NSEL Report Series
Report No. NSEL-005
December 2007

Multi-dimensional Mixed-mode Hybrid Simulation Control and Applications

Narutoshi Nakata

Billie F. Spencer, Jr.

Amr S. Elnashai

NEWMARK STRUCTURAL ENGINEERING LABORATORY

Department of Civil and Environmental Engineering
University of Illinois at Urbana-Champaign

UILU-ENG-2007-1805

ISSN: 1940-9826

The Newmark Structural Engineering Laboratory (NSEL) of the Department of Civil and Environmental Engineering at the University of Illinois at Urbana-Champaign has a long history of excellence in research and education that has contributed greatly to the state-of-the-art in civil engineering. Completed in 1967 and extended in 1971, the structural testing area of the laboratory has a versatile strong-floor/wall and a three-story clear height that can be used to carry out a wide range of tests of building materials, models, and structural systems. The laboratory is named for Dr. Nathan M. Newmark, an internationally known educator and engineer, who was the Head of the Department of Civil Engineering at the University of Illinois [1956-73] and the Chair of the Digital Computing Laboratory [1947-57]. He developed simple, yet powerful and widely used, methods for analyzing complex structures and assemblages subjected to a variety of static, dynamic, blast, and earthquake loadings. Dr. Newmark received numerous honors and awards for his achievements, including the prestigious National Medal of Science awarded in 1968 by President Lyndon B. Johnson. He was also one of the founding members of the National Academy of Engineering.

Contact:
Prof. B.F. Spencer, Jr.
Director, Newmark Structural Engineering Laboratory
2213 NCEL, MC-250
205 North Mathews Ave.
Urbana, IL 61801
Telephone (217) 333-8630
E-mail: bfs@uiuc.edu

This technical report is based on the first author's doctoral dissertation under the same title which was completed in July 2007. The second and third authors of the report served as dissertation advisors for this work.

Financial support for this research was provided in part by the Mid-America Earthquake Center under National Science Foundation (NSF) grant EEC-9701785 and through the George E. Brown, Jr. Network for Earthquake Engineering Simulation (NEES) Program under NSF grant CMS-0217325. This support is gratefully acknowledged.

The cover photographs are used with permission. The Trans-Alaska Pipeline photograph was provided by Terra Galleria Photography (http://www.terragalleria.com/).

Abstract

Hybrid simulation is an effective method for the assessment of the seismic response of structures, combining laboratory testing, computational simulation, and numerical time-step integration of the equations of motion. While this approach has been used for evaluation of the seismic performance of a variety of structures, applications to date have been limited to planar loading and to relatively simple structural systems. In contrast, actions during strong earthquakes are three-dimensional and continuously varying and modern structures can be extremely complex. Further development is required to evaluate the seismic performance of structures, in particular complex structural systems, under realistic loading.

The objectives of this study are to develop a multi-dimensional hybrid simulation framework using a six-actuator, self-reaction, loading system, referred to as the Load and Boundary Condition Box (LBCB), for evaluation of the seismic performance of large and complex structural systems and to demonstrate the framework through three-dimensional hybrid simulation of a skew reinforced concrete (RC) bridge. This report contains results for four major tasks that are intended to provide enhanced seismic performance evaluation using advance experimental techniques.

The first task is the calibration of the LBCB in global Cartesian coordinates. Due to imperfections in system geometry (e.g., the actuator configuration), errors in the Cartesian measurements are generated from errors in the transformation from actuator to Cartesian space. A sensitivity-based external calibration method is developed to improve the precision by which the LBCB can be controlled in Cartesian space.

The second task is to develop, implement, and experimentally verify a mixed load and displacement (mixed-mode) control strategy. A mixed-mode control capability is required, for example, to simulate gravity loads in the axial direction and displacements in the other directions on structural members such as RC piers in hybrid simulation. However, because of the nonlinear nature of the coordinate transformation, mixed-mode control for a multi-axial loading system is still a major theoretical and practical challenge. The mixed-mode control strategy developed in this study accounts for the spatial interaction of actuators both in displacement and load, and the stiffness variation of the structure specimen.

The third task is to integrate the control system and its capabilities into a hybrid simulation framework. The framework needs to also incorporate robust network communication for hybrid simulation.

The fourth and final task is to validate the hybrid simulation framework through the study of the three-dimensional behavior of a skew RC bridge. First, extensive analyses of skew bridges are conducted to prepare for the hybrid simulation. Subsequently, a small-scale RC pier is experimentally tested as a physical substructure, while the rest of the piers and the bridge deck are analyzed using a finite element model. The mixed-mode control capability is employed to impose on the RC pier simultaneous gravity loads in the axial direction and earthquake-induced displacements in the other directions. The experimental results show that the multi-dimensional hybrid simulation with versatile six degrees-of-freedom loading capability is a promising approach that provides a reliable means for evaluation of the seismic performance of large and complex structural systems.

Contents

Page

INTRODUCTION

1.1 Background

Severe earthquakes have repeatedly demonstrated the vulnerability of civil infrastructure systems including buildings, bridges, life-line structures, etc. Damage to these infrastructures causes not only loss of human lives and disruption of lifelines, but also long-term impact on the local, regional, and sometime national and international economies. For example, the 1994 Northridge earthquake showed various types of damage that could be inflicted on any heavily populated urban area; a total of 58 people were killed; many two and three-story apartment and several large commercial buildings collapsed; seven major highway bridges and eight large public parking structures suffered severe damage; water mains broke and caused flooding; gas lines broke and started fires; the entire Los Angeles area lost electric power. Economic loss was estimated at approximately $40 billion (Todd et al. 1994).

Mitigation of seismic risk is one of the challenges that our modern societies are facing from not only engineering but also social, economical, and political aspects. To reduce seismic risk, substantial preparedness and proper actions need to be taken before and after an event: improving earthquake-resistance of structures, education and training of evacuation plan, risk management and disaster contingency planning, recovery and reconstruction measurements, etc. Design codes and guidelines for structures have significantly improved in the last 30 years, reflecting lessons learned from past earthquakes. However, among these, improving the earthquake-resistance of structures is still the most important task because it is the primary means that can directly reduce the effects of such disasters.

Recent development of multi-performance seismic assessment and design approaches has emphasized limit state concepts for existing and new structures. Unlike a single design level approach in load and resistance factor design, structures are designed to meet multiple target performance (functional) levels for different ground motion levels. Therefore, the owners' or clients' opinions can be well incorporated in terms of performance, safety, and costs into the design process. Performance-based seismic engineering provides flexibility in the assessment and design processes, better performance prediction for earthquake events, and quantitative judgment based on the acceptance criteria. One of the keys in the performance-based seismic design is an evaluation of the seismic performance of structures. Accuracy in seismic performance evaluation significantly affects overall design qualities and outcomes. The need for seismic performance evaluation has increased not only for improving our understanding of structures, refining new analytical tools, and predicting seismic damage, but also for the performance-based seismic design procedure.

1.2 Statement of the Problem

The seismic performance of structures under strong earthquakes is a highly coupled cause-effect problem. Understanding the cause (action or demand) and its effect (behavior or capacity) is a key for evaluation of the seismic performance. Actions on structures during strong earthquakes are generally multi-dimensional and continuously varying due to the time-dependent nature of the input ground motion as well as the continuous change of the system stiffness. Assessment of such multi-dimensionally varying actions on the structural components is still a challenging problem, especially for critical components of large and complex structural systems. Furthermore, even with the proper assessment of seismic action, associated behavior of the component is difficult to obtain. For example, under significant influence of gravity loads, vertical structural components (e.g., bridge pier, building column, etc.) exhibit behavior to combined flexural, shear, and torsional actions that is distinct from those under no axial loads. There are not only the second order ($p\text{-}\Delta$) effects, but also response interactions such that shear capacity is influenced by axial, flexural, and torsional capacities, and vice versa. Analytical models are often ill-suited to capture such complex behavior; if the actions are multi-dimensional and extreme, analytical solutions sometimes may not converge. Additional experimental studies are, therefore, required to increase the level of understanding, to build better analytical models, and to ultimately enhance the safety of the structural systems.

Hybrid simulation is an effective experimental method that combines numerical time-step integration of equations of motion with laboratory testing. Utilizing the substructure technique, hybrid simulation allows for large-scale component testing in a system level simulation accounting for earthquake ground motion as well as its system response. It has been used for performance assessment of building and bridge structures. Although the method is not limited to simple structures, hybrid simulations to date are limited to only one- or two-dimensional applications with a small number of degrees-of-freedom (DOF). In fact, hybrid simulations that account for three-dimensional response of structures and 6DOF load and boundary conditions in testing have not been reported to date. To evaluate the seismic performance of a large and complex structural system and its components, hybrid simulation needs to be expanded to three-dimensions while accounting for all 6DOF load and boundary conditions and dealing with large interfaces between the various components.

1.3 Objectives of the Study

A state-of-the-art, six-actuator, self-reacting, loading system, referred to as the Load and Boundary Condition Box (LBCB), has been designed and assembled for evaluation of structural performance under 6DOF loading at the University of Illinois at Urbana-Champaign (UIUC). A facility at UIUC, including three LBCBs, a reaction wall, a strong floor, computer resources, software, etc., provides a complete testing and simulation environment that is capable of handling various types of applications for assessment of

structural and geotechnical systems. However, a general framework with versatile control strategies is required to fully utilize the LBCB in hybrid simulation.

The objectives of this study are to develop a multi-dimensional hybrid simulation framework using the LBCB and its versatile 6DOF loading capability for evaluation of the seismic performance of complex structural systems and to demonstrate the framework through three-dimensional hybrid simulation of a skew reinforced concrete (RC) bridge. The research herein is comprised of four main tasks that are intended to overcome the associated challenges to fulfill the objectives of this study.

The first task is to develop a calibration method for the multi-axial loading system in global Cartesian coordinates. Due to the nonlinear nature of the coordinate transformation and the difficulty to define a precise initial zero position for the platform in global coordinates, evaluation and calibration of multi-axial loading systems are challenging endeavors. A systematic calibration method is required to improve accuracy in all 6DOFs.

The second task is to develop, implement, and verify a mixed load and displacement (mixed-mode) control strategy that is required for the framework. In many cases, hybrid simulation requires mixed-mode control (e.g., to impose the gravity loads in the vertical direction while simultaneously applying the earthquake-induced displacements in the other directions). If a loading system exhibits coupling between actuator and Cartesian coordinates (e.g., as in the LBCB), mixed-mode control cannot be achieved with a combination of independent displacement-controlled and force-controlled actuators. Therefore, a mixed-mode control algorithm accounting for spatial coupling is required to allow accurate structural testing using multi-axis loading systems.

The third task is to integrate the LBCB loading system into a hybrid simulation framework. The framework needs to incorporate not only various control strategies and data processing and archiving features, but also network communication capability for hybrid simulation. The NEESgrid Tele-operation Control Protocol (NTCP; Pearlman et al. 2004) is implemented into the hybrid simulation framework as the network communication protocol.

The fourth and final task is to demonstrate the efficacy of the hybrid simulation framework through the study of the three-dimensional behavior of a skew RC bridge. First, extensive analyses of skew bridges are conducted to preparation for the hybrid simulation. These analytical results are used to determine which hybrid simulation should be performed. Subsequently, a small-scale RC pier is experimentally tested as a physical substructure, while the rest of the piers and the bridge deck are analyzed using a finite element model. The application example presented in this report is the first ever three-dimensional hybrid simulation controlling 6DOF at the interface between components.

1.4 Organization of the Report

This report is organized in the following nine chapters.

Chapter 1 provides general motivation and an overview of the report. Chapter 2 reviews previous studies and the fundamentals of hybrid simulation. Following a brief

review of experimental methods for seismic performance evaluation of structures, an overview of hybrid simulation is presented including the current study.

The experimental facility for hybrid simulation at UIUC is introduced in Chapter 3. Details of the LBCB loading system are described, including its features, capacity, hardware architecture, etc.

Chapter 4 proposes a calibration method for multi-axial loading systems. Following a description of actuator kinematics and errors induced by inaccuracies in the initial parameters, a sensitivity-based external calibration method and its experimental verification are presented.

Chapter 5 discusses a mixed load and displacement control strategy. The proposed mixed load and displacement control algorithm is based on the load-displacement conversion using a stiffness Jacobian. The estimation of the stiffness Jacobian, iterative algorithm, and its implementation are presented. Experimental verifications conducted for different specimens and loadings are also examined.

An analytical study of skew bridges is performed in this report, as described in Chapter 6. After a description of a reference skew bridge, the natural frequencies and mode shapes of the reference bridge are investigated using finite element model. The purpose of the modal analysis is to evaluate the effect of the skew angle on the global bridge behavior and RC piers.

Chapter 7 presents nonlinear and inelastic analysis of the reference skew bridge. Material and geometrical nonlinearities as well as local effects such as pounding are considered. Pushover analysis is performed to evaluate the force-displacement relationships of the RC piers. Moreover, parametric nonlinear dynamic analysis is carried out with the aim of investigating the effect of the skew angle on the seismic response of the bridge and its components.

A verification case of a three-dimensional hybrid simulation of a skew RC bridge using the LBCB is described in Chapter 8. Test results, as well as details of the system configuration and the simulation environment, are presented. The effectiveness of multi-dimensional hybrid simulation using the LBCB is discussed.

Finally, Chapter 9 summarizes the observations and conclusions of this report. The remaining challenges and future studies are also presented in this last chapter.

OVERVIEW OF HYBRID SIMULATION

2.1 Seismic Performance Evaluation Tools

Structural damage is a major contributing factor to the casualties and economic loss in earthquakes. Prediction and reduction of potential future earthquake damage are essential challenges for earthquake engineers and cannot be improved without reliable means for seismic performance evaluation of structures. There are three major tools for seismic performance evaluation: field observation, analysis, and testing. Lessons from past earthquakes have indicated that all available tools must be interactively deployed to improve seismic performance evaluation and to mitigate seismic hazards (Elnashai 2006).

Field observations are the most realistic way to evaluate the effects of earthquakes. Detailed and comprehensive data have been collected and compiled after major earthquakes in the last 40 years (Elnashai et al. 2000; Kawashima et al. 1998; Jennings 1971; Todd et al. 1994). Field observations are also important sources that help earthquake engineers identify problems and assess the outcome of efforts in structural design and retrofitting. However, due to the uniqueness of each data set (e.g., structural type, material properties, age, foundation, site condition, etc.), its use is limited to the investigation of failure mechanisms in damaged structures and verification of analysis and testing. Because none of the structures have all the same properties and conditions with the ones examined on site, field observation data are of limited value for the prediction of damage and the performance evaluation of existing and new structures in a reliability-based context.

Analysis is the most powerful tool in the sense that behavior of a large number of structures can be easily studied at relatively low cost. In particular, it is quite effective for iterative design processes, as well as a quantitative assessment of the influence of parameters under investigation. For seismic performance evaluation, pushover analysis and dynamic analysis are the most widely used analytical methods. Material inelasticity and geometric nonlinearity are normally incorporated in those analyses. With recent advancements in constitutive modeling of materials, numerical techniques, and computer technology, analytical capabilities have significantly progressed to the extent where nonlinear dynamic analysis of large three-dimensional structural models can be run on a personal computer in a short time (Elnashai 2006). However, analysis is not without limitations. Analytical models are often ill-suited to capture the complex behavior of local structural components under extreme loading (i.e., severe damage and failure). In addition, analytical results can vary significantly depending on the modeling, method, and input. Interpretation of analytical results is sometimes not straightforward; hence, analysis needs to be combined with in-depth understanding and experience to make it effective.

Compared to the two tools listed above, experimental testing is arguably the most effective manner for prediction of structural response and performance evaluation. Unlike field observations, which are obtained from regions selected by the earthquake, not the earthquake engineer, testing allows control of the details of the system under investigation. Additionally, testing does not require modeling assumption if tested at prototype scale. Because cause (input) and effect (response) can be measured during the test, the behavior of the structural components or systems can be well understood from measured data. Test data make it possible to assess the variation in materials and geometric effect, such as yielding, hardening, pinching, etc. In addition, testing allows monitoring of damage progression during the loading as well as damage state at post-loading. Both quantitative and qualitative data are essential for seismic performance evaluation and retrofitting scheme development for structures. However, similar to other tools, testing also has limitations. In general, it is not possible to reproduce complete on-site conditions in terms of size, boundary conditions, foundation, soil conditions, etc. because of the limited space, cost, and capacity of experimental equipment. To overcome some of the limitations in experimental testing, numerous methods and techniques have been developed to improve the seismic performance evaluation of structures.

In the following section, experimental approaches for seismic performance evaluation are further discussed.

2.2 Experimental Approaches

There are three major experimental methods widely used for the seismic performance evaluation of structures: shaking table, quasi-static, and hybrid (pseudo-dynamic) tests. The advantages and disadvantages of these methods are discussed below, with focus being placed on their effectiveness for seismic performance evaluation of large and complex structural systems.

Shaking table tests are a direct approach for the evaluation of seismic performance of structures. Because dynamic effects are accounted for in loading, shaking table tests provide more realistic response in time-scale than any other approach. However, shaking table tests also have drawbacks. In general, shaking table facilities are limited in dimension, payload, degrees-of-freedom (DOF), and dynamic capacity. Therefore, reduced scale or partial models of the structure are usually employed. One of the difficulties in dynamic tests with reduced scale specimens is a fulfillment of dynamic similitude; either additional mass or compression of time-axis, or a combination of both is needed. Shaking table tests with partial models can suffer from difficulties in the interpretation of the effect of boundary conditions that are neglected in the test. Recently, the E-defense facility in Japan (Ohtani et al. 2002) has constructed the world largest 15 m x 20 m shaking table. It has significantly expanded capabilities associated with scale in shaking table testing. However, even with this shaking table, horizontally extended structures such as bridges are still too large to test at large-scale. Needless to say, operational costs for such a large dynamic testing facility are problematic. Therefore, shaking table tests of large and complex structural systems are often not possible.

The quasi-static test method employs a slow-loading scheme with predetermined input histories in either displacement or force control, or combination thereof. Input loadings are usually monotonic or cyclic. Quasi-static testing has several advantages over the shaking table test. Quasi-static loading is well-suited method for the evaluation of important characteristics of structures such as yielding, limit state, ductility, etc. Because dynamic capabilities are not required in the loading system, the quasi-static test can be carried out at large scale. In addition, the slow loading, with the possibility to pause, makes it possible to carefully monitor the propagation of cracks and the evolution of damage. On the other hand, because input ground motion and the response of the structure are not taken into account, test results do not directly represent seismic behavior of the structure.

Hybrid simulation is an alternative approach to shaking table and quasi-static tests for understanding the dynamic response of structural systems, combining numerical time-step integration and experimental testing. Because critical reaction forces are experimentally evaluated, simulation results provide more accurate response of the structure than those in numerical analysis. Since its initial development (Hakuno et al. 1969, 1972; Takanashi et al. 1975), hybrid simulation has been used extensively for the seismic assessment of structures (Molina et al. 1999; Seible et al. 1996). One of the key features of hybrid simulation is substructuring, which allows modeling of an entire structural system as a combination of experimental and analytical substructures (Dermitzakis and Mahin 1985; see Figure 2.1).

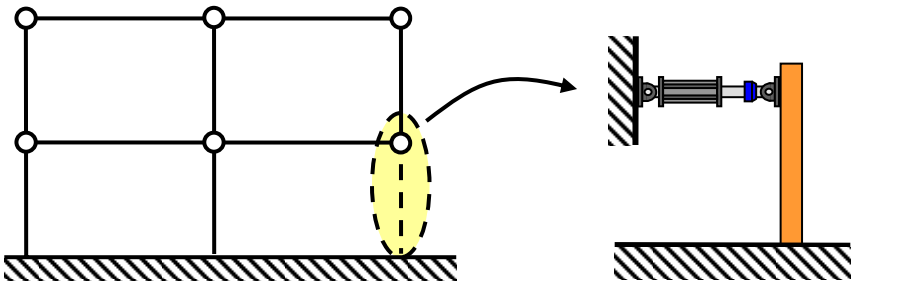

Figure 2.1. Illustration of substructure technique.

The substructure technique makes it possible to experimentally evaluate only the components that are difficult to model, while well-understood components are modeled analytically. Therefore, modeling efficiency can be significantly improved in terms of scale and cost. If experimental substructures are not highly dependent on the loading rate, hybrid simulation can be carried out using quasi-static loading facilities, which allows for testing at large scale (Chen et al. 2003). Compared to quasi-static loading tests where the input loading on the structural components is predetermined, hybrid simulation can be seen as a sophisticated structural component test that applies seismic loading in a system-

level simulation. However, there are also limitations in hybrid simulation. For example, hybrid simulation is not suitable for structures that are difficult to discretize such as dams (Shing et al. 1996). Although efforts have been made towards real-time testing in hybrid simulation, application to highly rate-dependent structures is still limited to quite simple models.

As briefly described in this section, each testing approach has advantages and disadvantages. A testing method must be carefully selected based on the purpose of the test, as well as the size and type of the structure of interest. Judging from the features of the three methods, hybrid simulation is the most attractive method for seismic performance evaluation of a significant class of large and complex structural systems. Therefore, hybrid simulation is further considered in this study.

2.3 Hybrid Simulation Methodology

2.3.1 Approach

The fundamental assumption in hybrid simulation is that the dynamic response of a structure can be represented by a discrete-parameter system with a finite number of DOF. The governing equations of motion for such an idealized model can be written as follows:

$$\mathbf{M}\ddot{\mathbf{x}}(t) + \mathbf{C}\dot{\mathbf{x}}(t) + \mathbf{r}(\mathbf{x}, \dot{\mathbf{x}}, t) = \mathbf{f}(t) \tag{2.1}$$

where $\ddot{\mathbf{x}}$, $\dot{\mathbf{x}}$, $\mathbf{x}$, and $\mathbf{f}$ are the acceleration, velocity, displacement, and input force vectors, respectively; $\mathbf{M}$ and $\mathbf{C}$ are the mass and damping matrices, and $\mathbf{r}$ is the reaction force vector. Equation (2.1) is discretized with respect to time t for numerical evaluation on digital computers:

$$\mathbf{M}\ddot{\mathbf{x}}_n + \mathbf{C}\dot{\mathbf{x}}_n + \mathbf{r}_n = \mathbf{f}_n \tag{2.2}$$

where a subscript n denotes that the variable is evaluated at the time-step n. The discrete-time equations of motion in Equation (2.2) are solved at each time-step incorporating the experimentally evaluated reaction force.

In general, each time-step in a hybrid simulation consists of four distinct phases (see Figure 2.2): (i) Calculation of the target displacement from the previous step responses or other system parameters depending on the integration algorithm; (ii) Imposition of the target displacement individually on both the experimental and analytical substructures; (iii) Collection of the measured and computational reaction forces from the experimental and analytical substructures; and (iv) Solution of the equations of motion at the current step using the combined reaction force term and the computationally calculated inertial, damping, and input force terms. Depending on the specific techniques employed for the integration algorithm, loading scheme, etc., the details in each phase can be different. Nevertheless, each of the four phases is essential in hybrid simulation, and repeated until the experiment is complete.

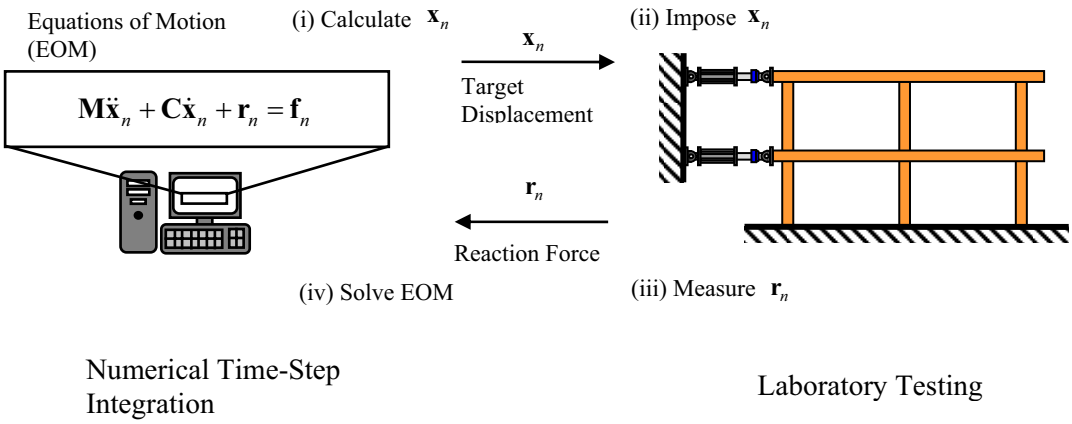

Figure 2.2. Schematics of hybrid simulation.

Although most hybrid simulations follow the basic philosophy above, applications vary widely; the model can be a single-DOF (SDOF) system or multi-dimensional geotechnical/structural system; the experimental substructures can be a single small-scale specimen or multiple full-scale specimens; the equipment can be comprised of one personal computer with a single actuator or integration of multiple geographically distributed facilities; the test duration can be of the same order as the earthquake input or last for several hours to days. These variations are mainly due to different scopes and objectives for the simulation, as well as techniques used in both the computational and experimental phases. Therefore, development of techniques and approaches must be carefully selected based on the objectives of the simulation.

2.3.2 Numerical time-step integration algorithms

The numerical time-step integration algorithm is one of the critical elements in hybrid simulation. A number of numerical integration algorithms have been developed for and deployed in hybrid simulation. Those algorithms can be categorized as either explicit or implicit scheme.

Explicit integration algorithms have been widely used because of their simplicity in implementation (Chang 2002; Shing and Mahin 1985). However, stability is conditional. The time step size needs to be selected based on the highest natural frequency of the model. Therefore, in general, explicit methods are effective for simple structural systems, but not applicable for large complex structural systems with relatively high natural frequencies.

Implicit integration algorithms have also been thoroughly evaluated for application to hybrid simulation (Shing et al. 1991; Thewalt and Mahin 1995). Implicit methods are generally superior to the explicit methods in terms of stability, accuracy, and error accumulation. However, the disadvantage of implicit methods is the requirement of

iteration to achieve equilibrium in the equations of motion. Nakashima et al. (1990) developed a non-iterative implicit algorithm using a predictor-corrector scheme, called the α-operator splitting (α-OS) method. The α-OS method provides unconditional stability for nonlinear structures with softening characteristics as well as simplicity in implementation. Because of those advantages, the α-OS method has been widely used for nonlinear structures (Pegon and Pinto 2000), and its properties have been well-studied (Combescure and Pegon 1997). The α-OS method will be adopted as the numerical integration algorithm for the studies in this report.

Alpha Operator-Splitting (α - OS) method

The formulation of equations of motion in the α method (Hilber et al. 1977) is modified from Equation (2.2) using a parameter α as follows:

$$\mathbf{M}\ddot{\mathbf{x}}_{n+1} + (1+\alpha)\mathbf{C}\dot{\mathbf{x}}_{n+1} - \alpha\mathbf{C}\dot{\mathbf{x}}_n + (1+\alpha)\mathbf{r}_{n+1} - \alpha\mathbf{r}_n = (1+\alpha)\mathbf{f}_{n+1} - \alpha\mathbf{f}_n \tag{2.3}$$

The parameter α represents the relative weight at the previous time-step for damping, stiffness, and input force terms.

Displacement and velocity at time-step n+1 can be formulated based on the integration approximation and further split into two terms: predictor and corrector.

$$\begin{aligned}\mathbf{x}_{n+1} &= \mathbf{x}_n + \Delta t\dot{\mathbf{x}}_n + \frac{\Delta t^2}{2}(1-2\beta)\ddot{\mathbf{x}}_n + \Delta t^2\beta\ddot{\mathbf{x}}_{n+1} \\ &= \tilde{\mathbf{x}}_{n+1} + \Delta t^2\beta\ddot{\mathbf{x}}_{n+1}\end{aligned} \tag{2.4}$$

$$\begin{aligned}\dot{\mathbf{x}}_{n+1} &= \dot{\mathbf{x}}_n + \Delta t(1-\gamma)\ddot{\mathbf{x}}_n + \Delta t\gamma\ddot{\mathbf{x}}_{n+1} \\ &= \tilde{\dot{\mathbf{x}}}_{n+1} + \Delta t\gamma\ddot{\mathbf{x}}_{n+1}\end{aligned} \tag{2.5}$$

where Δt is a time increment, and β and γ are the parameters of the algorithm, and selected using the parameter α.

$$\beta = (1-\alpha)^2/4 \tag{2.6}$$

$$\gamma = (1-2\alpha)/2 \tag{2.7}$$

If α satisfies the following criteria, the numerical algorithm is unconditionally stable.

$$-\frac{1}{3} \le \alpha \le 0 \tag{2.8}$$

When $\alpha = 0$, the numerical scheme becomes the well-known Newmark-β method.

The terms $\tilde{\mathbf{x}}_{n+1}$ and $\tilde{\dot{\mathbf{x}}}_{n+1}$, are called predictors and are written as follows:

$$\tilde{\mathbf{x}}_{n+1} = \mathbf{x}_n + \Delta t \dot{\mathbf{x}}_n + \frac{\Delta t^2}{2}\left(1-2\beta\right)\ddot{\mathbf{x}}_n \tag{2.9}$$

$$\tilde{\dot{\mathbf{x}}}_{n+1} = \dot{\mathbf{x}}_n + \Delta t\left(1-\gamma\right)\ddot{\mathbf{x}}_n \tag{2.10}$$

The predictor terms do not contain the responses at the current step n+1. Calculation of the predictor displacement in Equation (2.9) is the beginning of the process at each step in the α-OS method. Then, the predictor displacement $\tilde{\mathbf{x}}_{n+1}$ is treated as the target displacement, denoted here as $\tilde{\mathbf{x}}^{\mathrm{t}}_{n+1}$, that is imposed on the structure to obtain associated reaction force.

Following the execution of the target displacement $\tilde{\mathbf{x}}^{\mathrm{t}}_{n+1}$ by means of experimental loading system, the measured displacement $\tilde{\mathbf{x}}^{\mathrm{m}}_{n+1}$ and reaction force $\tilde{\mathbf{r}}^{\mathrm{m}}_{n+1}$ are obtained. Because of the nature of the loading and data acquisition systems, errors will exist to some extent (i.e., the measured displacement $\tilde{\mathbf{x}}^{\mathrm{m}}_{n+1}$ is not always equal to the target displacement $\tilde{\mathbf{x}}^{\mathrm{t}}_{n+1}$). Therefore, the reaction force at the predictor displacement $\tilde{\mathbf{x}}_{n+1}$ is approximated taking into account displacement error as follows:

$$\tilde{\mathbf{r}}_{n+1} \approx \tilde{\mathbf{r}}^{\mathrm{m}}_{n+1} - \mathbf{K}^{\mathrm{I}}\left(\tilde{\mathbf{x}}^{\mathrm{m}}_{n+1} - \tilde{\mathbf{x}}^{\mathrm{t}}_{n+1}\right) \tag{2.11}$$

where $\mathbf{K}^{\mathrm{I}}$ is the initial stiffness matrix of the structure. This error correction technique is called the I-modification (Nakashima and Kato 1987). If the tangent stiffness matrix is available, it can be used instead of the initial stiffness matrix.

Next, using $\tilde{\mathbf{r}}_{n+1}$ and $\tilde{\mathbf{x}}_{n+1}$ at the predictor step, and unknown displacement $\mathbf{x}_{n+1}$ at time-step n+1, the reaction force $\mathbf{r}_{n+1}$ is approximated in a manner similar to Equation (2.11).

$$\mathbf{r}_{n+1} \approx \tilde{\mathbf{r}}_{n+1} - \mathbf{K}^{\mathrm{I}}\left(\tilde{\mathbf{x}}_{n+1} - \mathbf{x}_{n+1}\right) \tag{2.12}$$

This process is called the corrector step, where the displacement and force relationship at time-step n+1 is obtained based on the experimental displacement and force in the predictor step.

Using Equations (2.4), (2.5), and (2.12), Equation (2.3) can be solved with respect to the acceleration $\ddot{\mathbf{x}}_{n+1}$ as follows:

$$\hat{\mathbf{M}}\ddot{\mathbf{x}}_{n+1} = \hat{\mathbf{f}}_{n+1} \tag{2.13}$$

where $\hat{\mathbf{M}}$ and $\hat{\mathbf{f}}_{n+1}$ are the equivalent mass matrix and equivalent input force vector, respectively, given by:

$$\hat{\mathbf{M}} = \mathbf{M} + \gamma\Delta t\left(1+\alpha\right)\mathbf{C} + \beta\Delta t^2\left(1+\alpha\right)\mathbf{K}^{\mathrm{I}} \tag{2.14}$$

$$\begin{aligned}\hat{\mathbf{f}}_{n+1} &= (1+\alpha)\mathbf{f}_{n+1} - \alpha\mathbf{f}_n + \alpha\tilde{\mathbf{r}}_n - (1+\alpha)\tilde{\mathbf{r}}_{n+1} \\ &\quad + \alpha\mathbf{C}\tilde{\dot{\mathbf{x}}}_n - (1+\alpha)\mathbf{C}\tilde{\dot{\mathbf{x}}}_{n+1} + \alpha\left(\gamma\Delta t\mathbf{C} + \beta\Delta t^2\mathbf{K}^{\mathrm{I}}\right)\ddot{\mathbf{x}}_n\end{aligned} \tag{2.15}$$

Once the acceleration $\ddot{\mathbf{x}}_{n+1}$ is obtained, the displacement $\mathbf{x}_{n+1}$ and velocity $\dot{\mathbf{x}}_{n+1}$ are calculated from Equations (2.4) and (2.5), respectively. These calculations are the end of the process at time-step $n+1$. After completion of the process at each time-step, the step number is incremented. The process is repeated until the simulation has finished.

Thus, the α-OS method is a non-iterative implicit method using a predictor-corrector scheme. With a proper parameter range for α, unconditional stability is guaranteed for structures with softening properties. Therefore, it is applicable for large and complex structural systems with nonlinear characteristics. Note that the α-OS method requires the initial stiffness matrix as a part of the initialization.

2.3.3 Loading rate and type

In physical testing, a target displacement is usually imposed on the experimental substructure using servo-controlled hydraulic actuators, and its reaction force is measured at every time-step. As previously mentioned, there are various experimental techniques and types for the execution and measurement processes. Among those, the loading rate is one of the important factors that influences both modeling and control accuracies, depending on the type of specimen and complexity of loading.

Traditional slow-rate, ramp-hold procedures allow for quasi-static actuators to be used in hybrid simulation, making tests of large-scale structural systems and components possible. Good control performance can be achieved in terms of accuracy even for very stiff test specimens. Because dynamic interaction of the actuators is assumed to be insignificant, synchronization of multiple actuators can be achieved with the least error and undesired motions during the ramp phase. Reaction forces are obtained by sampling and averaging during the holding phase where the actuators are held at the target command. Therefore, static reaction forces corresponding to the target displacement can be accurately obtained. However, the slow-rate, ramp-hold approach is limited to materials that are not highly rate-dependent, such as reinforced concrete (RC) and steel (Donea et al. 1996; i.e., $\mathbf{r}(\mathbf{x},\dot{\mathbf{x}},t) \cong \mathbf{r}(\mathbf{x})$). If test specimens under investigation are rate-dependent, such as isolation bearings and passive or semi-active dampers, slow-rate loading is not applicable. In addition, force-relaxation can also be a problem if the hold–period is too long. Slow-rate, ramp-hold procedures generally take more than 100 times longer than the actual simulation time.

To overcome the abovementioned pitfalls, continuous (Magonnete 2001; Mosqueda 2003) and real-time (Horiuchi et al. 1996; Nakashima et al. 1992) loading schemes have been developed and implemented. These techniques can reduce test duration, allow for rate-dependent materials to be tested, and avoid force relaxation. However, those techniques also have some limitations and challenges. The experimental components need to receive the target displacement at a deterministic rate to continuously move the actuators. Therefore, analytical models are limited to simple ones that can be performed

at a predetermined rate. In addition, continuous loading of multiple actuators is challenging in terms of accuracy and synchronization, especially for very stiff specimens. Real-time loading schemes are attractive for rate-dependent materials in hybrid simulation. However, due to the nature of the servo-actuator system, real-time control of actuator always has delays/lags, which introduce inherent errors. Therefore, in addition to the limitations and requirements for the continuous approach, actuator dynamics and its delay compensation need to be considered in real-time loading schemes. Current applications of real-time hybrid simulation are still limited to simple models that are intended for the development and verification of the testing scheme itself.

Thus, each loading scheme has both advantages and disadvantages. The loading scheme that should be selected depends on the type of material, size of specimen, and capacity of the equipment and hardware, etc. In this study, focus is placed on slow-rate, ramp-hold procedures.

2.3.4 Applications

Applications in hybrid simulation to date cover a wide range of structure and loading types. The type of applications and experimental setups are mainly dependent on the objective of the simulation that can be categorized as follows: building assessment, bridge assessment, and verification of method. In this section, those applications, experimental setups, and associated efforts are briefly reviewed focusing on the objective of the hybrid simulation.

Building assessment

Buildings are the primary application for hybrid simulation that are tested at large-scale. Seible et al. (1996) conducted a test of a full-scale, 5-story reinforced masonry building. The entire building is treated as a 5DOF system and tested using 10 actuators in a single, lateral direction. To overcome the displacement control error due to the actuator couplings resulting from the stiff nature of the multiple-DOF (MDOF) system, an iterative procedure incorporating external transducers and a scaling matrix was developed. The experimental results showed that their testing procedure allowed accurate simulation of the dynamic structural response of a stiff building under seismic loads. Molina et al. (1999) conducted a bi-directional hybrid simulation of a full-scale, 3-story building. In their test, each floor was subjected to two horizontal and one rotational displacements using four actuators; geometric nonlinearity is accounted for large displacements in the control process. Their test was successfully extended to bi-directional hybrid simulation of a full-scale building. Tsai et al. (2004) tested a full-scale 3-story, 3-bay concrete-filled steel tube (CFT) column and buckling restrained braced (BRB) composite frame in hybrid simulation. Their experimental results confirm that the global dynamic responses of the prototype CFT-BRB frame specimen can be satisfactorily predicted by analytical models. Other than those above, there are more hybrid simulations applied for building applications.

In general, for building applications, a large portion of the structure (e.g., frames, shear walls, or even entire buildings) is tested experimentally. Loadings are usually imposed at the floor level considering in-plane displacement.

Bridge assessment

In contrast with building applications, bridge applications typically experimentally test only a small portion of structure, such as piers or bearings. This assumption is because bridges are generally too large to test experimentally in the laboratory, and bridge damage under severe earthquake tends to be concentrated at the piers or surrounding connections. Pinto et al. (2004) carried out a hybrid simulation of a large-scale model of an existing six-pier bridge. In their simulation, two piers with different heights were experimentally tested in the laboratory under loading in lateral direction only, whereas the remaining four piers were modeled using 2D nonlinear fiber elements; the deck was modeled using 3D linear elements. The α-OS method and the ramp-hold procedure were used as the time-step integration algorithm and loading scheme, respectively. The experimental results confirmed that poor seismic behavior was experienced by bridges with limited displacement capacity. Nagata et al. (2005) conducted hybrid simulation of a bridge employing RC C-bent columns; the columns were tested under unilateral and bilateral excitations. The experimental results showed that the effect of the bilateral loading is significant on the performance of the C-bent column. There are several other bridge applications in hybrid simulation. Nevertheless, for bridge application using hybrid simulation, vertical components such as piers and bearings are usually tested experimentally; in most cases, only translational loadings are taken into account such as simple uni-lateral or bi-lateral loading with vertical gravity loading.

Method verification

Although hybrid simulation has been studied almost 40 years, major applications and efforts are still directed towards verification and demonstration of new methods and developments. Nakashima et al. (1999) presented a real-time hybrid simulation technique using an interpolation and extrapolation scheme. Seismic response of a MDOF base-isolated building was simulated where a rubber bearing was tested as an SDOF model using a single actuator. A series of tests demonstrated the effectiveness of the real-time hybrid simulation technique. Park et al. (2005) carried out a geographically distributed hybrid simulation at several institutions in Japan and Korea over the internet. The application structure was a base-isolated bridge with four continuous spans; the bridge was idealized as a 4DOF model in the longitudinal direction. Their test successfully demonstrated the feasibility of distributed hybrid simulation using the internet. Mosqueda (2003) conducted a geographically distributed continuous hybrid simulation using an event-driven scheme. The application was a simple two-story shear building where two identical small-scale cantilever columns were tested as an SDOF model by single actuators. Test results showed that the proposed system is effective for geographically distributed simulation in terms of accuracy, reliability, and network communication.

As briefly reviewed above, significant efforts have been allocated to the development of new methods for hybrid simulation. However, the majority of applications for verification were simple structural models with a limited number of DOF. Although hybrid simulation has been recognized as an effective tool for seismic evaluation of structural systems, available techniques have yet to be applied to realistic structural models, in terms of scale and complexity.

2.4 Network for Earthquake Engineering Simulation (NEES)

The National Science Foundation (NSF) created the George E. Brown, Jr. Network for Earthquake Engineering Simulation (NEES) to improve our understanding of earthquakes and their effects. The NEES is a national, shared-use experimental resource for advancing knowledge and technology to enhance the design and performance of the nation's civil and mechanical infrastructure when subjected to earthquake excitation and tsunami. The NEES is comprised of 15 experimental facilities and a network cyber-infrastructure that provide educators, students, practitioners, and the general public with a versatile earthquake engineering research and educational environment. Figure 2.3 shows the locations of the experimental facilities.

Figure 2.3. NEES equipment sites (Courtesy of NEES.org).

The facilities at the NEES equipment sites fall into the following five general categories:

1) Shaking table facilities:

   University of Nevada, Reno

University of California, San Diego

University of Buffalo, State University of New York

2) Tsunami wave basin facility:

   Oregon State University

3) Geotechnical centrifuge facilities:

   University of California, Davis

   Rensselaer Polytechnic Institute

4) Field experimentation and monitoring facilities:

   University of Texas at Austin

   University of California, Los Angeles

   University of California, Santa Barbara

5) Large-scale laboratory experimentation facilities:

   University of Minnesota

   University of Colorado at Boulder

   University of Illinois at Urbana-Champaign

   Lehigh University

   University of California, Berkeley

   Cornell University

Each site has unique testing capabilities that enable the evaluation of the seismic performance of structural and geotechnical systems in both conventional and innovative ways. Experimental facilities and resources are linked together via the NEES cyber-infrastructure that facilitates remote collaborations around the U.S. and even the world. The NEES cyber-infrastructure includes tools for the following items: Scheduled network and grid; data ingestion; data storage; collaboration; web; telepresence; data search and analysis; visualization; simulation.

Hybrid simulation is certainly one of the key experimental methods that the NEES is supporting. Large-scale experimental facilities in the NEES are intended to provide testing capabilities for collaborative simulation as well as to advance hybrid simulation test methods. Researchers involved in collaboration can benefit from the NEES by making maximum use of both facilities and cyber-infrastructure. Furthermore, with the NEES research environment, unprecedented comprehensive earthquake simulation can be scheduled, configured, and carried out in an efficient manner. Great advancements in hybrid simulation are also expected in terms of innovation, development, and application including multi-dimensional testing capabilities, real-time testing schemes, comprehensive simulation accounting for soil-structure interaction, etc. Advancement of

experimental methods will provide new ways of addressing earthquake engineering problems and bringing the earthquake engineering community to the next level.

The research presented in this study has been conducted as a part of the development of the NEES facility at UIUC to further advance multi-dimensional hybrid simulation capabilities.

2.5 Hybrid Simulation Framework

The main components of hybrid simulation are the experimental and analytical substructures and the time-step integration strategy. Each of these components can be executed on a single computer. However, in many cases, these components run on separate computers utilizing network communication for exchanging data. Because a digital servo-controller is usually site-specific, and various analysis programs are used for the analytical substructures, frameworks used for hybrid simulation tend to be simulation-specific; simulation-specific frameworks make it difficult to adopt and extend to other systems. Without a common framework, multi-site hybrid simulation utilizing different servo-controllers is much more difficult to perform because of the additional work for synchronization, collaboration, and configuration.

Recently, efforts have been made towards the development of generic hybrid simulation frameworks to support flexible configuration of substructures. UI-SimCor (Kwon et al. 2005) was developed at UIUC for multi-site distributed hybrid simulation. UI-SimCor supports the following communication protocols: (i) NTCP, (ii) raw TCP-IP, and (iii) NEESit's new secure NEES Hybrid Simulation Communications Protocol (NHCP). UI-SimCor provides for easy, flexible, and modular configuration of substructure components, including digital servo-controllers (see Figure 2.4). UI-SimCor supports multi-platform hybrid simulation where various analysis programs can be used for different substructures in a single simulation to improve modeling accuracy. Currently, the following analysis programs have been integrated and made available for simulation of the analytical components of complex structural-geotechnical systems: ZeusNL (Elnashai et al. 2002); OpenSees (Mazzoni et al. 2006); FedeasLab (Fillippou and Constantinides 2004); ABAQUS (ABAQUS, Inc. 2003); and VecTor2 (Vecchio and Wong 2003). Takahashi and Fenves (2006) developed an object-oriented software framework using the OpenSees platform. Their framework provides classes to configure various experimental setups, time-step integration algorithms, etc., in an abstract manner. The effort for development of hybrid simulation frameworks can be also seen internationally, e.g., Japan (Pan et al. 2006) and Taiwan (Wang et al. 2005).

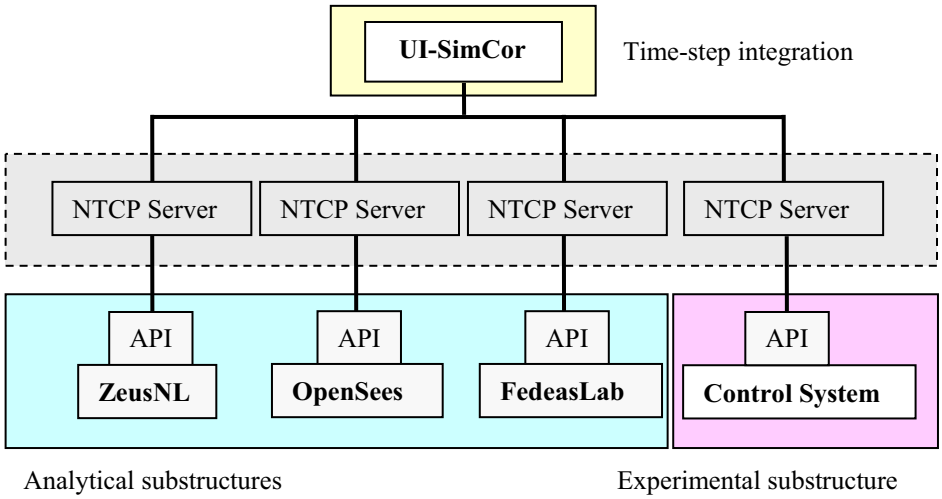

Figure 2.4. Configuration architecture in the UI-SimCor.

2.6 Summary

In the first part of this chapter, seismic performance evaluation tools were briefly reviewed, and the importance of experimental testing was addressed. Then, advantages and disadvantages of three experimental methods (i.e., shaking table, quasi-static, and hybrid tests) were summarized.

An overview of the hybrid simulation test method was given from several perspectives, such as numerical integration algorithm, loading rate, and applications. One of the advantages of hybrid simulation is to allow evaluation of the seismic performance of structural members under realistic loading in system level simulation. The efficiency and limitations of the hybrid simulation techniques were discussed with focus on the applications. An extensive review on applications indicated that much more development is required to utilize it for seismic performance evaluation. Those developments include multi-dimensional MDOF scheme, real-time loading scheme, etc.

The NEES, supported by the NSF, provides large-scale experimental facilities and cyber-infrastructure. Under the NEES, hybrid simulation can be further advanced in terms of innovation, development, and application. Development of the multi-dimensional MDOF hybrid simulation testing capability at the University of Illinois at Urbana-Champaign is well-suited for the current needs in earthquake engineering community.

EXPERIMENTAL FACILITIES FOR HYBRID SIMULATION

3.1 Introduction

The Multi-Axial Full-scale Sub-Structuring Testing and Simulation (MUST-SIM) facility at UIUC is one of the 15 equipment sites in the NSF's George E. Brown Jr. Network for Earthquake Engineering Simulation (NEES). The MUST-SIM facility is designed for large-scale testing of structural systems and components. One of the unique features of the MUST-SIM facility is a versatile six-degrees-of-freedom (6DOF) loading capability provided by a state-of-the-art, six-actuator, self-reaction loading system referred to as the Load and Boundary Condition Box (LBCB). The LBCBs, reaction wall, and strong floor laboratory enable complex testing configurations using multiple loading points on the experimental specimen. In addition, the MUST-SIM facility has a small-scale laboratory that contains $1/5^{th}$-scale LBCBs, reaction wall, and strong floor; this facility can be used for verification of testing methods and control algorithms and education of new users. Utilizing the NEES cyber-infrastructure, the MUST-SIM facility can be linked to the other facilities and resources, and used for geographically distributed hybrid simulation.

Figure 3.1 provides a schematic view of the MUST-SIM facility. The main components are the reaction wall, the strong floor, the LBCBs, the hydraulic power supply, the analog and digital controllers, and test specimen. For hybrid simulation, a personal computer should be added as a coordinator to exchange target and measured data with the digital controller.

In this chapter, a detailed description of the sites' experimental equipment is presented. Following the description of the reaction wall and strong floor, the LBCB and its control systems are provided. Then, the Krypton system that is used as an external measurement system of the LBCB is briefly introduced.

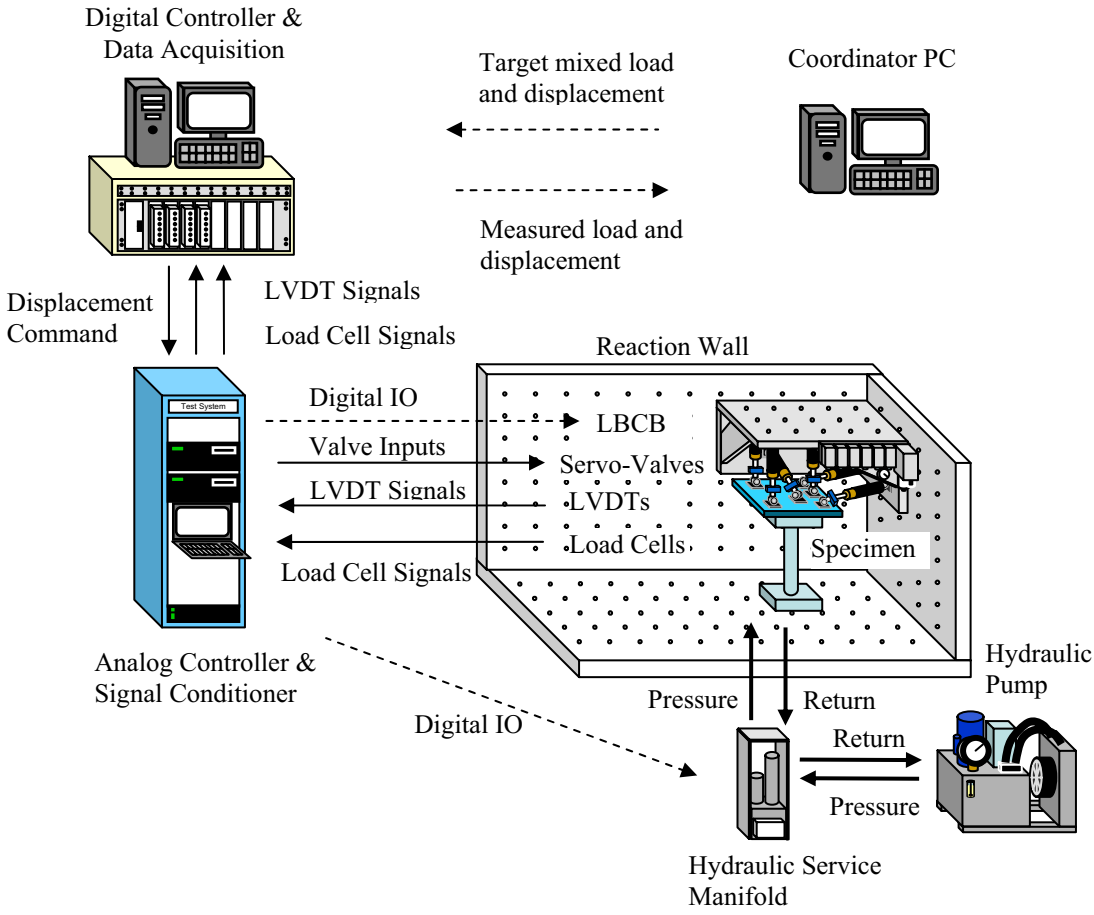

Figure 3.1. Schematic diagram of the testing system.

3.2 Reaction Wall and Strong Floor

An L-shaped reaction wall was constructed for use with the full-scale LBCBs in the Newmark Civil Engineering Laboratory at UIUC. The wall is made of 380 cubic yards of self-consolidating concrete with a total weight of 750 tons. The strong floor, with a size of 15 m × 40 m, for the MUST-SIM facility is a part of the Newmark Structural Engineering Laboratory. The reaction wall is post-tensioned to the strong floor by 81 ϕ 63.5mm high-strength rods with a total downward force of 2.2×10^5 kN. Figure 3.2 (a) shows photo of the full-scale reaction wall and the strong floor. The dimensions of the reaction wall are 15.2 m x 8.53 m x 9.14 m x 1.5 m (length x width x height x thickness). The reaction wall and strong floor have 76 mm-diameter tie-down holes on a 0.457 m and 0.914 m grid, respectively, to permit the modular installation of the loading equipments.

Three cranes with capacity of 40, 20, and 10 tons are equipped in the Newmark Laboratory. Moving and mounting the LBCBs as well as locating test specimens can be done using those cranes by machine shop personnel.

A 1/5th-scale reaction wall and strong floor of the full-scale one is designed for the small-scale loading equipments, and located at the NEES user studio in the Newmark Laboratory. Figure 3.2 (b) shows photo of the small-scale reaction wall and the strong floor. The small-wall and floor are made of aluminum with a waffle panel design on the back. A 1.5-ton capacity crane is available in the 1/5th-scale laboratory. Operation of the small-crane is allowed for trained students to configure their testing setups.

(a) Photo of full-scale facility

(b) Photo of 1/5th-scale facility

Figure 3.2. Reaction walls and floors at MUST-SIM facility.

3.3 Six-Actuator Self-Reaction Loading Systems

3.3.1 General description

The LBCBs are self-reaction loading systems consisting of six actuators, a reaction box, and a loading platform. The LBCBs are designed for quasi-static and hybrid simulation with 6DOF control capability. Figure 3.3 shows photos of the full- and 1/5th-scale LBCBs. The size of the full-scale LBCB is 4.0 m x 2.3 m x 2.0 m, and the weight is approximately 35 tons. Both LBCBs are servo-hydraulic controlled systems. Each actuator is equipped with a servo-valve, an embedded displacement transducer, and an in-line load cell for control and measurement. The 1/5th-scale LBCB is a miniature version of the full-scale LBCB. Other than the size, it has all the same features and control capabilities; it can be used for developing and debugging new control algorithms and testing concepts.

(a) Full-scale Load and Boundary Condition Box

(b) 1/5th-scale Load and Boundary Condition Box

Figure 3.3. Load and Boundary Condition Boxes.

Unlike traditional experimental equipment, the LBCB requires neither actuator assembly, nor actuator support frames. The LBCB can be attached directly to the reaction wall and strong floor in arbitrary location and orientation. Thus, the LBCB provides for flexible and modular testing configurations. Three LBCB units are available in both the full- and 1/5th-scales facilities. Use of multiple LBCBs allows for complex testing configuration such as MDOF multiple loading points testing, which is difficult to configure in the traditional loading systems. Figure 3.4 shows possible applications using the LBCBs. In addition to the flexibility and modularity in configuration, the LBCB provides high level of digital control software that incorporates various control algorithms and coordinate transformations. Therefore, regardless of the test configuration, users can utilize the LBCB software for their testing without redesigning the control system. Development of the control software as well as algorithms and its implementation is a part of the study in this report.

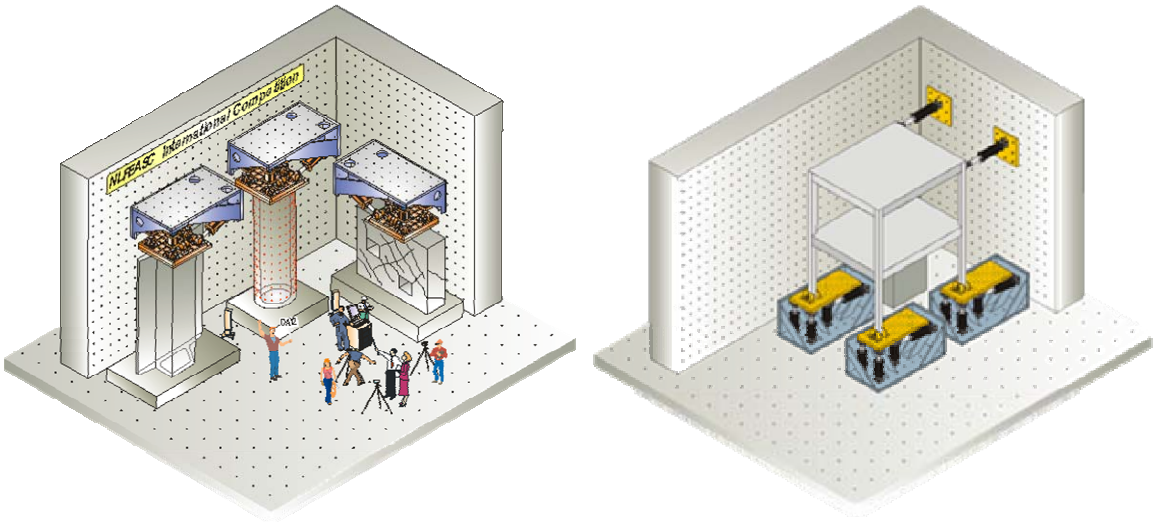

Figure 3.4. Possible applications using LBCBs.

3.3.2 Actuators, instrumentations, and hydraulic power supplies

The actuators for both the full- and 1/5th-scale LBCBs are manufactured by Shore Western, Inc. Figure 3.5 shows actuators for the full- and 1/5th-scale LBCBs. There are two different sizes of actuators assembled in each LBCB. In the full-scale LBCB, the two lateral actuators have a 20-inch stroke, while the others actuators have a 10-inch stroke. All actuators are connected to the reaction box and the loading platform with low-friction, swivel pin joints.

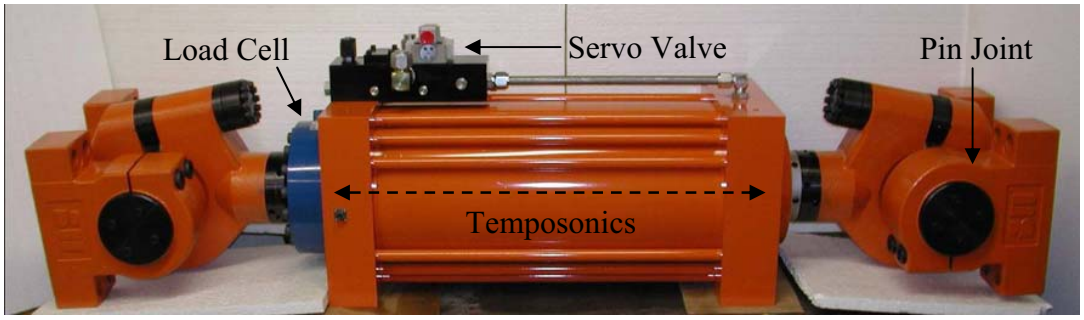

(a) Actuator in full-scale LBCB

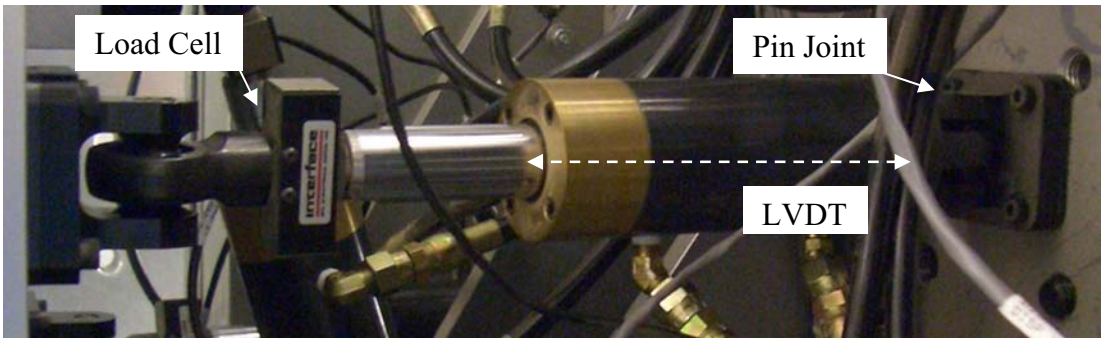

(b) Actuator in 1/5th-scale LBCB

Figure 3.5. Actuators in LBCB.

Each actuator is instrumented with a servo-valve, an embedded displacement transducer, and an in-line load cell. Two-stage electro-hydraulic servo-valves manufactured by Moog, Inc. are used for the actuator control: G761 series for the full-scale LBCB and G631 series for the 1/5th-scale LBCB. Temposonics G-Series position sensors manufactured by MTS are used for displacement measurement of the full-scale LBCB actuator: 10-inch stroke for longer actuators and 5-inch stroke for shorter actuators. Linear variable differential transformer (LVDT) manufactured by Trans-Tek, Inc. are used for displacement measurement of 1/5th-scale LBCB actuators: 4-inch stroke for longer actuators and 2-inch stroke for shorter actuators. Load cells manufactured by Interface, Inc. are used for force measurement: 1244CDL series for the full-scale LBCB and SML-1000 series for 1/5th-scale LBCB.

The hydraulic power supplier (HPS) is dedicated to the full-scale LBCBs. The HPS has two pumps, each with a capacity of 100 gallon per minutes (gpm) at 5000 psi. The 1/5th-scale facility has a dedicated HPS with a capacity of 10 gpm at 3000 psi. Each LBCB has a hydraulic service manifold that contains a hydraulic accumulator, filter, and solenoid switch for low- and high-pressure adjustment. The hydraulic accumulator helps to eliminate pressure spikes from the HPS, and the filter removes contaminants in the

hydraulic oil. For the full-scale LBCB, a lock-valve is installed for each actuator between accumulator and servo-valve, which regulates the hydraulic flow for initiating and terminating the operation as well as for emergency situations. The lock-valves and solenoids are controlled from the analog controller described in Section 3.4.1

3.3.3 Definition of the global Cartesian coordinates

The global coordinates in the LBCB follow the standard right-handed Cartesian coordinates. Figure 3.6 shows the Cartesian coordinates as well as the actuator labeling convention. The *x*-axis in the global coordinates is defined in the horizontal direction in the long-axis of the LBCB. The two actuators with principal directions in the *x*-axis are named X1 and X2 actuators. The *y*-axis is defined in the other horizontal direction orthogonal to the *x*-axis. The actuator with a principal direction in the *y*-axis is named Y1 actuator. Similarly, the *z*-axis is defined in the vertical direction, and the three actuators with principal directions in the *z*-axis are named Z1, Z2, and Z3 actuators.

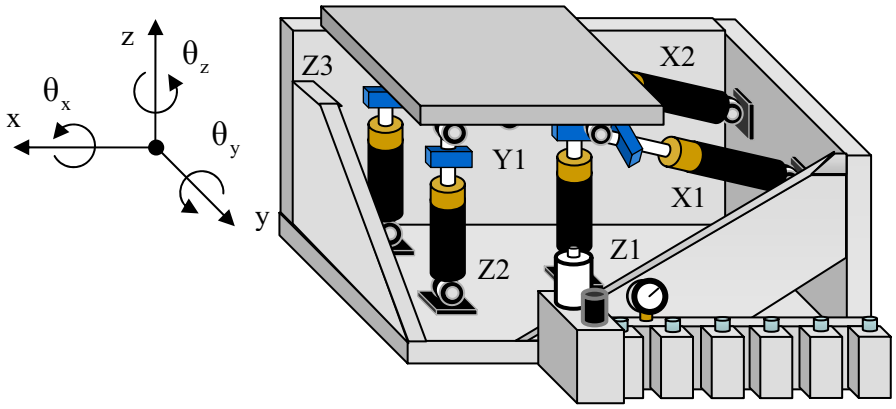

Figure 3.6. Global Cartesian and actuator coordinates of the LBCB.

From the control standpoint, the LBCB is a coupled multi-axial loading system [i.e., relationship between the actuator coordinates (i.e., actuator stroke and force) and the Cartesian coordinates at the loading platform is coupled in nonlinear manner]. Therefore, proper coordinate transformation is required for both control and measurement processes.

3.3.4 Displacement and load capacities

Displacement and load capacities are important system specifications in a loading system. Capacities of the LBCB in global Cartesian coordinates are governed by the area of the piston and the stroke of the actuator. The cross-coupling between Cartesian and actuator coordinates dictates that the range in one axis is highly dependent on the coordinates in other axes. For example, if the lateral displacement in the *x*-axis is held at zero, the rotational displacement in the *z*-axis has the full range of 16 degrees. However, if the lateral displacement in the *x*-axis is close to its limit, there is no stroke left in the X1 and X2 actuators for rotational displacement in the *z*-axis. Similar dependency among multiple axes can be seen in force and moment capacities. In other words, the displacement and load capacities of the LBCBs cannot be uniquely specified. A capacity can be specified only for a single axis when the other axes are fixed.

Table 3.1 lists nominal displacement and load capacities for the full- and 1/5th-scale LBCBs in global Cartesian coordinates. The nominal capacity here is defined with respect to the Cartesian coordinates being zero (except the axis of interest). The zero position in Cartesian coordinates is defined as the nominal platform position where all the actuator strokes are zero. For example, the lateral displacement capacity in the *x*-axis of the full-scale LBCB is ± 254.0mm when other axes are held at zero. Note that none of the two capacity limits can be hit at the same time.

Table 3.1. Specifications of the full- and 1/5th-scale LBCBs.

	Type	Axis	Full-scale	1/5th-scale
Displacement	Lateral (mm)	x	± 254.0	± 50.8
		y	± 127.0	± 25.4
		z	± 127.0	± 25.4
	Rotational (degree)	θ_x	± 16.0	± 16.0
		θ_y	± 11.8	± 12.0
		θ_z	± 16.0	± 16.0
Load	Force (kN)	F_x	± 2402	± 8.9
		F_y	± 1201	± 4.5
		F_z	± 3603	± 12.3
	Moment (kN*m)	M_x	± 862	± 1.13
		M_y	± 1152	± 2.03
		M_z	± 862	± 1.13

3.4 Hardware Components for the LBCB Control System

As shown in Figure 3.1, the LBCB control system consists of analog and digital controllers and associated hardware.

3.4.1 Analog controller and signal conditioner

A 6-channel programmable analog controller manufactured by Shore Western, Inc. is used to close actuator servo-loops with a proportional-integral-derivative (PID) control scheme (see Figure 3.7). The analog controller is composed of three SC6000 series high-precision control cards where each card has two channels of configurable analog feedback loops. Figure 3.8 shows a diagram of the control and data processing in the analog controller. Drive current to the servo-valve is sent directly from the analog controller. The analog controller also acts as a signal conditioner for the displacement transducers and load cells in the LBCB. In addition to the servo-loop settings (e.g., PID gains), settings for the signal conditioner such as excitation frequency and its level, signal amplifier, and settings for transducer demodulator and analog filter are adjustable in the analog controller. Conditioned signals from the displacement transducer and load cell, as well as servo-error, can be fed to the external digital controller for digital process and data acquisition through the analog controller. On the other hand, displacement command from an external source can be fed into the analog controller. Individual high-precision actuator control can be performed in the analog controller.

The analog controller also provides digital inputs/outputs (IOs) to the lock-valves (in the case of the large-scale LBCB), and solenoid switches for low and high pressures on the accumulator. Additionally, a hardware-based emergency stop is implemented and handled on the analog controller.

(a) Analog controller

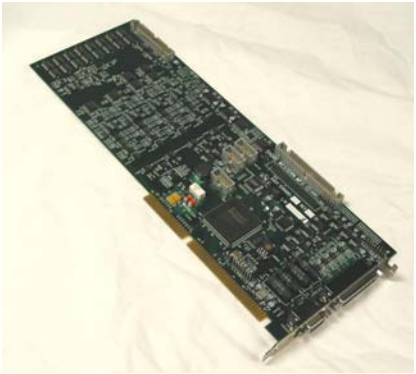

(b) SC6000 card

Figure 3.7. Shore Western analog controller.

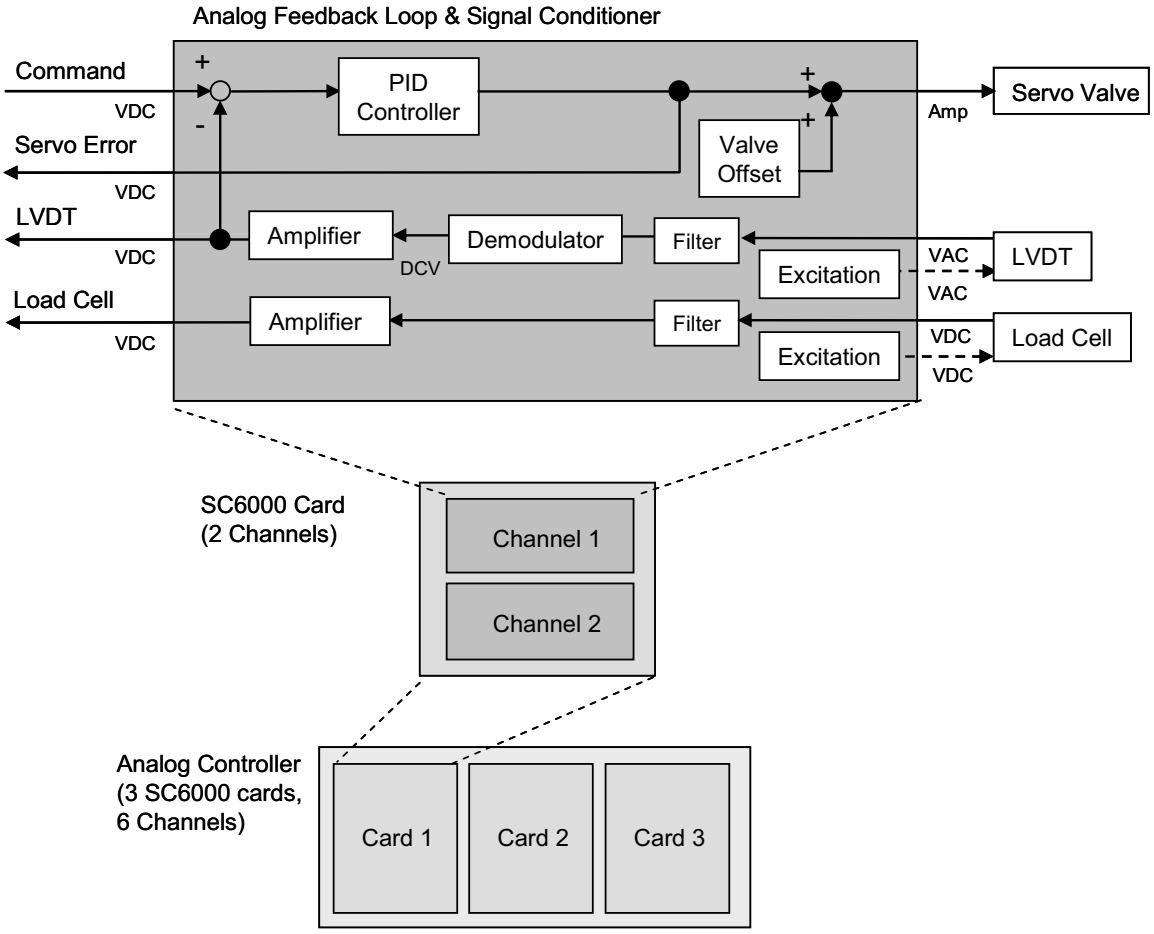

Figure 3.8. Control diagram in analog controller.

Due to the complex geometric transformations and actuator interactions, actuator commands cannot be explicitly specified either in displacement or force for mixed load and displacement command in global Cartesian coordinates. Therefore, in the LBCB control system, all of the actuator servo-loops are closed with the displacement feedback regardless of the control mode. Outside loop processes are performed in the digital controller, including coordinate transformations, the mixed load and displacement control algorithm, etc.

3.4.2 Digital controller and data acquisition

A digital controller consists of a personal computer, analog-to-digital (A/D) and digital-to-analog (D/A) converters, and associated hardware. Figure 3.10 shows the schematics of a digital controller.

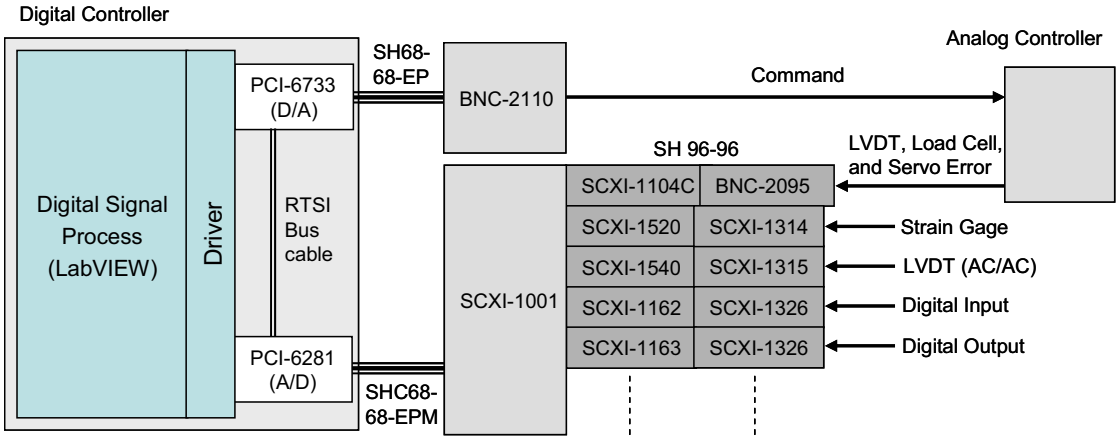

Figure 3.9. Schematics of digital controller.

A National Instruments (NI) PCI-6281 board is used for data acquisition as an A/D converter (see Figure 3.10). The PCI-6281 board is an 18-bit, 16-channel high-accuracy multifunction data acquisition board. With an SCXI-1001 chassis, it provides modular data acquisition system in terms of number of signals and types. All of the signals from the LBCB analog controller and additional sensor signals can be collected at the same sampling rate through the PCI-6281 board. These sampled data are available for signal processing via software and can be stored on the hard drive in the digital controller. An NI PCI-6733 D/A board is used with a BNC-2110 terminal block for actuator displacement command generation. The PCI-6733 board is a 16-bit, 8-channel high-speed analog output board. Synchronization of the operation of multiple boards, such as PCI-6281 and PCI-6733, is performed in both software and hardware using an RTSI-Bus cable. Analog signals are generated from the PCI-6733 based on the control algorithm. Those signals are fed into the LBCB analog controller as external inputs.

(a) Analog output board (PCI-6733)

(b) Analog input board (PI-6281)

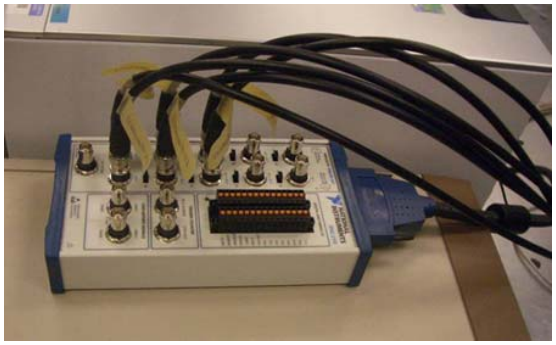

(c) BNC-2110

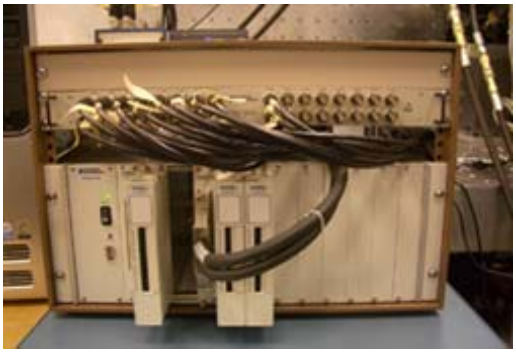

(d) SCXI-1001

Figure 3.10. Hardware components for digital controller.

The NI LabVIEW 7.1 is used as the environment for development and implementation of the digital controller for the LBCB system. All of the digital processes, including the mixed load and displacement control algorithm, coordinate transformations, and network communication, are implemented in the software developed in this study for the operation of the LBCBs in the hybrid simulation.

3.5 Krypton Dynamic Measurement Machine (DMM)

The Krypton DMM is a high-performance mobile coordinate measurement machine that provides high accuracy and a large measurement volume (Krypton Industrial Metrology, 2002). It consists of a camera system with three linear charge-coupled devices (CCDs), light emitting diodes (LEDs), a computer, and associated software. Figure 3.11 shows the hardware components of the Krypton system. The Krypton system at UIUC is capable of measuring the location of up to 256 LEDs in three-dimensional space with an accuracy of ±0.02 mm. The DMM software allows the user to define meaningful local coordinates as well as to measure rigid body motion of the target specified by multiple LEDs.

Figure 3.11. Krypton Dynamic DMM.

One of the challenges in the multi-axial loading system such as the LBCB is calibration in the global Cartesian coordinates. As a part of this study, a calibration method for the multi-axial loading systems was developed. In the calibration method described in Chapter 4, the Krypton DMM is used as an external measurement system that can directly measure the motion of the LBCB platform. The coordinate system and its origin defined by the Krypton system correspond to those in the LBCB global Cartesian coordinates. Multiple LEDs are attached on the LBCB platform and used to measure rigid body motion of the platform in the global coordinates. Thus, using the Krypton system, motion of the LBCB platform in the global coordinates is externally and accurately measured independent of the transformation of the internal actuator measurements.

3.6 Summary

This chapter presented the details of the experimental system for hybrid simulation at the UIUC MUST-SIM facility. The reaction wall and strong floor facility enables flexible and modular configuration of the testing setup. A state-of-the-art, six-actuator self-reaction loading system, the LBCB, was developed to allow 6DOF loading of test specimens in quasi-static and hybrid testing. Use of multiple LBCB makes it possible to conduct complex loading test such as multiple loading point tests. The hardware architecture for the LBCB control system provides flexible environment for the development of control and data acquisition systems. The Krypton system is capable of measuring the 6DOF motion of the LBCB platform independent of internal actuator measurement.

Next, control schemes need to be developed and implemented to fully incorporate the required functionalities into the LBCB control system. The first task for the use of the LBCB is calibration in global Cartesian coordinates. The following chapter presents an external calibration method for the multi-axial loading system.

EXTERNAL CALIBRATION METHOD OF MULTI-AXIAL LOADING SYSTEM

4.1 Introduction

Actions on structures during strong earthquakes are generally multi-dimensional, and continuously varying. For assessment of structures under such conditions, structural testing systems have become increasingly complex and sophisticated (see Figure 4.1). Many of today's modern facilities have multi-axial or multi-degrees-of-freedom (DOF) structural testing systems for hybrid simulation (Molina et al. 1999; Seible et al. 1996), as well as shaking tables (Mahin et al. 2006). A multi-axial loading system is an assemblage of servo-controlled hydraulic actuators; its accuracy is usually less than that of the individual actuator, due to the nonlinear nature of coordinate transformations and imperfections in system geometry. Appropriate evaluation and calibration of multi-axial loading systems are critical for their use in assessment of the seismic performance of structures.

Target control commands in structural tests are normally in global Cartesian coordinates, rather than directly in the actuator coordinates, and these Cartesian coordinates are with respect to the structure being tested. Accuracy in the actuator coordinates is dependent on the precision of the measurement device and on actuator calibration; typically, it can be achieved within 0.1% of full stroke. On the other hand, accuracy in the global coordinates is dependent not only on actuator calibration, but also on the accuracy of geometric parameters used in the transformation from the actuator coordinates. Moreover, errors in the global coordinates cannot be found or eliminated based solely on the actuator measurements. To date, very limited validation has been performed on the accuracy of multi-axial loading systems in global Cartesian coordinates.

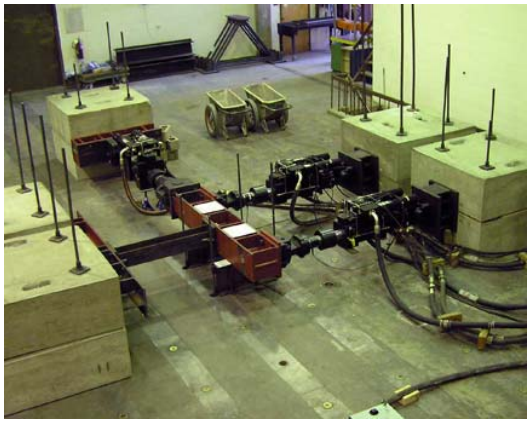

(a) NEES@Colorado
(Photo Credit: http://nees.colorado.edu/)

(b) NEES@Minnesota
(Photo Credit: http://nees.umn.edu/photo/)

Figure 4.1. Examples of multi-axial loading system.

Data acquisition technology has advanced significantly in the last decade. Commercially available sensing systems are now capable of directly measuring the motion of multiple target points in a three-dimensional space (Geodetic Systems, Inc. 2006; Krypton Industrial Metrology 2002). Utilizing an advanced measurement system, the accuracy of the multi-axial loading system in global Cartesian coordinates can be assessed independent of the individual actuator measurements. If significant errors exist between the command and the external global measurements, the loading system can be calibrated to improve control accuracy. However, a calibration method using external measurements needs to be developed for this purpose.

This chapter proposes a systematic strategy for calibration of multi-axial loading systems in global Cartesian coordinates. The proposed method utilizes an external measurement system that is independent of the internal measurements, and calibrates the loading system in global coordinates. The method is based on the sensitivity of the measured global coordinates with respect to the initial actuator lengths. To validate the method, the LBCB is employed as the multi-axial loading system, and the Krypton Dynamic Measurement Machine (DMM) is employed as the external measurement system.

4.2 Actuator Kinematics

4.2.1 Transformation between the Cartesian and actuator coordinates

In general, two coordinate systems are used in multi-axial loading systems: global and actuator coordinates. The global coordinates are usually defined in Cartesian space and referenced to the specimen. The actuator coordinates are defined with respect to each

actuator to support control and measurement operations. Both coordinates can be written in vector form as follows:

$$\mathbf{u} = \left[x, \quad y, \quad z, \quad \theta_x, \quad \theta_y, \quad \theta_z \right]^{\mathrm{T}} \tag{4.1}$$

$$\mathbf{l} = \left[l_1, \quad l_2, \quad l_3, \quad l_4, \quad l_5, \quad l_6 \right]^{\mathrm{T}} \tag{4.2}$$

The Cartesian coordinate vector $\mathbf{u}$ is with respect to the initial control point at which the target displacement is to be imposed. The actuator coordinate vector $\mathbf{l}$ herein is also referred to as the actuator length vector. Even if the loading system has redundant actuators (French et al., 2004), the actuator coordinates can be represented by at most the six actuator lengths in Equation (4.2). That is, the number of independent actuators can be reduced to the number of DOF from geometric constraints.

In a multi-axial loading system, the actuator's end connections to the base and loading platform are usually swivel joints with low-friction pins. The associated pin locations in three-dimensional space are key geometric parameters for the kinematic relationship between the global and actuator coordinates. The following notation is used to define the pin locations in vector form (see also Figure 4.2).

$\mathbf{v}_0$: initial control point
$\mathbf{v}$: current control point
$\mathbf{p}_{0j}$: initial platform pin location for the j-th actuator
$\mathbf{p}_j$: current platform pin location for the j-th actuator
$\mathbf{q}_{0j}$: base pin location for the j-th actuator

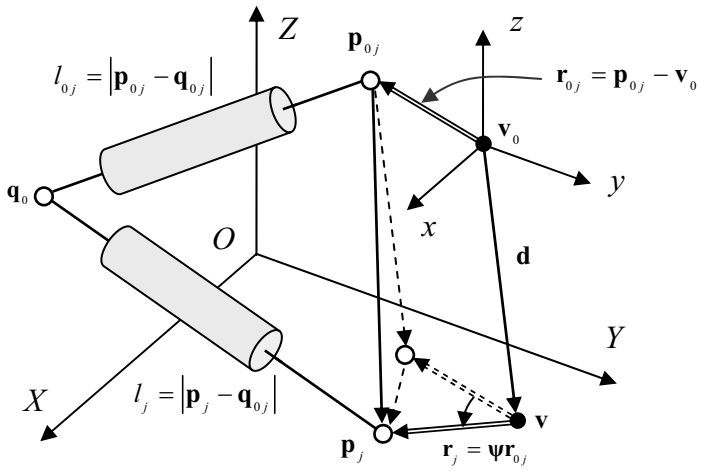

Figure 4.2. Actuator pin locations in the global coordinates.

The initial actuator length (i.e., length of actuator when the control point is at origin) in the *j*-the actuator l_{0j} can then be written in the following form:

$$l_{0j} = \left| \mathbf{p}_{0j} - \mathbf{q}_{0j} \right| \tag{4.3}$$

where $\left| \cdot \right|$ is the Euclidian norm.

The translational DOFs $\mathbf{d} = \left[x,\, y,\, z \right]^{\mathrm{T}}$ in $\mathbf{u}$ can be written in terms of the initial and current control points as follows:

$$\mathbf{v} = \mathbf{v}_0 + \mathbf{d} \tag{4.4}$$

Additionally, $\mathbf{r}_{0j}$ is defined as a vector from the initial control point to the initial platform pin location of the *j*-th actuator.

$$\mathbf{r}_{0j} = \mathbf{p}_{0j} - \mathbf{v}_0 \tag{4.5}$$

The rotational displacements $(\theta_x, \theta_y, \theta_z)$ result in a pure rotation of $\mathbf{r}_{0j}$.

$$\mathbf{r}_j = \boldsymbol{\psi} \mathbf{r}_{0j} \tag{4.6}$$

where rotational matrix $\boldsymbol{\psi}$ follows the Roll-Pitch-Yaw rotational convention and is given by:

$$\boldsymbol{\psi} = \begin{bmatrix} \cos\theta_z & -\sin\theta_z & 0 \\ \sin\theta_z & \cos\theta_z & 0 \\ 0 & 0 & 1 \end{bmatrix} \begin{bmatrix} \cos\theta_y & 0 & \sin\theta_y \\ 0 & \cos\theta_y & 0 \\ -\sin\theta_y & 0 & 1 \end{bmatrix} \begin{bmatrix} 1 & 0 & 0 \\ 0 & \cos\theta_x & -\sin\theta_x \\ 0 & \sin\theta_x & \cos\theta_x \end{bmatrix} \tag{4.7}$$

The current platform pin location $\mathbf{p}_j$ for the *j*-th actuator due to the motion $\mathbf{u}$ is a sum of the translational displacement vector at the control point $\mathbf{d}$ and rotated vector $\mathbf{r}_j$.

$$\begin{aligned} \mathbf{p}_j &= \mathbf{v} + \mathbf{r}_j \\ &= \mathbf{v}_0 + \mathbf{d} + \boldsymbol{\psi} \mathbf{r}_{0j} \end{aligned} \tag{4.8}$$

Finally, the current actuator length for the *j*-th actuator l_j can be written as follows:

$$\begin{aligned} l_j &= \left| \mathbf{p}_j - \mathbf{q}_{0j} \right| \\ &= \left| \mathbf{v}_0 + \mathbf{d} + \boldsymbol{\psi} \mathbf{r}_{0j} - \mathbf{q}_{0j} \right| \\ &= \left| \mathbf{p}_{0j} - \mathbf{r}_{0j} + \mathbf{d} + \boldsymbol{\psi} \mathbf{r}_{0j} - \mathbf{q}_{0j} \right| \\ &= \left| \mathbf{d} - \left(\mathbf{I} - \boldsymbol{\psi} \right) \mathbf{r}_{0j} + \mathbf{p}_{0j} - \mathbf{q}_{0j} \right| \end{aligned} \tag{4.9}$$

Equation (4.9) is a kinematic relationship between the *j*-th actuator length l_j and the global Cartesian coordinate vector $\mathbf{u} = \left[x, y, z, \theta_x, \theta_y, \theta_z \right]^{\mathrm{T}}$.

The transformation from the global to the actuator coordinates can be obtained directly from Equation (4.9) in closed-form:

$$\mathbf{l} = \boldsymbol{\Phi}\left(\mathbf{u}; \mathbf{l}_0\right) \tag{4.10}$$

where $\boldsymbol{\Phi}$ symbolically represents the transformation in Equation (4.9). For clarity in notation, the initial actuator length vector $\mathbf{l}_0$ is used as a parameter instead of the initial actuator directional vector $\mathbf{p}_{0j} - \mathbf{q}_{0j}$ in Equation (4.10); the six parameters in $\mathbf{l}_0$ represent the initial position of the platform.

Using symbolic notation, the transformation from the actuator to global coordinates is written in the following manner:

$$\mathbf{u} = \boldsymbol{\Omega}\left(\mathbf{l}; \mathbf{l}_0\right) \tag{4.11}$$

Equation (4.11) cannot be written in closed-form; rather an iterative numerical approach using the Newton-Raphson method is employed to solve Equation (4.11) for the Cartesian coordinates. Details of the solution procedure for Equation (4.11) are given in Appendix A.

4.2.2 Errors in the global Cartesian coordinates

As described in the previous section, the geometric parameters required for the transformation between global and actuator coordinates are actuator pin locations and initial actuator lengths at the zero position of the loading platform. Assuming that actuators are accurately calibrated, misrepresentations of these two parameters in the transformations are the sources of errors and crosstalk in global Cartesian coordinates. Manufacturing precision is typically high; therefore, errors in actuator pin locations are neglected. However, initial actuator lengths may not be accurate, because the zero position of the platform in global coordinates is difficult to determine. Direct measurement of actuator length between end pins in the assembled configuration is challenging. Therefore, misrepresentation of initial actuator length, defined as the initial actuator length error, is considered as a primary source of error in this study.

The actuator length vector $\mathbf{l}$ can be written as a sum of the initial actuator length vector $\mathbf{l}_0$ and the actuator stroke vector $\boldsymbol{\delta}\mathbf{l}$ as follows:

$$\mathbf{l} = \mathbf{l}_0 + \boldsymbol{\delta}\mathbf{l} \tag{4.12}$$

Because the actuator strokes can be accurately measured using the embedded displacement transducer, the actuator stroke vector $\boldsymbol{\delta}\mathbf{l}$ is assumed to be prescribed. The initial actuator length vector is an unknown vector written as follows:

$$\mathbf{l}_0 = \bar{\mathbf{l}} + \boldsymbol{\varepsilon}\mathbf{l} \tag{4.13}$$

where $\bar{\mathbf{l}}$ is the nominal initial actuator length vector used in the transformations, and $\boldsymbol{\varepsilon}\mathbf{l}$ is the initial actuator length error vector.

To illustrate errors in global Cartesian coordinates introduced by errors in the initial actuator length, a simple in-plane 3DOF system is considered. Figure 4.3 shows schematics of the actuators, a loading platform, and a control point in the 3DOF system, both with and without an initial actuator length error εl_1 in actuator 1. The global coordinates are defined in the Cartesian space (x, y, θ_z), whereas the actuator coordinates correspond to the actuator lengths (l_1, l_2, l_3) for actuators 1, 2, and 3, respectively. Initial actuator lengths, nominal initial actuator lengths, and actuator strokes are defined as (l_{01}, l_{02}, l_{03}), $(\bar{l}_1, \bar{l}_2, \bar{l}_3)$, and $(\delta l_1, \delta l_2, \delta l_3)$, respectively. In this case, the control point is located at the center of the platform which corresponds to the pin location of actuator 1.

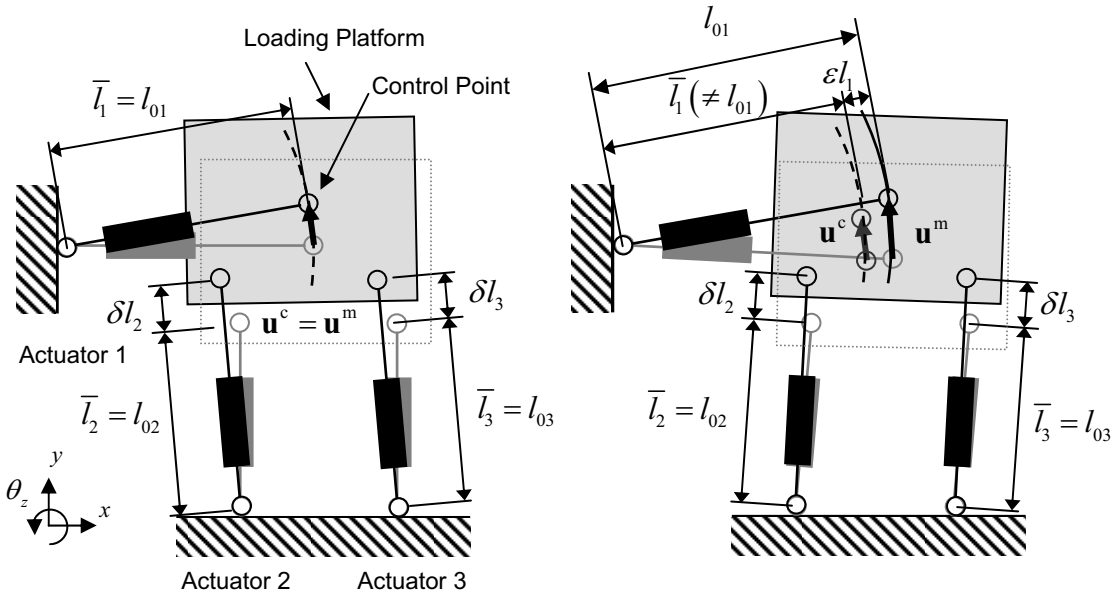

(a) Without initial length errors

(b) With initial length error in the actuator 1

Figure 4.3. Error in the global coordinates due to actuator length error.

If the initial actuator length error is zero [i.e., $\bar{\mathbf{l}} = \mathbf{l}_0$, see Figure 4.3(a)], the target platform motion in the global coordinates can be achieved and measured from coordinate transformations between the global and the actuator coordinates. For example, the actual platform motion, namely the measured displacement $\mathbf{u}^m$, when the actuator strokes are $(0, \delta l_2, \delta l_3)$, as described by the dashed arc, is equal to the internal measurements, namely calculated displacement $\mathbf{u}^c$. However, some errors in the initial actuator lengths usually exist (i.e., $\bar{\mathbf{l}} \neq \mathbf{l}_0$). Assuming an initial actuator length error for actuator 1, the

initial platform position, a dotted square in Figure 4.3(b), is no longer the same as the one without the error, a dotted square in Figure 4.3(a). Moreover, the actual platform motion, a solid arc $\mathbf{u}^{\mathrm{m}}$, does not correspond to the internal measurements without any error, a dashed arc $\mathbf{u}^{\mathrm{c}}$, despite that the actuator strokes $\left(0, \delta l_2, \delta l_3\right)$ are the same. Because the actuator coordinates $\left(l_1, l_2, l_3\right)$ in the transformation process are the same in both (a) and (b), the internal measurements $\mathbf{u}^{\mathrm{c}}$ are also the same. Thus, initial actuator length error causes a discrepancy between the internal measurements and the actual motion of the platform in the global Cartesian coordinates.

In addition to the error in the loading direction, initial actuator length error can also cause crosstalk among multiple axes in the global coordinates. Crosstalk is an undesired displacement in one axis due to the effect of a displacement in another axis. For example, although a command for translation in the *x*-axis is fixed as constant, some displacement in the *x*-axis may occur under pure rotational displacement about the *y*-axis. This feature is termed crosstalk between translation in the *x*-axis and rotation in the *y*-axis.

4.3 Sensitivity-based Calibration Method

4.3.1 Problem formulation

The problem herein is to determine the initial actuator length vector $\bar{\mathbf{l}}$ such that it minimizes the norm of the error between the measured and calculated displacements in global Cartesian coordinates, defined as the Cartesian coordinate error $\boldsymbol{\varepsilon}\mathbf{u}\big|_{\boldsymbol{\delta}\mathbf{l}}$, for a given actuator stroke $\boldsymbol{\delta}\mathbf{l}$, i.e.:

$$\min \left| \boldsymbol{\varepsilon}\mathbf{u}\big|_{\boldsymbol{\delta}\mathbf{l}} \right| \tag{4.14}$$

$$\boldsymbol{\varepsilon}\mathbf{u}\big|_{\boldsymbol{\delta}\mathbf{l}} = \mathbf{u}^{\mathrm{m}}\big|_{\boldsymbol{\delta}\mathbf{l}} - \mathbf{u}^{\mathrm{c}}\big|_{\boldsymbol{\delta}\mathbf{l}} \tag{4.15}$$

where $\mathbf{u}^{\mathrm{m}}\big|_{\boldsymbol{\delta}\mathbf{l}}$ is the measured Cartesian displacement that can be obtained from the external measurement system, and $\mathbf{u}^{\mathrm{c}}\big|_{\boldsymbol{\delta}\mathbf{l}}$ is the calculated Cartesian displacement assuming the actuator strokes are known and that there is no error in the initial actuator lengths, where

$$\mathbf{u}^{\mathrm{c}}\big|_{\boldsymbol{\delta}\mathbf{l}} = \boldsymbol{\Omega}\left(\bar{\mathbf{l}} + \boldsymbol{\delta}\mathbf{l}; \bar{\mathbf{l}}\right) \tag{4.16}$$

To obtain the initial actuator length error vector $\boldsymbol{\varepsilon}\mathbf{l}$, the following relationship is used:

$$\boldsymbol{\varepsilon}\mathbf{u}\big|_{\boldsymbol{\delta}\mathbf{l}} = \mathbf{S}\mathbf{u}\big|_{\boldsymbol{\delta}\mathbf{l}} \cdot \boldsymbol{\varepsilon}\mathbf{l} \tag{4.17}$$

$$\left[\mathbf{Su}\right]_{ij}\Big|_{\boldsymbol{\delta l}} = \left.\frac{\partial \boldsymbol{\Omega}_i}{\partial l_{0j}}\right|_{\boldsymbol{\delta l}} \tag{4.18}$$

where $\mathbf{Su}\big|_{\boldsymbol{\delta l}}$ is the sensitivity matrix of the Cartesian displacement with respect to the actuator length. Subscripts i and j denote the i-th component of the global Cartesian coordinates and the j-th actuator, respectively. Details of the sensitivity are described in the following section.

Once the initial actuator length error vector is obtained, the nominal initial actuator length vector $\bar{\mathbf{l}}$ is updated as follows:

$$\bar{\mathbf{l}}_{\text{updated}} = \bar{\mathbf{l}}_{\text{previous}} + \boldsymbol{\varepsilon l} \tag{4.19}$$

Because the sensitivity matrix is a linearized approximation, one step cannot guarantee the exact solution $\boldsymbol{\varepsilon l}$. Therefore, the calibration process proposed in the following section should be repeated until the norm in Equation (4.14) becomes small.

4.3.2 Determination of sensitivity matrix

The sensitivity matrix cannot be calculated analytically; therefore, it must be evaluated numerically. Defining a finite increment Δl in the j-th actuator length error, actuator length error vector can be written as:

$$\left\{\Delta\mathbf{l}^{(j)}\right\}_k = \Delta l \cdot \delta_{jk} \tag{4.20}$$

where $\left\{\Delta\mathbf{l}^{(j)}\right\}_k$ is the k-th component of $\Delta\mathbf{l}^{(j)}$, Δl is the scalar increment of initial actuator length error, and δ_{jk} is the Kronecker delta. Then, with this initial length error Δl in the j-th actuator, the global Cartesian displacement under a given actuator stroke $\boldsymbol{\delta l}$ can be calculated as follows:

$$\mathbf{u}^{\mathrm{c}}\Big|_{\boldsymbol{\delta l},\Delta\mathbf{l}^{(j)}} = \boldsymbol{\Omega}\left(\bar{\mathbf{l}} + \Delta\mathbf{l}^{(j)} + \boldsymbol{\delta l}; \bar{\mathbf{l}} + \Delta\mathbf{l}^{(j)}\right) \tag{4.21}$$

Error in the global Cartesian displacements due to the initial actuator length error Δl is as follows:

$$\begin{aligned}\Delta\mathbf{u}^{(j)}\Big|_{\boldsymbol{\delta l}} &= \mathbf{u}^{\mathrm{c}}\Big|_{\boldsymbol{\delta l},\Delta\mathbf{l}^{(j)}} - \mathbf{u}^{\mathrm{c}}\Big|_{\boldsymbol{\delta l}} \\ &= \boldsymbol{\Omega}\left(\bar{\mathbf{l}} + \Delta\mathbf{l}^{(j)} + \boldsymbol{\delta l}; \bar{\mathbf{l}} + \Delta\mathbf{l}^{(j)}\right) - \boldsymbol{\Omega}\left(\bar{\mathbf{l}} + \boldsymbol{\delta l}; \bar{\mathbf{l}}\right)\end{aligned} \tag{4.22}$$

Using Equation (4.21) and taking the linear approximation of Equation (4.18), the sensitivity can be estimated as follows:

$$\left[\mathbf{Su}\right]_{ij}\Big|_{\boldsymbol{\delta l}} \cong \frac{\boldsymbol{\Delta}\mathbf{u}_i^{(j)}\Big|_{\boldsymbol{\delta l}}}{\Delta l} = \frac{\boldsymbol{\Omega}_i\left(\bar{\mathbf{l}} + \boldsymbol{\Delta}\mathbf{l}^{(j)} + \boldsymbol{\delta}\mathbf{l}; \bar{\mathbf{l}} + \boldsymbol{\Delta}\mathbf{l}^{(j)}\right) - \boldsymbol{\Omega}_i\left(\bar{\mathbf{l}} + \boldsymbol{\delta}\mathbf{l}; \bar{\mathbf{l}}\right)}{\Delta l} \tag{4.23}$$

where $\boldsymbol{\Delta}\mathbf{u}_i^{(j)}\Big|_{\boldsymbol{\delta l}}$ is the i-th component of $\boldsymbol{\Delta}\mathbf{u}^{(j)}\Big|_{\boldsymbol{\delta l}}$, and $\left[\mathbf{Su}\right]_{ij}\Big|_{\boldsymbol{\delta l}}$ is the (i,j)-th component of $\mathbf{Su}\big|_{\boldsymbol{\delta l}}$ that represents the sensitivity of the i-th component of the Cartesian coordinate $\mathbf{u}\big|_{\boldsymbol{\delta l}}$ with respect to the j-th actuator's initial length error. Again, although $\boldsymbol{\Omega}_i$ is not in closed-form, the sensitivity $\left[\mathbf{Su}\right]_{ij}\Big|_{\boldsymbol{\delta l}}$ can be obtained numerically.

4.3.3 Solution of over-determined system of linear equations

To solve for the six unknown initial actuator length errors $\boldsymbol{\varepsilon}\mathbf{l}$ from the Cartesian coordinate errors $\boldsymbol{\varepsilon}\mathbf{u}$, at least six independent equations are required. Although a sensitivity matrix for a single actuator stroke path has a size of 6×6, it is not always well-conditioned and it can be even singular. Therefore, taking into account multiple actuator stroke paths $\boldsymbol{\delta}\mathbf{l}^{(k)}\left(k=1,\cdots,n\right)$, Equation (4.17) can be extended to an over-determined system of linear equations:

$$\boldsymbol{\varepsilon}\mathbf{U} = \mathbf{SU}\cdot\boldsymbol{\varepsilon}\mathbf{l} \tag{4.24}$$

where $\boldsymbol{\varepsilon}\mathbf{U}$ and $\mathbf{SU}$ are the extended Cartesian coordinate error vector $\left(6n\times 1\right)$ and the extended sensitivity matrix $\left(6n\times 6\right)$, respectively.

$$\boldsymbol{\varepsilon}\mathbf{U} = \left[\begin{array}{ccc}\boldsymbol{\varepsilon}\mathbf{u}\big|_{\boldsymbol{\delta}\mathbf{l}^{(1)}} & \cdots & \boldsymbol{\varepsilon}\mathbf{u}\big|_{\boldsymbol{\delta}\mathbf{l}^{(n)}}\end{array}\right]^{\mathrm{T}} \tag{4.25}$$

$$\mathbf{SU} = \left[\begin{array}{ccc}\mathbf{Su}\big|_{\boldsymbol{\delta}\mathbf{l}^{(1)}}{}^{\mathrm{T}} & \cdots & \mathbf{Su}\big|_{\boldsymbol{\delta}\mathbf{l}^{(n)}}{}^{\mathrm{T}}\end{array}\right]^{\mathrm{T}} \tag{4.26}$$

Note that the actuator stroke path $\boldsymbol{\delta}\mathbf{l}^{(k)}\left(k=1,\cdots,n\right)$ can be the combination of any arbitrary actuator stroke $\delta l_j\ \left(j=1,\cdots,6\right)$.

To solve Equation (4.24) with respect to $\boldsymbol{\varepsilon}\mathbf{l}$, the following condition needs to be satisfied.

$$\mathrm{rank}\left(\mathbf{SU}\right) = 6 \tag{4.27}$$

The solution of over-determined systems of linear equations with the condition in Equation (4.24) can be obtained in the following manner:

$$\begin{aligned}\boldsymbol{\varepsilon}\mathbf{l} &= \left(\mathbf{SU}^{\mathrm{T}}\cdot\mathbf{SU}\right)^{-1}\cdot\mathbf{SU}^{\mathrm{T}}\cdot\boldsymbol{\varepsilon}\mathbf{U} \\ &= \mathbf{SU}^{+}\cdot\boldsymbol{\varepsilon}\mathbf{U}\end{aligned} \tag{4.28}$$

where $\mathbf{SU}^{+}$ is given by:

$$\mathbf{SU}^{+} = \left(\mathbf{SU}^{\mathrm{T}} \cdot \mathbf{SU}\right)^{-1} \cdot \mathbf{SU}^{\mathrm{T}} \tag{4.29}$$

which is the Moore-Penrose matrix inverse (Campbell, 1991); $\boldsymbol{\varepsilon}\mathbf{l}$ is the solution in the least square sense.

4.3.4 Calibration procedure

Using the sensitivity matrix and an external measurement system, the proposed calibration method is established with the following three tasks: determination of sensitivity matrix, calibration, and verification.

Determination of sensitivity matrix

The goal of this process is to obtain a well-conditioned extended sensitivity matrix $\mathbf{SU}$ with a rank of 6. Steps in the first process are summarized as follow:

1) Select an actuator stroke path $\boldsymbol{\delta}\mathbf{l}^{(k)}$, and size of matrix n $\left(k = 1, \cdots, n\right)$. Note not all $\boldsymbol{\delta}\mathbf{l}^{(k)}$ are effective, and $\boldsymbol{\delta}\mathbf{l}^{(k)}$ needs to be chosen such that the errors $\boldsymbol{\varepsilon}\mathbf{l}$ are observable from $\boldsymbol{\varepsilon}\mathbf{U}$.
2) Calculate the sensitivity $\left[\mathbf{Su}\right]_{ij}\Big|_{\boldsymbol{\delta}\mathbf{l}}$ with respect to each actuator stroke path $\boldsymbol{\delta}\mathbf{l}^{(k)}$ $\left(k = 1, \cdots, n\right)$.
3) Construct the extended sensitivity matrix $\mathbf{SU}$ with rank of 6, and obtain the associated calculated Cartesian displacement $\mathbf{u}^{\mathrm{c}}\big|_{\boldsymbol{\delta}\mathbf{l}^{(k)}}$ $\left(k = 1, \cdots, n\right)$.

If the sensitivity matrix $\mathbf{SU}$ is not well-conditioned, steps 1-3 need to be repeated until a well-conditioned sensitivity matrix is obtained.

Calibration

The Calibration process is to measure the actual Cartesian displacement $\mathbf{u}^{\mathrm{m}}\big|_{\boldsymbol{\delta}\mathbf{l}^{(k)}}$ $\left(k = 1, \cdots, n\right)$ by imposing selected actuator path $\boldsymbol{\delta}\mathbf{l}^{(k)}$, to obtain extended Cartesian coordinate error $\boldsymbol{\varepsilon}\mathbf{U}$, and calculate the initial actuator length error vector $\boldsymbol{\varepsilon}\mathbf{l}$. For the measurement of actual Cartesian displacements, an external measurement system is used independent of the internal measurements. The steps in the calibration process are summarized as follow:

4) Impose $\boldsymbol{\delta}\mathbf{l}^{(k)}$ and measure $\mathbf{u}^{\mathrm{m}}\big|_{\boldsymbol{\delta}\mathbf{l}^{(k)}}$ $\left(k = 1, \cdots, n\right)$.
5) Obtain the extended Cartesian coordinate error vector $\boldsymbol{\varepsilon}\mathbf{U}$.
6) Calculate the initial actuator length error vector $\boldsymbol{\varepsilon}\mathbf{l}$ by solving the Equation (4.24).
7) Update the nominal actuator lengths $\bar{\mathbf{l}}$ by $\boldsymbol{\varepsilon}\mathbf{l}$ using Equation (4.19).

Because the sensitivity matrix is a linear approximation, one step cannot guarantee the exact solution $\boldsymbol{\varepsilon}\mathbf{l}$. Therefore, steps 4-7 should be repeated until the norm of the error

between the target and measured displacements in global Cartesian coordinates becomes small.

Verification

The verification process evaluates errors and crosstalk in global Cartesian coordinates. In the verification process, the multi-axial loading system is controlled in one axis of the global coordinates at a time, and accuracy in the loading direction and crosstalk are evaluated.

8) Verify accuracy and crosstalk in the global coordinates.

If the errors and crosstalk are not acceptable, the previous processes may need to be performed.

4.4 Calibration and Verification

Prior to the external calibration process, all actuators need to be precisely calibrated; the external calibration does not compensate for errors in internal calibration. Internal calibration refers to an individual actuator's calibration for the purpose of distinguishing it from the external calibration. In the proposed method, the actuator stroke vector **δl** is taken as a precisely known quantity; errors in the commanded displacement of the actuators are assumed to be zero in the external calibration process. Therefore, internal calibration has to be accurately performed prior to external calibration.

4.4.1 Sensitivity matrix for the LBCB

The first step in the process is to obtain a well-conditioned sensitivity matrix with a small condition number. Four different actuator stroke paths $\boldsymbol{\delta l}^{(k)}\ (k=1,\cdots,4)$ for the external calibration of the 1/5th-scale LBCB are selected and listed in Table 4.1. For example, in Loading Case 1 $(k=1)$, the actuators X1 and X2 are moved +45.72 mm in the same direction, while the other actuator strokes are held at zero stroke. Note that the maximum number of actuators that are moved in each path is two.

Table 4.1. Selected actuator stroke path $\boldsymbol{\delta l}^{(k)}$ for sensitivity matrix.

k	$\boldsymbol{\delta l}^{(k)}$ (mm)					
	$\delta l_1 = \delta$X1	$\delta l_2 = \delta$X2	$\delta l_3 = \delta$Y1	$\delta l_4 = \delta$Z1	$\delta l_5 = \delta$Z2	$\delta l_6 = \delta$Z3
1	45.72	45.72	0	0	0	0
2	0	0	22.86	0	0	0
3	0	0	0	20.32	0	0
4	0	0	0	0	12.70	-12.70

Tables 4.2 to 4.5 show sensitivity matrix for each actuator stroke path $\boldsymbol{\delta l}^{(k)}\left(k=1,\cdots,4\right)$. Shaded elements in the tables are dominant elements. For example, the sensitivity matrix for $\boldsymbol{\delta l}^{(1)}$ in Table 4.2 has dominant elements in columns for εX1, εX2, and $\varepsilon Z1$. Initial actuator length errors in the actuators X1, X2, and $Z1$ can be observed from the Cartesian coordinate errors under the stroke path $\boldsymbol{\delta l}^{(1)}$. However, those in actuator Y1, Z2, and Z3 are not likely to be observed because of their low sensitivity. Therefore, three more actuator paths are considered to observe the initial actuator length errors in all actuators (i.e., at least two dominant elements for each column can be found in the entire tables). Calculated Cartesian displacements for each stroke paths $\boldsymbol{\delta l}^{(k)}$ are also listed in the tables.

The extended sensitivity matrix **SU** is an assemblage of the sensitivity matrices in Tables 4.2 to 4.5. Because there are four stroke paths, the size of the extended sensitivity matrix is 24 x 6. The rank of the sensitivity matrix is equal to 6, and the condition number of the sensitivity matrix is 15.1. Thus, the sensitivity matrix is well-conditioned and the Moore-Penrose matrix inverse of the sensitivity matrix exists.

Table 4.2. Sensitivity matrix associated with $\boldsymbol{\delta l}^{(1)}$.

u	$\mathbf{u}^{c}\big\vert_{\boldsymbol{\delta l}^{(1)}}$	$\mathbf{Su}\big\vert_{\boldsymbol{\delta l}^{(1)}}\times 10^{-3}$ (mm/mm or degree/mm)					
		$\varepsilon l_1=\varepsilon$X1	$\varepsilon l_2=\varepsilon$X2	$\varepsilon l_3=\varepsilon$Y1	$\varepsilon l_4=\varepsilon$Z1	$\varepsilon l_5=\varepsilon$Z2	$\varepsilon l_6=\varepsilon$Z3
x	-49.084	-25.377	-12.755	-5.5374	-34.892	4.517	-1.539
y	-3.218	-41.805	-103.190	8.166	66.770	-19.424	1.799
z	-4.314	-97.758	-96.494	11.679	61.098	0.095	4.675
θ_x	0.000	-45.244	45.242	0.000	0.000	16.022	-16.018
θ_y	0.000	-2.906	2.999	0.000	-3.053	2.318	0.694
θ_z	0.000	9.143	-9.141	0.000	0.000	7.586	-7.585

* Dominant elements are shaded in the sensitivity matrix.

Table 4.3. Sensitivity matrix associated with $\boldsymbol{\delta l}^{(2)}$.

$\mathbf{u}$	$\mathbf{u}^{c}\big\|_{\boldsymbol{\delta l}^{(2)}}$	$\mathbf{Su}\big\|_{\boldsymbol{\delta l}^{(1)}} \times 10^{-3}$ (mm/mm or degree/mm)					
		$\varepsilon l_1 = \varepsilon$X1	$\varepsilon l_2 = \varepsilon$X2	$\varepsilon l_3 = \varepsilon$Y1	$\varepsilon l_4 = \varepsilon$Z1	$\varepsilon l_5 = \varepsilon$Z2	$\varepsilon l_6 = \varepsilon$Z3
x	0.477	47.090	-47.914	41.893	-7.938	-27.102	22.970
y	23.835	0.274	0.940	15.368	8.940	6.544	2.700
z	-1.001	-0.141	1.859	-88.355	12.132	25.954	-13.894
θ_x	0.000	0.428	-0.413	0.000	0.000	0.699	-0.724
θ_y	0.000	20.962	-20.964	0.000	-0.699	-6.206	6.906
θ_z	0.000	0.189	-0.210	0.000	0.000	0.336	-0.337

Table 4.4. Sensitivity matrix associated with $\boldsymbol{\delta l}^{(3)}$.

$\mathbf{u}$	$\mathbf{u}^{c}\big\|_{\boldsymbol{\delta l}^{(3)}}$	$\mathbf{Su}\big\|_{\boldsymbol{\delta l}^{(3)}} \times 10^{-3}$ (mm/mm or degree/mm)					
		$\varepsilon l_1 = \varepsilon$X1	$\varepsilon l_2 = \varepsilon$X2	$\varepsilon l_3 = \varepsilon$Y1	$\varepsilon l_4 = \varepsilon$Z1	$\varepsilon l_5 = \varepsilon$Z2	$\varepsilon l_6 = \varepsilon$Z3
x	3.146	-11.029	-0.047	-5.267	91.251	-11.217	-18.573
y	-3.12	-17.721	48.254	8.320	-38.783	-7.194	-4.286
z	10.210	14.037	14.674	11.846	-28.660	5.226	10.301
θ_x	0.000	24.506	-24.509	0.000	0.000	-8.910	8.914
θ_y	-3.967	-2.234	3.106	0.164	-1.261	1.605	-0.629
θ_z	0.000	2.943	-2.940	0.000	0.000	-14.411	14.411

Table 4.5. Sensitivity matrix associated with $\boldsymbol{\delta l}^{(4)}$.

$\mathbf{u}$	$\mathbf{u}^{c}\big\|_{\boldsymbol{\delta l}^{(4)}}$	$\mathbf{Su}\big\|_{\boldsymbol{\delta l}^{(4)}} \times 10^{-3}$ (mm/mm or degree/mm)					
		$\varepsilon l_1 = \varepsilon$X1	$\varepsilon l_2 = \varepsilon$X2	$\varepsilon l_3 = \varepsilon$Y1	$\varepsilon l_4 = \varepsilon$Z1	$\varepsilon l_5 = \varepsilon$Z2	$\varepsilon l_6 = \varepsilon$Z3
x	0.249	-13.197	12.502	-28.049	5.586	20.198	-17.899
y	-12.908	-14.581	11.896	0.825	-5.325	13.334	-39.368
z	-0.502	16.152	-15.365	21.748	-4.660	-39.721	37.577
θ_x	6.093	4.431	3.167	1.156	-9.445	3.967	2.754
θ_y	-0.182	23.264	-23.242	-7.544	-1.250	-13.407	15.083
θ_z	-2.021	2.798	0.778	0.013	-18.228	-1.1486	0.875

4.4.2 Calibration process

In the calibration process, all of the selected actuator stroke paths $\boldsymbol{\delta l}^{(k)}$ are executed by the servo-controller, and the global displacement is measured from the Krypton DMM system. Table 4.6 lists errors in the iterative process. The error in the global coordinate $\boldsymbol{\varepsilon u}\big|_{\boldsymbol{\delta l}^{(k)}}$ is the difference between the measured Cartesian displacement from the external measurement system $\mathbf{u}^{\mathrm{m}}\big|_{\boldsymbol{\delta l}^{(k)}}$ and the calculated Cartesian displacement $\mathbf{u}^{\mathrm{c}}\big|_{\boldsymbol{\delta l}^{(k)}}$. Using the Moore-Penrose matrix inverse of the sensitivity matrix $\mathbf{SU}$ and the Cartesian coordinate error vector $\boldsymbol{\varepsilon U}$, the initial actuator length error vector $\boldsymbol{\varepsilon l}$ can be calculated from Equation (4.29). As shown in Table 4.6, the initial actuator length error in the first iteration ranges from 0.1 to 2.3 mm. The nominal initial actuator length is updated using Equation (4.19). After the correction of actuator lengths, the same calibration process is repeated until errors in both the Cartesian coordinate and initial actuator length become small. In this study, the calibration process is repeated twice. Note that errors in both the Cartesian coordinate and initial actuator length in the second iteration become smaller than the ones in the first iteration.

4.4.3 Experimental verification

After two iterations of the calibration process, the verification process for the calibration method is performed. In the verification process, the LBCB platform is moved in one axis in the global coordinates at a time as opposed to the individual actuator control in the calibration process. Figure 4.4 shows step histories of 6DOF in the global coordinates measured from the external measurement system: (a) loading in only the *x*-direction, (b) loading in only the *y*-direction, (c) loading in only the *z*-direction, (d) loading in only the θ_x-direction, (e) loading in only the θ_y-direction, and (f) loading in only the θ_z-direction. As shown in the plots, crosstalk is reduced in most cases after the calibration process. For example, θ_x before the calibration in Figure 4.4 (a) has a maximum of about 0.04 degree crosstalk due to the loading in the *x*-direction; θ_x after the calibration, seen in the same plot, is reduced to the noise level. Table 4.7 summarizes the crosstalk normalized by the input amplitude. The values in the parenthesis are the original before calibration. Except in the cases in which the original is already small, overall crosstalk becomes significantly smaller than before calibration. The average reduction ratio of the crosstalk is about 40%. Thus, the proposed calibration method improved the crosstalk among multiple axes in all loading directions.

Figure 4.5 shows the three-dimensional and in-plane traces under translational loadings. These plots show reasonable alignment of axes between the control and the Krypton DMM systems after the calibration. Table 4.8 lists the control accuracy in the global coordinates in the loading direction. In all six directions, maximum errors are about three times smaller, and accuracy increases significantly. The accuracy in terms of the full stroke is around 0.35%. Considering that the actuator calibration can be 0.1% of full-stroke, the accuracy of 0.35% in the global coordinates is quite reasonable. Thus, the proposed calibration method improved control accuracy in the global coordinates in the loading direction.

Table 4.6. Errors in calibration process.

k	$\mathbf{u}$	$\boldsymbol{\varepsilon}\mathbf{u}\big\|_{\boldsymbol{\delta}\mathbf{l}^{(k)}}$ (mm or degree)			$\boldsymbol{\varepsilon}\mathbf{l}$ (mm)	
		Iteration 1	Iteration 2		Iteration 1	Iteration 2
1	x	-0.009	-0.020	εl_1	0.873	-0.025
	y	0.033	0.038	εl_2	-0.861	-0.125
	z	0.037	0.022	εl_3	0.260	-0.133
	θ_x	-0.047	0.001	εl_4	0.110	-0.175
	θ_y	-0.007	-0.007	εl_5	2.268	-0.165
	θ_z	0.043	0.012	εl_6	1.220	0.044
2	x	0.039	-0.005			
	y	0.059	0.015			
	z	0.048	0.016			
	θ_x	-0.001	0.002			
	θ_y	0.016	-0.003			
	θ_z	0.006	0.004			
3	x	-0.081	0.010			
	y	-0.075	-0.009			
	z	0.099	0.003			
	θ_x	0.003	0.001			
	θ_y	-0.104	-0.010			
	θ_z	0.003	0.019			
4	x	-0.009	-0.010			
	y	0.042	0.008			
	z	0.037	0.013			
	θ_x	-0.160	-0.031			
	θ_y	0.210	0.038			
	θ_z	0.077	0.030			

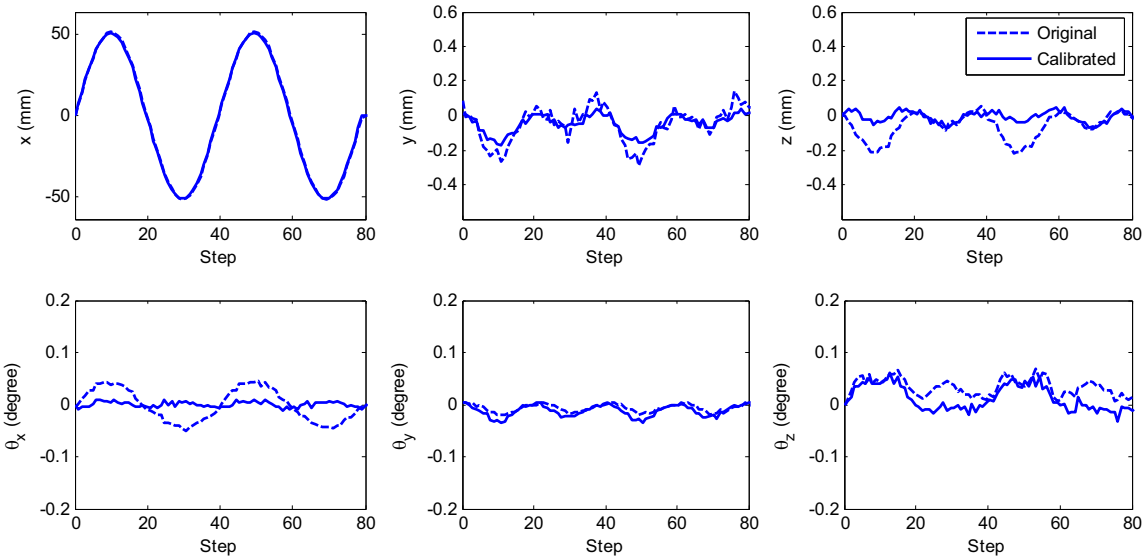

(a) Loading only in the *x*-direction (50.8 mm)

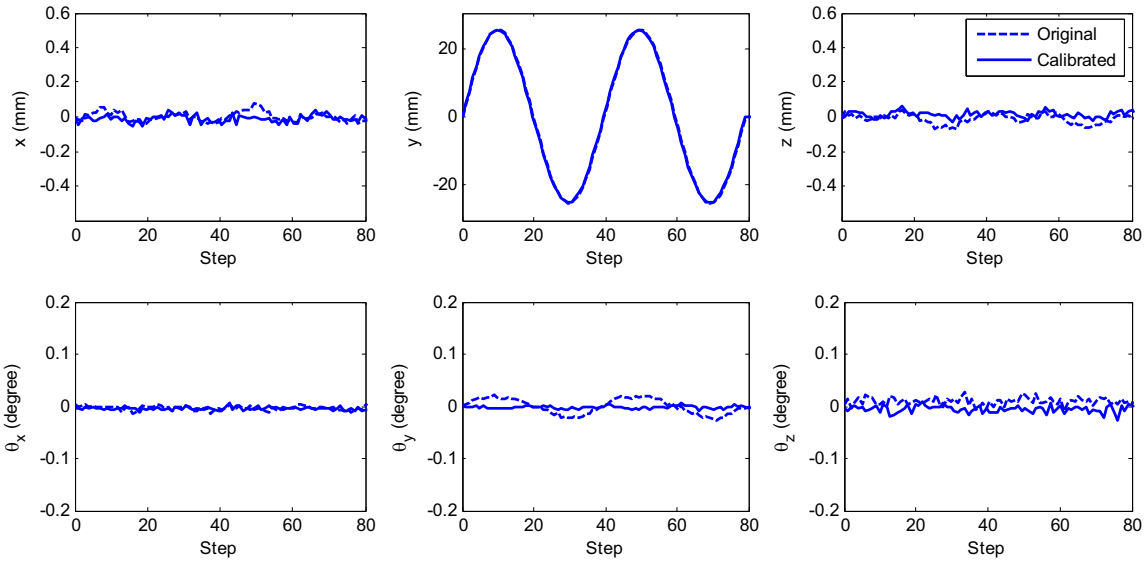

(b) Loading only in the *y*-direction (50.8 mm)

Figure 4.4. Verification of the proposed method in the global coordinates.

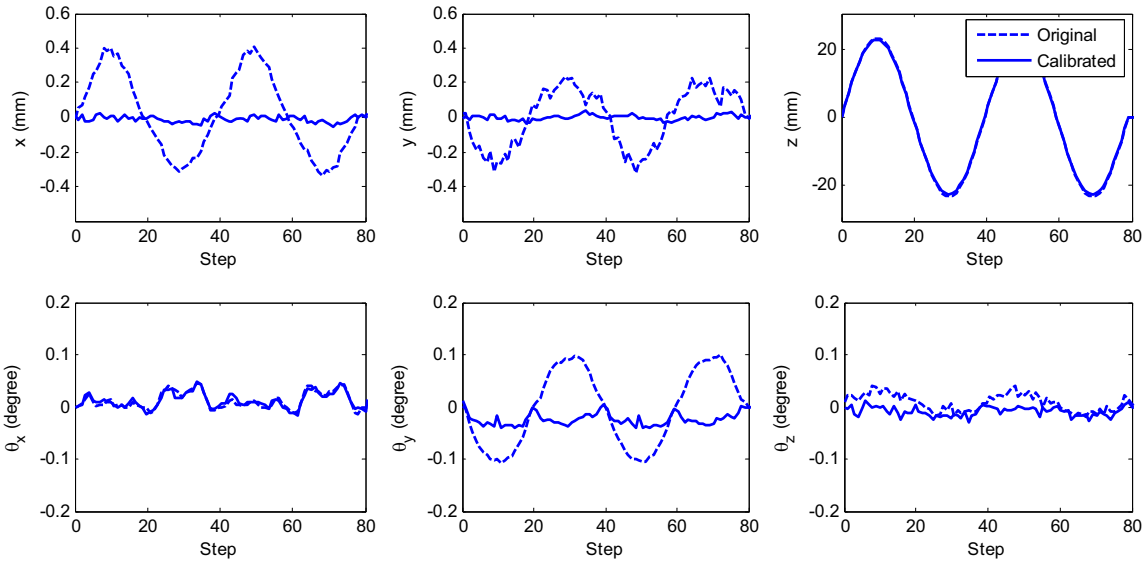

(c) Loading only in the z-direction (50.8 mm)

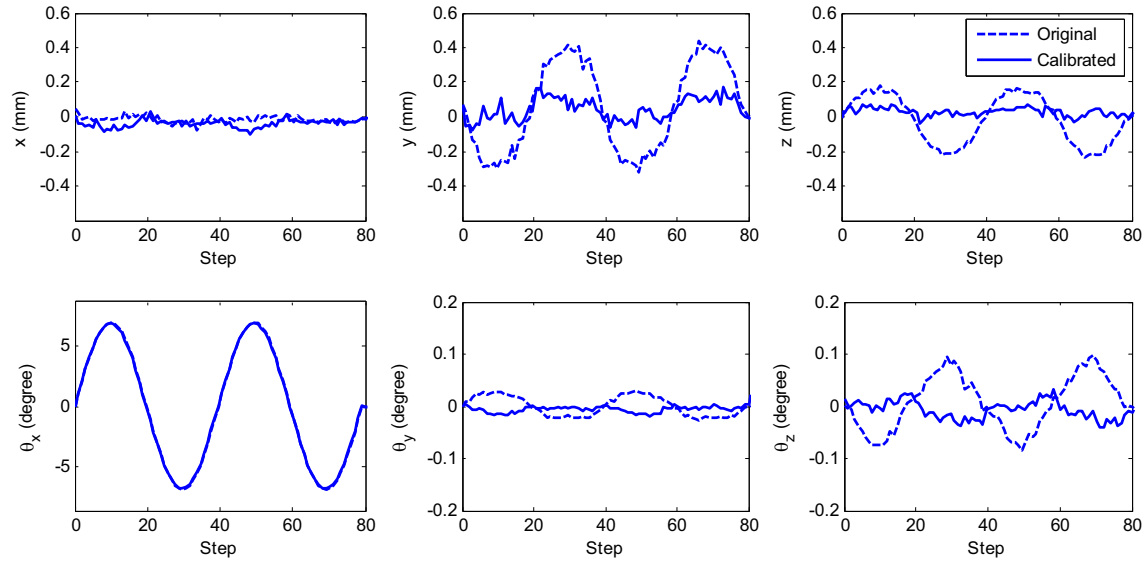

(d) Loading only in the θ_x-direction (50.8 mm)

Figure 4.4. Verification of the proposed method in the global coordinates (Continued).

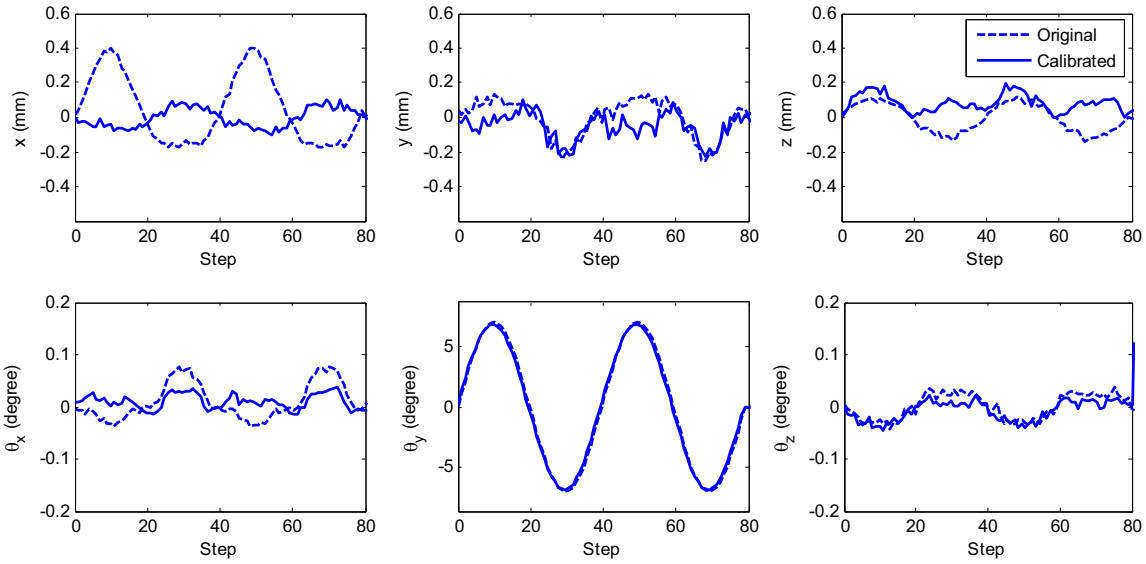

(e) Loading only in the θ_y-direction (50.8 mm)

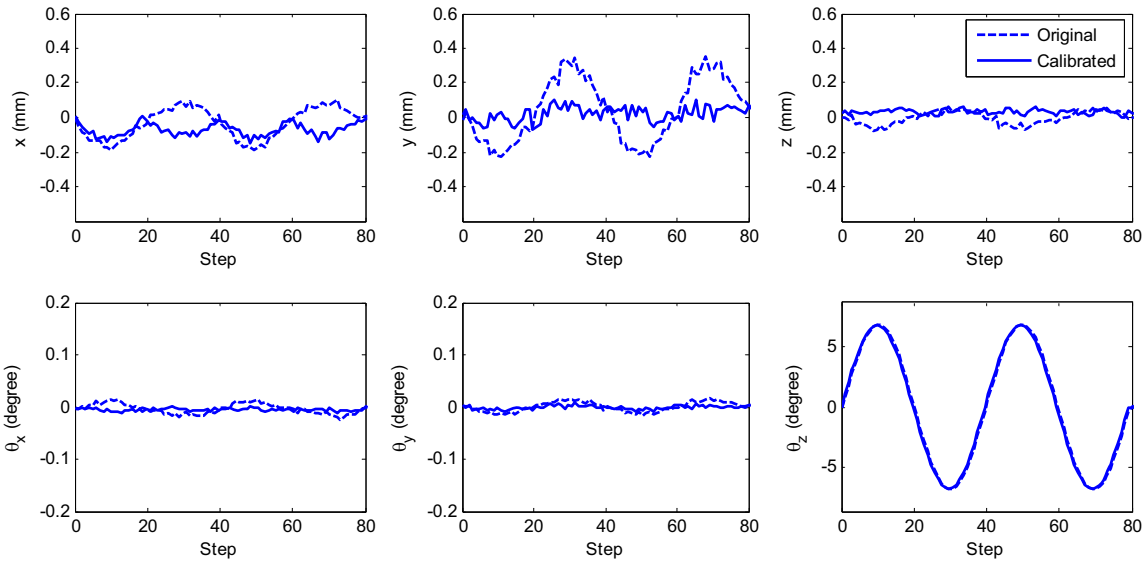

(f) Loading only in the θ_z-direction (50.8 mm)

Figure 4.4. Verification of the proposed method in the global coordinates (Continued).

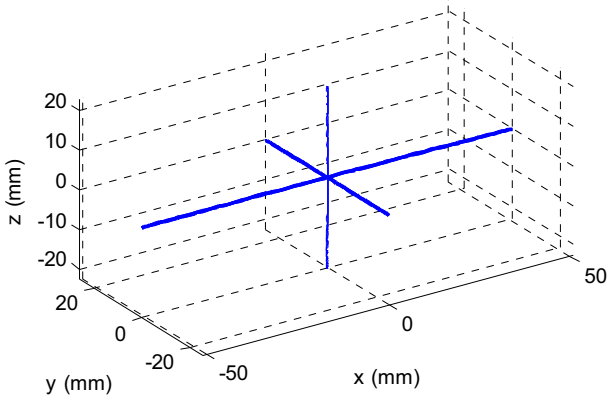

(a) Trace in 3-dimensional space under translational loading

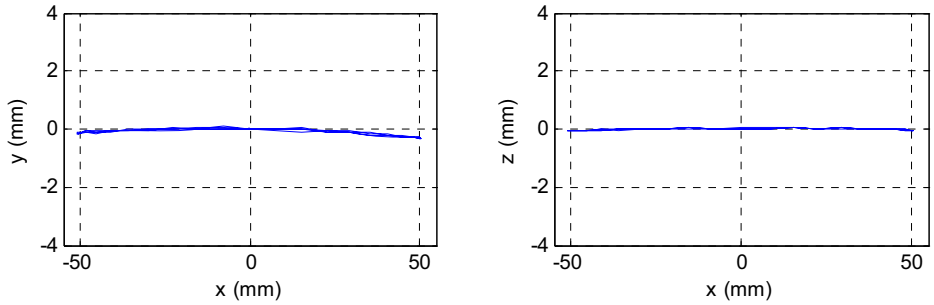

(b) Trace under loading in the *x*-direction

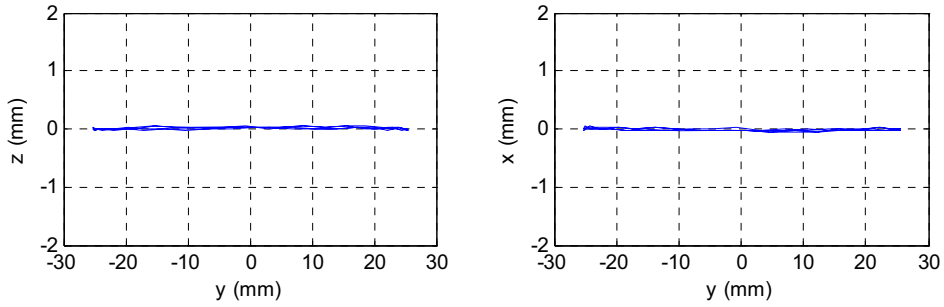

(c) Trace under loading in the *y*-direction

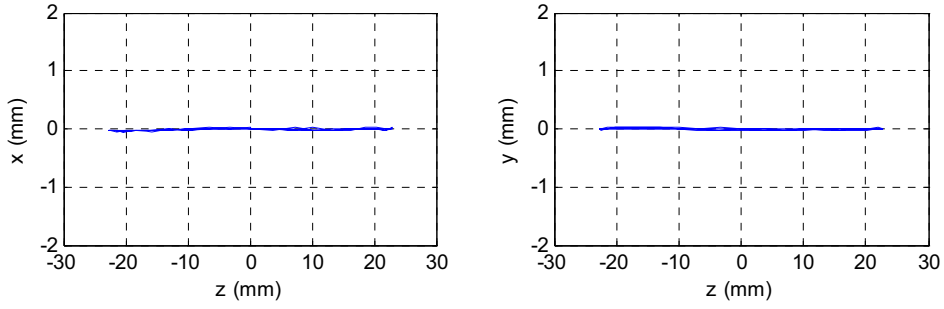

(d) Trace under loading in the *z*-direction

Figure 4.5. Traces under translational loadings.

Table 4.7. Cross talk.

		Measurement					
		x (mm)	y (mm)	z (mm)	θ_x (°)	θ_y (°)	θ_z (°)
Input	x (mm)		-0.0034 (-0.0057) (mm/mm)	-0.0014 (-0.0043) (mm/mm)	0.0002 (0.0010) (°/mm)	-0.0006 (-0.0004) (°/mm)	0.0012 (0.0013) (°/mm)
	y (mm)	-0.0022 (0.0030) (mm/mm)		-0.0024 (-0.0029) (mm/mm)	-0.0004 (-0.0005) (°/mm)	0.0003 (0.0010) (°/mm)	-0.0011 (0.0011) (°/mm)
	z (mm)	-0.0023 (0.0181) (mm/mm)	-0.0017 (-0.0142) (mm/mm)		0.0021 (0.0022) (°/mm)	-0.0018 (-0.0048) (°/mm)	-0.0013 (-0.0018) (°/mm)
	θ_x (°)	-0.0152 (-0.0111) (mm/°)	-0.0258 (-0.0643) (mm/°)	0.0109 (0.0342) (mm/°)		0.0029 (0.0046) (°/°)	-0.0060 (-0.0143) (°/°)
	θ_y (°)	-0.0153 (0.0594) (mm/°)	0.0330 (0.0375) (mm/°)	0.0290 (-0.0205) (mm/°)	0.0055 (-0.0114) (°/°)		-0.0066 (-0.0066) (°/°)
	θ_z (°)	-0.0219 (-0.0283) (mm/°)	-0.0272 (-0.0519) (mm/°)	0.0095 (-0.0114) (mm/°)	-0.0018 (-0.0036) (°/°)	-0.0015 (0.0025) (°/°)	

Calibrated
(Original)

Table 4.8. Accuracy in the global coordinates.

	Maximum Error (mm or °)	Accuracy (% of Full-Stroke)
x	0.378 (1.319)	0.37 (1.30)
y	0.195 (0.530)	0.39 (1.05)
z	0.147 (0.703)	0.33 (1.56)
θ_x	0.058 (0.097)	0.43 (0.72)
θ_y	0.045 (0.215)	0.33 (1.58)
θ_z	0.039 (0.203)	0.29 (1.50)

Calibrated
(Original)

4.5 Summary

This chapter proposes and verifies a systematic procedure for calibration of multi-axial loading systems in global Cartesian coordinates using an external measurement. The proposed method is based on the sensitivity of the measured global coordinates with respect to errors in the initial actuator length. The proposed procedure is verified experimentally using the LBCB at MUST-SIM facility as the multi-axial loading system and the Krypton DMM as the external measurement tool of the global Cartesian coordinates. Experimental results demonstrate that the proposed sensitivity-based external calibration method is very effective for improving control accuracy and reducing crosstalk for multi-axial loading systems in global Cartesian coordinates.

Using the proposed sensitivity-based external calibration method, the LBCB can been well-calibrated with respect to the global Cartesian coordinates. The next step is to develop a control system that utilizes the capabilities of the LBCBs and answers the needs of multi-axial hybrid simulation.

MIXED LOAD AND DISPLACEMENT CONTROL STRATEGIES

5.1 Introduction

Accounting for the effect of gravity loads is essential for the evaluation of the seismic performance of vertical structural components (i.e., building columns and bridge piers). Gravity load effects have been carefully considered in structural tests by many researchers, employing actuators in the vertical direction (Elnashai et al. 1998; Kawashima et al. 2004, 2005; Lynn et al. 1996). In those tests, actuators in the other directions are attached perpendicular to the vertical actuators at the initial position, and the assumption of decoupling of the actuator forces is made for the vertical load (see Figure 5.1). Therefore, vertical actuators are primarily in force control, whereas lateral actuators are in displacement control. In other words, gravity loads have been applied or considered only through actuators in the vertical direction, independent of forces in the lateral actuators. Note that under large deformation, lateral actuators will have a force component in the vertical direction that should be considered. Moreover, if a control system has coupling between actuator and Cartesian coordinates, mixed load and displacement (mixed-mode) control, including gravity load and lateral displacement control, cannot be achieved with independent control of each actuator. The challenge is due to the contribution of unknown displacements in the force-controlled actuators and the unknown forces in displacement-controlled actuators with respect to the target mixed load and displacement. In fact, mixed load and displacement commands cannot be explicitly decomposed into each actuator command in the coupled multi-axial control system. Therefore, versatile and generally-applicable mixed-mode control algorithms are required to take into account instantaneous and spatial coupling in the control systems. The mixed-mode control here includes various types of loading protocol such as multi-axes load control; it is not limited to the vertical force and lateral displacement control.

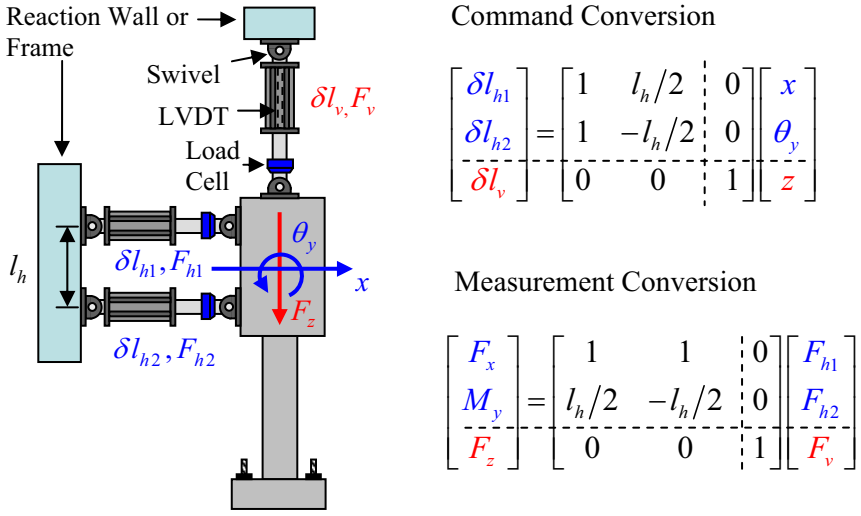

Figure 5.1. Illustration of traditional decoupling control system for vertical force.

This chapter presents control strategies for the use of the Load and Boundary Condition Box (LBCB) in hybrid simulation with all required functionalities including a general mixed-mode control algorithm. First, a digital integrator technique that compensates for the effect of reaction force from the test specimen on the actuator control accuracy is provided in Section 5.2. The digital integrator technique is specifically designed for ramp-hold loading procedure. Next, a mixed load and displacement control method which incorporates load-to-displacement conversion is presented in Section 5.3. The conversion is based on the incremental iteration process employing the Broyden (1965) update of the stiffness Jacobian of the tested structure. Following a description of the mixed-mode control algorithm, experimental verification is performed for aluminum column and RC pier specimens using the LBCB. Test results as well as control performance for the proposed method are presented. Then, supplemental and required control capabilities are introduced in Section 5.4. Those capabilities include an auto-balancing feedback loop that enables safe start even with specimen connected to the control system before pressure is supplied, and tele-operation control that allows network-based hybrid simulation.

5.2 Digital Integrator Technique for Ramp-Hold Procedure

A Proportional-Integral-Derivative (PID) controller is a widely used feedback control design for servo-hydraulic actuators. In practice, all of the PID terms are generally used with proper tuning for continuous and dynamic applications; tuning of the PID gains is performed by a trial-and-error based on the step responses of the actuator (i.e., rising and settling times, overshoot, etc). However, the conventional PID approach is not well-suited in terms of control performance and tuning for slow-rate, ramp-hold loading procedures

that are intended for stiff and non-repeatable testing structures. In this section, an actuator control technique for ramp-hold loading is proposed combining analog and digital controllers.

5.2.1 Effect of reaction forces on control accuracy

The ramp-hold loading procedure has two distinct phases as indicated by its title. The ramping phase imposes the target displacement from the previous position in a smooth fashion, either linear or half-sine shape. The holding phase averages measurement readings to obtain settled measurements corresponding to the target displacement. Because structures are generally path-dependent in the nonlinear response range, it is desirable to prevent overshoot. Therefore, proportional gain is usually set to modest levels to avoid overshoot and stability problems. Hence, the derivative term that is used to reduce the magnitude of the overshoot is generally not required. On the other hand, the integrator gain is difficult to tune for non-repeatable structural tests that do not allow the standard trial-and-error tuning process. To achieve the high control accuracy in structural tests, the control system needs to be well designed and evaluated.

First, a feedback control scheme with only a proportional loop is evaluated for the ramp-hold procedure. Employing the LBCB, an aluminum-column specimen is subjected to the lateral displacement, whereas the other degrees-of-freedom (DOF) are held at constant. The setup for the aluminum-column test is shown in Figure 5.2. For the details of the specimen, see Appendix B.

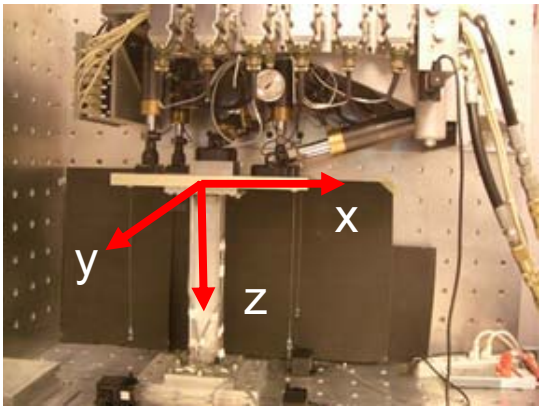

Figure 5.2. Setup for the aluminum column test.

Figure 5.3 shows step histories of the lateral and in-plane rotational displacements. As shown in the plots, the measured lateral displacement does not agree well with the target displacement. Moreover, the rotation in the y-direction θ_y shows undesired movement. Note that these errors do not occur without the specimen in place. These residual errors are due to the influence of the reaction force from the specimen on the control system.

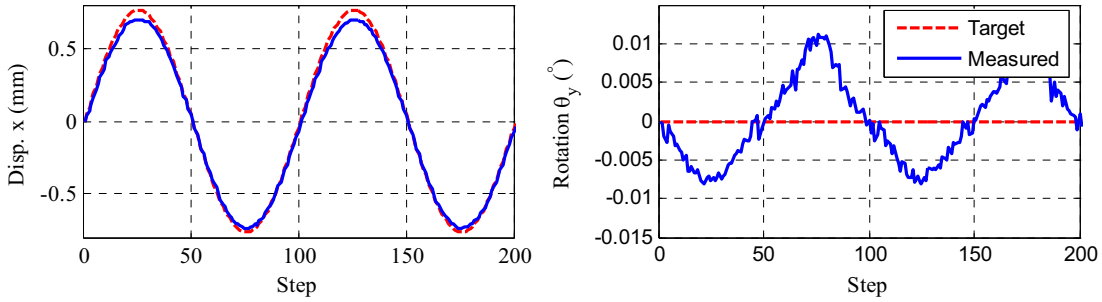

(a) Lateral displacement x (mm)

(b) Rotational displacement θ_y (degree)

Figure 5.3. Step-response of the lateral loading test without the integrator loop.

Figure 5.4 illustrates the influence of the reaction force of the test specimen on the actuator piston equilibrium. The servo-hydraulic control system consisting of the actuator and servo-valve is a mechanical system by which the equilibrium of the piston is affected by the reaction force transferred through piston rod. Without the influence of the reaction force, the drive current i holds the equilibrium pressures at both sides of the piston [see Figure 5.4(a)]. On the other hand, under the influence of relatively large reaction force, a drive current that gives equilibrium pressures is no longer the same current i [see Figure 5.4(b)]. This unbalanced valve current to the pressure equilibrium introduces a residual actuator displacement error. The errors in the lateral and rotational displacements are a reflection of the residual actuator displacement errors. In this test, actuators in the vertical direction are subjected to relatively large reaction forces due to the lateral displacement. Regardless of the holding time, the proportional loop does not eliminate the residual error. Thus, an integrator loop needs to be incorporated into the control system to reduce residual errors due to the influence of the reaction forces.

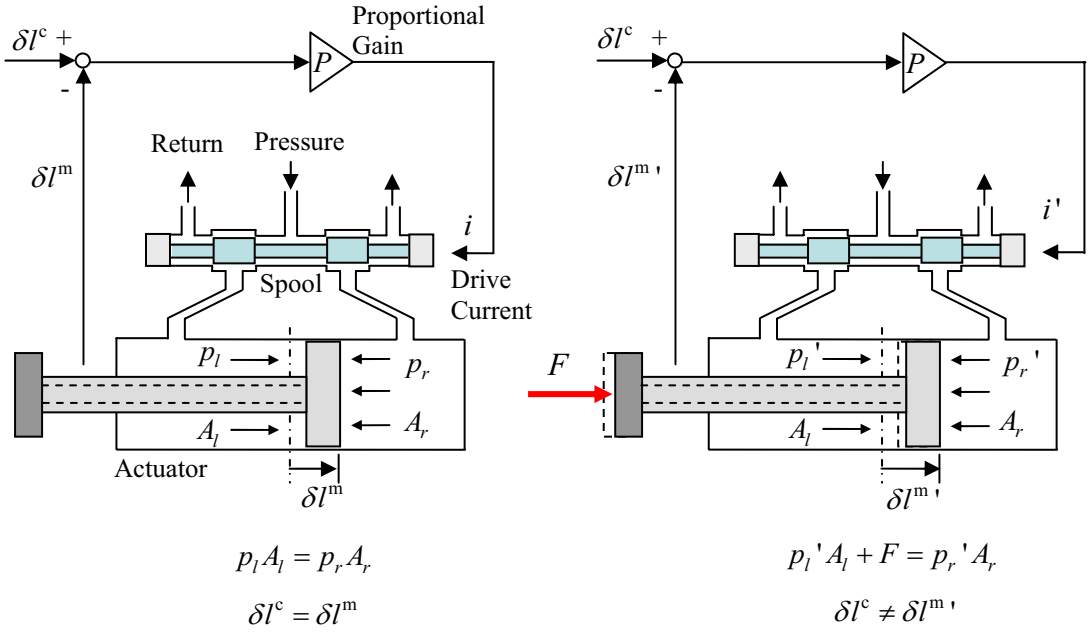

(a) Without influence of reaction force (b) With influence of reaction force

Figure 5.4. Illustration of the influence of reaction force on piston equilibrium.

5.2.2 Digital integrator technique

In this study, a digital integrator technique that activates an integrator loop only between the ramp and hold phase is proposed. Because the feedback of the integrated error in the ramping process becomes problematical for stiff specimen, it is desirable to disable the integrator loop in the ramping phase. The integrator loop on the analog controller used in this study cannot be turned on and off during operation. Therefore, the integrator technique is implemented here in the digital controller. Figure 5.5 shows a schematic of the single actuator control where continuous proportional loop is on the analog controller, and digital integrator loop is on the digital controller. Figure 5.6 shows the ramp-hold with digital integrator technique in the time domain. Because the integrator loop at global Cartesian coordinates level will increase the actuator interaction that may cause stability and convergence problem, the integrator loop here is all at the individual actuator level.

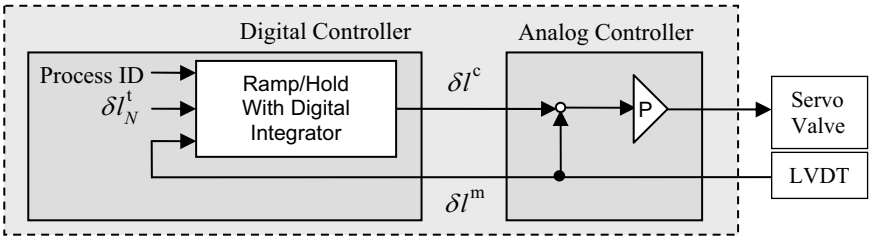

Figure 5.5. Schematic of actuator control for ramp-hold procedure.

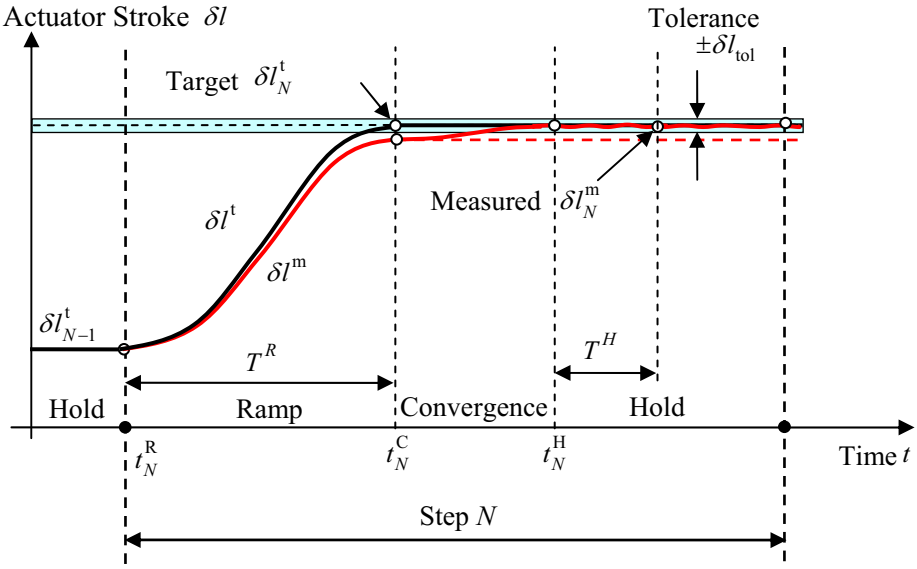

Figure 5.6. Ramp-hold with digital integrator technique in time domain.

The following is a command generation algorithm in the proposed digital integrator technique at main three phases: ramp, convergence, and hold.

i) Ramp phase

Each step starts with a ramp phase where a smooth increment in the command is generated from the previous target stroke to the current target stroke. The following expression describes the actuator stroke command:

$$\delta l^{\mathrm{c}}(t)=\frac{\left(\delta l_N^{\mathrm{t}}-\delta l_{N-1}^{\mathrm{t}}\right)}{2}\sin\pi\left(\frac{t-t_N^R}{T^R}-\frac{1}{2}\right)+\frac{\left(\delta l_N^{\mathrm{t}}+\delta l_{N-1}^{\mathrm{t}}\right)}{2}+\delta l^i \tag{5.1}$$

$$t_N^R \le t \le t_N^R + T^R \tag{5.2}$$

where δl^{c} is a generated actuator stroke command, $\delta l_{N-1}^{\mathrm{t}}$ and δl_N^{t} are the last and the new target actuator strokes, respectively, δl^{i} is the integrator constant at the last convergence step, T^R is a ramp time, t is a time constant, and t_N^R is the initial ramp time. Note the ramping process is a fixed time process with T^R. After ramping comes the convergence phase.

ii) Convergence phase

The first step in the convergence phase is to evaluate the actuator stroke error:

$$\left|\delta l_N^{\mathrm{t}}-\delta l^m\right| \le \delta l_{tol} \tag{5.3}$$

where δl^m is the measured actuator stroke, and δl_{tol} is the actuator stroke tolerance. If all of the actuator stroke errors are within the tolerance in Equation (5.3), the process moves to the hold phase. If not, the integrator constant is updated in the following manner:

$$\delta l_{\mathrm{new}}^i = \delta l_{\mathrm{previous}}^i + G_I\left(\delta l_N^{\mathrm{t}}-\delta l^m\right)\cdot\Delta t \tag{5.4}$$

where G_I is the integrator gain, and Δt is the time increment. Then, the actuator stroke command is updated with new integrator constant as follows:

$$\delta l^{\mathrm{c}}(t)=\delta l_N^{\mathrm{t}}+\delta l^i \tag{5.5}$$

The convergence phase is repeated until Equation (5.3) is satisfied in all actuators. Therefore, the convergence phase does not take a fixed amount of time.

iii) Hold phase

The hold phase is to average the measurement signals to obtain settled displacements and loads. The command in the hold phase remains at the last converged one in the convergence phase as follows:

$$\delta l^{\mathrm{c}}(t)=\delta l_N^{\mathrm{t}}+\delta l^i = const \tag{5.6}$$

After the hold time T^H elapses in the hold phase, the measured displacements and loads are returned corresponding to the converged target displacement. Because waiting time for the next step is not deterministic, the hold phase is not a fixed time process.

5.2.3 Experimental verification

Experimental verification is conducted using the aluminum column specimen under a lateral displacement. Based on the precision and noise level of the actuators, actuator stroke tolerances are set to 0.02 mm for the X1 and X2 actuators of 102 mm stroke, and 0.01 mm for the rest of the actuators of 51mm stroke. Figure 5.7 shows response-histories of the lateral and in-plane rotational displacements. The digital integrator technique ensured the actuator stroke accuracy is within the tolerance before moving to the next step. As a result, accuracy in both displacements is improved as compared to the ones without the integrator loops in Figure 5.3. Because the digital integrator technique is implemented at the actuator level, actuator interaction was not induced, and convergence was achieved in a smooth fashion. Thus, the digital integrator technique is proven to be effective for ramp-hold loading of structures in terms of control accuracy and robustness.

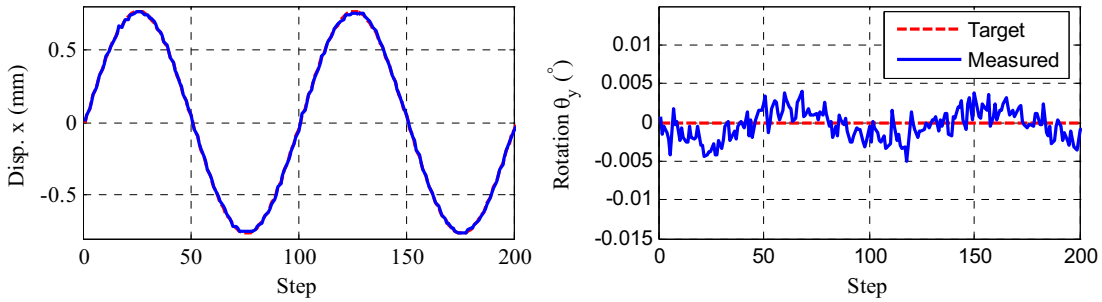

(a) Lateral displacement x (mm)

(b) Rotational displacement θ_y (degree)

Figure 5.7. Step-histories of lateral loading test with integrator loop.

Figure 5.8 shows comparison in displacement-load hysteresis between with and without integrator loops. The force-displacement and moment-displacement relationships obtained without discrete integrator loop produce significant errors. The errors are due to the inevitable in-plane rotation without discrete integrator loop. As shown in these plots, control accuracy is critical for the evaluation of the structural behavior, especially for MDOF systems. The proposed digital integrator technique is confirmed to be effective in providing accurate representation of the structural behavior.

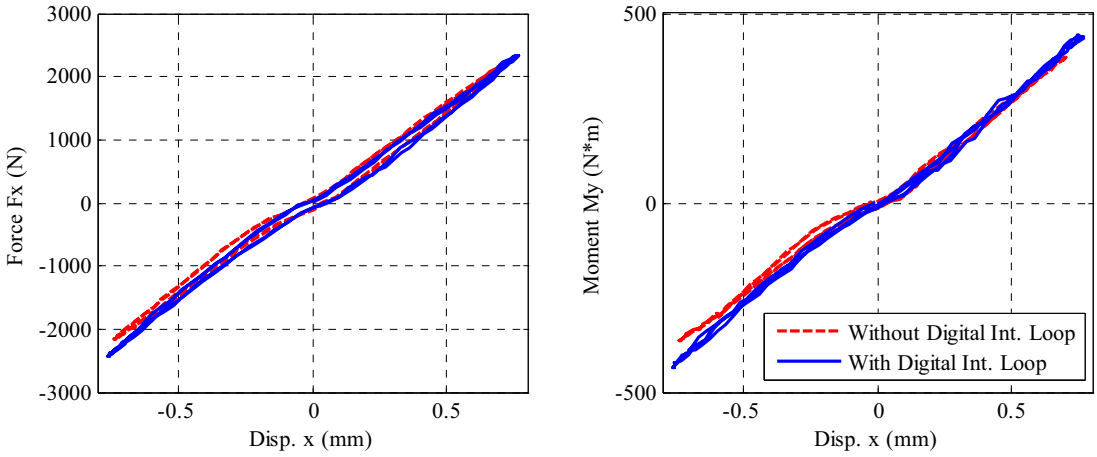

(a) Displacement x - Force F_x (b) Displacement x – Moment M_y

Figure 5.8. Comparison in hystereses between with and without integrator loop.

5.3 Mixed Load and Displacement Control

As previously mentioned, mixed load and displacement commands cannot be explicitly decomposed into the actuator command, either displacement or force, for coupled-control systems. This limitation is due to unknown displacements in the load-controlled axes and unknown loads in the displacement-controlled axes. To achieve a target mixed loads and displacement vector, it is essential to develop a control framework that can incorporate arbitrary control strategies. This section presents a general control framework that supports mixed load and displacement control algorithms for multi-axial loading systems.

5.3.1 Control system framework

Figure 5.9 shows schematics of the data flow and processes in the proposed control framework. The vectors **u** and **f** are the displacement and load vectors in Cartesian coordinates, whereas vectors **δl** and **r** are the displacement and force vectors in the actuator space. The superscripts *t*, *c*, and *m* denote the target, command, and measured data, respectively. Accents "¯" and "˜" denote data in the displacement- and force-controlled axes, respectively. The vector **p** is a vector of geometric parameters for actuator pin locations.

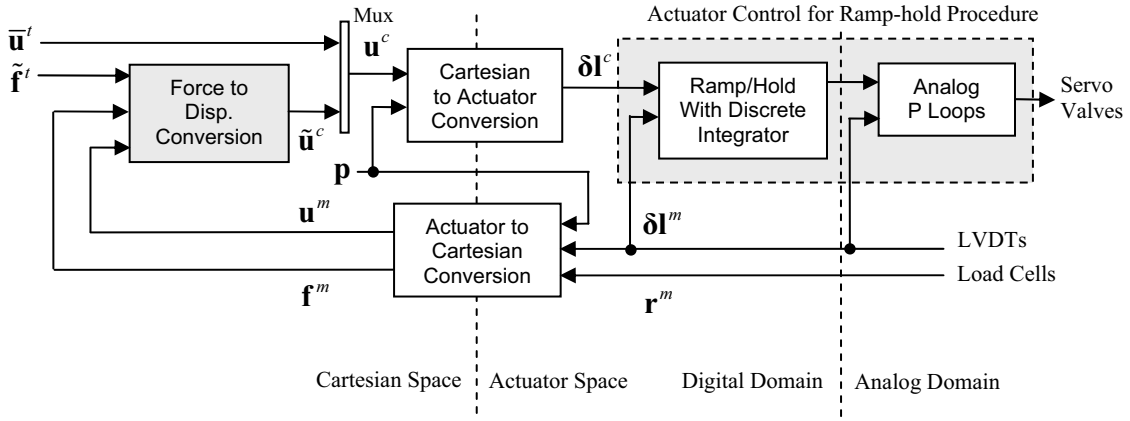

Figure 5.9. Block diagram of the proposed mixed-mode control strategy.

The first process in the proposed control framework is a load to displacement conversion. The Cartesian target load is converted into a Cartesian command displacement in all axes. The Cartesian command displacements for the load-controlled axes are estimated based on the approximation of the stiffness Jacobian. Once Cartesian commands are all specified in the displacement, they can be further decomposed into each actuator command displacement. This process is a geometric transformation using coordinates of the actuator pin locations with respect to the control point. Because there are no decoupling requirements between displacement- and load-controlled axes, an exact geometric transformation can be used instead of geometric approximation used in the traditional decoupling approach. This exact coordinate transformation from the Cartesian to the actuator coordinates ensures the validity of the control system even under large deformation. Then, using the ramp-hold process coupled with the digital integrator technique, all of the actuator commands are simultaneously executed. The dotted rectangle represents the actuator control strategy presented in the previous section. Following the convergence of the actuator displacements, the measured actuator displacements and force from the LVDT and load cell, respectively, are converted into the Cartesian measured displacement and load. In general, the transformation from actuator to Cartesian coordinates is an iterative process of solving a set of nonlinear kinematic relationships. At the end of each step, the measured mixed loads and displacements are compared with the target mixed loads and displacements. Depending on the acceptable tolerance in all the axes, the process iterates or goes to the next step.

In the proposed control framework, all of the actuator servo-loops are closed with displacement feedback regardless of the load-controlled axes. This approach is versatile for mixed load and displacement control of multi-axial loading systems. Moreover, because all the actuators are operated in displacement control, the system is more robust than the traditional mixed load and displacement control approach that has force-controlled actuators.

5.3.2 Iterative procedure for load convergence

In the proposed framework, the target mixed load and displacement command is achieved through a process that comprises directional and iterative ramps. First, the directional ramp is executed with an updated command in the displacement-controlled axes, whereas the command in the load-controlled axes remains the ones at the end of the previous step. Then, iterative ramps are repeated with an updated command in the load-controlled axes until convergence to the target load is achieved. After each ramp, an approximation of the stiffness Jacobian is updated using Broyden's method. A single step in the mixed mode control procedure is described below:

i) Directional ramp at step *N*:

The command displacement vector in the directional ramp is as follows:

$$\bar{\mathbf{u}}^{c}_{N(0)} = \bar{\mathbf{u}}^{t}_{N} \tag{5.7}$$

$$\tilde{\mathbf{u}}^{c}_{N(0)} = \tilde{\mathbf{u}}^{c}_{N-1} \tag{5.8}$$

where $\bar{\mathbf{u}}^{c}_{N(0)}$ and $\tilde{\mathbf{u}}^{c}_{N(0)}$ are the command displacement at the directional ramp in the *N*-th step in the displacement- and load-controlled axes, respectively; $\bar{\mathbf{u}}^{t}_{N}$ is a target displacement in the displacement controlled axes at step *N*; and $\tilde{\mathbf{u}}^{c}_{N-1}$ is a command displacement in the load-controlled axes at step *N*–1.

ii) Update the stiffness Jacobian after the directional ramp:

$$\mathbf{K}_{N(0)} = \mathbf{K}_{N-1} + \frac{\left(\Delta\mathbf{f}^{m}_{N(0)} - \mathbf{K}_{N-1}\cdot\Delta\mathbf{u}^{m}_{N(0)}\right)\cdot\left(\Delta\mathbf{u}^{m}_{N(0)}\right)^{\mathrm{T}}}{\left\|\Delta\mathbf{u}^{m}_{N(0)}\right\|^{2}} \tag{5.9}$$

where $\mathbf{K}_{N(0)}$ is an updated stiffness Jacobian after the directional ramp at the *N*-th step, $\Delta\mathbf{u}^{m}_{N(0)}$ and $\Delta\mathbf{f}^{m}_{N(0)}$ are the measured incremental displacement and load vectors, respectively, and are written as follows:

$$\Delta\mathbf{u}^{m}_{N(0)} = \mathbf{u}^{m}_{N(0)} - \mathbf{u}^{m}_{N-1} \tag{5.10}$$

$$\Delta\mathbf{f}^{m}_{N(0)} = \mathbf{f}^{m}_{N(0)} - \mathbf{f}^{m}_{N-1} \tag{5.11}$$

Equation (5.9) is known as Broyden update of the Jacobian, which satisfies the following relationship:

$$\Delta\mathbf{f}^{m}_{N(0)} = \mathbf{K}_{N(0)}\Delta\mathbf{u}^{m}_{N(0)} \tag{5.12}$$

iii) Iterative ramp at *i*-th iteration at step *N*:

The command displacement vector in the load-controlled axes is updated in the iterative ramp is as follows:

$$\bar{\mathbf{u}}^{c}_{N(i)} = \bar{\mathbf{u}}^{t}_{N} \tag{5.13}$$

$$\tilde{\mathbf{u}}^{c}_{N(i)} = \tilde{\mathbf{u}}^{c}_{N(i-1)} + \tilde{\mathbf{G}} \cdot \tilde{\mathbf{K}}_{N(i-1)} \cdot \left(\tilde{\mathbf{f}}^{t}_{N} - \tilde{\mathbf{f}}^{m}_{N(i-1)} \right) \tag{5.14}$$

where $\tilde{\mathbf{G}}$ is a mixed-mode gain matrix in the load-controlled axes and $\tilde{\mathbf{K}}_{N(i-1)}$ is the updated stiffness Jacobian after the *i*-th iteration at the *N*-th step in the load-controlled axes.

iv) Update the stiffness Jacobian after the *i*-th iterative ramp:

$$\mathbf{K}_{N(0)} = \mathbf{K} \frac{\left(\Delta \mathbf{f}^{m}_{N(i)} - \mathbf{K}_{N(i-1)} \cdot \Delta \mathbf{u}^{m}_{N(i)} \right) \cdot \left(\Delta \mathbf{u}^{m}_{N(i)} \right)^{\mathrm{T}}}{\left\| \Delta \mathbf{u}^{m}_{N(i)} \right\|^{2}} \tag{5.15}$$

where $\mathbf{K}_{N(i)}$ is an updated stiffness Jacobian after the *i*-th iterative ramp at the *N*-th step. The displacement and force increment vector $\Delta \mathbf{u}^{m}_{N(i)}$ and $\Delta \mathbf{f}^{m}_{N(i)}$ are written as follows:

$$\Delta \mathbf{u}^{m}_{N(i)} = \mathbf{u}^{m}_{N(i)} - \mathbf{u}^{m}_{N(i-1)} \tag{5.16}$$

$$\Delta \mathbf{f}^{m}_{N(i)} = \mathbf{f}^{m}_{N(i)} - \mathbf{f}^{m}_{N(i-1)} \tag{5.17}$$

v) Convergence evaluation:

The convergence of the load-controlled axes is evaluated as follows:

$$\left| \tilde{\mathbf{f}}^{t}_{N} - \tilde{\mathbf{f}}^{m}_{N(i)} \right| \leq e\tilde{\mathbf{f}} \tag{5.18}$$

where $e\tilde{\mathbf{f}}$ is a load tolerance vector in the load-controlled axes. If Equation (5.18) is not satisfied, the process goes back to (iii) and is repeated until the convergence criterion is satisfied. Following convergence, the process goes to step *N*+1 with the following relationships:

$$\tilde{\mathbf{u}}^{c}_{N} = \tilde{\mathbf{u}}^{c}_{N(i)} \tag{5.19}$$

$$\tilde{\mathbf{f}}^{m}_{N} = \tilde{\mathbf{f}}^{m}_{N(i)} \tag{5.20}$$

Because of the updating feature, the proposed method takes into account material inelasticity and geometric nonlinearity, as well as other abrupt effects such as cracking, in the control process. Therefore, the proposed method is robust and efficient in terms of the load control in multi-axial control systems. Most importantly, with small increments in the directional ramp, this method is capable of producing the desired mixed load and displacement loading history even for path-dependent structures.

Figure 5.10 shows the block diagram for the load-to-displacement conversion. Here, $\boldsymbol{\varepsilon}\tilde{\mathbf{f}}$ and $\Delta\tilde{\mathbf{u}}^c$ are the load error and displacement increment vectors in the load-controlled axes, respectively, while $\mathbf{K}$ and $\mathbf{G}$ are the stiffness Jacobian and mixed-mode gain matrices, respectively.

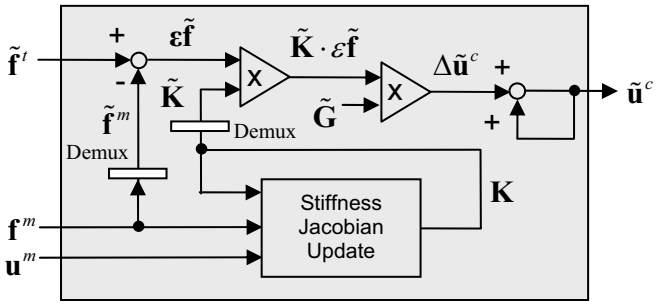

Figure 5.10. Block diagram for force to displacement conversion.

5.3.3 Experimental verifications

Experimental verification of the proposed mixed-mode control algorithm is conducted using the 1/5th-scale LBCB. To rigorously evaluate the performance of the proposed control algorithm, a series of tests have been performed using several types of specimens and loading protocols. In this section, test results are provided for two types of specimens and two types of loading protocols.

Aluminum specimen: Lateral displacement and vertical force controlled test

The first mixed-mode experiment is a lateral displacement and axial force controlled test of an aluminum-column specimen with bolted connections. For the details of the aluminum-column specimen, see Appendix B. The test setup for the aluminum specimen is the same as Figure 5.2. The lateral displacement input is a sinusoidal wave with increasing amplitude and the axial force input is 1350 N constant compression throughout the test. Note that positive *z*-direction is downwards from the loading platform. The other four DOFs, i.e. displacement in the *y*-direction and all the rotations, are commanded to be zero.

Figure 5.11 shows sample results from the lateral displacement and axial force controlled test. The top two plots are the controlled lateral displacement and axial force, respectively. The force tolerance in the axial direction is set to 50 N in this test. The middle two plots correspond to force and displacement in the lateral and axial directions, respectively. The variation in the axial displacement is a result of the axial force control and effect of the lateral displacement. The bottom two plots are representative of the hysteresis in the test. The force versus lateral displacement relationship shows a typical bilinear hysteresis, whereas the lateral and vertical displacement relationship exhibits complex nonlinear behavior. Complex variation of the axial displacement due to the lateral displacement under constant load is difficult to simulate in the analytical model. Despite those nonlinear inelastic behaviors of the aluminum specimen, the control objective is successfully achieved through the entire test.

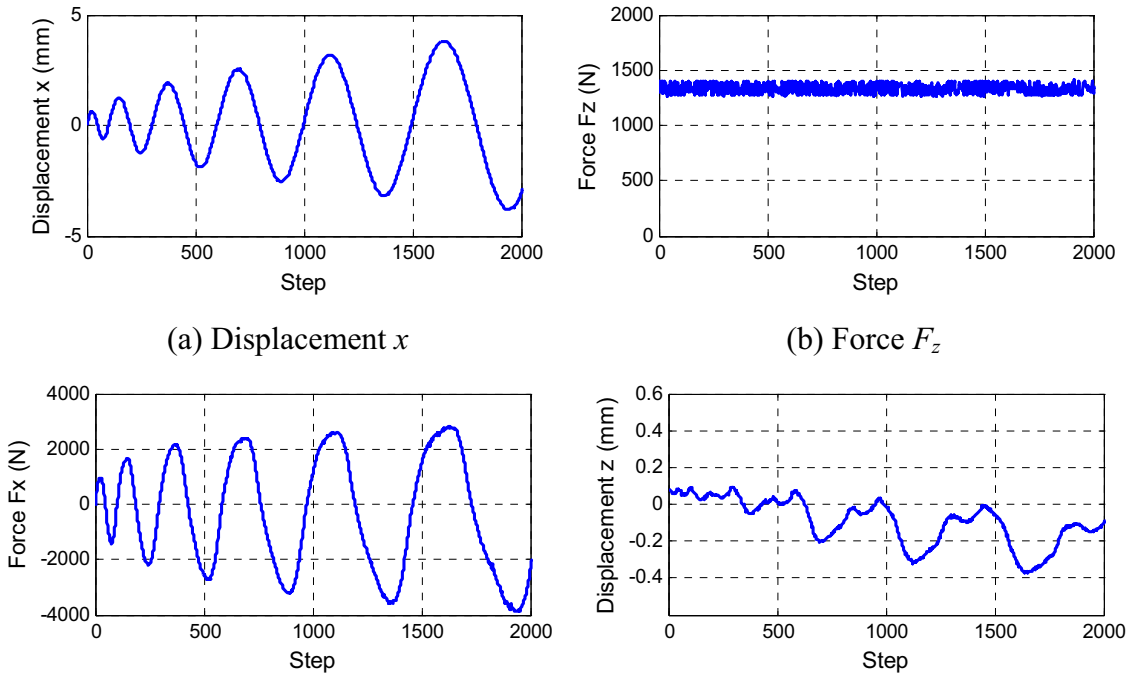

(a) Displacement x (b) Force F_z

(c) Force F_x (d) Displacement z

Figure 5.11. Lateral displacement and vertical force controlled test results for aluminum-specimen with angle connections.

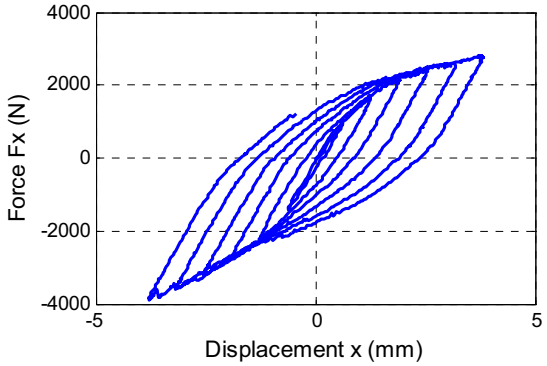

(e) Displacement x – Force F_x

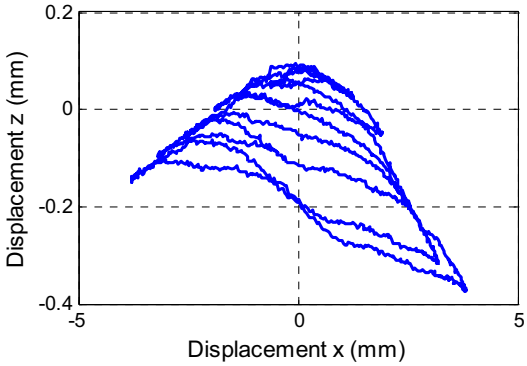

(f) Displacement x – Displacement z

Figure 5.11. Lateral displacement and vertical force controlled test results for aluminum specimen with angle connections (Continued).

RC pier specimen: Lateral displacement and vertical force controlled test

The second mixed-mode experiment is for a small-scale reinforced concrete pier specimen. For the details of the RC specimen, see Appendix B. The test setup for the RC specimen is shown in Figure 5.12. The loading protocol is the same as the previous example. However, the RC specimen exhibits more complex and brittle behavior than the aluminum specimen. Therefore, the control performance of the proposed algorithm can be evaluated under more challenging conditions.

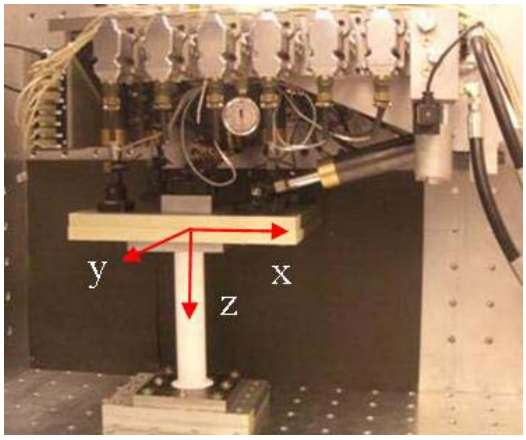

Figure 5.12. Setup for the RC pier test.

Figure 5.13 shows sample results from the lateral and axial loading test of the RC specimen. In this test, the axial load level is set to 4448 N constant compression with a tolerance of 40 N. The test was conducted in the large deformation range, where total shear failure of the RC pier was observed [see also Figure 5.15(a)]. The lateral

displacement and force relationship shows the typical nonlinear inelastic behavior of RC members, including cracking, yielding, and even pinching. On the other hand, the lateral and axial displacement relationship exhibits peculiar behavior as a result of the axial force control and the effect of the lateral displacement. From these plots, it can be seen that the properties of the specimen are changing in a drastic and complex manner. Despite these complex nonlinear inelastic behaviors, lateral displacement and axial force are controlled throughout the test. Thus, the proposed mixed-mode control method exhibits very good performance and robustness even for the inelastic response of the RC specimen.

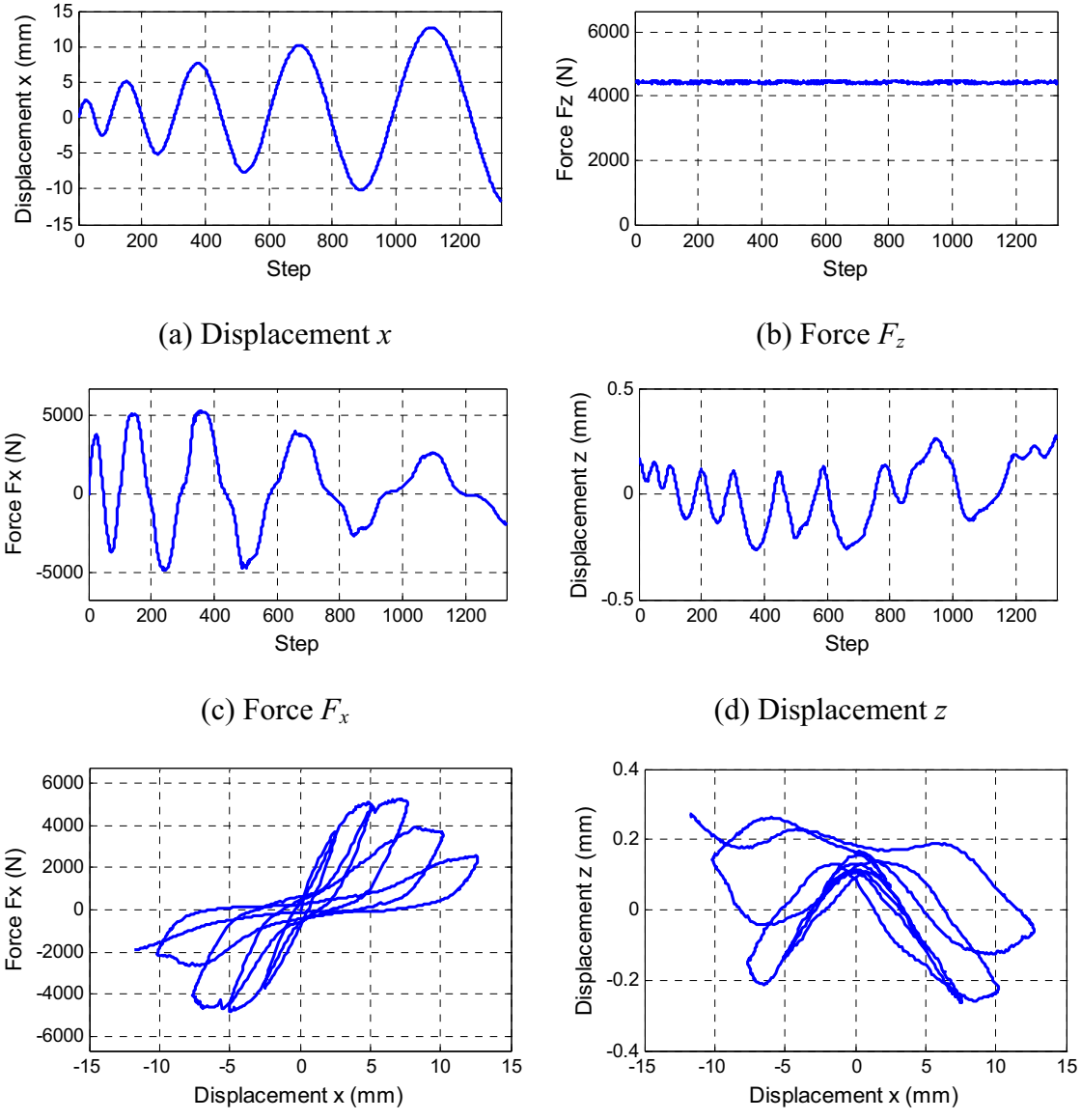

(a) Displacement x

(b) Force F_z

(c) Force F_x

(d) Displacement z

(e) Displacement x – Force F_x

(f) Displacement x – Displacement z

Figure 5.13. Lateral displacement and vertical force controlled test results for reinforced concrete pier specimen.

RC pier specimen: Torsional rotation and vertical force controlled test

The third mixed-mode experiment is a mixed torsional rotation and axial force controlled test of an RC pier specimen. The torsional rotation input is a sinusoidal wave with increasing amplitude; the axial force input is a 2224 N constant compression throughout the test. The other DOFs are under displacement control with constant zero inputs.

Figure 5.14 shows sample results from the torsional rotation-axial force controlled test. Similar to the previous example, cracks and strength reduction are also observed in this test [see Figure 5.15(b)]. The variation of the axial displacement is a result of the axial force control and effect of the torsional rotation. Ductile behavior and energy dissipation can be seen in the torsional rotation and moment relationship. Similar to the previous tests, the proposed mixed-mode control method shows very good control performance and robustness in torsional rotation and axial force controlled test even in the inelastic range of the response.

As shown in the test results, the proposed mixed load and displacement control algorithm is proved to be effective for complex behaviors of the test specimens and various loading protocols. At this stage, the mixed load and displacement control is ready to be utilized in hybrid simulation to represent the gravity loads in the axial direction and earthquake induced displacements in the other directions.

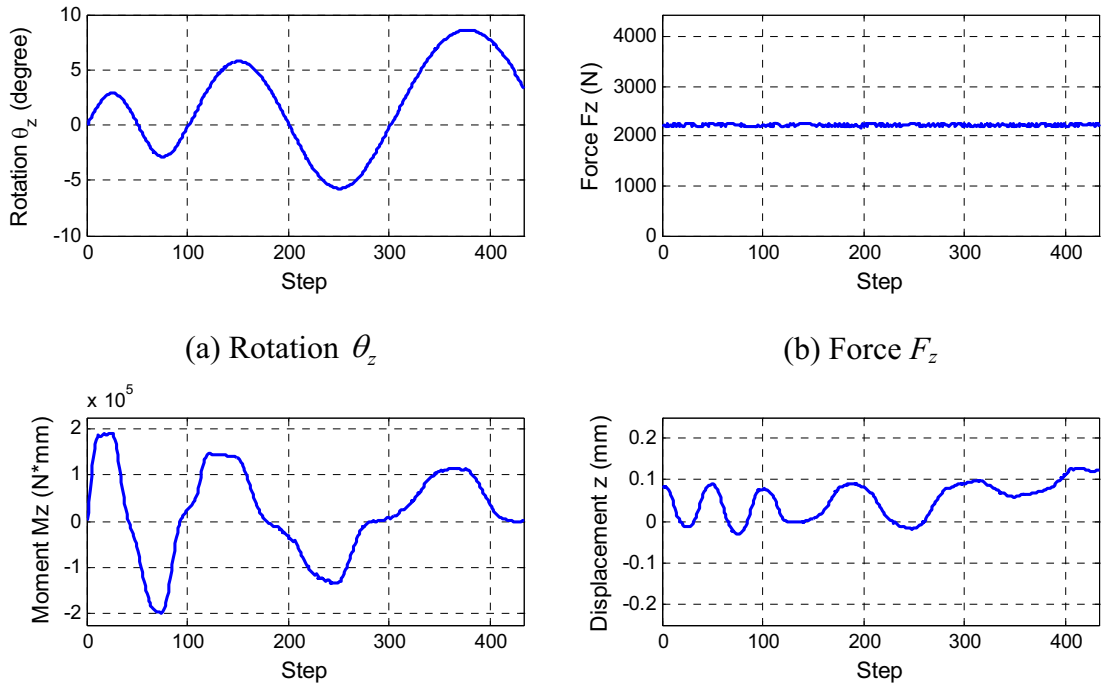

(a) Rotation θ_z (b) Force F_z

(c) Moment M_z (d) Displacement z

Figure 5.14. Torsional rotation and vertical force controlled test results for reinforced concrete pier specimen.

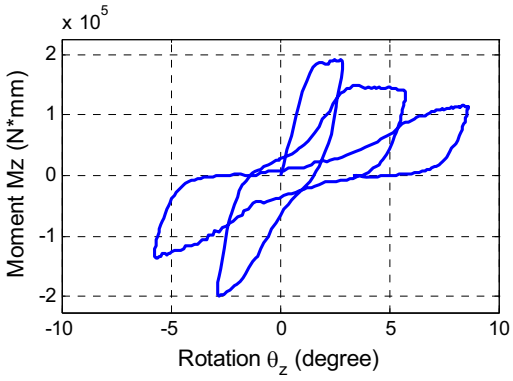

(e) Rotation θ_z – Moment M_z

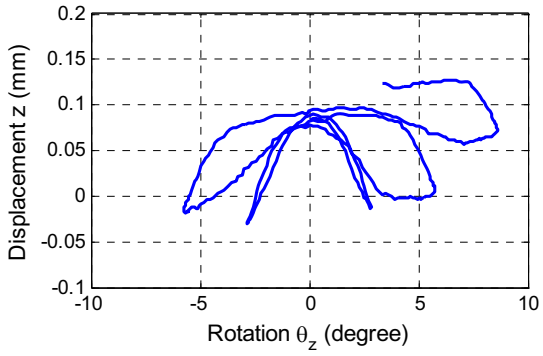

(f) Rotation θ_z – Displacement z

Figure 5.14. Torsional rotation and vertical force controlled test results for reinforced concrete pier specimen (Continued).

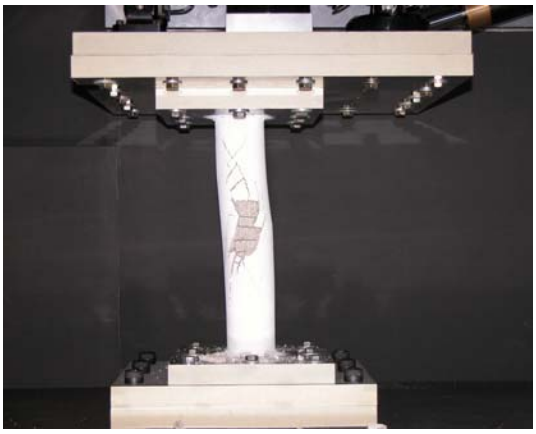

(a) Lateral displacement – axial load controlled test

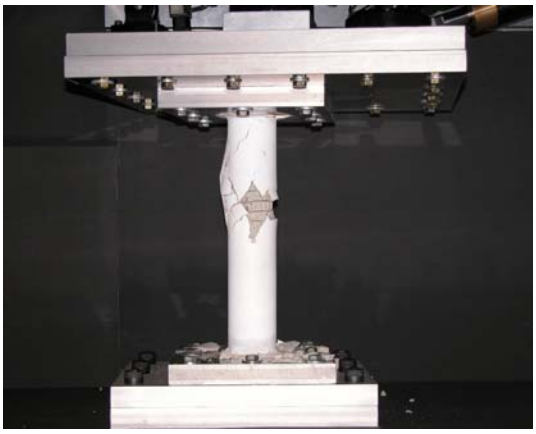

(b) Torsional rotation – axial load controlled test

Figure 5.15. Specimens after the completion of the tests.

5.4 Supplemental Digital Servo-Control Capabilities and Control Software

In addition to the digital integrator technique and the mixed load and displacement control algorithm, several other control techniques are developed and incorporated into a digital servo-control software that comprise a major part of the framework. Those supplemental techniques and the digital servo-control software are presented in this section.

5.4.1 Auto-balancing feedback control for safe start

Structural testing generally takes long preparation, execution, and teardown time periods. In particular, large-scale tests require weeks or even months for setting up instrumentation and a control system. Therefore, before an actual test is started, the specimens are usually already connected to the loading system. When hydraulic power is turned on to provide pressure to the loading system, the actuators may move to the command position. If the command does not correspond to the actuator initial position at rest, the actuators are likely to have a pulse response to the command position that can in turn cause damage to the test specimens. To avoid such undesired incidences, an auto-balancing feedback technique is developed that provides for safe-start of the control system.

The servo-error, which is the error between the command and the transducer feedback, is one of the indices to evaluate whether the servo-hydraulic system is in an equilibrium state. With certain pressure, the servo-error is constant when the servo-valve spool is in the proper position. After proper mechanical and electrical valve balancing, the servo-error can be adjusted to zero. The auto-balance of servo-valves can be achieved by setting the servo-error to this constant value. Figure 5.16 shows an auto-balance feedback loop implemented in the digital control system developed in this study. Prior to turning on the hydraulic power supply, the auto-balance feedback loop sets the servo-error to the target value. Once all the auto-balance loops converge, the command at the target servo-error is set as the initial command, and control system gets ready to be pressurized. Auto-balancing loops are implemented for all the actuators; therefore, the control system provides a safe start mechanism regardless of the initial position of the actuators, types of specimen, and number of actuators.

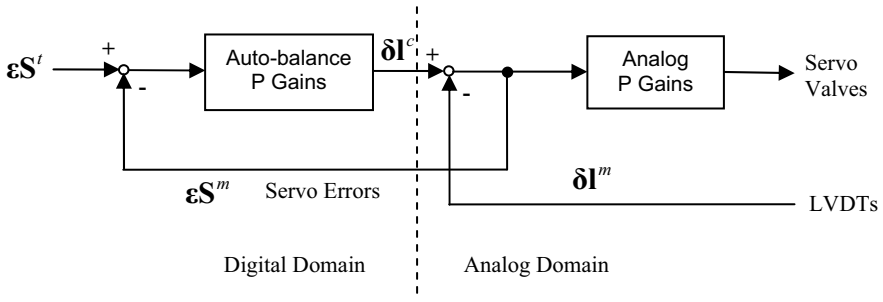

Figure 5.16. Auto-balance feedback loop block diagram.

5.4.2 Digital servo-control software

As a part of this study, digital servo-control software, named the LBCB operation manager, has been built in the process of the development of the various control strategies and for the needs of prospective users. Figure 5.17 shows the graphical user interface of the LBCB operation manager. The LBCB operation manager was written in the National Instruments LabVIEW environment and compiled into an executable application. To enhance its performance, computational processes are incorporated into the LBCB operation manager in the form of a dynamic link library (DLL), in which the programs are written in the C++ programming language. The LBCB operation manager is a multi-threaded programming application that independently handles main, control, monitor, and event-driven processes. The LBCB operation manager provides users with three major panels; settings, control, and monitoring.

Settings in the LBCB operation manager allow flexible configurations for structural testing. It can be configured for the full-scale and $1/5^{th}$-scale LBCBs for both right- and left-handed box configurations. The control point can be set at any point relative to the center of the loading platform so that control and measurements are achieved with respect to the control point. All of the gains and limit settings are also configurable to enhance the performance of the controller and satisfy the safety requirements of each test. In addition to these settings, all of the configurations can be saved in and loaded from configuration files in the HTML format so that multiple users can use the same controller using their own configurations.

The LBCB operation manager incorporates various control loops including auto-balance feedback, digital integrator technique, and mixed load and displacement feedbacks. When the application is launched, it starts with the auto-balance process so that the system ensures a safe-start. Once auto-balancing is achieved, it can be switched to the command feedback that provides several control capabilities, such as manual actuator control, manual Cartesian control, function generator, step-wise ramp generator, etc. All of the control panels grouped in the left top side of the interface are synchronized. Therefore, switching between different control panels can be smoothly performed. Input for the step-wise ramp can be taken from a text file, as well as manual input and network-based remote input.

The LBCB operation manager also provides data acquisition, monitoring, and archiving functions. The monitoring panel located at the bottom of the interface provides several types of data viewers including actuator signal waveform, Cartesian signal waveform, digital numerical data, X-Y plots, and stiffness Jacobian and properties for mixed load and displacement control. The monitoring rate is adjustable independent from the control rate without degrading system performance. The X-Y plots allow monitoring of the step-wise relationship between two signals. Two data archiving schemes are implemented in the LBCB operation manager: continuous and step-wise archiving. Continuous data archiving allows detail diagnostic of the data during the entire test, whereas the step-wise archiving provides data at each step in the event-driven manner. In addition to the default signals including servo-error, LVDT, and load cell, other transducer signals can be sampled, processed, and archived at the same rate.

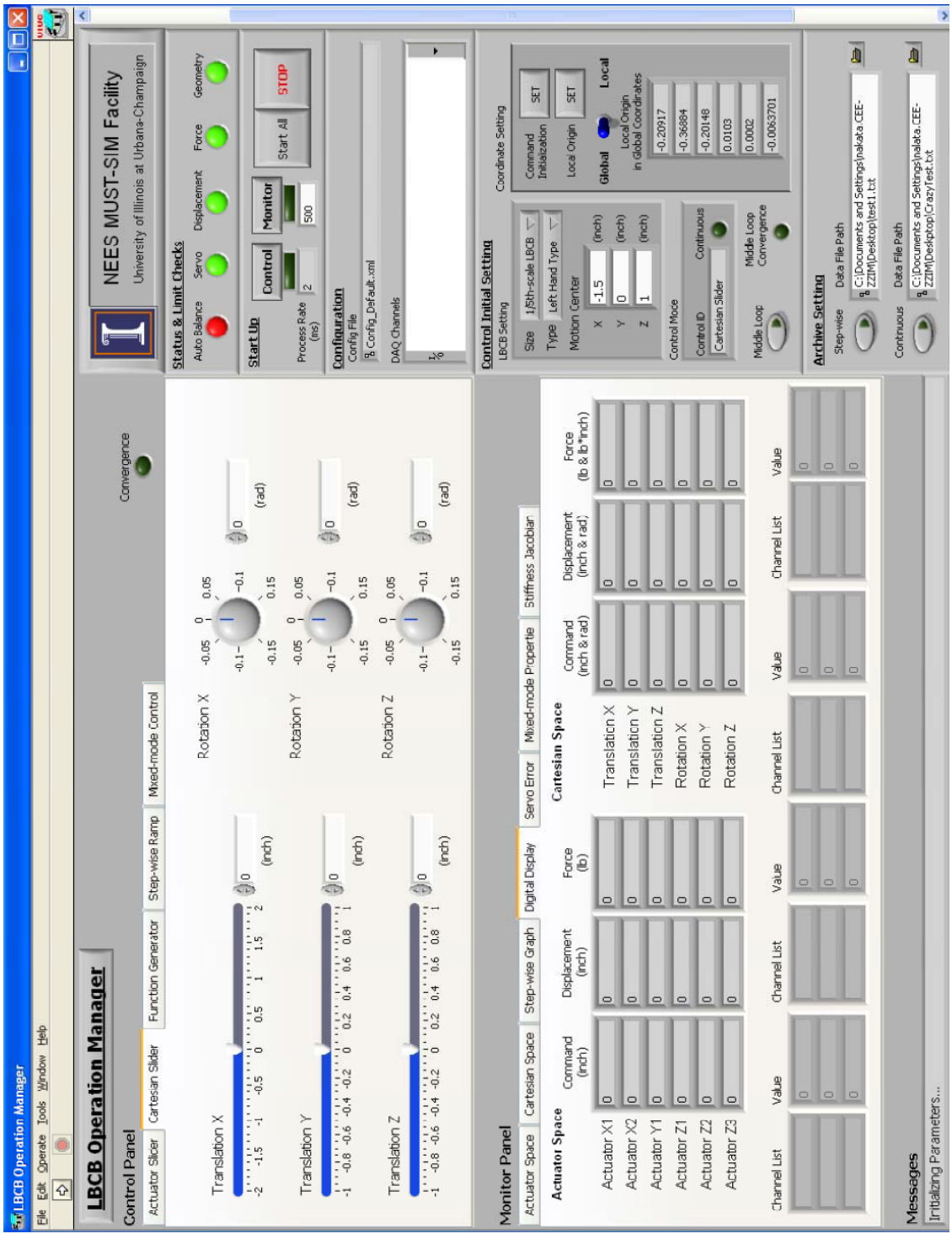

Figure 5.17. Graphical user interface of the LBCB operation manager.

5.4.3 Tele-operation control

Tele-operation remote control is an essential capability in the control system for network-based hybrid simulation. To incorporate an experimental model as a substructure of the system of interest, the control system should be able to handle commands from a remote client and to exchange required data in the simulation. Remote clients can be computational simulation or coordinator of the simulation such as UI-SimCor (Kwon et al. 2005).

Safe execution of the test is the highest priority, regardless of the scale of the testing. Due to the nature of network communication and uncertainty in the incoming commands, direct connection between the remote client and the digital servo-control software is at high risk from system failure that may cause an undesired effect on the loading system. Therefore, a gateway application has been developed to handle the network connection for the digital servo-control software for security reasons. Figure 5.18 shows the graphical user interface of the gateway application for the LBCB operation manager. The gateway application acts as a server for the remote client, and passes only the processed command to the LBCB operation manager. Because the LBCB operation manager does not open ports for communication, it cannot be accessed directly from the outside.

Transactions of the command are processed through the NEES Tele-operation Control Protocol (NTCP). The NTCP is implemented in the gateway application so that any remote client using The NTCP can request the commands to the LBCB operation manger through the gateway application. Table 5.1 lists the command available in the NTCP. The NTCP is currently widely used in the hybrid simulation. However, if there is a need for other communication protocol, it can be implemented in the gateway application without any modification on the LBCB operation manager.

Table 5.1. Commands in the NTCP.

Command	Description
Open Session	Hand shaking and initiate network connection
Close Session	Close session and terminate the network connection
Set Parameter	Set simulation parameter
Get Parameter	Get simulation parameter
Propose	Send the proposed target command
Execute	Request the execution of the proposed target command
Query	Request the measured data
Cancel	Cancel the previous command

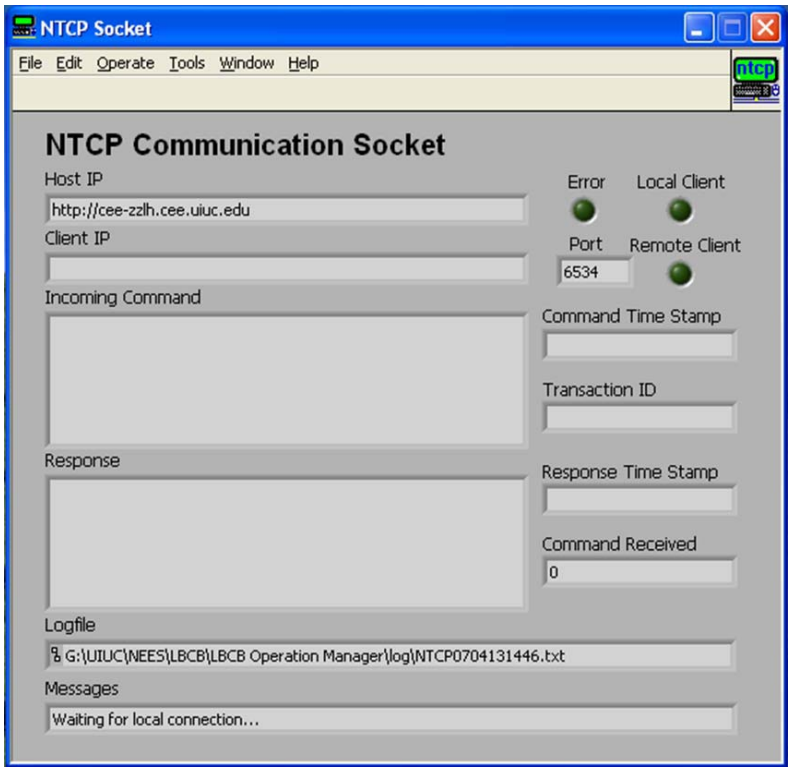

Figure 5.18. Gateway application for the LBCB operation manager.

5.5 Summary

This chapter presented control strategies for the LBCB in hybrid simulation. The digital integrator technique was shown to be effective for improving control accuracy during the experiment. The digital integrator technique presented herein is specifically designed for the ramp-hold loading procedure.

A new mixed load and displacement control strategy was developed for the multi-axial loading system. The control algorithm incorporates the load to displacement conversion using the stiffness Jacobian at every time step. Experimental test results showed that the proposed mixed load and displacement control algorithm works well for complexity of nonlinear responses and loading protocols.

In addition to the development of the control strategies, digital servo-control software was developed that implements these control strategies. The digital servo-control software, referred to as the LBCB operation manager, provides flexible configuration for structural and geometrical tests, and versatile control and monitoring capabilities. The LBCB operation manager developed in this study allows users to perform network-based hybrid simulation using the mixed load and displacement control strategy.

ASSESSMENT OF SKEW BRIDGES

6.1 Introduction

To demonstrate the efficacy of the framework developed in this study for multi-dimensional hybrid simulation, a skew bridge is employed as an application example. Prior to the hybrid simulation, extensive analyses are conducted to study the seismic behavior of skew bridges and to inform selection of the hybrid simulation scenario. Chapters 6 and 7 present these studies.

Highway transportation systems comprise a major part of the nation's civil infrastructures, connecting cities and economies across the entire United States. Among the various highway components and their roles, interchanges are critical parts of a transportation network that govern the serviceability of the highway systems. Highway interchanges generally consist of overpass bridges that maintain the main traffic streams, and one or more ramps that provide smooth transition from one route to another without crossing any other traffic streams. Such overpass bridges at highway interchanges are one of the most common types of bridge in the U.S., and in fact, many mid- and short-span bridges also belong to this class of bridges.

Intersecting highways are not always perpendicular to each other, and many overpass bridges are constructed at skewed angles. According to the summary of the statistics of the National Bridge Inventory (NBI) database (Nielson 2005), 34% of highway bridges have skew angles to some extent. Those bridges with skew angles and associated parallelogram decks are often referred to and categorized as skew bridges (see Figure 6.1).

Figure 6.1. A skew bridge at highway intersection.

Despite the number of skew bridges, the seismic design guidelines for skew bridges, i.e., capacity and demand, in the American Association of State Highway and Transportation Officials, Inc. (AASHTO) is not clearly specified. Although skew bridges have different dynamic characteristics than their straight counterparts, skew angle is not treated as an irregularity in the current design code. If bridges satisfy a criteria for regular bridges (i.e., straight, span length ratio less than 2, and maximum bent/pier stiffness ratio less than 4), then such bridges can be designed as straight bridges using either the uniform load method or the single-mode spectral method, regardless of the skew angle. The specification provides a recommendation to treat skew bridges as irregular structures and to use nonlinear three-dimensional time-history analysis depending on their criticality. However, the decision on the analytical procedure is left to the designers. In addition to these nonrestrictive design guidelines, the lack of understanding of the behavior of skew bridges still leaves large uncertainties in their seismic performance.

Assessing the seismic behavior of skew bridges from both the global and local perspective is important. This chapter provides a literature review of previously conducted skew bridge studies so that gaps in knowledge and needs can be identified. In Section 6.3, a reference skew bridge used in this research is presented in detail. Then, modeling techniques used to capture the global behavior of the reference bridges are described in Section 6.4. A detailed finite element model of the reference bridge is developed and used to assess the effects of skew angle, span length ratio, and varying skew angle on the bridge's modal behavior. Those results are discussed in Section 6.5. Finally, a summary of this chapter is provided.

6.2 Literature Review of Skew Bridge Investigations

Numerous studies have been conducted for the seismic assessment of skew bridges. As a whole, those studies can be classified into the following categories: field surveys, analytical and numerical studies, modeling considerations, and component assessments.

6.2.1 Field surveys

Skew bridges sustain a variety of failures during earthquakes. Limited studies of the seismic performance of skew highway bridges have been reported to date. Jennings (1971) reported the damage of several skew bridges at the Golden State-Foothill freeway interchange area due to the 1971 San Fernando Earthquake [Figure 6.2(a)]. Severe pier damage and substantial abutment and soil movement were observed as a result of the earthquake. Most of the skew bridges tended to suffer permanent displacements in the direction of increasing skewness in this earthquake. Gavin Canyon Undercrossing bridges suffered major damage such that the deck cantilever portion fell onto the roadway below during the 1994 Northridge Earthquake [Figure 6.2(b)]. This damage was largely due to the failure of cable restrainers to limit the superstructure's movement. Schiff (1995) reported that this failure may have resulted from a tendency of highly skew bridges to rotate out of their hinge supports. Yashinsky (1998) summarized the impact of the Loma Prieta earthquake on highway systems including some skew bridges. The Loma Prieta earthquake resulted in some positive changes for highway systems, such as the California

Department of Transportation (Caltrans) Bridge Seismic Retrofit Program to upgrade the seismic performance of the nation's highways (J. Robert 1994).

(a) Foothill Boulevard Undercrossing (b) Gavin Canyon Undercrossing

Figure 6.2. Damage of skew bridges.

In the 1995 Kobe Earthquake, two skew highway RC bridges, the Mukogawa and Kawaraginishi, suffered severe damage. Abutment bearing failure, restrainer failure, bent flexural damage, and shear failure of the piers were observed, resulting in the collapse of the superstructure (Schiff 1995). Kawashima et al. (1997) summarized the damage features of highway bridges as a result of this earthquake, and described a series of actions that were taken for seismic design and seismic strengthening of highway bridges. The Arifiye over-crossing suffered severe damage due to the 1999 Kocaeli Earthquake in Turkey. This skew bridge collapsed because of the fault rapture between the north abutment and the first pier. The fault movement pulled the north abutment and dropped the first span, resulting in the south end of the other three spans falling off their supports (Tang 2000).

Field survey data for skew bridges are important sources of performance evaluation; however, the effect of the skew angle on the failure cannot be evaluated only from the seismic reconnaissance data. Further assessment is essential to improve the understanding of skew bridge behavior.

6.2.2 Analytical and numerical studies

Based on earthquake reports and field surveys, some researchers conducted analytical and numerical studies to understand the cause of skew bridge failures. For example, several studies were carried out for the Foothill Boulevard undercrossing, a skew bridge that suffered severe RC pier damage due to the San Fernando Earthquake. Ghobarah (1974) analyzed the failure mechanism and concluded that the failure was attributed to the coupled flexural and torsional motions of the bridge deck that led to

compression failures of the columns. However, Wakefield et al. (1991), using a simplified beam model and a build-up plate model, concluded that if the deck is not rigidly connected to the abutments dynamic response of the bridge was dominated by in-plane rigid body motion of the deck rather than by flexural and torsional modes. Meng et al. (2000) also studied the failure mechanism of the same bridge using an elastic deck model and presented the conclusion that deck flexibility induced axial forces to the columns and inadequate shear strength in the columns was the major cause of the failure.

As reviewed above, forensic assessment of the failure mechanisms can vary widely. This fact is a clear indication that thorough and comprehensive studies are necessary for seismic assessment of skew bridges and that special care is needed to assess possible failure mechanisms.

6.2.3 Modeling consideration

One of the most important aspects of skew bridge studies is the modeling approach. Various types of models have been developed, analyzed, and validated. Modeling techniques reviewed here include only those used for the seismic evaluation or equivalent for skew bridges. Maragakis et al. (1987) developed a rigid bar model for the bridge deck with spring elements at piers and abutments to capture the kinematics features of rigid body motions of skew bridges. Planar rigid body rotations of decks are induced primarily as a result of deck skewness and the impact between deck and abutment. Maleki (2000) employed a rigid deck model for concrete decks considering the elastomeric bearing stiffness to determine periods of vibration. The researcher derived equations for determination of translational and in-plane rotational (yaw of the bridge) periods of vibration of a symmetric skew bridge. Meng et al. (2002) proposed a refined dual-beam stick model to represent torsional flexibility of the deck (roll of the bridge) and compared the vibration modes and natural frequencies with those from a finite element model using detailed meshed shell elements. Continuous differential equation models (Alfawakhiri et al. 2000; Ghobarah et al. 1974) are also used for bridge deck modeling. Finite element models including beam, brick, and shell elements have been used by numerous researchers to validate their modeling techniques (Maleki 2002; Meng et al. 2000, 2002; Wakefield et al. 1991).

At present, most commercial finite element programs are capable of including nonlinear material and geometric properties in static and dynamic analysis (Kankam 1995; McCallen 1994). Some researchers have employed experimental data in skew bridge studies. Ebeido et al. (1996) reported laboratory-scale experimental results of a skew bridge in comparison with the AASHTO specification. Huang et al. (2004) applied field measurement techniques in a skew bridge study to establish an analytical model based on the measured data. However, these investigations were aimed at determining the load distribution factor and not for seismic specification. Experimental study of seismic related issues for skew bridges was reported by Meng et al. (2004). Those researchers constructed a 1/6th-scale steel skew bridge deck model and conducted static and dynamic tests. Finite element and dual-beam models were calibrated based on the experimental data, and then natural frequencies and modal of those models were compared with their experimental counterparts.

In general, laboratory testing and finite element models are used to provide the reference model in a global sense to calibrate or validate other modeling approaches. For the investigation of the seismic performance of skew bridges, modeling of critical members at the component level needs to be also considered to capture local behavior that may govern bridge failure.

6.2.4 Component assessments

Rigorous studies related to seismic assessment of bridge components have been conducted. Elnashai et al. (1996) investigated the effect of deck, pile, and soil structure interaction on concrete bridge pier performance and showed that the modeling assumption and the boundary conditions significantly affected the overall behavior of concrete bridge piers. Tirashit et al. (2005) conducted a series of RC pier tests to evaluate the effect of interaction between bending and torsion that is likely to happen in skew bridges. Their experimental results clearly showed that the combined flexural and torsional loadings significantly affect the performance of reinforced concrete columns. Saiidi et al. (2001) evaluated the existing restrainer design method recommended by AASHTO and Caltrans and proposed new restrainer design methods considering the skewness of the bridge deck. Watanabe et al. (2004) analyzed the effect of pounding and three types of cable restrainers for skew bridges to mitigate deck rotation. Robson et al. (2001) evaluated the effectiveness of seismic isolation of the superstructure from the substructure of highly skew bridge. The maximum pier moment and shear of a skew bridge can be reduced by the seismic isolation.

Component level assessment is essential to investigate bridge behavior under severe seismic loading. However, those assessments are usually conducted independent of the system behavior or with simplified modeling for the rest of the structure. The behavior and performance of components are highly dependent on the interaction with adjacent members. Therefore, system level assessment taking into account member interaction is required for the seismic behavior and performance of components.

6.3 Selection of a Reference Skew Bridge

Design Example No. 4 (FHWA No. 4 bridge) in the FHWA's Seismic Design of Bridges (FHWA 1996) is selected for this study. This bridge is a 97.54 m-long three-span bridge. Span lengths are symmetric with respect to the center of bridge, and middle and side span lengths are 36.58 and 30.48 m, respectively. The bridge has a skew angle of 30° at the bents and abutments. Figures 6.3 and 6.4 show the plan and elevation views, respectively, for the FHWA No. 4 bridge.

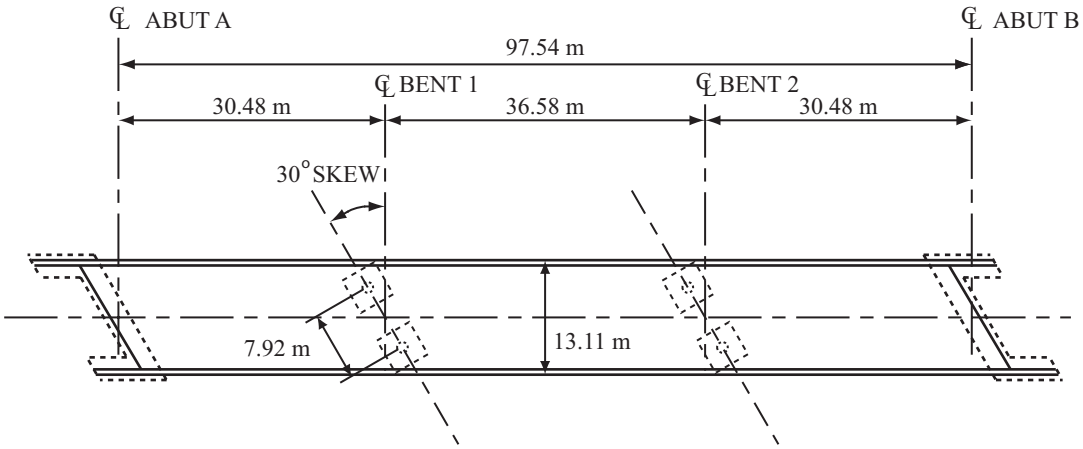

Figure 6.3. The plan view of the FHWA No. 4 bridge (Courtesy of the FHWA).

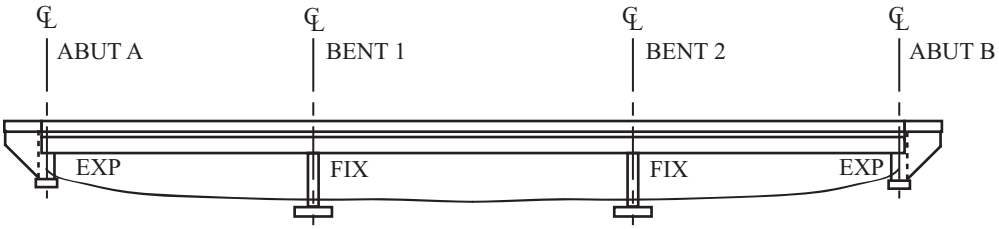

Figure 6.4. The elevation view of the FHWA No. 4 bridge (Courtesy of the FHWA).

The superstructure is a cast-in-place, continuous concrete box girder deck with two interior webs. Figure 6.5 shows the section view of the intermediate bent. The intermediate bents consist of a cap beam integrated in the box girder and two circular reinforced concrete piers. Because of the integrated cap beam, the connection between girder and piers is rigidly fixed. Pier supports are square-shaped spread footing foundations.

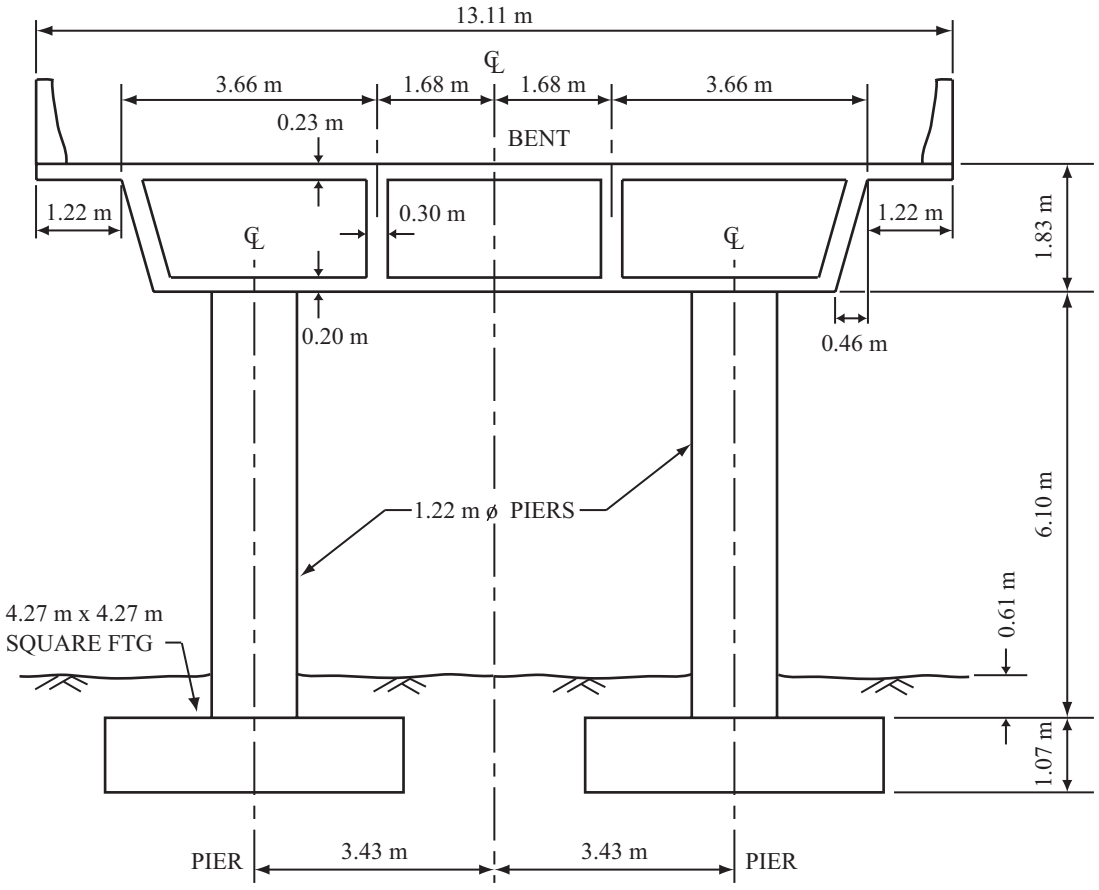

Figure 6.5. The section view of the FHWA No. 4 bridge (Courtesy of the FHWA).

The interface between the pier and footing is designed to be a pin connection using the Caltrans approach. However, the pier and footing connection is changed to be fixed in the following study so that the bridge has shorter vibration periods that respond to the majority of earthquake input motions.

Seat-type abutments on the spread footings are used with shear keys and bearings. Figure 6.6 (a) and (b) show the cross-sectional views of abutment in a direction parallel to the bents and parallel to the bridge center line, respectively. Longitudinal seismic loads in the deck are transferred to the abutment through elastomeric bearing and then resisted by soil pressure behind the back wall. Figure 6.7 shows the wingwall elevation view. Wingwalls transfer resistance soil pressure to the seismic loads in the transverse direction. Figure 6.8 shows the framing plan for the box girder superstructure. The end diaphragm and cap beam widths are 1.07 and 1.52 m, respectively. An intermediate diaphragm of 0.23 m width is used at the middle line of each span.

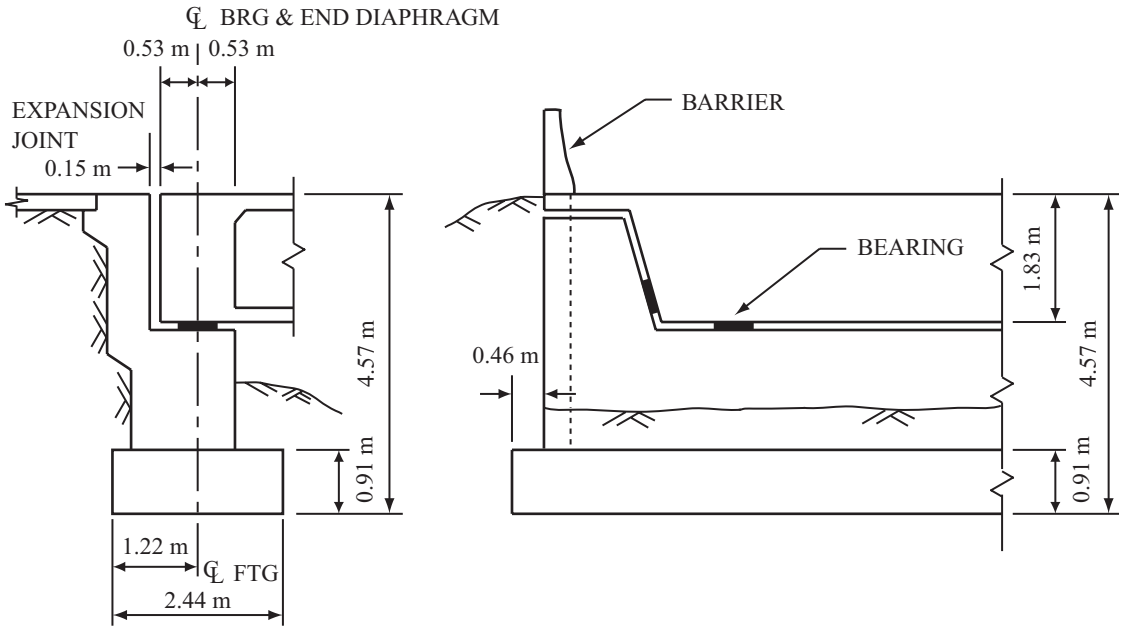

(a) Section View
(Looking parallel to bents)

(b) Section View
(Looking parallel to the bridge center line)

Figure 6.6. The abutment section view of the FHWA No. 4 bridge (Courtesy of the FHWA).

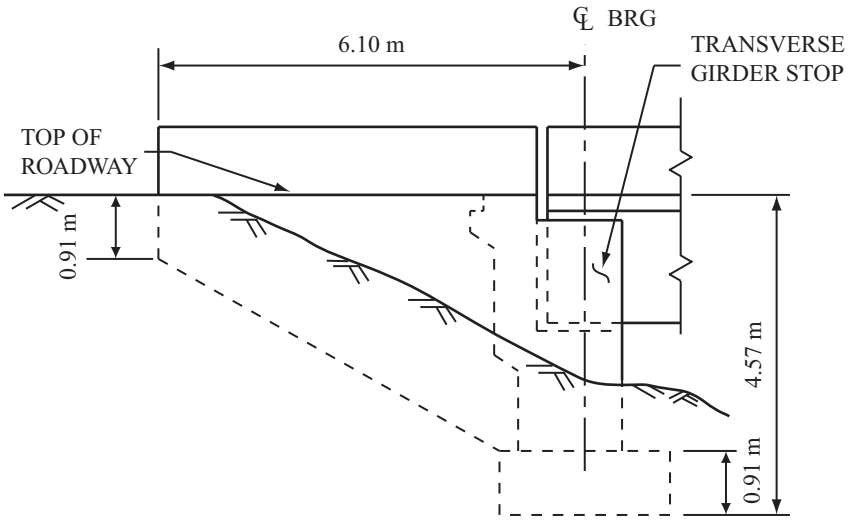

Figure 6.7. The wingwall elevation view of the FHWA No. 4 bridge (Courtesy of the FHWA).

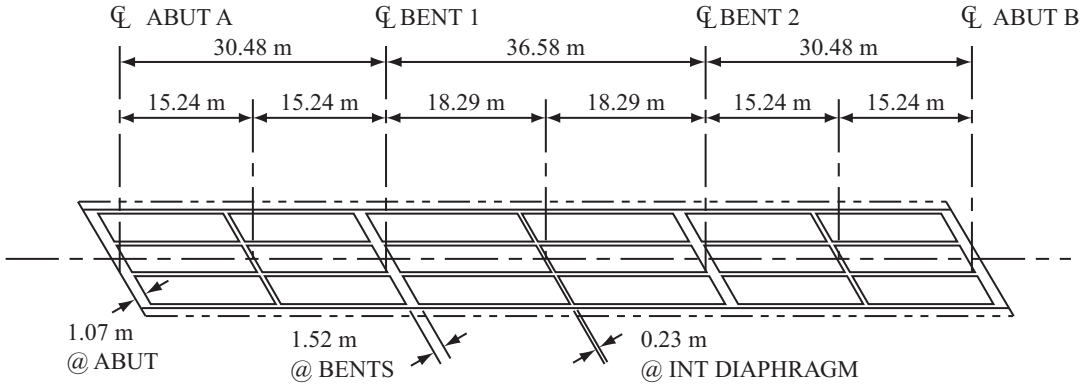

Figure 6.8. The framing plan of the FHWA No. 4 bridge (Courtesy of the FHWA).

Despite the skew angle, the FHWA No. 4 bridge belongs to the category of regular bridges, because it is straight, the maximum span-length ratio is less than 2, the maximum bent/pier stiffness ratio is less than 4, and the bridge is not critical. The minimum analysis required by the code is either the uniform load method or the single-mode spectral method. The multimode spectral method or the time-history method may be used in lieu of the former methods, but is not required. The FHWA No. 4 bridge can be seen as a typical multi-span, continuous concrete box girder bridge in the sense that the number of spans, maximum span length, deck width, and bent and abutment types fall within the majority of the class.

6.4 Modeling of the Reference Skew Bridge

The natural frequencies and mode shapes are some of the most important dynamic characteristics of a bridge, providing insight into global behavior of the structure. Improper assessment of the natural frequencies may yield erroneous estimates of the seismic behavior, capacity, and even failure mode of the structure. Therefore, the natural frequencies need to be properly evaluated for both the design and assessment processes. To accurately capture the effect of the skew angle on the fundamental natural frequencies and mode shapes, a finite element model is employed in the following modal analysis. For modeling and analysis, finite element software, DIANA (TNO DIANA 2002), is used.

6.4.1 Superstructure and bents

One of the distinct differences between straight and skew bridges is the shape of the deck (from the plan view): rectangle or parallelogram. To investigate the effect of skewness on global bridge behavior, the geometry in the superstructure should be properly modeled. For this purpose, the cross-section of the deck and framing plan, including internal webs and intermediate diaphragms, are taken into account in the

modeling, as shown in Figure 6.9. Considering the aspect ratios, the top and bottom deck plates, web geometry, and intermediate diaphragms are modeled using flat shell elements. End diaphragms and bents components, including cap beams, piers, and footings, are modeled using solid elements.

The material properties for the model are summarized in Table 6.1. Because the objective of this model is for modal analysis which is a linear analysis, elastic Young's modulus of concrete, 2.5×10^7 kN, is used for the entire model. In addition to the weight of the structural elements, dead loads of 34.3 kN per lineal meter of the superstructure, which are from traffic barriers and wearing surface overlay, are incorporated in the density of the bridge deck.

Figure 6.10 shows a finite element mesh of the FHWA No. 4 bridge model. The mesh size for the model is determined based on the convergence of the natural frequencies and computational time. The maximum aspect ratio of the shell elements is 1.24, and the total number of the nodes and elements are 5,314 and 11,747, respectively.

Table 6.1. Material properties of the FHWA No.4 bridge.

	Superstructure deck	Bents Cap beams, piers and footings
Young's Modulus (kN/m^2)	2.482×10^7	2.482×10^7
Density (kN/m^3)	2.915×10^3	2.403×10^3

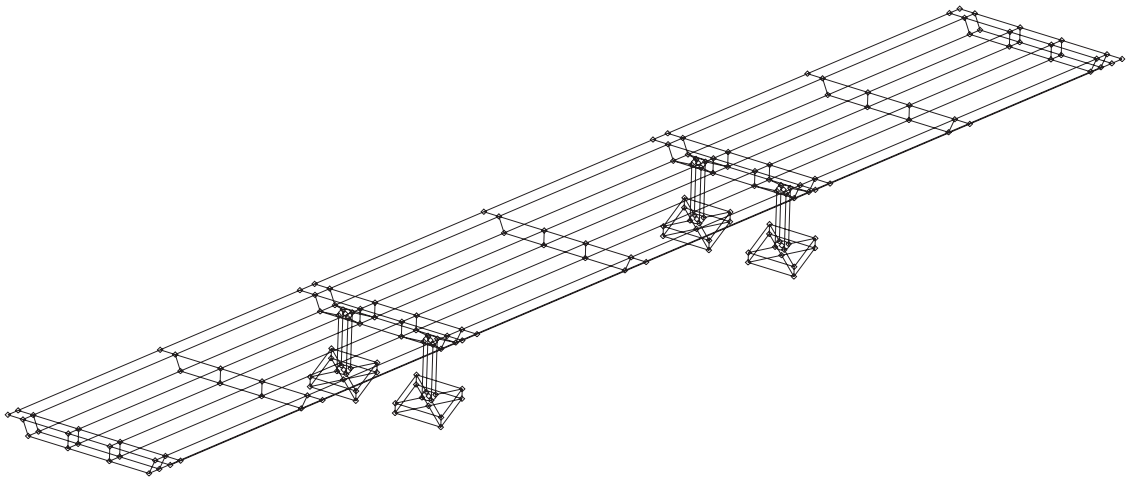

Figure 6.9. Finite element model of the FHWA No.4 bridge.

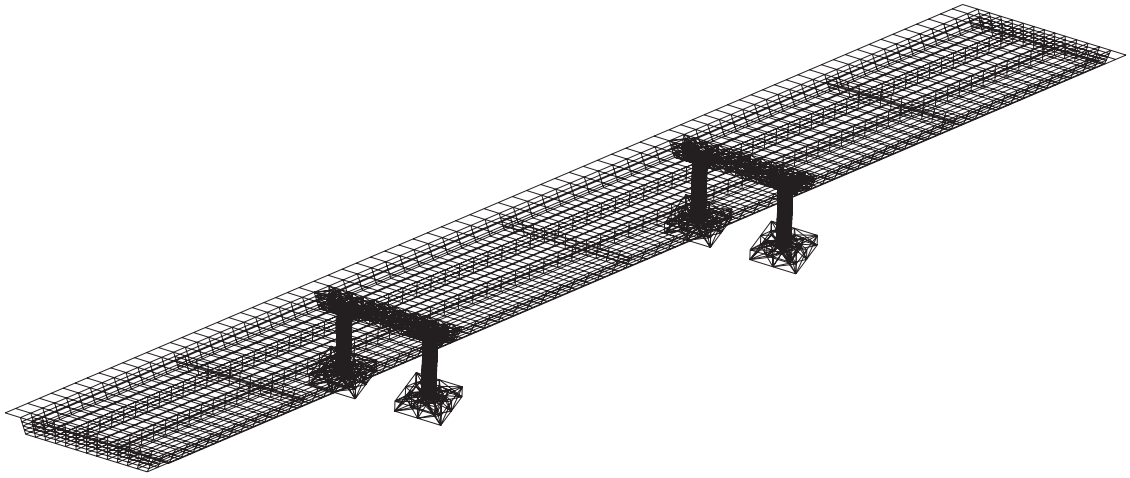

Figure 6.10. Finite element mesh of the FHWA No.4 bridge.

6.4.2 Abutments

The abutments not only provide vertical support for the superstructure, but also resist lateral loads at the ends of the bridge deck. Modeling of the abutments dictates the boundary conditions for the superstructure model and governs the overall behavior of the bridge structure. Needless to say, the abutments need to be carefully modeled.

As shown in Figure 6.6, the abutments for the FHWA No. 4 bridge are U-shaped, gravity-type with wingwalls. In the longitudinal direction, the expansion joint is provided to allow for expected seismic design displacements, and elastomeric bearings are used at the connection between the superstructure and abutment [see Figure 6.6 (a)]. So long as the deck displacement is less than the expansion joint gap, the forces developed in the longitudinal direction at the end of the deck are only due to the bearing stiffness.

Therefore, spring elements with the initial bearing stiffness are used at the ends of the deck for modeling of the abutment in the longitudinal direction in the following modal analysis. The spring element k_e in Figure 6.11 represents the elastomeric bearing in the longitudinal direction. An initial bearing stiffness of 3.4×10^3 kN/m, obtained for typical elastomeric bearing for concrete bridges (Nielson 2005), is adopted in this study.

The superstructure is restrained against translation in the transverse direction at the abutment by the girder stops on both side of the bridge (see Figure 6.6). Forces in the transverse direction at the abutments are transferred through a girder stop and resisted by soil pressure against the abutments and wingwalls. The Caltrans simple approach (1999) is used herein to determine the translational spring stiffness in the transverse direction; an initial compressive soil stiffness of 2.0×10^4 kN/m/m is multiplied by the wingwall length of 6.1 m and a reduction factor of 2/3. The property of 2.0×10^4 kN/m/m is a medium value in the Caltrans recommendations ranging, which is from 1.2×10^4 kN/m/m to 2.9×10^4 kN/m/m. A calculated effective soil stiffness of 1.2×10^5 kN/m is only for the compressive direction at one side of the deck. Therefore, the effective stiffness is equally divided into half at the support locations at the side of the deck. The spring element k_w in Figure 6.11 represents the transverse stiffness of the soil. Note that the direction of the soil spring element is in the transverse direction regardless of the skew angle.

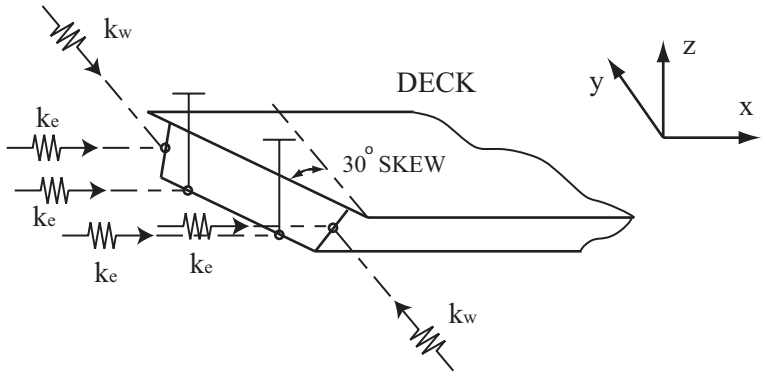

Figure 6.11. Spring elements at expansion joint.

The superstructure is fully restrained against vertical translation and deck torsional rotation (roll of the bridge) at the abutment, because of the gravity contact forces between the deck and the bearings, as well as the significant moment arm between the bearings (see Figure 6.11). Nonlinear characteristics such as deck pounding and bearing elasto-plastic behavior are discussed for seismic analysis of the bridge in the next chapter.

6.4.3 Bent foundations

Modeling of the soil and foundations is a complex problem. Soil stiffness is often simplified and modeled as linear springs for static, modal, and even seismic analyses. According to the FHWA design example (1997), any reasonable estimate of foundation stiffness will produce satisfactory results. Because discussion on the modeling of the soil

foundation is beyond the scope of this study, spring constants calculated in the FHWA design example are simply used here. In the FHWA design example, the elastic half-space method is employed with the equivalent radii for the footing. Values obtained using an elastic half-space approach are listed in Table 6.2. The definition of the spring directions is shown in Figure 6.12. For more detail regarding the elastic half-space method, see *the FHWA, Seismic Design and Retrofit Manual for Highway Bridges (1997).*

Table 6.2. Spring constants of the soil foundation.

	Direction	Stiffness
$k_{11}(kN/m)$	Translation, x-axis	1.503×10^{6}
$k_{22}(kN/m)$	Translation, y-axis	1.503×10^{6}
$k_{33}(kN/m)$	Translation, z-axis	1.377×10^{6}
$k_{44}(kN\cdot m/rad)$	Rotation, x-axis	9.653×10^{6}
$k_{55}(kN\cdot m/rad)$	Rotation, y-axis	9.653×10^{6}
$k_{66}(kN\cdot m/rad)$	Rotation, z-axis	1.559×10^{7}

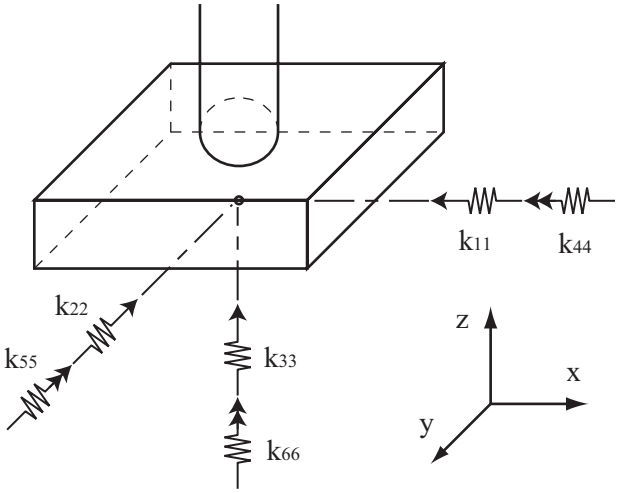

Figure 6.12. Spring elements at soil foundation.

6.5 Assessment of the Global Bridge Behavior

Conventional bridge design and analysis employ a decoupling approach where the bridge longitudinal and transverse directional responses are considered independently. One of the key factors that distinguish skew bridges from straight bridges is coupling among multiple directional responses (e.g., longitudinal and transverse) in each mode

shape. Any eccentricity in mass and stiffness can cause various coupling among multiple directional responses.

In this section, using the finite element model, modal analysis is carried out with focus placed on the effect of skew angle on the natural frequencies and mode shapes. In addition to the effect of the skew angle, effects of span ratio configuration in skew bridge and skew angle variation in a bridge are also investigated as possible sources of eccentricity.

6.5.1 Effect of the skew angle

At first, the effect of the skew angle is investigated. The skew angle is taken as a parameter ranging from 0° to 60° at each 15° increment (i.e., $\theta = 0^\circ$, 15°, 30°, 45°, and 60°). Note that a skew angle of 0° corresponds to a straight bridge. In the following parametric study, all of the geometric and material properties remain the same except the skew angle.

Figure 6.13 shows the first six mode shapes at straight and skew angle 30° cases as examples. Principle directions of the first three modes are longitudinal, transverse, and in-plane rotational (yaw of the bridge) modes, respectively; the fourth to sixth modes correspond to deck bending modes. The order of the mode types are the same for the rest of the cases, 15°, 45°, and 60°. However, there is discrepancy in mode shapes between straight and skew bridges. In the straight bridge case, all of the mode shapes are distinct such that the first mode is in the pure longitudinal direction and the second mode is in the pure transverse direction, and so on. On the other hand, in the skew bridge cases, each mode shape consists of multiple directional responses to some extent. For example, though it is difficult to observe from the plot, the first mode contains not only longitudinal, but also transverse directions. Similarly, the second mode contains both longitudinal and transverse responses. In other words, the deformation direction of the first mode is between the bridge longitudinal and skew longitudinal directions. The bridge longitudinal and the skew longitudinal directions are defined as being parallel to the bridge center line and the normal to the bent center line, respectively. Similarly, the deformation direction of the second mode is between the bridge transverse and the skew transverse directions. The bridge transverse and the skew transverse directions are normal to the bridge center line and parallel to the bent center line, respectively. These differences in the deformation direction of the mode shapes are due to the coupling of longitudinal and transverse responses resulting from the skew angle. Higher modes have more complex coupling among directional responses such as deck in-plane rotational (yaw of the bridge) and bending directions. The mode shapes for the other skew angles are shown in Appendix C.

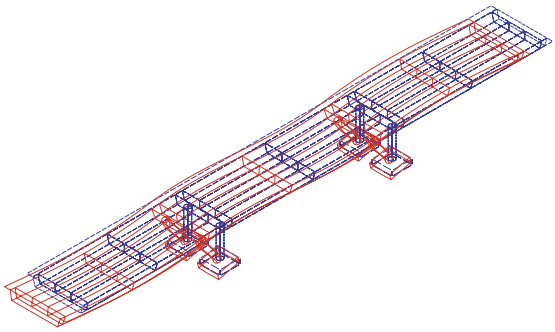

(a) Straight case $\left(f_1 = 1.97 \text{ Hz}\right)$

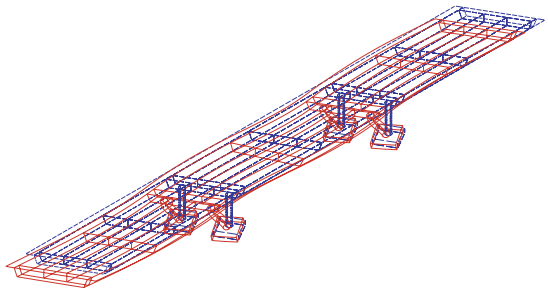

(b) Skew 30° case $\left(f_1 = 1.99 \text{ Hz}\right)$

1st mode (Longitudinal)

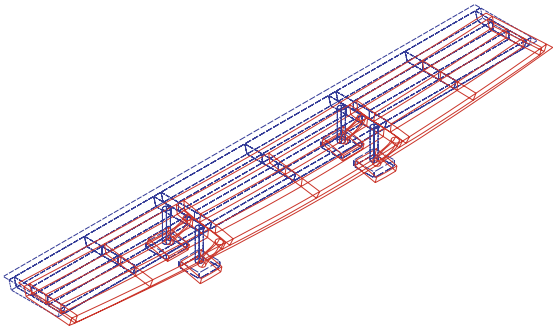

(c) Straight case $\left(f_2 = 2.42 \text{ Hz}\right)$

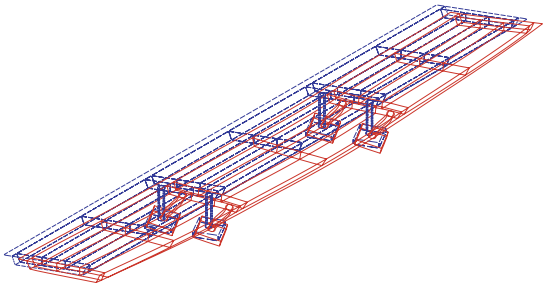

(d) Skew 30° case $\left(f_2 = 2.41 \text{ Hz}\right)$

2nd mode (Longitudinal)

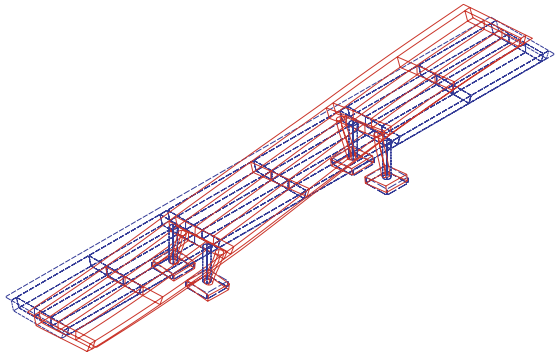

(e) Straight case $\left(f_3 = 2.99 \text{ Hz}\right)$

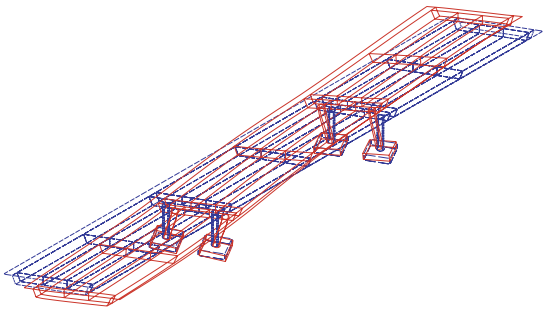

(f) Skew 30° case $\left(f_3 = 2.96 \text{ Hz}\right)$

3rd mode (Rotational)

Figure 6.13. Fundamental mode shapes.

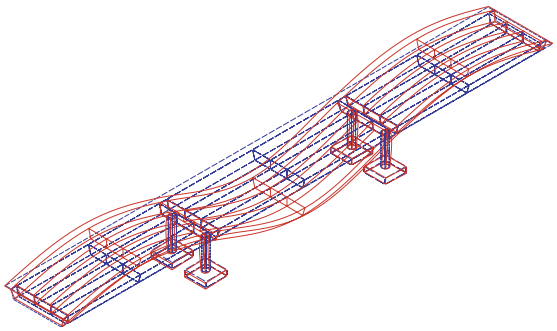

(g) Straight case $\left(f_4 = 3.09 \text{ Hz}\right)$

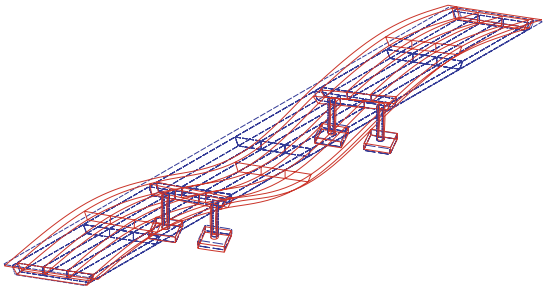

(h) Skew 30° case $\left(f_4 = 3.34 \text{ Hz}\right)$

4^{th} mode (Bending)

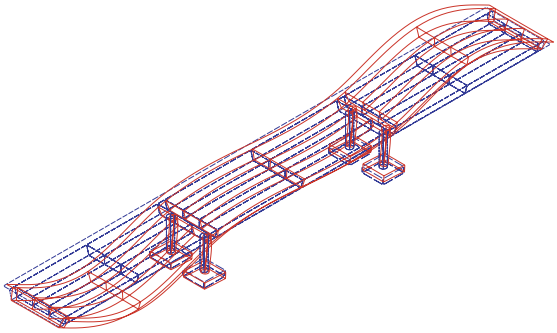

(i) Straight case $\left(f_5 = 4.00 \text{ Hz}\right)$

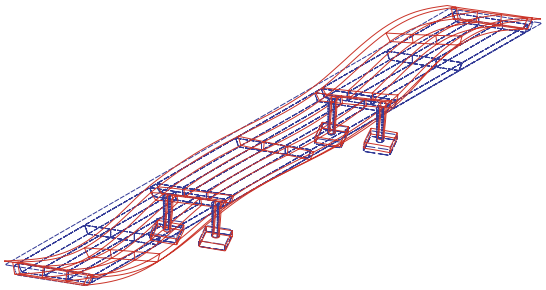

(j) Skew 30° case $\left(f_5 = 4.21 \text{ Hz}\right)$

5^{th} mode (Bending)

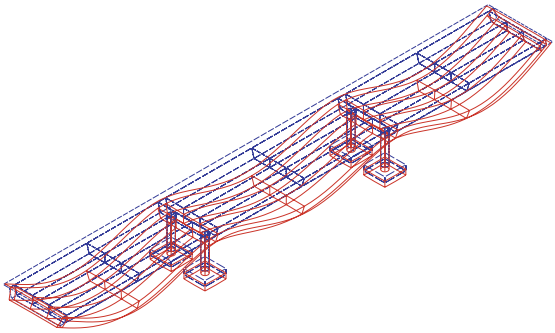

(k) Straight case $\left(f_6 = 4.47 \text{ Hz}\right)$

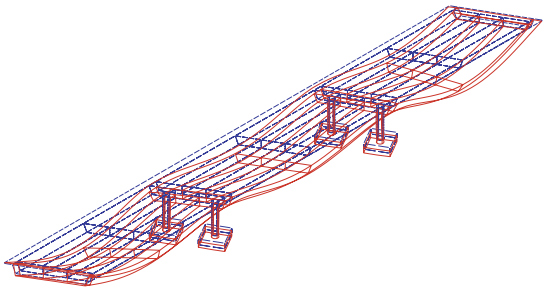

(l) Skew 30° case $\left(f_6 = 4.59 \text{ Hz}\right)$

6^{th} mode (Bending)

Figure 6.13. Fundamental mode shapes (Continued).

Figure 6.14 shows the relationships between each modal frequency and skew angle for the first six modes. The longitudinal frequency tends to increase, and the transverse frequency tends to decrease as the skew angle becomes larger. This effect is due to the increase in coupling between longitudinal and transverse directions with the skew angle. However, the overall changes in the first three fundamental frequencies are small. On the other hand, the frequencies of the bending modes increase significantly as the skew angle increases. These effects are considered to be a result of the changes in the deck boundary conditions due to the skew angle.

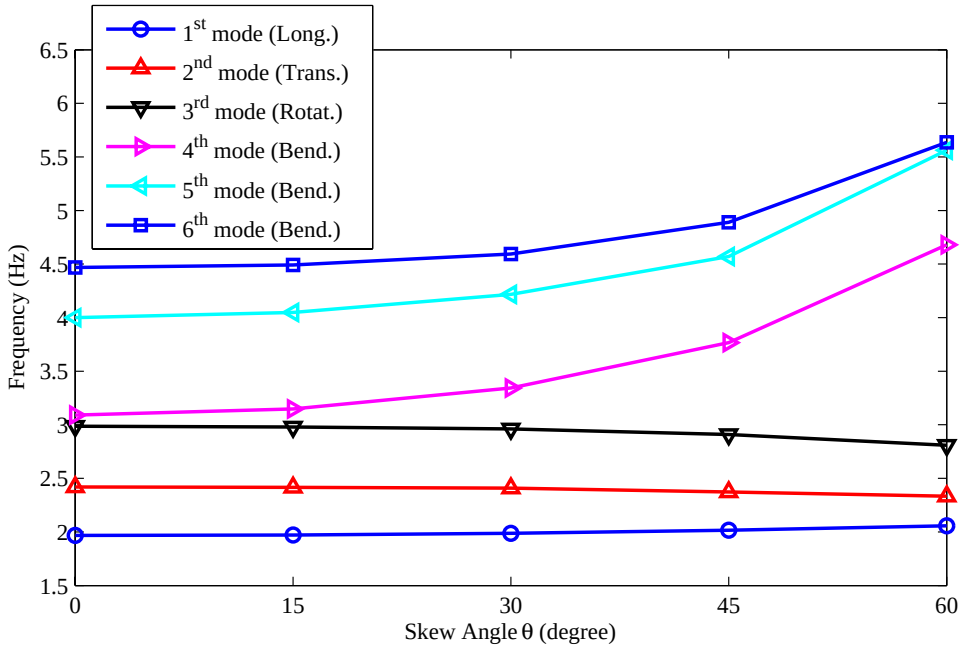

Figure 6.14. Effect of skew angle on the fundamental natural frequencies.

Based on the observation here, the effect of the skew angle is summarized as follows. In terms of natural frequencies, the effect of the skew angle is negligible for modest skew bridges, especially for those with a rigid deck in which bending modes are insignificant. For example, short span bridges with a skew angle of less than 30° have almost the same fundamental natural frequencies as the straight-bridge counterpart. If the bridges have a flexible deck, such as long span bridges, the bending natural frequencies are higher than those of straight bridge with the same geometric and material properties. However, as seen in the mode shapes, skew bridges tend to have coupling among multiple directional responses as the skew angle increases. In other words, the conventional decoupling approach where the bridge longitudinal and transverse directional responses are analyzed independently may not be appropriate for skew bridges. Further investigations for skew bridges need to be carried out with careful attention to modeling of skew angle.

6.5.2 Effect of the span length ratio

Span length ratios of the mid span to the end spans in the FHWA No. 4 bridge are both 1.2. Therefore, the locations for the bent are symmetric with respect to the mid point of the bridge. However, not all highway bridges have symmetric span ratio configurations. Again, any eccentricity in mass or stiffness causes coupling among multi-directional responses in the vibration modes (e.g., longitudinal and transverse response coupling). An asymmetric span ratio configuration is an additional source that may introduce eccentricity that results in coupled responses. In this section, the effect of the span ratio configuration with skew angle on the bridge behavior is investigated.

Both straight and skew bridges with different span length ratios are modeled using the finite element approach. The number of spans and total bridge length are fixed to those found in FHWA No. 4 bridge. Because the end spans are normally shorter than the mid spans in most bridges, span configurations with shorter end spans are considered in this study. AASHTO Division I-A (1995) defined a span length ratio that is less than 2.0 as one of the criteria for regular bridge. Therefore, the span length ratio of 2.0 is set to the upper limit of the parameter. Figure 6.15 shows six selected parametric models with different span ratio configurations. The *X* and *Y* axes are the span length ratios of mid span to the right-side and the left-side end spans, respectively. Three models, SR1.2-1.2, SR1.6-1.6, and SR2.0-2.0 have symmetric span ratio configurations, whereas the others, SR1.2-1.6, SR1.6-2.0, and SR1.2-2.0 have asymmetric span ratio configuration.

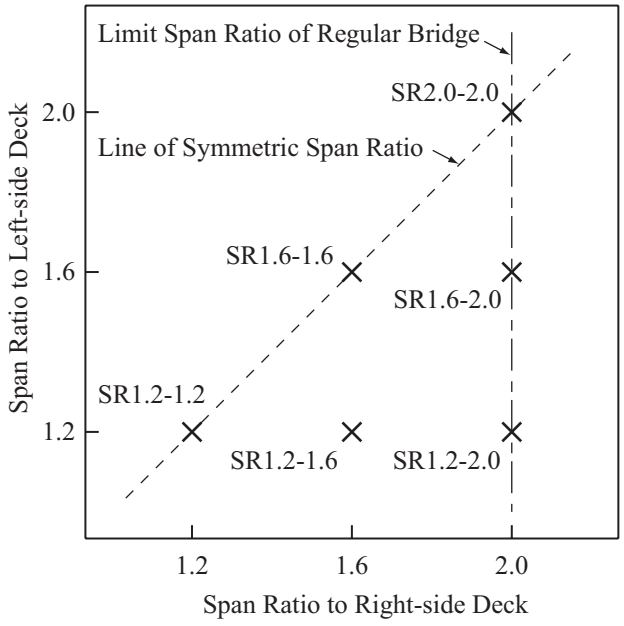

Figure 6.15. Span length configurations.

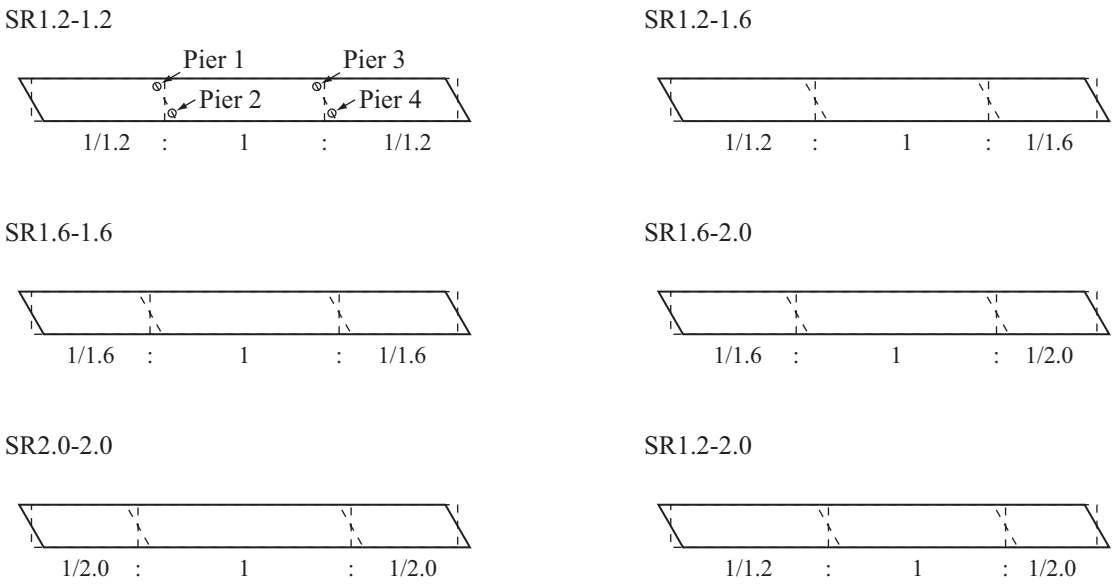

Figure 6.16. Layout of the span length configurations.

Figure 6.16 shows the plan views for each parametric model. For each span ratio configuration model, straight and skew 30° cases are considered. Bridges with symmetric span ratio configurations have the same span length at the end spans. On the other hand, bridges with asymmetric span ration configurations have different end span lengths. Piers are identified for assessment of the coupling effect as follows: Piers 1 and 2 are in the left side bent, and Piers 3 and 4 are in the right side bent. In the skew configuration, Piers 1 and 4 are on the obtuse side of the end span, whereas Piers 2 and 3 are on the acute side of the end span.

Modal analysis is carried out for 12 parametric models, i.e., straight and skew cases for 6 span ratio configurations. Figure 6.17 shows the relationships between the natural frequencies for the first four modes. For associated mode shapes, see Appendix C. As expected, the longitudinal and transverse modal frequencies hardly change, regardless of span ratio and skew angle. On the other hand, there is a tendency that bridges with longer mid-spans have higher in-plane rotational (yaw of the bridge) and lower bending frequencies. The effect of the skew angle is distinct at each mode type: For the skew bridge, the longitudinal and bending mode frequencies tend to become larger, while the transverse and rotational mode frequencies tend to become lower. As in the previous section, the effect of the skew angle is most significant on the bending natural frequency in the first four vibration modes. In general, the natural frequencies are not affected by the span length ratio configuration and skew angle.

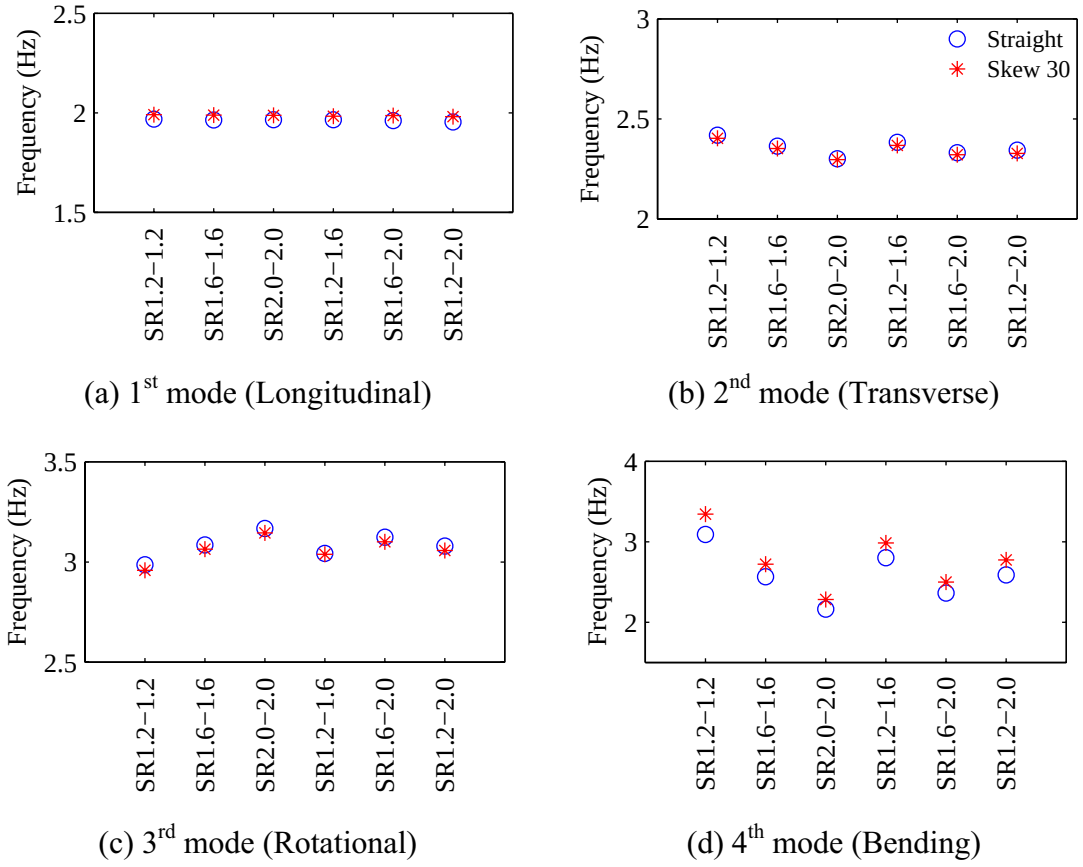

(a) 1st mode (Longitudinal) (b) 2nd mode (Transverse)

(c) 3rd mode (Rotational) (d) 4th mode (Bending)

Figure 6.17. Effect of span length ratio configuration on the natural frequencies.

In addition to considering the natural frequencies as an indicator of the global behavior, the coupling responses in the vibration modes are evaluated at the local level. As one of the coupling indices, the relative displacements at the piers are considered. The relative displacement here is defined as the difference between the top and bottom displacements. Because soil and footing displacements are not considered, the relative displacement can be seen as the actual deformation pattern subjected to the pier in the mode of interest. Figure 6.18 (a) shows the longitudinal to transverse (L/T) displacement ratios in the transverse mode in all the parametric models. The location of the bridge piers corresponds to the ones in Figure 6.16. For the case of symmetric span ratios with straight configurations (i.e., no skewness), the L/T ratios in the transverse mode for all the four piers are almost the same. On the other hand, in the symmetric span ratio case with nonzero skewness, the L/T ratios on the acute side of the mid-span (i.e., Piers 1 and 4) are much higher than those at the obtuse side of the mid-span (i.e., Piers 2 and 3). In the asymmetric span ratio case with straight configurations, the L/T ratios at the longer side of the end span (i.e., Piers 1 and 2) are smaller than those at the shorter side of the end span (i.e., Piers 3 and 4). In the asymmetric span ratio case with nonzero skewness, the L/T ratios have some scatter, and the ratio at Pier 4, which is on the obtuse side of the shorter end span, is much higher than those at the other piers.

Figure 6.18 (b) shows the in-plane rotational (yaw of the bridge) to transverse (Y/T) displacement ratios in the same transverse mode. The same trend can be seen in the Y/T ratios. Note that regardless of the span ratio configurations, the coupling effect on the pier in the same bent is almost the same as in the straight case. On the other hand, the coupling effect varies in the skew case, even in the same bent. As a summary, asymmetry in the span ratio configuration affects the coupling responses at the bent level. In addition, if the bridge is skewed, the coupling effects vary at each pier, depending on the location. Based on the study here, the pier on the obtuse side of the shorter end span tends to be subjected to higher coupling effect than the other piers.

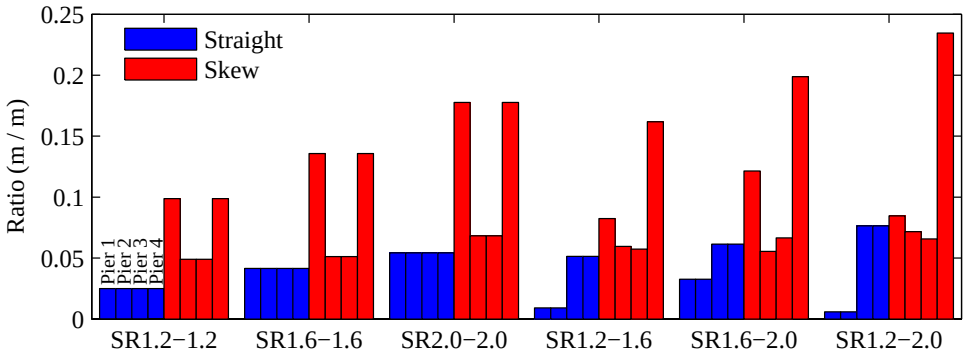

(a) Longitudinal/Transverse (L/T) ratio in the transverse mode.

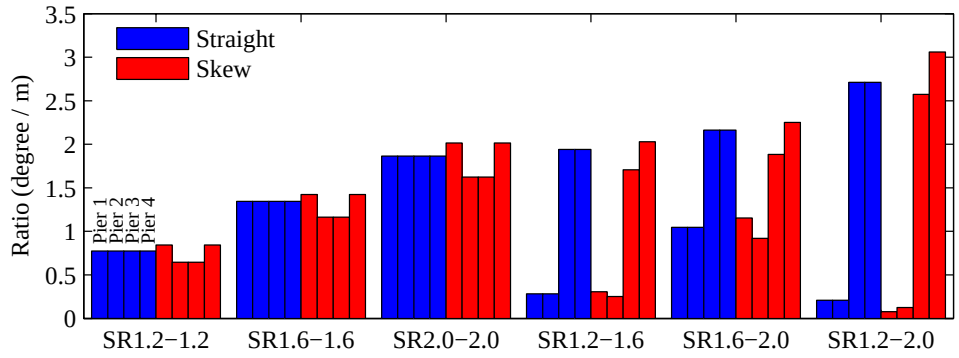

(b) Yaw/Transverse (Y/T) ratio in the transverse mode.

Figure 6.18. Coupling response indices.

6.5.3 Effect of skew angle variation in a bridge

Skew angles at abutment and bent are not always uniform. For example, Sierra Point Overhead has a 59° skew at the north abutment and a 72° skew at the south abutment (Yashinsky 1998). Skew angle variation can be viewed as one of the sources for the eccentricity that results in coupling responses. In this section, the effect of skew angle variation is investigated based on modal analysis. As parametric models, six bridge

configurations are considered as shown in Figure 6.19. Three models, ES15-15, ES30-30, and ES45-45, have symmetric skew angle configurations (i.e., skew angles at the abutments are the same as well as the skew angle at both bents). The other three models, ES15-30, ES15-45, and VS15-45, have asymmetric skew angle configurations (i.e., skew angles at the left- and right-side abutments are different). Because the main span between bents usually crosses straight objects such as a highway or river, the skew angles at bent are assumed to be the same, and are fixed at 30°, except the VS15-45 model. The total bridge length and span ratio configurations are also identical to those found in the FHWA No. 4 bridge.

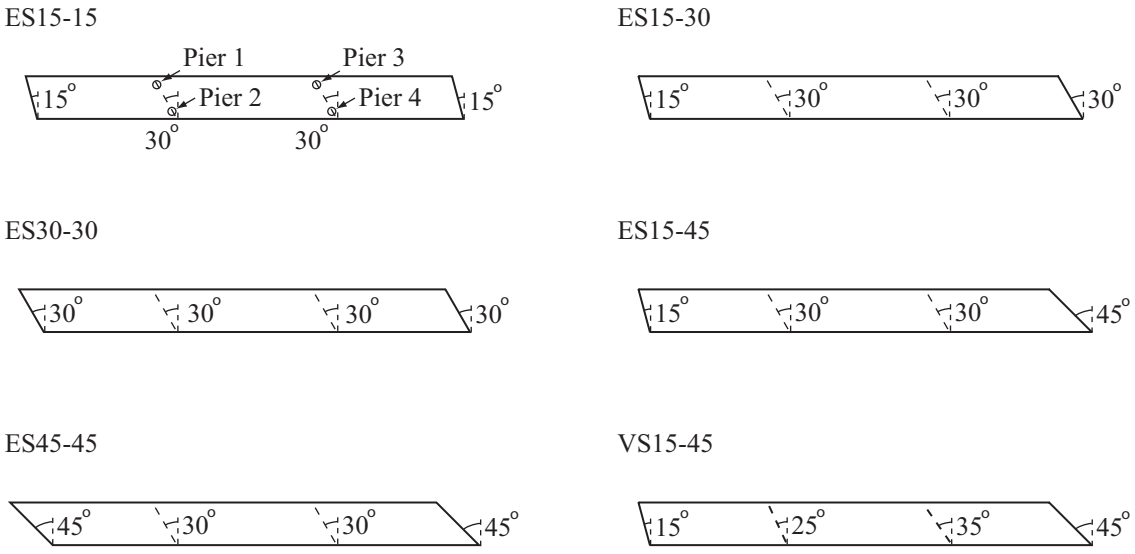

Figure 6.19. Layout of the span length configurations.

Figure 6.20 shows the natural frequencies for all of the various cases. Longitudinal and transverse natural frequencies do not change regardless of the skew angle configurations (this is to be expected because they are basically rigid body modes). On the other hand, the in-plane rotational (yaw of the bridge) natural frequency tends to become smaller, and the bending natural frequency tends to become larger if skew angle at any abutment or bent is increased. However, the overall effect of skew angle variation on the natural frequencies is very small.

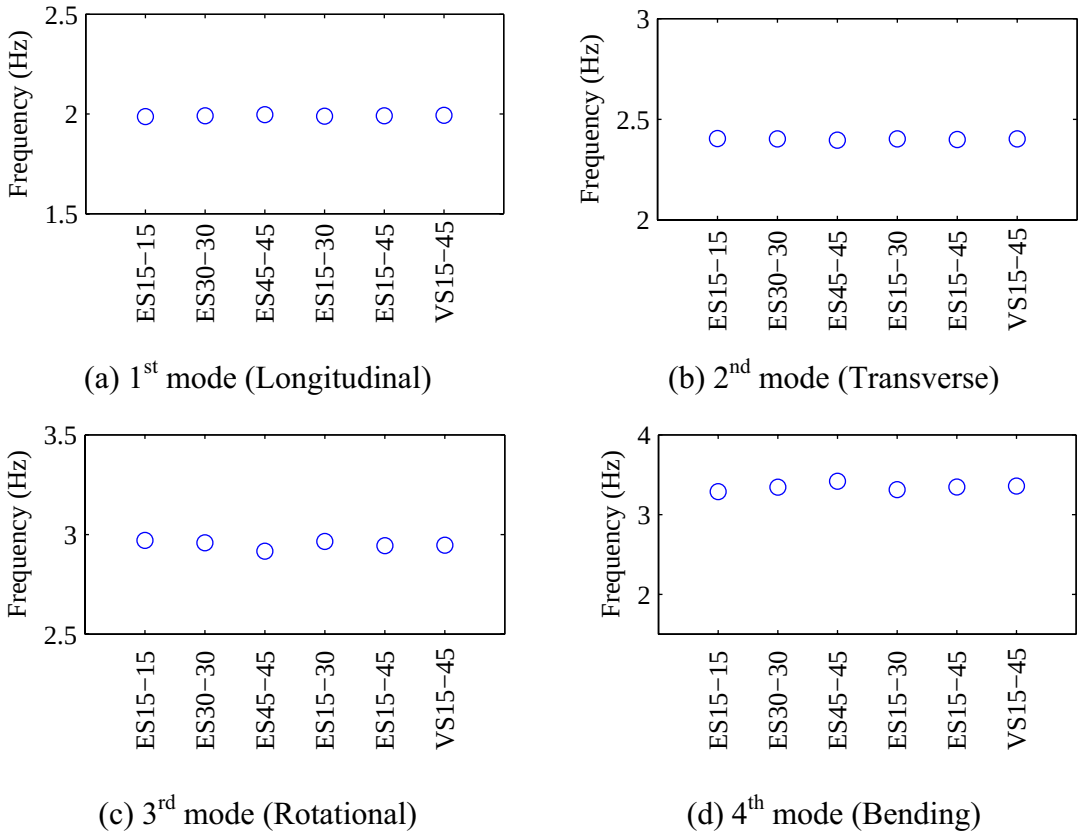

Figure 6.20. Effect of skew angle variation on the natural frequencies.

As in the previous section, the relative displacement at the piers is considered for evaluation of the coupling responses at the local level. Figure 6.21 shows the longitudinal to transverse (L/T) and yaw to transverse (Y/T) displacement ratios in the transverse mode. The coupling effect varies depending on the skew angle configuration. In varying skew angle cases, the highest L/T and R/T ratios occur at one of the piers on the obtuse side of the end span (i.e., Piers 1 or 4). This trend is consistent with the results in the evaluation of span ratio configurations in the previous section.

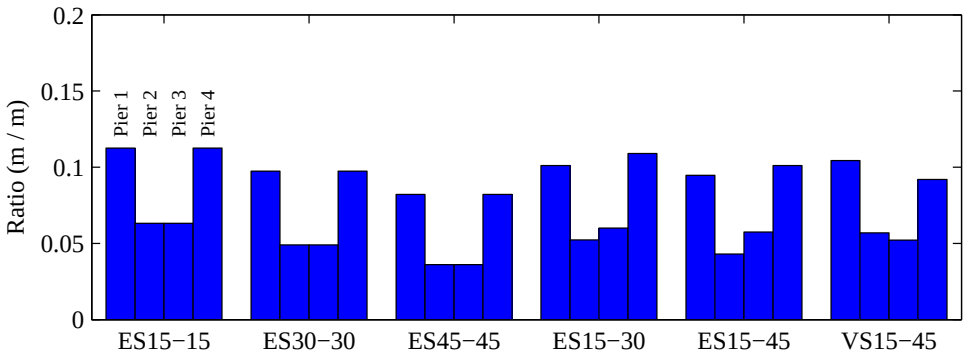

(a) Longitudinal/Transverse (L/T) ratio in the transverse mode.

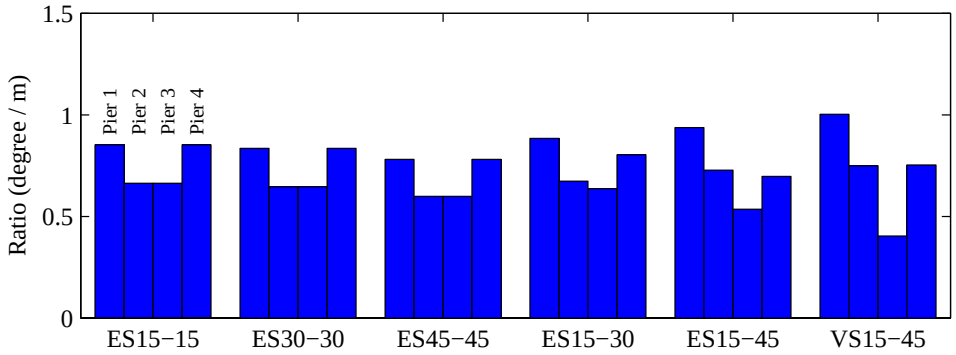

(b) Yaw/Transverse (Y/T) ratio in the transverse mode.

Figure 6.21. Coupling response indices for skew angle variation.

6.6 Summary

Skew bridges are introduced as an example of a structural system that still poses significant research challenges. Studies of skew bridges to date were carefully reviewed and categorized as either field surveys, analytical and numerical studies, modeling considerations, or component assessments.

Assessment from both global and local perspectives is important for the seismic performance of skew bridges. Following the selection of a reference skew bridge, the FHWA No. 4 bridge, a finite element model of the reference bridge was presented in detail. For the purpose of capturing both global and local behavior of bridges, three types of elements were employed (i.e., shell, solid, and spring elements) based on the geometric and material properties of the bridge deck, piers, connections, and foundations. Using the finite element model, a parametric study was carried out focusing on the effect of the skew angle, span length configuration, and skew angle variation in a bridge from the global prospective. Results from the parametric modal analysis showed that the effect of

the skew angle is negligible, judging only from the natural frequencies. However, due to eccentricities introduced by skew angle, skew bridges have complex coupling behavior among multiple directional responses such as longitudinal and transverse coupling. These coupling effects result in relatively large differences between skew and straight bridge responses at the component level. Further inelastic assessment is needed to evaluate the effect of the skew angle on the seismic performance of skew bridges and will be presented in the next chapter.

NONLINEAR INELASTIC ANALYSIS OF SKEW RC BRIDGE

7.1 Introduction

Under strong earthquakes, structural behavior is no longer linear and elastic, rather nonlinear and inelastic. Nonlinear, inelastic behavior refers to geometric nonlinearity, including the second-order effect and material inelasticity due to large stress and strain. Because structural damage and failure are associated with excessive nonlinear, inelastic behavior, it is essential to take into account such behavior in the evaluation of the seismic performance of structures.

In case of the RC bridges, RC piers are the primary components that exhibit the nonlinear, inelastic behavior under strong earthquakes, whereas the bridge deck usually remains linear and elastic. The inelasticity of RC pier behaviors is due to not only combined loading such as earthquake-induced displacements and gravity-induced axial load, but also the geometric (p-Δ) effect that introduces second-order moments. Furthermore, deformations larger than the joint gap between abutment and deck cause pounding that introduces a significant impact on the overall bridge behavior. Pounding is a highly nonlinear effect, hence, it cannot be evaluated in linear analysis. As presented in the previous chapter, skew angle causes coupling of vibration responses that induces complex responses at the local level. The effect of the skew angle on the seismic performance of bridges needs to be investigated taking into account nonlinear, inelastic responses of members.

In this chapter, nonlinear inelastic analyses of a skew RC bridge are carried out using the FHWA No. 4 bridge (FHWA 1996) as a reference bridge. The FHWA No. 4 bridge is a continuous three-span concrete box girder bridge with the skew angle of 30°. Following the description of model details, a pushover analysis is presented in section 7.3. A pushover analysis herein is conducted for a single RC pier, a bent, and the entire bridge for the evaluation of local and global limit states. Thereafter, nonlinear, inelastic, dynamic analysis is performed using a set of natural earthquake ground motion records. The selection and scaling of the ground motion records are described in section 7.4. Results of the nonlinear, inelastic, dynamic analysis are presented in section 7.5. A summary of this chapter is given in section 7.6.

7.2 Modeling for the Inelastic Analysis

Detailed finite element modeling provides a reasonable tool for the assessment of the global dynamic characteristics of structures. However, such a modeling approach requires large computational resources for nonlinear analyses, especially in dynamic analysis. To

assist in achieving a balance between performance and computational demand, the nonlinear inelastic analysis software, Zeus-NL (Elnashai et al. 2002), is used in this chapter after verification with the finite element model in the previous chapter. Zeus-NL incorporates accurate modeling of material inelasticity using fiber-based section analysis with beam element as well as geometric nonlinearity. Zeus-NL has been verified against experimental data for a wide range of members and structures (Jeong and Elnashai 2005).

7.2.1 Geometry of the model

The bridge superstructure is modeled using fiber-based beam elements. Figure 7.1 shows three-dimensional schematic of the model consisting of fiber-based beam element. The bridge deck is composed of three elements in the longitudinal direction to accurately model the deck torsional motion. To capture the curvature and stress-strain relationship of the RC piers, each pier is divided into eight beam elements with the shorter length at the end and the longer length in the middle, so that the pier model has Gauss points as close as possible to potential plastic hinge locations. Each fiber-based element consists of 200 through-the-section fibers to obtain detailed stress and strain information. Rigid beam elements are used at the connections between the cap beam and RC pier to represent offsets between centers of various intersecting elements.

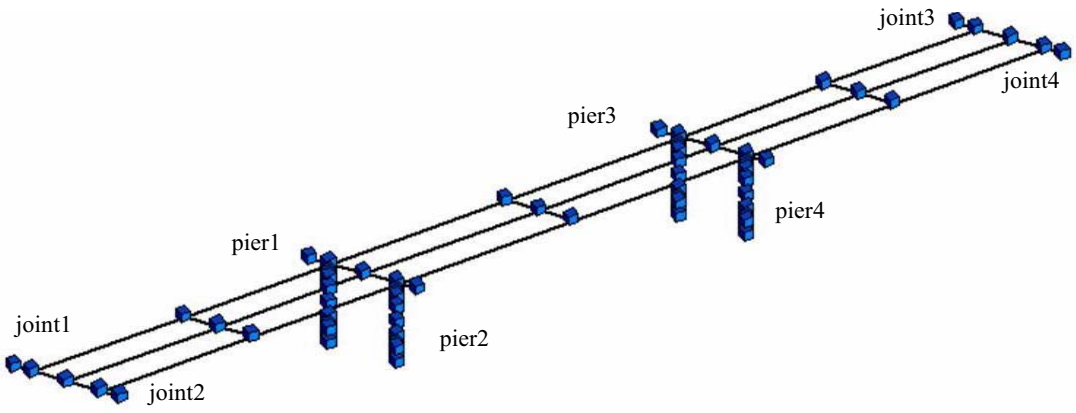

Figure 7.1. Modeling for the nonlinear analyses.

Boundary conditions and restraints are modeled similar to the finite element model in the previous chapter. Soil foundations are incorporated as spring elements at the end of footings and abutments. Distributed mass elements are used to represent the weight of the structure.

7.2.2 Material models

Materials used in the FHWA No. 4 bridge are reinforcing steel and concrete. The following are material models and properties used in the Zeus NL.

Steel

A bilinear kinematic-hardening elasto-plastic model is used to represent the stress-strain relationship of the reinforcing steel with a Young modulus of 200 kN/mm^2 and a yield strength of 500 kN/mm^2 [see Figure 7.2 (a)]. Kinematic strain hardening is incorporated in the Zeus-NL, and a hardening parameter of 0.05, the ratio between the initial and the post-yielding stiffness, is used for modeling of the post-yield behavior. The accuracy of this model is presented in Elnashai and Izzuddin (1993).

Concrete

A uniaxial constant confinement concrete model is used to represent both confined and unconfined concrete stress-strain relationships [see Figure 7.2 (b)). A compressive strength of 20 kN/mm^2, tensile strength of 2.2 kN/mm^2, and crushing strain of 0.002 are used for entire concrete model. Confinement factors for confined and unconfined regions are 1.2 and 1.0, respectively. Details of the model and comparisons with test data are presented in Madas and Elnashai (1992) and Martinez-Rueda and Elnashai (1996).

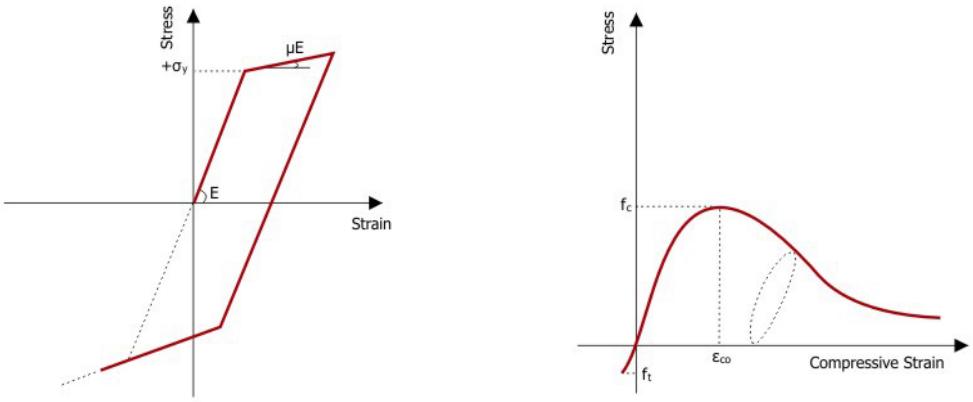

(a) Reinforcement (b) Concrete

Figure 7.2. Material models in nonlinear analyses (Courtesy of Zeus-NL).

7.2.3 Pounding model between abutment and deck

Under large displacements, bridge structures become susceptible to the pounding of adjacent segments at the joint regions. Recent earthquakes have demonstrated damages due to the effect of deck poundings. In general, pounding is treated using gap-contact

elements with impact models such as Kelvin and Herz models (Muthukumar and DesRoches 2006). In this study, a simple linear spring model is used for representing the pounding effect between deck and abutment. Figure 7.3 shows a schematic of the deck pounding model and force-displacement relationship of the linear spring model. A gap between abutment and deck in the FHWA No. 4 design is 150 mm. One of the reasons for the large gap is that pier and footing connection is assumed to be pin connection. In the modified bridge model in this study, the pier and footing connection is changed to a fixed connection that does not require such large gap at the abutment. Therefore, a gap width of 75mm is used to assess the effect of the pounding. A spring stiffness of 4000 kN/mm is determined based on previous study (Muthukumar and DesRoches, 2006).

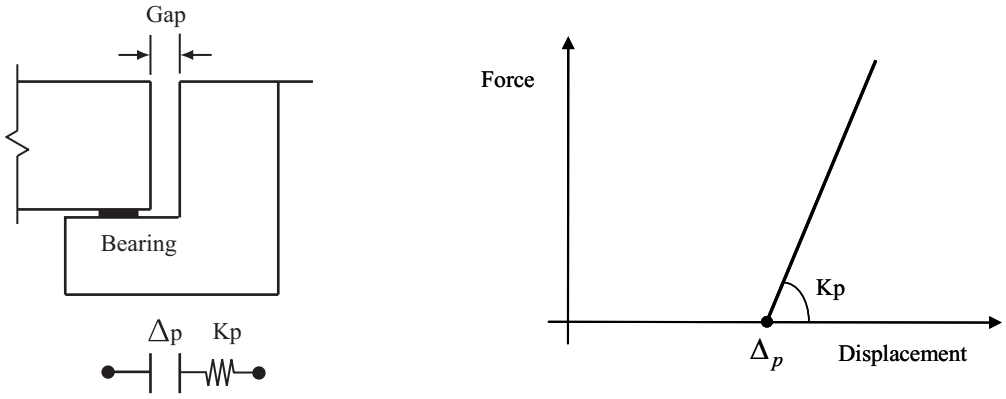

(a) Contact and spring elements (b) Force-displacement relationship

Figure 7.3. Modeling of the pounding between deck and abutment.

7.2.4 Modeling verification

Prior to nonlinear analyses, the fiber-based beam element model is verified in terms of accuracy of the global bridge behavior. For that purpose, natural frequencies of the fiber-based bridge model is compared with those of the finite element model. Table 7.1 summarizes the natural frequencies of the two models for straight and 30° skew bridges. For the first two natural frequencies, differences between the two models are quite small. Furthermore, the fiber-based bridge model captures the coupling tendency in which longitudinal and transverse frequencies get closer with increases in skew angle; longitudinal frequency increases and transverse frequency decreases with skew angle. Although the difference becomes larger for the higher mode frequencies, higher modes are not dominant for the global bridge behavior. Thus, the fiber-based bridge model provides a reasonable representation of the overall bridge behavior, and is used for the nonlinear analyses in the following sections.

Table 7.1. Comparison of natural frequencies between finite element and fiber element models.

Natural frequency (Hz)	Straight case		Skew 30° case	
	Finite Element Model	Fiber Beam Model	Finite Element Model	Fiber Beam Model
1st mode (Longitudinal)	1.97	1.96	1.99	1.97
2nd mode (Transverse)	2.42	2.37	2.41	2.32
3rd mode (Rotational)	2.98	2.89	2.96	2.83
4th mode (Bending)	3.09	3.39	3.34	3.89

7.3 Static Pushover Analysis

Structural capacity in earthquake engineering is evaluated in terms of the displacement ductility and associated load capacity. Static pushover analysis is a well-established analytical approach that provides back-borne curve of displacement and load relationship. Although real seismic loading is not monotonic, pushover is extensively used in the design and assessment processes for the evaluation of the structural load and displacement capacities. In this section, nonlinear, inelastic static pushover analysis is carried out to investigate the performance of the reference bridge and its components with a focus on the effect of skew angle.

7.3.1 Single RC pier

The four RC piers in the FHWA No. 4 bridge have the same sectional and material properties. Therefore, all of the piers can be assumed to have the same force-displacement relationship under the same boundary conditions. Furthermore, because the piers have a circular cross-section, the force-displacement relationship is also the same regardless of the loading direction, for single direction loading.

Figure 7.4 shows the model and result of a pushover analysis of the single RC pier. The pier model here includes a footing and rigid link at the top. The lateral displacement is imposed at the top of the rigid link incrementally. Constant gravity force is also imposed at the top of the rigid link, and the p-Δ effect is incorporated in the nonlinear pushover analysis. The boundary conditions at the top of the rigid link are free in this single RC pier pushover analysis. As shown in the plot, under the cantilever deformation shape with gravity load effect, the RC pier has approximately a peak resistance force of 1000 kN.

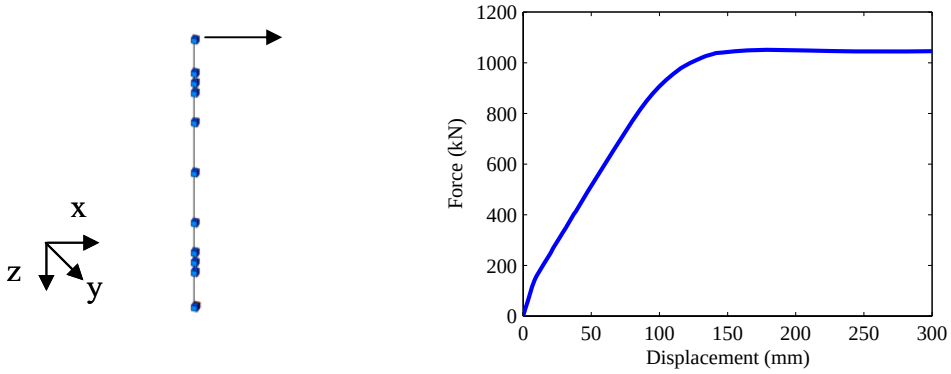

(a) RC pier model (b) Force-displacement relationship

Figure 7.4. Pushover analysis of single RC pier.

7.3.2 Bent

Bents are the main lateral force resisting components of bridges in both longitudinal and transverse directions. The bents in the FHWA No. 4 bridge consist of two RC piers and a connecting cap beam. Pushover analysis is conducted for skew 30° and straight configurations in both longitudinal and transverse directions, taking into account the gravity loads of the bridge deck.

Figure 7.5 (a) and (b) show the schematic of the model and results of the longitudinal pushover analysis of a bent, respectively. Longitudinal lateral resistance of piers in the straight bridge is identical to that of the single pier in the previous section. Because the cap beam is perpendicular to the longitudinal direction, the response mode is the same as the fixed-free (cantilever) mode of the piers. On the other hand, longitudinal lateral resistances of piers in the skew bridge are different in location and higher than those of the straight bridge. In the skew bridge, the longitudinal direction is not perpendicular to the cap beam. As a result, there is an interaction between cap beam and piers under longitudinal loading. In other words, the rigidity of the cap beam restrains the boundary conditions of the RC piers, and the resistance force level becomes higher than that fixed-free response mode of the straight bridge.

Figure 7.5 (c) and (d) show the schematic of the model and the result of the transverse pushover analysis, respectively. The effect of the cap beam rigidity on the boundary conditions of the piers is relatively large (i.e., piers are almost fixed against rotation in the longitudinal axis at the top). As a result, the transverse resistances of the piers are higher than 2000 kN.

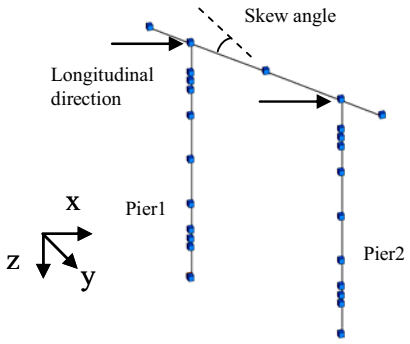

(a) Bent model and longitudinal loading

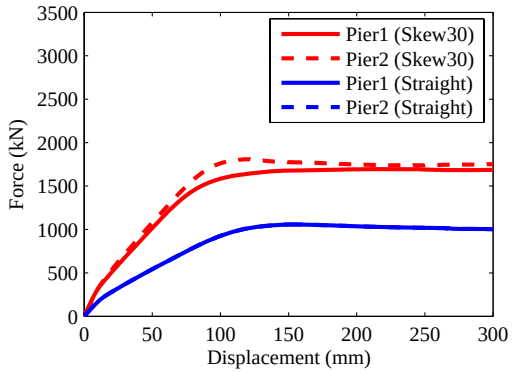

(b) Longitudinal force-displacement relationships

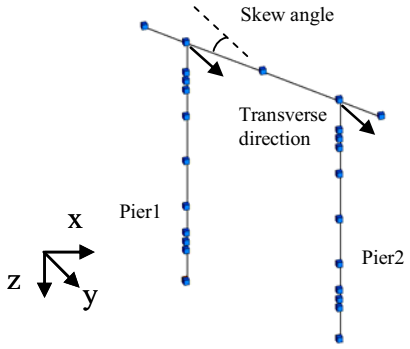

(c) Bent model and transverse loading

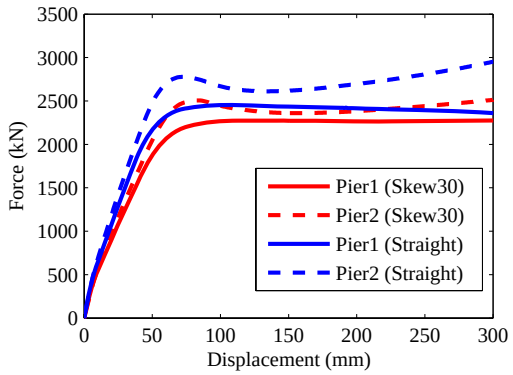

(d) Transverse force-displacement relationships

Figure 7.5. Pushover analysis of bent.

7.3.3 Complete bridge model

Pushover analysis is carried out for the entire bridge model taking into account the effect of the deck gravity loads. The loading points are at the top of the piers in both longitudinal and transverse loading cases. Figure 7.6 shows force-displacement relationships for the longitudinal and transverse direction loading, respectively. Because the behavior of the four piers in the longitudinal loading case is the same at each skew and straight bridge, Figure 7.6 (a) shows a force-displacement relationship of only pier 1 for both skew and straight bridges. Similarly, Figure 7.6 (b) shows force-displacement relationships of piers 1 and 2 for transverse loading case. As shown, the pushover analysis results of skew and straight bridges are quite similar in both longitudinal and transverse direction loadings. Because under a fixed loading direction, skewness does not affect the loading and boundary conditions at RC pier in the entire bridge case, the effect of skew angle cannot be seen in the force-displacement relationship of the RC pier. This observation emphasizes that pushover analysis is a 'capacity' and not a 'demand' assessment tool. The need for nonlinear, inelastic, dynamic analysis which is a combined

'capacity and demand' assessment tool is thus emphasized for investigation of the effect of skew angle.

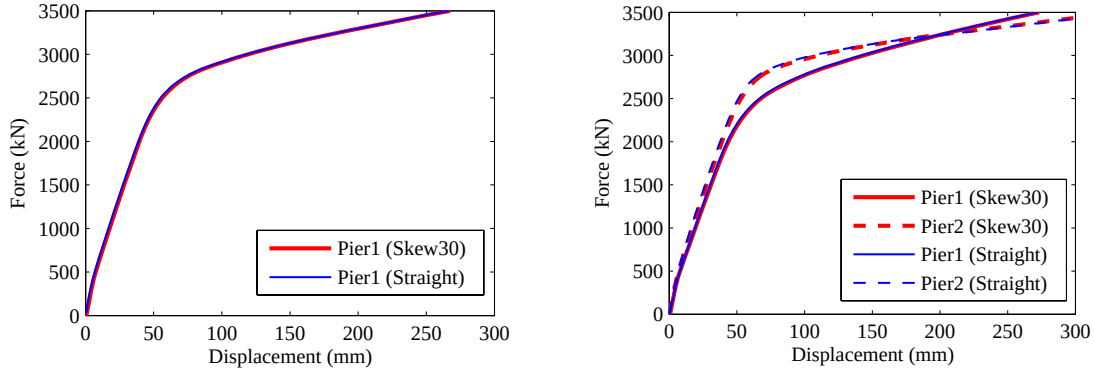

(a) Longitudinal force-displacement relationships

(b) Transverse force-displacement relationships

Figure 7.6. Pushover analysis of single RC pier.

7.4 Selection of the Ground Motion Records

Effects of earthquakes on structures vary due to the complex characteristics of ground motion at the site and their interaction with structural characteristics. For example, one strong-motion record may cause large damage on one type of structure but little damage on the other. Special attention and reasonable knowledge of strong-motion features and their effect on response is required for the selection of strong-motion records used in the dynamic analysis.

7.4.1 Criteria for selection

Characteristics of ground motion are highly dependent on the mechanism and magnitude of fault rapture, distance and direction to the site, characteristics of the travel path, and site condition. Many parameters are used to characterize strong ground motion, including peak ground acceleration (PGA), peak ground velocity (PGV), peak ground displacement (PGD), duration, dominant frequency, intensity measures, and power spectral density (PSD), among others. Furthermore, elastic and inelastic response spectra are also important ground motion properties that provide expected amplification of the response as a function of structural frequency and have been extensively used in the analysis and design processes.

The focus of the following nonlinear inelastic dynamic analysis presented thereafter is to study the effect of skew angle on the behavior of highway RC bridges under strong ground shaking. To cover a wide range of earthquake scenarios for skew bridges, selection of ground motion records was carefully made with a variety of characteristics.

Table 7.2. Properties of the selected ground motion records.

Distance to Fault Rapture (km)	Earthquake	Year	M_w	Station	Mechanism	PGA (g)		PGV (cm/sec)		PGD (cm)		Site Condition
						NS	EW	NS	EW	NS	EW	
0.6	Kobe	1995	6.9	KJMA	SS	0.82	0.60	81.3	74.3	17.7	20.0	B, B
7.3	Chi-Chi	1999	6.9	CHY028	RN	0.82	0.65	67.0	72.8	22.3	14.7	I, C
8.2	Duzce	1999	7.1	Lamont	SS	0.97	0.51	36.5	20.2	5.5	7.5	B, -
8.5	Coalinga	1983	6.4	Pleasant Valley	SS	0.59	0.55	60.2	36.4	8.8	4.0	D, -
10.6	Imperial Valley	1979	6.5	Calexico Fire Station	SS	0.28	0.20	21.2	16.0	9.0	9.2	D, C
12.8	Morgan Hill	1984	6.2	Gilroy Array	SS	0.22	0.35	19.3	17.4	4.3	3.1	D, C
21.2	Landers	1992	7.3	Coolwater	SS	0.28	0.42	25.6	42.3	13.7	13.8	D, B
64.0	Taiwan SMART1	1986	6.4	SMART1 E01	RO	0.20	0.18	36.5	15.1	7.6	3.1	D, -
77.4	Loma Prieta	1989	6.9	Oakland	RO	0.25	0.18	40.0	33.2	30.1	25.8	D, C
78.9	Kocaeli	1999	7.4	Ambarli	SS	0.20	0.24	19.9	36.1	3.5	7.2	E, D

M_w – Moment magnitude; PGA – Peak ground acceleration; PGV – Peak ground velocity; PGD – Peak ground displacement; SS- Strike sprit; RN – Reverse normal; RO – Reverse oblique; site condition – geomatrix, USGS

Table 7.2 summarizes 10 selected strong-motion records with respect to distance to the fault rapture. Selected strong-motion records are from different earthquakes. Distances to fault rapture range from 0.6 to 80 km, and fault mechanisms include strike strip, reverse normal, and reverse oblique. Site conditions of records also vary in type of both geomatrix and USGS. Thus, the selected ground motions cover a wide variety of earthquakes in terms of magnitude, distance, and site condition. In the following analysis, two horizontal components of the selected records are used as a set of earthquake ground motion.

7.4.2 Characteristics of the selected records

Response spectra are useful tools for assessment of the earthquake strong-motion on structural behavior. Acceleration spectra are commonly used in conventional design. Displacement spectra are increasingly being used in displacement-based design. Finally, velocity spectra have been used extensively to characterize the damage potential of earthquake ground motion, because they represent energy imparted into structures.

Figure 7.7 shows pseudo velocity spectrum (PVS) for the selected ground motions. For clarity of comparison, the PVSs are plotted in two groups. Group 1 contains records with the first short distance to the fault rapture in ascending order. Group 2 contains the rest of the five records also in increasing order of distance to the fault rapture. As a general tendency, the PVS of record with shorter distance has higher peaks than the one with longer distance. This tendency is consistent with PGA, PGV, and PGD listed in Table 7.2, and general attenuation relationships. Selected ground motions include various types of PVS. For example, PVSs of Kobe and Kocaeli records have high amplifications in low frequency less than 2 Hz; those of Chi-Chi and Landers have relatively wide high amplification ranging from 0.5 to 4 Hz. The PVS of Duzce has high amplification in high frequency. The PVS of Coalinga has unique characteristics such that the NS component has high amplification in low frequency, and the EW component has high amplification in high frequency. As a whole, those selected ground motion records have a variety of characteristics that lend credence to assessment results based on their use.

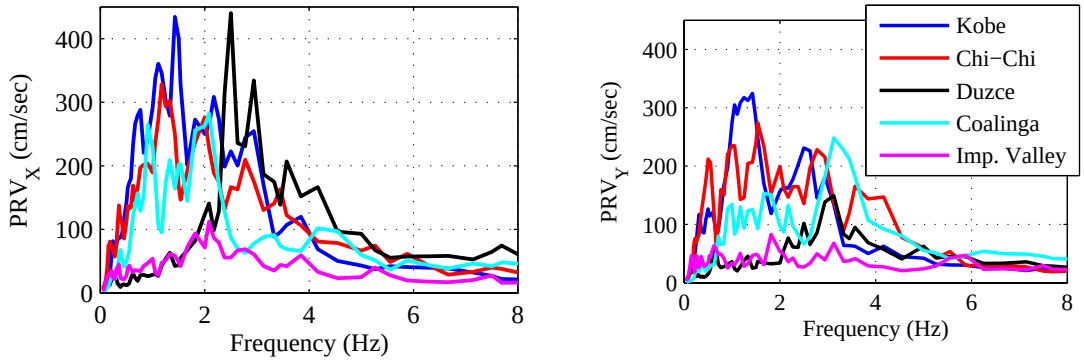

(a) NS components for Group 1 (b) EW components for Group 1

Figure 7.7. Pseudo velocity spectrum (PVS) of the selected ground motions.

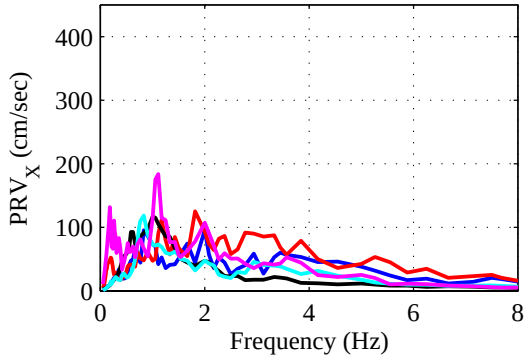

(c) NS components for Group 2

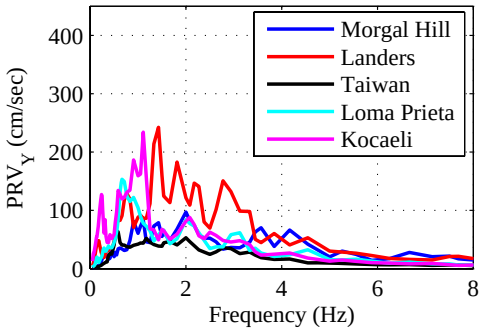

(d) EW components for Group 2

Figure 7.7. Pseudo velocity spectrum (PVS) of the selected ground motions. (Continued).

7.4.3 Baseline correction

Acceleration records of ground motion inevitably contain errors due to noise, quantization, and other sources. Ground displacement histories obtained from double integration of acceleration records often shift over time and contain nonzero end displacement resulting from permanent ground deformation and amplification of the errors due to integration. Residual ground displacement is certainly possible especially at sites close to the fault and on highly deformable soils. However, shifting ground displacement over a time is not a physical phenomenon. Therefore, acceleration records require modification so that the calculated ground displacement does not shift along the time axis with an assumption of zero residual displacement at the end of the record. This zero end displacement assumption obliterates possible genuine permanent ground deformations that would be of significance in asynchronous motion analysis of extended structures.

A simple linear baseline correction algorithm is used to modify the selected ground motion records. First, the original acceleration record is integrated twice using the trapezoid role to obtain calculated displacement history. A linear correction function is created based on the zero displacement at time zero and the residual displacement at the end of the record. The amplitude of the displacement in the linear correction function increases with time. The linear correction function is then subtracted from the calculated displacement time-history. The corrected displacement history has zero residual displacement at the end of the history, and looks as if the original displacement history is pivoted about the origin. Next, the corrected displacement time-history is differentiated twice to obtain the corrected acceleration time-history. Figure 7.8 shows original and corrected displacement and acceleration time-histories of the Imperial Valley earthquake. Although the corrected acceleration time-history is similar to the original, the zero residual ground displacement is guaranteed at the end of the record. All selected records are baseline corrected prior to dynamic analysis.

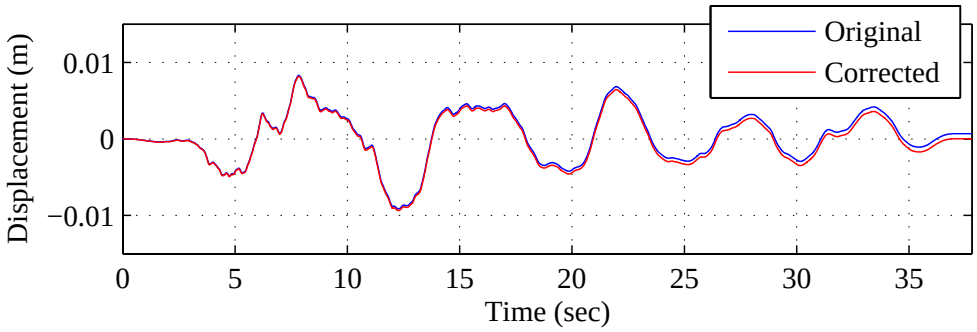

(a) Displacement time-histories

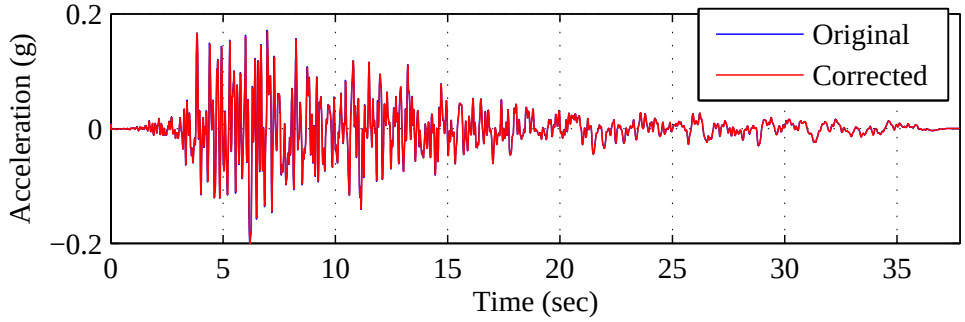

(b) Acceleration time-histories

Figure 7.8. Original and corrected time-histories.

7.4.4 Scaling of the ground motions

Selected ground motion records vary in scale such as PGA, PGV, and PGD. The difference in scale of input ground motion causes large differences in the behavior of skew bridges, and makes it difficult to investigate the effect of skew angle on bridge behavior. Because the focus of this study is to investigate the effect of skew angle, not the ground motion, the selected strong ground motion records need to be scaled so that all of the records have a consistent level of impact on the bridge structure.

The velocity spectral intensity (VSI) area under the velocity response spectrum is used frequently to measure the energy content of earthquake ground motion. As shown in Figure 7.4, each ground motion record has a unique energy distribution over the frequency range. Because the response of the bridge structures is primarily dominated by the low-frequency modes, the VSI within the frequency range of interest is used for the scaling process. The lower and upper limits of the frequency considered in the VSI are $0.6\,f_1$ and $1.4\,f_2$, where f_1 and f_2 are the first and second natural frequencies, respectively. Figure 7.9 shows the schematics of the VSI and its range of interest. Factors 0.6 and 1.4 cover the inelastic frequency of the first mode and uncertainty in the structural model as well.

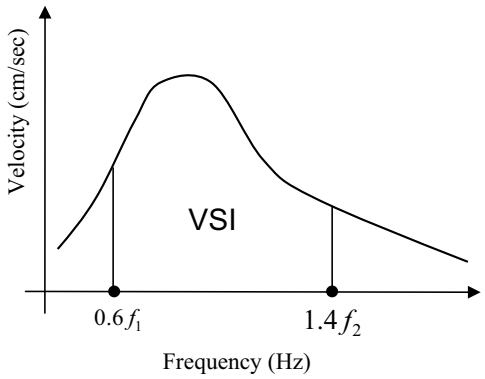

Figure 7.9. Velocity spectrum intensity and its range of interest.

Table 7.3. Scaling factors for the selected ground motions.

	Velocity spectral intensity VSI (cm/sec*Hz)			Normalized by Duzce VSI	Scaling factor
	NS	EW	Total		
Kobe	639.1	497.1	1136.2	2.10	0.48
Chi-Chi	504.0	460.9	964.9	1.79	0.56
Duzce	378.7	161.8	540.5	1.00	1.00
Coalinga	388.1	327.2	715.3	1.32	0.76
Imperial Valley	154.2	109.6	263.8	0.49	2.05
Morgan Hill	128.9	143.7	272.6	0.50	2.00
Landers	197.8	308.8	506.5	0.94	1.07
Taiwan SMART1	117.1	94.5	211.5	0.39	2.55
Loma Prieta	115.1	152.5	267.6	0.50	2.02
Kocaeli	175.6	190.3	365.9	0.68	1.48

Table 7.3 summarizes the VSI for the selected ground motion records. The total VSI is the sum of VSIs in NS and EW records. Total VSIs are normalized with respect to those of the Duzce record. The record is sufficiently damaging without scaling, and is therefore, used as a reference. Scaling factors are calculated based on the normalized VSIs. In the dynamic analysis that follows, the selected ground motion records are scaled by the factors obtained in this section.

7.5 Nonlinear Inelastic Dynamic Analysis

7.5.1 Analysis rationale

With appropriate modeling of response features, nonlinear dynamic analysis provides more accurate response of structures than linear dynamic analysis. However, because of its complexity and peculiarity of the simulation, general remarks are difficult to conclude from the limited number of analytical results. For example, the effect of the skew angle on the bridge behavior cannot be assessed from a single case study of nonlinear dynamic analysis.

The scope of the nonlinear, inelastic dynamic analysis presented hereafter is to capture the general aspects of the skew bridge behavior compared with straight bridges with focus on the effect of skew angle. Therefore, numerous nonlinear dynamic analyses are carried out to cover various analysis cases and to identify the extreme cases among them. As a parameter of the analyses, skew angles of 0°, 30°, and 60° are considered, and bridge models with those angles are constructed using the modeling techniques described in section 7.2. All of the properties and geometries of those three bridge models are identical except for the skew angle.

The ground motion records selected in the previous section contain a variety of features resulting from source, path, and site characteristics. In addition to those varieties in the records, input directions of the two sets of horizontal motion with respect to the bridge configuration can also be regarded as unknown properties. The direction of the input ground motion affects the bridge response even with the same set of horizontal records. Because there is no deterministic correlation between the model bridge configuration and the selected ground motion directions, three input directions are considered for each set of strong motion record: (i) 0°, in which the NS component of record is in the longitudinal direction of bridge, while the EW component of record is in the transverse direction of bridge; (ii) 45°, in which the NS component of record is in 45° from the longitudinal direction of bridge, and the EW component of record is perpendicular to the input direction of the NS component; and (iii) 90°, in which the NS component of record is in the transverse direction of bridge whereas the EW component of record is in the longitudinal direction of bridge.

Nonlinear dynamic analyses are carried out for three bridge configurations of skew angle of 0°, 30°, and 60° with ten sets of scaled ground motion records, and three input directions of each record [i.e., the total number of analyses is 90 (3 x 10 x 3)]. Because of the uniqueness of nonlinear analysis, quantitative judgment is difficult to make from each analytical result. However, a rich set of response data under various simulation scenarios provides sufficient basis to capture the difference between straight and skew bridge behavior. Analytical results are summarized in the following sections with focus on the effect of skew angle on the response of bridge structures. The detailed analysis results of all 90 cases are given in Appendix D.

7.5.2 Evaluation of maximum response quantities

The displacements that structures undergo during earthquakes are one of the most important response criteria. Relative displacement between the bridge deck and the soil foundation results in the displacement of the bridge pier that is highly correlated with pier damage and eventual failure. Relative displacement is used in the design process for bridge structures, and it needs to be carefully evaluated in the analytical process as well.

Longitudinal displacement

Longitudinal direction is generally in lower vibration modes of bridge structure and is one of the important indexes for the seismic assessment of bridges. As sample analytical results, Figure 7.10 shows longitudinal relative displacement time-histories at pier 4 for bridges with different skew angles subjected to the scaled earthquake record at station CHY028 collected during the 1999 Chi-Chi earthquake. The input angle of the ground motion is 0°, meaning that the NS component is in the longitudinal direction whereas the EW component is in the transverse direction. A difference can be seen among three bridge configurations compared in the small time range [see Figure 7.10 (b)]. However, overall bridge longitudinal responses are quite similar. In this simulation scenario, the difference in the maximum displacements is only 4%.

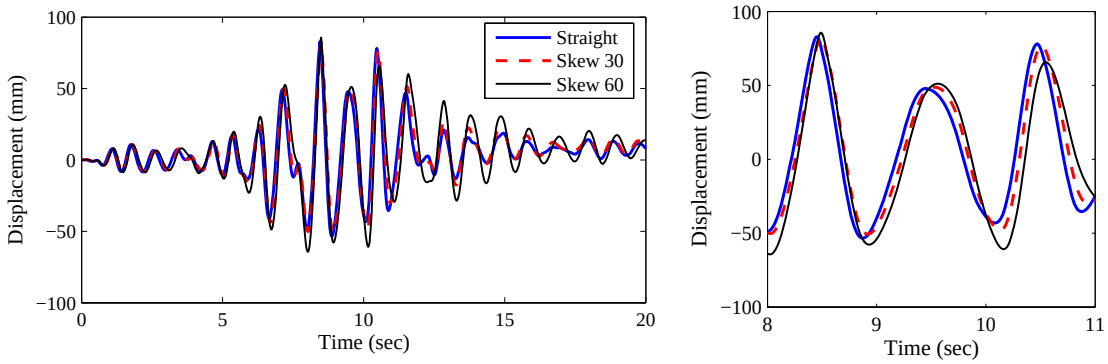

(a) Full time-histories

(b) Close-up of the large displacement range

Figure 7.10. Longitudinal displacement time-histories at RC pier, Chi-Chi IA00.

Maximum longitudinal relative displacements at RC piers are extracted from all simulation scenarios, and plotted in Figure 7.11. Labels IA00, IA45, and IA90, stand for the input angle of the ground motion, 0°, 45°, and 90°, respectively, as defined in the previous section. In most cases, the difference among the three bridge configurations is very small. Bridge configurations with the largest maximum displacement are also random. For example, maximum longitudinal displacements are the largest at 60° skew bridge and the smallest at straight bridge for Kobe IA00 input. However, the results are totally opposite for Taiwan IA90 input. In both cases, the differences between the two

maximum displacements are negligibly small. In other words, there is no clear indication of the effect of skew angle on the maximum longitudinal displacement. Note that despite the scaling of the strong-motion records based on the spectral intensity, maximum displacements vary for each simulation scenario ranging from 24 to 100mm. This variation is due to the different characteristics of the ground motion records.

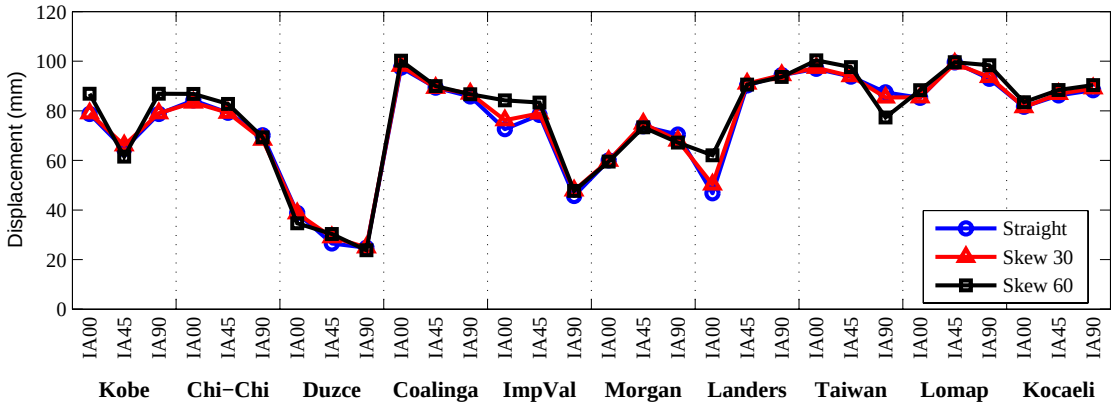

Figure 7.11. Maximum displacements at RC pier in the longitudinal direction.

Transverse displacement

For long-span bridges, the transverse response can be more significant than the longitudinal response. Current design codes of practice for highway bridges require minimum analytical procedures, such as the multi-spectral method, that usually takes into account transverse response except for a few simple analysis procedures.

Figure 7.12 shows the transverse relative displacement time-histories at pier 4 for three bridge configurations subjected to the Chi-Chi earthquake. Note that the phases of the time-histories are no longer similar for the three bridge configurations, especially the skew bridge with 60°. Furthermore, the peak transverse displacement for straight, skew 30°, and skew 60° bridges are 55, 70, and 85 mm, respectively, and their differences are also noticeable.

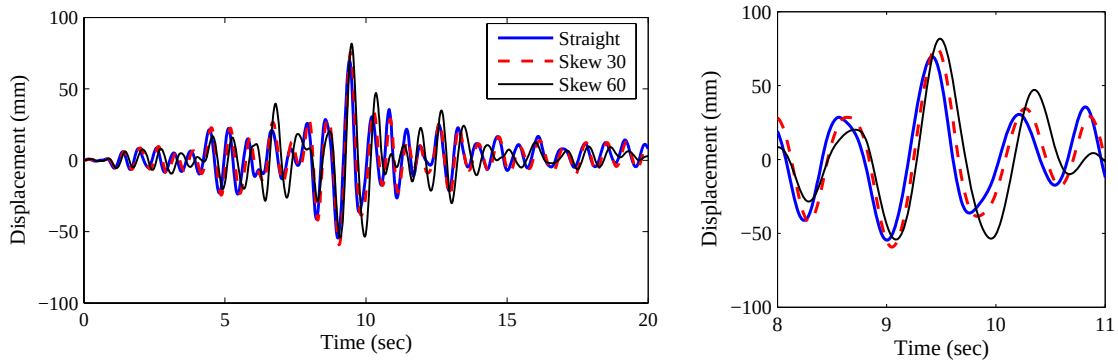

(a) Full time-histories

(b) Close-up of the large displacement range

Figure 7.12. Transverse displacement time-histories at RC pier, Chi-Chi IA00.

Similarly, the peak transverse relative displacements for all simulation scenarios are compiled and plotted in Figure 7.13. There is a general trend that the peak transverse displacements are higher for skew bridge than for straight bridges. Some exceptional cases such as Loma Prieta IA00 can be seen, but the 60° skew bridge has high peaks for most cases. This trend is considered to be the effect of the skew angle. Although the effect of the skew angle on the transverse vibration frequencies is slightly small, as related in the previous chapter, the transverse natural frequency tends to become lower as the skew angle increases. In general, lower vibration frequencies yield larger amplification for the same level of input. Response amplification due to the reduction in vibration frequency caused by the skew angle is consistent with the nonlinear dynamic analysis results. The average increase in the peak transverse displacement from straight to 60° skew bridge is 24%. The transverse response is more susceptible to the effect of the skew angle than the longitudinal response.

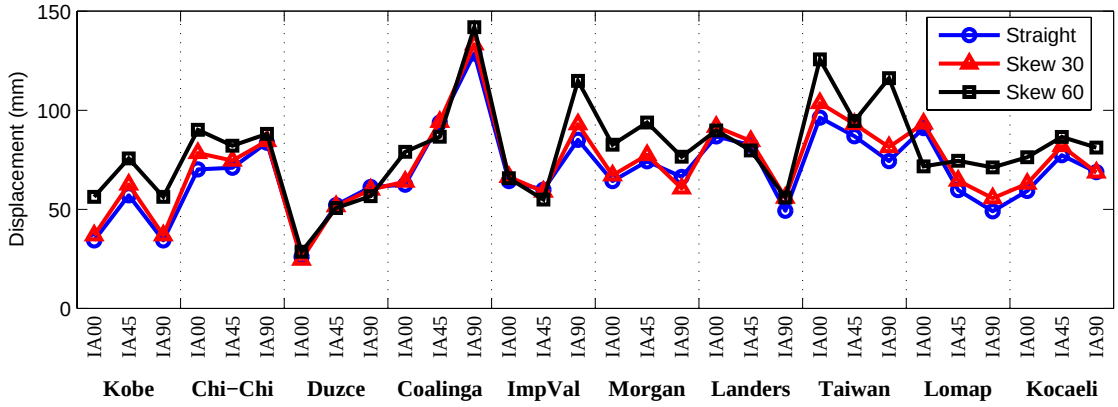

Figure 7.13. Maximum displacements at RC pier in the transverse direction.

Torsional rotation

Damage on the RC bridge pier is not only due to the lateral loading but also occasionally due to torsion. Torsional rotations induce shear on the pier, especially at the extreme fiber of the section that reduces total shear capacity. In most cases, torsional effects may not appear to be a major cause of the bridge pier failure. However, torsion has an inevitable effect and interaction with other directional capacities such as shear, flexure, axial, etc. Although most design guidelines for bridge piers do not take into account torsional effect, it is an important property to be considered for the seismic performance of the RC pier.

Figure 7.14 shows torsional rotation response histories at the RC pier for three bridge configurations subjected to the Chi-Chi IA00 earthquake records. Torsional rotation tends to become large as the skew angle increases. In this specific simulation scenario, increases in the peak torsional rotation from straight to skew 30° and 60° configurations are 13 and 56%, respectively.

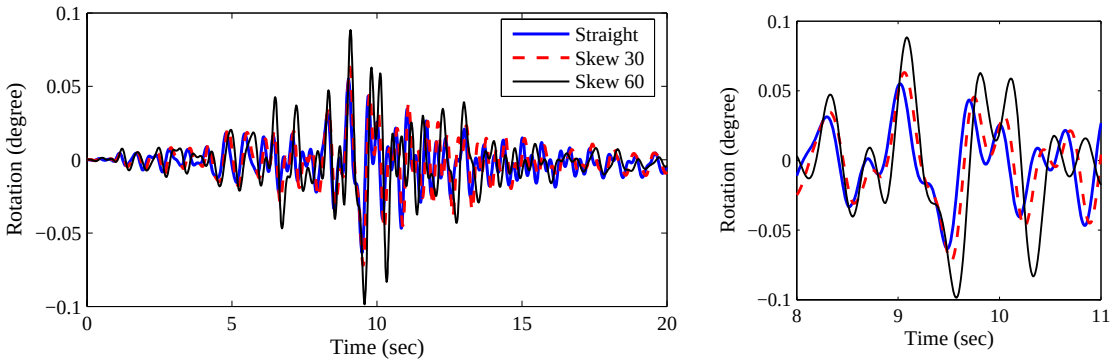

(a) Full time-histories

(b) Close-up of the large displacement range

Figure 7.14. Torsional rotation time-histories at RC pier, Chi-Chi IA00.

Peak torsional rotations for all simulation scenarios are summarized and plotted in Figure 7.15. As shown in the plot, peak torsional rotations vary for each bridge configuration, input ground motion, and direction. However, a clear tendency can be seen: The larger the skew angle, the higher the peak torsional rotation. The average increase in peak torsional rotation from straight bridge to skew 30° and 60° bridges are 10 and 68%, respectively.

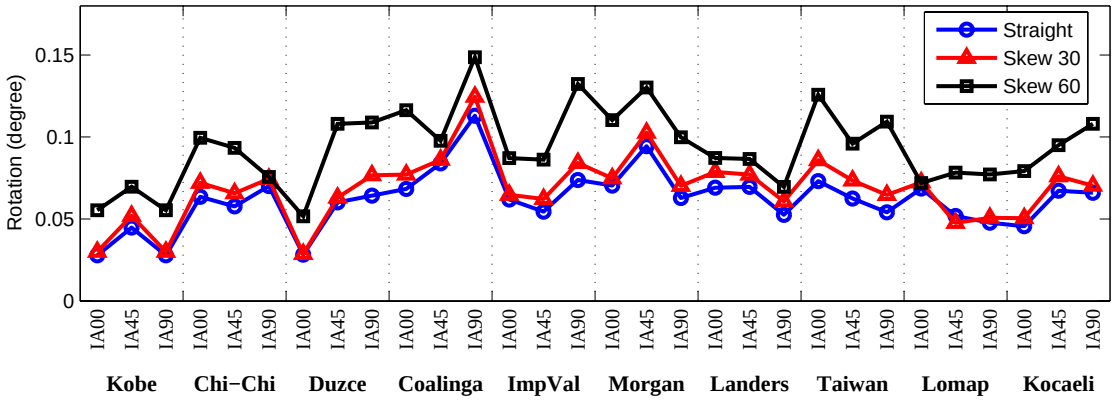

Figure 7.15. Maximum torsional rotation at RC pier.

The effect of the maximum responses at the RC pier is summarized in Table 7.4. Percentages of increase in longitudinal, transverse, and torsional responses at the RC pier are calculated and averaged with peak responses of straight bridge (i.e., skew angle 0°) as reference. As a general remark based on the brief parametric nonlinear dynamic analysis presented herein, the effect of the skew angle on the bridge behavior is relatively small on both the longitudinal displacement and transverse displacement, up to a moderate skew angle. On the other hand, the effect is noticeable on the transverse displacement with a large skew angle, and significant on torsional rotation.

Table 7.4. Average increase in peak responses due to the skew angle.

Skew angle	Longitudinal displacement	Transverse displacement	Torsional rotation
0° (reference)	0.0 %	0.0 %	0.0 %
30°	1.0 %	2.5 %	10.4 %
60°	2.5 %	23.6 %	68.2 %

7.5.3 Gap closing and pounding effect

Longitudinal displacements open and close gaps of expansion and seismic joints between the deck and abutment. Under the displacement capacity, the deck is resisted by elastomeric bearing anchored at the abutment. Once the longitudinal displacement exceeds the gap limit, pounding of the deck and abutment occurs, and large impact force is imposed on the deck and abutment. The pounding effect is a local feature that occurs only at the joints. However, it largely affects the behavior of the entire bridge structure and can cause serious damage.

Sample analytical results for displacement and force time-histories as well as force-displacement relationship at the joint are shown in Figure 7.16. This set of data is at joint 4 of the straight bridge under the Chi-Chi earthquake IA00. The longitudinal response of the deck exceeds the displacement limits at 8 and 11 seconds, and causes pounding between the deck and abutment. The force time-history clearly shows the amplitude and instance of impact forces. Small fluctuations in the force occur from the elastomeric bearing. Note that the displacement at pounding has sharper peaks than others. These short-duration reverses of longitudinal displacement are due to the impact force resulting from the pounding effect.

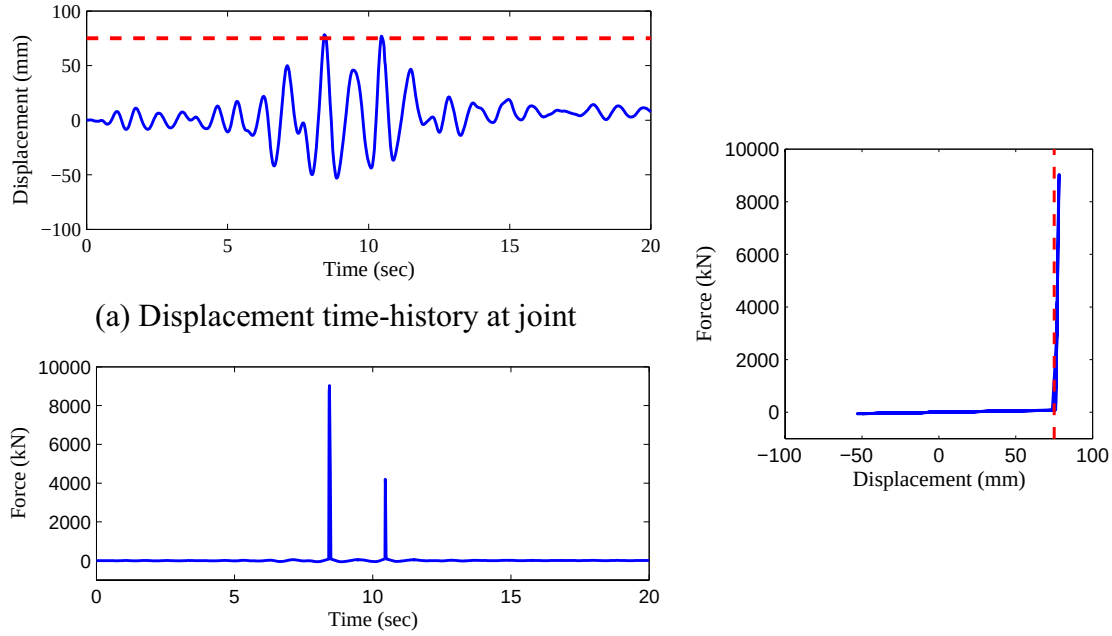

(a) Displacement time-history at joint

(b) Force time-history at joint

(c) Pounding force

Figure 7.16. Gap closing and pounding effect at joint.

The number of poundings for each simulation scenario is summarized in Figure 7.17. Locations of the four joints are shown in Figure 7.1. Joints 1 and 2 are the left side of the bridge, and joints 3 and 4 are the right side of the bridge. The number of poundings varies with the input ground motion, direction, and location of the joint. In addition, the effect of skew angle on pounding is not clear. This is because the poundings are highly associated with longitudinal response of bridges that is not affected by skew angle. This result is consistent with the finding in the previous section. The results show that numbers of poundings are equal for the same side of joints in most cases. However, there are some rare cases that the joints at the same side have a different number of poundings.

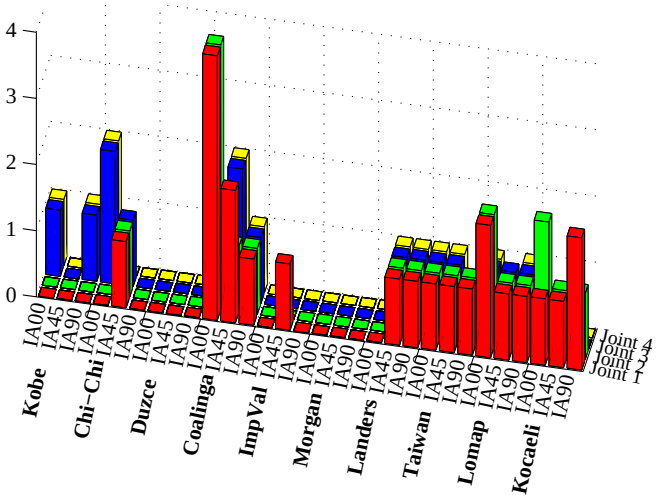

(a) Straight bridge

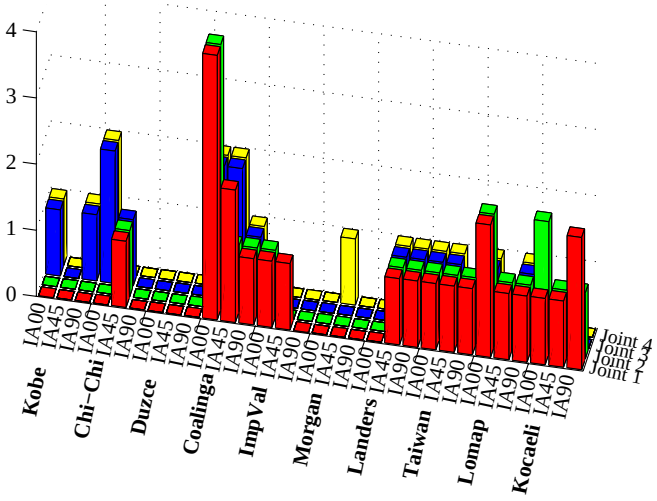

(b) Skew 30° bridge

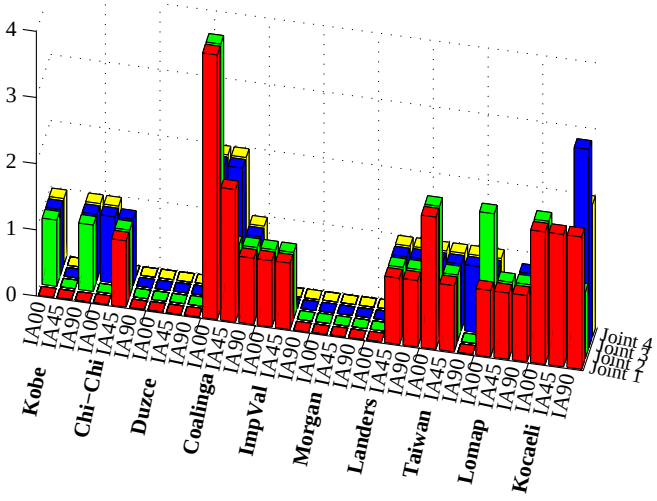

(c) Skew 60° bridge

Figure 7.17. Number of poundings for each simulation scenario.

7.5.4 Performance evaluation

Piers are the primary structural components to resist earthquake and gravity loads. In the design process, the performance of the RC pier is generally evaluated in terms of yield strength, ultimate strength, and ductility, using the demand from dynamic analysis and the supply from pushover analysis. Such evaluation is usually performed in each loading direction separately. However, actual loadings during earthquakes are generally multi-directional; hence, interaction of multi-directional responses may affect the performance of the RC pier. In addition, dynamic effects, such as damping and changing boundary conditions, also influence the response of the RC pier.

Sample force-displacement relationships of RC pier in nonlinear dynamic analysis are shown in Figure 7.18. These plots are longitudinal and transverse hysteresis loops of pier 4 of the straight bridge under the Chi-Chi IA00 earthquake ground motions. For comparison, backbone curves from pushover analysis are also plotted. Initial stiffness in dynamic and pushover analyses is quite similar in both longitudinal and transverse directions. However, it is interesting to note that the peak forces in the positive region from dynamic analysis are higher than the ones in the pushover analysis. This difference may be due to the interaction between longitudinal and transverse loadings and the differences in boundary conditions. Moreover, the unloading and reloading in dynamic analysis provide more detailed paths than the ones in the pushover analysis. Thus, compared to the pushover analysis, which is only for capacity assessment, nonlinear, inelastic dynamic analysis allows for both demand and capacity assessment of the structural members.

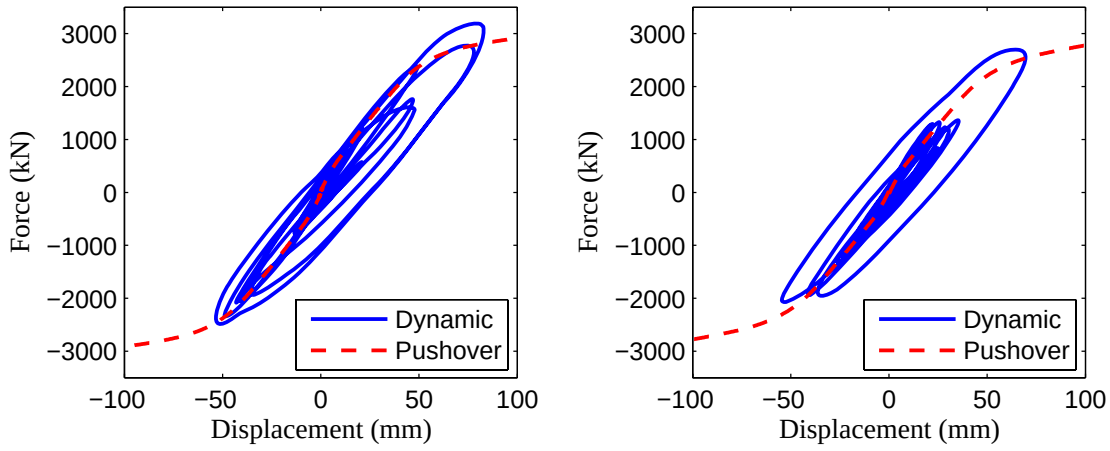

(a) Longitudinal direction (b) Transverse direction

Figure 7.18. Force-displacement relationships at RC pier.

7.6 Summary

In this chapter, nonlinear inelastic analyses were performed to investigate the seismic behavior of bridges with a focus on the effect of the skew angle. Modeling used for nonlinear analyses included material inelasticity for concrete and reinforcement, geometric nonlinearity, and pounding of deck and abutment. Prior to the nonlinear, inelastic dynamic analysis, pushover analysis was conducted to evaluate the capacity of the RC pier, bridge bent, and the entire bridge.

Ground motion records for dynamic analysis were carefully selected covering various fault rapture distances and mechanisms, soil conditions, etc. The selected ground-motion records are scaled based on the earthquake intensity, taking into account the relationship with the fundamental natural frequencies of the model bridge. Dynamic analyses were carried out for three bridge configurations with different skew angles, and each strong-motion record is used from three different input directions. The total number of nonlinear, inelastic dynamic analysis performed was 90, which is sufficient to obtain the general trends of the effect of the skew angle for this particular bridge layout (three spans, double column bent). The main findings from the nonlinear, inelastic dynamic analyses are as follows:

- Longitudinal response of bridges is not sensitive to skew angle.
- Transverse response of bridges tends to become larger as the skew angle increases.
- Torsional rotation increases significantly as the skew angle increases.

In the nonlinear analyses undertaken, the pounding effect between deck and abutment was observed, and the performance of the RC pier under multi-directional loading was investigated compared to the capacity estimates from pushover analysis.

MULTI-DIMENSIONAL HYBRID SIMULATION OF SKEW RC BRIDGE

8.1 Introduction

Hybrid simulation and associated techniques have been developed and employed for seismic assessment of structural systems. Hybrid simulations to date vary in structural model, scale, loading rate, dimension, degrees-of-freedom (DOF), etc. Despite the long-term devotion by many researchers, the method is still not fully matured for rigorous investigation of the seismic performance of structural components. In particular, loading conditions in hybrid simulation are in general simplified and poorly treated due to the high demand in testing equipment and challenges in the control system.

The six-actuator, self-reaction loading system, referred as the Load and Boundary Condition Box (LBCB), designed at the NEES MUST-SIM facility provides loading capability in 6DOF. To impose combined gravity load and earthquake-induced displacements, a mixed load and displacement control strategy was developed for such multi-axial loading systems. With tele-operation control capability, the LBCB loading system can be employed for network-based hybrid simulation that allows distributed hybrid simulations of structural systems under complex loading and boundary conditions.

As studied in Chapters 6 and 7, skew bridges have different modal vibration properties and dynamic responses from straight bridges. Despite their uniqueness, current design codes of practice do not consider the skew angle as an irregular property of bridges. In fact, a simple analysis procedure is allowed in the design process even if selected analysis procedures do not take into account coupled vibration responses. With such background, skew bridges certainly deserve more research attention.

In this chapter, multi-dimensional hybrid simulation of a skew RC bridge is presented to demonstrate all of the capabilities developed in this study and the effectiveness of the multi-dimensional mixed-mode hybrid simulation for complex structural systems. In the hybrid simulation presented herein, one of the RC piers is modeled experimentally and tested as a substructure of an entire skew bridge. At first, the skew bridge modeling used in the hybrid simulation is described, as well as the substructure components and their network configurations. Then, the hybrid simulation scenario is discussed in detail. Those scenarios include selection and scaling of strong ground motion and the control mode for the RC bridge pier in the experiment using the LBCB. The hybrid simulation is performed, accounting for three-dimensional 6DOF loading using the LBCB mixed load and displacement control capabilities. The experimental results and observations are provided and discussed focusing on the control performance of the LBCB and the behavior of the tested RC pier. Finally, a summary of this chapter is presented.

8.2 Hybrid Simulation Model

8.2.1 Structural modeling

The FHWA No. 4 skew bridge (FHWA 1996) that has been studied in Chapters 6 and 7 of this report is used as a model structure in the hybrid simulation. Vibration responses of skew bridges are coupled with each other to some extent; hence, dynamic responses of skew bridges are likely to be in multi-dimensional and complex. In other words, a skew bridge is an example of the type of structure for which responses need to be evaluated in multiple dimensions. Therefore, the skew bridge seems to be an appropriate structural model for demonstrating the effectiveness of multi-dimensional hybrid simulation.

Figure 8.1 shows the entire bridge model in the hybrid simulation. One of the RC piers is carefully modeled and designed, accounting for similitude of the prototype pier, and experimentally tested using the $1/5^{th}$-scale LBCB. The remaining RC piers are modeled in ZeusNL, with nonlinear inelastic behaviors the same as in Chapter 7. On the other hand, the bridge deck is further simplified from a nonlinear fiber element to a linear beam element; the response of bridge deck was linear elastic in most of the parametric nonlinear dynamic analyses. Linear models including the bridge deck, soil foundation, and elastomeric bearings are modeled in Matlab.

As a whole, the model structure is composed of five substructures, including one experimental substructure for a pier, three analytical substructures for the other piers in ZeusNL, and one analytical substructure for the rest of the bridge in Matlab.

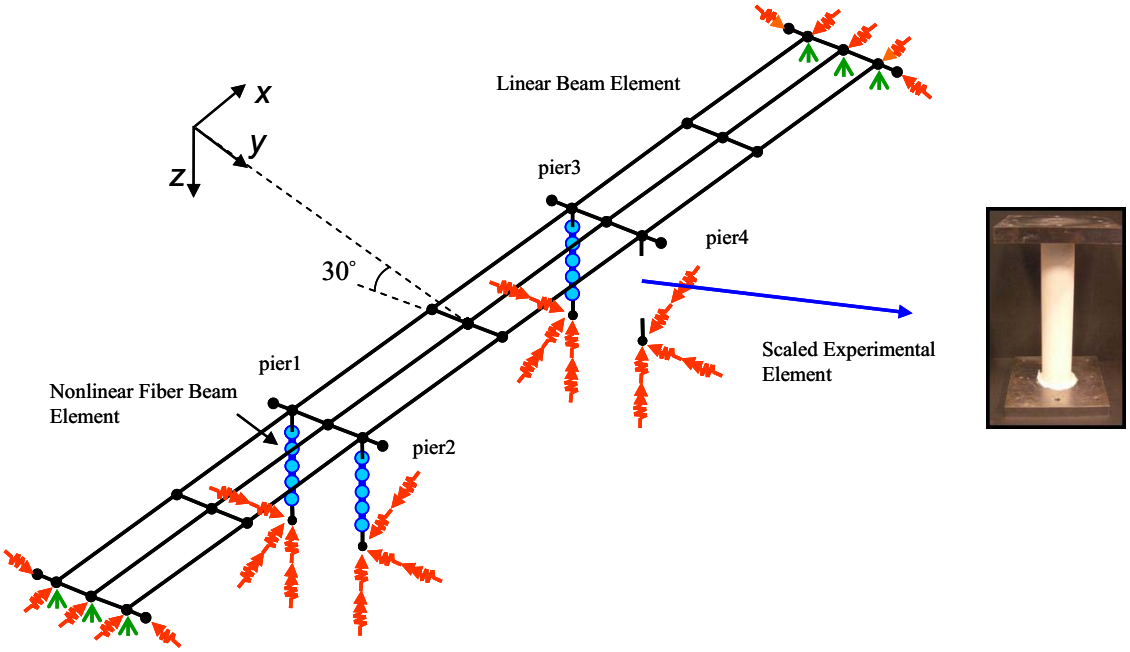

Figure 8.1. Bridge Modeling for hybrid simulation.

8.2.2 Network configuration

UI-SimCor (Kwon et al. 2005) is employed as a coordinator in the hybrid simulation. In addition to connecting the substructure modules, UI-SimCor also performs a time-step integration of equations of motion using the alpha-operator splitting method as the numerical integration algorithm.

Figure 8.2 shows the network configuration of the hybrid simulation. Three pier models in ZeusNL are connected to UI-SimCor through the NTCP server. Using the tele-operation control capability developed in this study, the experimental pier is also connected to UI-SimCor in the same way. On the other hand, the bridge deck model is integrated into the simulation in a different way. Because UI-SimCor and the bridge deck model are in the same software platform, Matlab, they are integrated into one Matlab program as shown in Figure 8.2. Therefore, although there are five substructures used for modeling of the reference bridge, there are only four modules that communicate with UI-SimCor through the network.

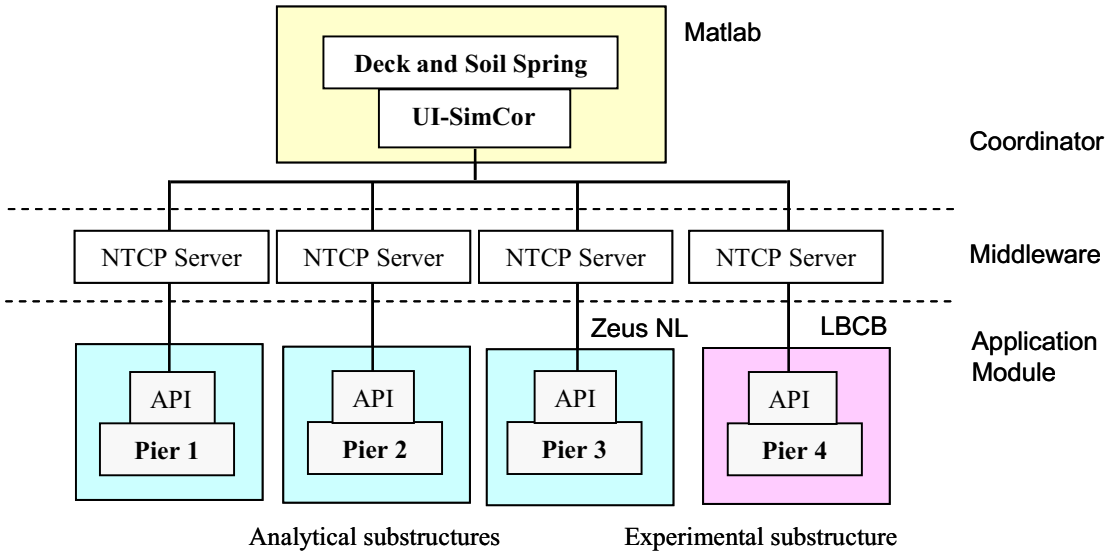

Figure 8.2. Bridge modeling for hybrid simulation.

8.3 Simulation Scenario

8.3.1 Similitude and scaling considerations

Similitude of RC members between two different scales is difficult to satisfy, especially when the model is extremely small compared to the prototype (Krawinkler 1988). Concrete has unique and different stress-strain relationships in compression and tension. Those material properties are dependent on not only scalable properties such as aggregate size, but also nonscalable properties such as confinement and bond-slip.

Furthermore, even if reasonable similitude in material properties is obtained, crack pattern, size, and propagation cannot be modeled in the small-scale. Those nonisotropic and nonscalable properties of concrete with inevitable scale effects make similitude of reinforced concrete a challenging, yet important research area (Noor and Boswell 1992).

The RC pier specimen used in the hybrid simulation is $1/20^{th}$ scale of the prototype bridge pier, which is categorized in extremely small-scaling. Therefore, although the cross-section, aspect ratio, reinforcement ratio, and concrete mixture design are carefully selected and monitored in the fabrication process, good similitude in the displacement and force relationships was not quantitatively obtained from the RC specimen. This quantitative disagreement of response was considered to be further affected by the boundary conditions where specimens are attached directly to steel plates without pier caps, which allow stress redistribution. Although the RC specimen does not exhibit quantitative similitude, it shows qualitative similitude of typical RC pier behavior such as cracking, yielding, post-peak, and pinching behavior as shown in Figure 5.13.

Because further discussion on the similitude of RC pier specimens is beyond the scope of this study, an artificial scaling factor is introduced for the response of the RC specimen in hybrid simulation as follows: (a) A preliminary uni-directional, quasistatic lateral loading test is conducted using an RC pier specimen to obtain the force-displacement relationships. (b) an analytical, quasistatic simulation is performed to obtain the force-displacement relationship employed in the analytical RC pier model; and (c) scaling factors are determined based on the agreement of the initial stiffness and ultimate strength between the experimental and analytical force-displacement relationships. Thus, scaling factors in this study are based on the lateral behavior of the RC pier, rather than on the dimension of the specimen. In the hybrid simulation, a target displacement is scaled down before execution, and the reaction force is scaled up after the measurement.

8.3.2 Selection of input ground motion

The Morgan Hill earthquake record of 1984 at station G06 is selected as the input ground motion for the hybrid simulation. The selected record has a relatively high pseudo velocity response spectrum around the first and second natural frequencies of the model bridge. Two horizontal components of the record are input in the longitudinal and transverse directions, respectively.

A parametric analytical study is carried out prior to the hybrid simulation to determine the amplification of the components in both the longitudinal and transverse directions. Based on the expected displacement feasible in the loading system, amplifications of the longitudinal and transverse components are determined to be 1.5 and 1.0, respectively. Figure 8.3 shows the amplified acceleration histories used in the hybrid simulation. Note that a baseline correction of the selected record was made to modify the ground displacement to zero at the end of the record.

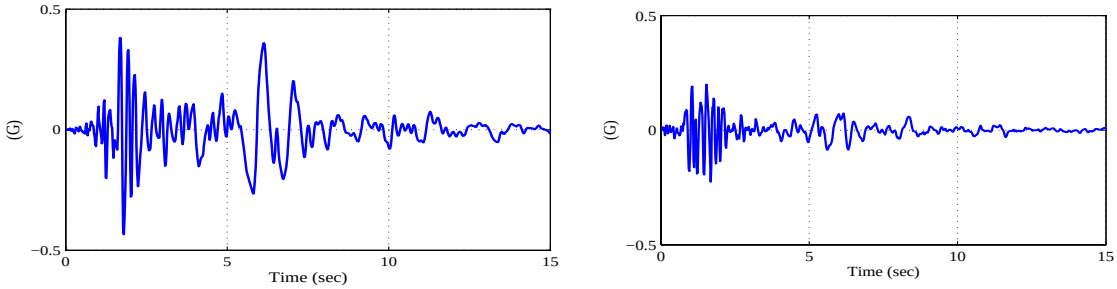

(a) Longitudinal direction (b) Transverse direction

Figure 8.3. Scaled ground motion-records.

8.3.3 Control mode in the axial direction of RC pier

Most numerical integration algorithms in hybrid simulation, including the alpha-OS method, calculate a target command that is to be imposed on the structure in the form of a displacement at each time step. For nonlinear structures, the target displacement is a predicted displacement based on the initial stiffness matrix. The displacement-driven algorithms are well-suited for DOFs for which force can be reasonably predicted by the initial stiffness in a linear manner. However, for DOFs where the initial stiffness is insufficient to predict the response, energy can be introduced into the model as a result of error propagation and accumulation.

As shown in Section 5.3.3, the axial force in RC piers is not only a function of axial displacement, but also subjected to the geometric nonlinearity as well as interaction with displacements and forces in other axes. Such complex behavior in the axial direction cannot be modeled by the linear initial stiffness. Because the axial direction is much stiffer than the other directions, any erroneous target displacement in the axial direction can cause unrealistic axial force variation. The effect of the axial load is significant on the behavior of the RC pier. Such undesired force variation in the axial direction is likely to result in the poor performance evaluation of the RC pier under unrealistic boundary conditions.

Governing actions on the RC piers during an earthquake are gravity loads in the axial direction and earthquake-induced displacements in the other directions. To impose appropriate load and boundary conditions on the RC pier in the hybrid simulation, the axial direction of the RC pier is controlled in force at a scaled constant initial gravity load level, rather than driven by the predicted displacements. The rest of the DOF are controlled in displacement based on the numerical integration algorithm. The mixed load and displacement control method developed in this study is employed to allow such combined actions on the RC pier.

8.4 Experimental Results

A hybrid simulation of the skew RC bridge is performed using the 1/5th-scale LBCB to demonstrate the effectiveness of multi-dimensional hybrid simulation for complex structural systems. Simulation results are discussed in each category in the following sections.

8.4.1 Multi-dimensional loadings

Figure 8.4 shows lateral and rotational displacement time-histories imposed on the RC pier specimen. The *x*, *y*, and *z*-axes correspond to the longitudinal, transverse, and vertical directions of the bridge, respectively. Although the input ground motion is considered only in two horizontal directions, three dimensional responses are induced for the entire bridge. As a result, the RC pier is subjected to loading in all 6DOF. Because of the large input motion in the longitudinal direction, large responses of the RC pier are seen in the longitudinal displacement and rotation around the transverse axis. The vertical displacement exhibits peculiar behavior compared with the other direction. This response is a result of the controlled axial force and the effect of the displacements in the other axes.

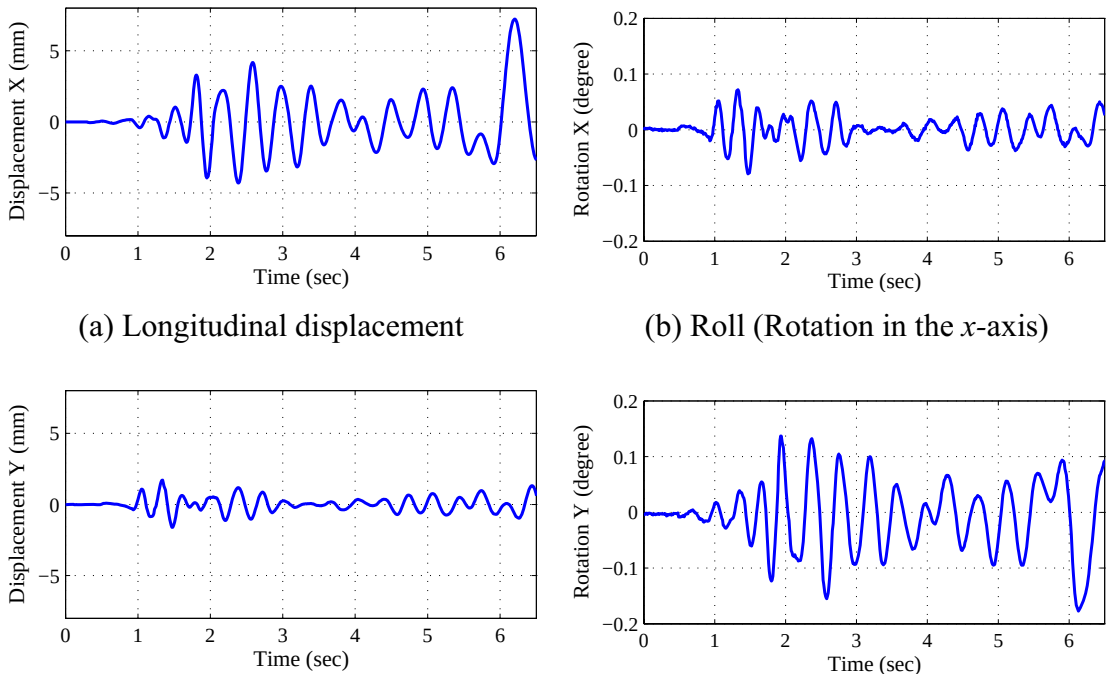

(a) Longitudinal displacement

(b) Roll (Rotation in the *x*-axis)

(c) Transverse displacement

(d) Pitch (Rotation in the *y*-axis)

Figure 8.4. Displacement and rotation time-histories at the RC pier.

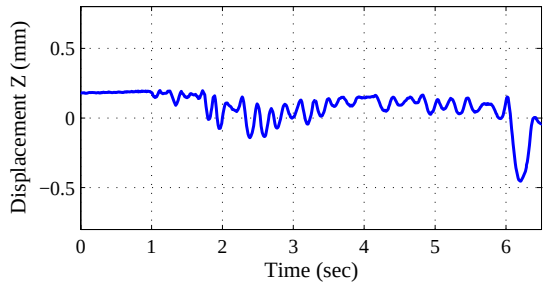

(e) Vertical displacement

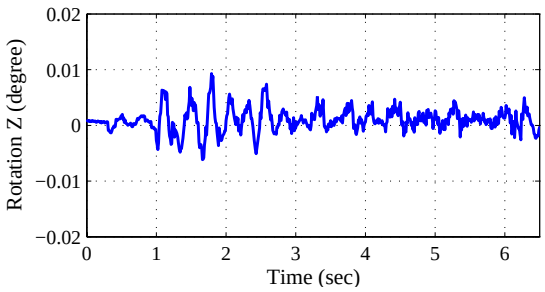

(f) Yaw (Rotation in the *z*-axis)

Figure 8.4. Displacement and rotation time-histories at the RC pier. (Continued).

In-plane lateral displacement trajectories are shown in Figure 8.5. These plots show the displacement paths at the top of the RC pier in three-dimensional space. To impose such continuously changing three-dimensional boundary conditions on structural components is quite challenging. These plots clearly indicate the spatial control capability of the LBCB and control system.

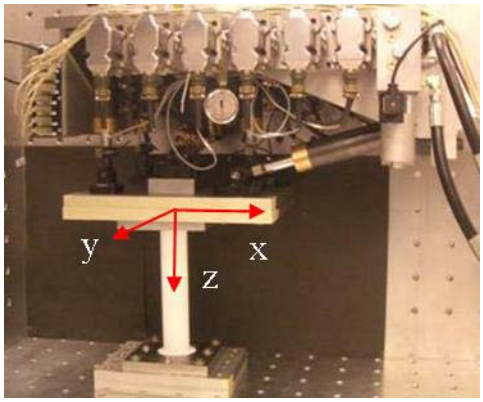

(a) Coordinates on the pier

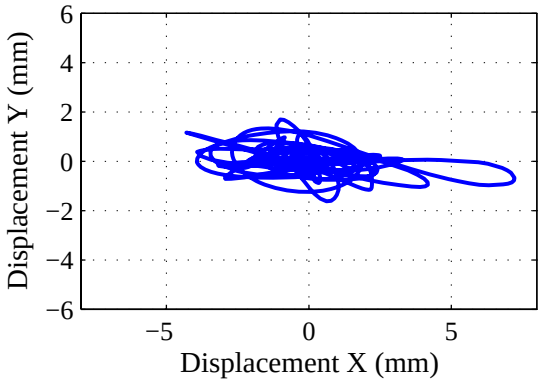

(b) Longitudinal - transverse

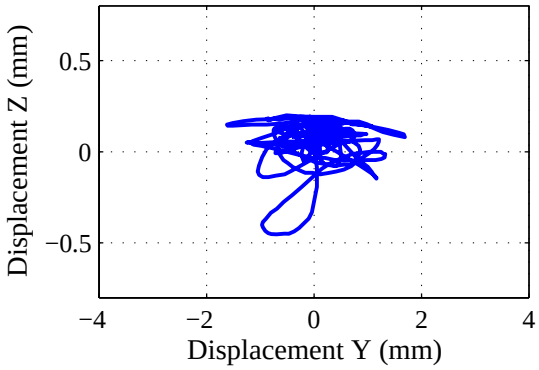

(c) Transverse - vertical

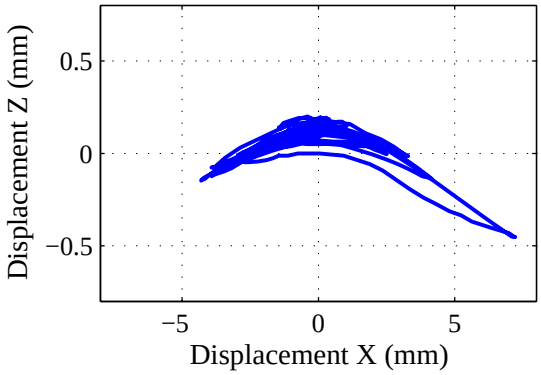

(d) Longitudinal - vertical

Figure 8.5. Lateral displacement trajectories at the RC pier.

8.4.2 Force and displacement relationships

Force and displacement relationships in the longitudinal and transverse directions are shown in Figure 8.6. The longitudinal response exhibits an inelastic hysteresis loop including yielding, pinching, and post-peak behavior. A relatively large amount of energy dissipation can be seen in the hysteresis of the peak cycle. On the other hand, the transverse response does not exhibit any significant nonlinear behavior. However, note that the transverse response shows two distinct stiffnesses (i.e., slopes). An observation showed that the transverse stiffness dropped by about 50% after the peak strength in the longitudinal direction is reached. This stiffness reduction is due to the interaction between the longitudinal and transverse behaviors. Damage in the longitudinal direction affects the strength in the transverse direction. These results demonstrate that multi-dimensional hybrid simulation allows the seismic performance evaluation of the structural elements under realistic load and boundary conditions, including the interactions among multiple directional behaviors; such multi-directional interactions cannot be evaluated in a simple in-plane simulation.

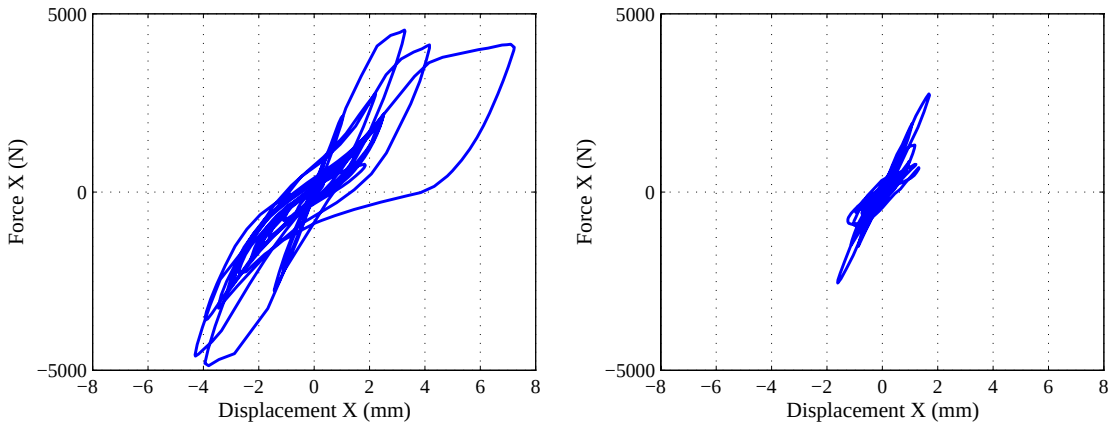

(a) Longitudinal direction (b) Transverse direction

Figure 8.6. Force-displacement relationships at the RC pier.

8.4.3 Mixed load and displacement control

Force and moment time-histories at the RC pier are shown in Figure 8.7. Similar to the lateral and rotational displacement time-histories, reaction forces and moments of the RC pier can be seen in all 6DOF. During the test, the development of small cracks is observed in the longitudinal direction. Despite the inelastic behavior of the RC pier and multi-dimensional loadings, the axial force in the vertical direction is controlled and remains constant at the initial gravity load level within the tolerance of 20N through the simulation. As shown here, the mixed load and displacement control capability is demonstrated in the multi-dimensional hybrid simulation of the RC specimen subjected to the multi-directional actions and exhibiting nonlinear inelastic behavior.

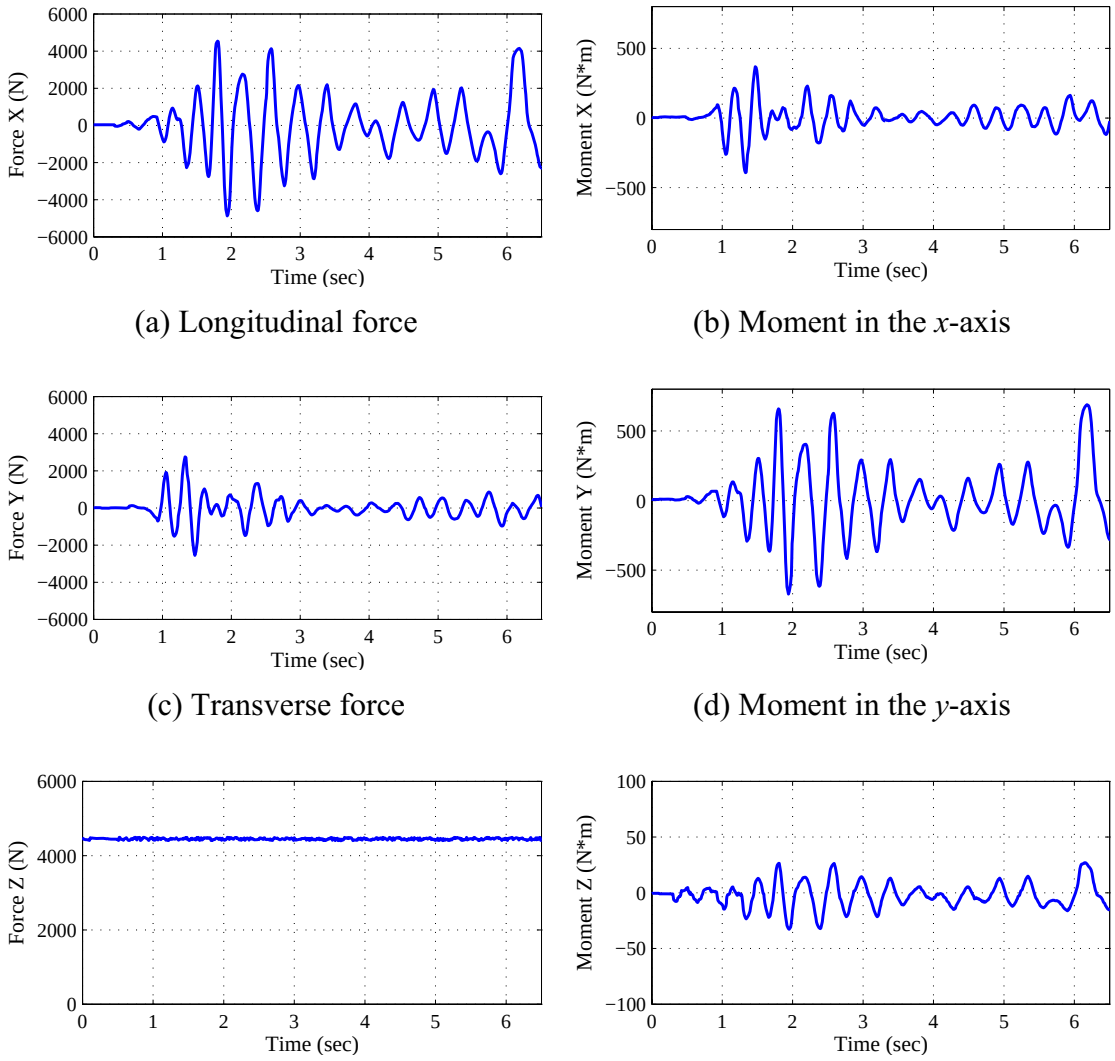

(a) Longitudinal force (b) Moment in the *x*-axis

(c) Transverse force (d) Moment in the *y*-axis

(e) Vertical force (f) Moment in the *z*-axis

Figure 8.7. Force and moment time-histories at the RC pier.

8.4.4 Control errors

Any errors introduced in the simulation affect the accuracy of the results. Needless to say, experimental errors such as control and measurement errors are not exceptional.

High control accuracy in multi-axial loading is challenging to achieve due to crosstalk. Furthermore, residual control errors in the actuator displacements are likely to be introduced by large reaction forces from a stiff specimen such as the RC pier discussed herein. It is of interest to investigate and evaluate control accuracy in multi-dimensional mixed-mode hybrid simulation. Figure 8.8 shows the lateral and rotational control errors in global coordinates. Errors in both lateral and rotational displacements are within a certain range, regardless of the amplitude of the imposed displacements and rotations. In

other words, any residual errors are not induced by the interaction with the specimen during the simulation. This high accuracy resulted from the high performance of the digital integrator technique described in Section 5.2.2. In the hybrid simulation, the digital integrator technique is employed for each actuator with a tolerance of 0.02 mm for longer stroke actuators and 0.01 mm for shorter stroke actuators. The test results confirm that the high accuracy in the actuator displacement using the discrete integrator technique reduces the errors in the global coordinates in a certain range.

The force control is applied only in the vertical direction in the hybrid simulation. As previously mentioned, its error is within the +-20 N, which is about 0.5% of the target force of 4500 N. Taking into account the challenges in mixed load and displacement control, the force error and tolerance are also very small. Thus, the control system developed in this study provides high accuracy in both displacement and load control in combined manner even in the hybrid simulation under 6DOF loading.

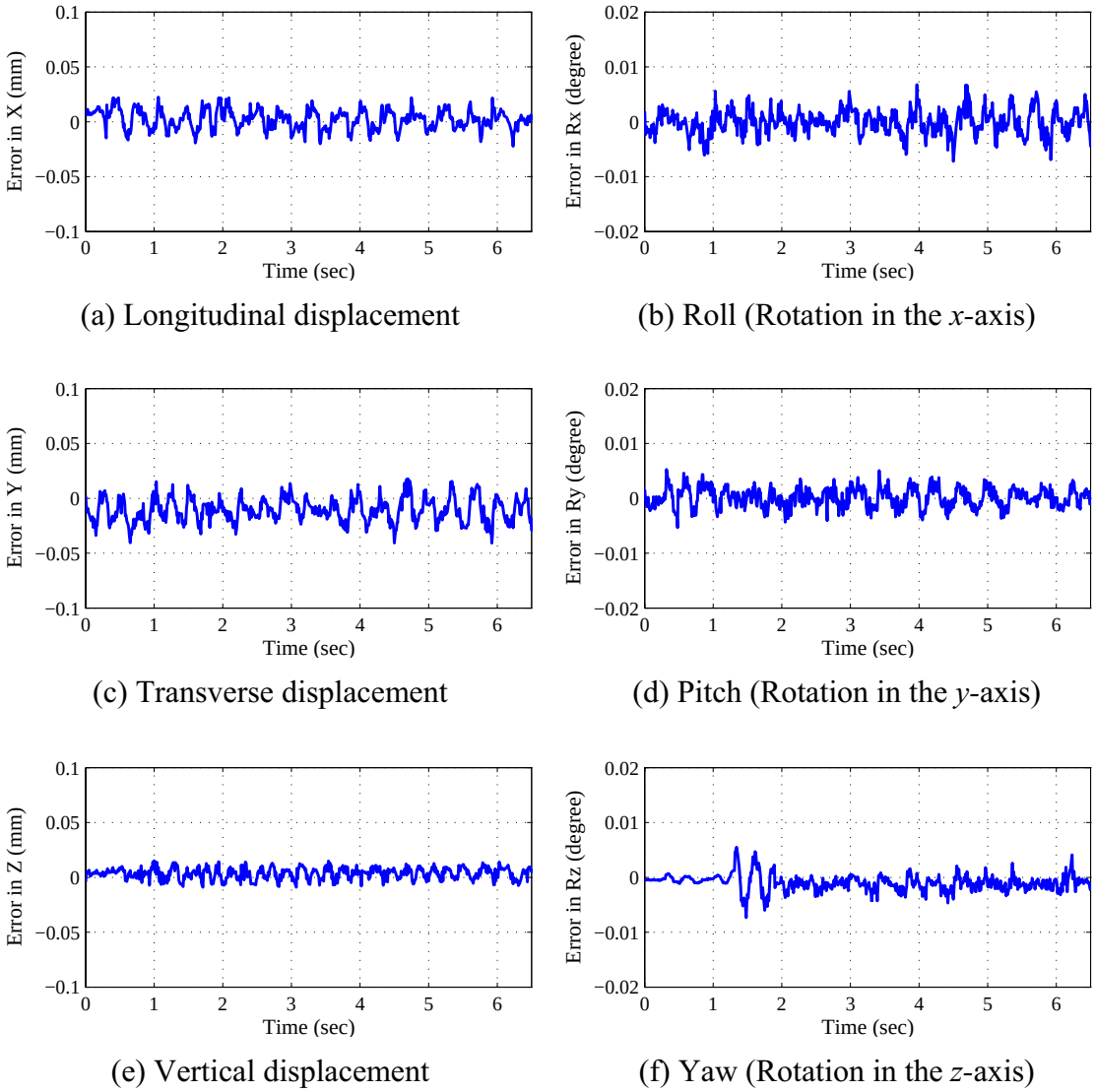

(a) Longitudinal displacement

(b) Roll (Rotation in the *x*-axis)

(c) Transverse displacement

(d) Pitch (Rotation in the *y*-axis)

(e) Vertical displacement

(f) Yaw (Rotation in the *z*-axis)

Figure 8.8. Control error time-histories at the RC pier.

8.4.5 Comparison with analytical simulation

The scope of this study is to demonstrate the effectiveness of multi-dimensional mixed-mode hybrid simulation using the small-scale RC pier specimen. Because of the scaling and fixture conditions of the RC pier specimen, the test results do not necessarily represent the actual bridge behavior. However, for the purpose of evaluating the test results, experimental results are compared with analytical results where all the piers are modeled analytically.

Figure 8.9 shows comparisons between analytical and experimental results of the force-displacement relationships and displacement time-histories in longitudinal and transverse directions. These comparisons are made at the simulation scale such that the experimental data is scaled up to the simulation level. Although scaling factors are carefully determined from the preliminary experimental results and analytical pier models, prior to the simulation, a large difference can be seen in the longitudinal force-displacement relationship, especially at the peak strength. This difference can be considered due to the uncertainties in the strength of the small-scale, reinforced concrete and the effect of fixture conditions between concrete and steel plates. On the other hand, the transverse response shows reasonable agreement between experimental and analytical results.

The difference at the global level can be evaluated from displacement time-histories. Transverse responses show good agreement between experimental and analytical results through simulation [see Figure 8.9 (d)]. Longitudinal response also shows reasonable agreement between experimental and analytical results at the first 2 seconds. After reaching the peak strength at 2 seconds, the differences in the displacement time-histories increase. This difference is due to the accumulation of the reaction force error between experiment and analysis through the simulation. However, the overall difference in the displacement time-history is not as significant as the difference in the force-displacement hysteresis.

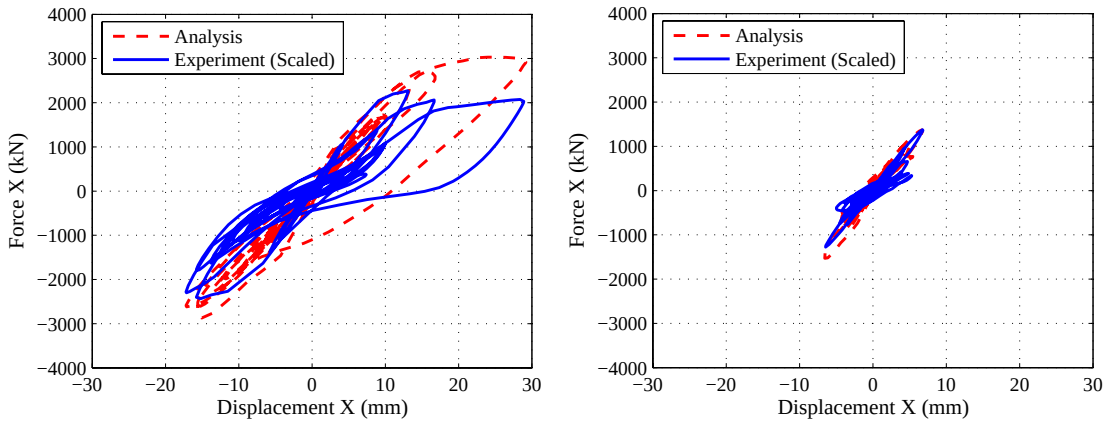

(a) Longitudinal hysteresis (b) Transverse hysteresis

Figure 8.9 Comparison between experimental and analytical results.

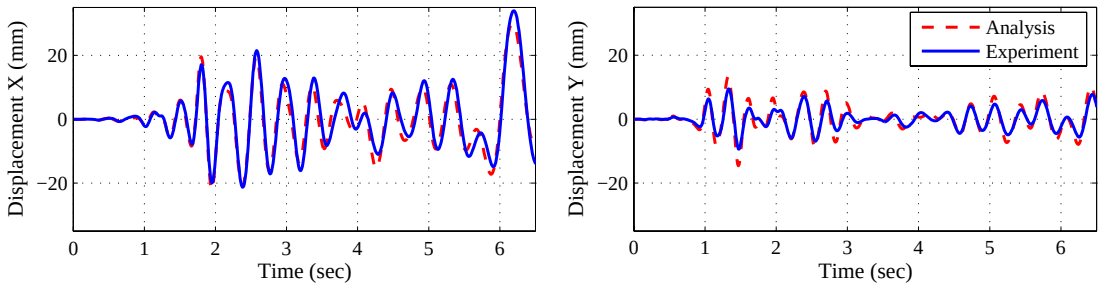

(c) Longitudinal time-histories (d) Transverse time-histories

Figure 8.9. Comparison between experimental and analytical results. (Continued).

8.5 Summary

This chapter presented a multi-dimensional hybrid simulation of a skew RC bridge. The model structure was divided into five substructures: one RC pier experimental model, three RC pier nonlinear computational models, and one linear computational model of the deck. Those substructures were connected to the UI-SimCor as a coordinator of the simulation. Similitude and scaling factors were considered to incorporate the small-scale RC pier specimen with analytical substructures at different scales in the bridge simulation.

The small-scale RC pier was experimentally tested in the hybrid simulation using the $1/5^{th}$-scale LBCB under 6DOF loadings. To simulate gravity loads in the axial direction and earthquake-induced displacements in the other directions, the mixed load and displacement control strategy developed in this study was employed in combination with the digital integrator technique. The test results demonstrated that three-dimensional hybrid simulation using the LBCB allows for component testing of complex structural systems under realistic loading in all 6DOF. This versatile testing capability with high accuracy in both displacement and load provides a more realistic and reliable means for the seismic assessment of structural systems.

CONCLUSIONS AND FUTURE STUDIES

9.1 Conclusions

The studies in this report have addressed a number of challenges facing wider use of hybrid simulation. Focus has been placed on the development of control strategies for multi-axial loading systems, seismic assessment of skew RC bridges, and demonstration of multi-dimensional hybrid simulation for a skew RC bridge. This study constitutes the first hybrid simulations accounting for all six-degrees-of-freedom (6DOF) in loading and employing mixed load and displacement control. The key contributions and findings in this report are summarized below.

A summary of hybrid simulation methodology has been provided including the substructure technique and numerical integration algorithms. One of the advantages of hybrid simulation is that it allows evaluation of the seismic performance of structural members under realistic loading in a system-level simulation. This literature review revealed that the loading in most experiments is simplified to match experimental capabilities; testing under complete 6DOF load and boundary conditions has not been reported for hybrid simulation.

Experimental facilities for hybrid simulation at the University of Illinois at Urbana-Champaign were presented in detail with specifications and capabilities. The six-actuator self-reaction loading system, referred as the Load and Boundary Condition Box (LBCB), was shown to be a versatile, state-of-the-art, 6DOF loading unit.

Transformations between actuator and global coordinates are essential processes in the control of multi-axial loading systems such as the LBCB. Any misrepresentation of parameters in the transformation introduces errors and crosstalk in the global Cartesian coordinates (i.e., specimen coordinates). However, such errors and crosstalk cannot be observed or eliminated based on actuator measurements; hence, evaluation and calibration of multi-axial loading systems is challenging. A systematic calibration method for multi-axial loading systems was developed utilizing an independent, external measurement system. The method is based on the sensitivity of the global coordinates with respect to the initial actuator length. A theoretical background and calibration procedure was given in a general framework. Calibration and verification using the proposed method were performed using the $1/5^{th}$-scale LBCB as the multi-axial loading system, and the Krypton Dynamic Measurement Machine as the external measurement system. Experimental results demonstrated that the proposed sensitivity-based external calibration method is effective for improving control accuracy and reducing crosstalk of multi-axial loading systems in global Cartesian coordinates.

Mixed load and displacement control capabilities were developed to simulate gravity loads in the axial direction and displacements in the other directions on the RC pier.

Because of the nonlinear nature of the coordinate transformations and cross-coupling of actuator forces in global coordinates, mixed load and displacement control for multi-axial loading system posed major theoretical and practical challenges. The mixed load and displacement control strategy was developed utilizing an incremental iterative approach. Broyden's method was used to update the stiffness Jacobian of the test specimen. The proposed mixed load and displacement control strategy was implemented into the LBCB control system, and verified using the $1/5^{th}$-scale LBCB for three types of specimens under two loading protocols. The experimental test results exhibited excellent control performance and robustness, even when the specimens were highly inelastic and material properties vary over a wide range.

In addition to development of the mixed load and displacement control strategy, several other control strategies were developed and implemented for the LBCB, including a digital integrator technique, tele-operation control, etc. These control strategies and capabilities were integrated, compiled, and made available as digital servo-control software, termed the LBCB Operation Manager. The LBCB Operation Manager has been used by researchers for testing using the LBCBs both for small- and full-scale hybrid simulation.

Skew bridges were introduced as examples of structural systems that exhibit complex multi-dimensional responses. A literature review of skew bridge studies was provided in a category of field surveys, analytical and numerical studies, modeling considerations, and component assessments.

Using a finite element model, parametric modal analysis was carried out with focus on the effect of the skew angle, span length configuration, and skew angle variation on global bridge behavior. The analytical results showed that the effect of the skew angle is negligible judging from the natural frequencies. However, due to eccentricities introduced by the skew angle, skew bridges have complex modal responses that couple the responses in the principle directions (i.e., longitudinal, transverse, and yaw).

For preparation and selection prior to the hybrid simulation, nonlinear pushover analyses were carried out considering material nonlinearity reinforced concrete, geometric nonlinearities, and local phenomena such as pounding of the deck and abutments. Results showed that the capacities of the RC pier are highly dependent on the boundary conditions, which can change significantly during an earthquake event.

Parametric nonlinear dynamic analyses were carried out with focus on the effect of the skew angle on bridge responses. Ground motion records were carefully selected to cover uncertainties in the ground motion, soil conditions, and input direction, and to properly scale the records based on the associated spectral intensity. Analytical results from the simulation scenarios are summarized as follows: (a) longitudinal response of bridges is not susceptible to skew angle; (b) transverse response of bridges tends to become larger as skew angle increases; and (c) the yaw of the bridge that results in torsional rotation at piers increases significantly as the skew angle increases. The pounding effect was observed in most of the simulation cases. However, the relationships between the skew angle and the pounding effect could not be determined.

A multi-dimensional hybrid simulation of the skew RC bridge was performed based on the analytical study on skew RC bridges using the control strategies developed in this study. The model structure was divided into five substructures: one RC pier experimental model tested in the 1/5th-scale facility, three RC pier nonlinear computational models, and one linear deck computational model. These five substructures were connected to UI-SimCor through the network using the NTCP communication protocol. The small-scale RC pier was experimentally tested under 6DOF loading with appropriate scaling considerations. The mixed load and displacement control strategy was employed to simulate gravity loads in the axial direction and earthquake-induced displacements in the other directions. Test results successfully demonstrated that a three-dimensional hybrid simulation using the LBCB allows for component testing of complex structural systems under realistic loading in all 6DOF. This versatile testing capability with high accuracy in both displacement and load provides a more realistic and reliable means for seismic assessment of structural systems using hybrid simulation.

9.2 Future Studies

This study has successfully accomplished the goal of enhancing hybrid simulation techniques used for seismic performance evaluation of complex structural systems accounting for multi-directional loadings. However, challenges still remain. The remainder of this chapter presents directions and suggestions for future studies.

9.2.1 Mixed load and displacement control

In this study, mixed load and displacement control was verified and applied using the 1/5th-scale LBCB with a small-scale specimen. Although the same control algorithm and digital controller can be used with the full-scale LBCB, issues and challenges may exist that were not observed in the small-scale testing. Therefore, it is recommended that the mixed load and displacement control using the full-scale LBCB should be verified prior to its application in hybrid simulation.

Possible applications of the mixed load and displacement control are not limited to seismic simulation of axial members that require load control in the axial direction and displacement control in the other directions. For some cases, load control in more than two axes may be needed, such as axial, shear, and moment-controlled test. The algorithm developed in this study is theoretically able to handle any loading protocols. However, the mixed load and displacement control needs to be verified for other applications with various specimens.

The mixed load and displacement control strategy developed in this study takes an iterative approach using a ramp-hold procedure. This approach is not suitable for structural specimens that have high relaxation and rate dependency. Further development of control algorithms is essential to expand the applicability of the mixed load and displacement control in continuous loading.

9.2.2 Assessment of skew RC bridges

In this study, the assessment of a skew RC bridge was conducted using the FHWA No. 4 bridge as a reference model. Although various types of skew bridges based on the reference model were covered in the parametric analyses, results do not necessarily reveal all of the possible effects of the skew angle on bridge behavior. For example, if a bridge has a single pier per each bent as opposed to two piers per bent, the torsional effect on the RC pier can be more significant. For an investigation of the current design codes of practice, further study needs to be carried out to improve our understanding of the effect of the skew angle on bridge behavior.

9.2.3 Hybrid simulation

Multi-dimensional hybrid simulation allows for the assessment of complex structural and geotechnical systems. Utilizing the multi-directional mixed load and displacement control capability developed herein for hybrid simulation, seismic performance of critical structural component can be assessed, taking into account system level responses. Multi-dimensional hybrid simulation must be further explored in various applications, especially those that have complex, coupled, multi-directional responses.

In general, numerical integration algorithms used in hybrid simulation are displacement-based; the target command is determined in the form of lateral and rotational displacements. The accuracy of such algorithms in the load-governed axes (e.g., vertical direction of bridge RC piers) needs to be evaluated, taking into account the effect of the error on the behavior of the associated members. If necessary, hybrid (mixed load and displacement-based) algorithms need to be developed to improve the accuracy of hybrid simulation.

Finally, the versatility of the hybrid simulation framework developed herein should be verified with various types of hybrid simulation, such as full-scale and geographically distributed hybrid simulation.

REFERENCES

AASHTO. (1995). "Standard Specifications for Highway Bridges, Division I-A: Seismic Design." *American Association of State Highway and Transportation Officials, Inc*., 15th Edition, as amended by the Interim Specification – Bridges, Washington, DC.

AASHTO. (1998). "LRFD Bridge Design Specification, 2nd ed." *American Association of State Highway and Transportation Officials, Inc*., Washington, DC.

ABAQUS, Inc. (2003). "ABAQUA Analysis User's Manual."

Aschheim, M., Gulkan, P., Sezen, H., Bruneau, M., Elnashai, A., Halling, M., Love, J., and Rahnama, M. (2000). "Performance of Buildings." *Earthquake Spectra*, 16(S1): 237-279.

Caltrans. (1995). "Bridge Design Details Manual, Section 7 – Bents." *State of California, Department of Transportation*, Sacramento, CA.

Caltrans. (1995). "Bridge Design Specifications, Section 8 – Reinforced Concrete." *State of California, Department of Transportation*, Sacramento, CA.

Campbell, S. L., and Meyer, C. D. (1991). "Generalized Inverses of Linear Transformations." New York, Dover.

Chang, S-Y. (2002). "Explicit Pseudodynamic Algorithm with Unconditional Stability." *Journal of Engineering Mechanics*, 128(9): 935-947.

Chen, C-H., Lai, W-C., Cordova, P., Deierlein, G. G., and Tsai, K-C. (2003). "Pseudo-Dynamic Test of A Full-Scale RCS Frame: Part 1 – Design, Construction and Testing." *International Workshop on Steel and Concrete Composite Constructions*, Taipei.

Combescure, D., and Pegon, P. (1997). "Alpha-Operator Splitting Time Integration Technique for Pseudodynamic Testing Error Propagation Analysis." *Soil Dynamics and Earthquake Engineering*, 16(7-8): 427-443.

Dermitzakis, S. N., and Mahin, S. A. (1985). "Development of Substructuring Techniques for On-line Computer Controlled Seismic Performance Testing." *Report UCB/EERC-85/04*, Earthquake Engineering Research Center, University of California, Berkeley.

Donea, J., Magonette, G., Negro, P., Pegon, P., Pinto, A., and Verzeletti, G. (1996). "Pseudodynamic Capabilities of the ELSA Laboratory for Earthquake Testing of Large Structures." *Earthquake Spectra*, 12(1): 163-180.

Elnashai, A. S. and Izzuddin, B. A. (1993). "Modeling of Material Nonlinearities in Steel Structures Subjected to Transient Dynamic Loading." *Earthquake Engineering and Structural Dynamics*, 22(6): 509-532.

Elnashai, A. S., and McClure, D. C. (1996). "Effect of Modelling Assumption and Input Motion Characteristics on Seismic Design Parameters of RC Bridge Piers." *Earthquake Engineering and Structural Dynamics*, 25(5): 435-463.

Elnashai, A. S. (1998). "Earthquake Resistance of High Strength Reinforced Concrete Buildings." *Seismic Design Practice into the Next Century*, Booth(ed.), Balkema, Rotterdam, 3-14.

Elnashai, A. S., Goodfellow, R. G. C., and Chana, P. S. (1998). "Flexural Ductility of High Strength Reinforced Concrete Structures." *Proc. of the 2nd Japan-UK Workshop on Implications of Recent Earthquake on Seismic Risk*, 145-157, Tokyo, Japan.

Elnashai, A. S., and Antoniou, S. (2000). "Implications of Recent Earthquakes on Seismic Risk." *Series on Innovation in Structures and Construction*, 2, Imperial College Press.

Elnashai, A. S., Papanikolaou, V., and Lee, D. (2002). "Zeus NL, A System for Inelastic Analysis of Structures." *Mid-America Earthquake Center*, University of Illinois at Urbana-Champaign, Program Release September 2002. http://mae.ce.uiuc.edu/software_and_tools/index.html

Elnashai, A. S. (2006). "Assessment of Seismic Vulnerability of Structures." *Journal of Constructional Steel Research*, 62: 1134-1147.

FHWA. (1996). "Seismic Design of Bridges – Design Example No. 4 Three-Span Continuous CIP Concrete Bridge," *FHWA-SA-97-009*, Federal Way, Washington, DC.

Fillippou, F., and Constantinides, M. (2004). "FEDEASLab Getting Started Guide and Simulation Examples." *Technical Report, NEESgrid-2004-22*, http://it.nees.org/.

French, C. W., Schultz, A. E., Hajjar, J. F., Shield, C. K., Ernie, D. W., Dexter, R. J., Du, D. H.-C., Olson, S. A., Daugherty, D. J., and Wan, C. P. (2004). "Multi-Axial Subassemblage Testing (MAST) System: Description and Capabilities." *Proc. of the 13th World Conference on Earthquake Engineering*, Vancouver, B.C., Canada.

Geodetic Systems, Inc. 3D Industrial Measurement Systems. (2006). "The Basics of Photogrammetry." http://www.geodetic.com/Whatis.htm

Ghobarah, A. A., and Tso, W. K. (1974). "Seismic Analysis of Skewed Highway Bridges with Intermediate Supports." *Earthquake Engineering and Structural Dynamics*, 2(3): 235-248.

Hakuno, M., Shidawara M., and Hara T. (1969). "Dynamic Destructive Test of a Cantilever Beam, Controlled by an Analog-Computer." *Journals of the Japan Society of Civil Engineers*, 171: 1-9 (In Japanese).

Hakuno M., Yokoyama K., and Sato Y. (1972). "Real Time Dynamic Test on a Model Pile Foundation." *Journals of the Japan Society of Civil Engineers*, 200: 85-90 (In Japanese).

Hilber, H. M., Huges, T. J. R., and Taylor, R. L. (1977). "Improved Numerical Dissipation for Time Integration Algorithms in Structural Dynamics." *Earthquake Engineering and Structural Dynamics*, 5(3): 283-292.

Holub, C. (2005). "Similitude Considerations for Small Scale Distributed Hybrid Testing of Reinforced Concrete Bridges." *Master Thesis*, University of Illinois at Urbana-Champaign.

Horiuchi, T., Inoue, M., Konno, T., and Namita, Y. (1999). "Real-Time Hybrid Experimental System with Actuator Delay Compensation and Its Application to a Piping System with Energy Absorber." *Earthquake Engineering and Structural Dynamics*, 28(10): 1121-1141.

Huang, H., Shenton, H. W., and Chajes, M. J. (2004). "Load Distribution for a Highly Skewed Bridge: Testing and Analysis." *Journal of Bridge Engineering*, 9(6): 558-562.

Japanese Society of Civil Engineering. (1996). "Special Task Committee of Earthquake Resistance of Civil Engineering Structures: Proposal on Earthquake Resistance for Civil Engineering."

Jennings, P. C. (1971) "Engineering features of the San Fernando earthquake." *Report No. EERL 71-02*, California Institute of Technology, Pasadena, CA: 366-433.

Jeong, S-H., and Elnashai, A. S. (2005). "Analytical Assessment of an Irregular RC Frame for Full-Scale 3D Pseudo-Dynamic Testing Part I: Analytical Model Verification." *Journal of Earthquake Engineering*, 9(1): 95-128.

Kankam, J. A., and Dagher, H. J. (1995). "Nonlinear FE Analysis of RC Skewed Slab Bridges." *Journal of Structural Engineering*, 121(9): 1338-1345.

Kawashima K., and Unjoh, S. (1998). "The Damage of Highway Bridges in the 1995 Hyogo-ken Nanbu Earthquake and Its Impact on Japanese Seismic Design." *Journal of Earthquake Engineering*, 1(3): 505-541.

Kawashima K., and Unjoh, S. (2000). "Damage of Transportation Facility in the 1999 Kocaeli and Duzce, Turkey Earthquakes and the 1999 Chi-Chi, Taiwan Earthquake." *Proc. of the 34th Joint Meeting of US-Japan Panel on Wind and Seismic Effects*, UJNR, NIST Special Publication, 904: 159-174.

Krawinkler, H. (1988). "Scale Effects in Static and Dynamic Model Testing of Structures." *Proc. of the 9th World Conference on Earthquake Engineering*, 8: 865-876.

Krypton Industrial Metrology. (2003). "Krypton Help Pages on DMM Modular."

Kwon, O. S., Nakata, N., Elnashai, A. S., and Spencer, B. F. (2005). "A Framework for Multi-Site Distributed Simulation and Application to Complex Structural Systems." *Journal of Earthquake Engineering*, 9(5): 741-753.

Madas, P., and Elnashai, A. S. (1992). "A New Passive Confinement Model for the Analysis of Concrete Structures Subjected to Cyclic and Transient Loading." *Earthquake Engineering and Structural Dynamics*, 21(5): 409-431.

Magonette, G. (2001). "Development and Application of Large-scale Continuous Pseudo-dynamic Testing Techniques." *Dynamic Testing of Theme, Philosophical Transactions of the Royal Society: Mathematical, Physical and Engineering Sciences*, 359: 1771-1799.

Mahin, S. A., and Shing, P. B. (1985). "Pseudodynamic Method for Seismic Testing." *Journal of Structural Engineering*, 111(7): 1482-1503.

Mahin, S. A., Sakai, J., and Chang, H. (2006). "Use of Partially Prestressed Reinforcement Concrete Columns to Reduce Post-Earthquake Residual Displacements of Bridges." *Proc of the 5th National Seismic Conference on Bridges & Highways*, San Francisco, CA.

Maleki, S. (2001). "Free Vibration of Skewed Bridges." *Journal of Vibration and Control*, 7(7): 935-952.

Maleki, S. (2002). "Deck Modeling for Seismic Analysis of Skewed Slab-Girder Bridges." Engineering Structures, 24(10): 1315-1326.

Maragakis, E., and Jennings, P. (1987). "Analytical Models for the Rigid Body Motions of Skew Bridges." *Earthquake Engineering and Structural Dynamics*, 15(8): 923-944.

Martinez-Rueda, J. E., and Elnashai, A. S. (1997). "Confined Concrete Model under Cyclic Load." *Materials and Structures*, 30(3); 139-147.

Mathworks. (2003). "Matlab, the Language of Technical Computing." *The Mathworks, Inc*., MA.

Mazzoni, S., McKenna, F., Scot, M. H., and Fenves, G. L. (2006). "Open System for Earthquake Engineering Simulation User Command-Language Manual." *Pacific Earthquake Engineering Research Center*, University of California, Berkeley, OpenSees version 1.7.3 http://opensees.berkeley.edu/index.php

McCallen, D. B., and Romstad, K. M. (1994). "Dynamic Analysis of a Skewed Short-Span, Box-Girder Overpass." *Earthquake Spectra*, 10(4): 729-755.

Meng, J. Y., and Lui, E. M. (2000). "Seismic Analysis and Assessment of a Skew Highway Bridge." *Engineering Structures*, 22(11): 1433-1452.

Meng, J. Y., and Lui, E. M. (2002). "Refined Stick Model for Dynamic Analysis of Skew Highway Bridges." *Journal of Bridge Engineering*, 7(3): 184-194.

Meng, J. Y., Ghasemi, H., and Lui, E. M. (2004). "Analytical and Experimental Study of a Skew Bridge Model." *Engineering Structures*, 26(8): 1127-1142.

Mizusawa, T., Kajita, T., and Naruoka, M. (1980). "Analysis of Skew Plate Problems with Various Constraints." *Journal of Sound and Vibration*, 73(4): 575-584.

Molina, F. J., Verzeletti, G., Magonette, G, Buchet, PH., and Geradin, M. (1999). "Bi-Directional Pseudodynamic Test of a Full-Size Three-Storey Building." *Earthquake Engineering and Structural Dynamics*, 28(12): 1541-1566.

Mosqueda, G. (2003). "Continuous Hybrid Simulation with Geographically Distributed Substructures." *Ph.D. Thesis*, University of California, Berkeley.

Muthukumar, S., and DesRoches, R. (2006). "A Hertz Contact Model with Non-Linear Damping for Pounding Simulation." *Earthquake Engineering and Structural Dynamics*, 35(7): 811-828.

Nakashima, M., and Kato, H. (1987). "Experimental Error Growth Behavior and Error Growth Control in On-line Computer Test Control Method." *Building Research Institute, BRI-Report 123*, Ministry of Construction, Tsukuba, Japan.

Nakashima, M., Kaminosono, T., Ishida, I., and Ando, K. (1990). "Integration Techniques for Substructure Pseudodynamic Test." *Proc. of the 4th U.S. National Conference on Earthquake Engineering,* 2: 515-524, Palm Springs, CA.

Nakashima, M., Kato, M., and Takaoka, E. (1992). "Development of Real-Time Pseudodynamic Testing." *Earthquake Engineering and Structural Dynamics*, 21(1): 79-92.

Nakata, N., Spencer, B. F., and Elnashai, A. S. (2006). "Mixed Load / Displacement Control Strategy for Hybrid Simulation." *Proc. of the 4th International Conference on Earthquake Engineering*, Taiwan.

Nakata, N., Spencer, B. F., and Elnashai, A. S. (2007). "Sensitivity-Based External Calibration Method for Multi-Axial Loading System." *Journal of Structural Engineering* (to be submitted).

Nakata, N., Elnashai, A. S., and Spencer, B. F. (2007). "Multi-Dimensional Hybrid Simulation Using a Six-Actuator Self-Reaction Loading System." *Earthquake Spectra* (to be submitted).

Negro, P., Verzeletti, G., Magonette, G., and Pinto, A. (1994). "Test on A Four-Storey RC Frame Designed According to Eurocodes 8 and 2." *Preliminary Report*, EUR 15879 EN, Joint Research Center, Commission of the European Communities, Ispra, Italy.

Nielson, B. (2005). "Analytical Fragility Curves for Highway Bridges in Moderate Seismic Zones." *Ph.D. Thesis*, Georgia Institute of Technology.

Noor, F. A., and Boswell, F. L. (1992). "Small Scale Modeling of Concrete Structures." Elsevier, New York.

Ohtani, K., Ogawa, N., Katayama, T., and Shibata, H. (2002). "3-D Full-scale Earthquake Testing Facility and Earthquake Engineering Network." *Proc. of the 3rd World Conference on Structural Control*, Como, Italy.

Pearlman, L., D'Arcy, M., Johnson, E., Kesselman, C., and Plaszczak, P. (2004). "NEESgrid Teleoperation Control Protocol (NTCP)." *Technical Report, NEESgrid-2004-23*, http://it.nees.org/.

Pen, P., Tomofuji, H., Wang, T., Nakashima, M., Ohsaki, M., and Mosalam, M. (2006). "Development of Peer-to-Peer (P2P) Internet Online Hybrid Test System." *Earthquake Engineering and Structural Dynamics*, **35**(7): 867-890.

Robert, J. E. (1994). "Highway Bridges." Chapter 6 in *Practical Lessons from the Loma Prieta Earthquake*, National Research Council, National Academies Press, Washington, DC.

Robson, B. N., Harik, I. E., and Gupta, V. (2001). "Effectiveness of Seismic Isolation of Highly Skewed P/C I-Girder Bridge." *Journal of Bridge Engineering*, 6(3): 221-224.

Schiff, A. (1995). "Northridge Earthquake, Lifeline performance and post-earthquake response." *Technical Council on Lifeline Earthquake Engineering*, Monograph No.8, ASCE.

Schiff, A. (1998). "Hyogoken-Nanbu (Kobe) Earthquake of January 17, 1995, -Lifeline Performance." *Technical Council on Lifeline Earthquake Engineering*, Monograph No. 14, ASCE.

Schneider, S., and Roeder, C. (1994). "An Inelastic Substructure Technique for the Pseudodynamic Test Method." *Earthquake Engineering and Structural Dynamics*, 23(7): 761-775.

Seible, F., Hegemier, G., and Igarashi, A. (1996). "Simulated Seismic Laboratory Load Testing of Full-Scale Buildings." *Earthquake Spectra*, 12(1): 57-86.

Shing, P. B., and Mahin, S. A. (1983). "Experimental Error Propagation in Pseudodynamic Testing." *UCB/EERC-83/12, Earthquake Engineering Research Center*, University of California, Berkeley.

Shing, P. B., and Mahin, S. A. (1985). "Computational Aspects of A Seismic Performance Test Method Using On-line Computer Control." *Earthquake Engineering and Structural Dynamics*, 13(4): 507-526.

Shing, P. B., and Mahin, S. A. (1988). "Rate-of-Loading Effect on Pseudodynamic Tests." *Journal of Structural Engineering*, 114(11): 2403-2420.

Shing, P. B., Vannan, M. T., and Carter, E. W. (1991). "Implicit Time Integration for Pseudodynamic Test." *Earthquake Engineering and Structural Dynamics*, 20(6): 551-571.

Shing, P. B., Nakashima, M., and Bursi, O. (1996). "Application of Pseudodynamic Test Method to Structural Research." *Earthquake Spectra*, 12(1): 29-56.

Spencer, B. F., Elnashai, A. S., Nakata, N., Seliem, H., Yang, G., Futrelle, J., Glick, W., Marcusiu, D., Ricker, K., Finholt, T., Horn, D., Hubbard, P., Keahey, K., Liming, L., Zaluzec, N., Pearlman, L., and Stauffer, E. (2004). "The MOST Experiment: Earthquake Engineering on the Grid." *Technical Report*, NEESgrid-2004-41.

Tagami, J., Ishii, T., Iizuka, S., and Ishida, M. (1990). "Application of Substructure Pseudo Dynamic Test to Base Isolated Structure." *Proc. of the 4th U.S. National Conference on Earthquake Engineering*, 3:599-608, Palm Springs, CA.

Takahashi, Y., and Fenves, G. L. (2006). "Software Framework for Distributed Experimental-Computational Simulation of Structural Systems." *Earthquake Engineering and Structural Dynamics*, 35(3): 267-291.

Takanashi, K., Udagawa, K., Seki, M., Okada, T., and Tanaka, H. (1975) "Nonlinear Earthquake Response Analysis of Structures by A Computer-Actuator On-Line System" *Bulletin of Earthquake Resistant Structure Research Center 8*, Institute of Industrial Science, University of Tokyo.

Takanashi, K., and Nakashima M. (1987). "Japanese Activities On-Line Testing." *Journal of Engineering Mechanics*, 113(7): 1014-1032.

Tang, A. (2000). "Izmit (Kocaeli), Turkey, Earthquake of August 17, 1999, including Duzce Earthquake of November 12, 1999, -Lifeline Performance." *Technical Council on Lifeline Earthquake Engineering*, Monograph No. 17, ASCE.

Thewalt, C. R., and Mahin, S. A. (1995). "An Unconditionally Stable Hybrid Pseudodynamic Algorithm." *Earthquake Engineering and Structural Dynamics*, 24(5): 723-731.

Thewalt, C. R., and Mahin, S. A. (1995). "Nonplaner Pseudodynamic Testing." Earthquake Engineering and Structural Dynamics, 24(5): 733-746.

Tirasit, P, Kawashima, K., and Watanabe, G. (2005). "An Experimental Study on the Performance of RC Columns Subjected to Cyclic Flexural-Torsional Loading." *Proc. of the 2nd International Conference on Urban Earthquake Engineering*, 357-364.

TNO Diana. (2005). "DIANA User's Manual Release 9." *TNO Diana B.V.*, Netherland.

Todd, D., Carino, N., Chung, R. M., Lew, H. S., Taylor, A. W., Walton, W. D., Cooper, J. D., and Nimis, R. (1994). "1994 Northridge Earthquake –Performance of Structures, Lifelines, and Fire Protection Systems." *NIST Special Publication*, 862, ICSSC TR14.

Tsai, K. C., Li, J., and Wang, T. (1994). "Pseudodynamic Performance of Steel Plate Energy-Dissipating Substructures." *Proc. of the 5th U.S. National Conference on Earthquake Engineering*, 735-744, Earthquake Engineering Research Institute, Chicago.

Tsai, K. C., Lai, J. W., Chen, C. H., Hsiao, B. C., Weng, Y. T., and Lin, M. L. (2004). "Pseudo Dynamic Tests of a Full Scale CFT/BRB Composite Frame." *Proc. of Structures Congress 2004*, Tennessee.

Tsutumi, H., Ando, K., and Sato, K. (1990). "Substructure Pseudo Dynamic Test with Rotation Control." *Proc. of the 4th U.S. National Conference on Earthquake Engineering,* 2: 525-534, Palm Springs, CA.

Vecchio, F. J., and Wong, P. (2003). "VecTor2 and FormWorks Manual." *Software Manual*, VecTor Analysis Group, University of Toronto.

Wakefield, R., Nazmy, A., and Billington, D. (1991). "Analysis of Seismic Failure in Skew RC Bridges." *Journal of Structural Engineering*, 117(3): 972-986.

Wang, K. J., Wang, S. J., Cheng, W. C., Yang, Y. S., and Tsai, K. C. (2005). "A Platform for Networked Collaborative Structural Experiments." *Proc of the 1st Conference on Advanced in Experimental Structural Engineering*, Nagoya, Japan.

Watanabe, G., and Kawashima, K. (2004). "Seismic Response of a Skewed Bridge." *Proc. of the 13th World Conference on Earthquake Engineering*, Vancouver, B.C., Canada.

Yashinsky, M. (1998). "The Loma Prieta, California, Earthquake of October 17, 1989 - Highway Systems." *U.S. Geological Survey Professional Paper,* 1552-B.

TRANSFORMATION FROM ACTUATOR TO GLOBAL COORDINATES

The transformation from the actuator to the global coordinates is not straight-forward. Six sets of Equation (4.11) need to be solved with respect to the global displacement **u** from the actuator length l_j $\left(j=1,\cdots,6\right)$. Equation (4.11) is a highly nonlinear equation. It is not possible to solve six of these equations explicitly and to identify one correct solution from the multiple possible solutions. As an alternative, an iterative numerical approach can be applied to solve this problem using the modified Newton-Raphson method with a kinematic Jacobian. Taking the square of Equation (4.11), the following relation can be obtained,

$$l_i^2 = \Phi_i\left(x, y, z, \theta_x, \theta_y, \theta_z\right) \tag{A.1}$$

where Φ_i is a symbolic notation of the function to square of the actuator length in Equation (4.11). Φ_i is continuous and differentiable with respect to all variables in **u**. Partial derivative of Φ_i can be taken for each variable as follows:

$$2l_i\frac{\partial l_i}{\partial u} = \frac{\partial \Phi_i}{\partial u}\left(x, y, z, \theta_x, \theta_y, \theta_z\right) du:\ \left(u = x, y, z, \theta_x, \theta_y, \theta_z\right) \tag{A.2}$$

Considering that actuator lengths are always greater than zero $l_i > 0$, the increment Δl_i can be approximated as the summation of the partial derivatives as follows:

$$\begin{aligned}\Delta l_i &= \frac{\partial l_i}{\partial x}\Delta x + \frac{\partial l_i}{\partial y}\Delta y + \frac{\partial l_i}{\partial z}\Delta z + \frac{\partial l_i}{\partial \theta_x}\Delta\theta_x + \frac{\partial l_i}{\partial \theta_y}\Delta\theta_y + \frac{\partial l_i}{\partial \theta_z}\Delta\theta_z \\ &= \frac{1}{2l_i}\left(\frac{\partial \Phi_i}{\partial x}\Delta x + \frac{\partial \Phi_i}{\partial y}\Delta y + \frac{\partial \Phi_i}{\partial z}\Delta z + \frac{\partial \Phi_i}{\partial \theta_x}\Delta\theta_x + \frac{\partial \Phi_i}{\partial \theta_y}\Delta\theta_y + \frac{\partial \Phi_i}{\partial \theta_z}\Delta\theta_z\right)\end{aligned} \tag{A.3}$$

From the relationship in Equation (A.3), a kinematics Jacobian $\mathbf{J}_k$ can be constructed as follows:

$$\begin{bmatrix} \Delta l_1 \\ \Delta l_2 \\ \Delta l_3 \\ \Delta l_4 \\ \Delta l_5 \\ \Delta l_6 \end{bmatrix} = \begin{bmatrix} \frac{1}{l_1}\frac{\partial \Phi_1}{\partial x} & \frac{1}{l_1}\frac{\partial \Phi_1}{\partial y} & \frac{1}{l_1}\frac{\partial \Phi_1}{\partial z} & \frac{1}{l_1}\frac{\partial \Phi_1}{\partial \theta_x} & \frac{1}{l_1}\frac{\partial \Phi_1}{\partial \theta_y} & \frac{1}{l_1}\frac{\partial \Phi_1}{\partial \theta_z} \\ \frac{1}{l_2}\frac{\partial \Phi_2}{\partial x} & \cdots & \cdots & \cdots & \cdots & \cdots \\ \frac{1}{l_3}\frac{\partial \Phi_3}{\partial x} & \cdots & \cdots & \cdots & \cdots & \cdots \\ \frac{1}{l_4}\frac{\partial \Phi_4}{\partial x} & \cdots & \cdots & \cdots & \cdots & \cdots \\ \frac{1}{l_5}\frac{\partial \Phi_5}{\partial x} & \cdots & \cdots & \cdots & \cdots & \cdots \\ \frac{1}{l_6}\frac{\partial \Phi_6}{\partial x} & \cdots & \cdots & \cdots & \cdots & \cdots \end{bmatrix} \begin{bmatrix} \Delta x \\ \Delta y \\ \Delta z \\ \Delta \theta_x \\ \Delta \theta_y \\ \Delta \theta_z \end{bmatrix} \tag{A.4}$$

$$\mathbf{\Delta l} = \mathbf{J}_k \mathbf{\Delta u}$$

The kinematic Jacobian $\mathbf{J}_k$ gives a relationship between an increment in the actuator length $\mathbf{\Delta l}$ and the global displacement $\mathbf{\Delta u}$. Note that the kinematic Jacobian is a function of the global displacement $\mathbf{u}$.

The modified Newton-Raphson method using the kinematic Jacobian $\mathbf{J}_k$ for transformation from the actuator to the global coordinates is summarized in Figure A.1. After the actuator strokes are measured, those measured actuator strokes are compared with the estimated actuator strokes. At the first iteration, the previous actuator strokes are used as the estimated actuator strokes. If all of the errors between measured and estimated actuator strokes are within an acceptable range, the global displacement used for the estimated actuator strokes is an approximated numerical solution. If not, the kinematic Jacobian is calculated at the previous global displacement. Then, the global displacement is updated based on the kinematic Jacobian and the error between the measured and estimated actuator strokes. Once the global displacement is updated, the process goes back to step 2 in Figure A.1 to recalculate the estimated actuator strokes. This process will be repeated until all of the errors between the measured and estimated actuator strokes are within an acceptable range.

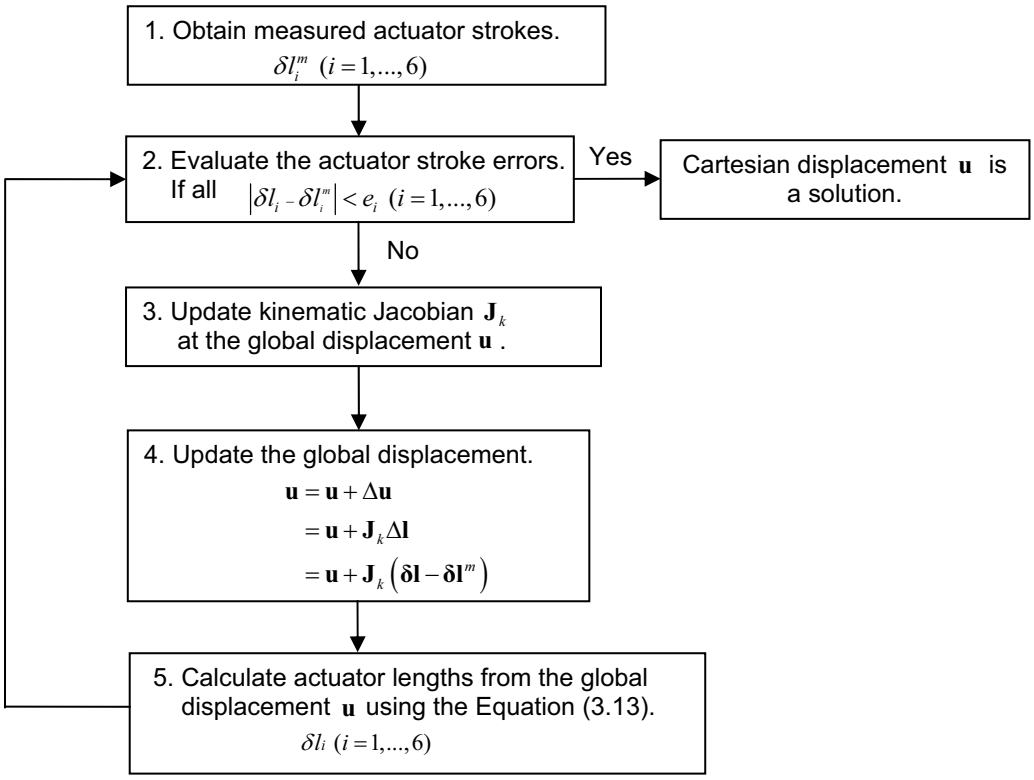

Figure A.1. Flowchart of the transformation from the actuator to the global coordinates.

TEST SPECIMENS

Two types of specimens are used in the study: small-scale reinforced concrete (RC) piers and aluminum columns. The following is a description of those specimens.

B.1 Reinforced Concrete Piers

In the multi-dimensional hybrid simulation utilizing six-degrees-of-freedom (6DOF), versatile control capabilities of the Load and Boundary Condition Box (LBCB), a small-scale RC pier has been tested as an experimental substructure of a skew RC bridge. The same RC piers have been also extensively used for the verification of control algorithms developed in this study. Those small-scale RC piers are designed with similitude considerations of the prototype RC pier as well as the capacity of the LBCB, and fabricated using carefully selected materials.

Prototype bridge pier

Design Example No. 4 from the Federal Highway Administration (FHWA) Seismic Design of Bridges (FHWA 1996) is used as a prototype bridge. The FHWA No. 4 bridge has four identical circular RC piers with a height of 6096 mm and a diameter of 1219 mm. The cross-section of the prototype RC pier is shown in Figure B.1(a). The prototype bridge pier has a continuous cap beam and spread footing. However, because of the constructability of the small-scale RC pier, only the cylinder portion of the RC pier is modeled in the test specimen.

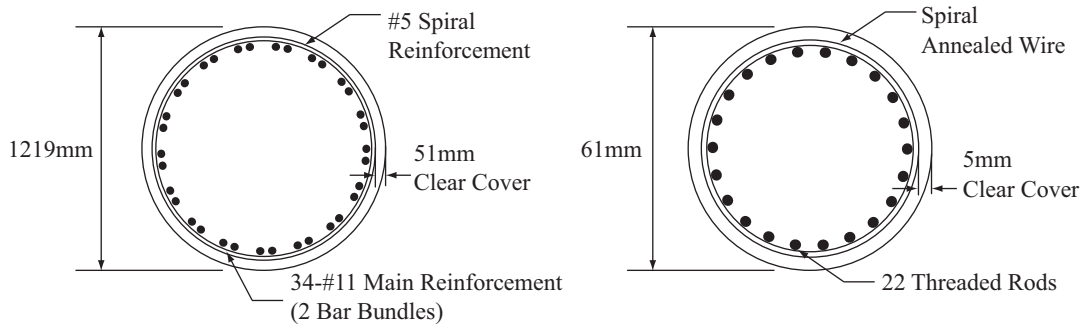

(a) Prototype RC Pier (b) Small-scaled RC Pier

Figure B.1. RC pier cross sections.

Scaling considerations

The design of scaled specimens generally takes an iterative process to satisfy and optimize multiple criteria under the constraints of testing system capabilities. For the small-scaled RC pier specimen employed herein, the following two constraints are considered: The first constraint is that the specimens can be tested up to failure in lateral loading within the capacity of the LBCB. Because severe loading and nonlinear behavior in the hybrid simulation is of interest in the study, this criteria needs to be satisfied. The second constraint is that a reasonably scaled axial load can be imposed within the capacity of the LBCB. The axial load level governs behaviors in shear, flexure, and torsion. Therefore, even for a small-scaled specimen, consideration of the axial loading is important for reinforced concrete axial members. Under the constraints above, an iterative design process has been performed keeping the same aspect and reinforcement rations of the prototype pier. Figure B.2 (b) shows the cross section of the designed small-scale RC pier with scale factor of 20. A summary of the designed small-scale pier is listed in Table B.1.

Material properties

In addition to the scaling of the geometry, modeling of material is also an important aspect to fulfill similitude. Microconcrete with aggregate graded through a #10 sieve (opening size of 1.6 mm) is used for producing the microconcrete. The mix design of the microconcrete [i.e., water/cement (W/C) and aggregate/cement (A/C) ratios] is selected based on the prototype pier compressive strength of 27.6 MPa and the previous study by Holub (2005). Details of the mix design and averaged compressive strength from cylinder tests are listed in Table B.1.

Threaded rod and annealed wire are used as longitudinal and spiral reinforcement, respectively. The threaded rods are heat treated to obtain a satisfactory yield strength. The temperature for the heat treatment is selected to 590^{o}c from the preliminary test. The yield strengths of the heat-treated threaded rod and annealed wire are 350 and 420 MPa, respectively.

Table B.1. Properties of prototype and small-scaled RC piers.

		Prototype	Scaled Model	Scale Factor
Geometry	Height	6096mm	305mm	20.0
	Diameter	1219mm	61mm	20.0
	Core Diameter	1107mm	51mm	21.7
	Area (A_c)	$1.17\times10^{6}\,\text{mm}^2$	$2.92\times10^{3}\,\text{mm}^2$	400.0 $(=20\times20)$
	Aspect Ratio	5.0	5.0	NA
Concrete	Type	Standard	Microconcrete	NA
	W/C	NA	0.65	NA
	A/C	NA	3.25	NA
	Compressive Strength	27.6MPa	31.0MPa	NA
Longitudinal Reinforcement	Type	#11 Bar	Threaded Rod	NA
	Diameter	35.8mm	2.24mm	16.0
	# of Bars	34	22	NA
	Area (A_s)	$3.42\times10^{4}\,\text{mm}^2$	86.7mm^2	394.5 $(=19.8\times19.8)$
	Ratio (A_s / A_c)	2.93%	2.97%	NA
	Yield Strength	345MPa	350MPa	NA
Transverse Reinforcement	Type	Spiral #5 Bar	Spiral Annealed Wire	NA
	Diameter	15.9mm	0.83mm	18.9
	Spacing	88.9mm	12.7mm	7.0
	Yield Strength	414MPa	420MPa	NA

Fabrication process

To increase the cost- and time-effectiveness of the fabrication of the designed small-scale RC piers, four specimens are manufactured at the same time using reusable and disposable materials. The fabrication process consists of the following six steps (see Figure B.2): (1) prepare materials and tools including heat-treatment and cutting of RC rods; (2) tie-up spiral reinforcement with longitudinal reinforcement; (3) complete four reinforcement cages; (4) assemble and bolt-down the formwork; (5) mix aggregate, cement, and water, and cast it into the formwork; and (6) after curing of 14 days, remove formwork, finish and paint surface, and attach steel plates at the both sides. The total labor time for one specimen excluding curing time is approximately 16 hours.

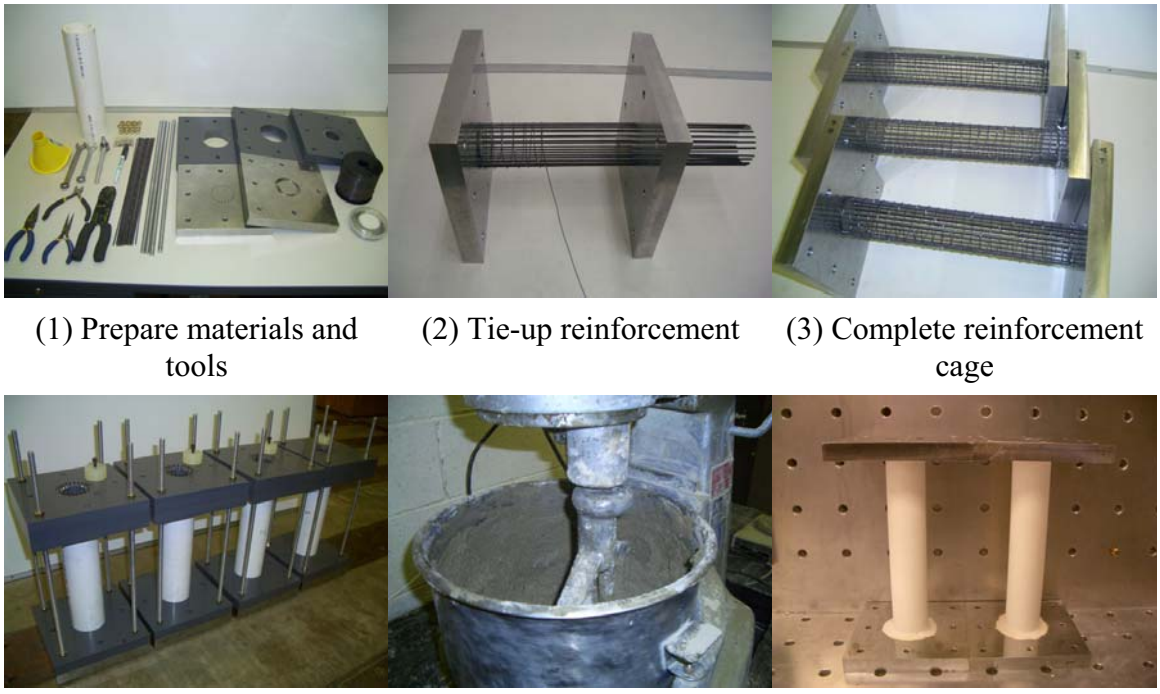

(1) Prepare materials and tools | (2) Tie-up reinforcement | (3) Complete reinforcement cage

(4) Assemble formwork | (5) Mix and cast concrete | (6) Attach steel plates

Figure B.2. Scaled RC pier fabrication process.

B.2 Aluminum columns

Two types of aluminum column specimens that have either welded- or bolted-angle connection are also used in this study (see Figure B.3). The aluminum specimens have an I-shape cross-section, and their height is 457mm. Those specimens are originally designed for modeling of building columns and have been used for demonstration of hybrid simulation using the LBCB. Unlike the RC specimens, the aluminum specimens can be used repeatedly. The specimen with the welded connection is linear elastic under

the loading capacity of the LBCB. Therefore, it can be used for debugging of control algorithms under large loads. On the other hand, the specimen with the bolted-angle connection provides nonlinear inelastic behavior by slip and yielding of the angles. This specimen can be used for the verification of the control system for nonlinear, hysteretic structures. Angles are easily replaceable at a low cost, and can be used repeatedly.

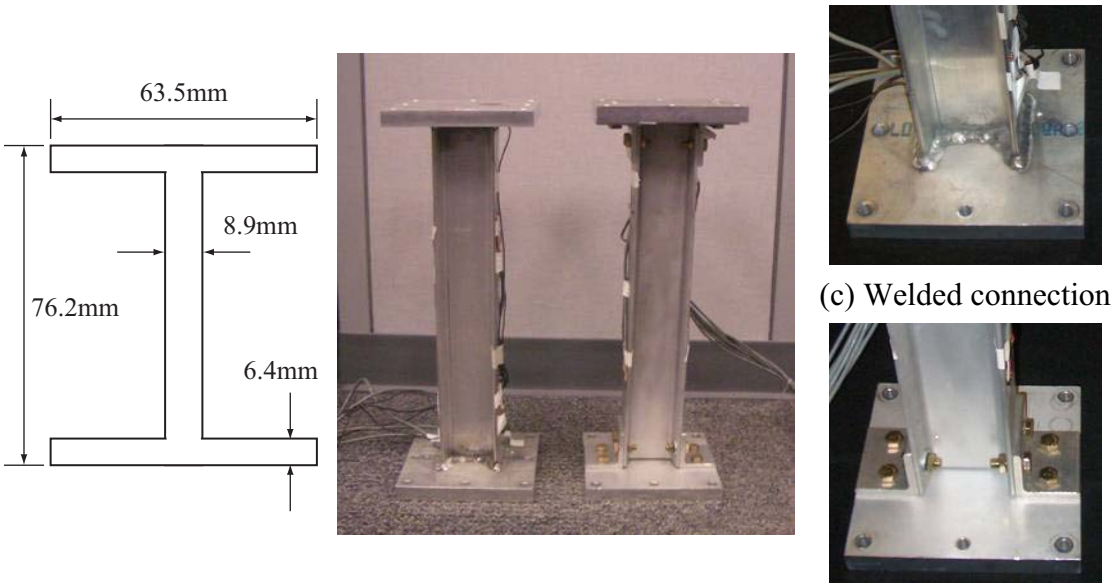

(a) Cross-section (b) Front view (c) Welded connection (d) Bolted connection

Figure B.3. Aluminum Specimens.

VIBRATION MODE SHAPES OF THE REFERENCE SKEW BRIDGE

The first six vibration mode shapes of each parametric skew bridge model are presented in the following; Figures C.1 – C.5 are for bridges with different skew angle; Figures C.6 – C.17 are for bridges with different span ratio configuration; and Figures C.18 – C.23 are for bridges with varying skew angles in a bridge.

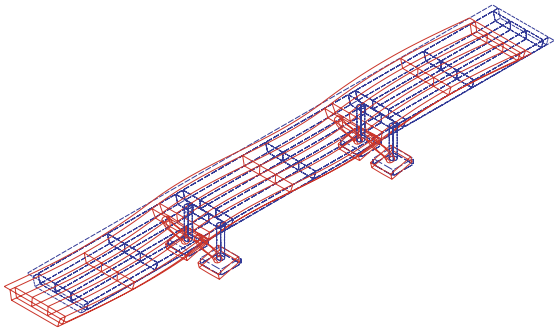

(a) 1st mode $\left(f_1 = 1.97 \text{ Hz}\right)$

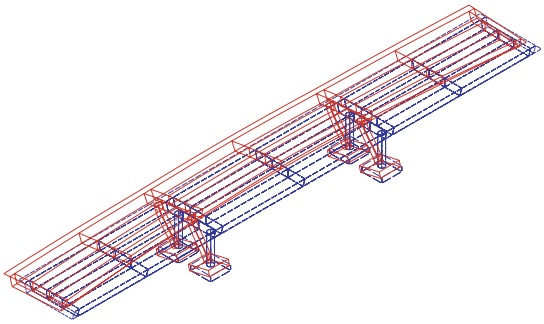

(b) 2nd mode $\left(f_2 = 2.42 \text{ Hz}\right)$

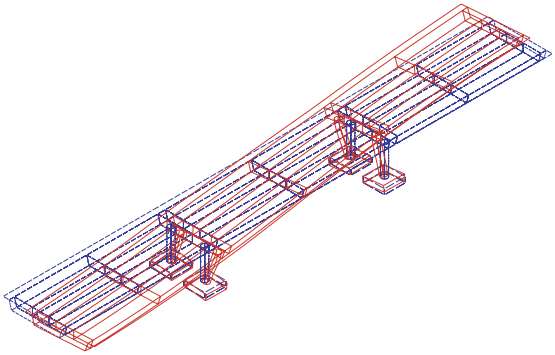

(c) 3rd mode $\left(f_3 = 2.99 \text{ Hz}\right)$

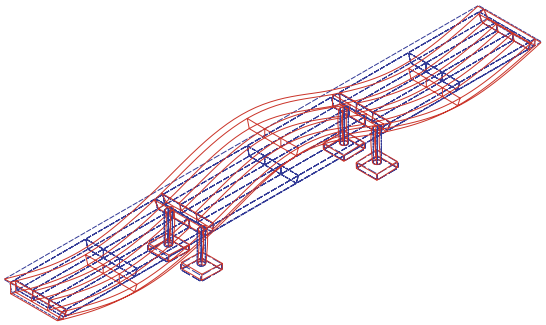

(d) 4th mode $\left(f_4 = 3.09 \text{ Hz}\right)$

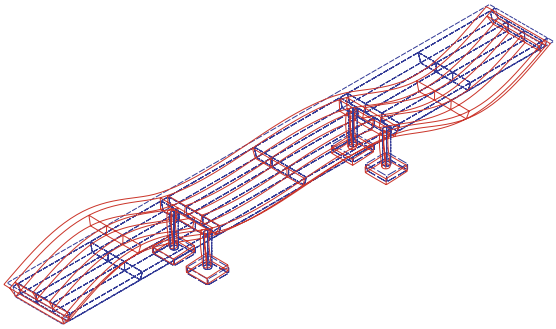

(e) 5th mode $\left(f_5 = 4.00 \text{ Hz}\right)$

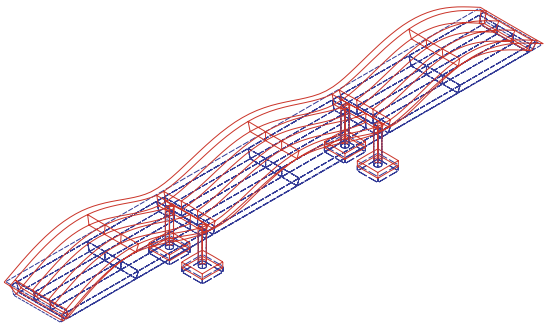

(f) 6th mode $\left(f_6 = 4.47 \text{ Hz}\right)$

Figure C.1. Fundamental mode shapes (Straight).

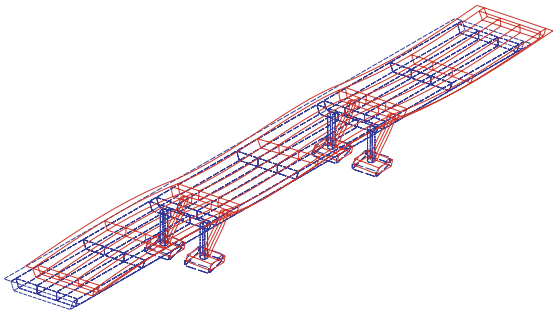

(a) 1st mode $\left(f_1 = 1.97 \text{ Hz}\right)$

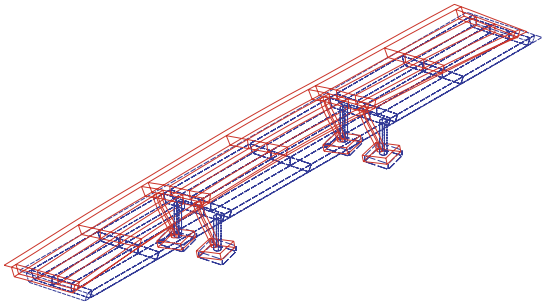

(b) 2nd mode $\left(f_2 = 2.42 \text{ Hz}\right)$

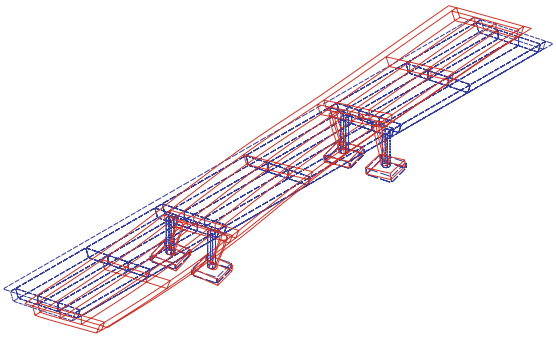

(c) 3rd mode $\left(f_3 = 2.98 \text{ Hz}\right)$

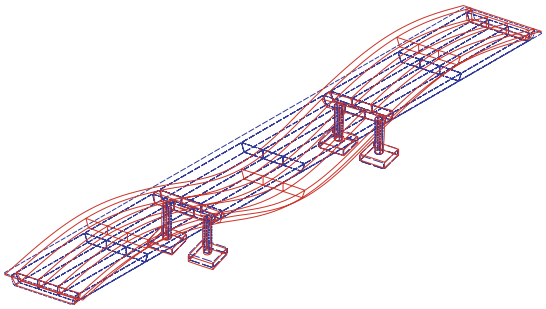

(d) 4th mode $\left(f_4 = 3.15 \text{ Hz}\right)$

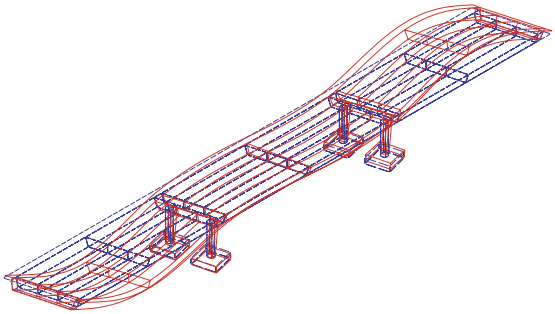

(e) 5th mode $\left(f_5 = 4.05 \text{ Hz}\right)$

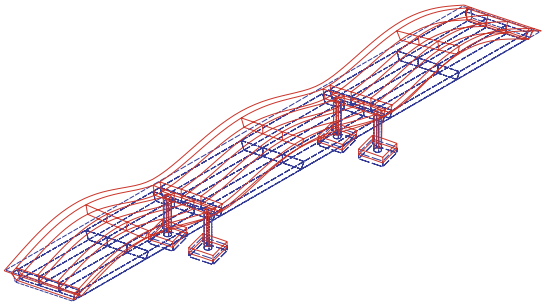

(f) 6th mode $\left(f_6 = 4.49 \text{ Hz}\right)$

Figure C.2. Fundamental mode shapes (Skew 15°).

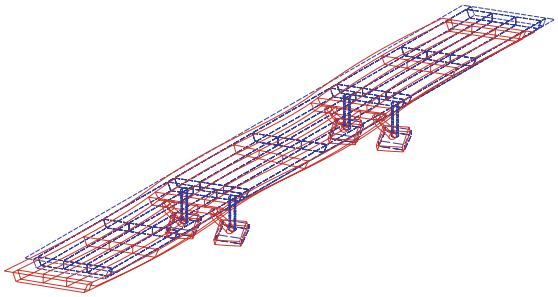

(a) 1st mode $\left(f_1 = 1.99 \text{ Hz}\right)$

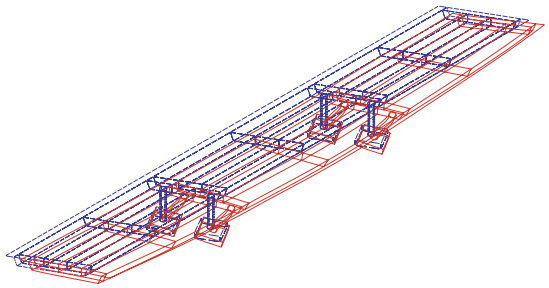

(b) 2nd mode $\left(f_2 = 2.41 \text{ Hz}\right)$

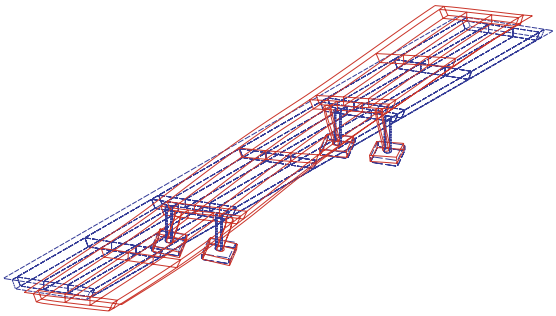

(c) 3rd mode $\left(f_3 = 2.96 \text{ Hz}\right)$

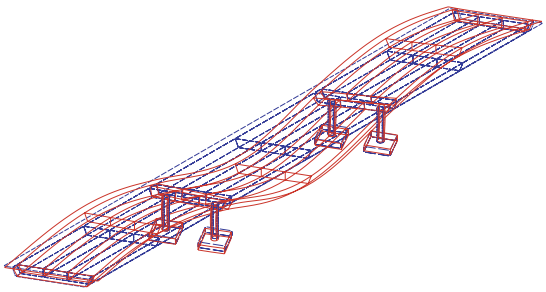

(d) 4th mode $\left(f_4 = 3.34 \text{ Hz}\right)$

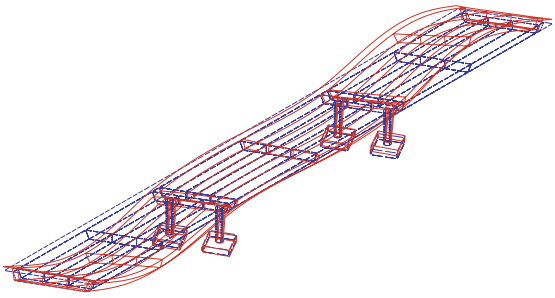

(e) 5th mode $\left(f_5 = 4.22 \text{ Hz}\right)$

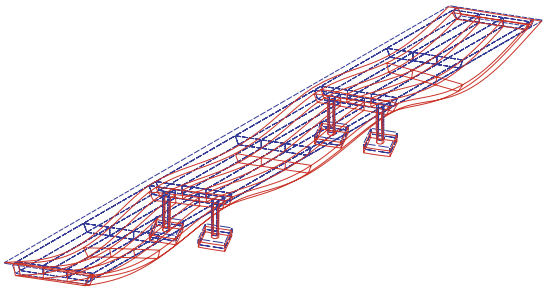

(f) 6th mode $\left(f_6 = 4.59 \text{ Hz}\right)$

Figure C.3. Fundamental mode shapes (Skew 30°).

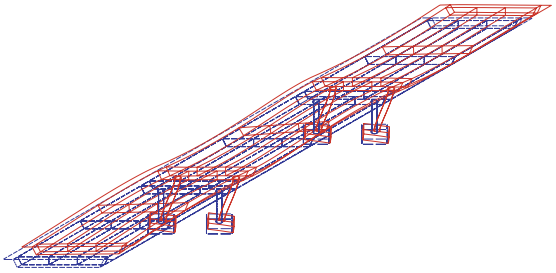

(a) 1st mode $\left(f_1 = 2.02 \text{ Hz}\right)$

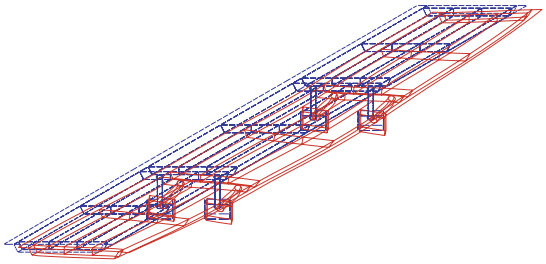

(b) 2nd mode $\left(f_2 = 2.37 \text{ Hz}\right)$

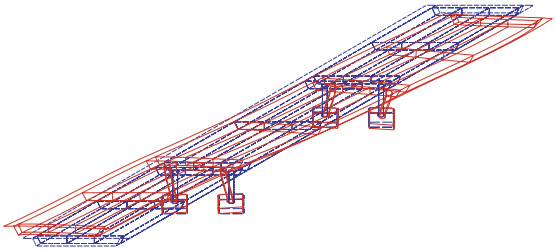

(c) 3rd mode $\left(f_3 = 2.91 \text{ Hz}\right)$

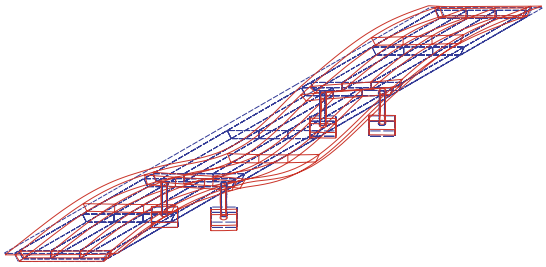

(d) 4th mode $\left(f_4 = 3.77 \text{ Hz}\right)$

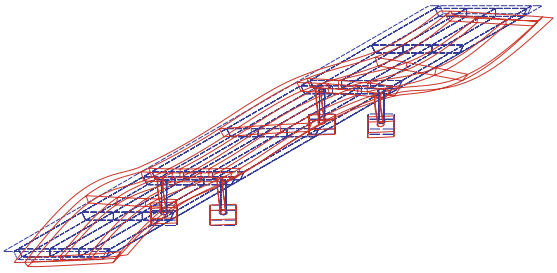

(e) 5th mode $\left(f_5 = 4.57 \text{ Hz}\right)$

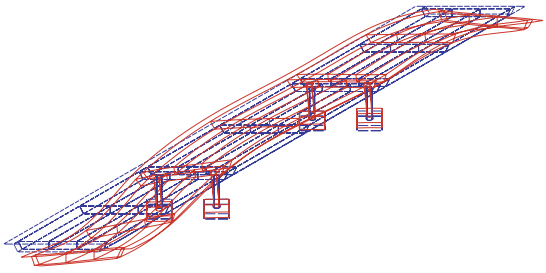

(f) 6th mode $\left(f_6 = 4.80 \text{ Hz}\right)$

Figure C.4. Fundamental mode shapes (Skew 45°).

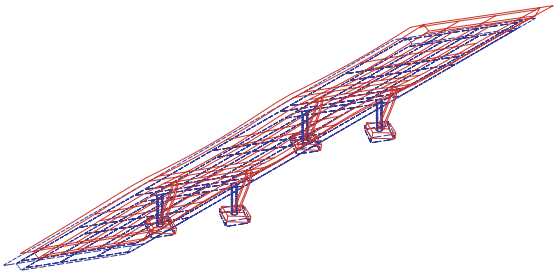

(a) 1st mode $\left(f_1 = 2.06 \text{ Hz}\right)$

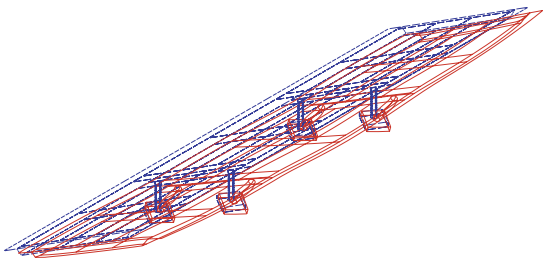

(b) 2nd mode $\left(f_2 = 2.33 \text{ Hz}\right)$

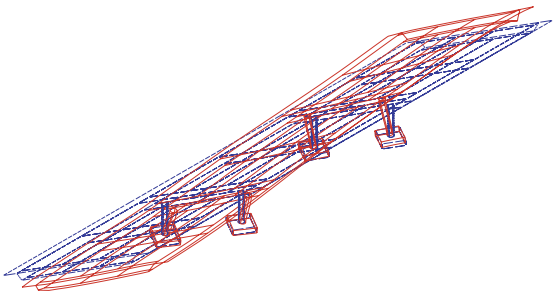

(c) 3rd mode $\left(f_3 = 2.81 \text{ Hz}\right)$

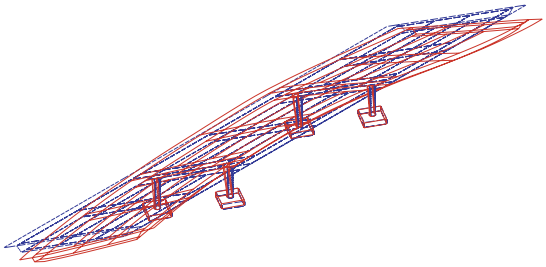

(d) 4th mode $\left(f_4 = 4.65 \text{ Hz}\right)$

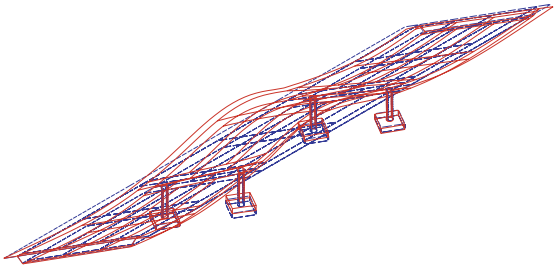

(e) 5th mode $\left(f_5 = 4.68 \text{ Hz}\right)$

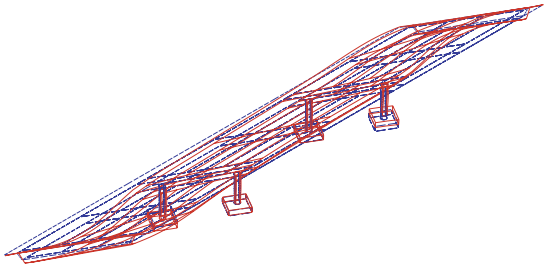

(f) 6th mode $\left(f_6 = 5.56 \text{ Hz}\right)$

Figure C.5. Fundamental mode shapes (Skew 60°).

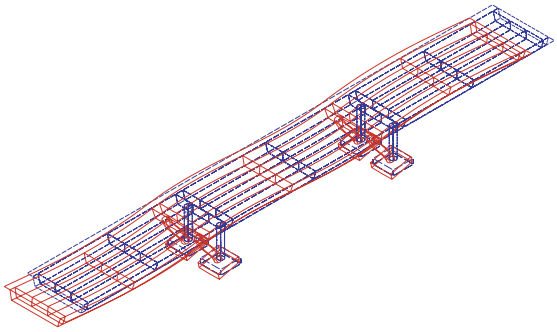

(a) 1st mode $\left(f_1 = 1.97 \text{ Hz}\right)$

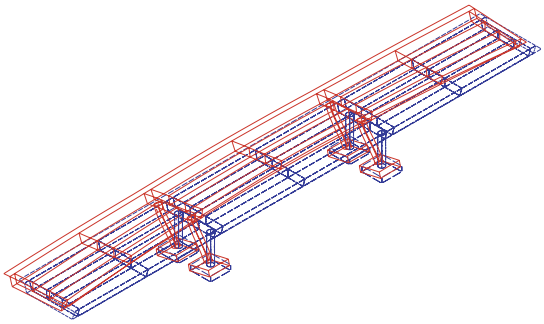

(b) 2nd mode $\left(f_2 = 2.42 \text{ Hz}\right)$

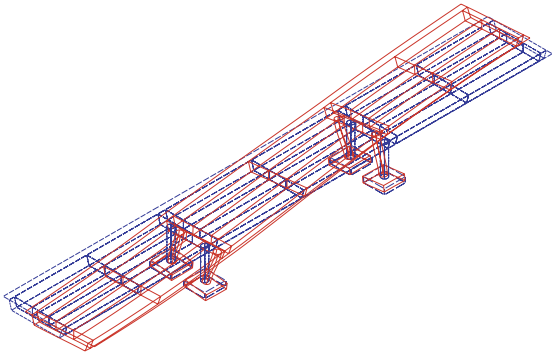

(c) 3rd mode $\left(f_3 = 2.99 \text{ Hz}\right)$

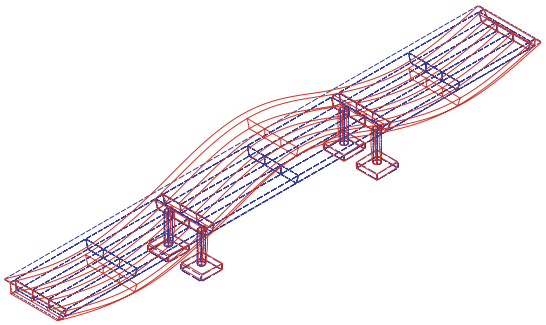

(d) 4th mode $\left(f_4 = 3.09 \text{ Hz}\right)$

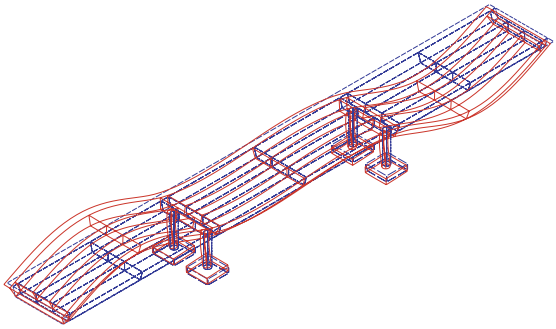

(e) 5th mode $\left(f_5 = 4.00 \text{ Hz}\right)$

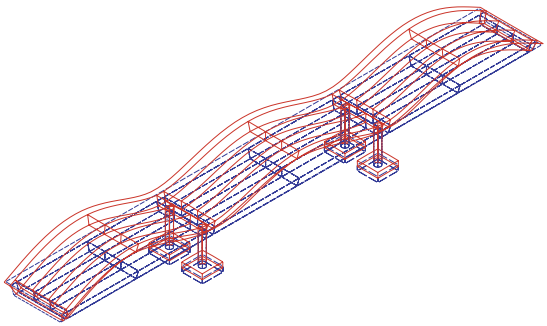

(f) 6th mode $\left(f_6 = 4.47 \text{ Hz}\right)$

Figure C.6. Fundamental mode shapes (SR1.2-1.2, Straight).

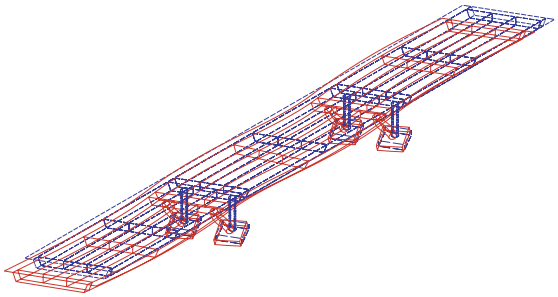

(a) 1st mode $\left(f_1 = 1.99 \text{ Hz}\right)$

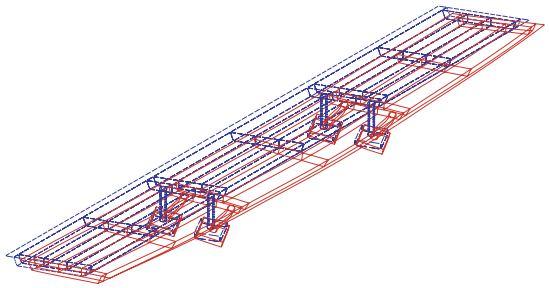

(b) 2nd mode $\left(f_2 = 2.41 \text{ Hz}\right)$

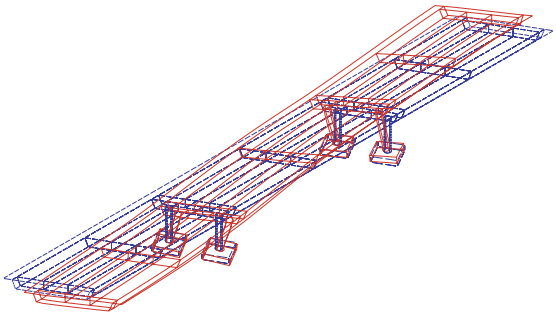

(c) 3rd mode $\left(f_3 = 2.96 \text{ Hz}\right)$

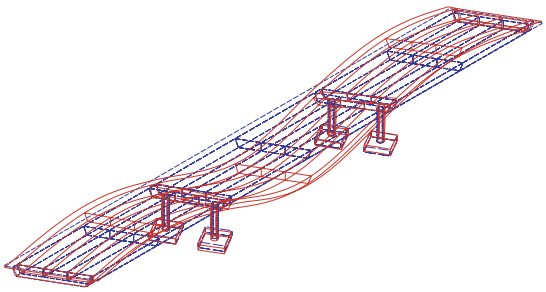

(d) 4th mode $\left(f_4 = 3.34 \text{ Hz}\right)$

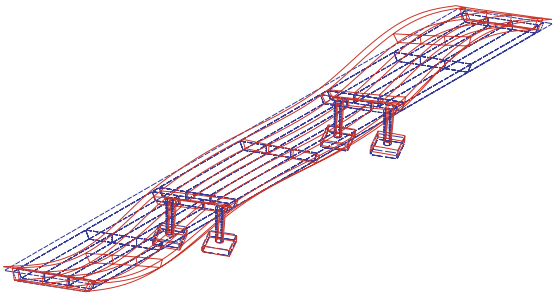

(e) 5th mode $\left(f_5 = 4.22 \text{ Hz}\right)$

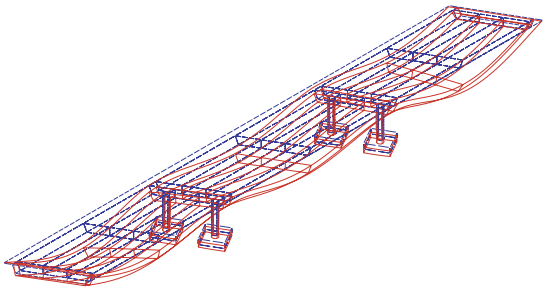

(f) 6th mode $\left(f_6 = 4.59 \text{ Hz}\right)$

Figure C.7. Fundamental mode shapes (SR1.2-1.2, Skew 30°).

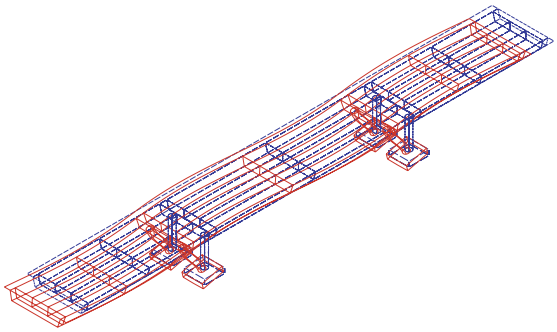

(a) 1st mode $\left(f_1 = 1.96 \text{ Hz}\right)$

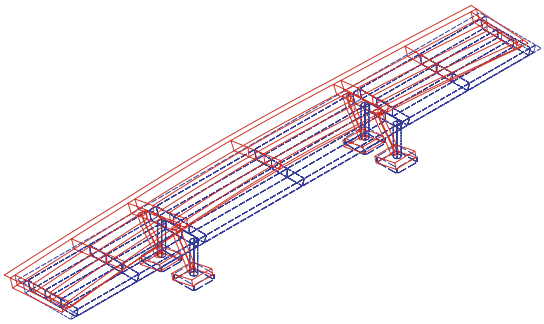

(b) 2nd mode $\left(f_2 = 2.36 \text{ Hz}\right)$

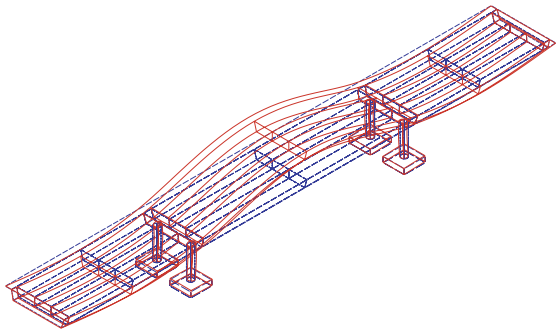

(c) 3rd mode $\left(f_3 = 2.57 \text{ Hz}\right)$

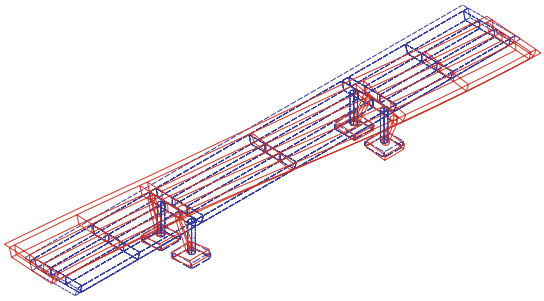

(d) 4th mode $\left(f_4 = 3.08 \text{ Hz}\right)$

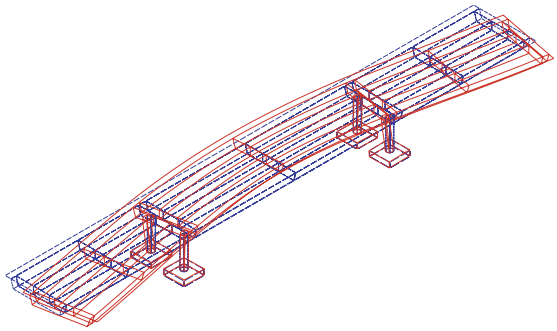

(e) 5th mode $\left(f_5 = 4.75 \text{ Hz}\right)$

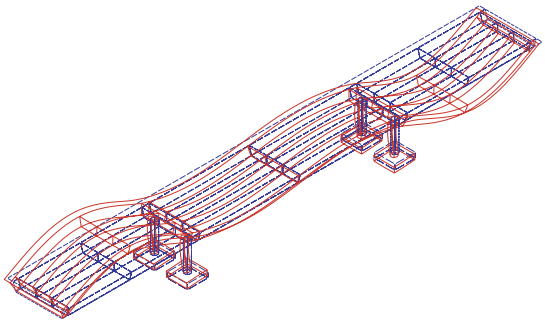

(f) 6th mode $\left(f_6 = 4.77 \text{ Hz}\right)$

Figure C.8. Fundamental mode shapes (SR1.6-1.6, Straight).

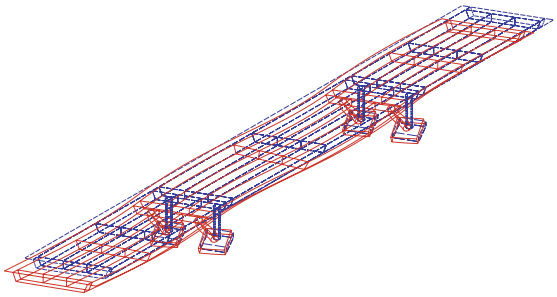

(a) 1st mode $\left(f_1 = 1.99 \text{ Hz}\right)$

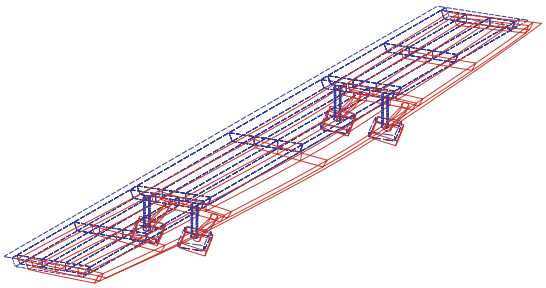

(b) 2nd mode $\left(f_2 = 2.35 \text{ Hz}\right)$

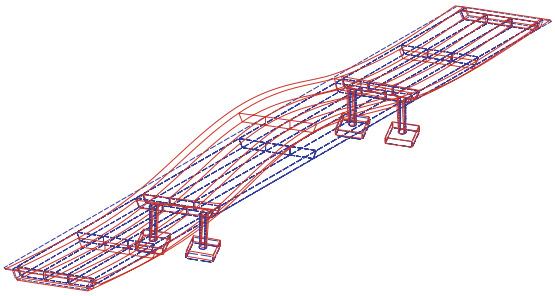

(c) 3rd mode $\left(f_3 = 2.72 \text{ Hz}\right)$

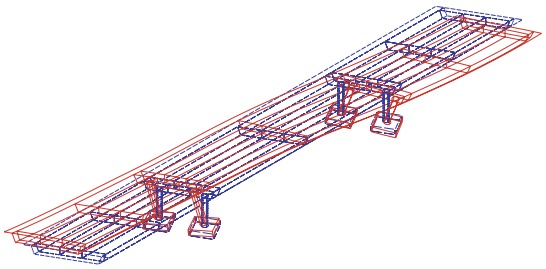

(d) 4th mode $\left(f_4 = 3.06 \text{ Hz}\right)$

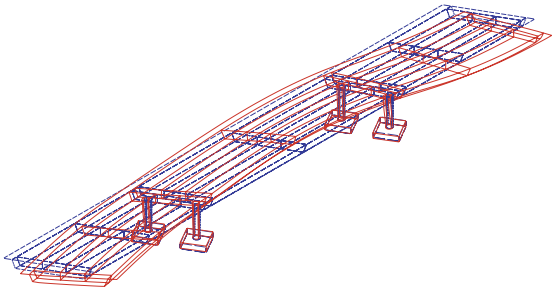

(e) 5th mode $\left(f_5 = 4.71 \text{ Hz}\right)$

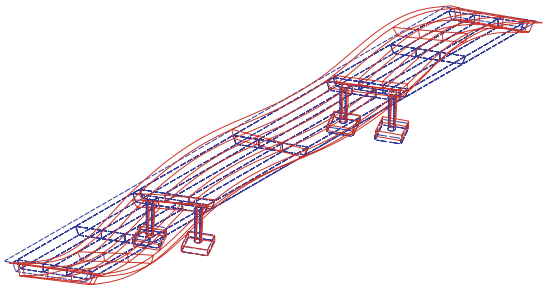

(f) 6th mode $\left(f_6 = 5.06 \text{ Hz}\right)$

Figure C.9. Fundamental mode shapes (SR1.6-1.6, Skew 30°).

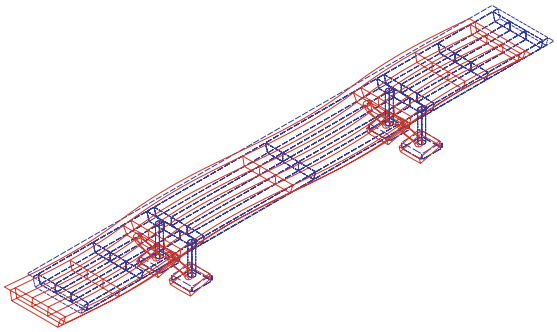

(a) 1st mode $\left(f_1 = 1.96 \text{ Hz}\right)$

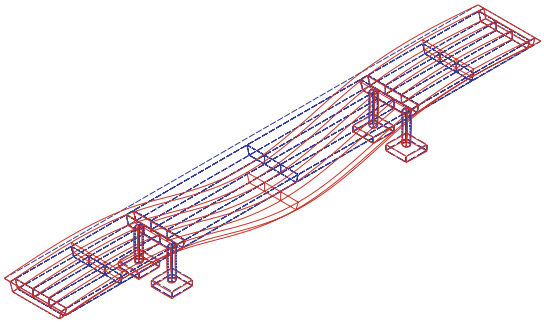

(b) 2nd mode $\left(f_2 = 2.16 \text{ Hz}\right)$

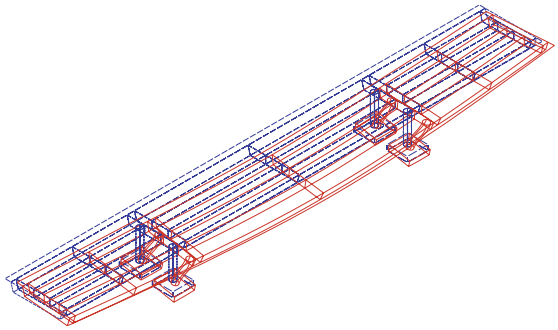

(c) 3rd mode $\left(f_3 = 2.30 \text{ Hz}\right)$

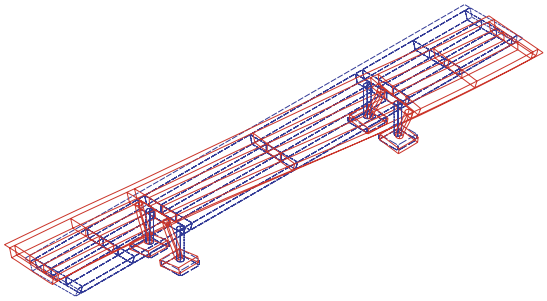

(d) 4th mode $\left(f_4 = 3.17 \text{ Hz}\right)$

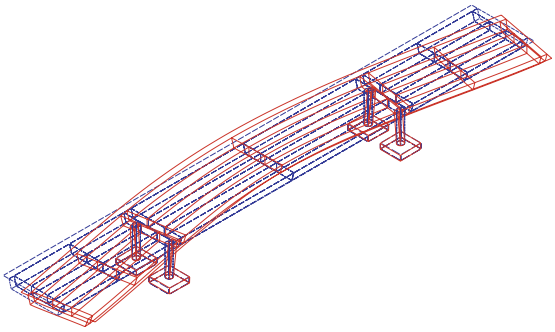

(e) 5th mode $\left(f_5 = 4.74 \text{ Hz}\right)$

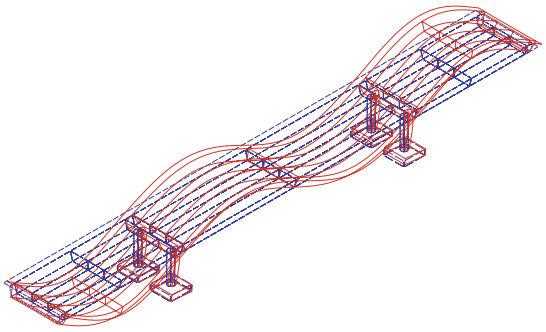

(f) 6th mode $\left(f_6 = 5.38 \text{ Hz}\right)$

Figure C.10. Fundamental mode shapes (SR2.0-2.0, Straight).

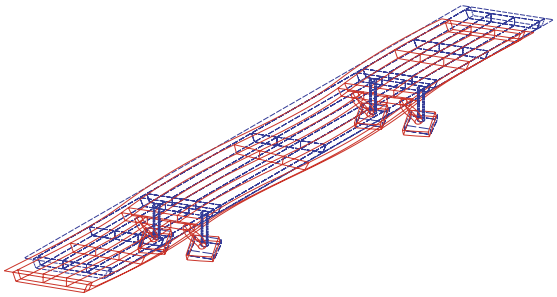

(a) 1st mode $\left(f_1 = 1.99 \text{ Hz}\right)$

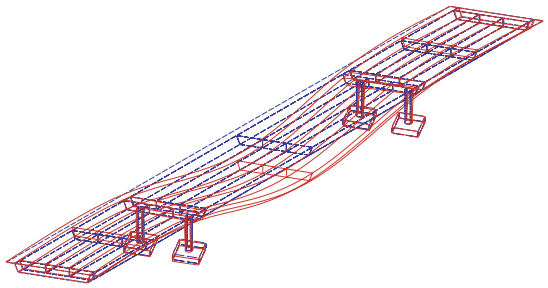

(b) 2nd mode $\left(f_2 = 2.28 \text{ Hz}\right)$

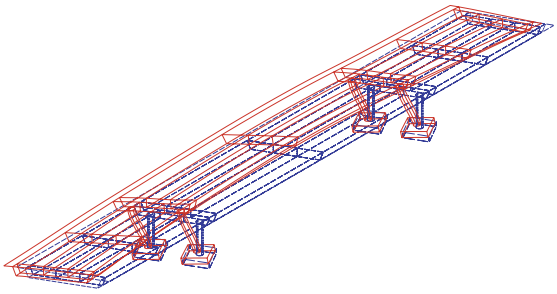

(c) 3rd mode $\left(f_3 = 2.30 \text{ Hz}\right)$

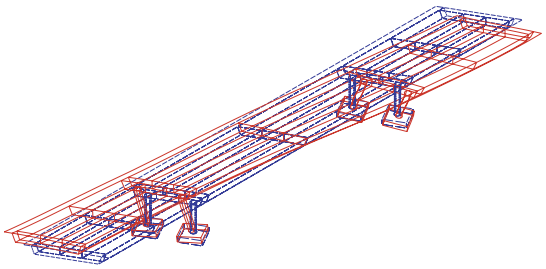

(d) 4th mode $\left(f_4 = 3.15 \text{ Hz}\right)$

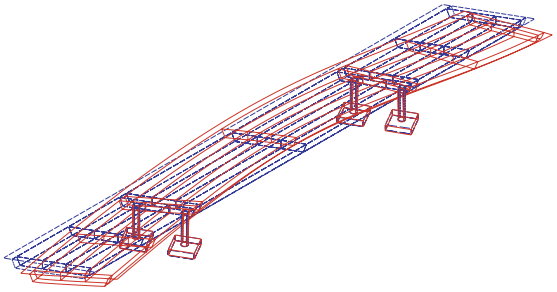

(e) 5th mode $\left(f_5 = 4.71 \text{ Hz}\right)$

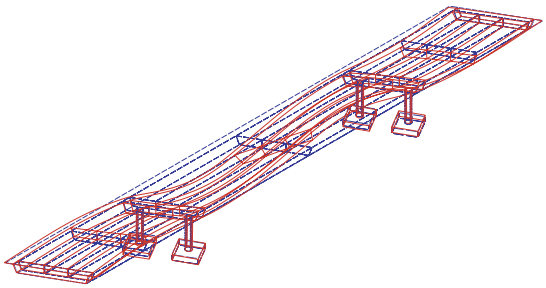

(f) 6th mode $\left(f_6 = 5.28 \text{ Hz}\right)$

Figure C.11. Fundamental mode shapes (SR2.0-2.0, Skew 30°).

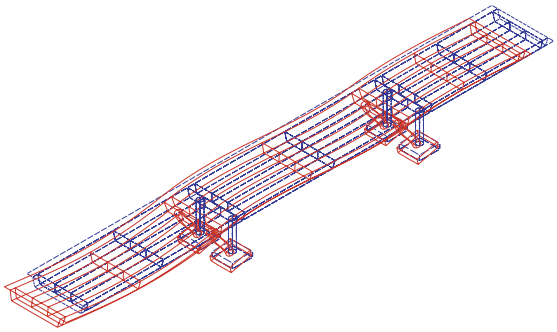

(a) 1st mode $\left(f_1 = 1.96 \text{ Hz}\right)$

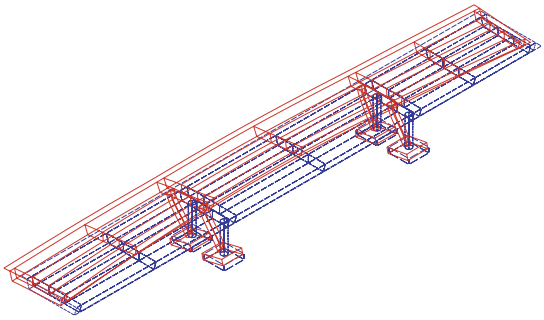

(b) 2nd mode $\left(f_2 = 2.38 \text{ Hz}\right)$

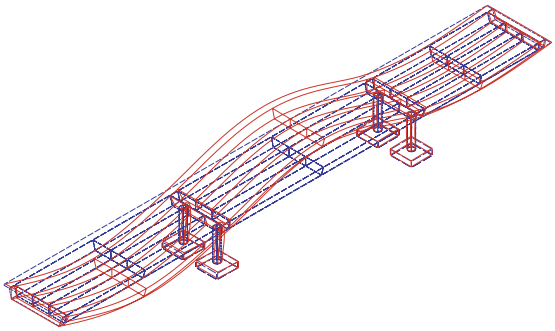

(c) 3rd mode $\left(f_3 = 2.80 \text{ Hz}\right)$

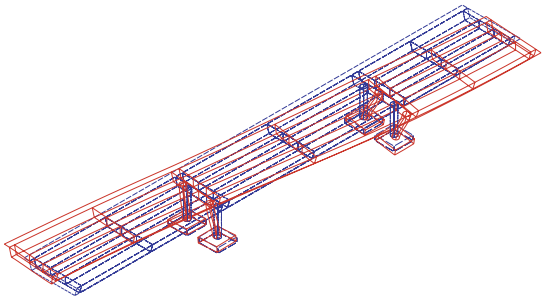

(d) 4th mode $\left(f_4 = 3.04 \text{ Hz}\right)$

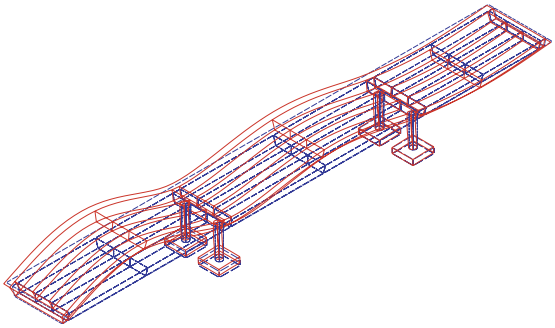

(e) 5th mode $\left(f_5 = 3.74 \text{ Hz}\right)$

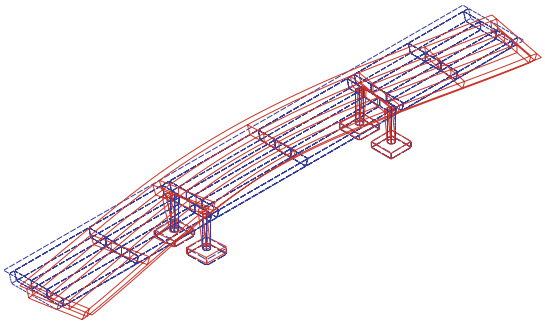

(f) 6th mode $\left(f_6 = 4.78 \text{ Hz}\right)$

Figure C.12. Fundamental mode shapes (SR1.2-1.6, Straight).

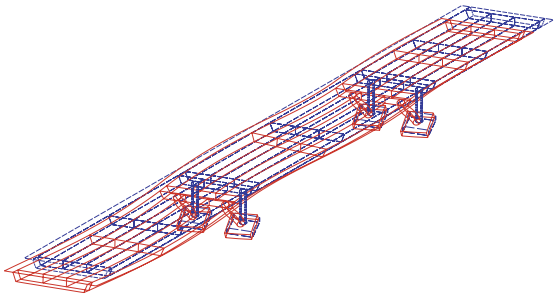

(a) 1st mode $\left(f_1 = 1.98 \text{ Hz}\right)$

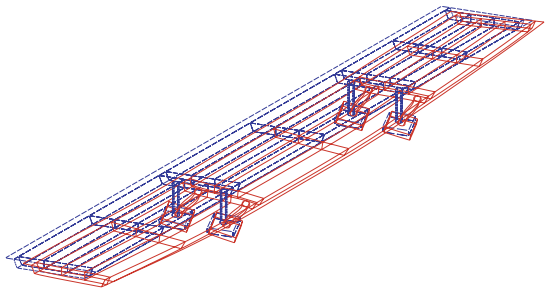

(b) 2nd mode $\left(f_2 = 2.37 \text{ Hz}\right)$

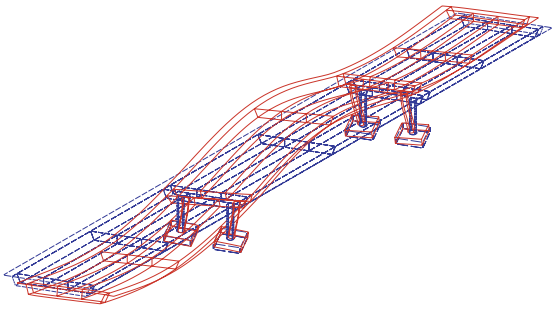

(c) 3rd mode $\left(f_3 = 2.99 \text{ Hz}\right)$

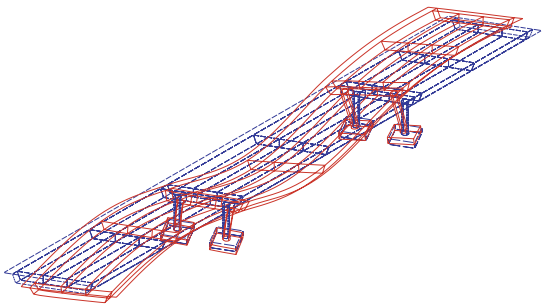

(d) 4th mode $\left(f_4 = 3.04 \text{ Hz}\right)$

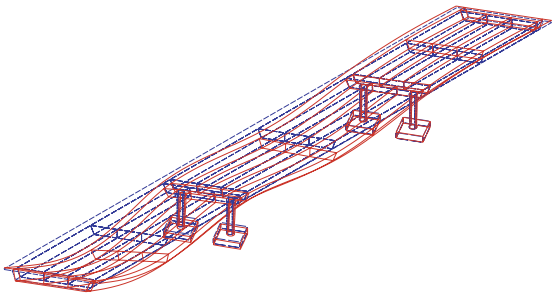

(e) 5th mode $\left(f_5 = 3.90 \text{ Hz}\right)$

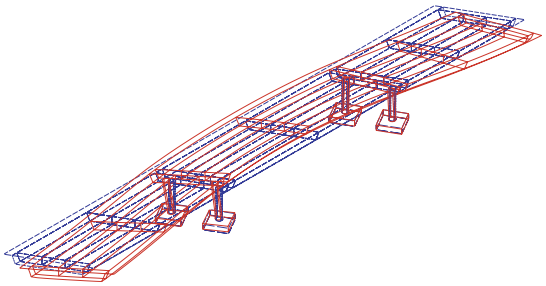

(f) 6th mode $\left(f_6 = 4.76 \text{ Hz}\right)$

Figure C.13. Fundamental mode shapes (SR1.2-1.6, Skew 30°).

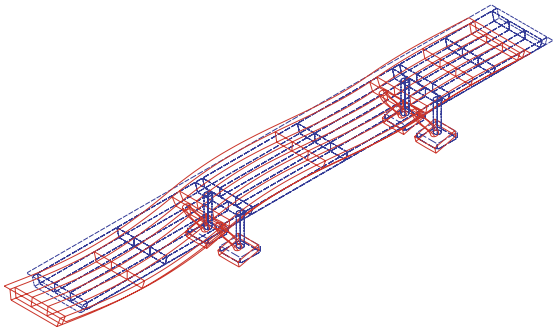

(a) 1st mode $\left(f_1 = 1.95 \text{ Hz}\right)$

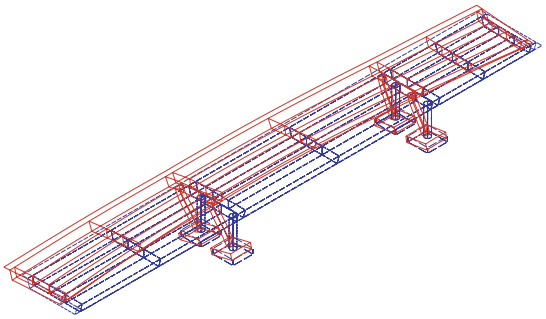

(b) 2nd mode $\left(f_2 = 2.34 \text{ Hz}\right)$

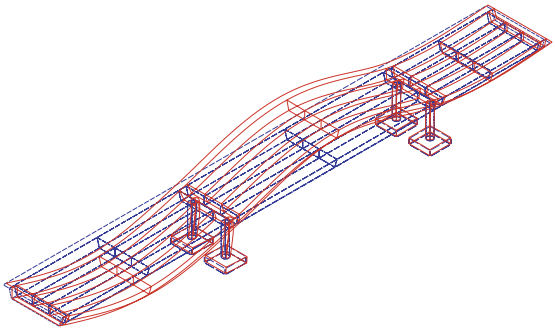

(c) 3rd mode $\left(f_3 = 2.59 \text{ Hz}\right)$

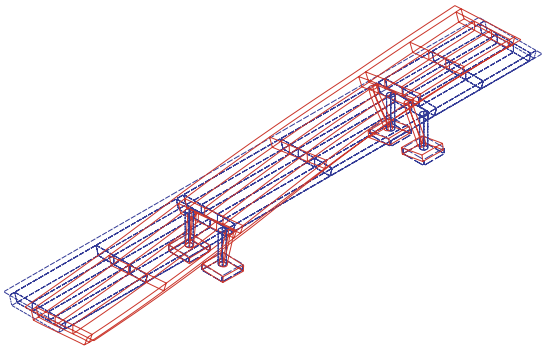

(d) 4th mode $\left(f_4 = 3.08 \text{ Hz}\right)$

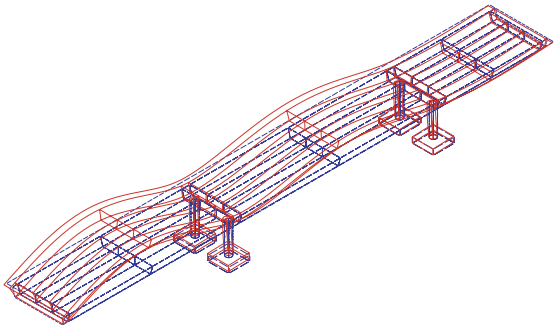

(e) 5th mode $\left(f_5 = 3.45 \text{ Hz}\right)$

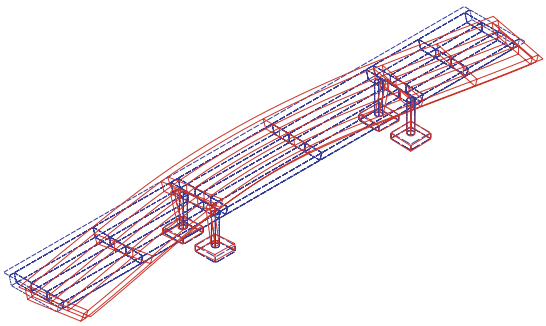

(f) 6th mode $\left(f_6 = 4.81 \text{ Hz}\right)$

Figure C.14. Fundamental mode shapes (SR1.2-2.0, Straight).

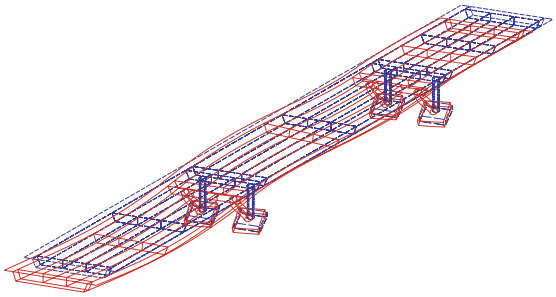

(a) 1st mode $\left(f_1 = 1.98 \text{ Hz}\right)$

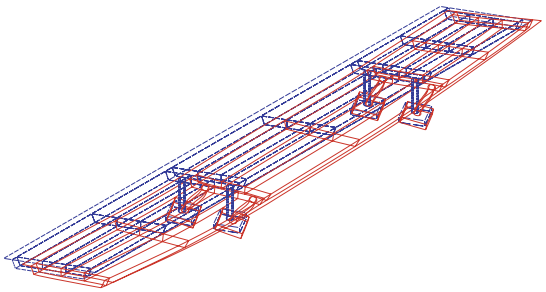

(b) 2nd mode $\left(f_2 = 2.32 \text{ Hz}\right)$

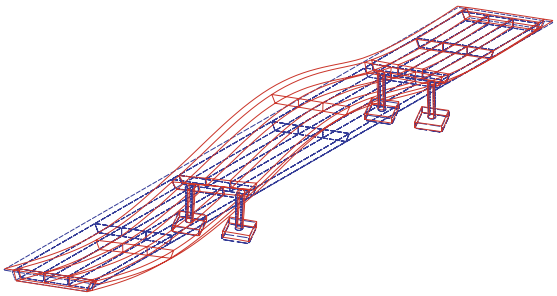

(c) 3rd mode $\left(f_3 = 2.77 \text{ Hz}\right)$

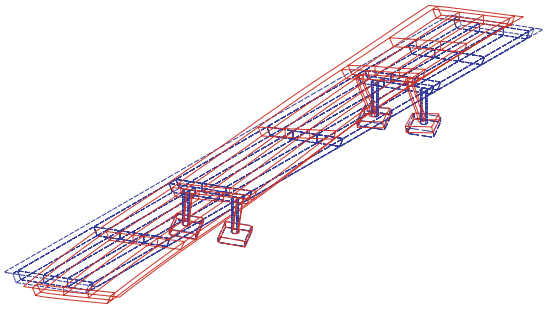

(d) 4th mode $\left(f_4 = 3.06 \text{ Hz}\right)$

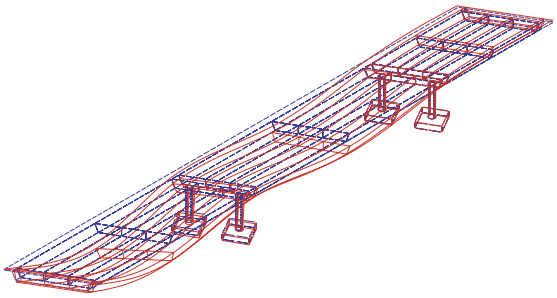

(e) 5th mode $\left(f_5 = 3.59 \text{ Hz}\right)$

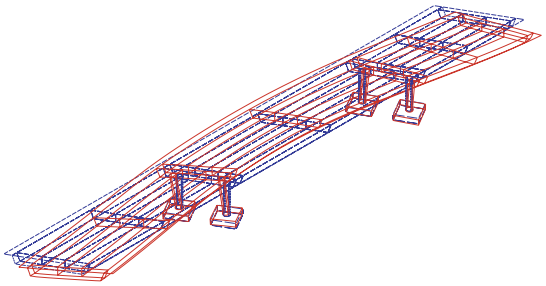

(f) 6th mode $\left(f_6 = 4.79 \text{ Hz}\right)$

Figure C.15. Fundamental mode shapes (SR1.2-2.0, Skew 30°).

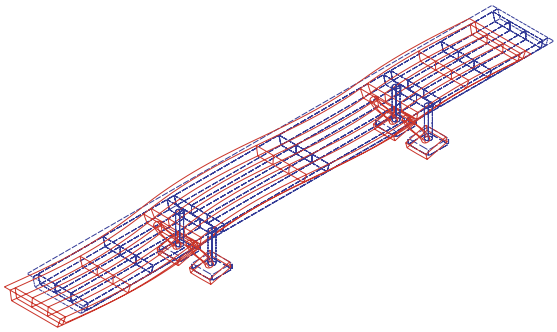

(a) 1st mode $\left(f_1 = 1.96 \text{ Hz}\right)$

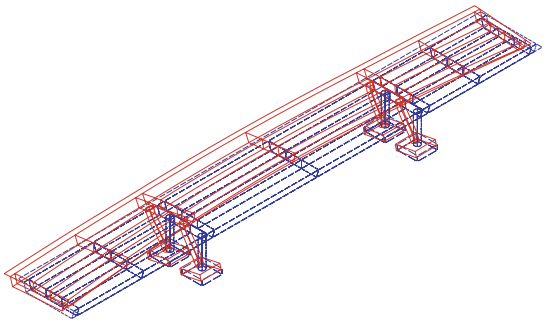

(b) 2nd mode $\left(f_2 = 2.33 \text{ Hz}\right)$

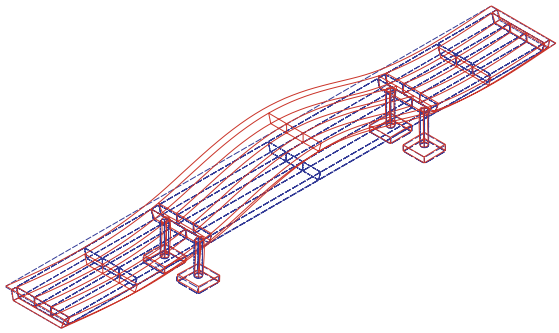

(c) 3rd mode $\left(f_3 = 2.36 \text{ Hz}\right)$

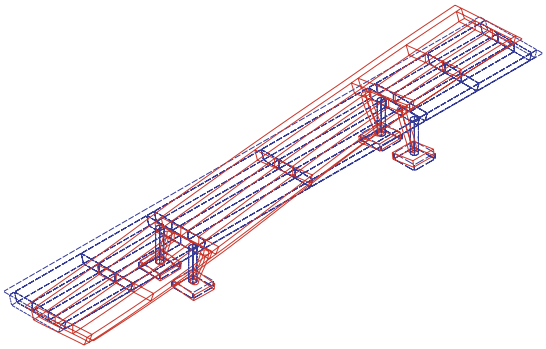

(d) 4th mode $\left(f_4 = 3.12 \text{ Hz}\right)$

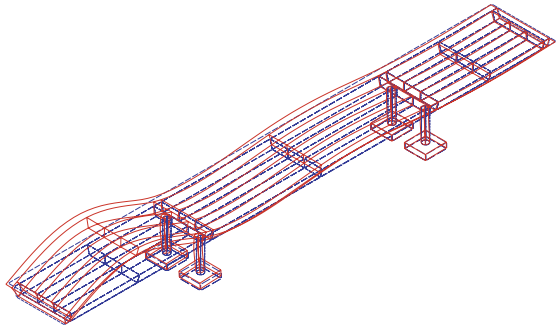

(e) 5th mode $\left(f_5 = 4.43 \text{ Hz}\right)$

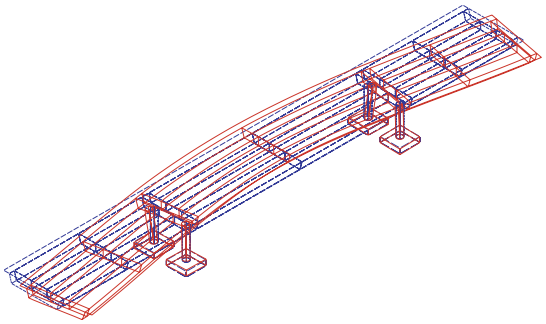

(f) 6th mode $\left(f_6 = 4.75 \text{ Hz}\right)$

Figure C.16. Fundamental mode shapes (SR1.6-2.0, Straight).

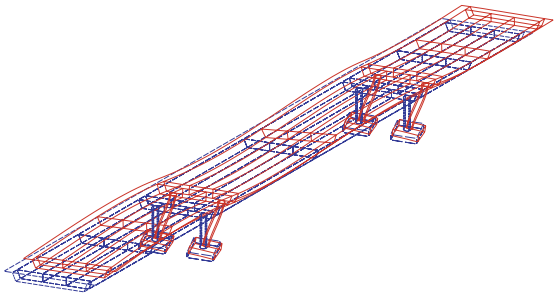

(a) 1st mode $\left(f_1 = 1.99 \text{ Hz}\right)$

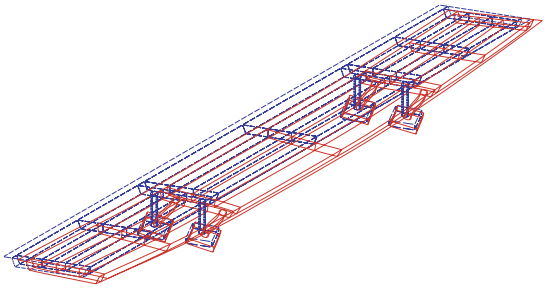

(b) 2nd mode $\left(f_2 = 2.32 \text{ Hz}\right)$

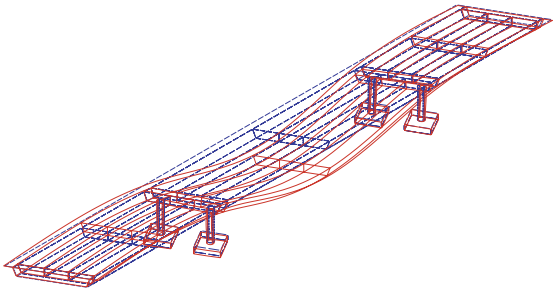

(c) 3rd mode $\left(f_3 = 2.50 \text{ Hz}\right)$

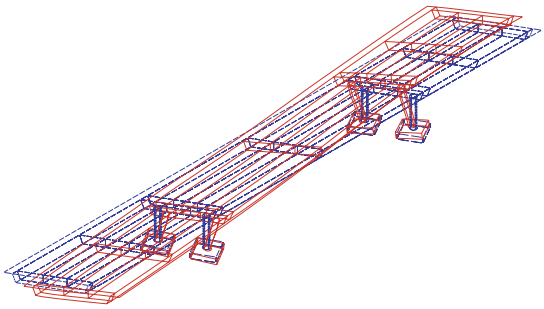

(d) 4th mode $\left(f_4 = 3.10 \text{ Hz}\right)$

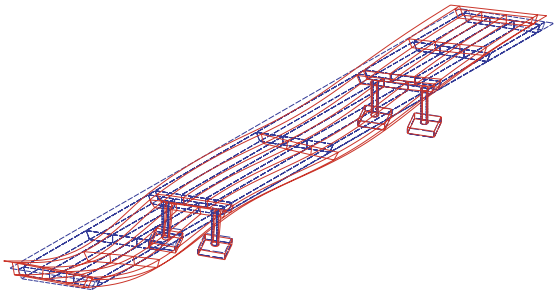

(e) 5th mode $\left(f_5 = 4.64 \text{ Hz}\right)$

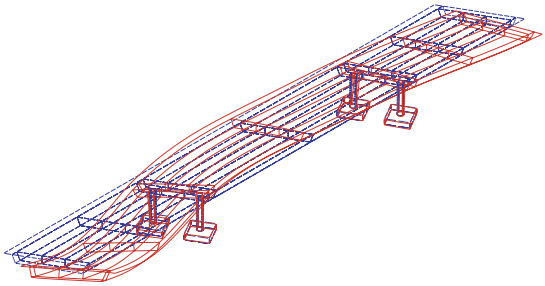

(f) 6th mode $\left(f_6 = 4.76 \text{ Hz}\right)$

Figure C.17. Fundamental mode shapes (SR1.6-2.0, Skew 30°).

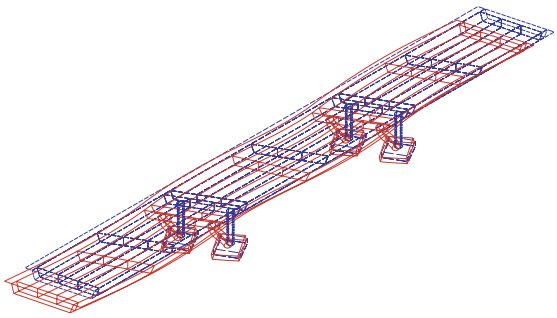

(a) 1st mode $\left(f_1 = 1.99 \text{ Hz}\right)$

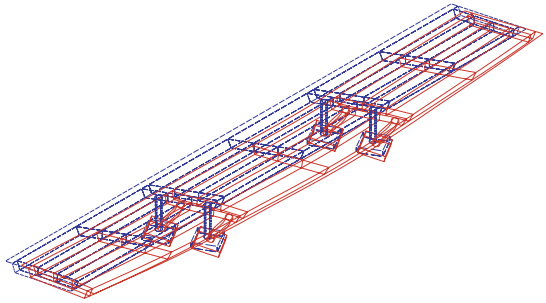

(b) 2nd mode $\left(f_2 = 2.40 \text{ Hz}\right)$

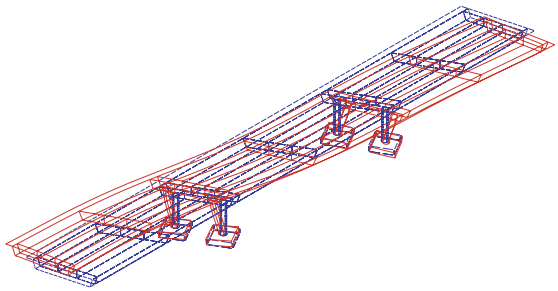

(c) 3rd mode $\left(f_3 = 2.97 \text{ Hz}\right)$

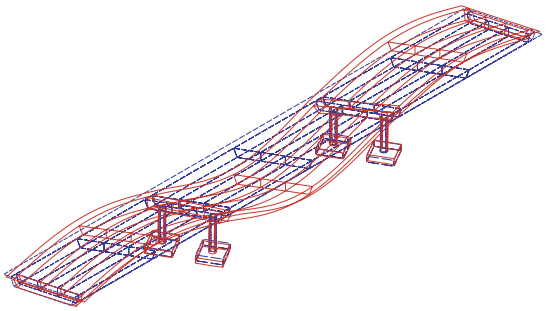

(d) 4th mode $\left(f_4 = 3.29 \text{ Hz}\right)$

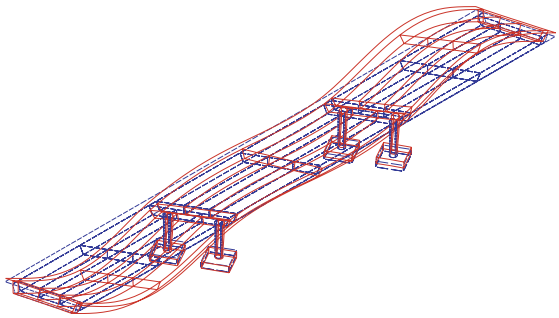

(e) 5th mode $\left(f_5 = 4.13 \text{ Hz}\right)$

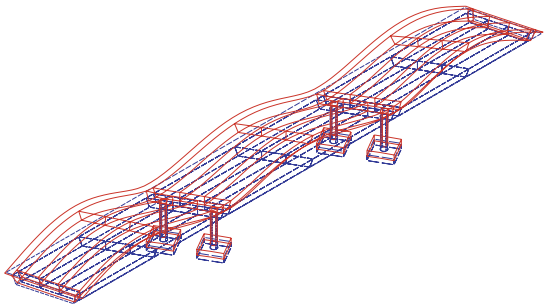

(f) 6th mode $\left(f_6 = 4.56 \text{ Hz}\right)$

Figure C.18. Fundamental mode shapes (ES15-15).

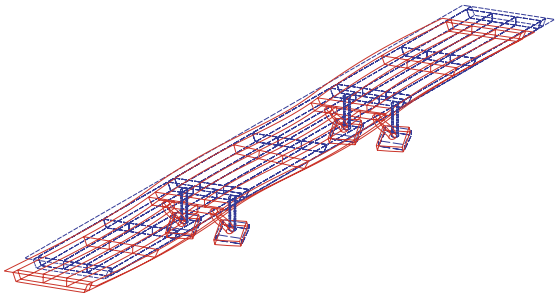

(a) 1st mode $\left(f_1 = 1.99 \text{ Hz}\right)$

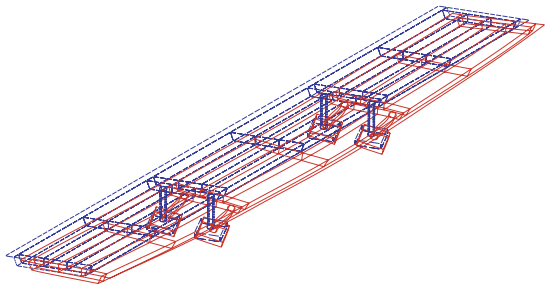

(b) 2nd mode $\left(f_2 = 2.41 \text{ Hz}\right)$

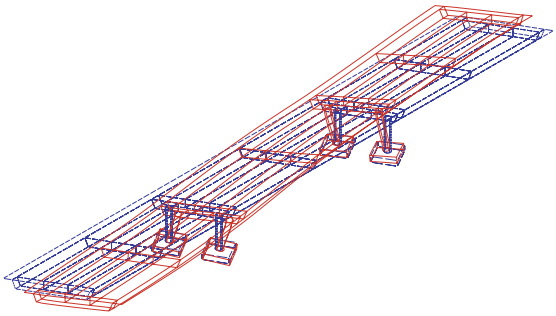

(c) 3rd mode $\left(f_3 = 2.96 \text{ Hz}\right)$

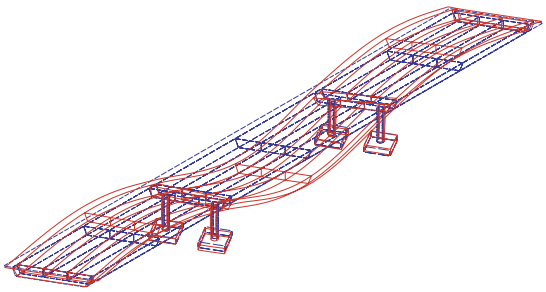

(d) 4th mode $\left(f_4 = 3.34 \text{ Hz}\right)$

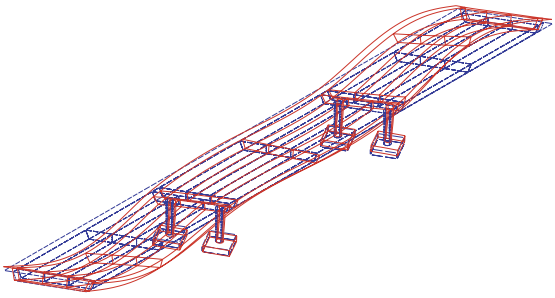

(e) 5th mode $\left(f_5 = 4.22 \text{ Hz}\right)$

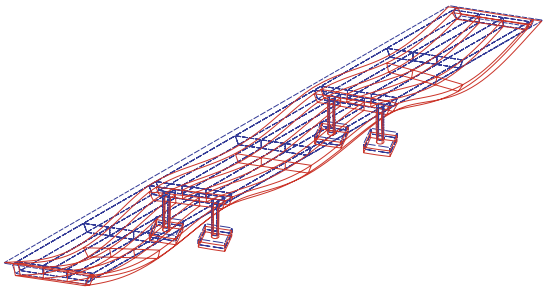

(f) 6th mode $\left(f_6 = 4.59 \text{ Hz}\right)$

Figure C.19. Fundamental mode shapes (ES30-30).

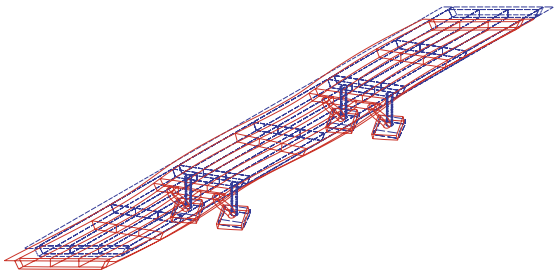

(a) 1st mode $\left(f_1 = 2.00 \text{ Hz}\right)$

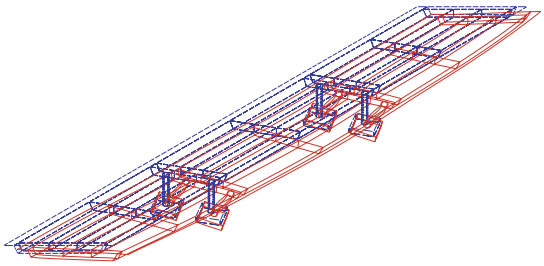

(b) 2nd mode $\left(f_2 = 2.40 \text{ Hz}\right)$

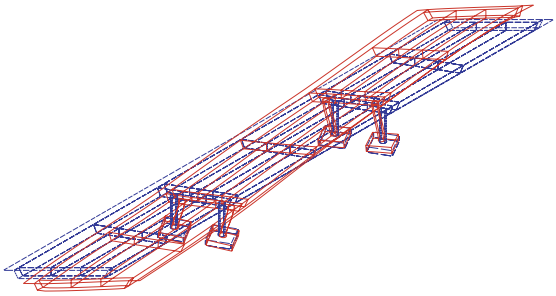

(c) 3rd mode $\left(f_3 = 2.92 \text{ Hz}\right)$

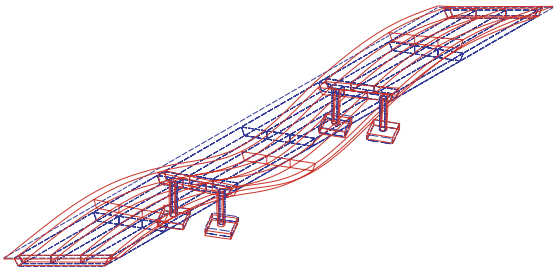

(d) 4th mode $\left(f_4 = 3.42 \text{ Hz}\right)$

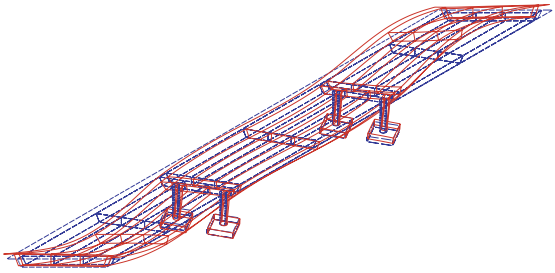

(e) 5th mode $\left(f_5 = 4.31 \text{ Hz}\right)$

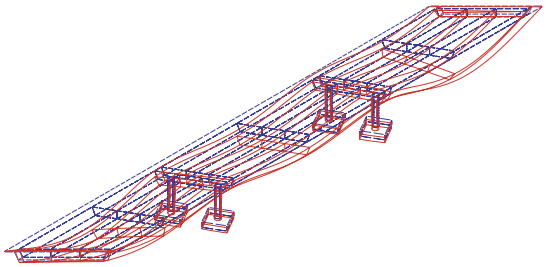

(f) 6th mode $\left(f_6 = 4.62 \text{ Hz}\right)$

Figure C.20. Fundamental mode shapes (ES45-45).

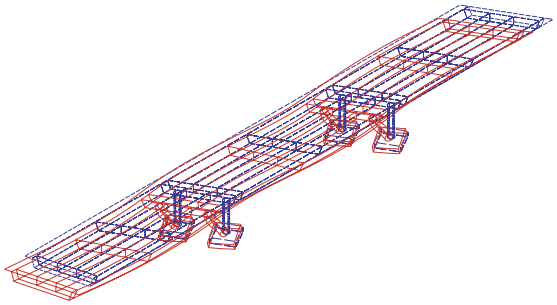

(a) 1st mode $\left(f_1 = 1.99 \text{ Hz}\right)$

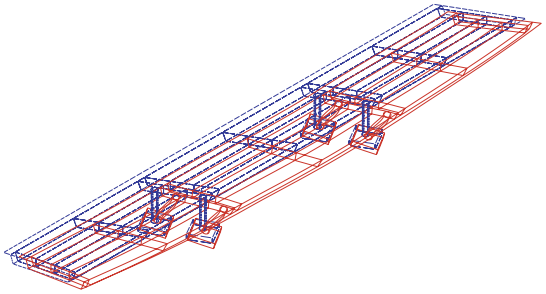

(b) 2nd mode $\left(f_2 = 2.40 \text{ Hz}\right)$

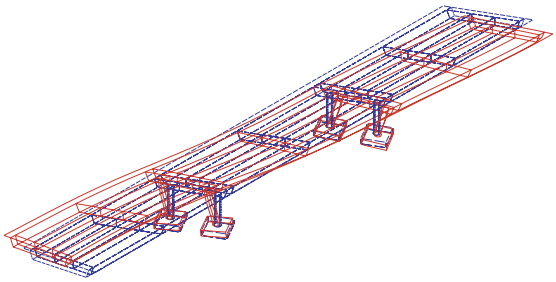

(c) 3rd mode $\left(f_3 = 2.96 \text{ Hz}\right)$

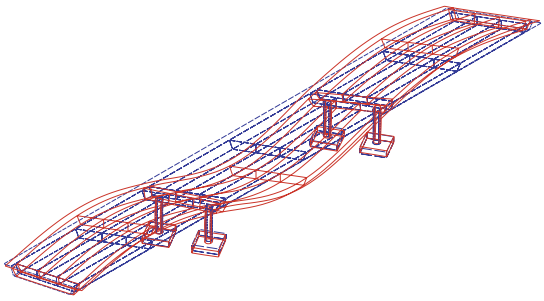

(d) 4th mode $\left(f_4 = 3.31 \text{ Hz}\right)$

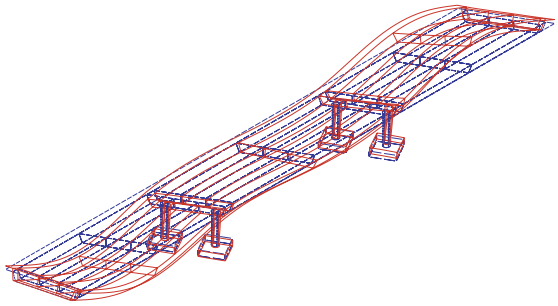

(e) 5th mode $\left(f_5 = 4.17 \text{ Hz}\right)$

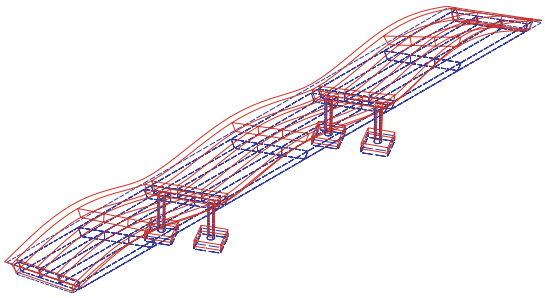

(f) 6th mode $\left(f_6 = 4.58 \text{ Hz}\right)$

Figure C.21. Fundamental mode shapes (ES15-30).

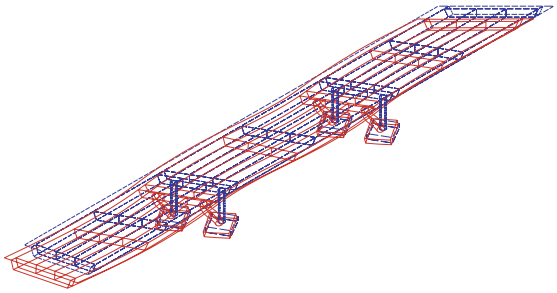

(a) 1st mode $\left(f_1 = 1.99 \text{ Hz}\right)$

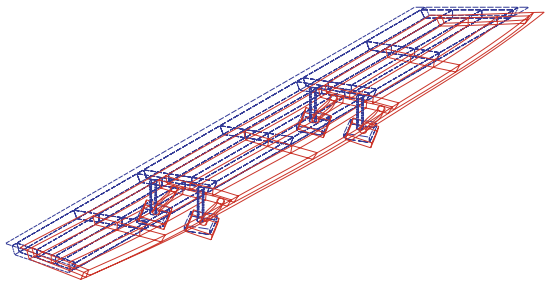

(b) 2nd mode $\left(f_2 = 2.40 \text{ Hz}\right)$

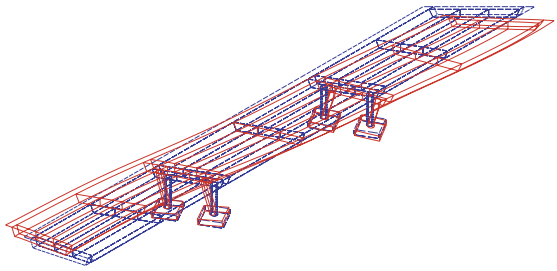

(c) 3rd mode $\left(f_3 = 2.94 \text{ Hz}\right)$

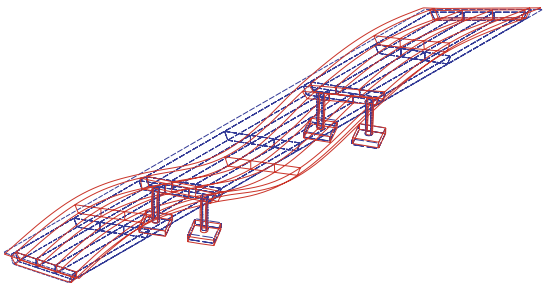

(d) 4th mode $\left(f_4 = 3.35 \text{ Hz}\right)$

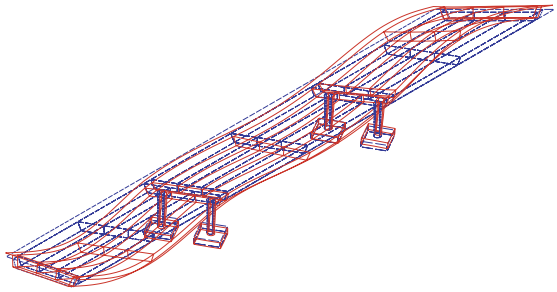

(e) 5th mode $\left(f_5 = 4.23 \text{ Hz}\right)$

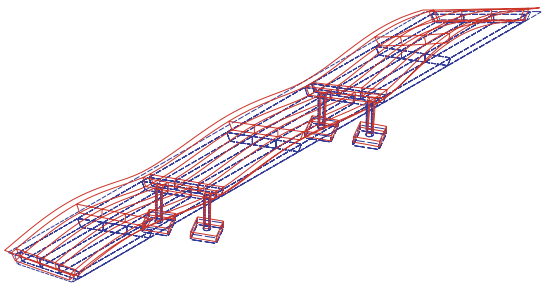

(f) 6th mode $\left(f_6 = 4.59 \text{ Hz}\right)$

Figure C.22. Fundamental mode shapes (ES15-45).

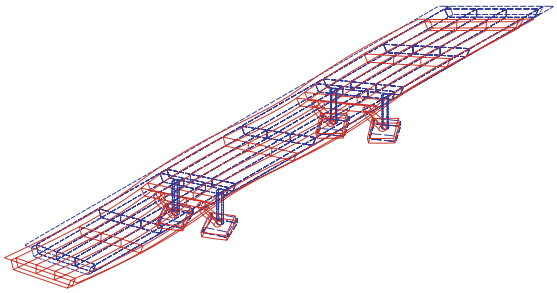

(a) 1st mode $\left(f_1 = 1.99 \text{ Hz}\right)$

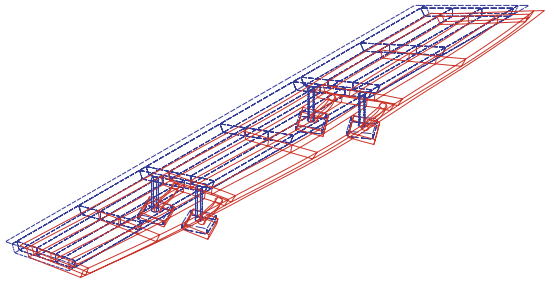

(b) 2nd mode $\left(f_2 = 2.40 \text{ Hz}\right)$

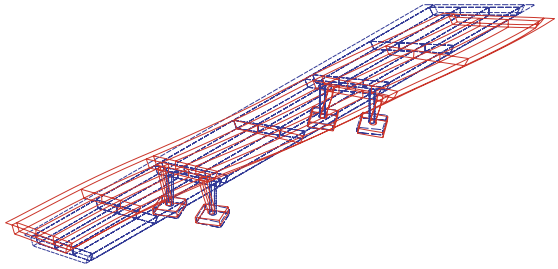

(c) 3rd mode $\left(f_3 = 2.95 \text{ Hz}\right)$

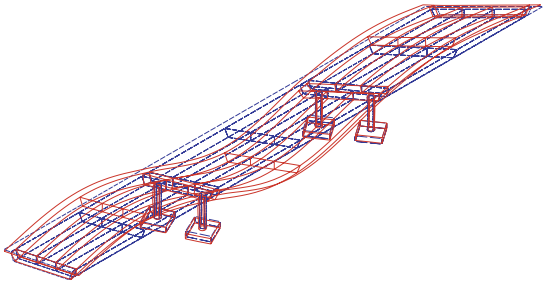

(d) 4th mode $\left(f_4 = 3.36 \text{ Hz}\right)$

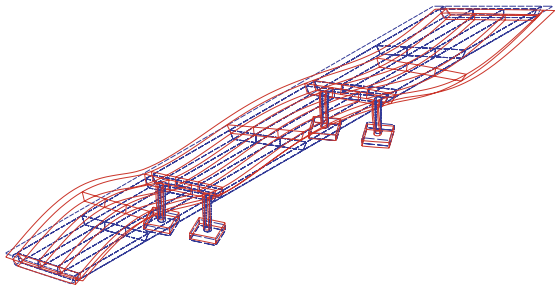

(e) 5th mode $\left(f_5 = 4.24 \text{ Hz}\right)$

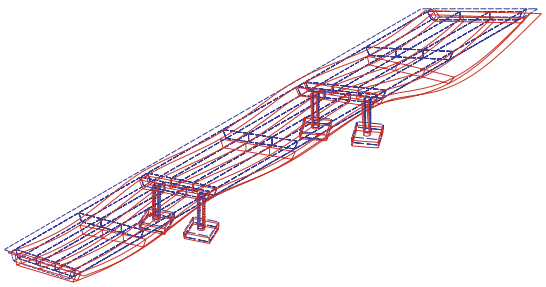

(f) 6th mode $\left(f_6 = 4.63 \text{ Hz}\right)$

Figure C.23. Fundamental mode shapes (VS15-45).

RESULTS OF PARAMETRIC NONLINEAR DYNAMIC ANALYSIS

The following is a summary of each nonlinear inelastic dynamic analysis. Each page has a template with the name, scale, and direction of the ground-motion record, skew angle configuration, response time-histories at one of the RC piers (pier 4), and maximum responses and pounding effects at representative locations of the bridge.

Input Earthquake: Kobe, 1995 **Station**: KJM **Scaling Factor**: 0.48

Input Direction: Longitudinal – 00 comp.
Transverse – 90 comp.

Skew Angle: 0 degree

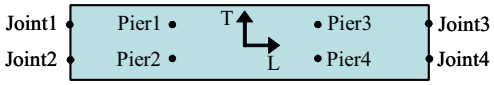

Input Time-histories

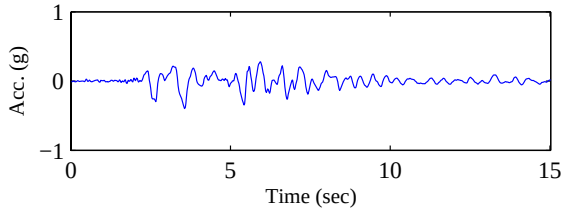

(a) Longitudinal Input

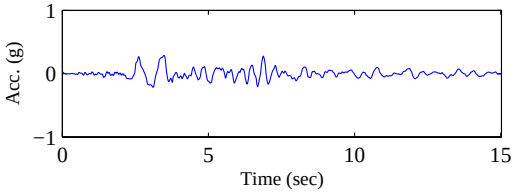

(b) Transverse Input

RC Pier Responses (Pier4)

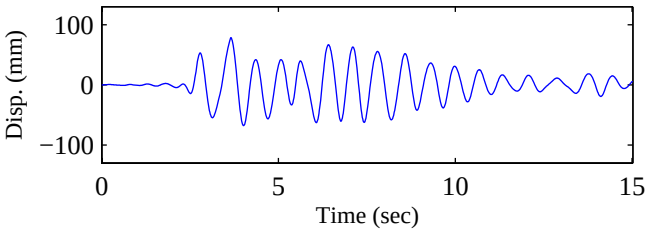

(c) Longitudinal displacement

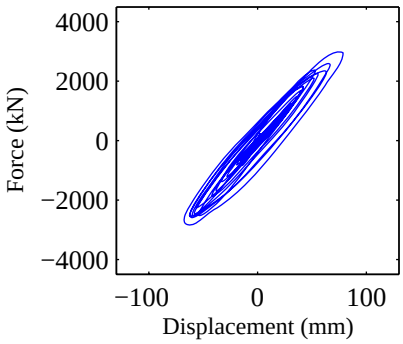

(f) Longitudinal disp.-force

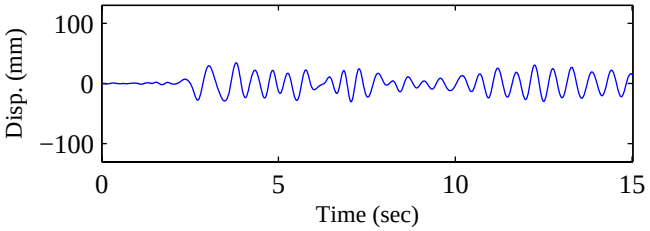

(d) Transverse displacement

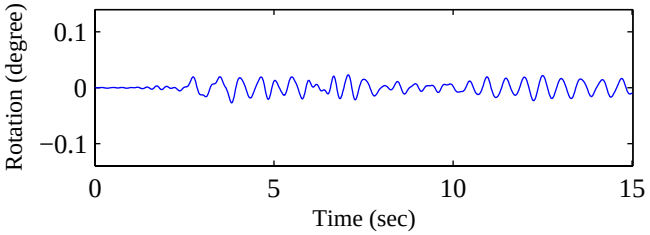

(e) Rotational displacement

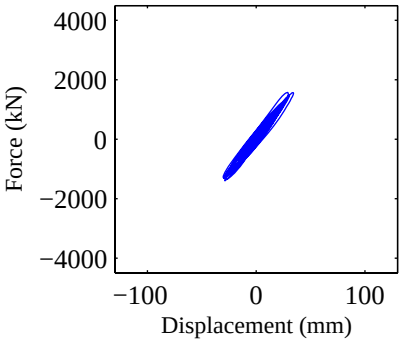

(g) Transverse disp.-force

Response Summary

	Pier1	Pier2	Pier3	Pier4	Joint1	Joint2	Joint3	Joint4
Max Long. Disp.(mm)	77.8	77.7	78.7	78.5	77.0	77.0	79.3	79.1
Max Trans. Disp.(mm)	33.9	33.9	34.3	34.3	15.4	15.4	15.8	15.8
Max Tor. Rot.(degree)	0.028	0.028	0.027	0.027	0.036	0.036	0.037	0.037
Pounding Events	NA	NA	NA	NA	0	0	1	1

Input Earthquake: Kobe, 1995 **Station**: KJM **Scaling Factor**: 0.48

Input Direction: Longitudinal – 00 comp.
Transverse – 90 comp.

Skew Angle: 30 degree

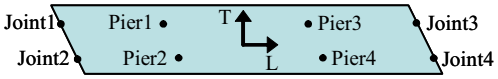

Input Time-histories

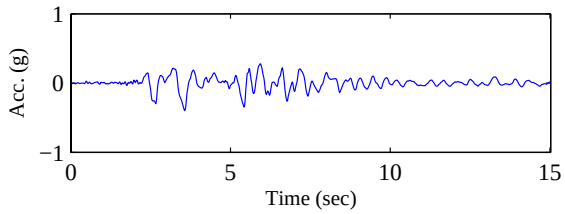

(a) Longitudinal Input

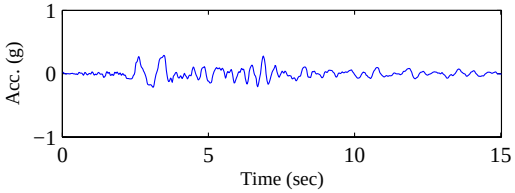

(b) Transverse Input

RC Pier Responses (Pier4)

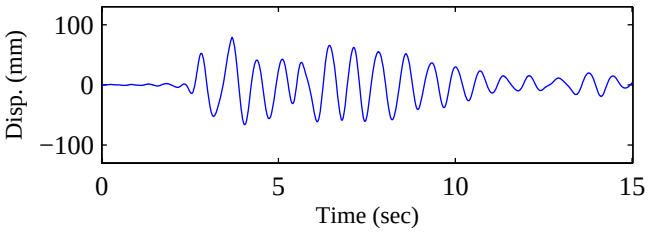

(c) Longitudinal displacement

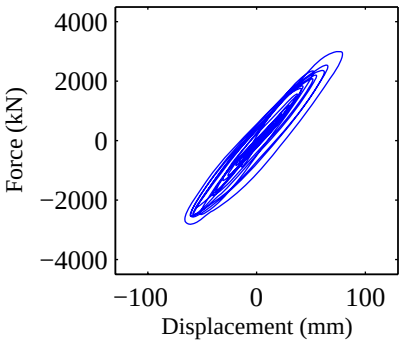

(f) Longitudinal disp.-force

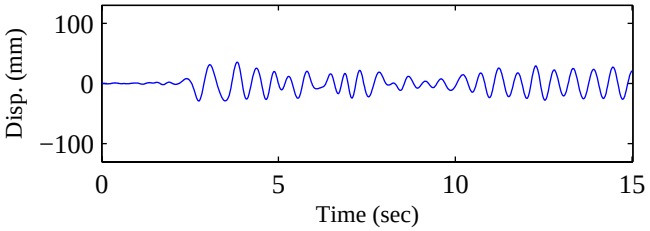

(d) Transverse displacement

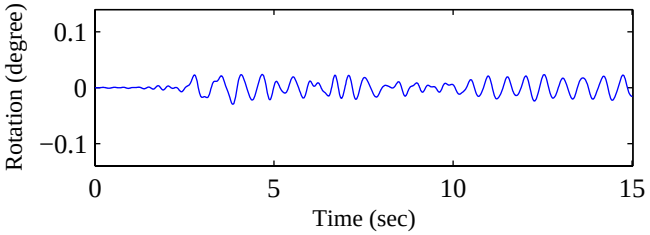

(e) Rotational displacement

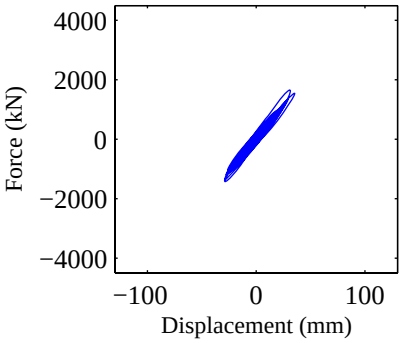

(g) Transverse disp.-force

Response Summary

	Pier1	Pier2	Pier3	Pier4	Joint1	Joint2	Joint3	Joint4
Max Long. Disp.(mm)	78.1	78.0	79.0	79.0	77.2	77.1	79.6	79.8
Max Trans. Disp.(mm)	36.7	35.2	35.5	36.9	17.8	16.0	16.2	18.1
Max Tor. Rot.(degree)	0.027	0.030	0.030	0.027	0.037	0.038	0.037	0.036
Pounding Events	NA	NA	NA	NA	0	0	1	1

Input Earthquake: Kobe, 1995 **Station**: KJM **Scaling Factor**: 0.48

Input Direction: Longitudinal – 00 comp.
Transverse – 90 comp.

Skew Angle: 60 degree

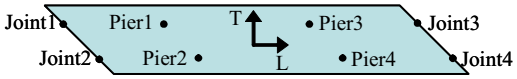

Input Time-histories

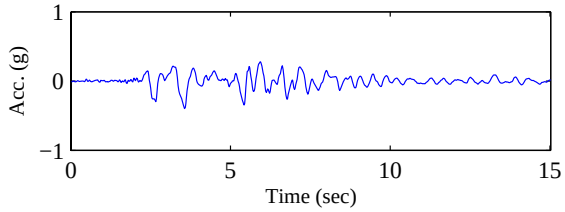

(a) Longitudinal Input

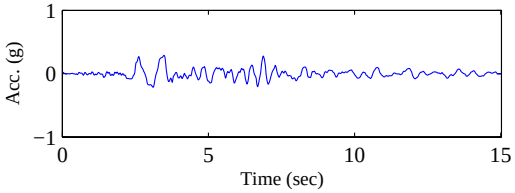

(b) Transverse Input

RC Pier Responses (Pier4)

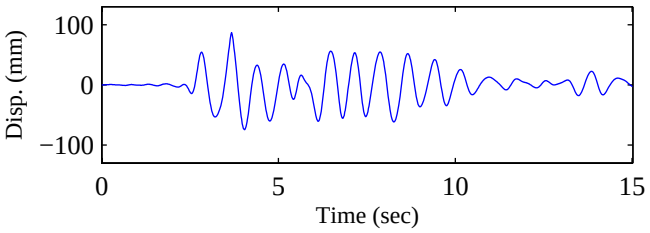

(c) Longitudinal displacement

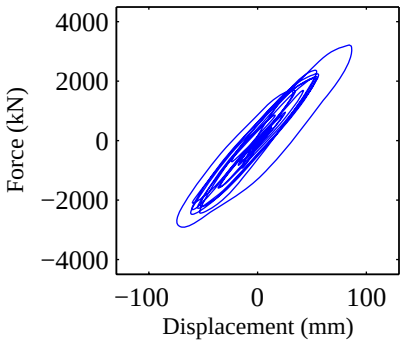

(f) Longitudinal disp.-force

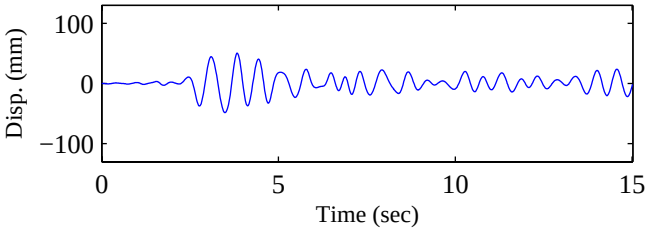

(d) Transverse displacement

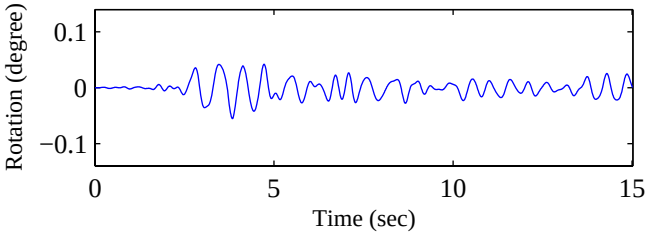

(e) Rotational displacement

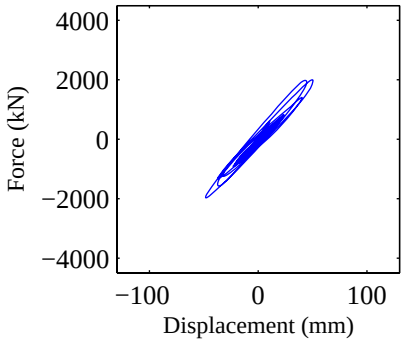

(g) Transverse disp.-force

Response Summary

	Pier1	Pier2	Pier3	Pier4	Joint1	Joint2	Joint3	Joint4
Max Long. Disp.(mm)	82.7	82.9	86.9	86.3	79.2	79.3	88.6	87.8
Max Trans. Disp.(mm)	55.8	50.0	50.5	56.3	27.4	18.3	18.2	27.0
Max Tor. Rot.(degree)	0.040	0.055	0.055	0.042	0.049	0.053	0.053	0.049
Pounding Events	NA	NA	NA	NA	0	1	1	1

Input Earthquake: Kobe, 1995 **Station**: KJM **Scaling Factor**: 0.48

Input Direction: Diagonal 1 – 00 comp.
Diagonal 2 – 90 comp.

Skew Angle: 0 degree

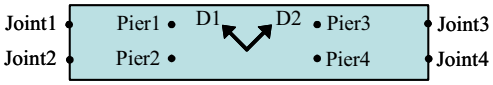

Input Time-histories

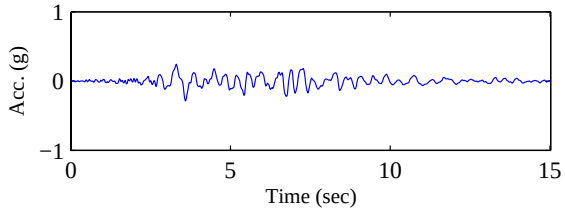

(a) Longitudinal Input

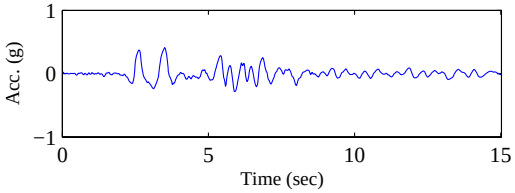

(b) Transverse Input

RC Pier Responses (Pier4)

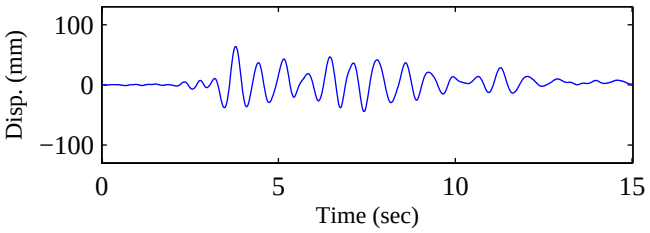

(c) Longitudinal displacement

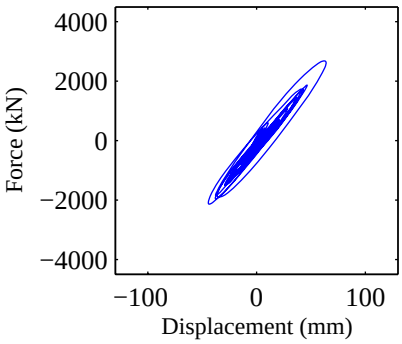

(f) Longitudinal disp.-force

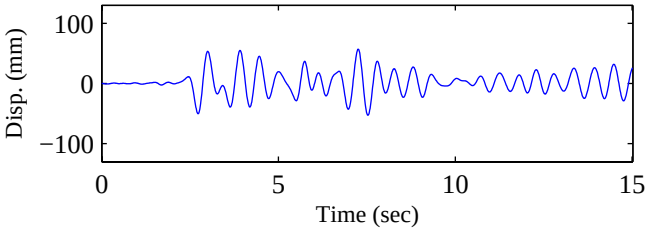

(d) Transverse displacement

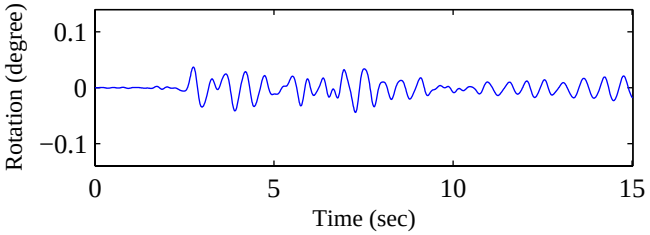

(e) Rotational displacement

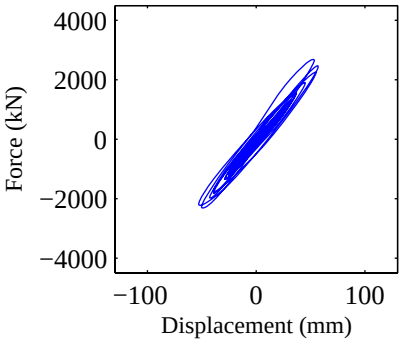

(g) Transverse disp.-force

Response Summary

	Pier1	Pier2	Pier3	Pier4	Joint1	Joint2	Joint3	Joint4
Max Long. Disp.(mm)	64.5	63.9	63.9	64.6	65.3	63.9	63.9	65.4
Max Trans. Disp.(mm)	56.9	56.9	57.0	57.1	23.2	23.2	23.1	23.1
Max Tor. Rot.(degree)	0.044	0.044	0.044	0.045	0.060	0.060	0.060	0.060
Pounding Events	NA	NA	NA	NA	0	0	0	0

Input Earthquake: Kobe, 1995 **Station**: KJM **Scaling Factor**: 0.48

Input Direction: Diagonal 1 – 00 comp.
Diagonal 2 – 90 comp.

Skew Angle: 30 degree

Input Time-histories

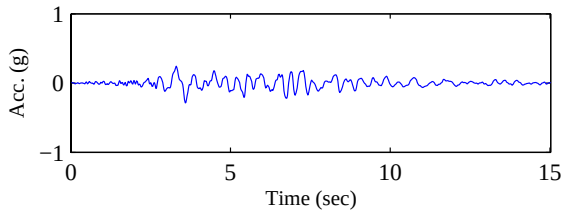

(a) Longitudinal Input

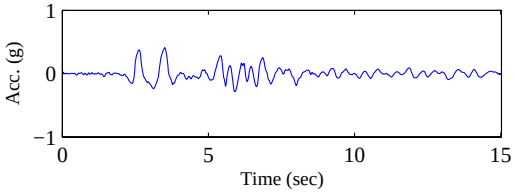

(b) Transverse Input

RC Pier Responses (Pier4)

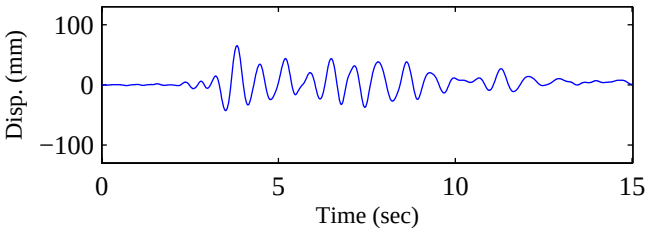

(c) Longitudinal displacement

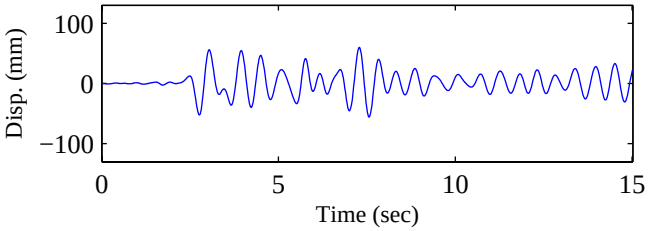

(d) Transverse displacement

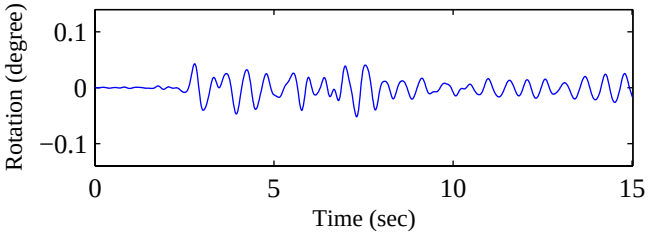

(e) Rotational displacement

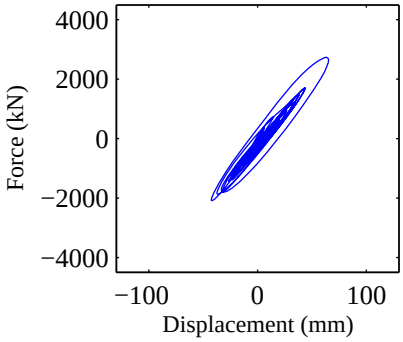

(f) Longitudinal disp.-force

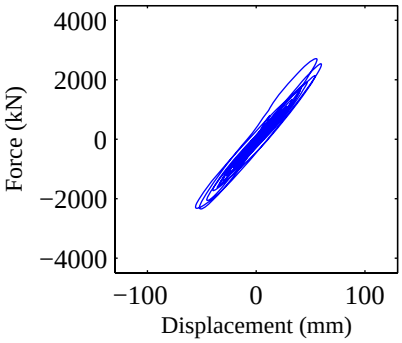

(g) Transverse disp.-force

Response Summary

	Pier1	Pier2	Pier3	Pier4	Joint1	Joint2	Joint3	Joint4
Max Long. Disp.(mm)	66.1	65.3	65.3	66.1	67.0	65.2	65.2	67.1
Max Trans. Disp.(mm)	62.4	60.1	60.1	62.5	26.0	22.3	22.7	26.4
Max Tor. Rot.(degree)	0.046	0.052	0.052	0.047	0.064	0.065	0.065	0.064
Pounding Events	NA	NA	NA	NA	0	0	0	0

Input Earthquake: Kobe, 1995 **Station**: KJM **Scaling Factor**: 0.48

Input Direction: Diagonal 1 – 00 comp.
Diagonal 2 – 90 comp.

Skew Angle: 60 degree

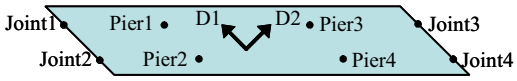

Input Time-histories

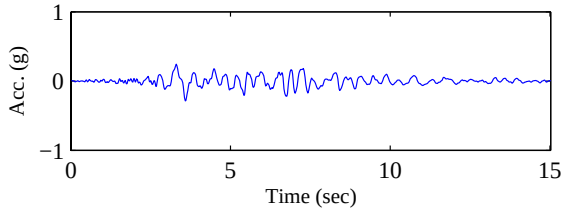

(a) Longitudinal Input

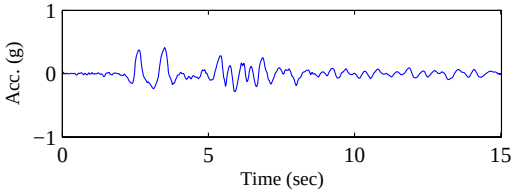

(b) Transverse Input

RC Pier Responses (Pier4)

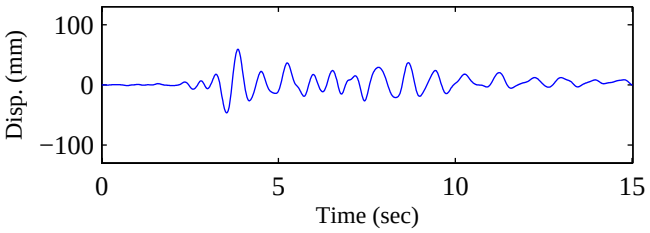

(c) Longitudinal displacement

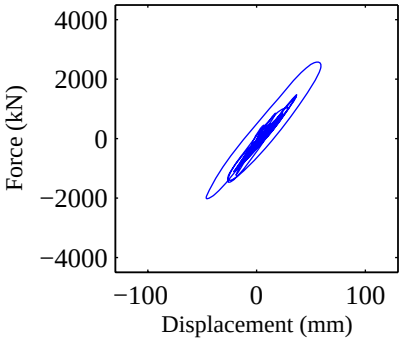

(f) Longitudinal disp.-force

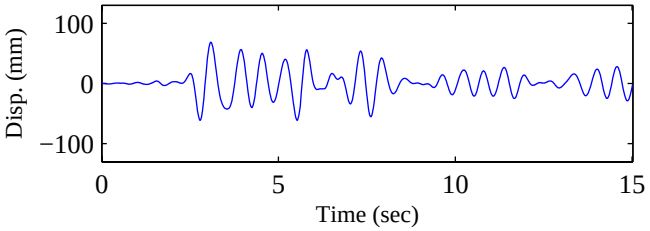

(d) Transverse displacement

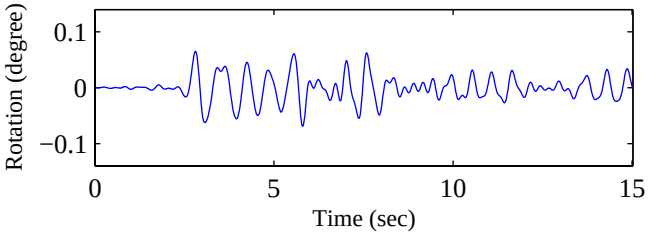

(e) Rotational displacement

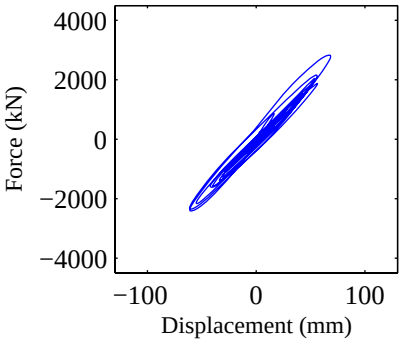

(g) Transverse disp.-force

Response Summary

	Pier1	Pier2	Pier3	Pier4	Joint1	Joint2	Joint3	Joint4
Max Long. Disp.(mm)	61.5	59.2	59.2	61.5	63.1	58.6	58.6	63.1
Max Trans. Disp.(mm)	74.9	68.3	68.5	75.6	36.2	23.4	23.6	36.6
Max Tor. Rot.(degree)	0.051	0.070	0.069	0.050	0.061	0.068	0.069	0.063
Pounding Events	NA	NA	NA	NA	0	0	0	0

Input Earthquake: Kobe, 1995 **Station**: KJM **Scaling Factor**: 0.48

Input Direction: Longitudinal – 90 comp.
Transverse – 00 comp.

Skew Angle: 0 degree

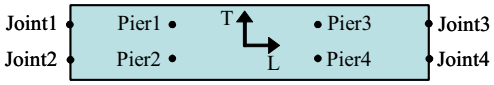

Input Time-histories

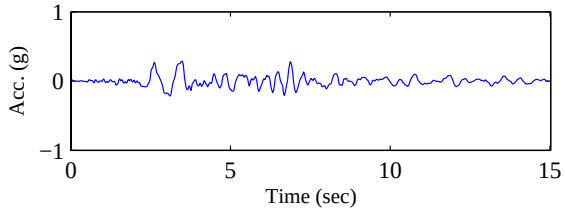

(a) Longitudinal Input

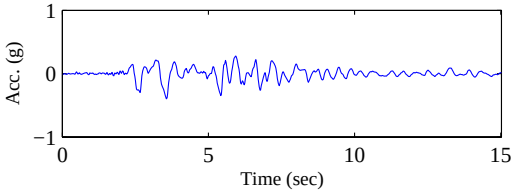

(b) Transverse Input

RC Pier Responses (Pier4)

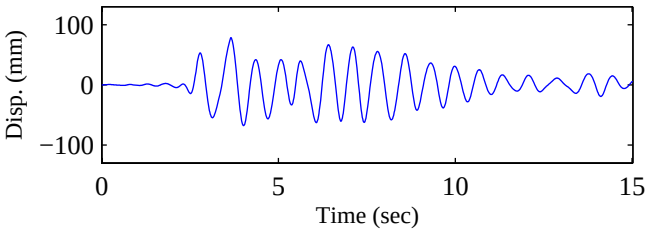

(c) Longitudinal displacement

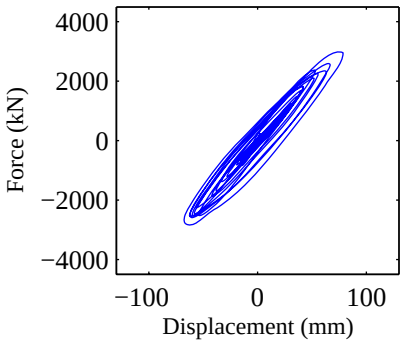

(f) Longitudinal disp.-force

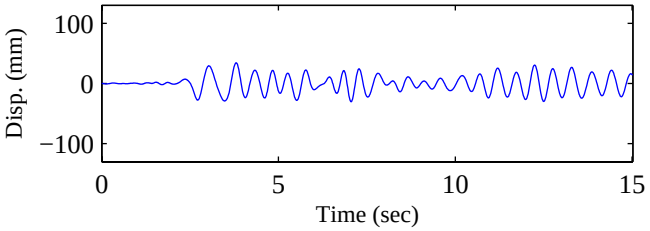

(d) Transverse displacement

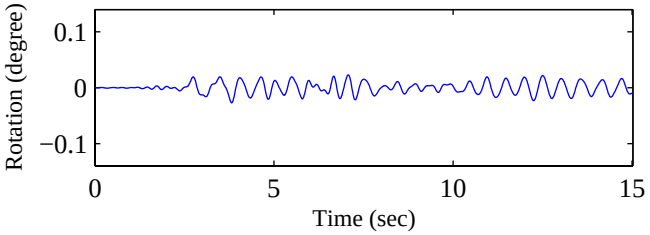

(e) Rotational displacement

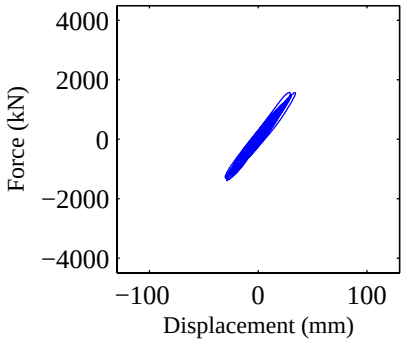

(g) Transverse disp.-force

Response Summary

	Pier1	Pier2	Pier3	Pier4	Joint1	Joint2	Joint3	Joint4
Max Long. Disp.(mm)	77.8	77.7	78.7	78.5	77.0	77.0	79.3	79.1
Max Trans. Disp.(mm)	33.9	33.9	34.3	34.3	15.4	15.4	15.9	15.9
Max Tor. Rot.(degree)	0.028	0.027	0.027	0.027	0.036	0.036	0.037	0.037
Pounding Events	NA	NA	NA	NA	0	0	1	1

Input Earthquake: Kobe, 1995 **Station**: KJM **Scaling Factor**: 0.48

Input Direction: Longitudinal – 90 comp.
Transverse – 00 comp.

Skew Angle: 30 degree

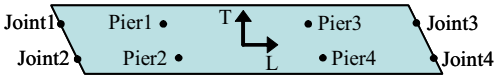

Input Time-histories

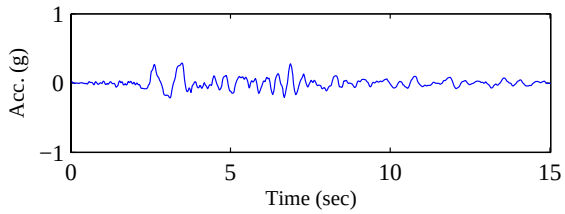

(a) Longitudinal Input

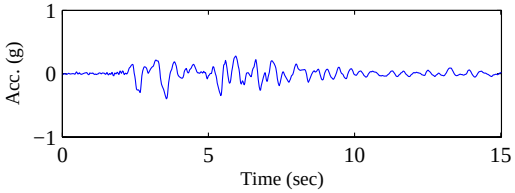

(b) Transverse Input

RC Pier Responses (Pier4)

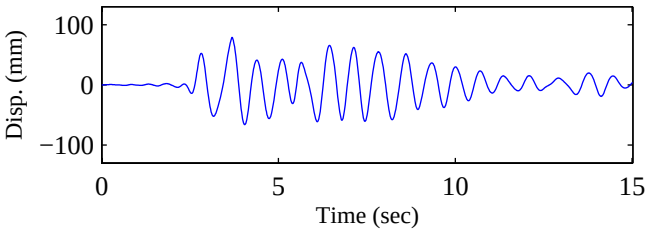

(c) Longitudinal displacement

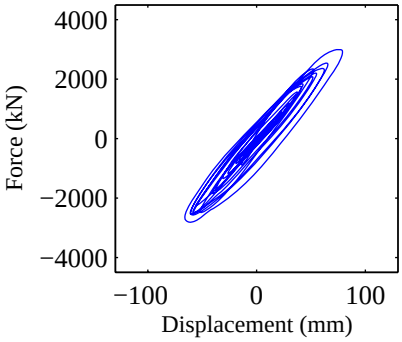

(f) Longitudinal disp.-force

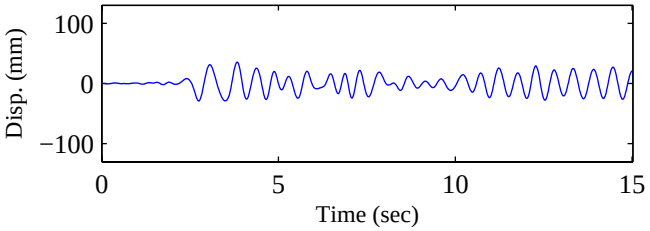

(d) Transverse displacement

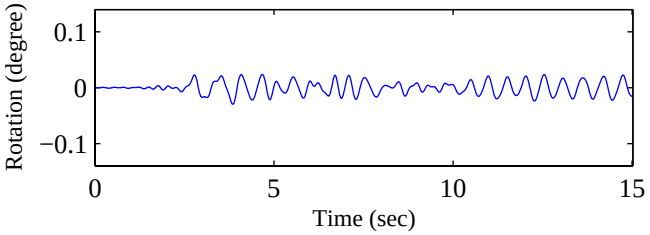

(e) Rotational displacement

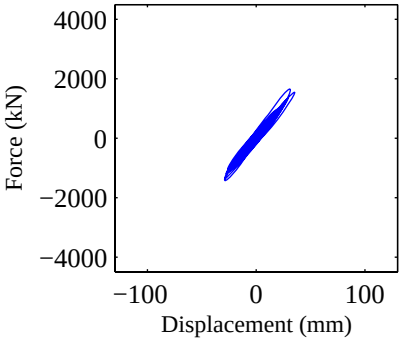

(g) Transverse disp.-force

Response Summary

	Pier1	Pier2	Pier3	Pier4	Joint1	Joint2	Joint3	Joint4
Max Long. Disp.(mm)	78.1	78.0	79.0	79.0	77.2	77.1	79.6	79.8
Max Trans. Disp.(mm)	36.7	35.2	35.5	36.8	17.8	16.0	16.2	18.0
Max Tor. Rot.(degree)	0.027	0.030	0.030	0.027	0.037	0.038	0.037	0.036
Pounding Events	NA	NA	NA	NA	0	0	1	1

Input Earthquake: Kobe, 1995 **Station**: KJM **Scaling Factor**: 0.48

Input Direction: Longitudinal – 90 comp.
Transverse – 00 comp.

Skew Angle: 60 degree

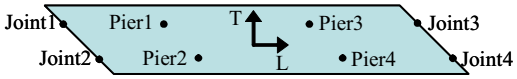

Input Time-histories

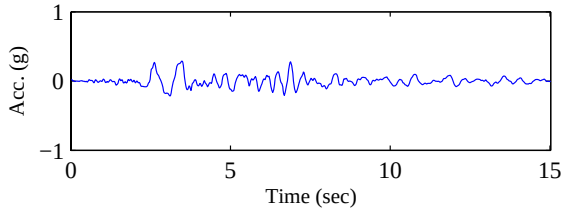

(a) Longitudinal Input

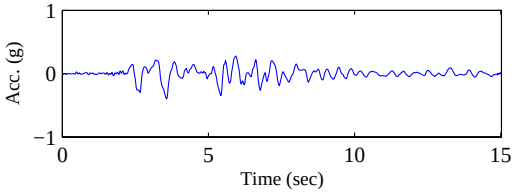

(b) Transverse Input

RC Pier Responses (Pier4)

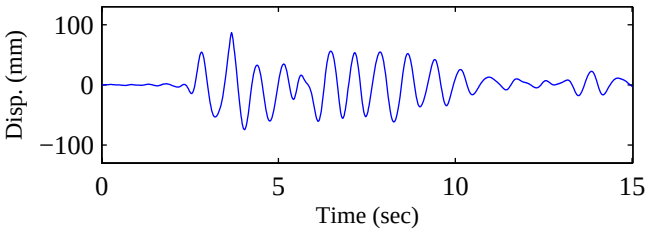

(c) Longitudinal displacement

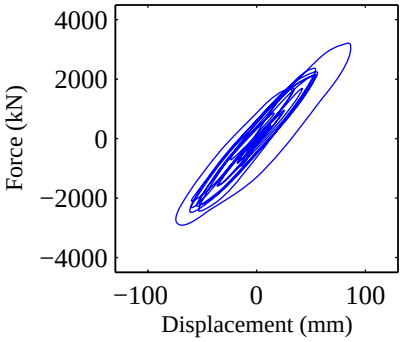

(f) Longitudinal disp.-force

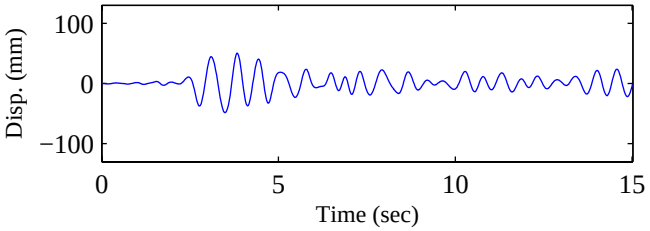

(d) Transverse displacement

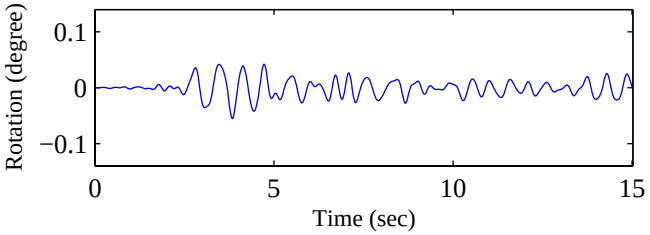

(e) Rotational displacement

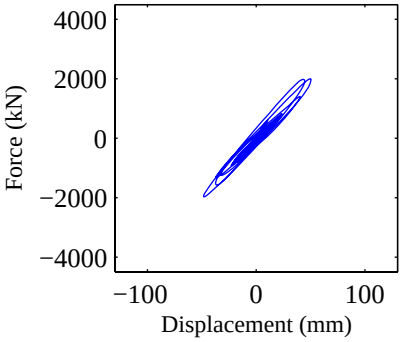

(g) Transverse disp.-force

Response Summary

	Pier1	Pier2	Pier3	Pier4	Joint1	Joint2	Joint3	Joint4
Max Long. Disp.(mm)	82.7	82.9	86.9	86.3	79.2	79.3	88.6	87.8
Max Trans. Disp.(mm)	55.8	50.0	5.5	56.3	27.4	18.3	18.2	27.0
Max Tor. Rot.(degree)	0.040	0.055	0.055	0.042	0.049	0.053	0.053	0.049
Pounding Events	NA	NA	NA	NA	0	1	1	1

Input Earthquake: Chi-Chi, 1999 **Station**: CHY028 **Scaling Factor**: 0.56

Input Direction: Longitudinal – NS comp.
Transverse – EW comp.

Skew Angle: 0 degree

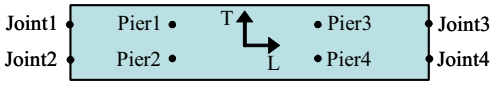

Input Time-histories

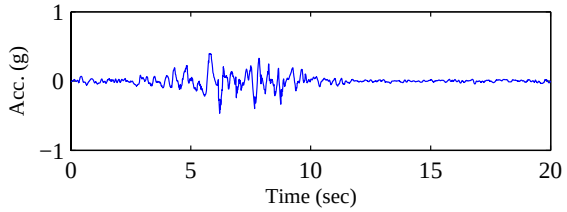

(a) Longitudinal Input

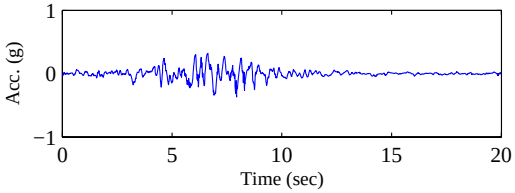

(b) Transverse Input

RC Pier Responses (Pier4)

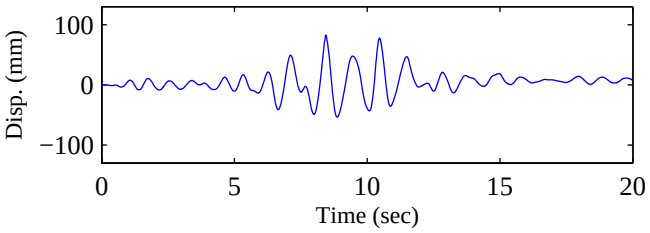

(c) Longitudinal displacement

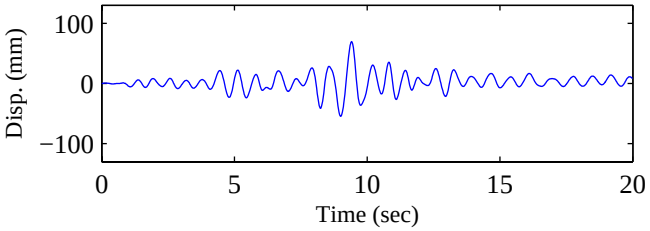

(d) Transverse displacement

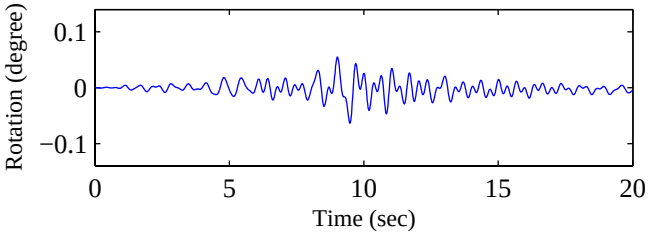

(e) Rotational displacement

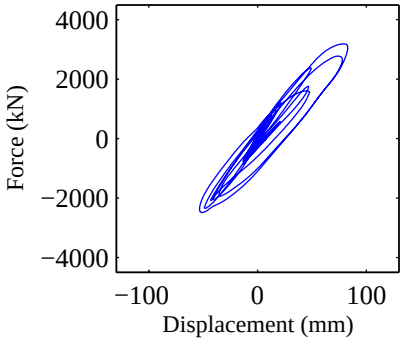

(f) Longitudinal disp.-force

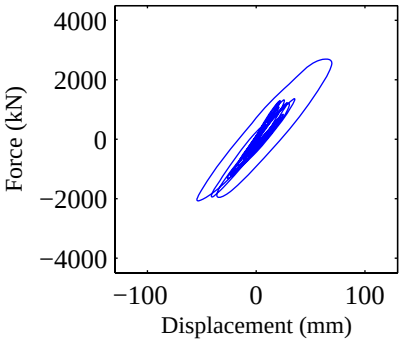

(g) Transverse disp.-force

Response Summary

	Pier1	Pier2	Pier3	Pier4	Joint1	Joint2	Joint3	Joint4
Max Long. Disp.(mm)	81.3	80.7	82.8	84.2	78.8	78.2	83.7	85.9
Max Trans. Disp.(mm)	70.1	70.1	69.6	69.6	36.6	36.6	36.8	36.8
Max Tor. Rot.(degree)	0.060	0.062	0.063	0.061	0.076	0.076	0.076	0.076
Pounding Events	NA	NA	NA	NA	0	0	2	2

Input Earthquake: Chi-Chi, 1999 **Station**: CHY028 **Scaling Factor**: 0.56

Input Direction: Longitudinal – NS comp.
Transverse – EW comp.

Skew Angle: 30 degree

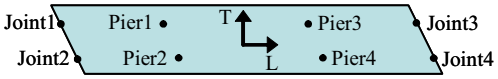

Input Time-histories

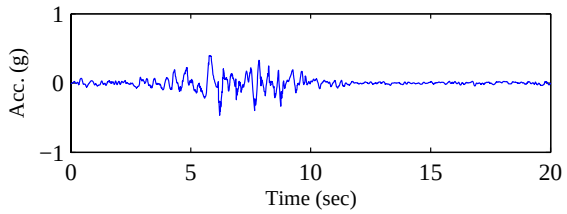

(a) Longitudinal Input

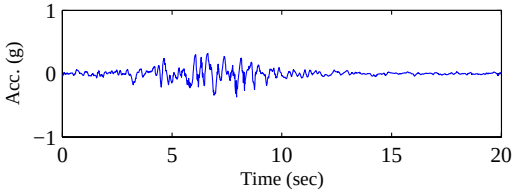

(b) Transverse Input

RC Pier Responses (Pier4)

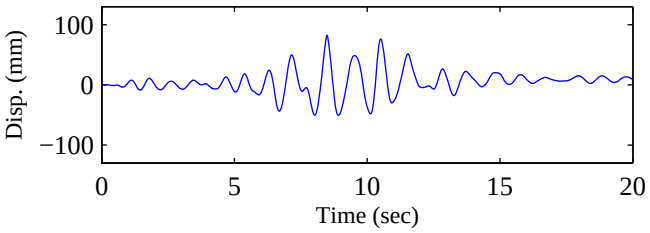

(c) Longitudinal displacement

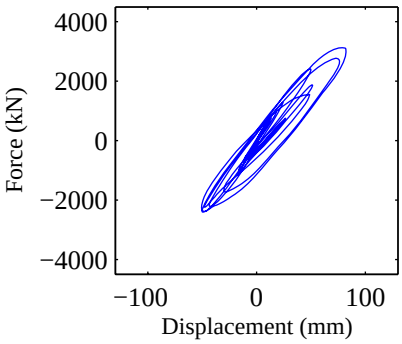

(f) Longitudinal disp.-force

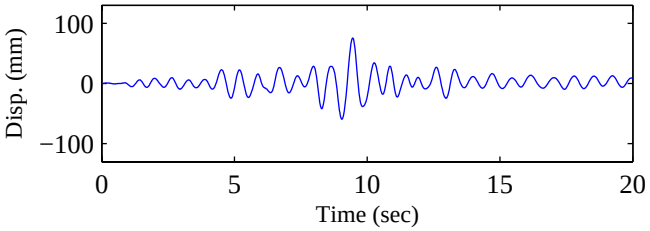

(d) Transverse displacement

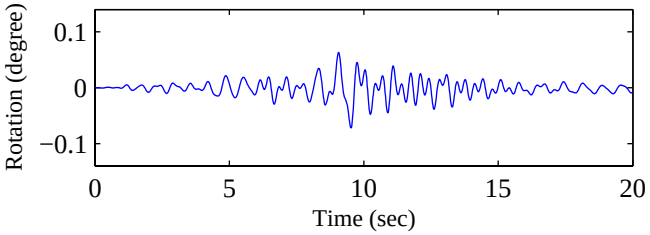

(e) Rotational displacement

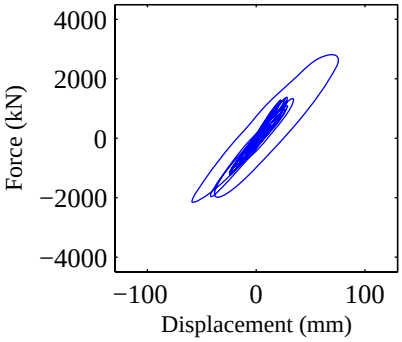

(g) Transverse disp.-force

Response Summary

	Pier1	Pier2	Pier3	Pier4	Joint1	Joint2	Joint3	Joint4
Max Long. Disp.(mm)	80.8	80.4	82.5	83.3	78.6	78.2	83.3	84.7
Max Trans. Disp.(mm)	78.4	75.7	75.6	78.4	39.5	35.6	35.6	39.8
Max Tor. Rot.(degree)	0.062	0.071	0.072	0.063	0.081	0.082	0.082	0.081
Pounding Events	NA	NA	NA	NA	0	0	2	2

Input Earthquake: Chi-Chi, 1999 **Station**: CHY028 **Scaling Factor**: 0.56

Input Direction: Longitudinal – NS comp.
Transverse – EW comp.

Skew Angle: 60 degree

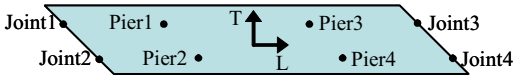

Input Time-histories

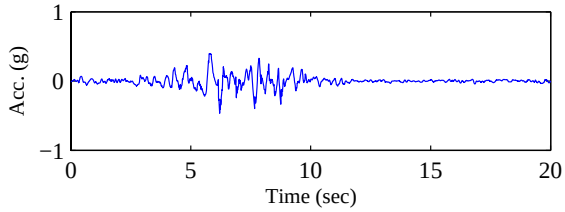

(a) Longitudinal Input

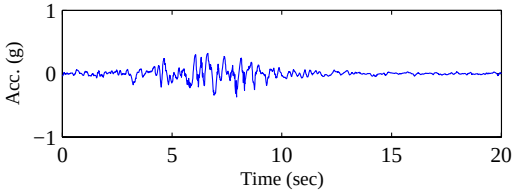

(b) Transverse Input

RC Pier Responses (Pier4)

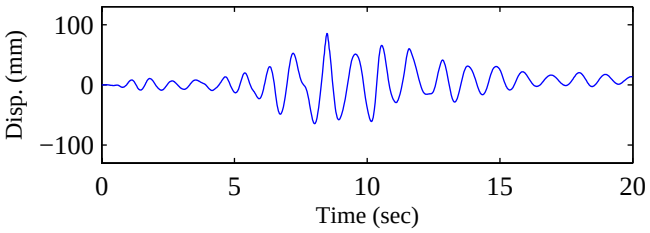

(c) Longitudinal displacement

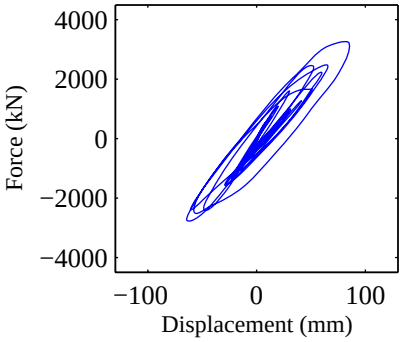

(f) Longitudinal disp.-force

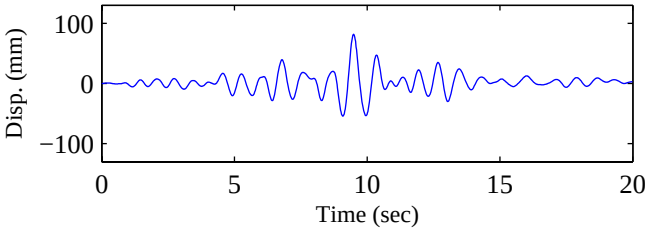

(d) Transverse displacement

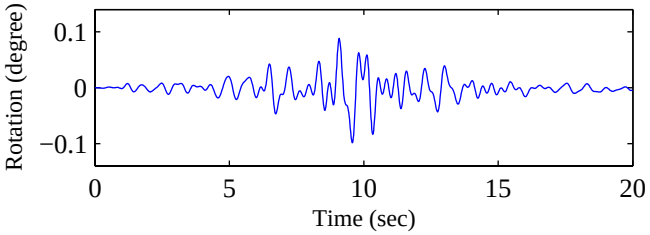

(e) Rotational displacement

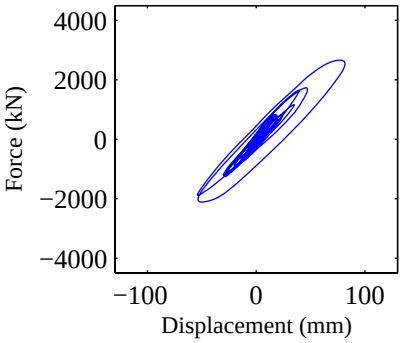

(g) Transverse disp.-force

Response Summary

	Pier1	Pier2	Pier3	Pier4	Joint1	Joint2	Joint3	Joint4
Max Long. Disp.(mm)	83.1	82.3	85.6	86.8	79.6	78.9	87.0	88.7
Max Trans. Disp.(mm)	88.9	81.4	81.7	90.1	50.0	38.6	37.1	49.7
Max Tor. Rot.(degree)	0.073	0.099	0.099	0.073	0.083	0.089	0.088	0.082
Pounding Events	NA	NA	NA	NA	0	0	1	1

Input Earthquake: Chi-Chi, 1999 **Station**: CHY028 **Scaling Factor**: 0.56

Input Direction: Diagonal 1 – NS comp.
Diagonal 2 – EW comp.

Skew Angle: 0 degree

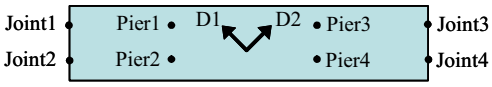

Input Time-histories

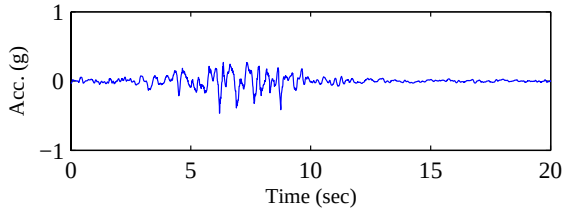

(a) Longitudinal Input

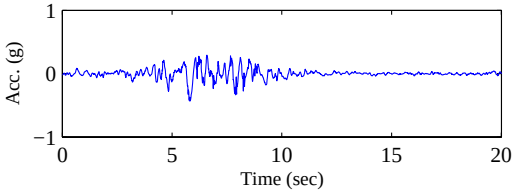

(b) Transverse Input

RC Pier Responses (Pier4)

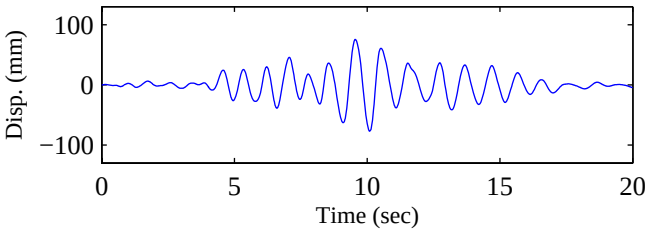

(c) Longitudinal displacement

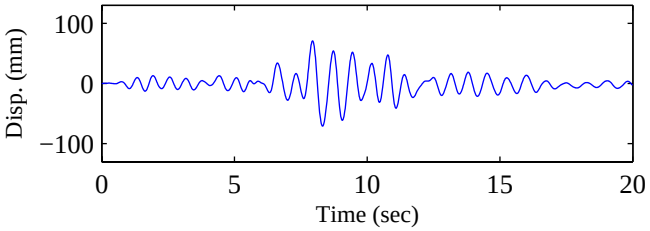

(d) Transverse displacement

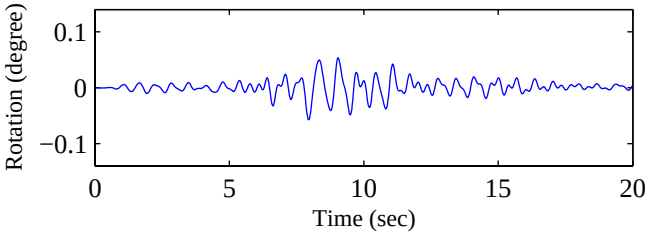

(e) Rotational displacement

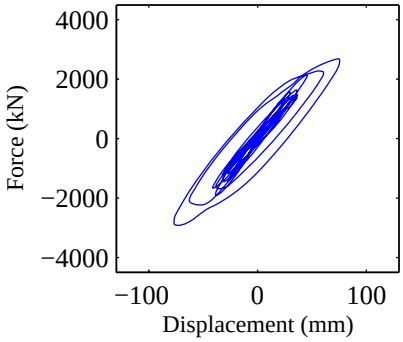

(f) Longitudinal disp.-force

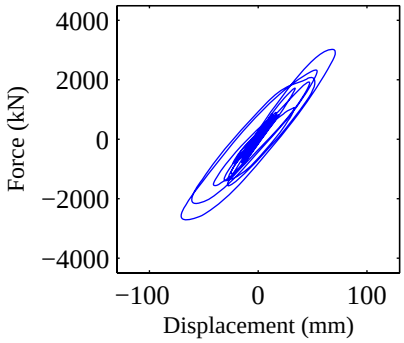

(g) Transverse disp.-force

Response Summary

	Pier1	Pier2	Pier3	Pier4	Joint1	Joint2	Joint3	Joint4
Max Long. Disp.(mm)	77.5	77.7	77.0	79.2	77.4	78.8	77.0	80.8
Max Trans. Disp.(mm)	70.8	70.8	71.0	71.0	27.4	27.4	27.8	27.8
Max Tor. Rot.(degree)	0.058	0.058	0.057	0.057	0.077	0.077	0.077	0.077
Pounding Events	NA	NA	NA	NA	1	1	1	0

Input Earthquake: Chi-Chi, 1999 **Station**: CHY028 **Scaling Factor**: 0.56

Input Direction: Diagonal 1 – NS comp.
Diagonal 2 – EW comp.

Skew Angle: 30 degree

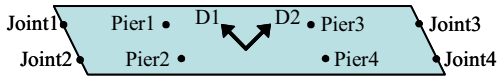

Input Time-histories

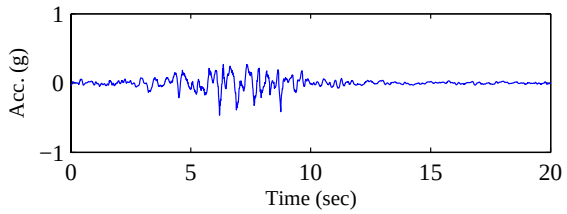

(a) Longitudinal Input

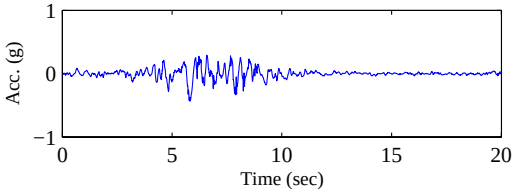

(b) Transverse Input

RC Pier Responses (Pier4)

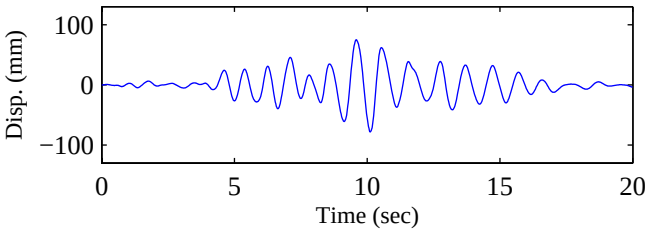

(c) Longitudinal displacement

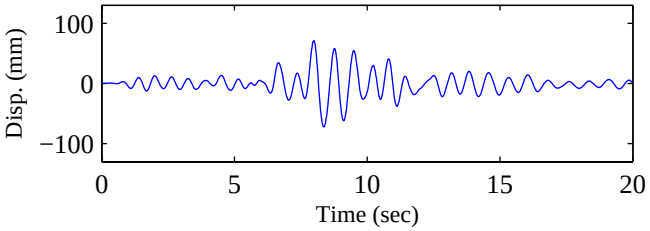

(d) Transverse displacement

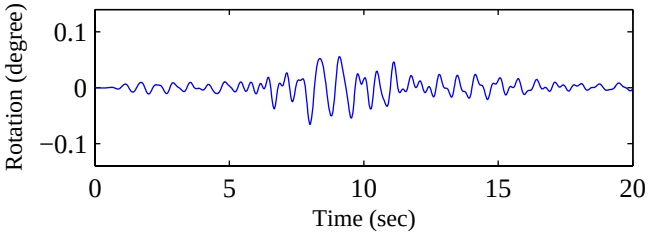

(e) Rotational displacement

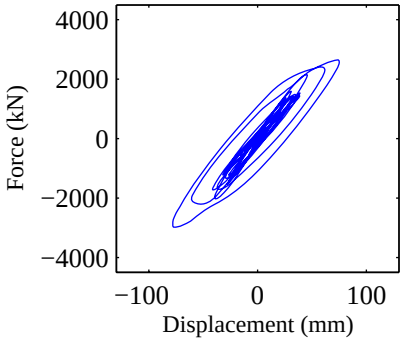

(f) Longitudinal disp.-force

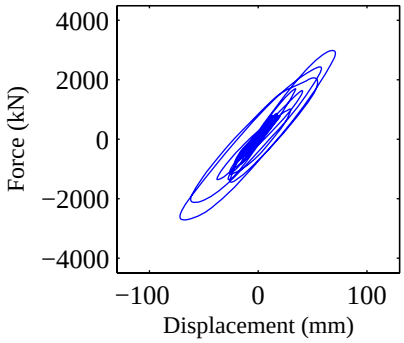

(g) Transverse disp.-force

Response Summary

	Pier1	Pier2	Pier3	Pier4	Joint1	Joint2	Joint3	Joint4
Max Long. Disp.(mm)	79.2	79.2	78.1	78.8	79.4	80.3	77.3	80.6
Max Trans. Disp.(mm)	74.5	72.0	72.1	74.6	32.3	27.4	27.4	32.2
Max Tor. Rot.(degree)	0.058	0.066	0.066	0.058	0.078	0.079	0.080	0.078
Pounding Events	NA	NA	NA	NA	1	1	1	0

Input Earthquake: Chi-Chi, 1999 **Station**: CHY028 **Scaling Factor**: 0.56

Input Direction: Diagonal 1 – NS comp.
Diagonal 2 – EW comp.

Skew Angle: 60 degree

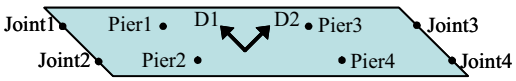

Input Time-histories

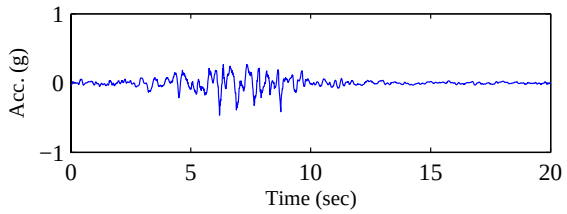

(a) Longitudinal Input

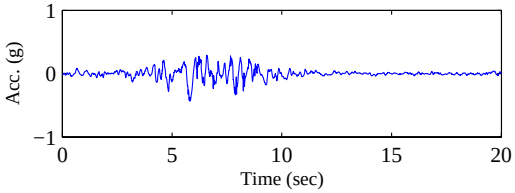

(b) Transverse Input

RC Pier Responses (Pier4)

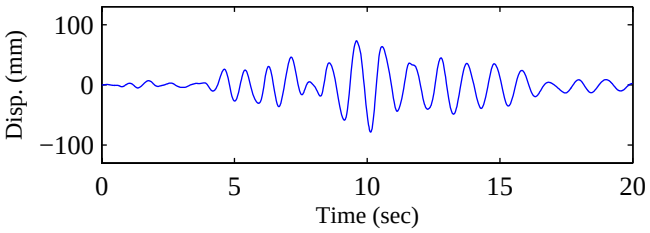

(c) Longitudinal displacement

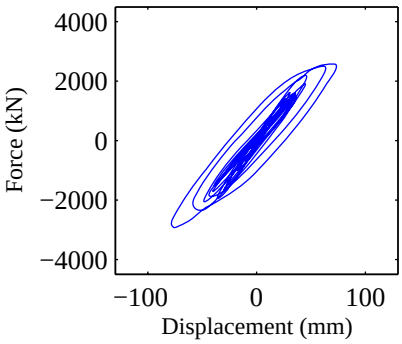

(f) Longitudinal disp.-force

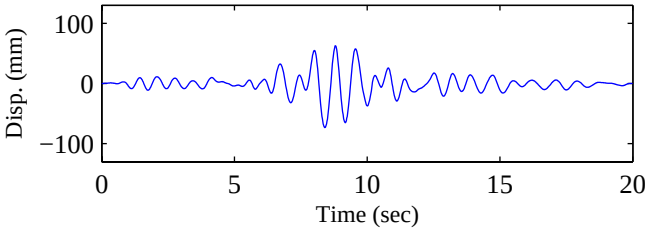

(d) Transverse displacement

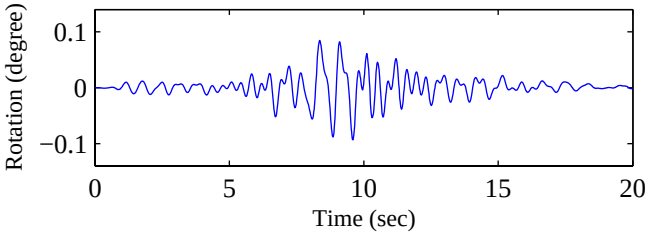

(e) Rotational displacement

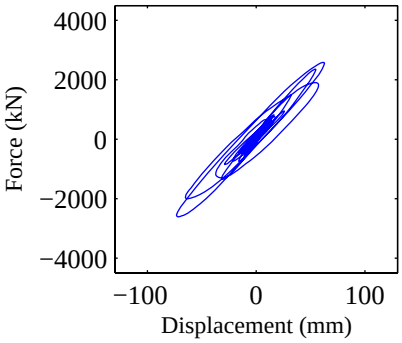

(g) Transverse disp.-force

Response Summary

	Pier1	Pier2	Pier3	Pier4	Joint1	Joint2	Joint3	Joint4
Max Long. Disp.(mm)	82.8	79.9	78.4	80.6	84.6	80.3	77.0	81.3
Max Trans. Disp.(mm)	82.1	73.2	73.2	81.4	38.9	27.4	30.2	38.8
Max Tor. Rot.(degree)	0.071	0.092	0.093	0.068	0.075	0.081	0.078	0.073
Pounding Events	NA	NA	NA	NA	1	1	1	0

Input Earthquake: Chi-Chi, 1999 **Station**: CHY028 **Scaling Factor**: 0.56

Input Direction: Longitudinal – EW comp.
Transverse – NS comp.

Skew Angle: 0 degree

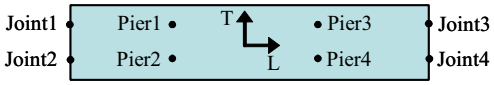

Input Time-histories

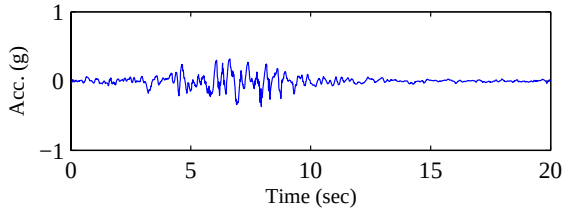

(a) Longitudinal Input

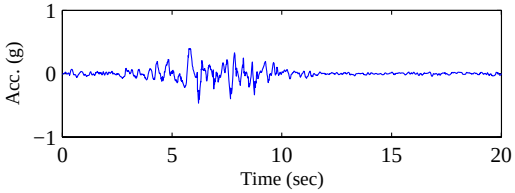

(b) Transverse Input

RC Pier Responses (Pier4)

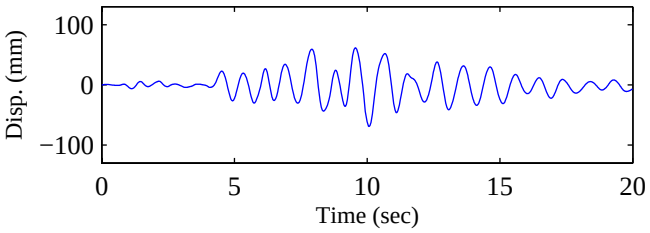

(c) Longitudinal displacement

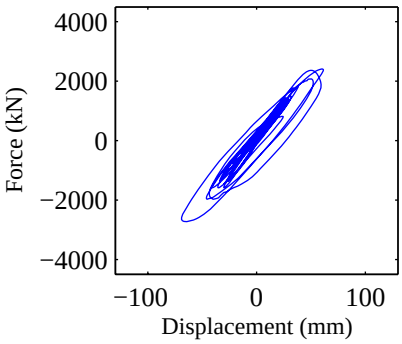

(f) Longitudinal disp.-force

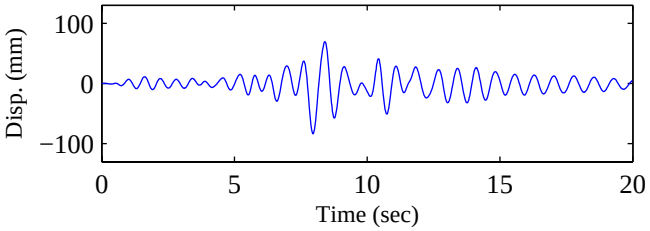

(d) Transverse displacement

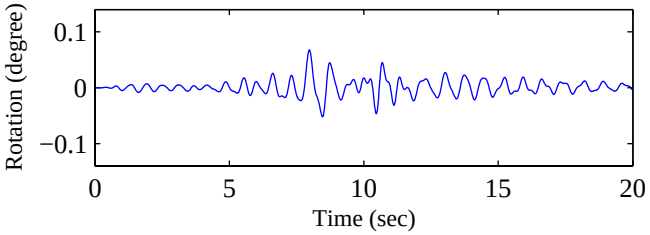

(e) Rotational displacement

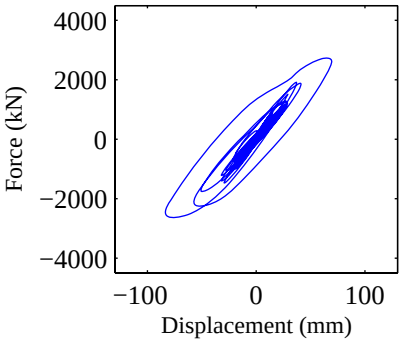

(g) Transverse disp.-force

Response Summary

	Pier1	Pier2	Pier3	Pier4	Joint1	Joint2	Joint3	Joint4
Max Long. Disp.(mm)	70.1	69.0	69.1	70.0	71.0	68.9	68.9	70.9
Max Trans. Disp.(mm)	83.2	83.2	83.6	83.6	31.4	31.4	31.8	31.8
Max Tor. Rot.(degree)	0.070	0.068	0.068	0.070	0.091	0.091	0.092	0.092
Pounding Events	NA	NA	NA	NA	0	0	0	0

Input Earthquake: Chi-Chi, 1999 **Station**: CHY028 **Scaling Factor**: 0.56

Input Direction: Longitudinal – EW comp.
Transverse – NS comp.

Skew Angle: 30 degree

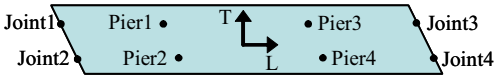

Input Time-histories

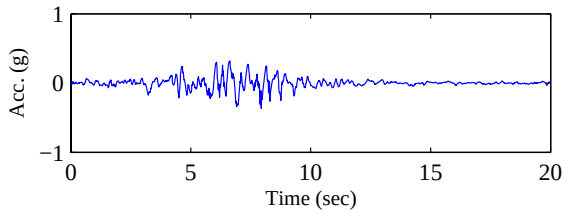

(a) Longitudinal Input

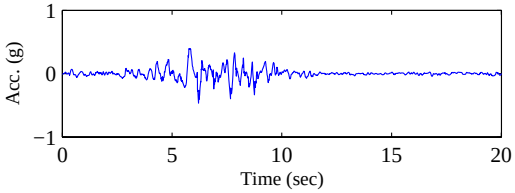

(b) Transverse Input

RC Pier Responses (Pier4)

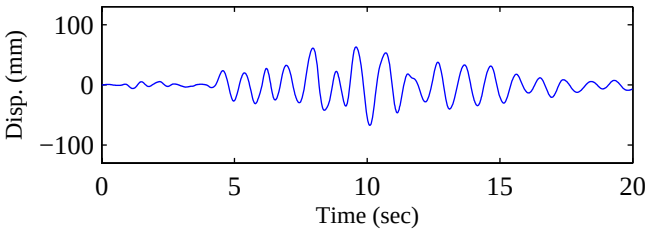

(c) Longitudinal displacement

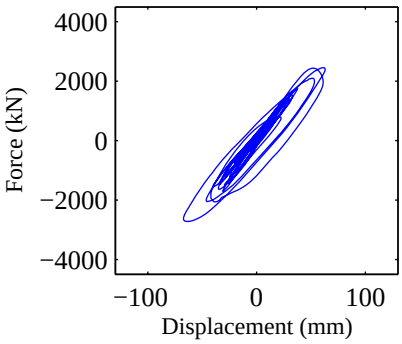

(f) Longitudinal disp.-force

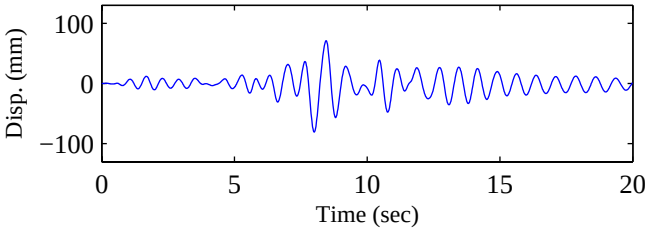

(d) Transverse displacement

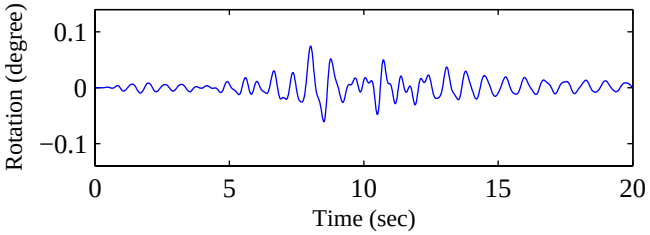

(e) Rotational displacement

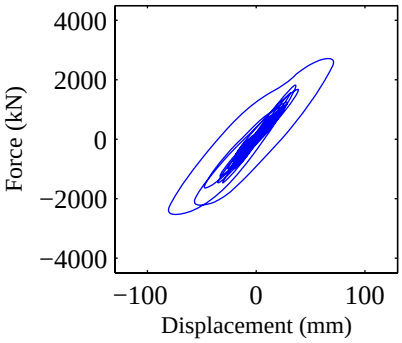

(g) Transverse disp.-force

Response Summary

	Pier1	Pier2	Pier3	Pier4	Joint1	Joint2	Joint3	Joint4
Max Long. Disp.(mm)	68.3	67.3	67.3	68.3	69.2	67.2	67.2	69.1
Max Trans. Disp.(mm)	84.4	80.9	80.7	84.2	35.0	31.2	32.0	35.8
Max Tor. Rot.(degree)	0.068	0.074	0.074	0.068	0.090	0.091	0.091	0.090
Pounding Events	NA	NA	NA	NA	0	0	0	0

Input Earthquake: Chi-Chi, 1999 **Station**: CHY028 **Scaling Factor**: 0.56

Input Direction: Longitudinal – EW comp.
Transverse – NS comp.

Skew Angle: 60 degree

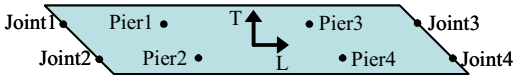

Input Time-histories

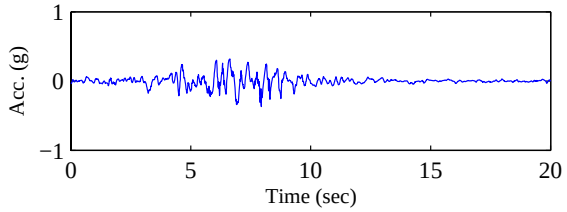

(a) Longitudinal Input

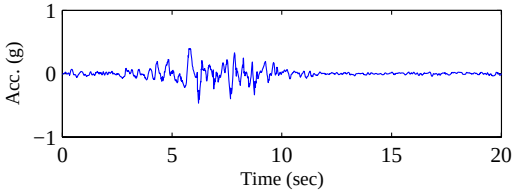

(b) Transverse Input

RC Pier Responses (Pier4)

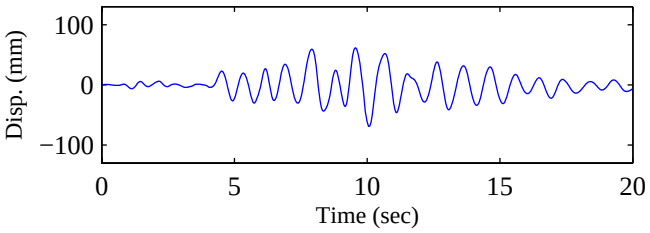

(c) Longitudinal displacement

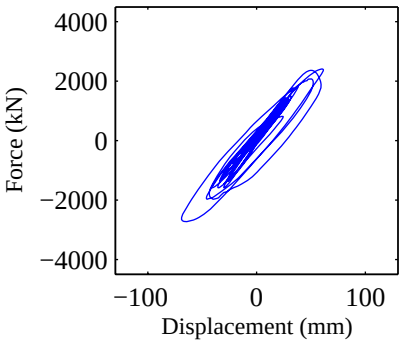

(f) Longitudinal disp.-force

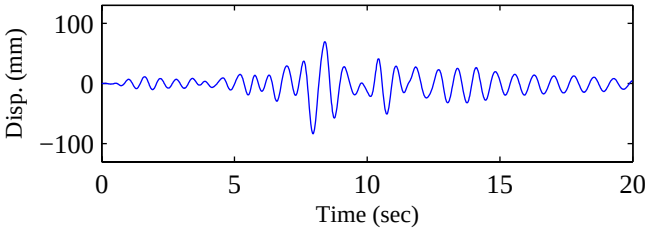

(d) Transverse displacement

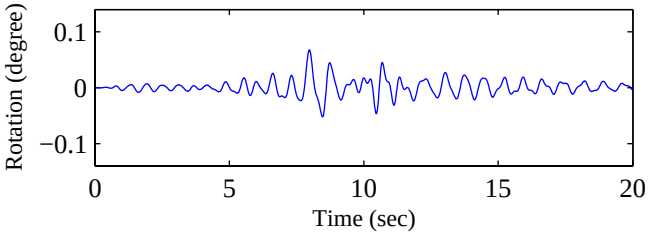

(e) Rotational displacement

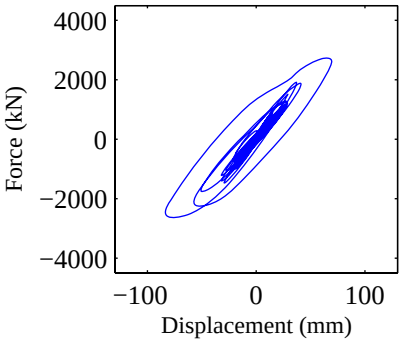

(g) Transverse disp.-force

Response Summary

	Pier1	Pier2	Pier3	Pier4	Joint1	Joint2	Joint3	Joint4
Max Long. Disp.(mm)	68.4	69.3	69.3	68.4	68.6	69.9	69.9	68.6
Max Trans. Disp.(mm)	87.7	80.0	80.4	88.0	43.4	29.2	30.2	44.3
Max Tor. Rot.(degree)	0.056	0.076	0.076	0.056	0.073	0.080	0.080	0.073
Pounding Events	NA	NA	NA	NA	0	0	0	0

Input Earthquake: Duzce, 1999 **Station**: Lamont 375 **Scaling Factor**: 1.0

Input Direction: Longitudinal – 00 comp.
Transverse – 90 comp.

Skew Angle: 0 degree

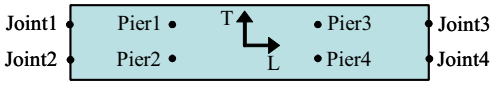

Input Time-histories

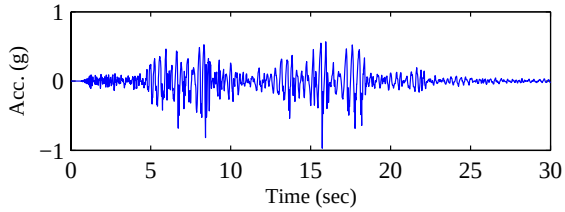

(a) Longitudinal Input

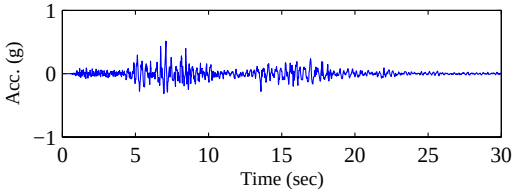

(b) Transverse Input

RC Pier Responses (Pier4)

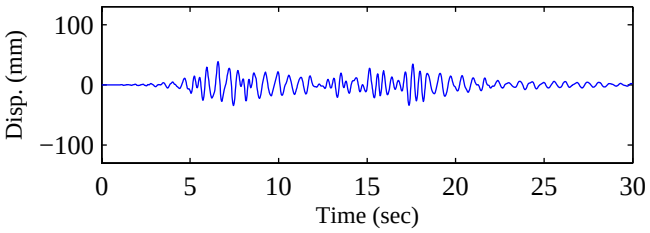

(c) Longitudinal displacement

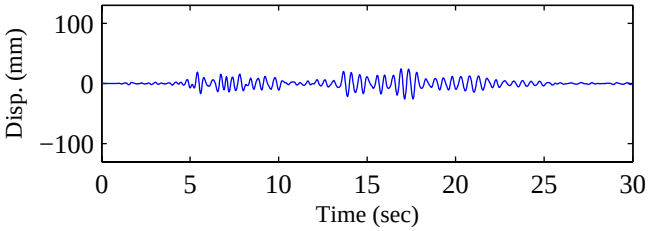

(d) Transverse displacement

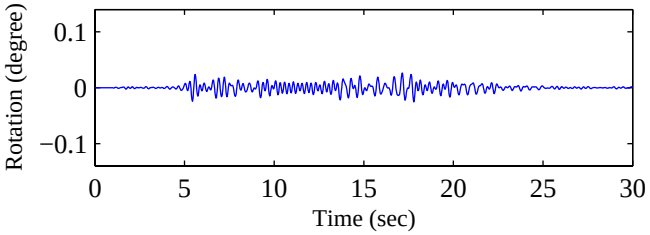

(e) Rotational displacement

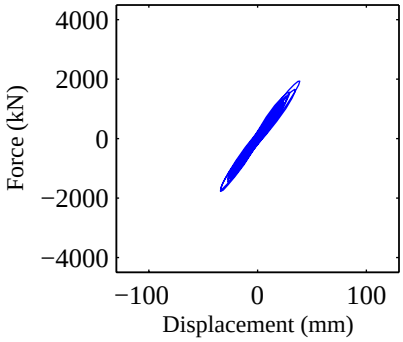

(f) Longitudinal disp.-force

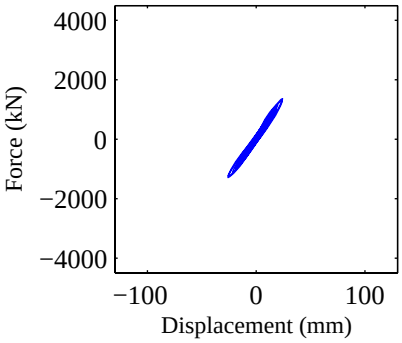

(g) Transverse disp.-force

Response Summary

	Pier1	Pier2	Pier3	Pier4	Joint1	Joint2	Joint3	Joint4
Max Long. Disp.(mm)	37.7	38.7	38.8	37.6	37.5	39.4	39.4	37.5
Max Trans. Disp.(mm)	25.9	25.9	26.0	26.0	14.0	14.0	14.0	14.0
Max Tor. Rot.(degree)	0.028	0.027	0.026	0.028	0.032	0.032	0.032	0.032
Pounding Events	NA	NA	NA	NA	0	0	0	0

Input Earthquake: Duzce, 1999 **Station**: Lamont 375 **Scaling Factor**: 1.0

Input Direction: Longitudinal – 00 comp.
Transverse – 90 comp.

Skew Angle: 30 degree

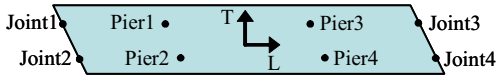

Input Time-histories

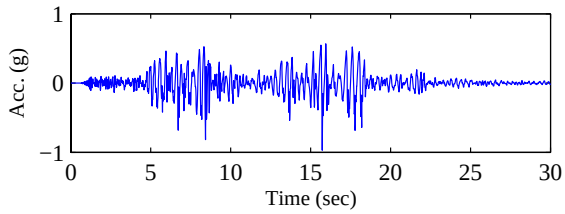

(a) Longitudinal Input

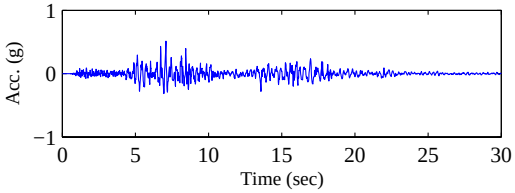

(b) Transverse Input

RC Pier Responses (Pier4)

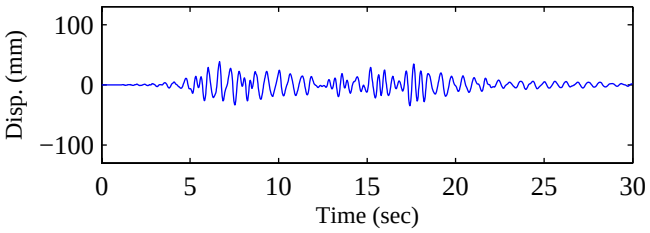

(c) Longitudinal displacement

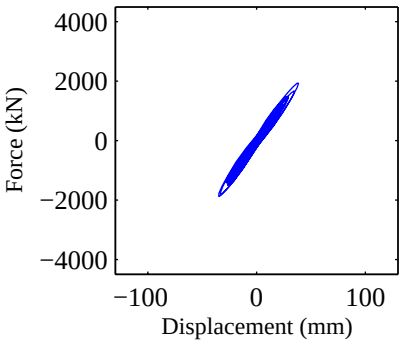

(f) Longitudinal disp.-force

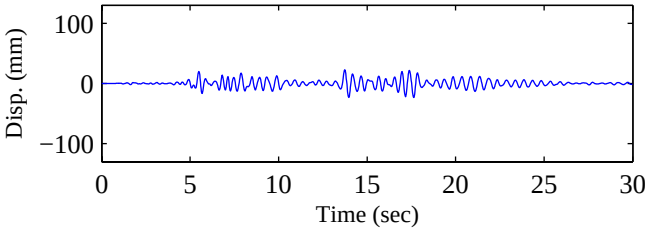

(d) Transverse displacement

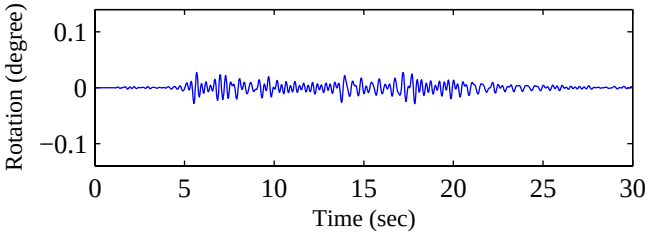

(e) Rotational displacement

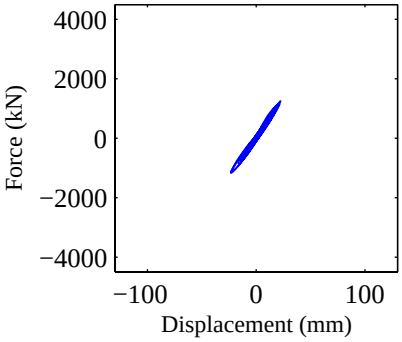

(g) Transverse disp.-force

Response Summary

	Pier1	Pier2	Pier3	Pier4	Joint1	Joint2	Joint3	Joint4
Max Long. Disp.(mm)	37.7	38.6	38.6	37.7	37.6	39.2	39.2	37.6
Max Trans. Disp.(mm)	24.4	23.6	23.3	24.1	14.7	13.8	14.1	15.0
Max Tor. Rot.(degree)	0.027	0.028	0.029	0.028	0.029	0.029	0.028	0.028
Pounding Events	NA	NA	NA	NA	0	0	0	0

Input Earthquake: Duzce, 1999 **Station**: Lamont 375 **Scaling Factor**: 1.0

Input Direction: Longitudinal – 00 comp.
Transverse – 90 comp.

Skew Angle: 60 degree

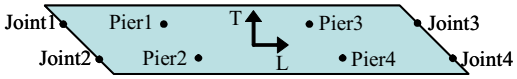

Input Time-histories

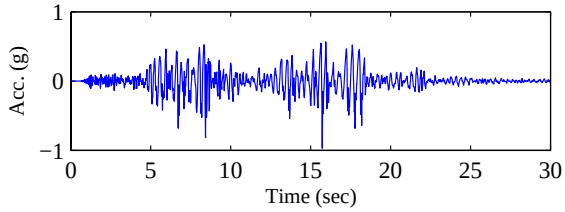

(a) Longitudinal Input

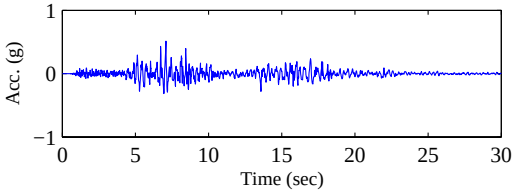

(b) Transverse Input

RC Pier Responses (Pier4)

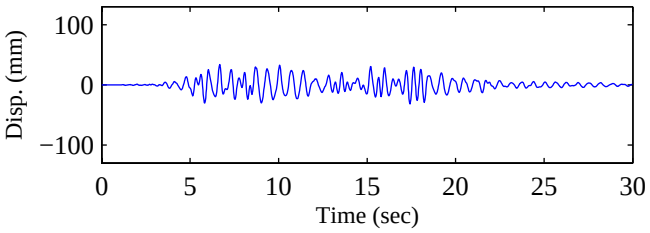

(c) Longitudinal displacement

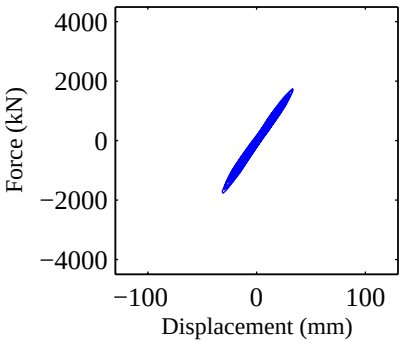

(f) Longitudinal disp.-force

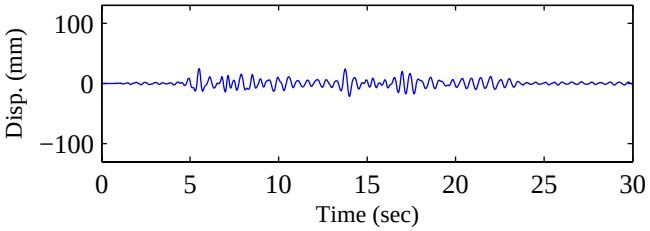

(d) Transverse displacement

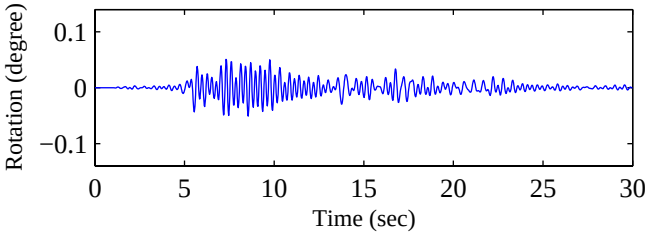

(e) Rotational displacement

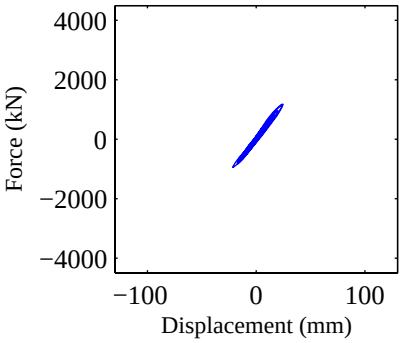

(g) Transverse disp.-force

Response Summary

	Pier1	Pier2	Pier3	Pier4	Joint1	Joint2	Joint3	Joint4
Max Long. Disp.(mm)	34.5	33.8	33.8	34.5	34.8	34.0	34.0	34.9
Max Trans. Disp.(mm)	27.9	24.5	24.6	28.3	21.4	22.7	22.5	21.8
Max Tor. Rot.(degree)	0.044	0.051	0.051	0.044	0.032	0.032	0.033	0.032
Pounding Events	NA	NA	NA	NA	0	0	0	0

Input Earthquake: Duzce, 1999 **Station**: Lamont 375 **Scaling Factor**: 1.0

Input Direction: Diagonal 1 – NS comp.
Diagonal 2 – EW comp.

Skew Angle: 0 degree

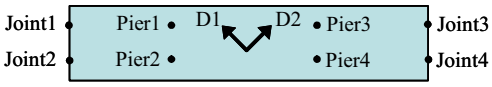

Input Time-histories

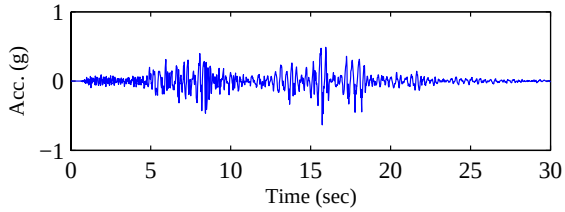

(a) Longitudinal Input

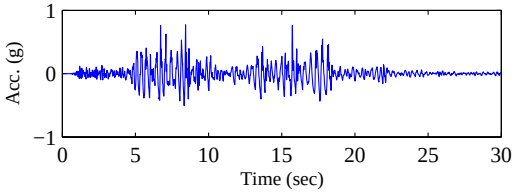

(b) Transverse Input

RC Pier Responses (Pier4)

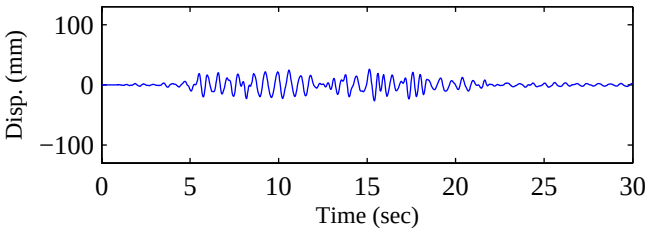

(c) Longitudinal displacement

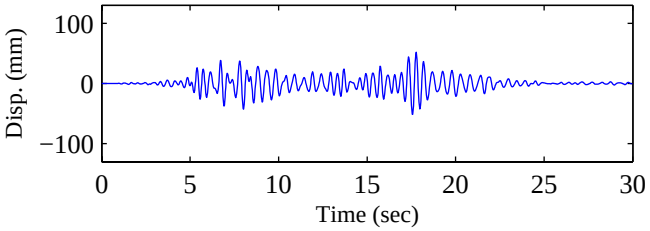

(d) Transverse displacement

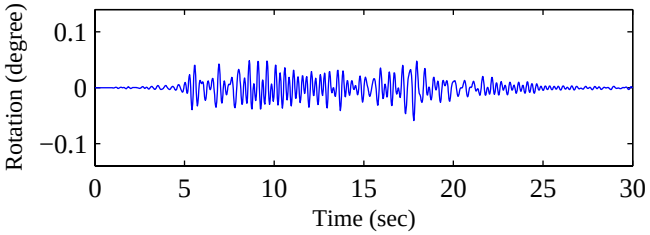

(e) Rotational displacement

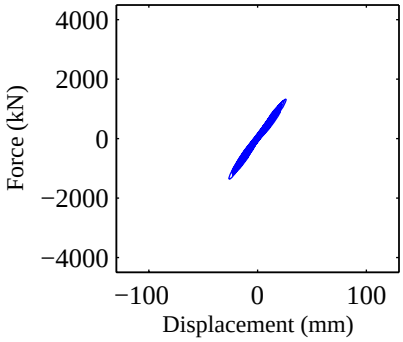

(f) Longitudinal disp.-force

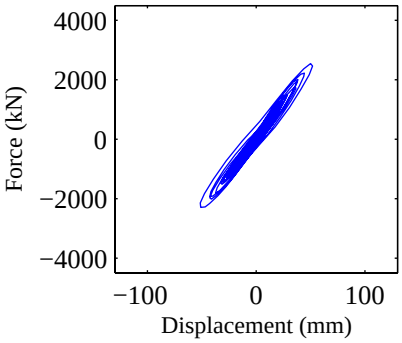

(g) Transverse disp.-force

Response Summary

	Pier1	Pier2	Pier3	Pier4	Joint1	Joint2	Joint3	Joint4
Max Long. Disp.(mm)	25.9	26.5	26.5	26.0	25.9	27.0	27.1	25.9
Max Trans. Disp.(mm)	52.0	52.0	51.9	51.9	27.1	27.1	27.4	27.4
Max Tor. Rot.(degree)	0.060	0.059	0.059	0.060	0.066	0.066	0.065	0.065
Pounding Events	NA	NA	NA	NA	0	0	0	0

Input Earthquake: Duzce, 1999 **Station**: Lamont 375 **Scaling Factor**: 1.0

Input Direction: Diagonal 1 – NS comp.
Diagonal 2 – EW comp.

Skew Angle: 30 degree

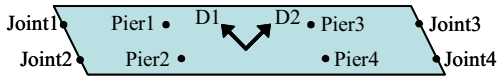

Input Time-histories

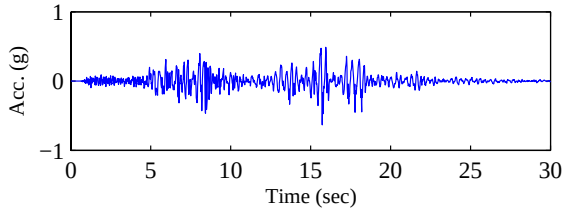

(a) Longitudinal Input

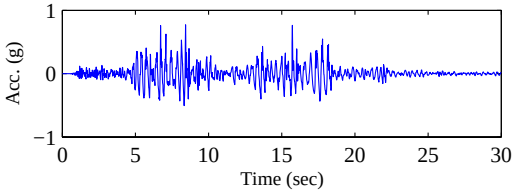

(b) Transverse Input

RC Pier Responses (Pier4)

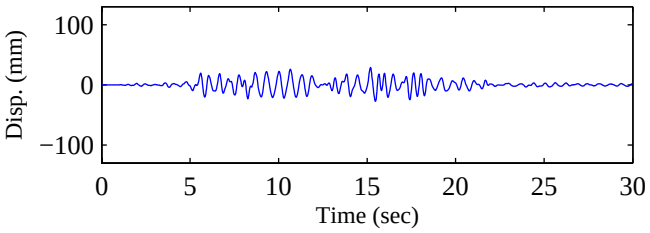

(c) Longitudinal displacement

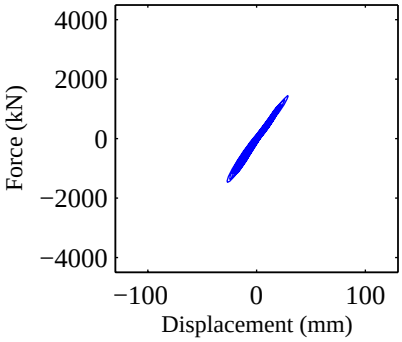

(f) Longitudinal disp.-force

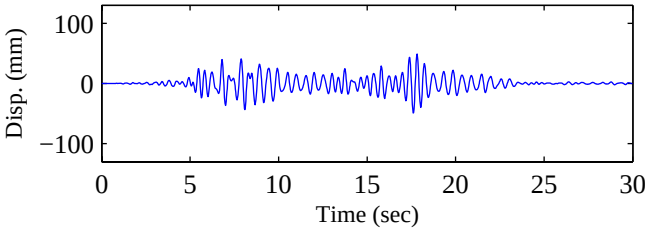

(d) Transverse displacement

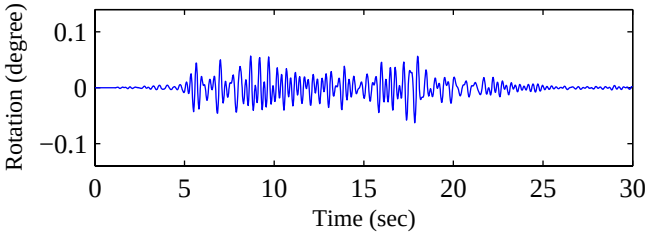

(e) Rotational displacement

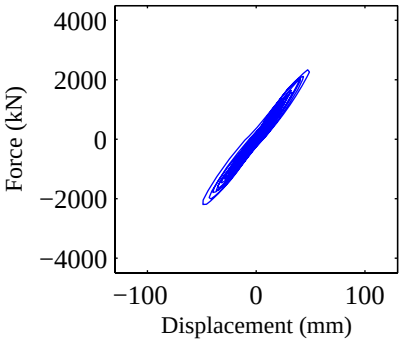

(g) Transverse disp.-force

Response Summary

	Pier1	Pier2	Pier3	Pier4	Joint1	Joint2	Joint3	Joint4
Max Long. Disp.(mm)	27.6	28.9	29.0	27.6	27.6	29.7	29.8	27.7
Max Trans. Disp.(mm)	51.1	49.2	49.1	51.6	29.6	28.5	28.4	29.5
Max Tor. Rot.(degree)	0.057	0.062	0.063	0.058	0.063	0.063	0.064	0.064
Pounding Events	NA	NA	NA	NA	0	0	0	0

Input Earthquake: Duzce, 1999 **Station**: Lamont 375 **Scaling Factor**: 1.0

Input Direction: Diagonal 1 – NS comp.
Diagonal 2 – EW comp.

Skew Angle: 60 degree

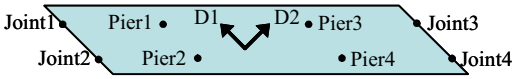

Input Time-histories

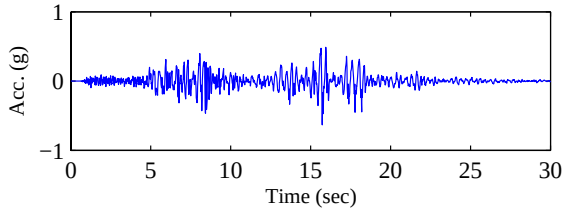

(a) Longitudinal Input

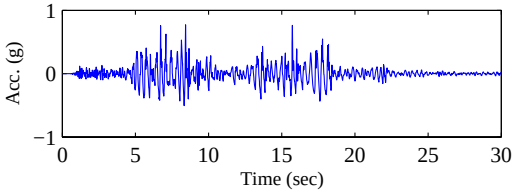

(b) Transverse Input

RC Pier Responses (Pier4)

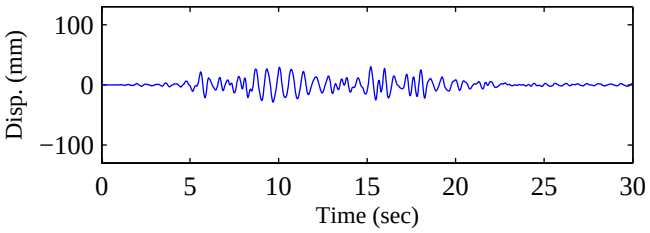

(c) Longitudinal displacement

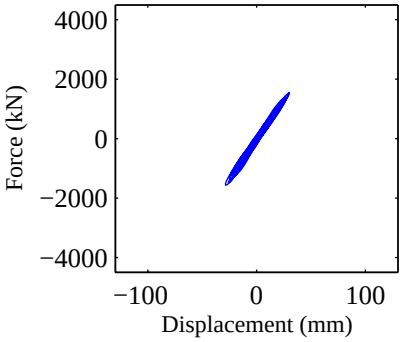

(f) Longitudinal disp.-force

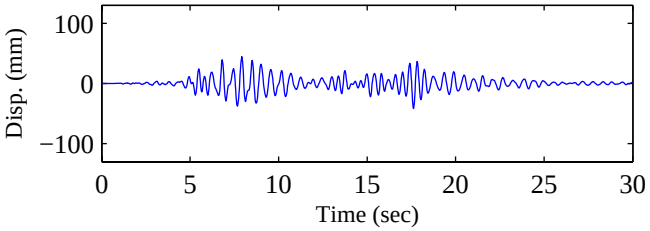

(d) Transverse displacement

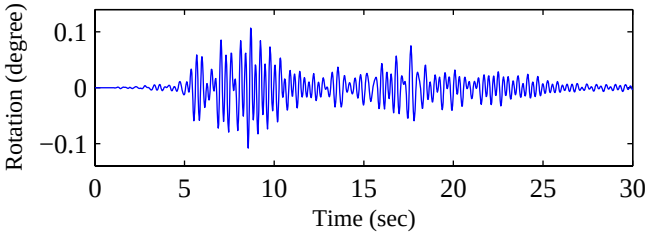

(e) Rotational displacement

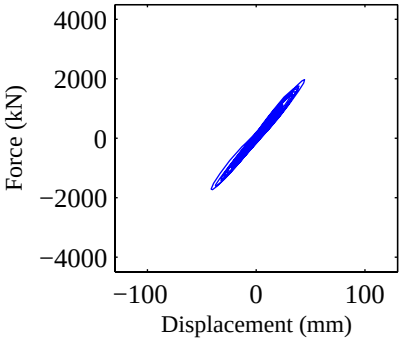

(g) Transverse disp.-force

Response Summary

	Pier1	Pier2	Pier3	Pier4	Joint1	Joint2	Joint3	Joint4
Max Long. Disp.(mm)	28.9	30.2	30.2	28.9	28.8	30.9	31.0	28.8
Max Trans. Disp.(mm)	49.6	44.3	44.6	50.5	43.2	44.5	43.6	42.9
Max Tor. Rot.(degree)	0.086	0.107	0.108	0.088	0.068	0.068	0.069	0.070
Pounding Events	NA	NA	NA	NA	0	0	0	0

Input Earthquake: Duzce, 1999 **Station**: Lamont 375 **Scaling Factor**: 1.0

Input Direction: Longitudinal – 90 comp.
Transverse – 00 comp.

Skew Angle: 0 degree

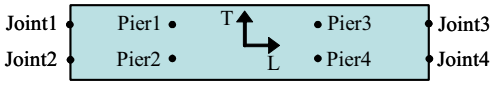

Input Time-histories

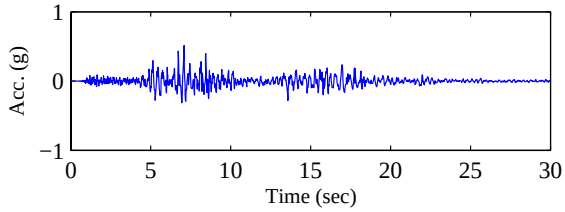

(a) Longitudinal Input

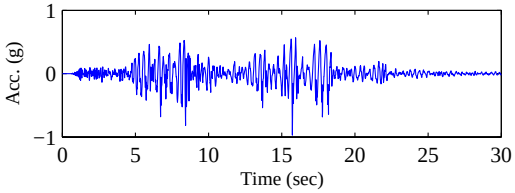

(b) Transverse Input

RC Pier Responses (Pier4)

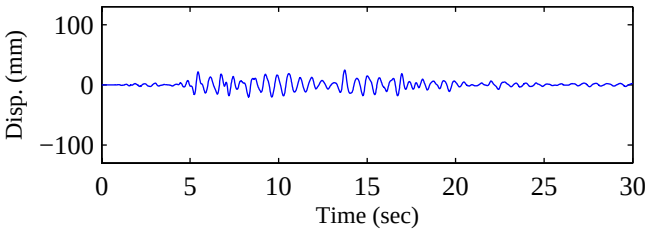

(c) Longitudinal displacement

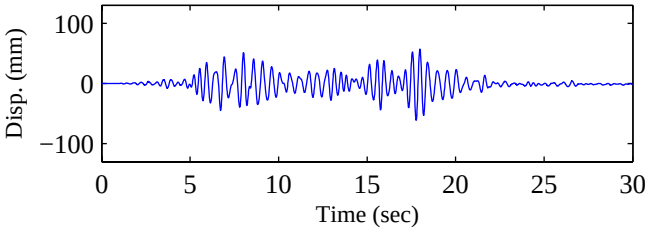

(d) Transverse displacement

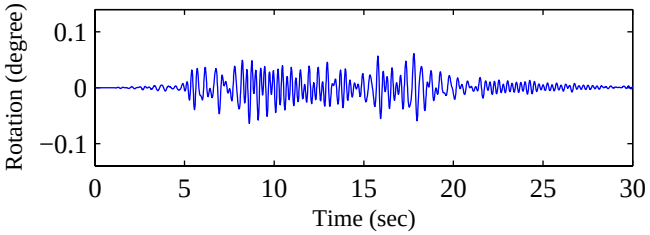

(e) Rotational displacement

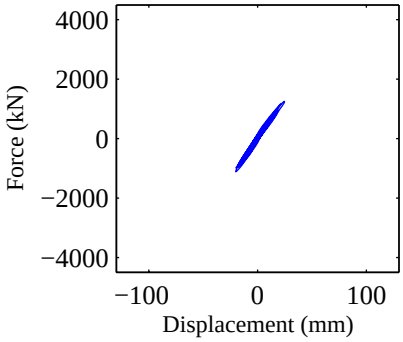

(f) Longitudinal disp.-force

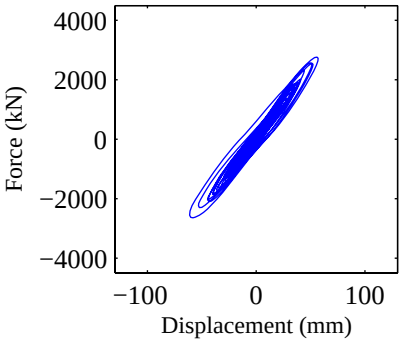

(g) Transverse disp.-force

Response Summary

	Pier1	Pier2	Pier3	Pier4	Joint1	Joint2	Joint3	Joint4
Max Long. Disp.(mm)	23.3	24.8	24.8	23.3	23.4	25.2	25.2	23.4
Max Trans. Disp.(mm)	61.1	61.1	61.2	61.2	33.7	33.7	33.8	33.8
Max Tor. Rot.(degree)	0.063	0.064	0.064	0.063	0.073	0.073	0.073	0.073
Pounding Events	NA	NA	NA	NA	0	0	0	0

Input Earthquake: Duzce, 1999 **Station**: Lamont 375 **Scaling Factor**: 1.0

Input Direction: Longitudinal – 90 comp.
Transverse – 00 comp.

Skew Angle: 30 degree

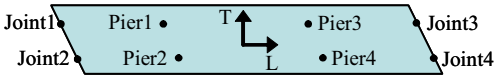

Input Time-histories

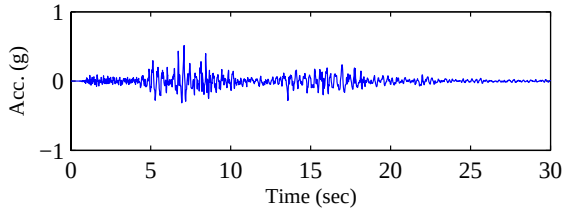

(a) Longitudinal Input

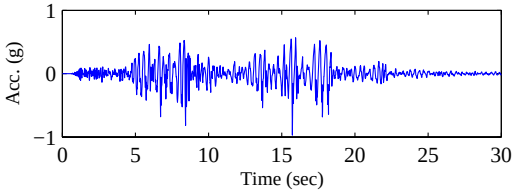

(b) Transverse Input

RC Pier Responses (Pier4)

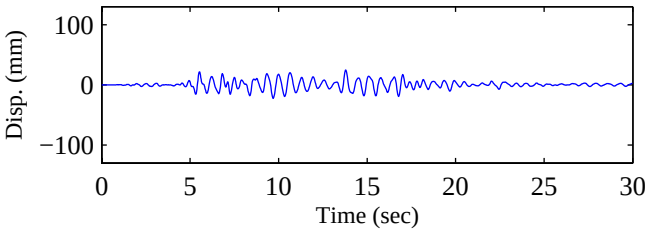

(c) Longitudinal displacement

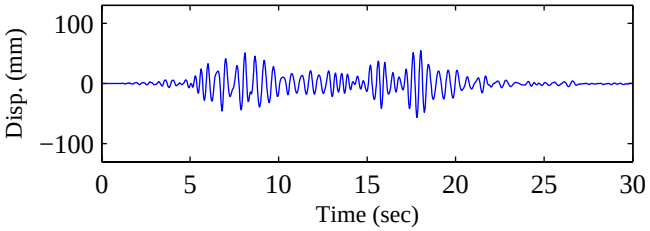

(d) Transverse displacement

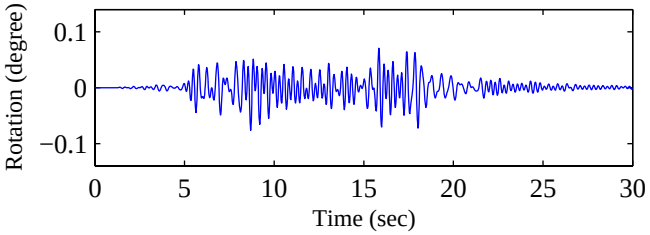

(e) Rotational displacement

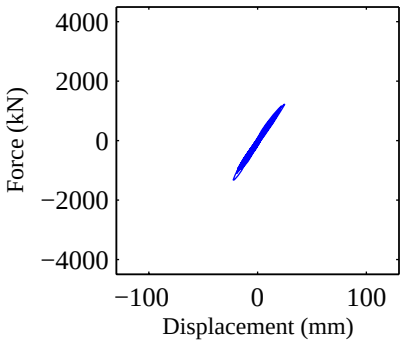

(f) Longitudinal disp.-force

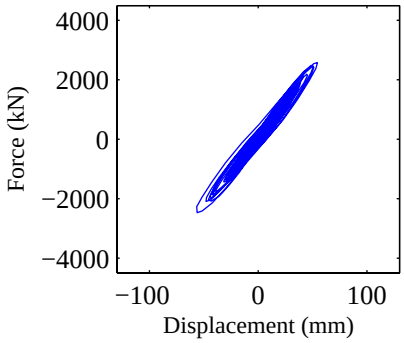

(g) Transverse disp.-force

Response Summary

	Pier1	Pier2	Pier3	Pier4	Joint1	Joint2	Joint3	Joint4
Max Long. Disp.(mm)	23.1	24.9	24.9	23.2	23.0	25.3	25.3	23.1
Max Trans. Disp.(mm)	59.6	57.0	56.6	59.1	36.8	35.5	35.8	37.1
Max Tor. Rot.(degree)	0.069	0.076	0.076	0.070	0.071	0.071	0.073	0.073
Pounding Events	NA	NA	NA	NA	0	0	0	0

Input Earthquake: Duzce, 1999 **Station**: Lamont 375 **Scaling Factor**: 1.0

Input Direction: Longitudinal – 90 comp.
Transverse – 00 comp.

Skew Angle: 60 degree

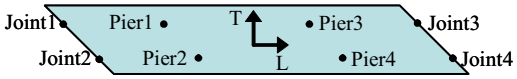

Input Time-histories

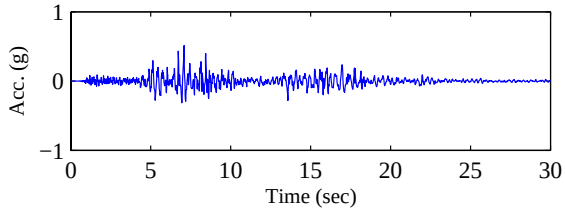

(a) Longitudinal Input

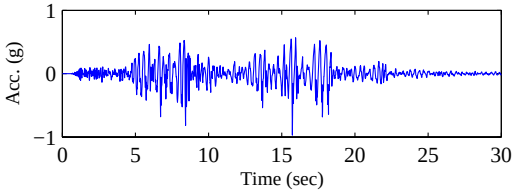

(b) Transverse Input

RC Pier Responses (Pier4)

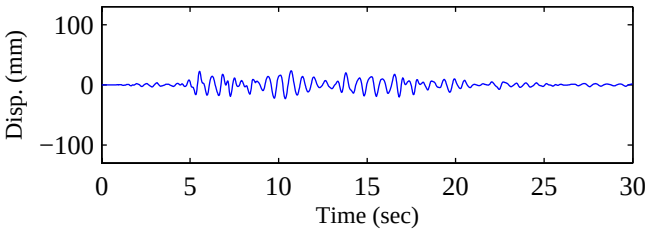

(c) Longitudinal displacement

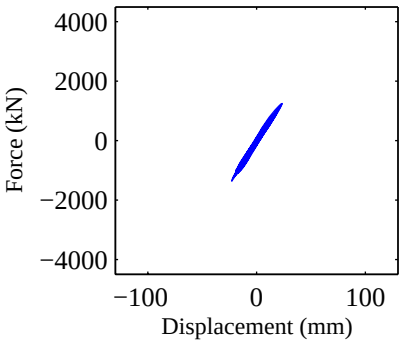

(f) Longitudinal disp.-force

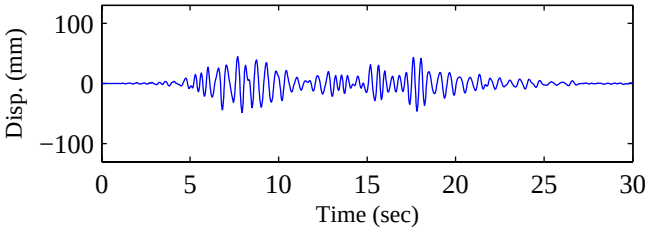

(d) Transverse displacement

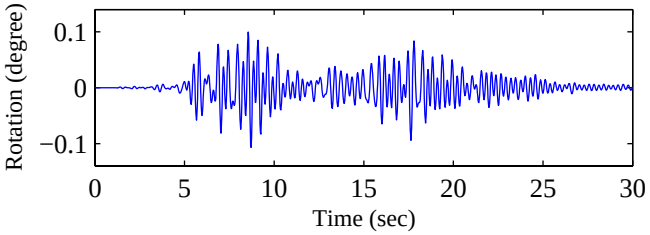

(e) Rotational displacement

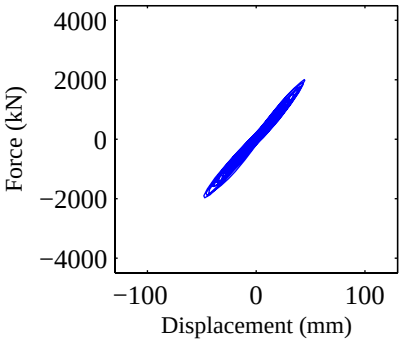

(g) Transverse disp.-force

Response Summary

	Pier1	Pier2	Pier3	Pier4	Joint1	Joint2	Joint3	Joint4
Max Long. Disp.(mm)	22.8	23.7	23.7	22.9	22.6	24.3	24.3	22.7
Max Trans. Disp.(mm)	56.7	48.5	48.1	55.3	42.5	41.3	42.2	42.7
Max Tor. Rot.(degree)	0.085	0.108	0.107	0.085	0.072	0.071	0.069	0.069
Pounding Events	NA	NA	NA	NA	0	0	0	0

Input Earthquake: Coalinga, 1983 **Station**: Pleasant Valley **Scaling Factor**: 0.76

Input Direction: Longitudinal – 00 comp.
Transverse – 90 comp.

Skew Angle: 0 degree

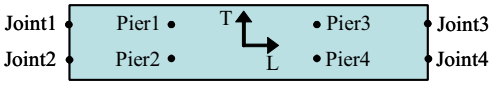

Input Time-histories

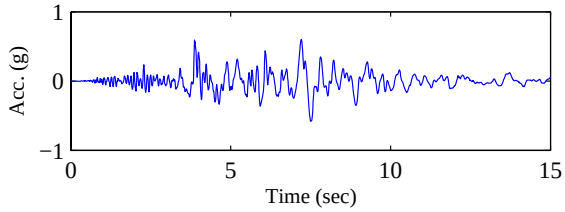

(a) Longitudinal Input

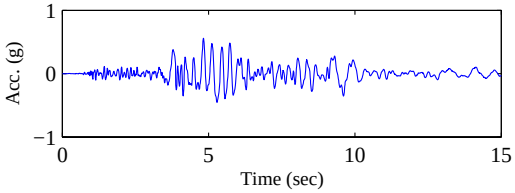

(b) Transverse Input

RC Pier Responses (Pier4)

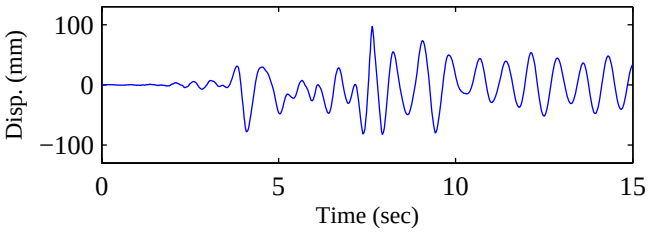

(c) Longitudinal displacement

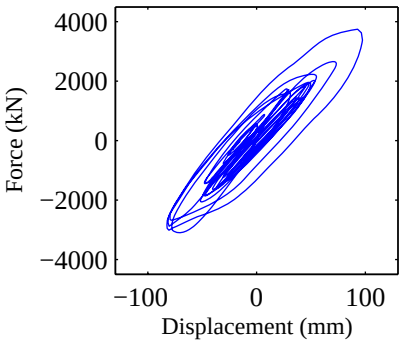

(f) Longitudinal disp.-force

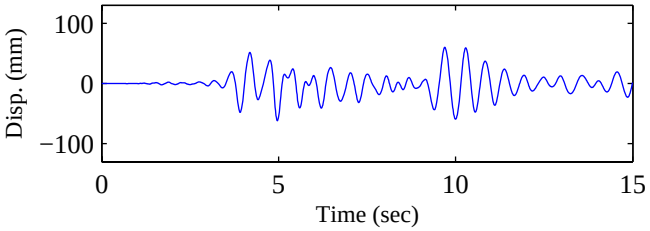

(d) Transverse displacement

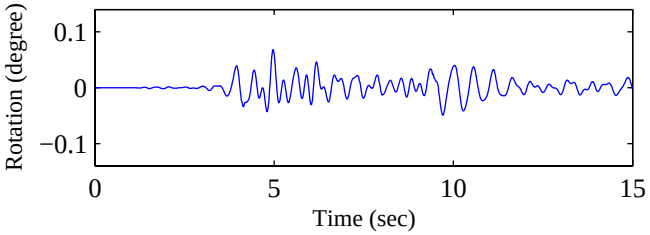

(e) Rotational displacement

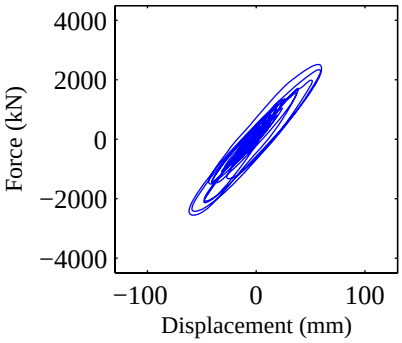

(g) Transverse disp.-force

Response Summary

	Pier1	Pier2	Pier3	Pier4	Joint1	Joint2	Joint3	Joint4
Max Long. Disp.(mm)	89.5	89.8	97.4	97.0	87.8	86.8	100.3	99.8
Max Trans. Disp.(mm)	62.5	62.4	61.9	61.9	26.6	26.6	25.8	25.8
Max Tor. Rot.(degree)	0.066	0.068	0.068	0.066	0.079	0.079	0.077	0.077
Pounding Events	NA	NA	NA	NA	4	4	1	1

Input Earthquake: Coalinga, 1983 **Station**: Pleasant Valley **Scaling Factor**: 0.76

Input Direction: Longitudinal – 00 comp.
Transverse – 90 comp.

Skew Angle: 30 degree

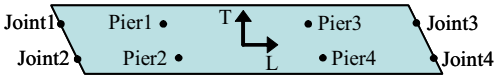

Input Time-histories

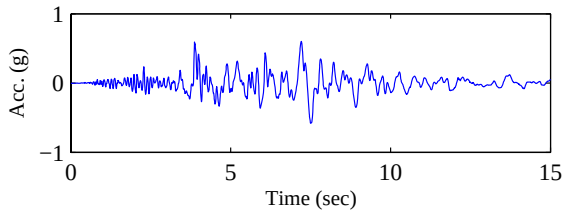

(a) Longitudinal Input

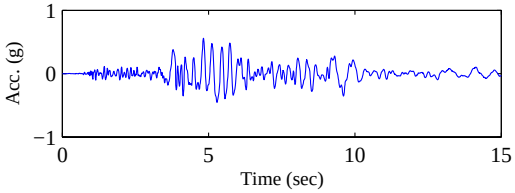

(b) Transverse Input

RC Pier Responses (Pier4)

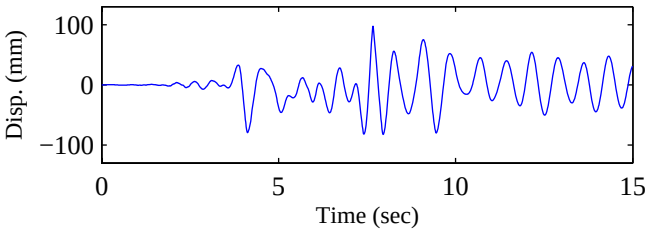

(c) Longitudinal displacement

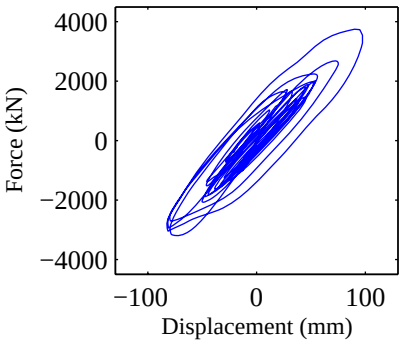

(f) Longitudinal disp.-force

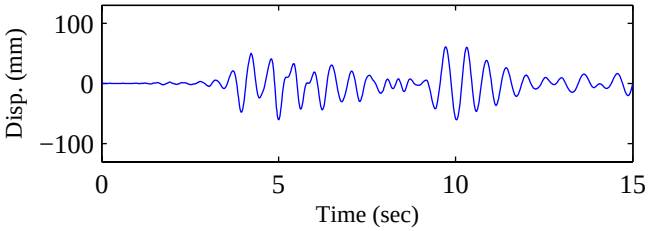

(d) Transverse displacement

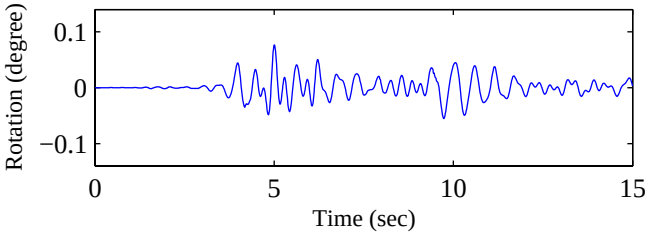

(e) Rotational displacement

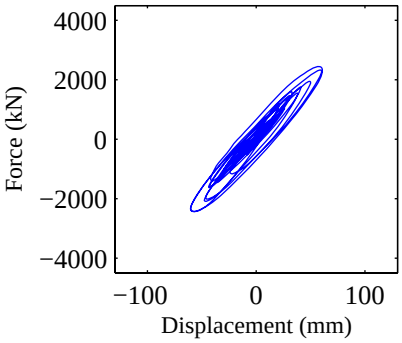

(g) Transverse disp.-force

Response Summary

	Pier1	Pier2	Pier3	Pier4	Joint1	Joint2	Joint3	Joint4
Max Long. Disp.(mm)	90.1	90.1	97.5	97.9	88.4	86.5	100.4	101.0
Max Trans. Disp.(mm)	64.0	60.5	60.9	63.6	29.0	25.4	25.1	27.5
Max Tor. Rot.(degree)	0.068	0.077	0.077	0.067	0.079	0.080	0.078	0.077
Pounding Events	NA	NA	NA	NA	4	4	1	1

Input Earthquake: Coalinga, 1983 **Station**: Pleasant Valley **Scaling Factor**: 0.76

Input Direction: Longitudinal – 00 comp.
Transverse – 90 comp.

Skew Angle: 60 degree

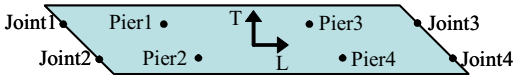

Input Time-histories

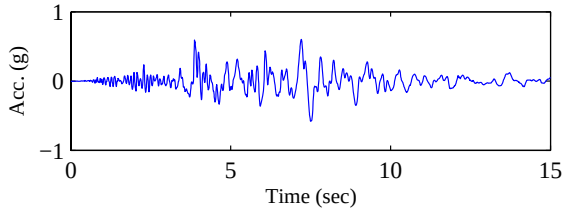

(a) Longitudinal Input

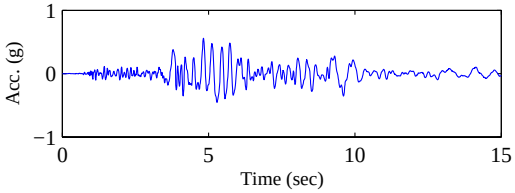

(b) Transverse Input

RC Pier Responses (Pier4)

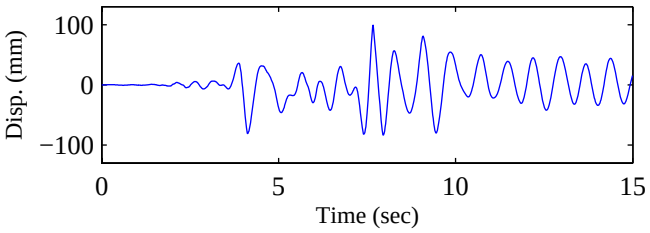

(c) Longitudinal displacement

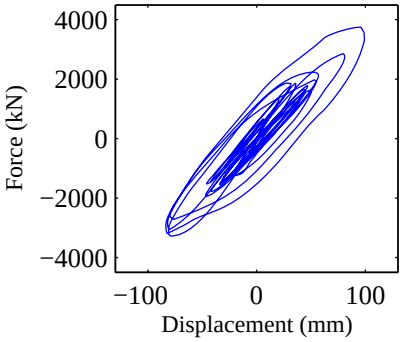

(f) Longitudinal disp.-force

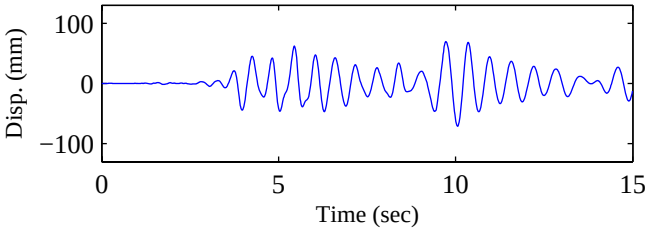

(d) Transverse displacement

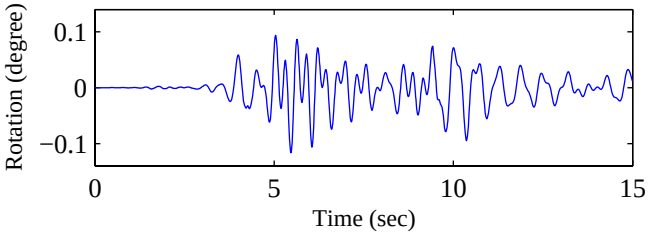

(e) Rotational displacement

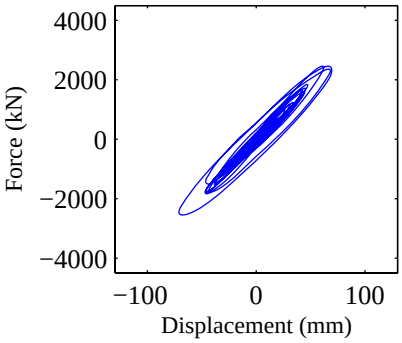

(g) Transverse disp.-force

Response Summary

	Pier1	Pier2	Pier3	Pier4	Joint1	Joint2	Joint3	Joint4
Max Long. Disp.(mm)	91.6	90.9	99.2	100.1	89.1	88.8	102.3	103.7
Max Trans. Disp.(mm)	76.5	69.1	71.0	79.0	44.3	39.7	40.1	40.4
Max Tor. Rot.(degree)	0.089	0.116	0.116	0.089	0.086	0.089	0.090	0.088
Pounding Events	NA	NA	NA	NA	4	4	2	2

Input Earthquake: Coalinga, 1983 **Station**: Pleasant Valley **Scaling Factor**: 0.76

Input Direction: Diagonal 1 – NS comp.
Diagonal 2 – EW comp.

Skew Angle: 0 degree

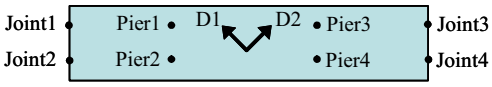

Input Time-histories

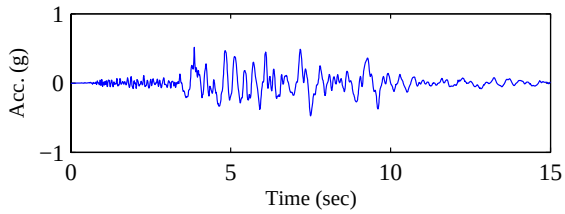

(a) Longitudinal Input

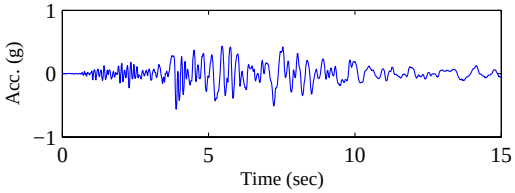

(b) Transverse Input

RC Pier Responses (Pier4)

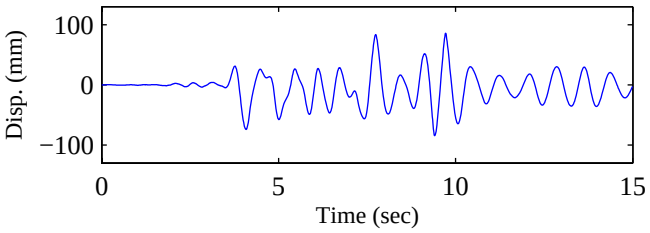

(c) Longitudinal displacement

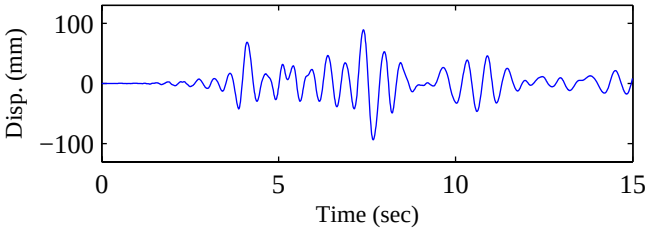

(d) Transverse displacement

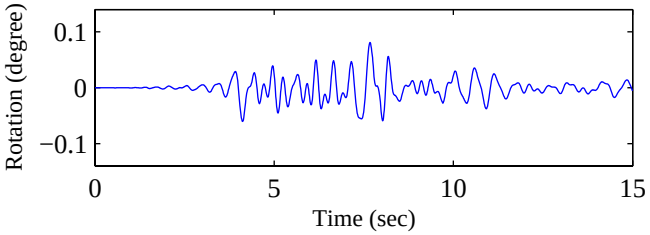

(e) Rotational displacement

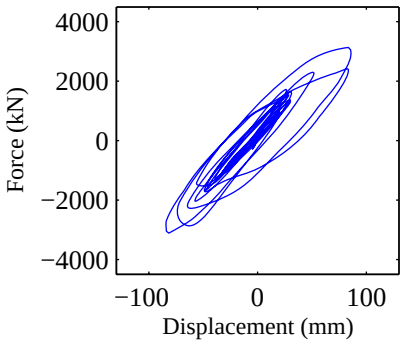

(f) Longitudinal disp.-force

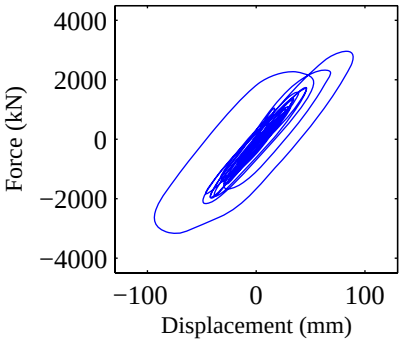

(g) Transverse disp.-force

Response Summary

	Pier1	Pier2	Pier3	Pier4	Joint1	Joint2	Joint3	Joint4
Max Long. Disp.(mm)	89.3	88.8	86.1	88.5	91.3	90.6	87.1	90.8
Max Trans. Disp.(mm)	93.8	93.8	93.7	93.7	36.9	37.0	36.8	36.8
Max Tor. Rot.(degree)	0.083	0.080	0.081	0.084	0.105	0.105	0.106	0.106
Pounding Events	NA	NA	NA	NA	2	1	2	2

Input Earthquake: Coalinga, 1983 **Station**: Pleasant Valley **Scaling Factor**: 0.76

Input Direction: Diagonal 1 – NS comp.
Diagonal 2 – EW comp.

Skew Angle: 30 degree

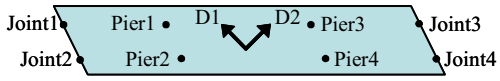

Input Time-histories

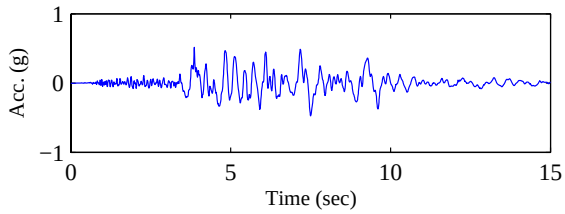

(a) Longitudinal Input

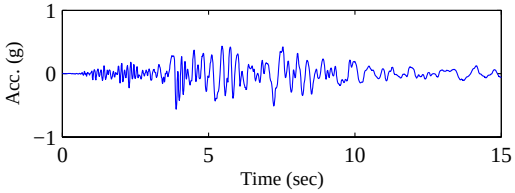

(b) Transverse Input

RC Pier Responses (Pier4)

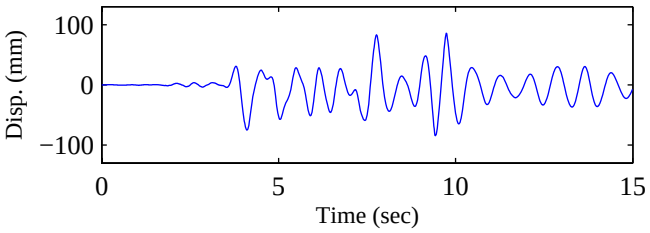

(c) Longitudinal displacement

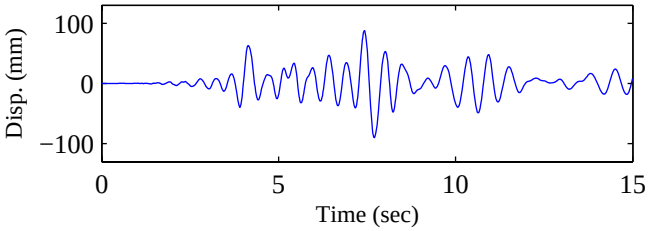

(d) Transverse displacement

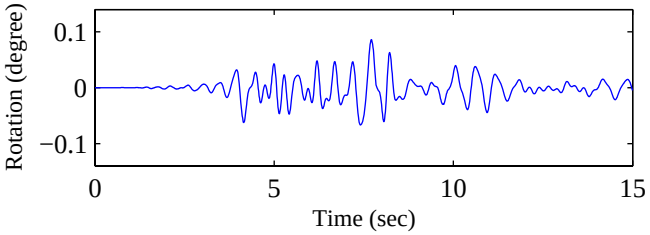

(e) Rotational displacement

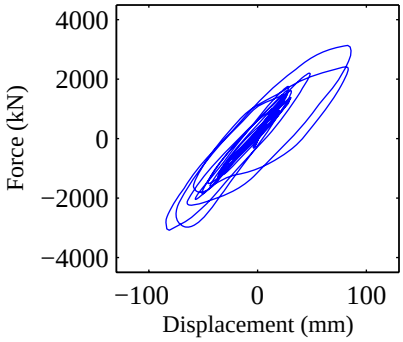

(f) Longitudinal disp.-force

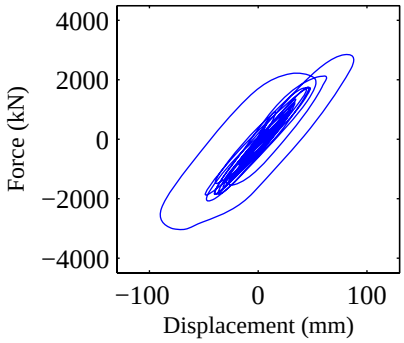

(g) Transverse disp.-force

Response Summary

	Pier1	Pier2	Pier3	Pier4	Joint1	Joint2	Joint3	Joint4
Max Long. Disp.(mm)	89.3	88.6	86.0	88.7	91.3	90.2	87.0	91.0
Max Trans. Disp.(mm)	94.1	90.1	90.1	94.2	35.9	30.8	30.1	35.7
Max Tor. Rot.(degree)	0.079	0.085	0.086	0.080	0.102	0.103	0.104	0.103
Pounding Events	NA	NA	NA	NA	2	1	2	2

Input Earthquake: Coalinga, 1983 **Station**: Pleasant Valley **Scaling Factor**: 0.76

Input Direction: Diagonal 1 – NS comp.
Diagonal 2 – EW comp.

Skew Angle: 60 degree

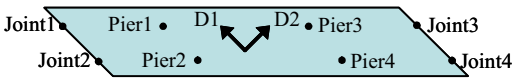

Input Time-histories

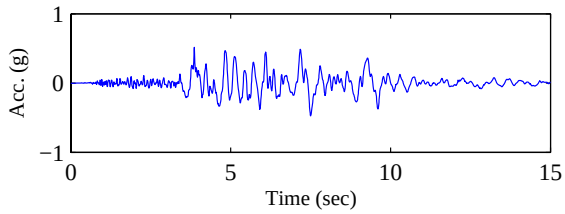

(a) Longitudinal Input

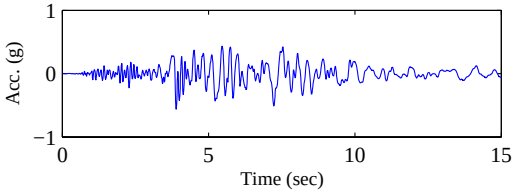

(b) Transverse Input

RC Pier Responses (Pier4)

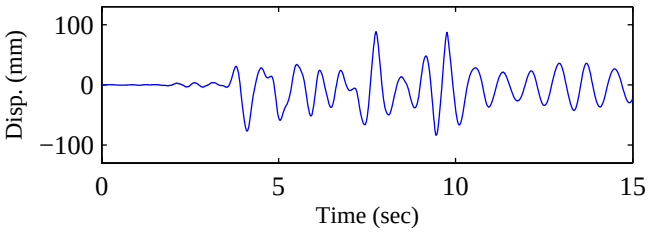

(c) Longitudinal displacement

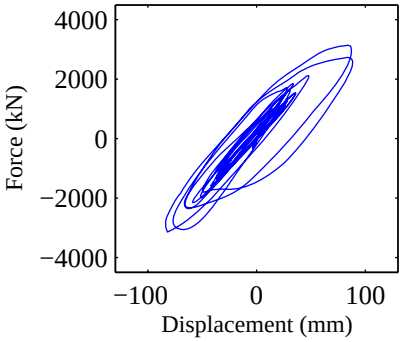

(f) Longitudinal disp.-force

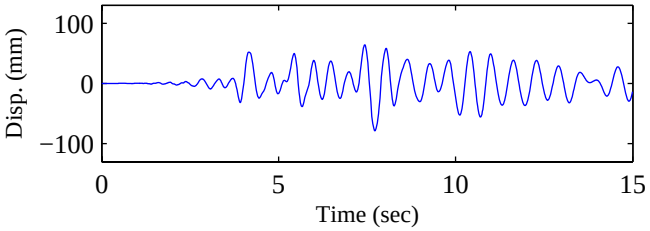

(d) Transverse displacement

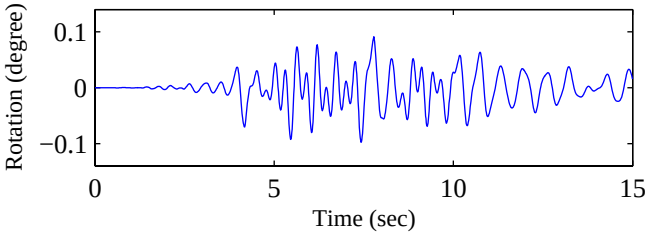

(e) Rotational displacement

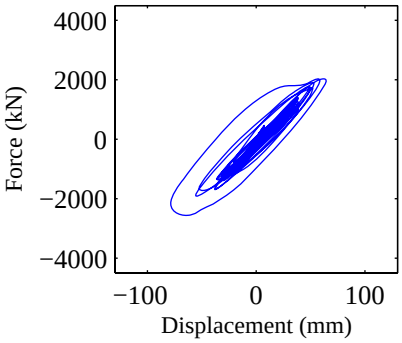

(g) Transverse disp.-force

Response Summary

	Pier1	Pier2	Pier3	Pier4	Joint1	Joint2	Joint3	Joint4
Max Long. Disp.(mm)	89.0	87.7	88.5	89.9	91.2	89.5	91.7	92.8
Max Trans. Disp.(mm)	86.6	79.2	78.7	86.5	45.3	32.8	33.1	45.3
Max Tor. Rot.(degree)	0.076	0.098	0.098	0.078	0.078	0.082	0.091	0.088
Pounding Events	NA	NA	NA	NA	2	1	2	2

Input Earthquake: Coalinga, 1983 **Station**: Pleasant Valley **Scaling Factor**: 0.76
Input Direction: Longitudinal – 90 comp.
Transverse – 00 comp.
Skew Angle: 0 degree

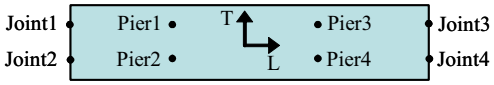

Input Time-histories

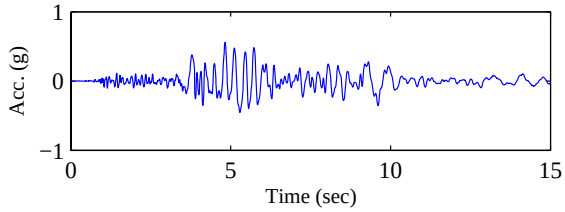

(a) Longitudinal Input

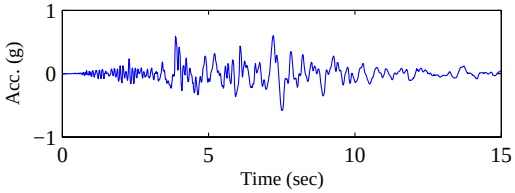

(b) Transverse Input

RC Pier Responses (Pier4)

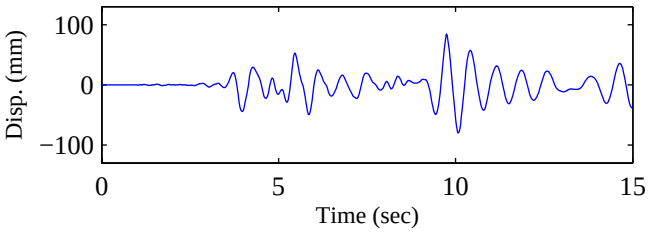

(c) Longitudinal displacement

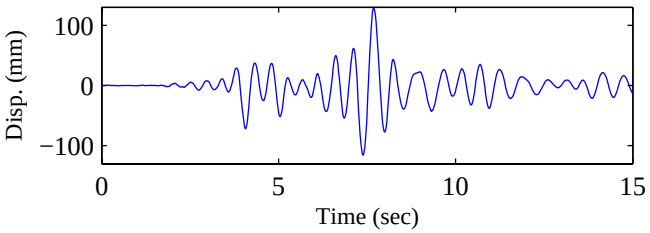

(d) Transverse displacement

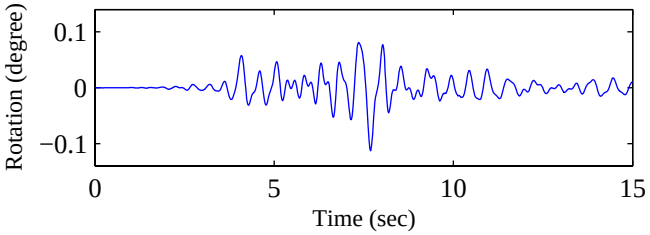

(e) Rotational displacement

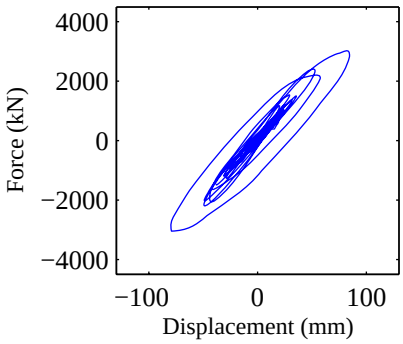

(f) Longitudinal disp.-force

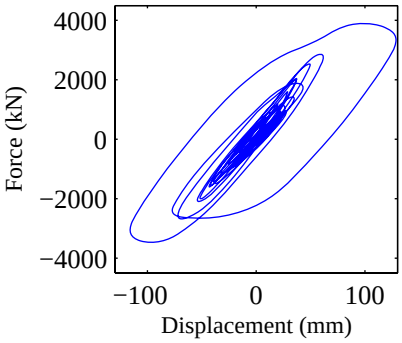

(g) Transverse disp.-force

Response Summary

	Pier1	Pier2	Pier3	Pier4	Joint1	Joint2	Joint3	Joint4
Max Long. Disp.(mm)	82.0	82.0	84.6	85.8	81.4	83.3	85.5	87.6
Max Trans. Disp.(mm)	128.7	128.7	128.7	128.7	42.6	42.6	42.5	42.5
Max Tor. Rot.(degree)	0.112	0.113	0.113	0.113	0.146	0.146	0.146	0.146
Pounding Events	NA	NA	NA	NA	1	1	1	1

Input Earthquake: Coalinga, 1983 **Station**: Pleasant Valley **Scaling Factor**: 0.76

Input Direction: Longitudinal – 90 comp.
Transverse – 00 comp.

Skew Angle: 30 degree

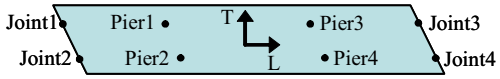

Input Time-histories

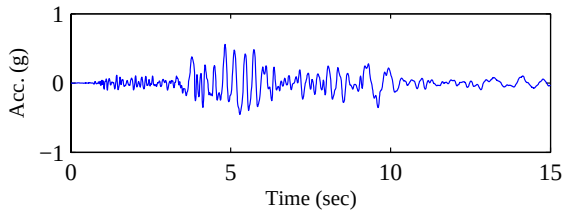

(a) Longitudinal Input

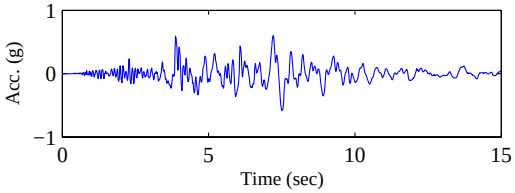

(b) Transverse Input

RC Pier Responses (Pier4)

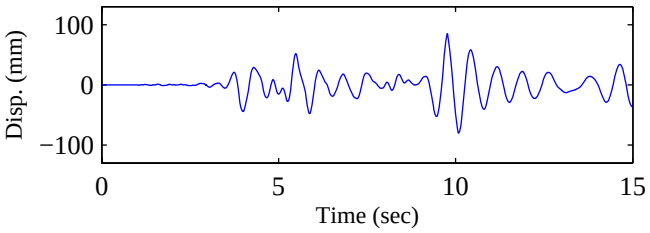

(c) Longitudinal displacement

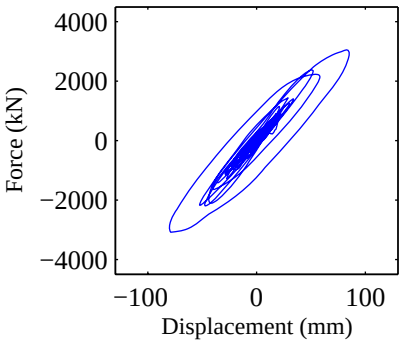

(f) Longitudinal disp.-force

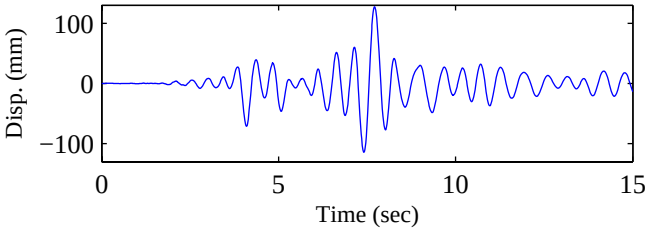

(d) Transverse displacement

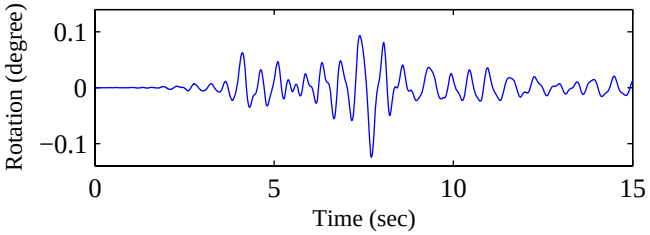

(e) Rotational displacement

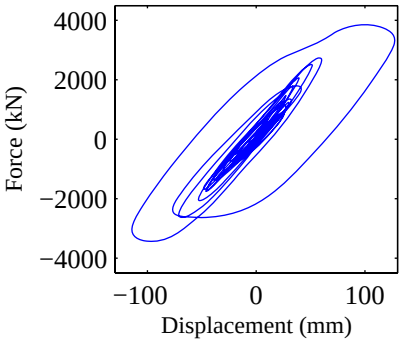

(g) Transverse disp.-force

Response Summary

	Pier1	Pier2	Pier3	Pier4	Joint1	Joint2	Joint3	Joint4
Max Long. Disp.(mm)	82.7	82.4	85.2	86.9	82.5	83.7	86.4	88.9
Max Trans. Disp.(mm)	133.0	127.2	127.4	133.3	44.9	39.4	39.2	44.9
Max Tor. Rot.(degree)	0.112	0.125	0.124	0.112	0.145	0.148	0.148	0.146
Pounding Events	NA	NA	NA	NA	1	1	1	1

Input Earthquake: Coalinga, 1983 **Station**: Pleasant Valley **Scaling Factor**: 0.76
Input Direction: Longitudinal – 90 comp.
Transverse – 00 comp.
Skew Angle: 60 degree

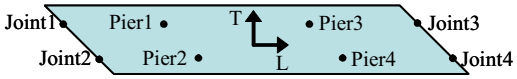

Input Time-histories

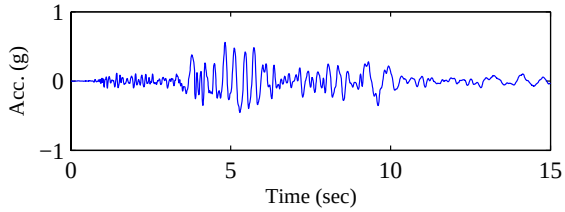

(a) Longitudinal Input

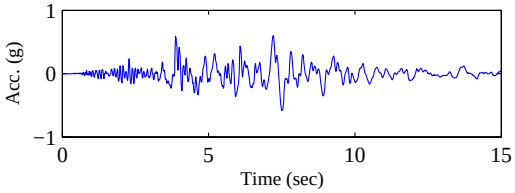

(b) Transverse Input

RC Pier Responses (Pier4)

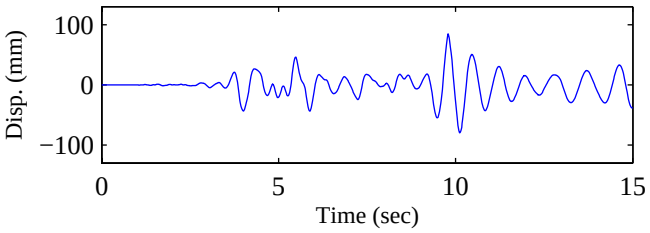

(c) Longitudinal displacement

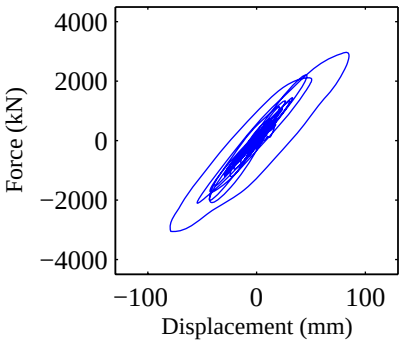

(f) Longitudinal disp.-force

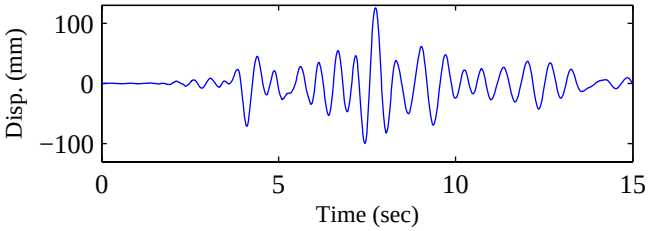

(d) Transverse displacement

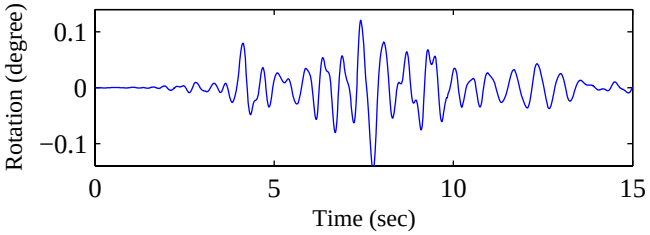

(e) Rotational displacement

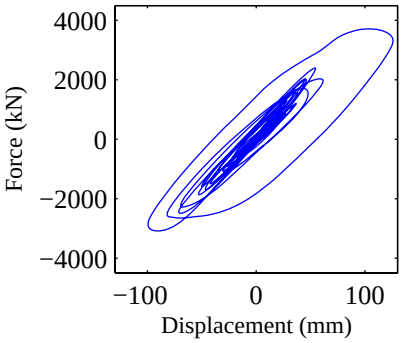

(g) Transverse disp.-force

Response Summary

	Pier1	Pier2	Pier3	Pier4	Joint1	Joint2	Joint3	Joint4
Max Long. Disp.(mm)	82.7	82.1	84.9	86.6	82.9	82.5	85.8	89.0
Max Trans. Disp.(mm)	141.5	125.7	125.7	141.9	58.0	39.5	38.9	58.1
Max Tor. Rot.(degree)	0.109	0.149	0.148	0.110	0.133	0.142	0.142	0.133
Pounding Events	NA	NA	NA	NA	1	1	1	1

Input Earthquake: Imperial Valley, 1979 **Station**: Galexico Fire Station

Scaling Factor: 2.05

Input Direction: Longitudinal – 00 comp.
Transverse – 90 comp.

Skew Angle: 0 degree

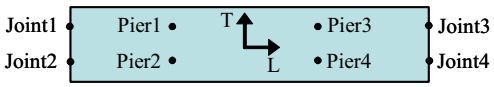

Input Time-histories

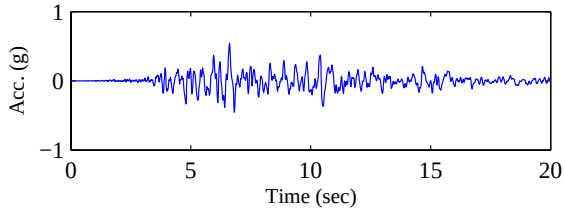

(a) Longitudinal Input

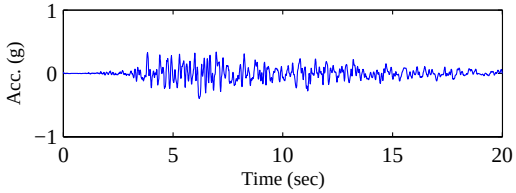

(b) Transverse Input

RC Pier Responses (Pier4)

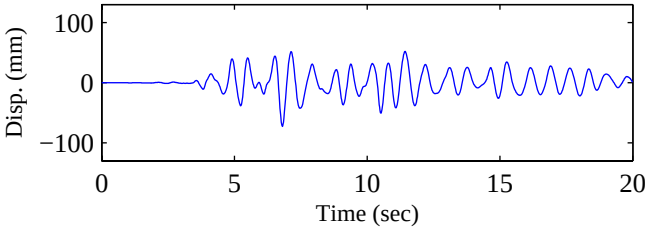

(c) Longitudinal displacement

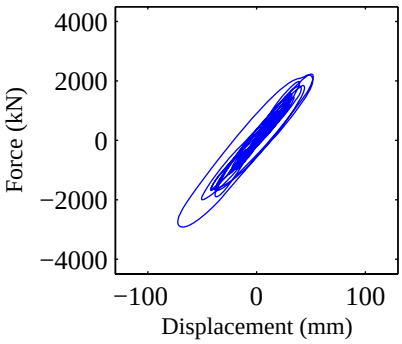

(f) Longitudinal disp.-force

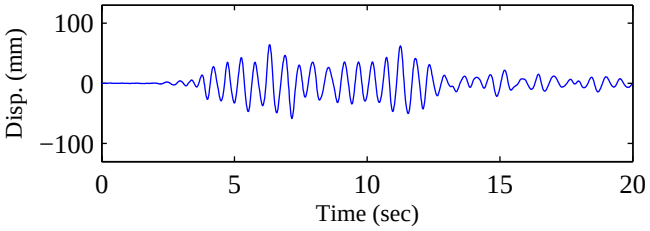

(d) Transverse displacement

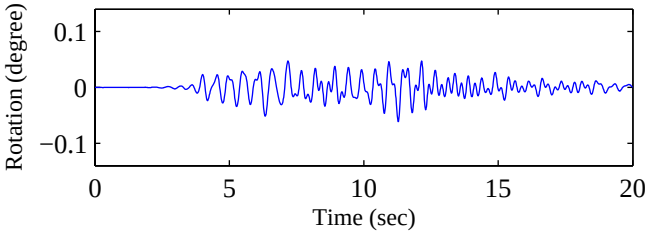

(e) Rotational displacement

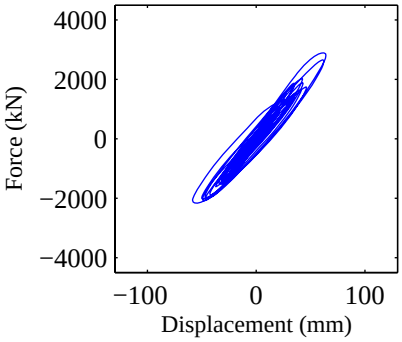

(g) Transverse disp.-force

Response Summary

	Pier1	Pier2	Pier3	Pier4	Joint1	Joint2	Joint3	Joint4
Max Long. Disp.(mm)	71.1	72.6	72.5	71.2	70.8	73.7	73.6	70.8
Max Trans. Disp.(mm)	64.1	64.1	64.2	64.2	30.6	30.6	30.6	30.6
Max Tor. Rot.(degree)	0.060	0.062	0.061	0.060	0.073	0.073	0.073	0.073
Pounding Events	NA	NA	NA	NA	0	0	0	0

Input Earthquake: Imperial Valley, 1979 **Station**: Galexico Fire Station

Scaling Factor: 2.05

Input Direction: Longitudinal – 00 comp.
Transverse – 90 comp.

Skew Angle: 30 degree

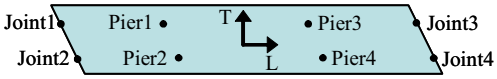

Input Time-histories

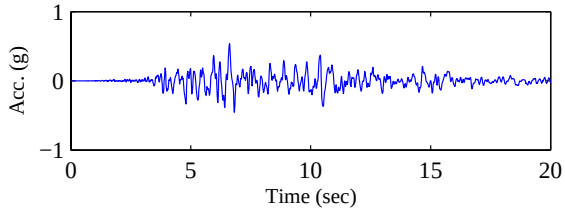

(a) Longitudinal Input

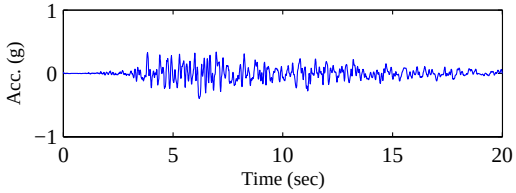

(b) Transverse Input

RC Pier Responses (Pier4)

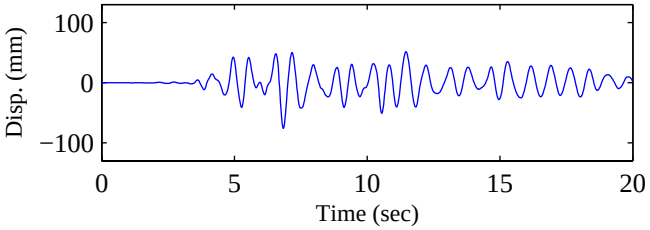

(c) Longitudinal displacement

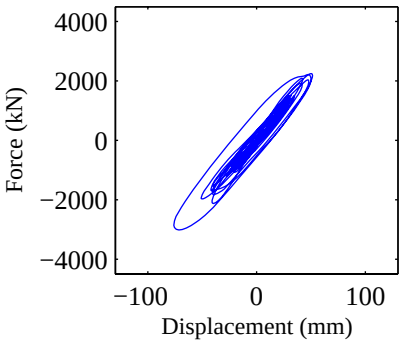

(f) Longitudinal disp.-force

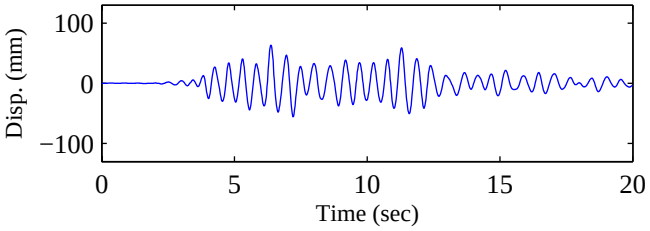

(d) Transverse displacement

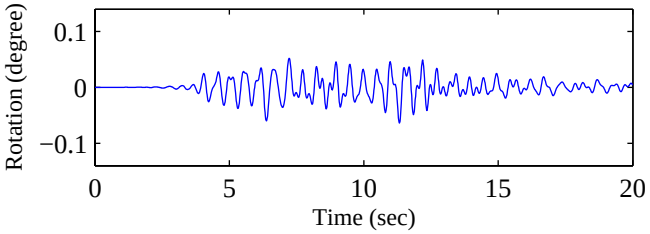

(e) Rotational displacement

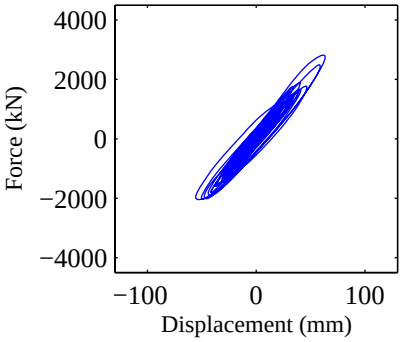

(g) Transverse disp.-force

Response Summary

	Pier1	Pier2	Pier3	Pier4	Joint1	Joint2	Joint3	Joint4
Max Long. Disp.(mm)	75.2	76.2	76.1	75.2	75.1	77.0	76.5	75.1
Max Trans. Disp.(mm)	65.9	63.2	63.5	66.3	32.5	29.8	29.6	32.4
Max Tor. Rot.(degree)	0.057	0.065	0.064	0.056	0.070	0.071	0.072	0.071
Pounding Events	NA	NA	NA	NA	1	1	0	0

Input Earthquake: Imperial Valley, 1979 **Station**: Galexico Fire Station

Scaling Factor: 2.05

Input Direction: Longitudinal – 00 comp.
Transverse – 90 comp.

Skew Angle: 60 degree

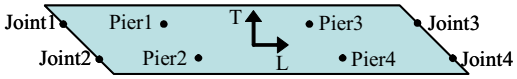

Input Time-histories

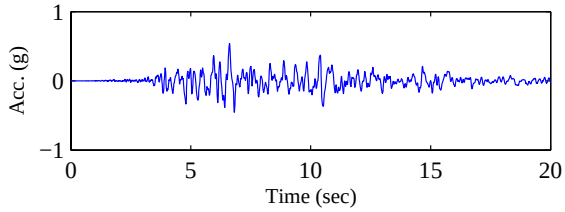

(a) Longitudinal Input

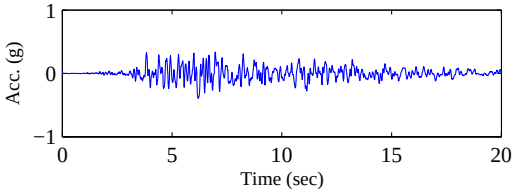

(b) Transverse Input

RC Pier Responses (Pier4)

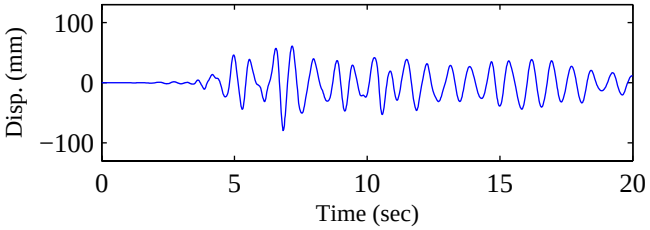

(c) Longitudinal displacement

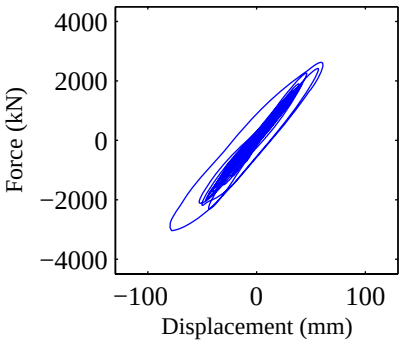

(f) Longitudinal disp.-force

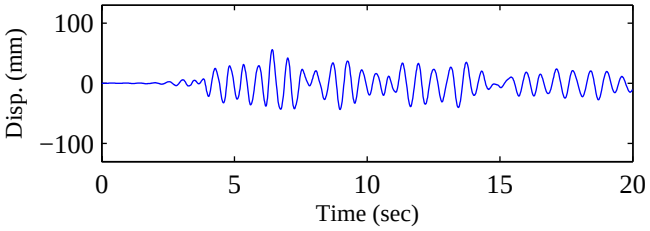

(d) Transverse displacement

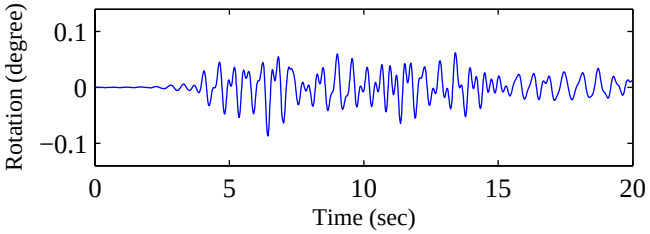

(e) Rotational displacement

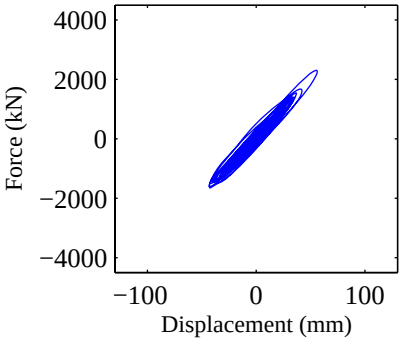

(g) Transverse disp.-force

Response Summary

	Pier1	Pier2	Pier3	Pier4	Joint1	Joint2	Joint3	Joint4
Max Long. Disp.(mm)	84.2	81.2	79.6	81.4	86.1	81.8	77.7	79.3
Max Trans. Disp.(mm)	64.7	56.0	56.2	65.6	32.7	27.4	27.4	32.3
Max Tor. Rot.(degree)	0.063	0.087	0.087	0.063	0.067	0.071	0.074	0.070
Pounding Events	NA	NA	NA	NA	1	1	0	0

Input Earthquake: Imperial Valley, 1979 **Station**: Galexico Fire Station

Scaling Factor: 2.05

Input Direction: Diagonal 1 – NS comp.
Diagonal 2 – EW comp.

Skew Angle: 0 degree

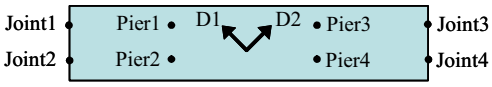

Input Time-histories

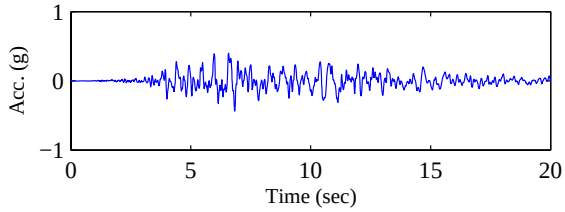

(a) Longitudinal Input

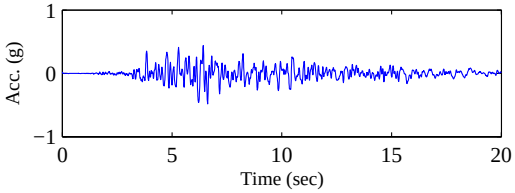

(b) Transverse Input

RC Pier Responses (Pier4)

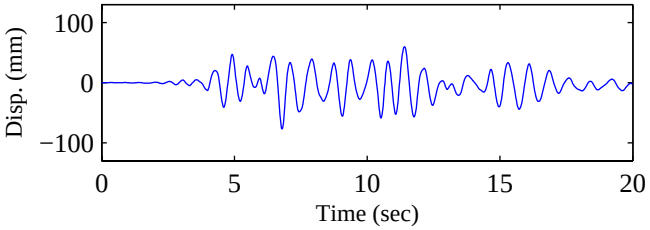

(c) Longitudinal displacement

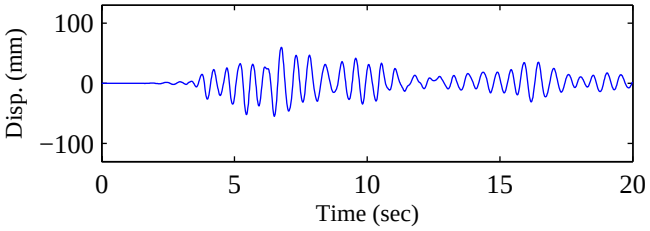

(d) Transverse displacement

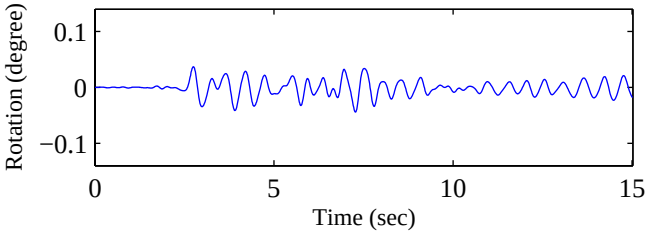

(e) Rotational displacement

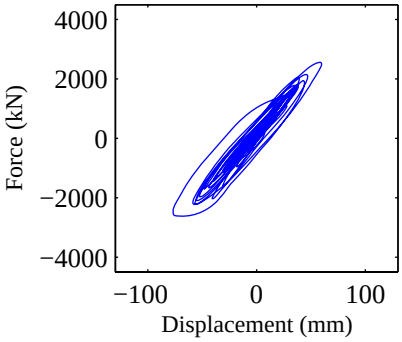

(f) Longitudinal disp.-force

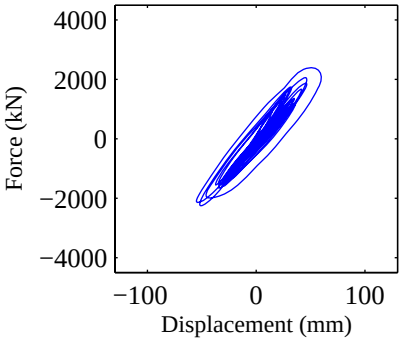

(g) Transverse disp.-force

Response Summary

	Pier1	Pier2	Pier3	Pier4	Joint1	Joint2	Joint3	Joint4
Max Long. Disp.(mm)	74.3	78.3	76.8	74.3	73.2	80.4	77.4	72.8
Max Trans. Disp.(mm)	59.9	59.9	59.9	59.9	27.0	27.0	27.1	27.1
Max Tor. Rot.(degree)	0.054	0.053	0.053	0.054	0.065	0.065	0.065	0.065
Pounding Events	NA	NA	NA	NA	1	0	0	0

Input Earthquake: Imperial Valley, 1979 **Station**: Galexico Fire Station

Scaling Factor: 2.05

Input Direction: Diagonal 1 – NS comp.
Diagonal 2 – EW comp.

Skew Angle: 30 degree

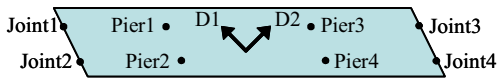

Input Time-histories

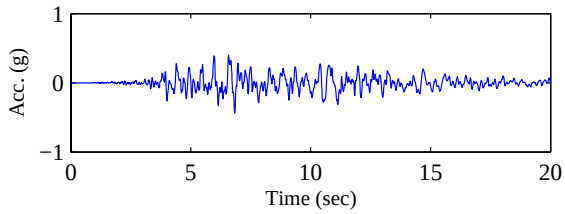

(a) Longitudinal Input

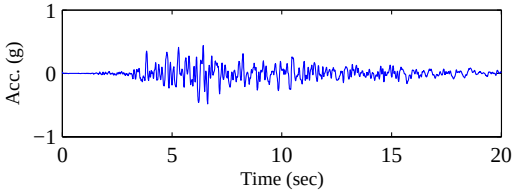

(b) Transverse Input

RC Pier Responses (Pier4)

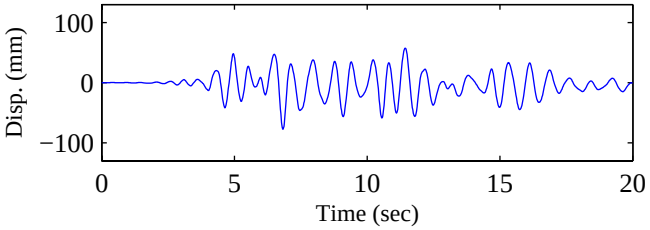

(c) Longitudinal displacement

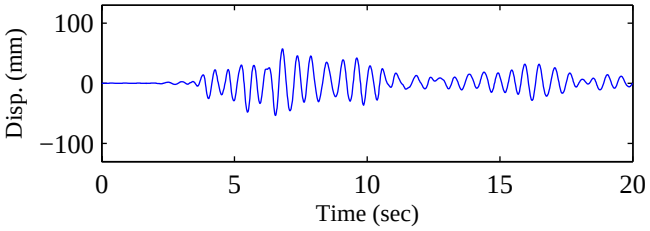

(d) Transverse displacement

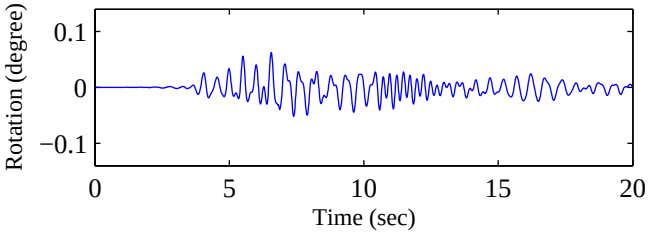

(e) Rotational displacement

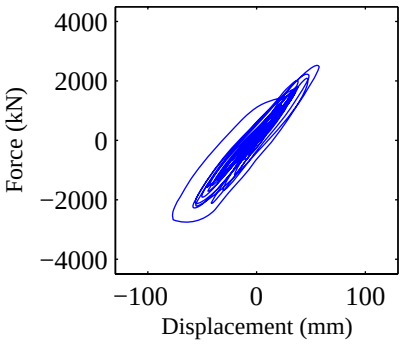

(f) Longitudinal disp.-force

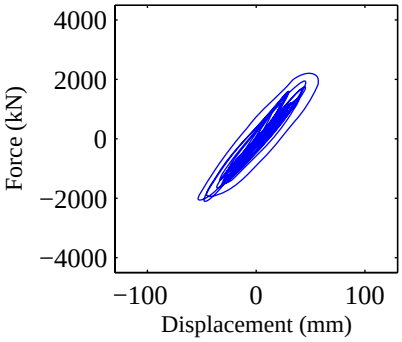

(g) Transverse disp.-force

Response Summary

	Pier1	Pier2	Pier3	Pier4	Joint1	Joint2	Joint3	Joint4
Max Long. Disp.(mm)	75.3	78.9	77.4	75.3	74.4	81.1	77.6	73.9
Max Trans. Disp.(mm)	58.6	56.8	57.2	58.9	29.6	26.2	26.2	29.6
Max Tor. Rot.(degree)	0.058	0.062	0.062	0.058	0.067	0.068	0.068	0.067
Pounding Events	NA	NA	NA	NA	1	0	0	0

Input Earthquake: Imperial Valley, 1979 **Station**: Galexico Fire Station

Scaling Factor: 2.05

Input Direction: Diagonal 1 – NS comp.
Diagonal 2 – EW comp.

Skew Angle: 60 degree

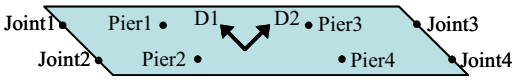

Input Time-histories

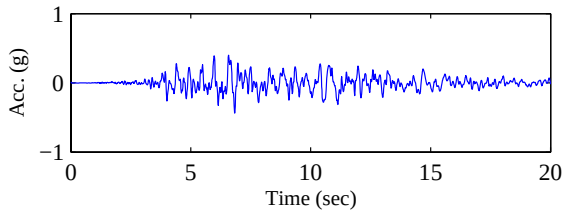

(a) Longitudinal Input

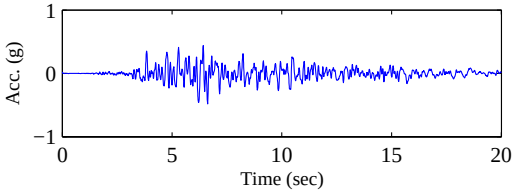

(b) Transverse Input

RC Pier Responses (Pier4)

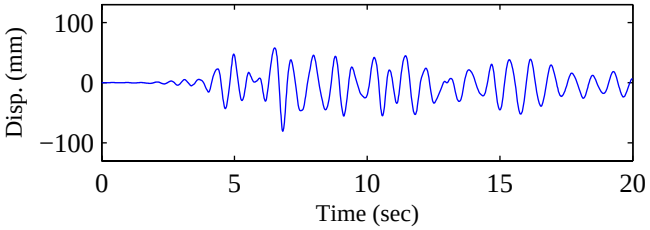

(c) Longitudinal displacement

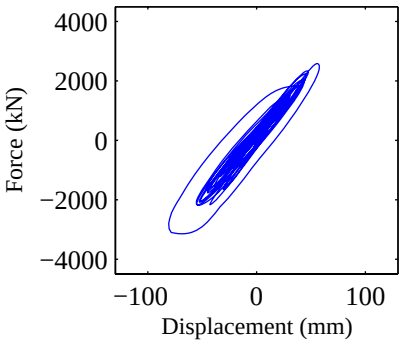

(f) Longitudinal disp.-force

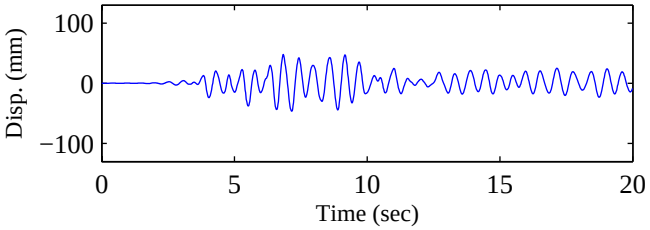

(d) Transverse displacement

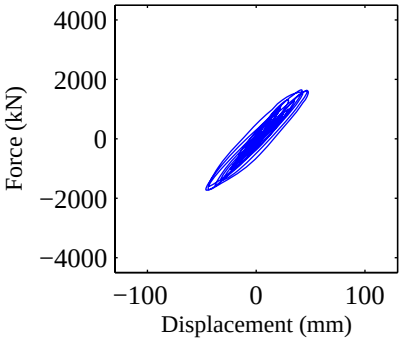

(g) Transverse disp.-force

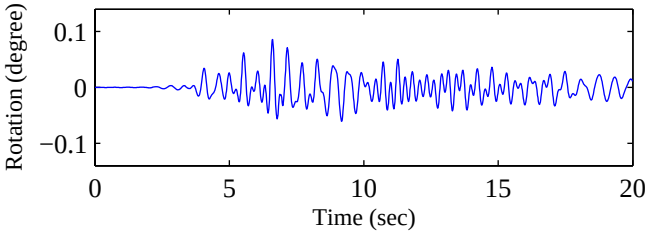

(e) Rotational displacement

Response Summary

	Pier1	Pier2	Pier3	Pier4	Joint1	Joint2	Joint3	Joint4
Max Long. Disp.(mm)	80.7	83.2	80.8	79.4	80.6	85.3	78.9	77.3
Max Trans. Disp.(mm)	54.9	47.3	48.0	54.1	30.7	25.3	28.8	32.3
Max Tor. Rot.(degree)	0.069	0.086	0.086	0.068	0.064	0.065	0.063	0.062
Pounding Events	NA	NA	NA	NA	1	1	0	0

Input Earthquake: Imperial Valley, 1979 **Station**: Galexico Fire Station

Scaling Factor: 2.05

Input Direction: Longitudinal – 90 comp.
Transverse – 00 comp.

Skew Angle: 0 degree

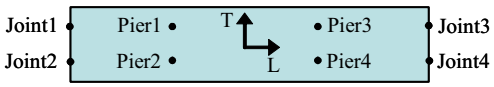

Input Time-histories

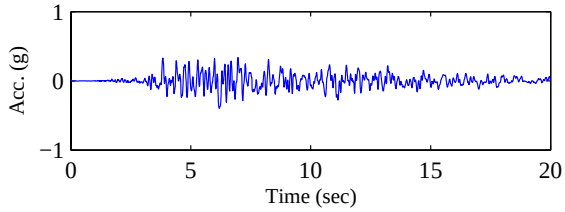

(a) Longitudinal Input

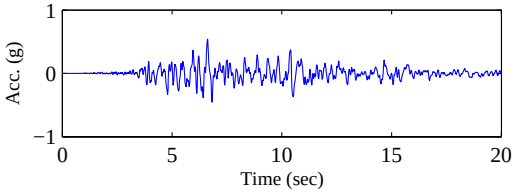

(b) Transverse Input

RC Pier Responses (Pier4)

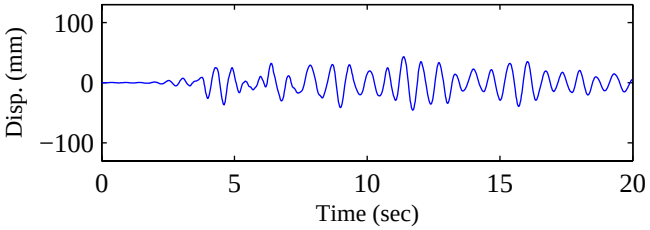

(c) Longitudinal displacement

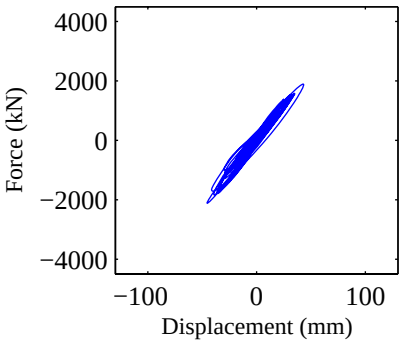

(f) Longitudinal disp.-force

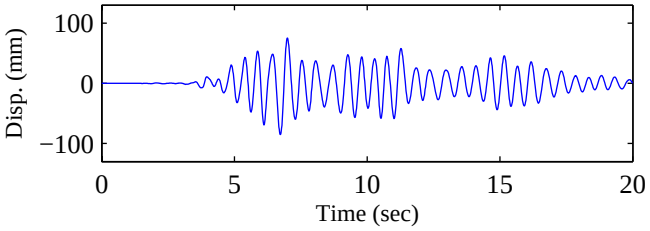

(d) Transverse displacement

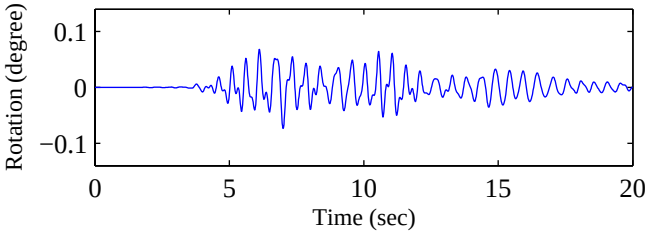

(e) Rotational displacement

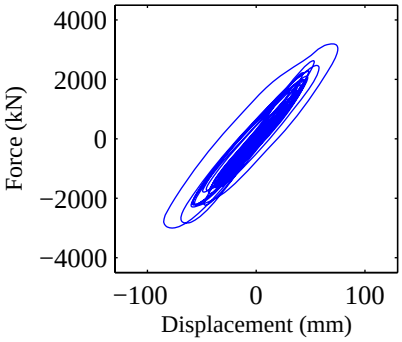

(g) Transverse disp.-force

Response Summary

	Pier1	Pier2	Pier3	Pier4	Joint1	Joint2	Joint3	Joint4
Max Long. Disp.(mm)	45.0	45.6	45.6	45.0	46.1	46.0	46.0	46.2
Max Trans. Disp.(mm)	84.9	84.9	85.1	85.1	37.6	37.6	37.9	37.9
Max Tor. Rot.(degree)	0.073	0.074	0.074	0.073	0.089	0.089	0.089	0.089
Pounding Events	NA	NA	NA	NA	0	0	0	0

Input Earthquake: Imperial Valley, 1979 **Station**: Galexico Fire Station

Scaling Factor: 2.05

Input Direction: Longitudinal – 90 comp.
Transverse – 00 comp.

Skew Angle: 30 degree

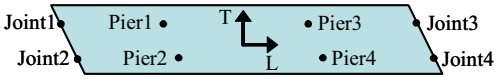

Input Time-histories

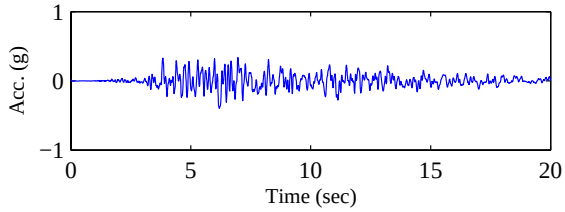

(a) Longitudinal Input

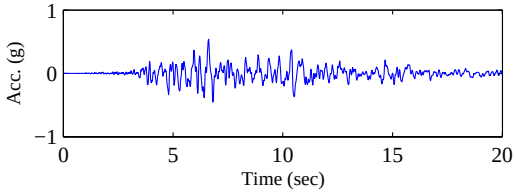

(b) Transverse Input

RC Pier Responses (Pier4)

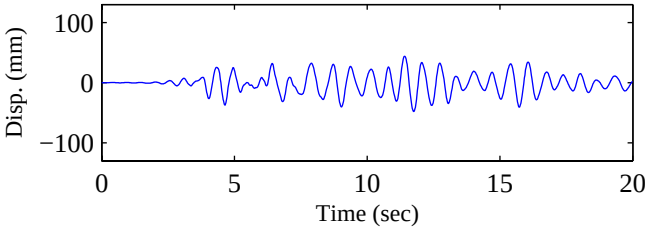

(c) Longitudinal displacement

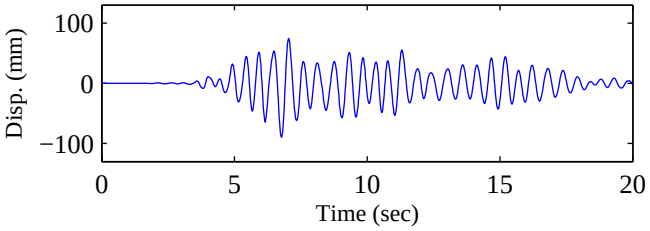

(d) Transverse displacement

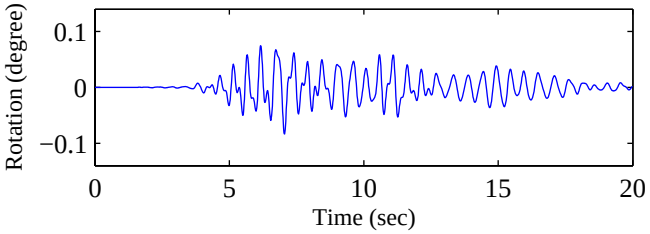

(e) Rotational displacement

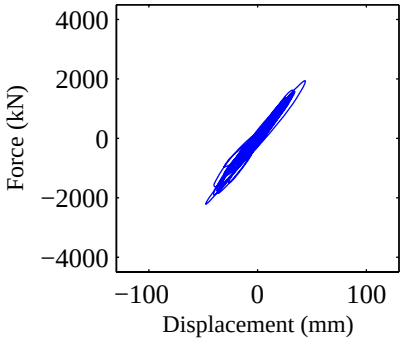

(f) Longitudinal disp.-force

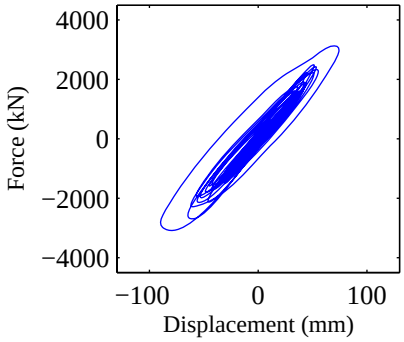

(g) Transverse disp.-force

Response Summary

	Pier1	Pier2	Pier3	Pier4	Joint1	Joint2	Joint3	Joint4
Max Long. Disp.(mm)	42.2	47.9	47.9	47.2	47.5	48.2	48.2	47.5
Max Trans. Disp.(mm)	93.0	89.9	89.8	92.7	42.4	36.6	36.7	42.4
Max Tor. Rot.(degree)	0.075	0.084	0.083	0.074	0.090	0.091	0.092	0.090
Pounding Events	NA	NA	NA	NA	0	0	0	0

Input Earthquake: Imperial Valley, 1979 **Station**: Galexico Fire Station

Scaling Factor: 2.05

Input Direction: Longitudinal – 90 comp.
Transverse – 00 comp.

Skew Angle: 60 degree

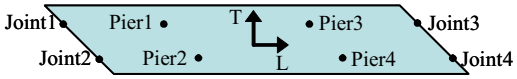

Input Time-histories

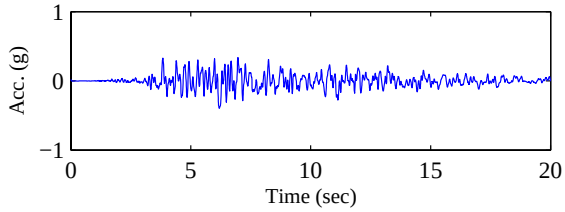

(a) Longitudinal Input

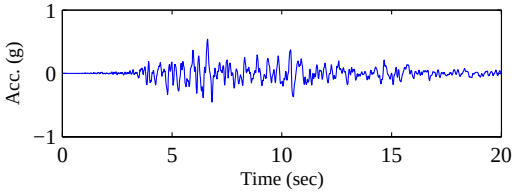

(b) Transverse Input

RC Pier Responses (Pier4)

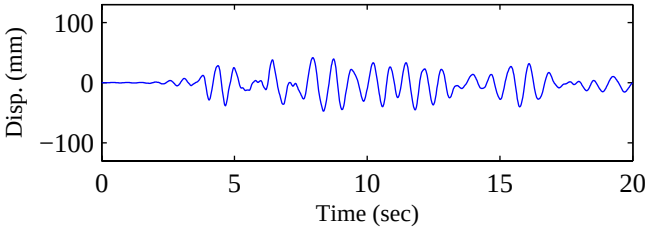

(c) Longitudinal displacement

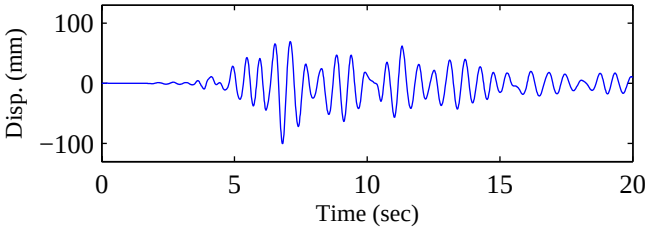

(d) Transverse displacement

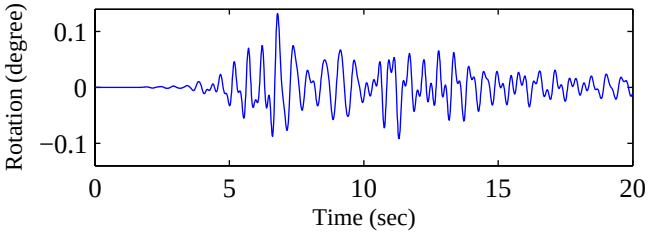

(e) Rotational displacement

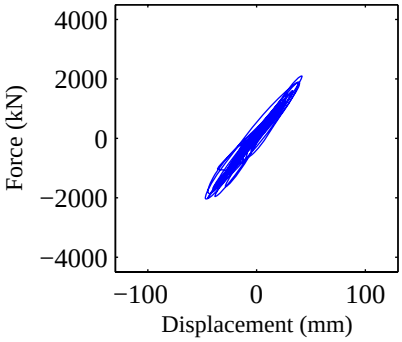

(f) Longitudinal disp.-force

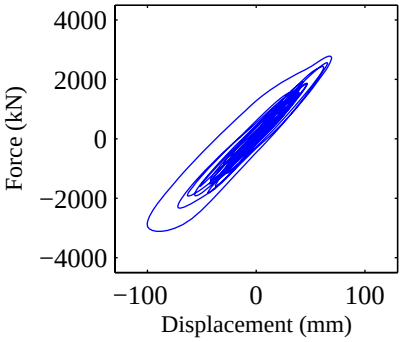

(g) Transverse disp.-force

Response Summary

	Pier1	Pier2	Pier3	Pier4	Joint1	Joint2	Joint3	Joint4
Max Long. Disp.(mm)	47.7	47.3	47.2	47.7	49.6	47.8	47.8	49.5
Max Trans. Disp.(mm)	114.8	100.5	100.4	113.9	47.5	39.7	40.3	48.3
Max Tor. Rot.(degree)	0.097	0.132	0.132	0.096	0.113	0.120	0.118	0.111
Pounding Events	NA	NA	NA	NA	0	0	0	0

Input Earthquake: Morgan Hill, 1984 **Station**: Gilroy Array **Scaling Factor**: 2.00

Input Direction: Longitudinal – 00 comp.
Transverse – 90 comp.

Skew Angle: 0 degree

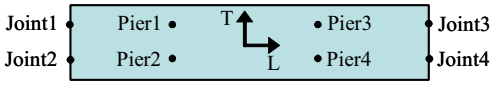

Input Time-histories

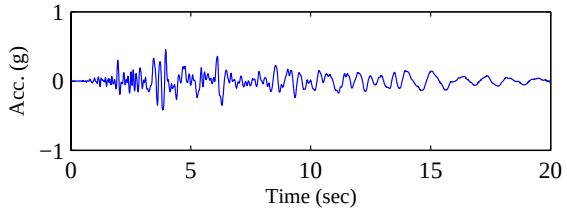

(a) Longitudinal Input

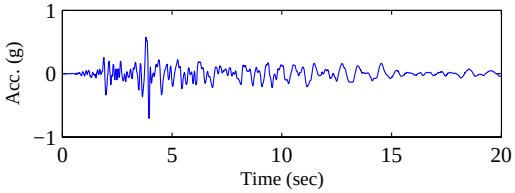

(b) Transverse Input

RC Pier Responses (Pier4)

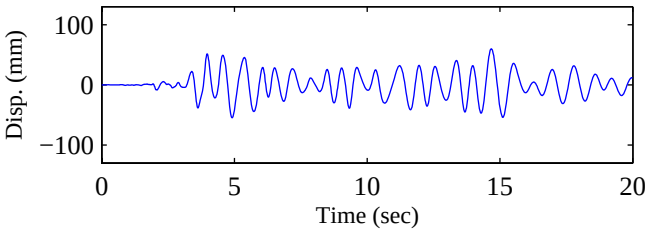

(c) Longitudinal displacement

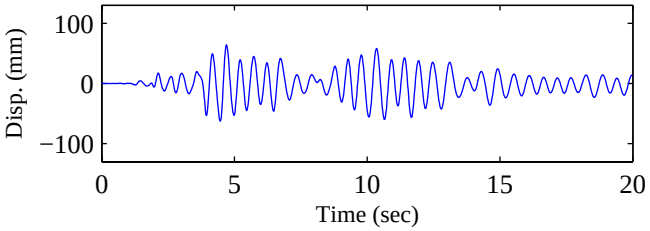

(d) Transverse displacement

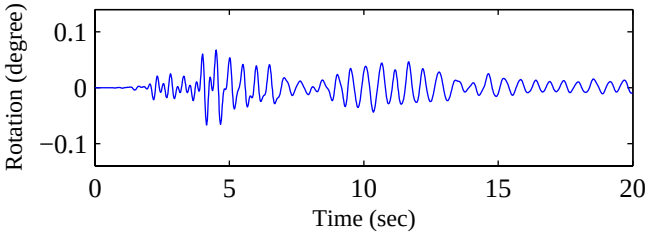

(e) Rotational displacement

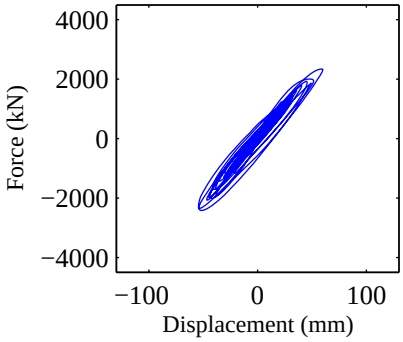

(f) Longitudinal disp.-force

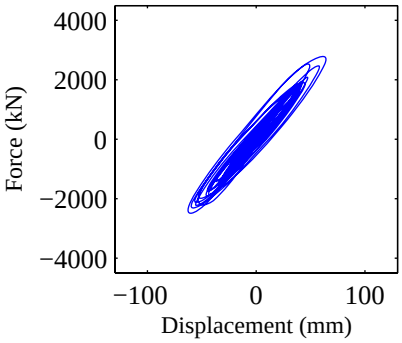

(g) Transverse disp.-force

Response Summary

	Pier1	Pier2	Pier3	Pier4	Joint1	Joint2	Joint3	Joint4
Max Long. Disp.(mm)	57.9	59.9	60.0	57.9	57.3	61.2	61.2	57.3
Max Trans. Disp.(mm)	63.5	63.5	64.1	64.1	38.4	38.4	38.4	38.4
Max Tor. Rot.(degree)	0.070	0.068	0.067	0.070	0.077	0.077	0.077	0.077
Pounding Events	NA	NA	NA	NA	0	0	0	0

Input Earthquake: Morgan Hill, 1984 **Station**: Gilroy Array **Scaling Factor**: 2.00

Input Direction: Longitudinal – 00 comp.
Transverse – 90 comp.

Skew Angle: 30 degree

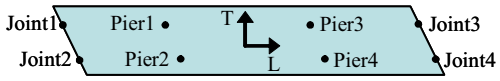

Input Time-histories

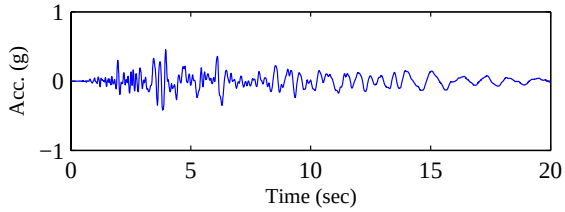

(a) Longitudinal Input

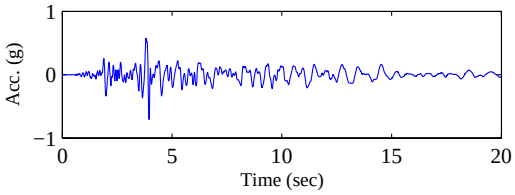

(b) Transverse Input

RC Pier Responses (Pier4)

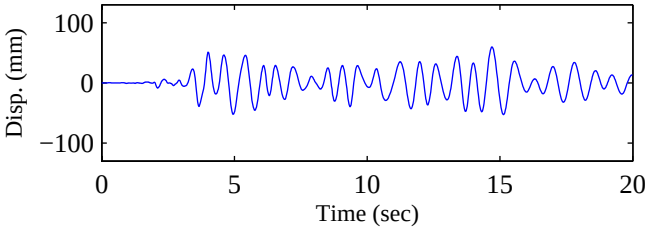

(c) Longitudinal displacement

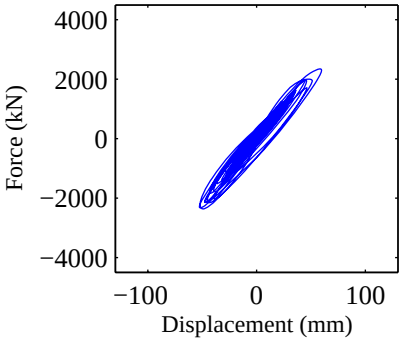

(f) Longitudinal disp.-force

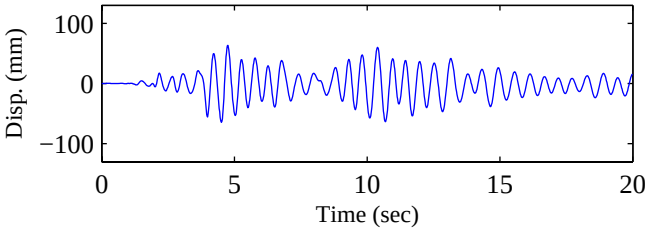

(d) Transverse displacement

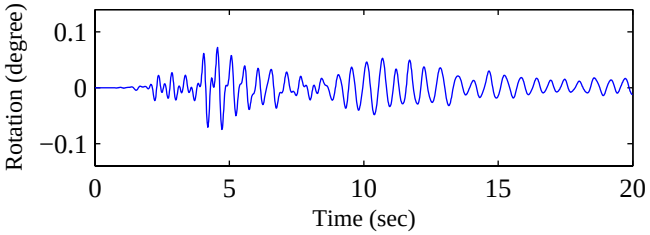

(e) Rotational displacement

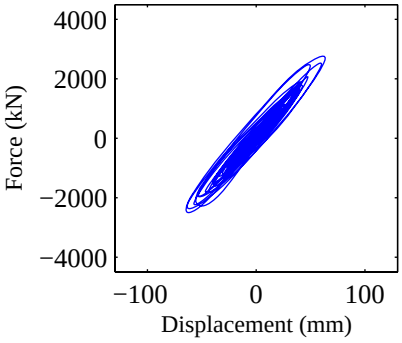

(g) Transverse disp.-force

Response Summary

	Pier1	Pier2	Pier3	Pier4	Joint1	Joint2	Joint3	Joint4
Max Long. Disp.(mm)	57.7	59.8	59.8	57.7	57.1	61.1	61.1	57.0
Max Trans. Disp.(mm)	66.8	64.3	64.5	67.0	39.3	36.9	37.5	39.7
Max Tor. Rot.(degree)	0.068	0.074	0.075	0.068	0.076	0.077	0.077	0.076
Pounding Events	NA	NA	NA	NA	0	0	0	0

Input Earthquake: Morgan Hill, 1984 **Station**: Gilroy Array **Scaling Factor**: 2.00

Input Direction: Longitudinal – 00 comp.
Transverse – 90 comp.

Skew Angle: 60 degree

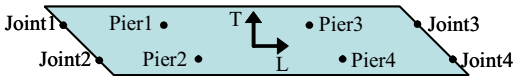

Input Time-histories

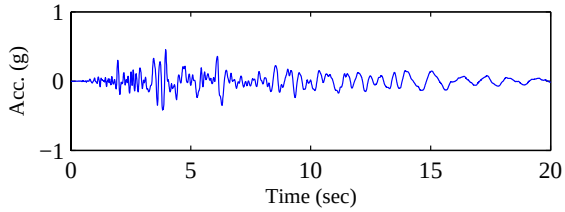

(a) Longitudinal Input

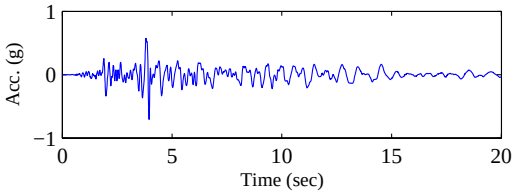

(b) Transverse Input

RC Pier Responses (Pier4)

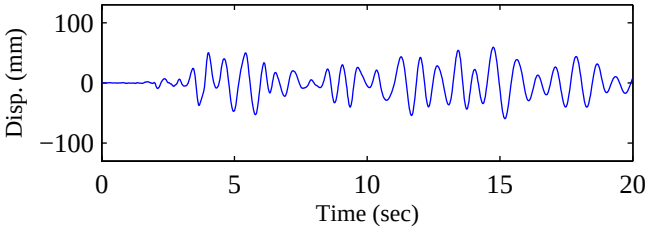

(c) Longitudinal displacement

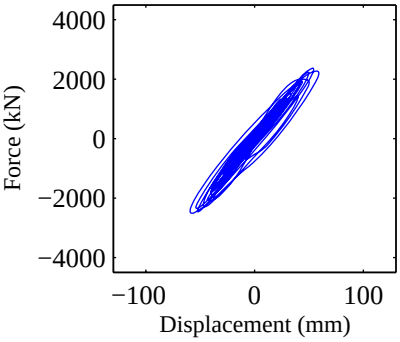

(f) Longitudinal disp.-force

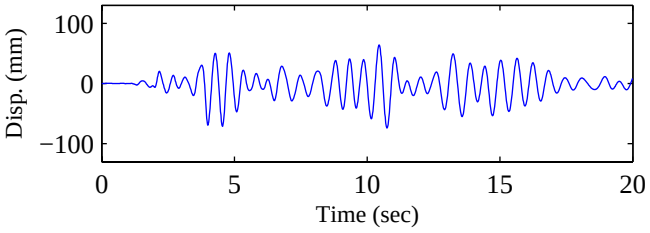

(d) Transverse displacement

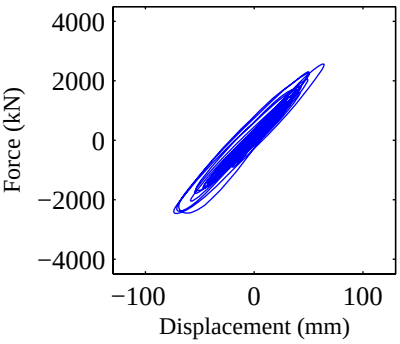

(g) Transverse disp.-force

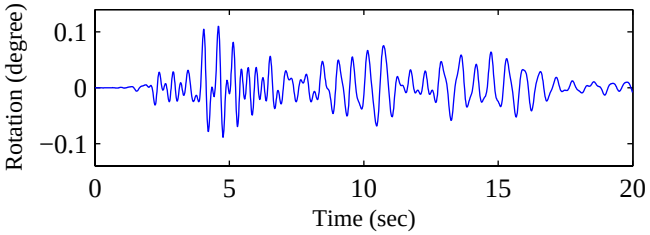

(e) Rotational displacement

Response Summary

	Pier1	Pier2	Pier3	Pier4	Joint1	Joint2	Joint3	Joint4
Max Long. Disp.(mm)	59.5	59.4	59.3	59.5	60.2	60.9	61.0	60.2
Max Trans. Disp.(mm)	82.6	74.1	74.0	82.1	41.5	35.3	36.0	41.9
Max Tor. Rot.(degree)	0.086	0.110	0.110	0.086	0.087	0.090	0.090	0.087
Pounding Events	NA	NA	NA	NA	0	0	0	0

Input Earthquake: Morgan Hill, 1984 **Station**: Gilroy Array **Scaling Factor**: 2.00
Input Direction: Diagonal 1 – NS comp.
Diagonal 2 – EW comp.
Skew Angle: 0 degree

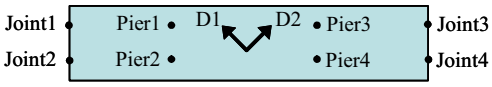

Input Time-histories

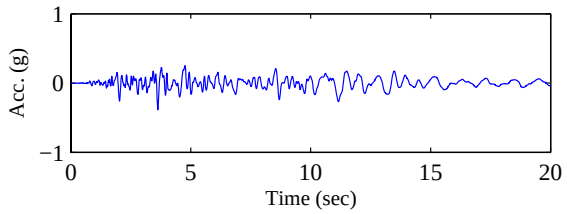

(a) Longitudinal Input

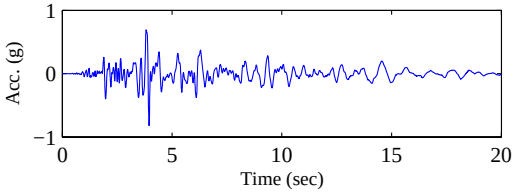

(b) Transverse Input

RC Pier Responses (Pier4)

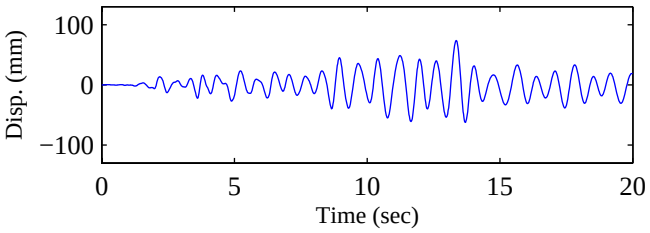

(c) Longitudinal displacement

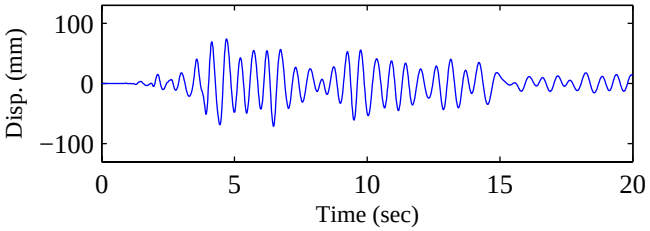

(d) Transverse displacement

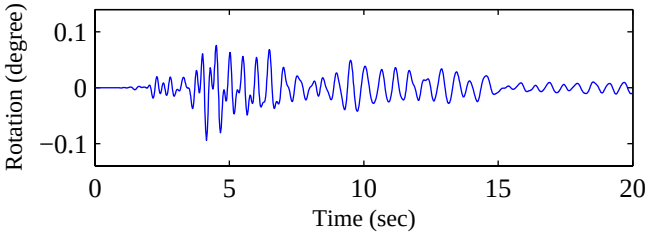

(e) Rotational displacement

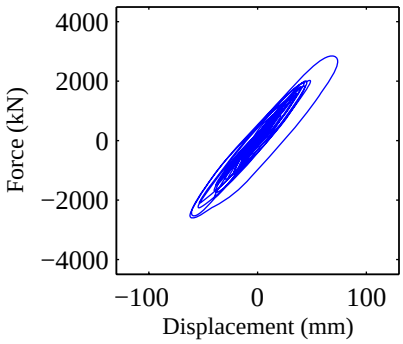

(f) Longitudinal disp.-force

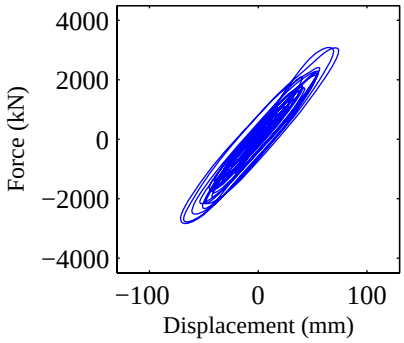

(g) Transverse disp.-force

Response Summary

	Pier1	Pier2	Pier3	Pier4	Joint1	Joint2	Joint3	Joint4
Max Long. Disp.(mm)	72.3	73.7	73.8	72.3	72.0	74.8	74.8	72.0
Max Trans. Disp.(mm)	74.1	74.1	74.2	74.2	49.3	49.3	49.1	49.1
Max Tor. Rot.(degree)	0.094	0.094	0.094	0.094	0.099	0.099	0.099	0.099
Pounding Events	NA	NA	NA	NA	0	0	0	0

Input Earthquake: Morgan Hill, 1984 **Station**: Gilroy Array **Scaling Factor**: 2.00
Input Direction: Diagonal 1 – NS comp.
Diagonal 2 – EW comp.
Skew Angle: 30 degree

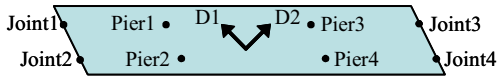

Input Time-histories

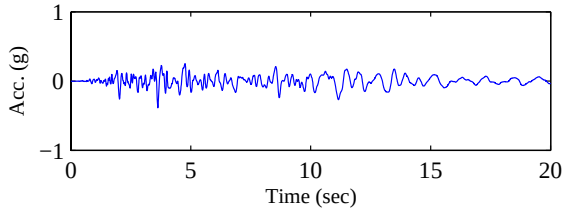

(a) Longitudinal Input

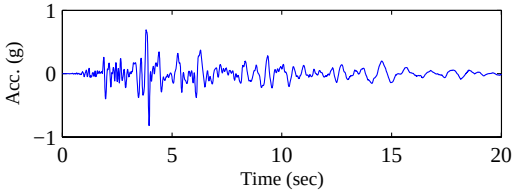

(b) Transverse Input

RC Pier Responses (Pier4)

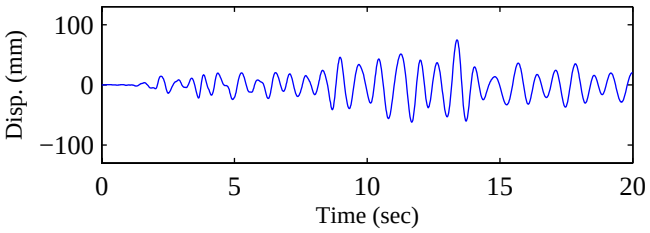

(c) Longitudinal displacement

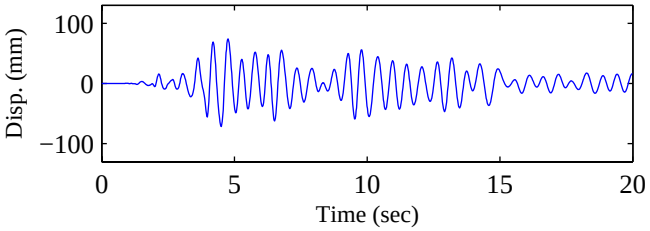

(d) Transverse displacement

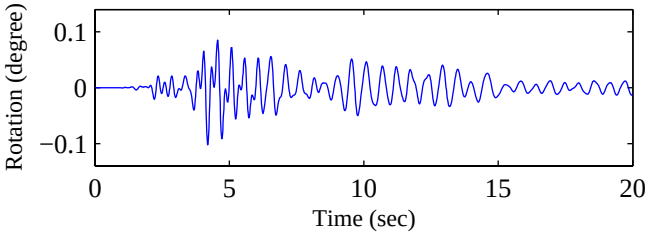

(e) Rotational displacement

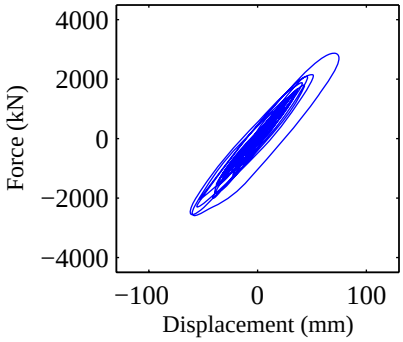

(f) Longitudinal disp.-force

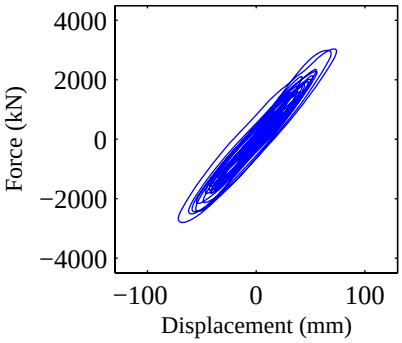

(g) Transverse disp.-force

Response Summary

	Pier1	Pier2	Pier3	Pier4	Joint1	Joint2	Joint3	Joint4
Max Long. Disp.(mm)	73.8	74.7	74.8	73.8	73.7	75.7	75.8	73.7
Max Trans. Disp.(mm)	77.3	74.0	74.0	77.3	51.5	49.1	49.4	51.8
Max Tor. Rot.(degree)	0.093	0.102	0.102	0.094	0.098	0.099	0.100	0.099
Pounding Events	NA	NA	NA	NA	0	0	0	1

Input Earthquake: Morgan Hill, 1984 **Station**: Gilroy Array **Scaling Factor**: 2.00
Input Direction: Diagonal 1 – NS comp.
Diagonal 2 – EW comp.
Skew Angle: 60 degree

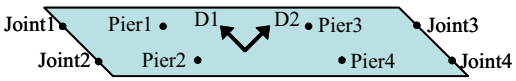

Input Time-histories

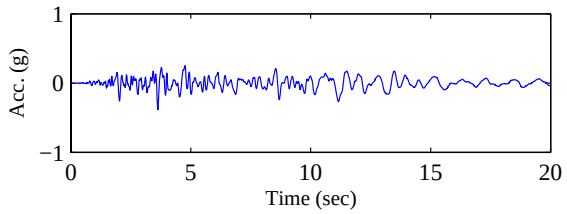

(a) Longitudinal Input

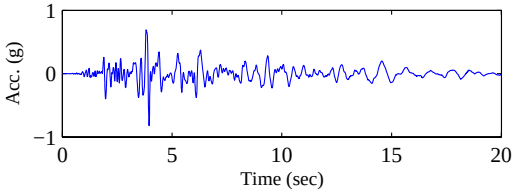

(b) Transverse Input

RC Pier Responses (Pier4)

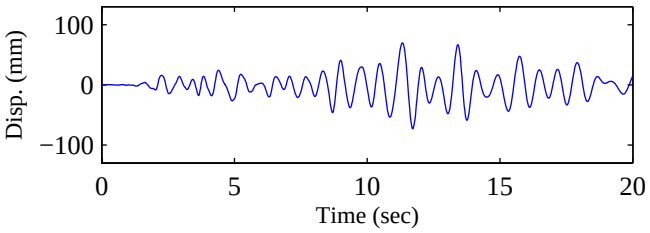

(c) Longitudinal displacement

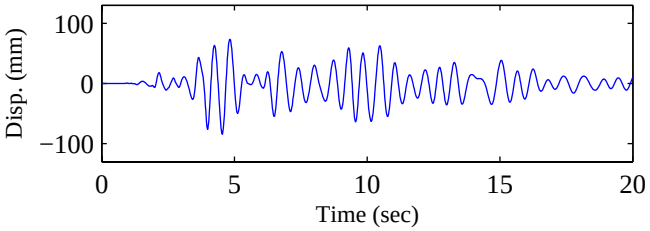

(d) Transverse displacement

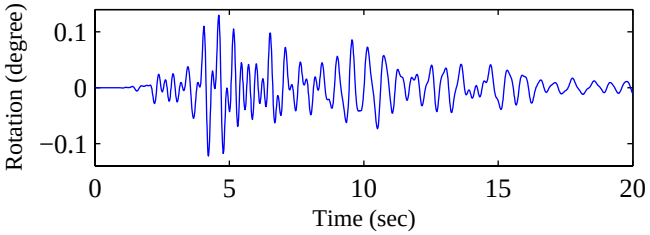

(e) Rotational displacement

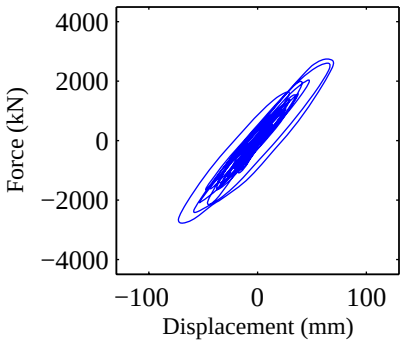

(f) Longitudinal disp.-force

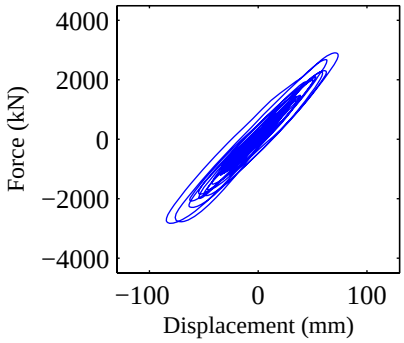

(g) Transverse disp.-force

Response Summary

	Pier1	Pier2	Pier3	Pier4	Joint1	Joint2	Joint3	Joint4
Max Long. Disp.(mm)	73.2	73.0	72.9	73.3	73.7	73.3	73.3	73.7
Max Trans. Disp.(mm)	93.6	84.5	84.5	93.3	60.1	51.7	52.1	60.2
Max Tor. Rot.(degree)	0.102	0.129	0.130	0.101	0.099	0.103	0.102	0.098
Pounding Events	NA	NA	NA	NA	0	0	0	0

Input Earthquake: Morgan Hill, 1984 **Station**: Gilroy Array **Scaling Factor**: 2.00
Input Direction: Longitudinal – 90 comp.
Transverse – 00 comp.
Skew Angle: 0 degree

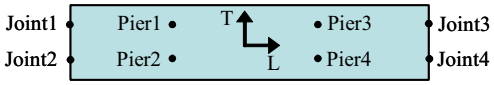

Input Time-histories

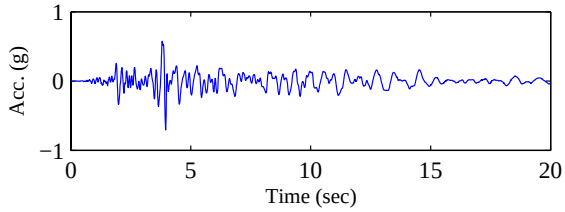

(a) Longitudinal Input

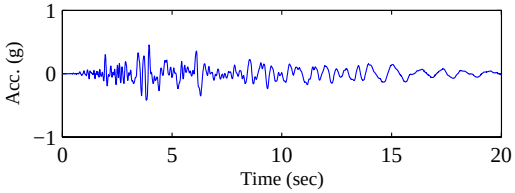

(b) Transverse Input

RC Pier Responses (Pier4)

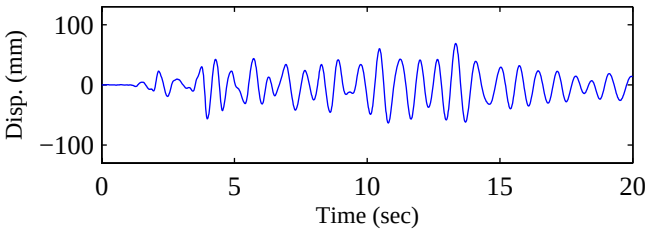

(c) Longitudinal displacement

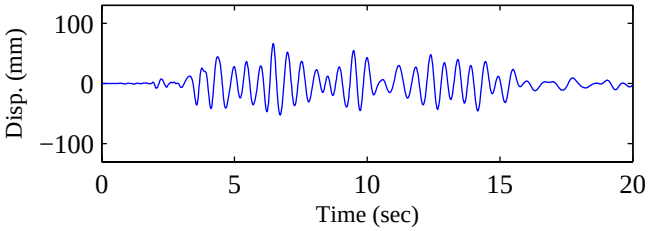

(d) Transverse displacement

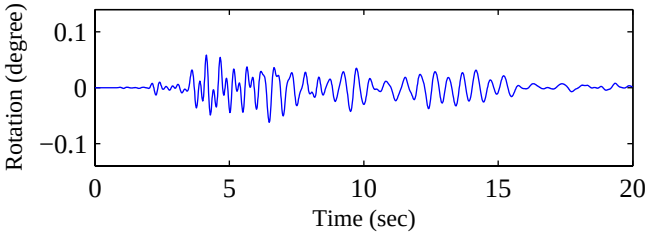

(e) Rotational displacement

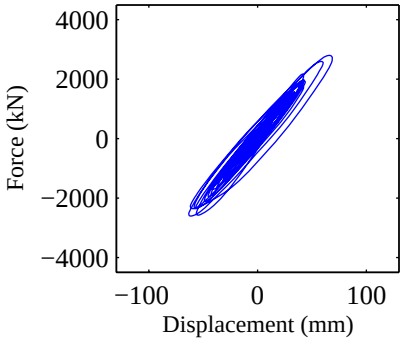

(f) Longitudinal disp.-force

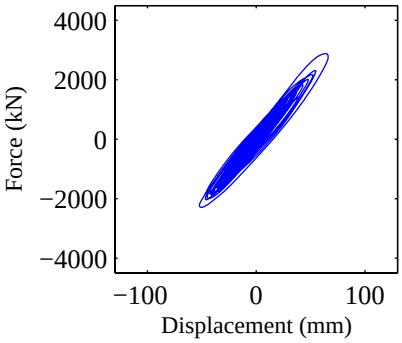

(g) Transverse disp.-force

Response Summary

	Pier1	Pier2	Pier3	Pier4	Joint1	Joint2	Joint3	Joint4
Max Long. Disp.(mm)	70.3	68.9	68.8	70.4	71.4	68.5	68.5	71.5
Max Trans. Disp.(mm)	66.3	66.3	66.3	66.3	34.1	34.1	33.9	33.9
Max Tor. Rot.(degree)	0.063	0.062	0.062	0.063	0.078	0.077	0.077	0.077
Pounding Events	NA	NA	NA	NA	0	0	0	0

Input Earthquake: Morgan Hill, 1984 **Station**: Gilroy Array **Scaling Factor**: 2.00
Input Direction: Longitudinal – 90 comp.
Transverse – 00 comp.
Skew Angle: 30 degree

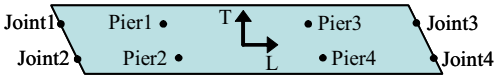

Input Time-histories

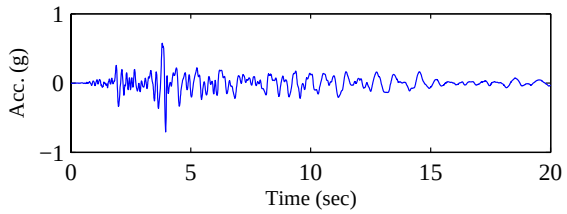

(a) Longitudinal Input

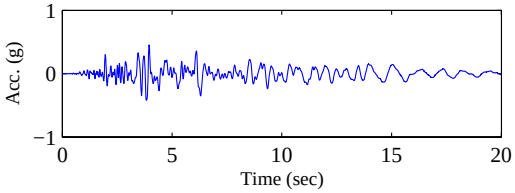

(b) Transverse Input

RC Pier Responses (Pier4)

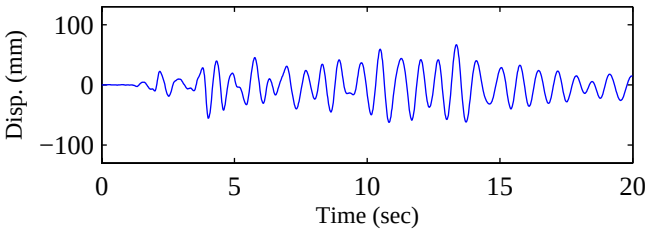

(c) Longitudinal displacement

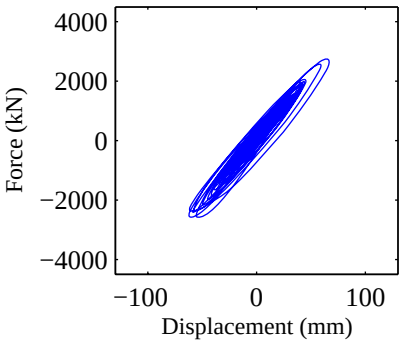

(f) Longitudinal disp.-force

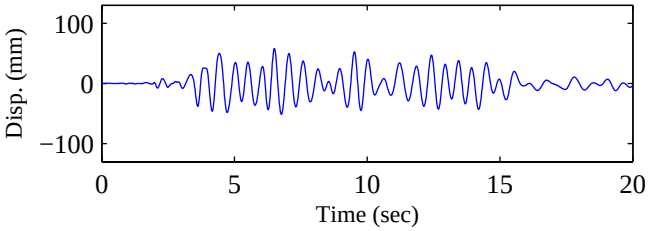

(d) Transverse displacement

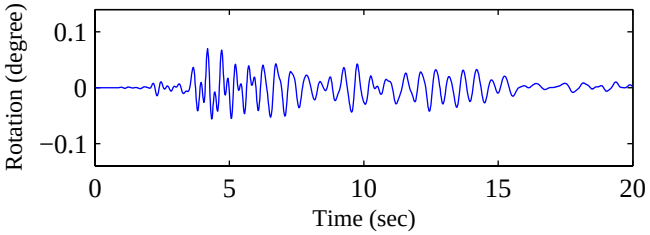

(e) Rotational displacement

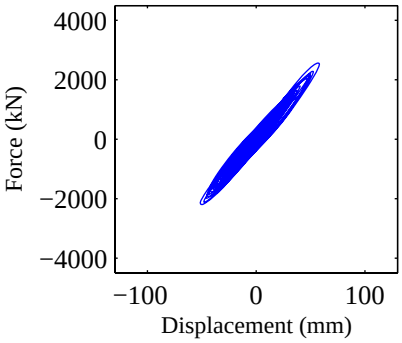

(g) Transverse disp.-force

Response Summary

	Pier1	Pier2	Pier3	Pier4	Joint1	Joint2	Joint3	Joint4
Max Long. Disp.(mm)	68.0	66.8	66.8	68.0	69.0	66.5	66.5	69.1
Max Trans. Disp.(mm)	60.1	57.9	58.2	60.6	39.2	37.1	36.6	38.8
Max Tor. Rot.(degree)	0.065	0.070	0.070	0.064	0.066	0.067	0.066	0.066
Pounding Events	NA	NA	NA	NA	0	0	0	0

Input Earthquake: Morgan Hill, 1984 **Station**: Gilroy Array **Scaling Factor**: 2.00
Input Direction: Longitudinal – 90 comp.
Transverse – 00 comp.
Skew Angle: 60 degree

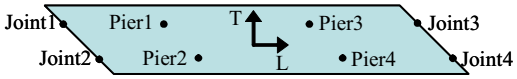

Input Time-histories

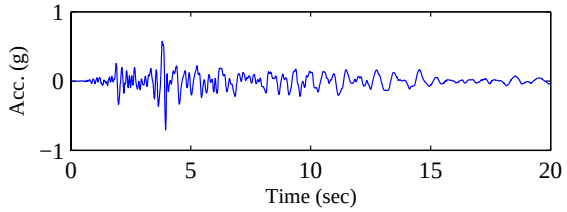

(a) Longitudinal Input

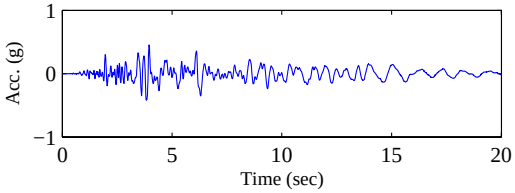

(b) Transverse Input

RC Pier Responses (Pier4)

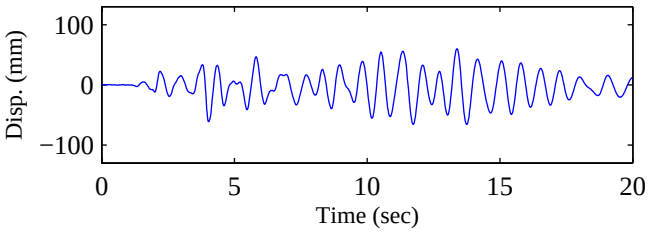

(c) Longitudinal displacement

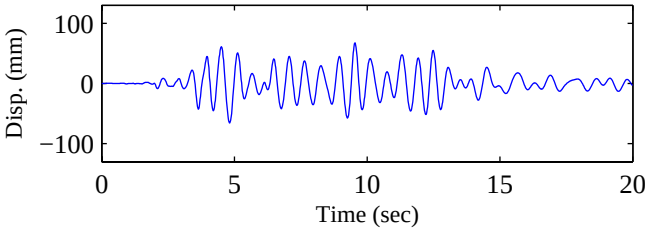

(d) Transverse displacement

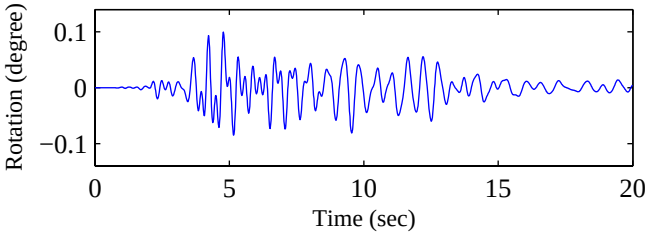

(e) Rotational displacement

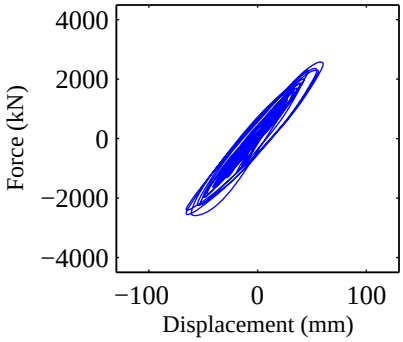

(f) Longitudinal disp.-force

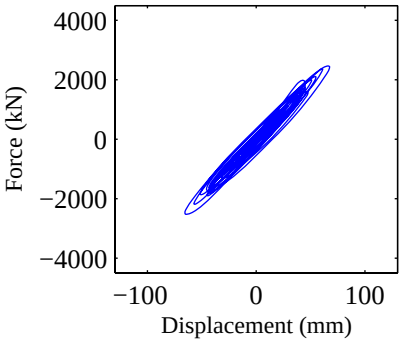

(g) Transverse disp.-force

Response Summary

	Pier1	Pier2	Pier3	Pier4	Joint1	Joint2	Joint3	Joint4
Max Long. Disp.(mm)	67.2	65.9	65.8	67.1	68.4	66.0	65.9	68.4
Max Trans. Disp.(mm)	76.1	67.5	67.6	76.4	49.9	42.7	41.9	49.6
Max Tor. Rot.(degree)	0.075	0.100	0.100	0.074	0.077	0.080	0.080	0.076
Pounding Events	NA	NA	NA	NA	0	0	0	0

Input Earthquake: Landers, 1992 **Station**: Coolwater **Scaling Factor**: 1.07

Input Direction: Longitudinal – 00 comp.
Transverse – 90 comp.

Skew Angle: 0 degree

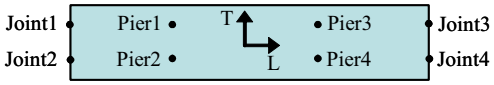

Input Time-histories

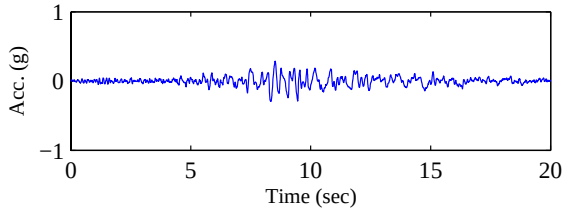

(a) Longitudinal Input

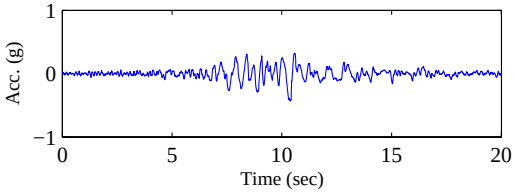

(b) Transverse Input

RC Pier Responses (Pier4)

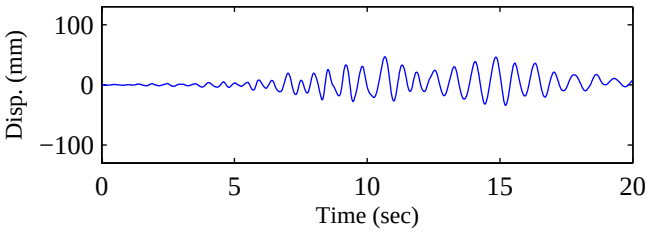

(c) Longitudinal displacement

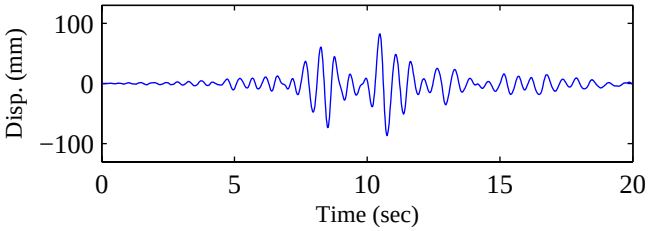

(d) Transverse displacement

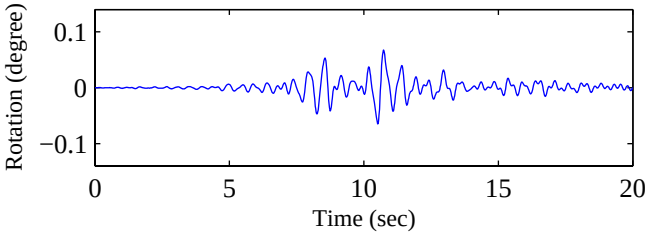

(e) Rotational displacement

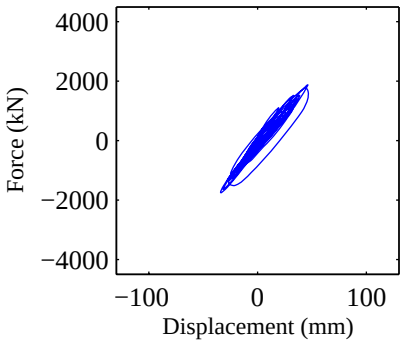

(f) Longitudinal disp.-force

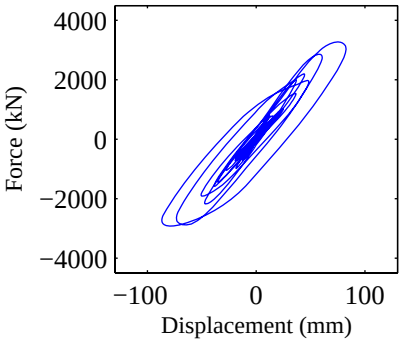

(g) Transverse disp.-force

Response Summary

	Pier1	Pier2	Pier3	Pier4	Joint1	Joint2	Joint3	Joint4
Max Long. Disp.(mm)	45.3	46.7	46.7	45.3	45.1	48.5	48.6	45.1
Max Trans. Disp.(mm)	86.6	86.6	86.8	86.7	37.1	37.1	37.0	37.1
Max Tor. Rot.(degree)	0.069	0.068	0.068	0.069	0.092	0.092	0.092	0.093
Pounding Events	NA	NA	NA	NA	0	0	0	0

Input Earthquake: Landers, 1992 **Station**: Coolwater **Scaling Factor**: 1.07

Input Direction: Longitudinal – 00 comp.
Transverse – 90 comp.

Skew Angle: 30 degree

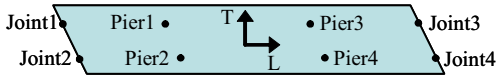

Input Time-histories

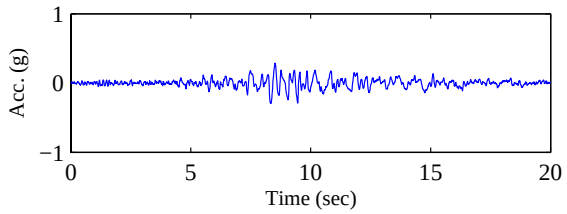

(a) Longitudinal Input

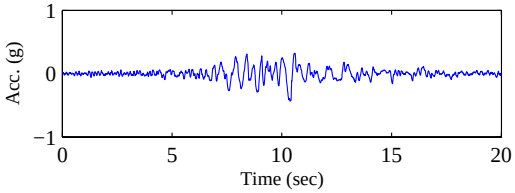

(b) Transverse Input

RC Pier Responses (Pier4)

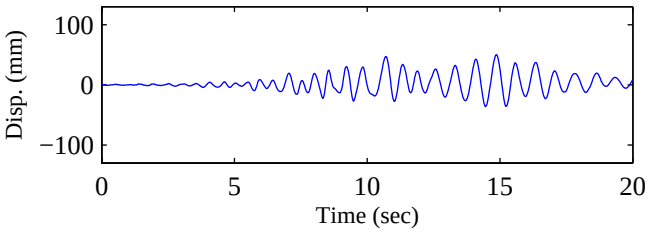

(c) Longitudinal displacement

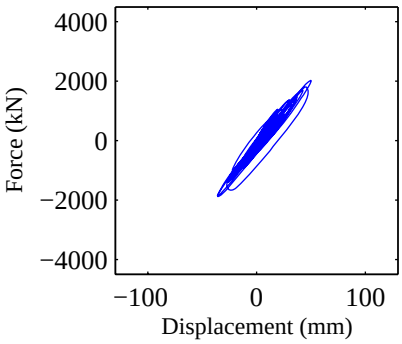

(f) Longitudinal disp.-force

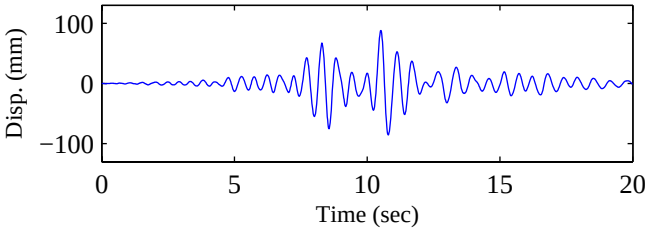

(d) Transverse displacement

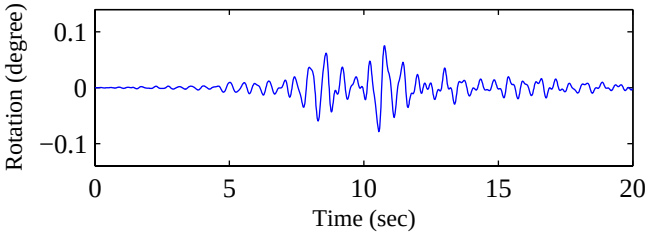

(e) Rotational displacement

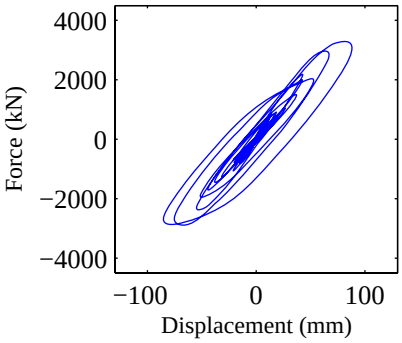

(g) Transverse disp.-force

Response Summary

	Pier1	Pier2	Pier3	Pier4	Joint1	Joint2	Joint3	Joint4
Max Long. Disp.(mm)	49.2	50.2	50.3	49.1	49.0	50.9	51.0	48.9
Max Trans. Disp.(mm)	91.4	88.2	88.3	91.6	41.8	37.0	36.9	41.8
Max Tor. Rot.(degree)	0.069	0.078	0.079	0.069	0.093	0.094	0.095	0.093
Pounding Events	NA	NA	NA	NA	0	0	0	0

Input Earthquake: Landers, 1992 **Station**: Coolwater **Scaling Factor**: 1.07

Input Direction: Longitudinal – 00 comp.
Transverse – 90 comp.

Skew Angle: 60 degree

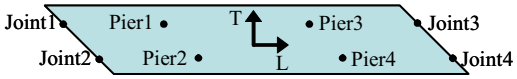

Input Time-histories

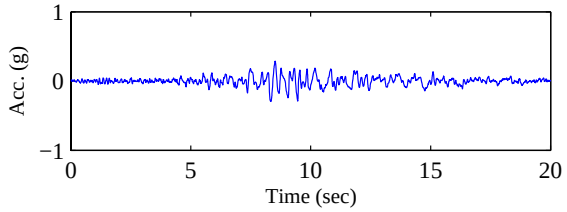

(a) Longitudinal Input

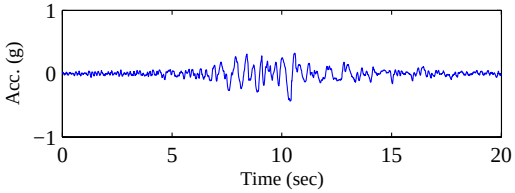

(b) Transverse Input

RC Pier Responses (Pier4)

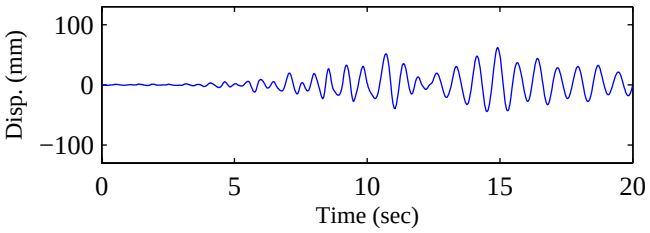

(c) Longitudinal displacement

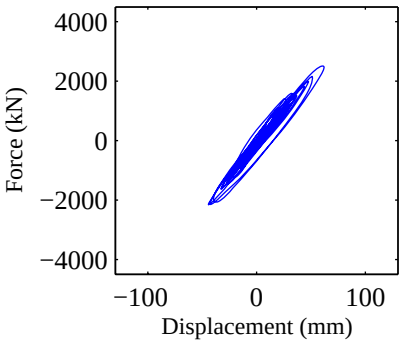

(f) Longitudinal disp.-force

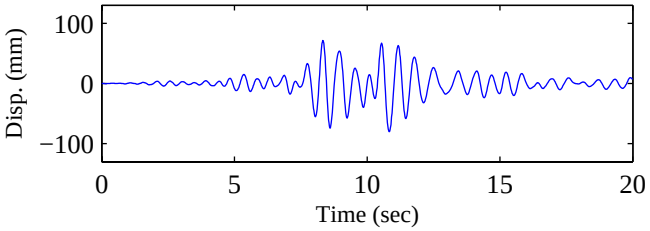

(d) Transverse displacement

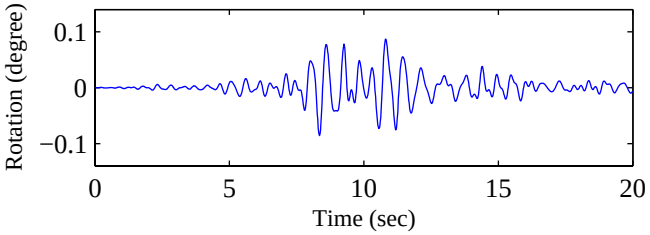

(e) Rotational displacement

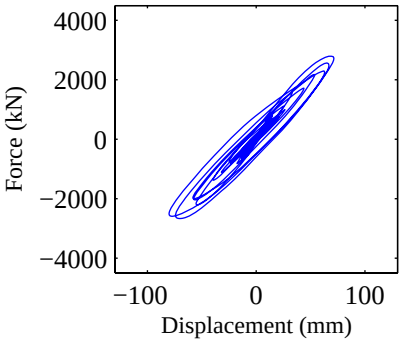

(g) Transverse disp.-force

Response Summary

	Pier1	Pier2	Pier3	Pier4	Joint1	Joint2	Joint3	Joint4
Max Long. Disp.(mm)	60.9	62.0	62.1	60.8	60.8	62.7	62.8	60.8
Max Trans. Disp.(mm)	89.7	80.1	80.2	89.3	37.6	23.1	23.0	37.5
Max Tor. Rot.(degree)	0.062	0.087	0.087	0.063	0.081	0.087	0.085	0.079
Pounding Events	NA	NA	NA	NA	0	0	0	0

Input Earthquake: Landers, 1992 **Station**: Coolwater **Scaling Factor**: 1.07

Input Direction: Diagonal 1 – NS comp.
Diagonal 2 – EW comp.

Skew Angle: 0 degree

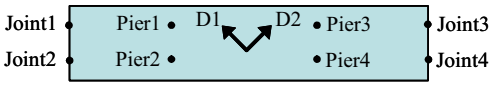

Input Time-histories

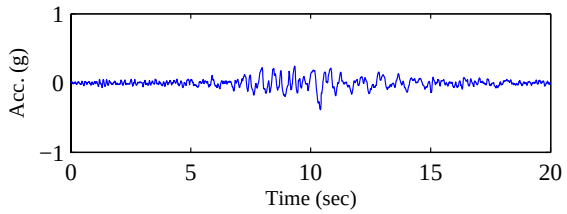

(a) Longitudinal Input

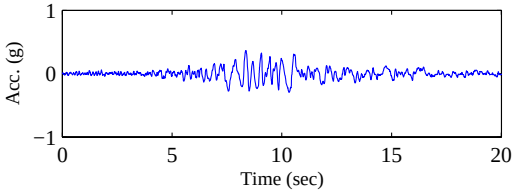

(b) Transverse Input

RC Pier Responses (Pier4)

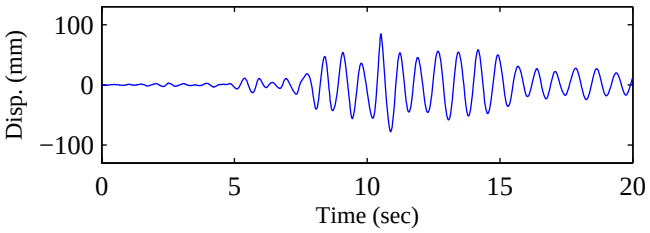

(c) Longitudinal displacement

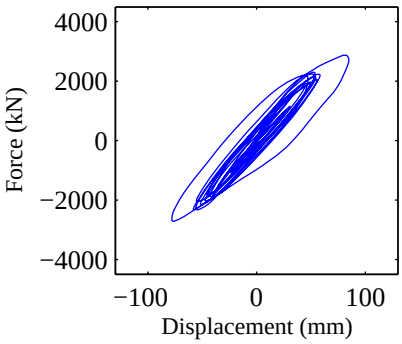

(f) Longitudinal disp.-force

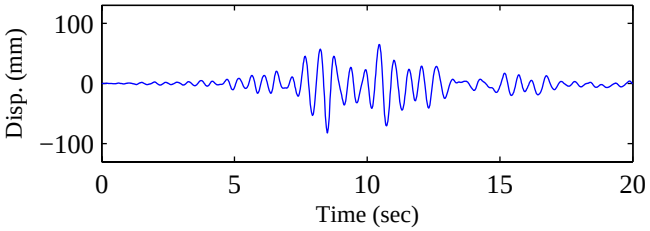

(d) Transverse displacement

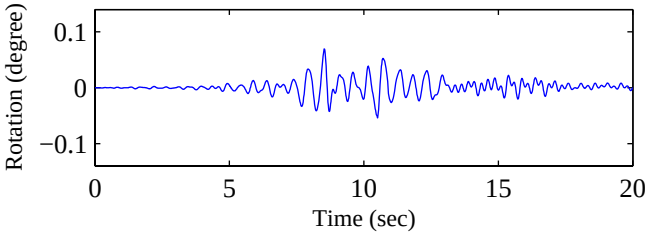

(e) Rotational displacement

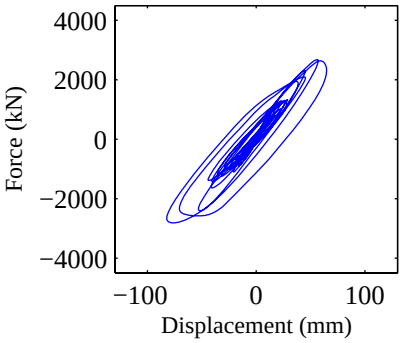

(g) Transverse disp.-force

Response Summary

	Pier1	Pier2	Pier3	Pier4	Joint1	Joint2	Joint3	Joint4
Max Long. Disp.(mm)	84.5	82.8	84.8	90.2	80.5	79.2	84.9	93.0
Max Trans. Disp.(mm)	82.2	82.2	82.2	82.2	31.4	31.4	30.9	30.9
Max Tor. Rot.(degree)	0.069	0.069	0.070	0.069	0.090	0.090	0.090	0.090
Pounding Events	NA	NA	NA	NA	1	1	1	1

Input Earthquake: Landers, 1992 **Station**: Coolwater **Scaling Factor**: 1.07

Input Direction: Diagonal 1 – NS comp.
Diagonal 2 – EW comp.

Skew Angle: 30 degree

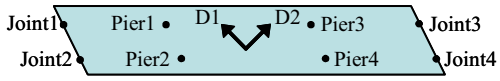

Input Time-histories

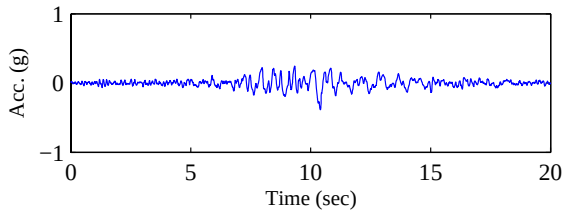

(a) Longitudinal Input

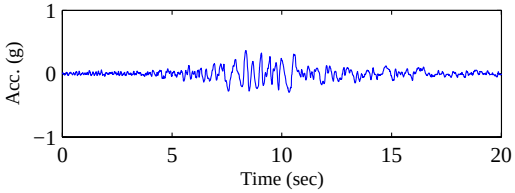

(b) Transverse Input

RC Pier Responses (Pier4)

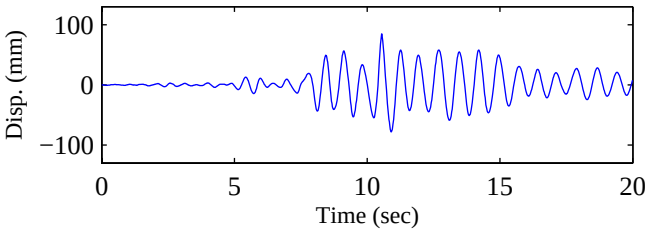

(c) Longitudinal displacement

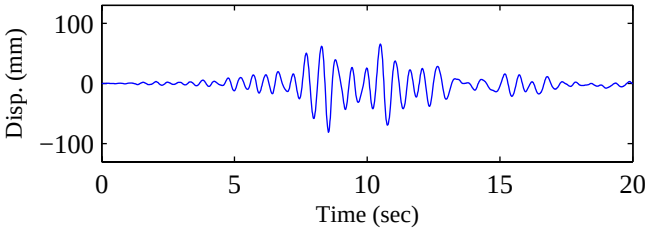

(d) Transverse displacement

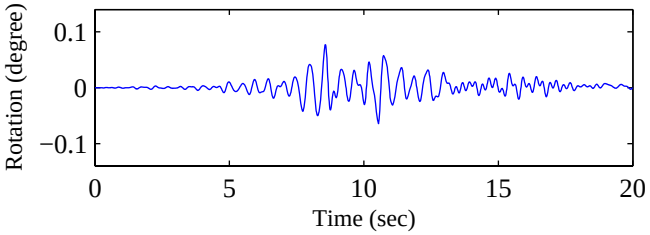

(e) Rotational displacement

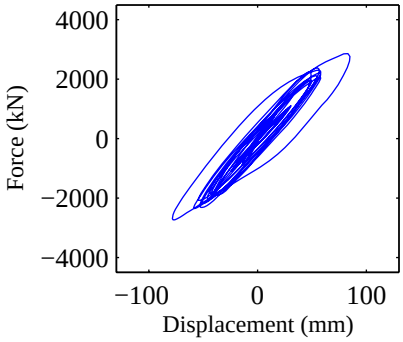

(f) Longitudinal disp.-force

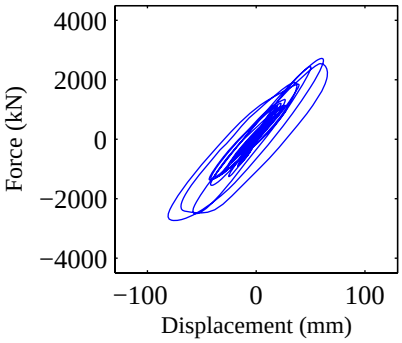

(g) Transverse disp.-force

Response Summary

	Pier1	Pier2	Pier3	Pier4	Joint1	Joint2	Joint3	Joint4
Max Long. Disp.(mm)	86.8	85.7	82.6	82.8	88.8	87.0	79.0	79.4
Max Trans. Disp.(mm)	81.9	78.5	78.5	81.7	32.8	28.8	28.8	32.8
Max Tor. Rot.(degree)	0.067	0.076	0.076	0.067	0.088	0.089	0.089	0.087
Pounding Events	NA	NA	NA	NA	1	1	0	0

Input Earthquake: Landers, 1992 **Station**: Coolwater **Scaling Factor**: 1.07

Input Direction: Diagonal 1 – NS comp.
Diagonal 2 – EW comp.

Skew Angle: 60 degree

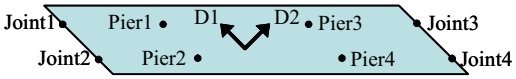

Input Time-histories

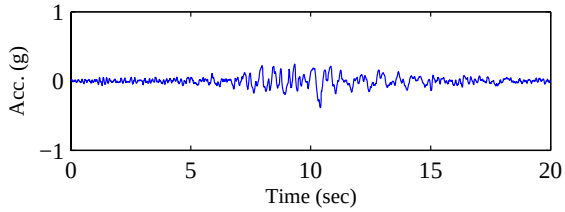

(a) Longitudinal Input

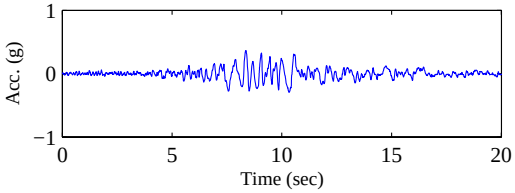

(b) Transverse Input

RC Pier Responses (Pier4)

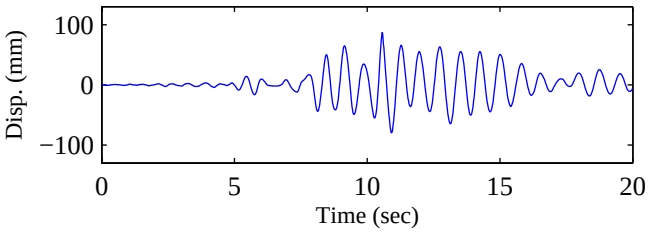

(c) Longitudinal displacement

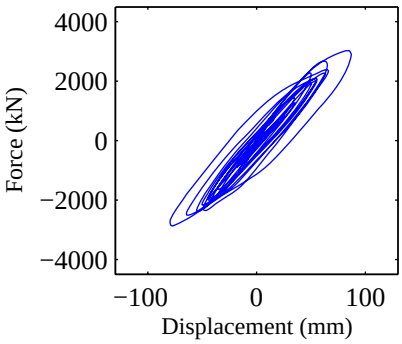

(f) Longitudinal disp.-force

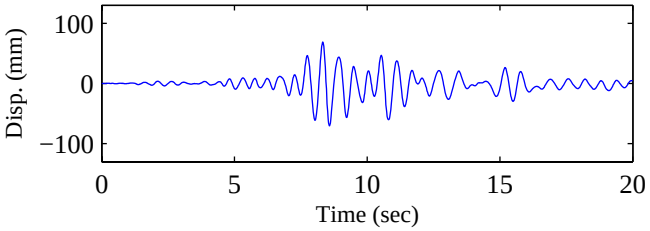

(d) Transverse displacement

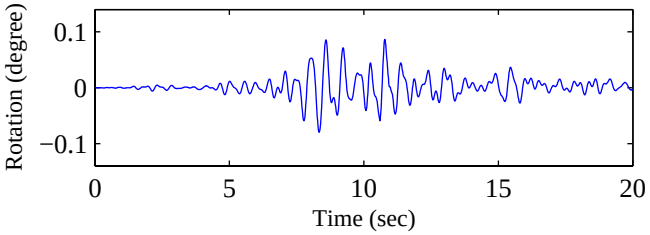

(e) Rotational displacement

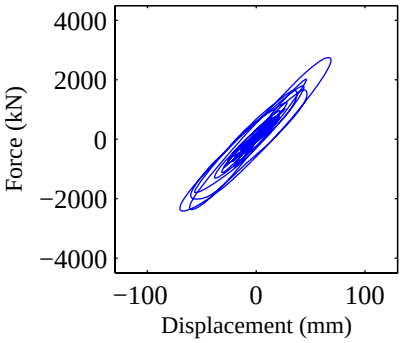

(g) Transverse disp.-force

Response Summary

	Pier1	Pier2	Pier3	Pier4	Joint1	Joint2	Joint3	Joint4
Max Long. Disp.(mm)	85.0	83.6	87.1	90.5	84.2	82.3	87.8	93.6
Max Trans. Disp.(mm)	79.7	70.3	70.5	79.5	34.2	23.9	24.2	33.9
Max Tor. Rot.(degree)	0.062	0.086	0.087	0.064	0.076	0.081	0.080	0.075
Pounding Events	NA	NA	NA	NA	1	1	1	1

Input Earthquake: Landers, 1992 **Station**: Coolwater **Scaling Factor**: 1.07

Input Direction: Longitudinal – 90 comp.
Transverse – 00 comp.

Skew Angle: 0 degree

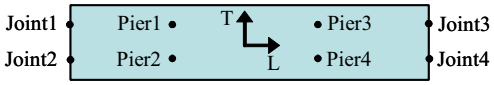

Input Time-histories

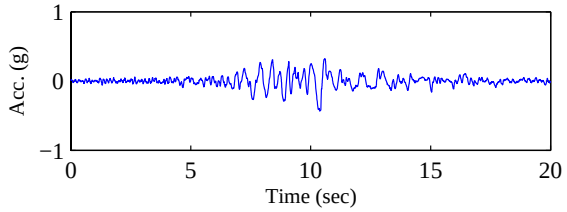

(a) Longitudinal Input

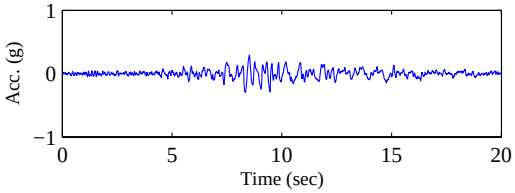

(b) Transverse Input

RC Pier Responses (Pier4)

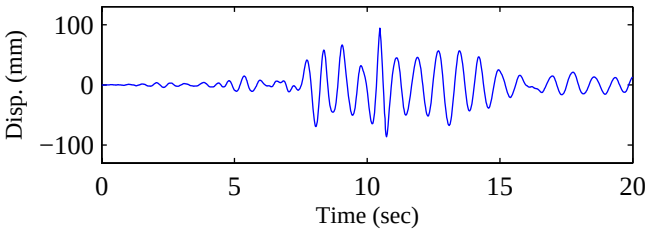

(c) Longitudinal displacement

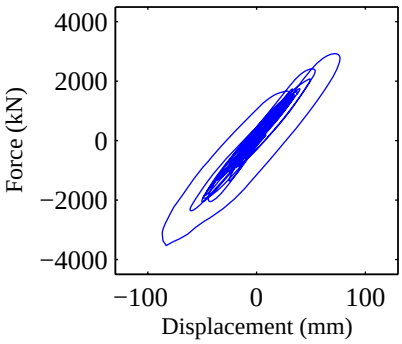

(f) Longitudinal disp.-force

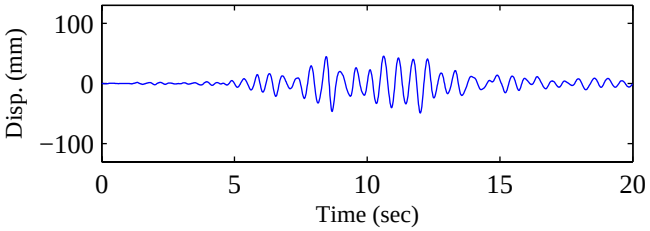

(d) Transverse displacement

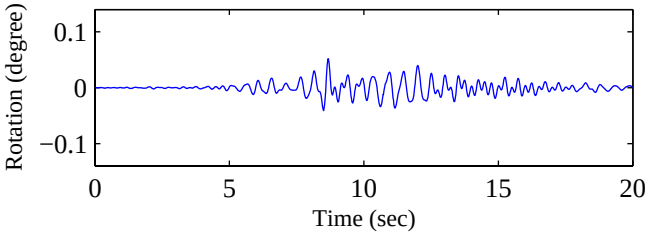

(e) Rotational displacement

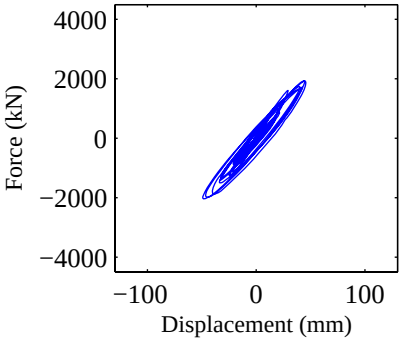

(g) Transverse disp.-force

Response Summary

	Pier1	Pier2	Pier3	Pier4	Joint1	Joint2	Joint3	Joint4
Max Long. Disp.(mm)	90.3	92.1	94.4	93.7	91.9	94.6	96.8	96.1
Max Trans. Disp.(mm)	49.2	49.2	49.2	49.2	23.5	23.5	23.2	23.2
Max Tor. Rot.(degree)	0.050	0.053	0.052	0.050	0.059	0.059	0.058	0.058
Pounding Events	NA	NA	NA	NA	1	1	1	1

Input Earthquake: Landers, 1992 **Station**: Coolwater **Scaling Factor**: 1.07

Input Direction: Longitudinal – 90 comp.
Transverse – 00 comp.

Skew Angle: 30 degree

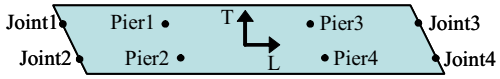

Input Time-histories

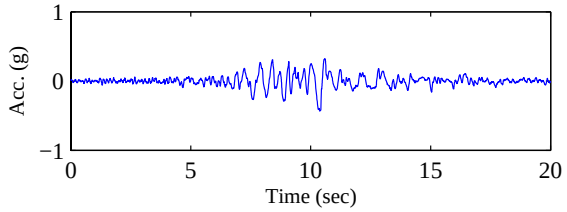

(a) Longitudinal Input

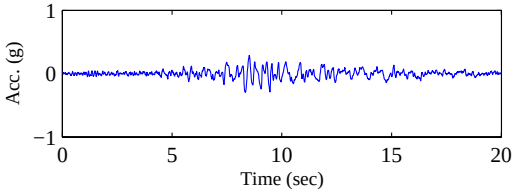

(b) Transverse Input

RC Pier Responses (Pier4)

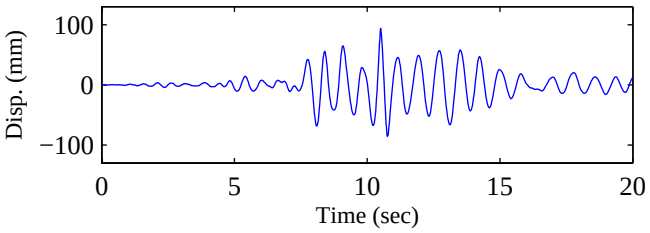

(c) Longitudinal displacement

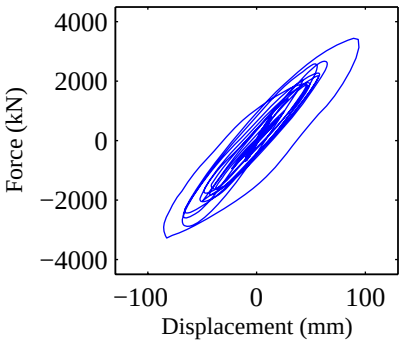

(f) Longitudinal disp.-force

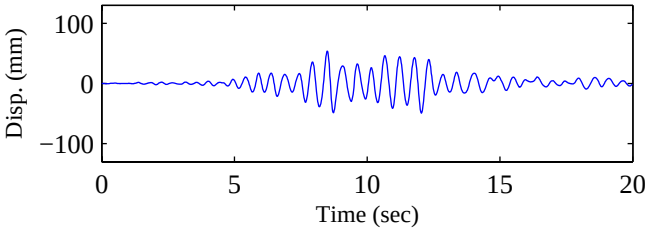

(d) Transverse displacement

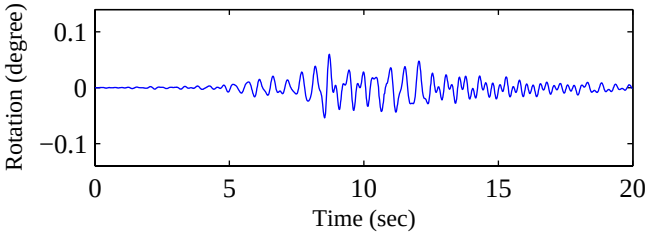

(e) Rotational displacement

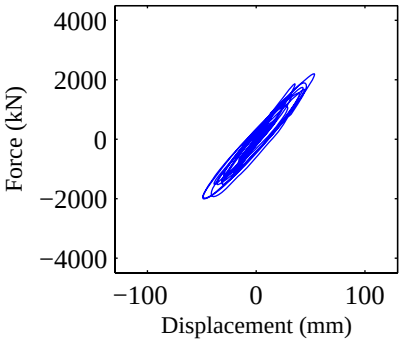

(g) Transverse disp.-force

Response Summary

	Pier1	Pier2	Pier3	Pier4	Joint1	Joint2	Joint3	Joint4
Max Long. Disp.(mm)	89.4	91.3	94.2	92.9	91.0	93.8	96.8	95.4
Max Trans. Disp.(mm)	55.6	53.6	53.7	55.9	27.5	24.9	24.9	27.6
Max Tor. Rot.(degree)	0.053	0.061	0.060	0.052	0.062	0.063	0.062	0.061
Pounding Events	NA	NA	NA	NA	1	1	1	1

Input Earthquake: Landers, 1992 **Station**: Coolwater **Scaling Factor**: 1.07

Input Direction: Longitudinal – 90 comp.
Transverse – 00 comp.

Skew Angle: 60 degree

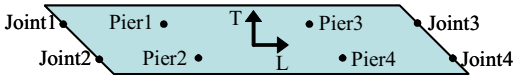

Input Time-histories

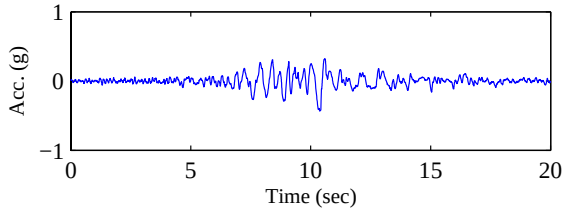

(a) Longitudinal Input

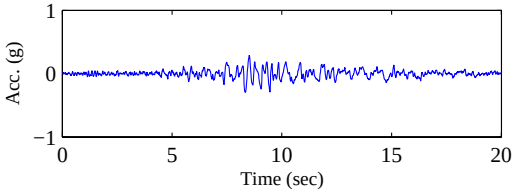

(b) Transverse Input

RC Pier Responses (Pier4)

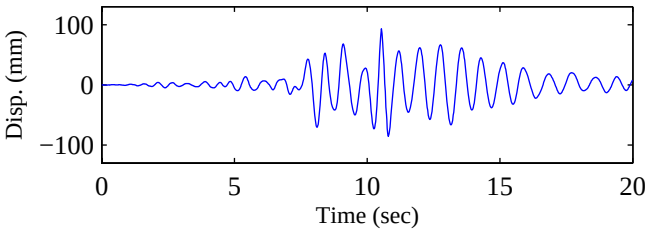

(c) Longitudinal displacement

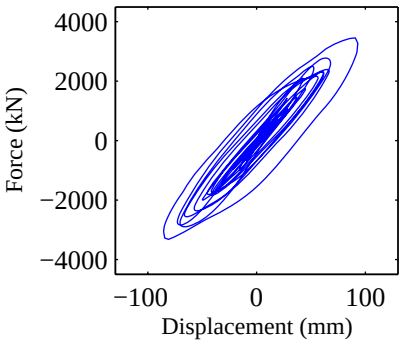

(f) Longitudinal disp.-force

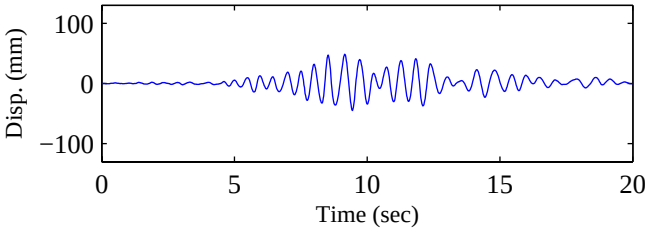

(d) Transverse displacement

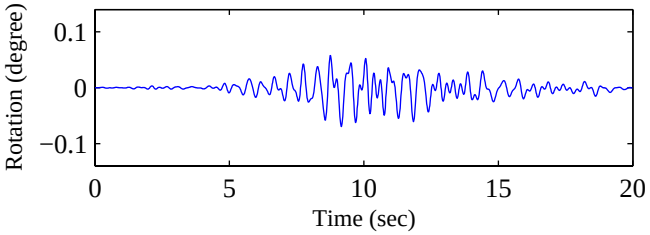

(e) Rotational displacement

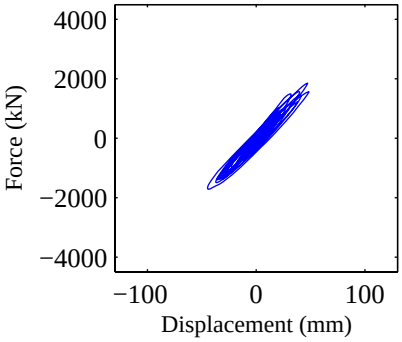

(g) Transverse disp.-force

Response Summary

	Pier1	Pier2	Pier3	Pier4	Joint1	Joint2	Joint3	Joint4
Max Long. Disp.(mm)	88.7	90.9	93.2	93.6	90.2	93.3	95.6	95.9
Max Trans. Disp.(mm)	55.7	48.4	48.5	55.9	29.4	22.3	22.3	29.4
Max Tor. Rot.(degree)	0.049	0.069	0.069	0.049	0.057	0.061	0.061	0.057
Pounding Events	NA	NA	NA	NA	1	1	1	1

Input Earthquake: Taiwan SMART1, 1986 **Station**: SMART1 E01

Scaling Factor: 2.55

Input Direction: Longitudinal – 00 comp.
Transverse – 90 comp.

Skew Angle: 0 degree

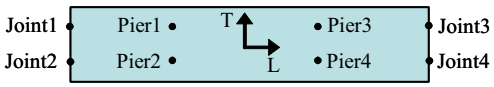

Input Time-histories

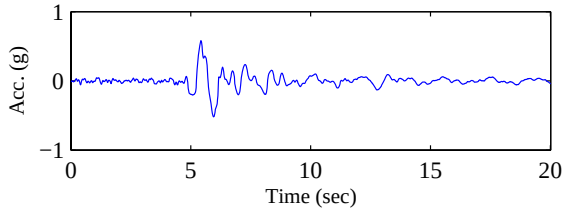

(a) Longitudinal Input

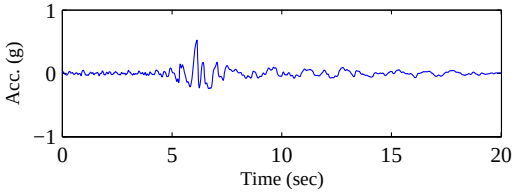

(b) Transverse Input

RC Pier Responses (Pier4)

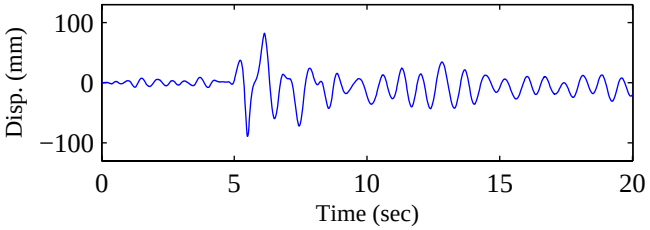

(c) Longitudinal displacement

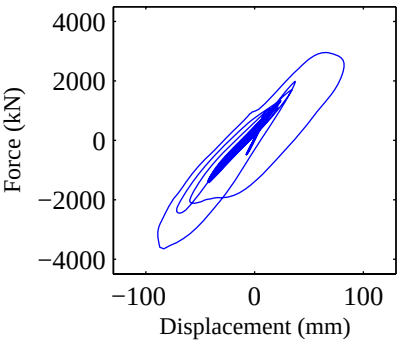

(f) Longitudinal disp.-force

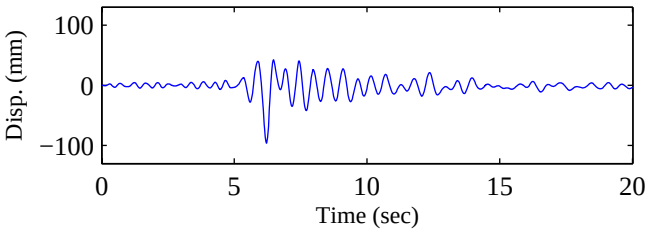

(d) Transverse displacement

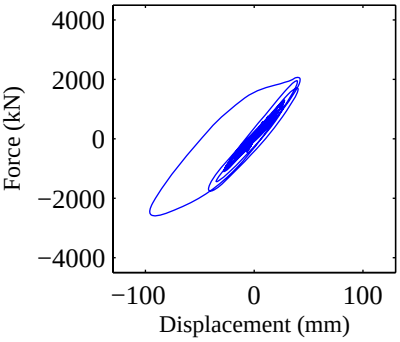

(g) Transverse disp.-force

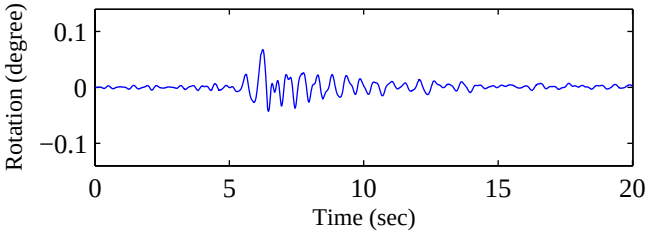

(e) Rotational displacement

Response Summary

	Pier1	Pier2	Pier3	Pier4	Joint1	Joint2	Joint3	Joint4
Max Long. Disp.(mm)	96.8	96.0	89.1	89.3	99.9	98.4	84.9	82.0
Max Trans. Disp.(mm)	94.6	94.6	96.2	96.2	40.7	40.7	33.8	33.8
Max Tor. Rot.(degree)	0.073	0.073	0.068	0.068	0.099	0.099	0.101	0.101
Pounding Events	NA	NA	NA	NA	1	1	1	1

Input Earthquake: Taiwan SMART1, 1986 **Station**: SMART1 E01

Scaling Factor: 2.55

Input Direction: Longitudinal – 00 comp.
Transverse – 90 comp.

Skew Angle: 30 degree

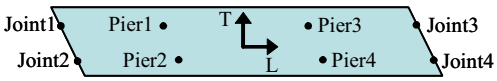

Input Time-histories

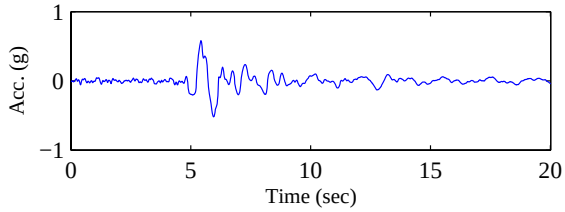

(a) Longitudinal Input

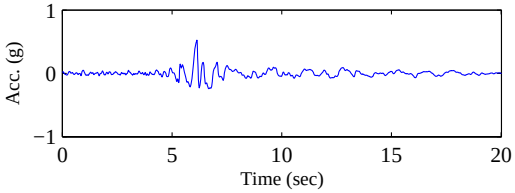

(b) Transverse Input

RC Pier Responses (Pier4)

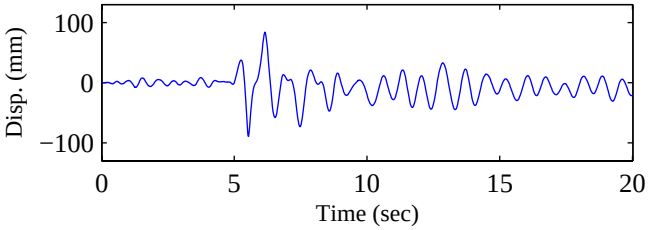

(c) Longitudinal displacement

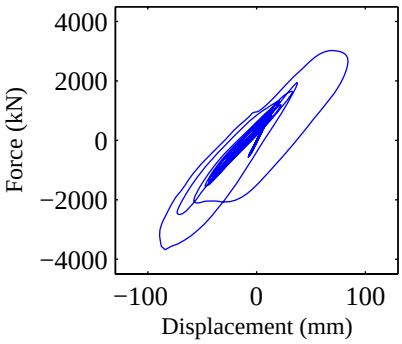

(f) Longitudinal disp.-force

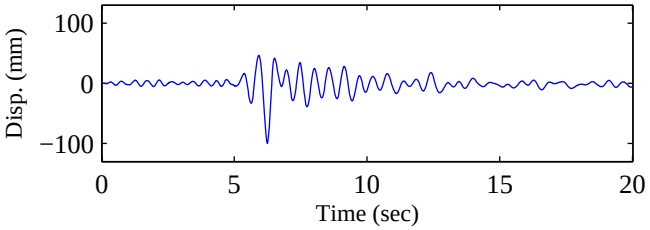

(d) Transverse displacement

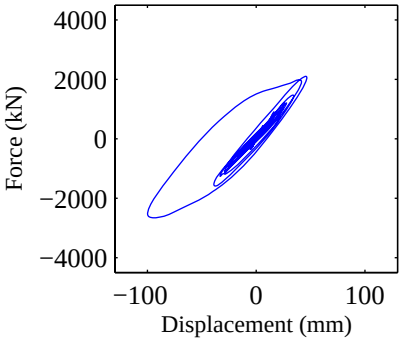

(g) Transverse disp.-force

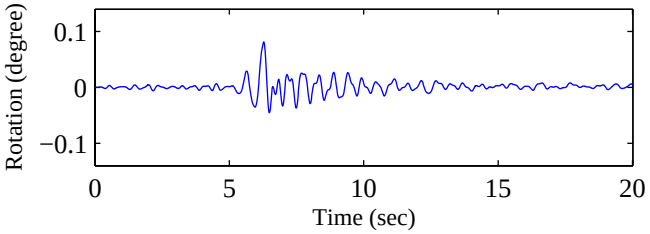

(e) Rotational displacement

Response Summary

	Pier1	Pier2	Pier3	Pier4	Joint1	Joint2	Joint3	Joint4
Max Long. Disp.(mm)	97.1	96.3	89.3	89.5	100.4	98.6	86.5	82.1
Max Trans. Disp.(mm)	103.5	99.9	99.9	103.6	44.4	39.1	31.6	38.5
Max Tor. Rot.(degree)	0.077	0.086	0.081	0.073	0.107	0.109	0.106	0.105
Pounding Events	NA	NA	NA	NA	1	1	1	1

Input Earthquake: Taiwan SMART1, 1986 **Station**: SMART1 E01

Scaling Factor: 2.55

Input Direction: Longitudinal – 00 comp.
Transverse – 90 comp.

Skew Angle: 60 degree

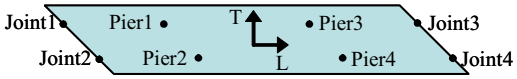

Input Time-histories

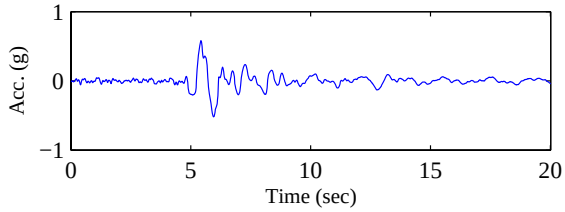

(a) Longitudinal Input

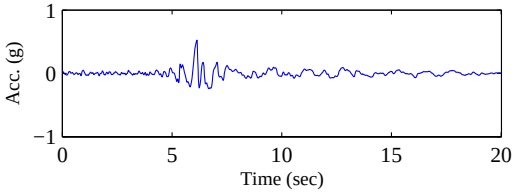

(b) Transverse Input

RC Pier Responses (Pier4)

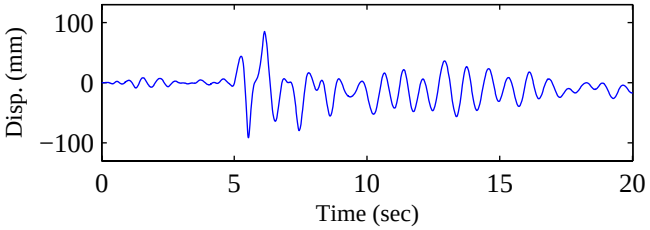

(c) Longitudinal displacement

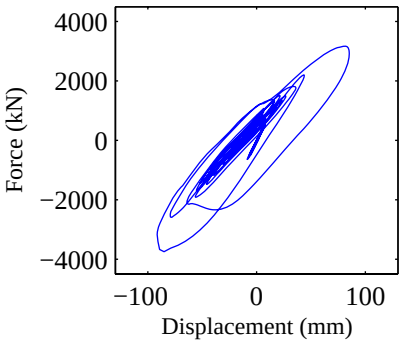

(f) Longitudinal disp.-force

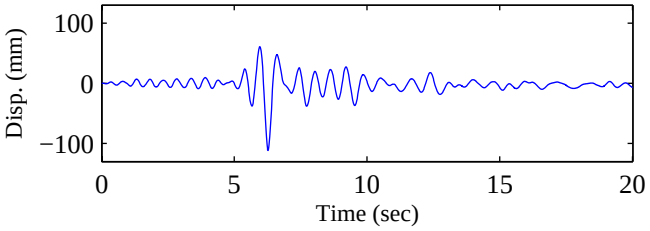

(d) Transverse displacement

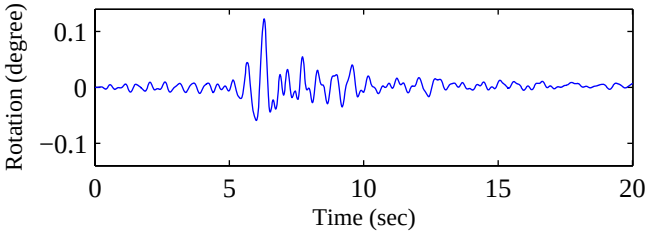

(e) Rotational displacement

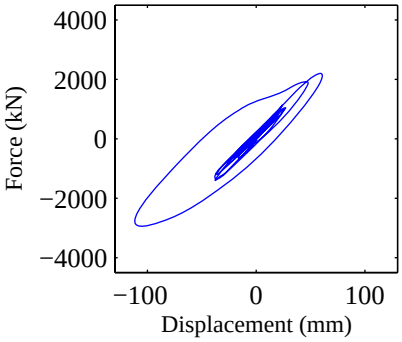

(g) Transverse disp.-force

Response Summary

	Pier1	Pier2	Pier3	Pier4	Joint1	Joint2	Joint3	Joint4
Max Long. Disp.(mm)	100.2	100.3	91.4	91.5	103.7	103.4	87.5	85.2
Max Trans. Disp.(mm)	125.6	110.9	111.8	123.2	50.6	32.1	26.4	47.3
Max Tor. Rot.(degree)	0.096	0.126	0.123	0.093	0.115	0.124	0.119	0.111
Pounding Events	NA	NA	NA	NA	2	2	1	1

Input Earthquake: Taiwan SMART1, 1986 **Station**: SMART1 E01

Scaling Factor: 2.55

Input Direction: Diagonal 1 – NS comp.
Diagonal 2 – EW comp.

Skew Angle: 0 degree

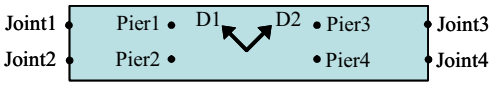

Input Time-histories

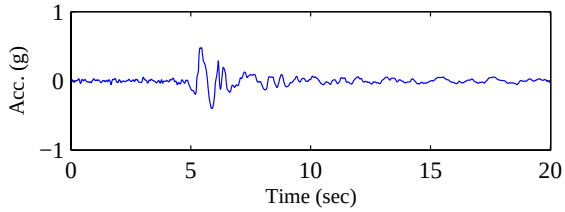

(a) Longitudinal Input

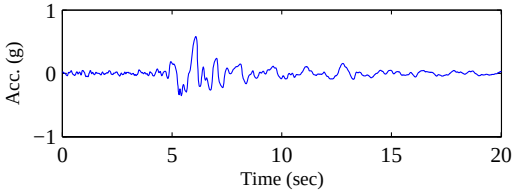

(b) Transverse Input

RC Pier Responses (Pier4)

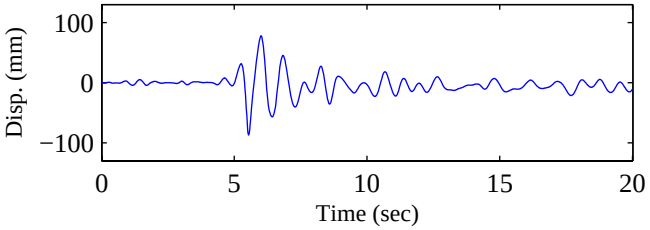

(c) Longitudinal displacement

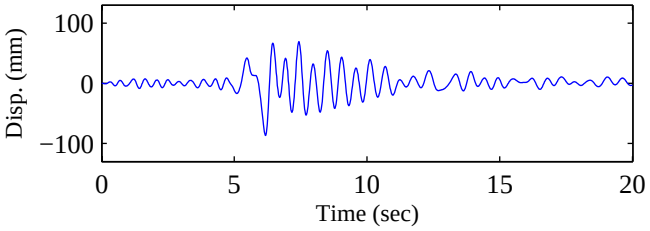

(d) Transverse displacement

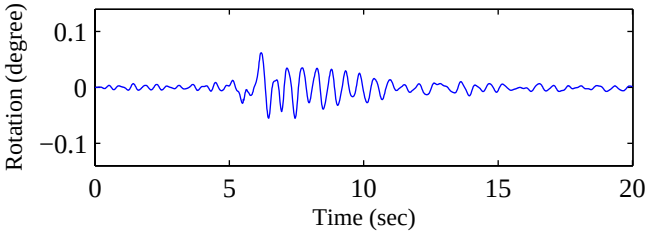

(e) Rotational displacement

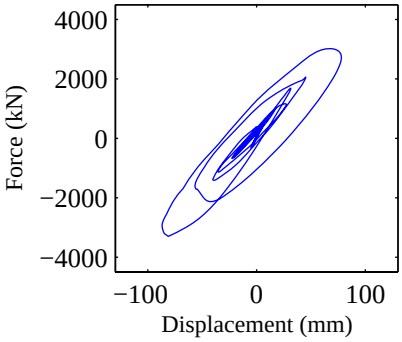

(f) Longitudinal disp.-force

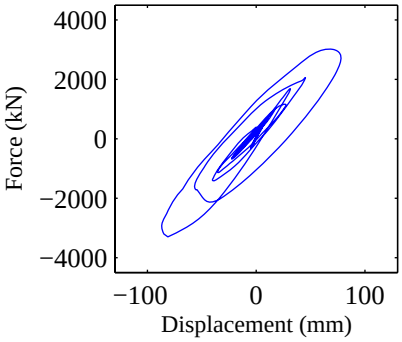

(g) Transverse disp.-force

Response Summary

	Pier1	Pier2	Pier3	Pier4	Joint1	Joint2	Joint3	Joint4
Max Long. Disp.(mm)	90.6	93.8	87.0	85.9	91.8	97.0	81.3	80.1
Max Trans. Disp.(mm)	86.0	85.9	86.8	86.8	31.3	31.3	31.6	31.6
Max Tor. Rot.(degree)	0.062	0.063	0.062	0.061	0.089	0.089	0.090	0.090
Pounding Events	NA	NA	NA	NA	1	1	1	1

Input Earthquake: Taiwan SMART1, 1986 **Station**: SMART1 E01

Scaling Factor: 2.55

Input Direction: Diagonal 1 – NS comp.
Diagonal 2 – EW comp.

Skew Angle: 30 degree

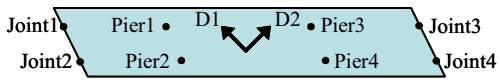

Input Time-histories

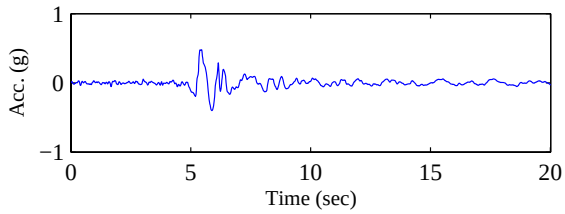

(a) Longitudinal Input

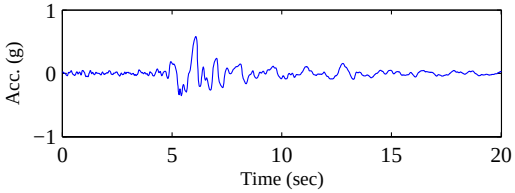

(b) Transverse Input

RC Pier Responses (Pier4)

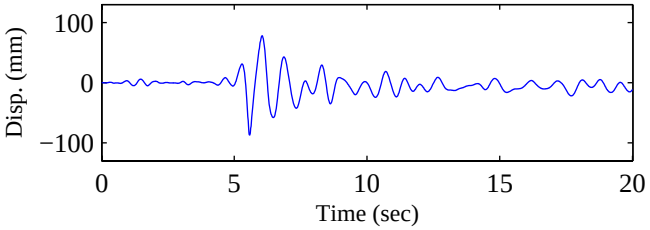

(c) Longitudinal displacement

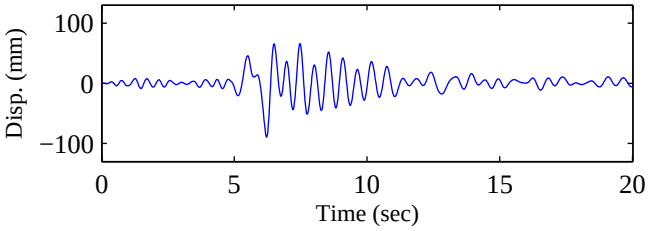

(d) Transverse displacement

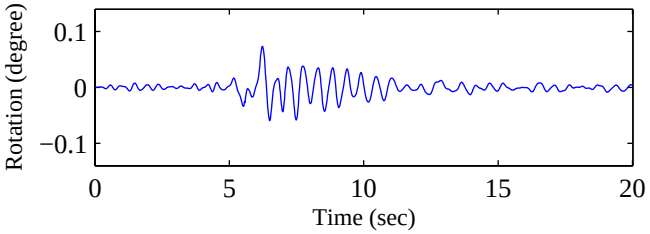

(e) Rotational displacement

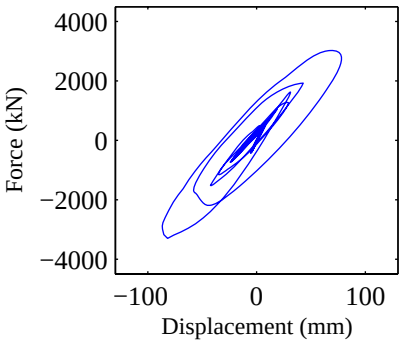

(f) Longitudinal disp.-force

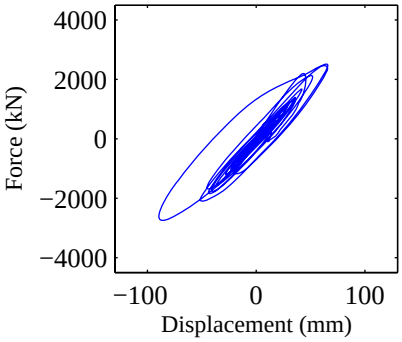

(g) Transverse disp.-force

Response Summary

	Pier1	Pier2	Pier3	Pier4	Joint1	Joint2	Joint3	Joint4
Max Long. Disp.(mm)	90.6	94.0	86.9	86.1	91.8	97.1	81.2	80.1
Max Trans. Disp.(mm)	92.0	88.6	89.5	93.0	35.3	29.4	30.1	35.5
Max Tor. Rot.(degree)	0.063	0.073	0.073	0.064	0.092	0.094	0.097	0.095
Pounding Events	NA	NA	NA	NA	1	1	1	1

Input Earthquake: Taiwan SMART1, 1986 **Station**: SMART1 E01

Scaling Factor: 2.55

Input Direction: Diagonal 1 – NS comp.
Diagonal 2 – EW comp.

Skew Angle: 60 degree

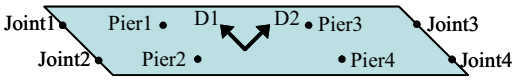

Input Time-histories

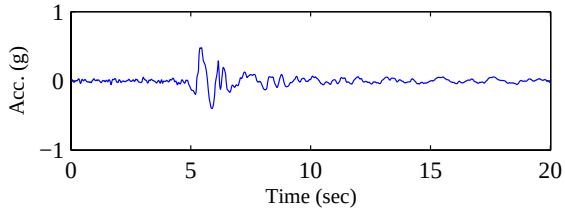

(a) Longitudinal Input

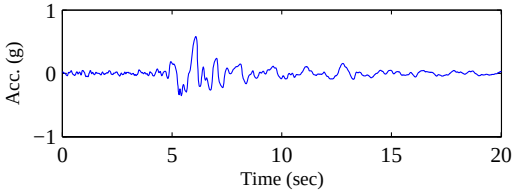

(b) Transverse Input

RC Pier Responses (Pier4)

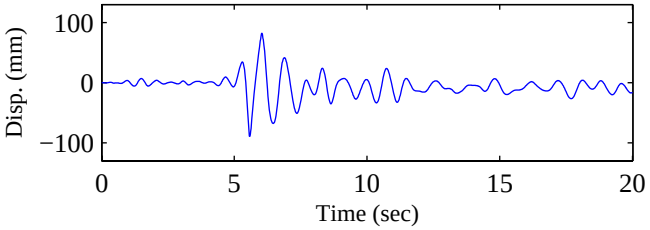

(c) Longitudinal displacement

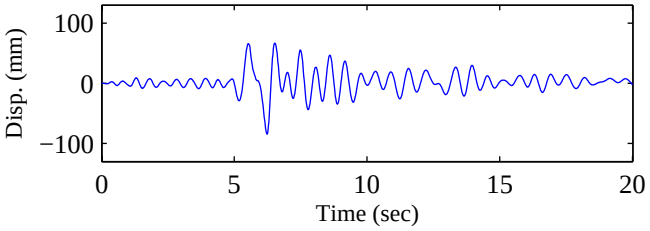

(d) Transverse displacement

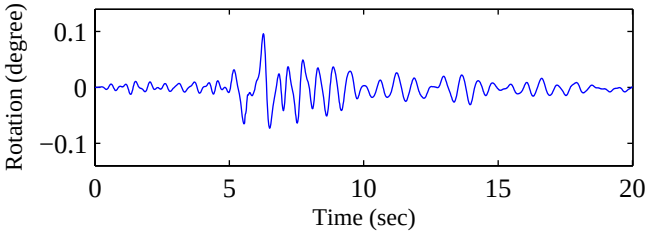

(e) Rotational displacement

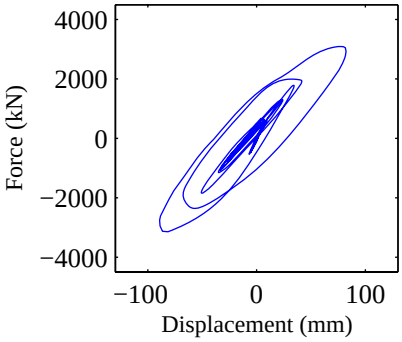

(f) Longitudinal disp.-force

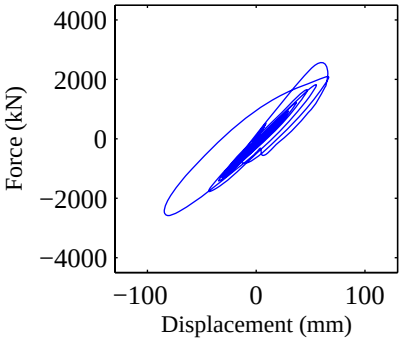

(g) Transverse disp.-force

Response Summary

	Pier1	Pier2	Pier3	Pier4	Joint1	Joint2	Joint3	Joint4
Max Long. Disp.(mm)	92.8	97.4	89.2	87.9	93.8	101.2	83.8	81.3
Max Trans. Disp.(mm)	94.6	84.0	84.5	93.9	38.9	28.7	32.4	44.0
Max Tor. Rot.(degree)	0.066	0.094	0.096	0.068	0.087	0.094	0.094	0.088
Pounding Events	NA	NA	NA	NA	1	1	1	1

Input Earthquake: Taiwan SMART1, 1986 **Station**: SMART1 E01

Scaling Factor: 2.55

Input Direction: Longitudinal – 90 comp.
Transverse – 00 comp.

Skew Angle: 0 degree

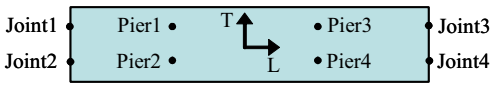

Input Time-histories

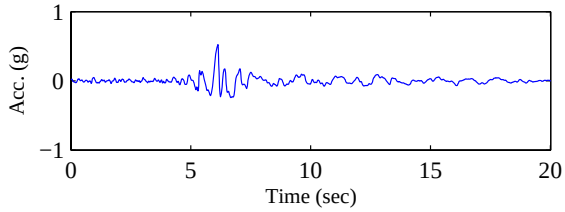

(a) Longitudinal Input

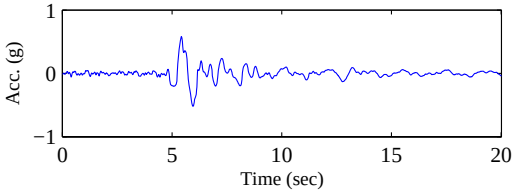

(b) Transverse Input

RC Pier Responses (Pier4)

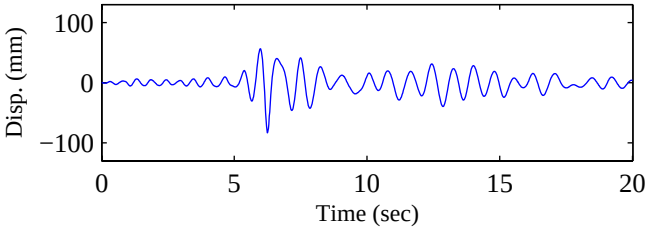

(c) Longitudinal displacement

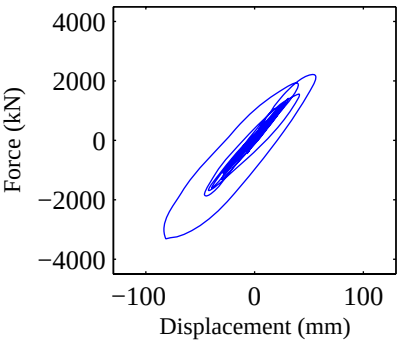

(f) Longitudinal disp.-force

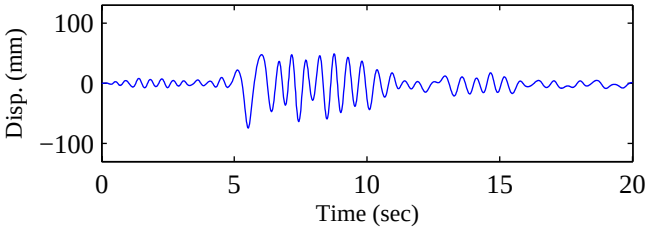

(d) Transverse displacement

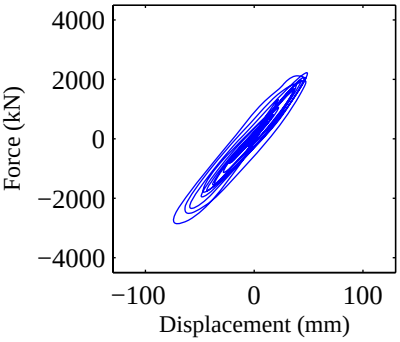

(g) Transverse disp.-force

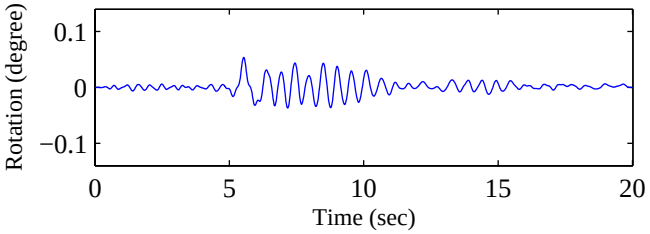

(e) Rotational displacement

Response Summary

	Pier1	Pier2	Pier3	Pier4	Joint1	Joint2	Joint3	Joint4
Max Long. Disp.(mm)	87.2	87.4	83.4	83.5	88.9	88.9	79.6	79.6
Max Trans. Disp.(mm)	74.1	74.1	74.3	74.3	29.5	29.5	29.6	29.6
Max Tor. Rot.(degree)	0.053	0.054	0.054	0.053	0.076	0.076	0.076	0.076
Pounding Events	NA	NA	NA	NA	1	1	0	0

Input Earthquake: Taiwan SMART1, 1986 **Station**: SMART1 E01

Scaling Factor: 2.55

Input Direction: Longitudinal – 90 comp.
Transverse – 00 comp.

Skew Angle: 30 degree

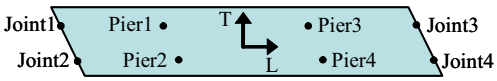

Input Time-histories

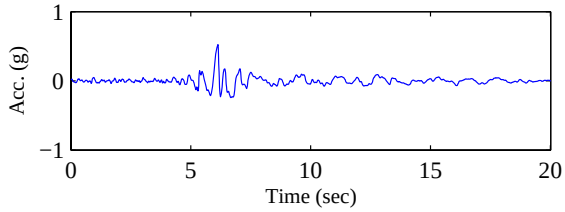

(a) Longitudinal Input

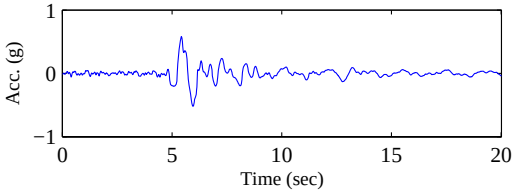

(b) Transverse Input

RC Pier Responses (Pier4)

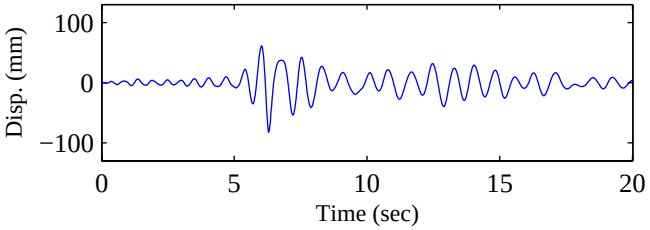

(c) Longitudinal displacement

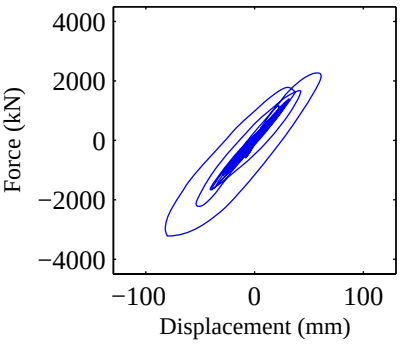

(f) Longitudinal disp.-force

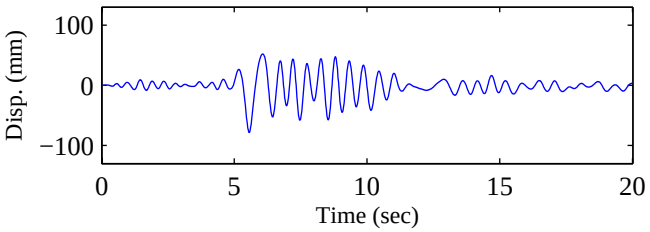

(d) Transverse displacement

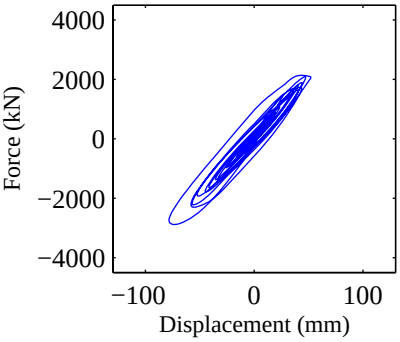

(g) Transverse disp.-force

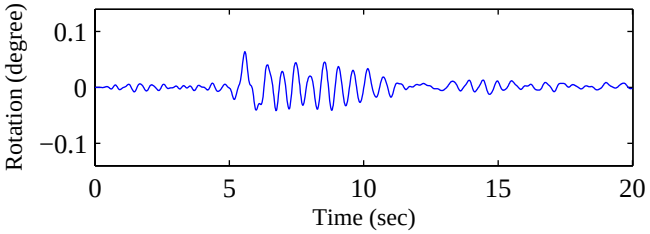

(e) Rotational displacement

Response Summary

	Pier1	Pier2	Pier3	Pier4	Joint1	Joint2	Joint3	Joint4
Max Long. Disp.(mm)	85.4	85.3	82.1	82.2	86.9	86.3	79.0	79.1
Max Trans. Disp.(mm)	81.4	78.4	78.4	81.3	34.3	30.0	29.8	34.1
Max Tor. Rot.(degree)	0.056	0.065	0.064	0.055	0.081	0.083	0.082	0.080
Pounding Events	NA	NA	NA	NA	1	1	0	0

Input Earthquake: Taiwan SMART1, 1986 **Station**: SMART1 E01

Scaling Factor: 2.55

Input Direction: Longitudinal – 90 comp.
Transverse – 00 comp.

Skew Angle: 60 degree

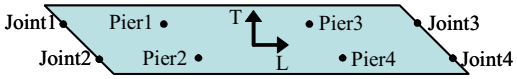

Input Time-histories

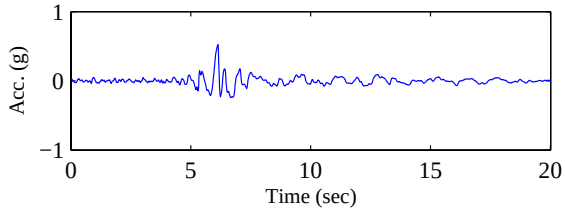

(a) Longitudinal Input

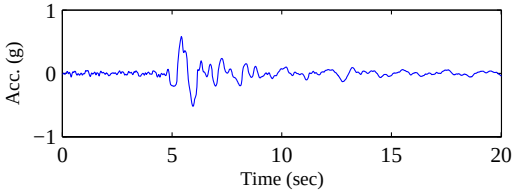

(b) Transverse Input

RC Pier Responses (Pier4)

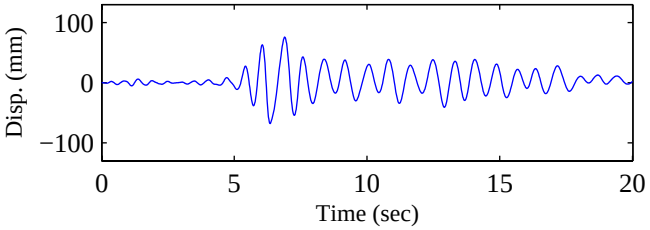

(c) Longitudinal displacement

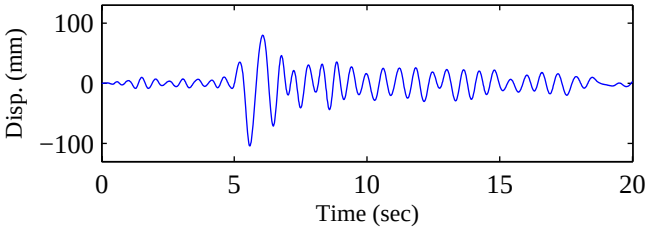

(d) Transverse displacement

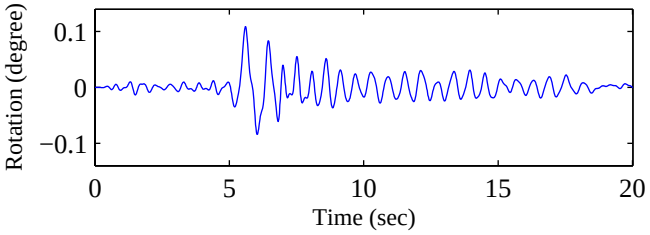

(e) Rotational displacement

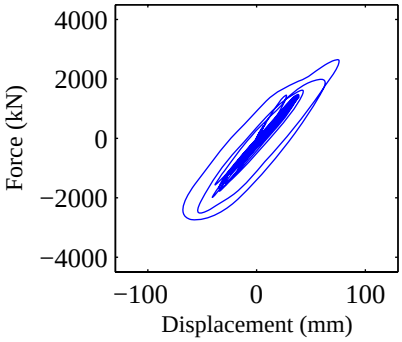

(f) Longitudinal disp.-force

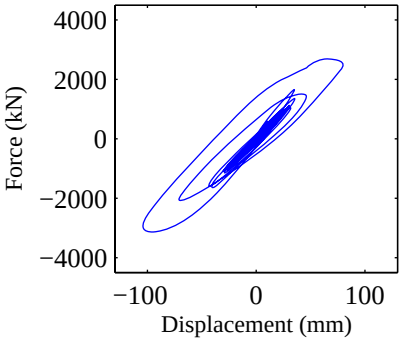

(g) Transverse disp.-force

Response Summary

	Pier1	Pier2	Pier3	Pier4	Joint1	Joint2	Joint3	Joint4
Max Long. Disp.(mm)	76.7	75.8	76.0	77.3	76.9	75.9	76.2	78.4
Max Trans. Disp.(mm)	116.1	103.8	104.1	115.8	49.5	32.3	32.3	49.5
Max Tor. Rot.(degree)	0.077	0.109	0.109	0.076	0.103	0.112	0.110	0.101
Pounding Events	NA	NA	NA	NA	0	0	1	1

Input Earthquake: Loma Prieta, 1986 **Station**: Oakland **Scaling Factor**: 2.02

Input Direction: Longitudinal – 00 comp.
Transverse – 90 comp.

Skew Angle: 0 degree

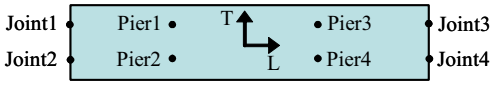

Input Time-histories

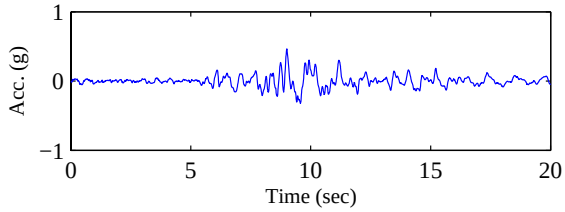

(a) Longitudinal Input

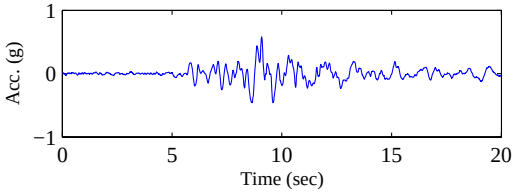

(b) Transverse Input

RC Pier Responses (Pier4)

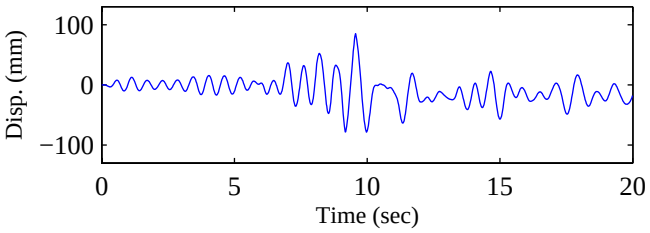

(c) Longitudinal displacement

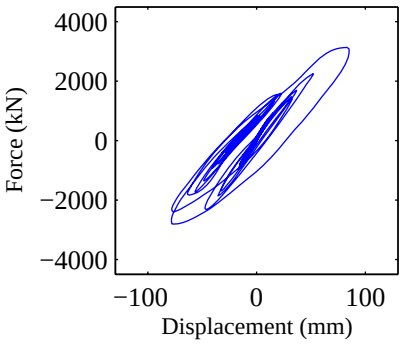

(f) Longitudinal disp.-force

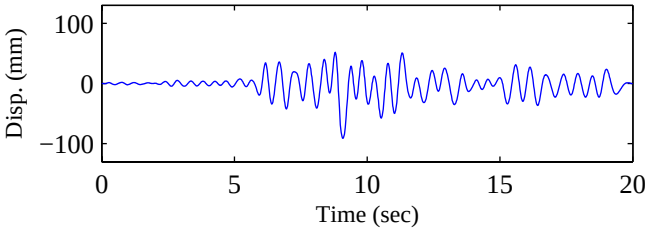

(d) Transverse displacement

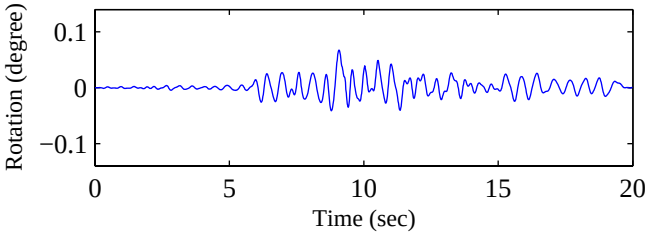

(e) Rotational displacement

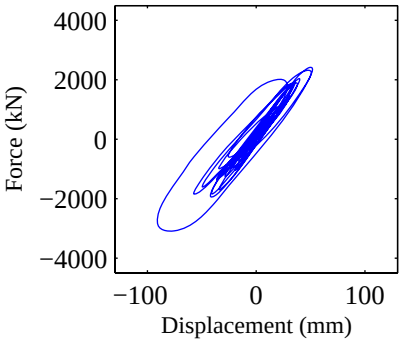

(g) Transverse disp.-force

Response Summary

	Pier1	Pier2	Pier3	Pier4	Joint1	Joint2	Joint3	Joint4
Max Long. Disp.(mm)	83.0	81.6	85.1	82.1	85.8	79.2	87.2	82.7
Max Trans. Disp.(mm)	90.7	90.7	91.0	91.0	33.4	33.4	34.4	34.4
Max Tor. Rot.(degree)	0.066	0.069	0.067	0.065	0.095	0.095	0.094	0.094
Pounding Events	NA	NA	NA	NA	2	2	1	1

Input Earthquake: Loma Prieta, 1986 **Station**: Oakland **Scaling Factor**: 2.02

Input Direction: Longitudinal – 00 comp.
Transverse – 90 comp.

Skew Angle: 30 degree

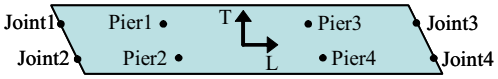

Input Time-histories

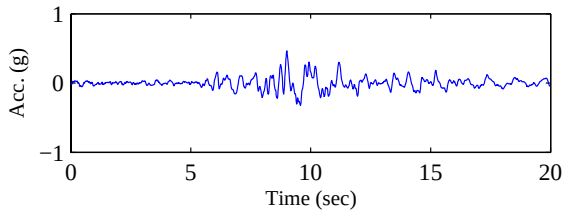

(a) Longitudinal Input

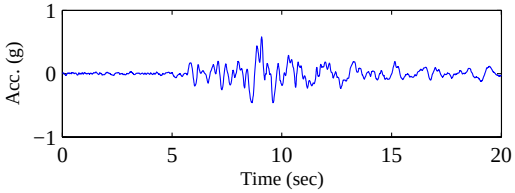

(b) Transverse Input

RC Pier Responses (Pier4)

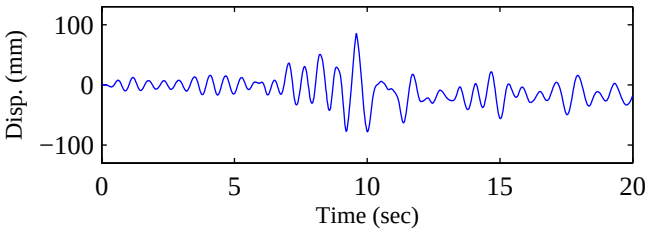

(c) Longitudinal displacement

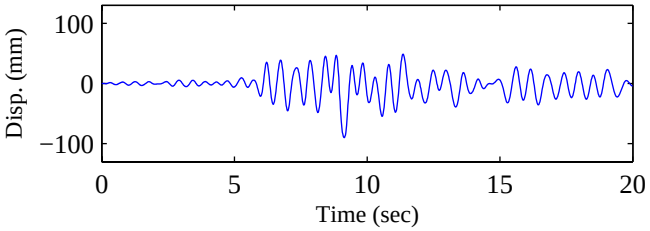

(d) Transverse displacement

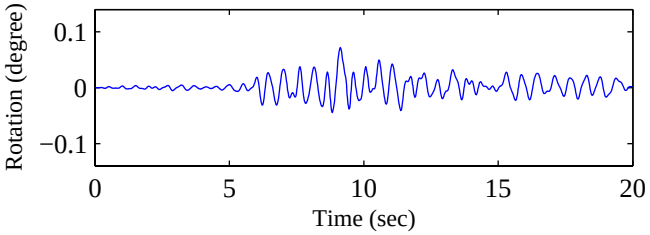

(e) Rotational displacement

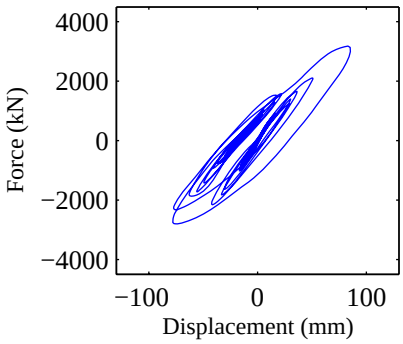

(f) Longitudinal disp.-force

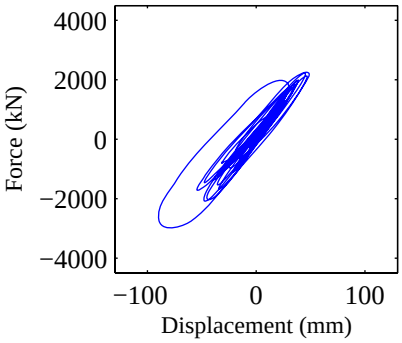

(g) Transverse disp.-force

Response Summary

	Pier1	Pier2	Pier3	Pier4	Joint1	Joint2	Joint3	Joint4
Max Long. Disp.(mm)	82.6	81.8	85.4	83.0	85.6	78.9	87.3	83.9
Max Trans. Disp.(mm)	93.2	89.8	89.9	93.2	37.3	31.2	33.4	36.9
Max Tor. Rot.(degree)	0.061	0.072	0.072	0.061	0.092	0.094	0.093	0.091
Pounding Events	NA	NA	NA	NA	2	2	1	1

Input Earthquake: Loma Prieta, 1986 **Station**: Oakland **Scaling Factor**: 2.02
Input Direction: Longitudinal – 00 comp.
Transverse – 90 comp.
Skew Angle: 60 degree

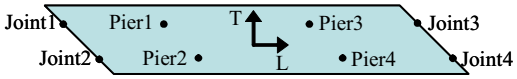

Input Time-histories

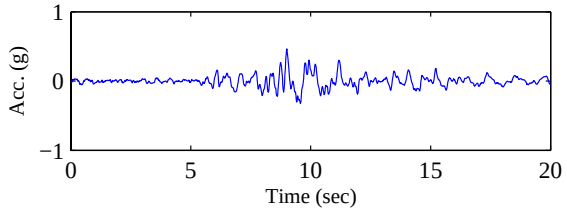

(a) Longitudinal Input

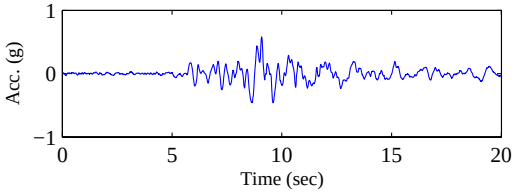

(b) Transverse Input

RC Pier Responses (Pier4)

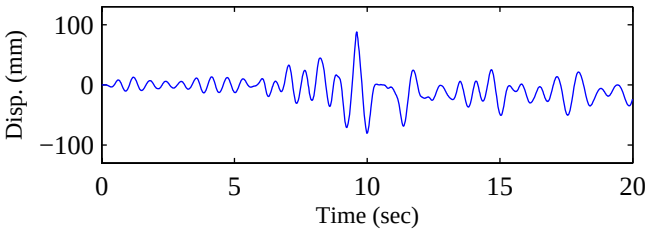

(c) Longitudinal displacement

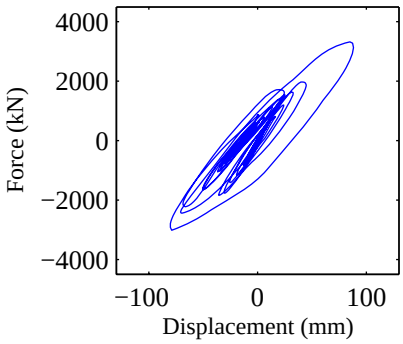

(f) Longitudinal disp.-force

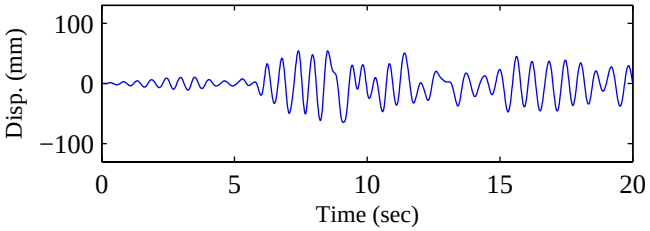

(d) Transverse displacement

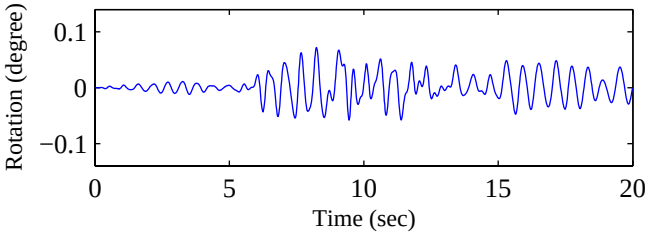

(e) Rotational displacement

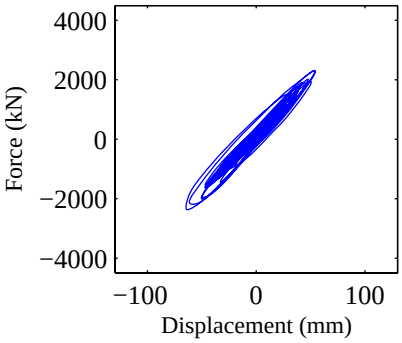

(g) Transverse disp.-force

Response Summary

	Pier1	Pier2	Pier3	Pier4	Joint1	Joint2	Joint3	Joint4
Max Long. Disp.(mm)	83.0	83.8	88.3	86.4	84.7	83.2	90.4	87.9
Max Trans. Disp.(mm)	71.6	64.2	64.6	71.5	36.9	26.3	26.8	37.2
Max Tor. Rot.(degree)	0.052	0.071	0.072	0.053	0.064	0.069	0.069	0.065
Pounding Events	NA	NA	NA	NA	1	2	1	1

Input Earthquake: Loma Prieta, 1986 **Station**: Oakland **Scaling Factor**: 2.02

Input Direction: Diagonal 1 – NS comp.
Diagonal 2 – EW comp.

Skew Angle: 0 degree

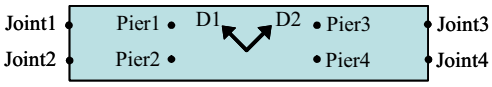

Input Time-histories

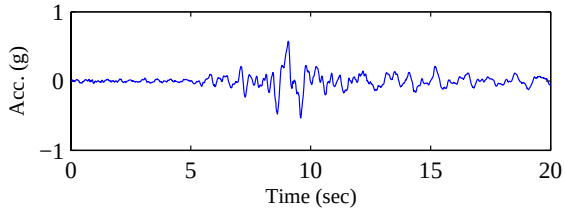

(a) Longitudinal Input

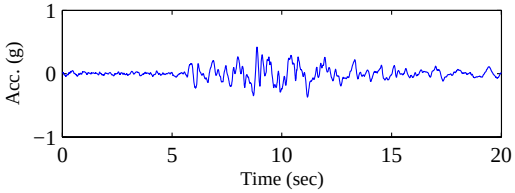

(b) Transverse Input

RC Pier Responses (Pier4)

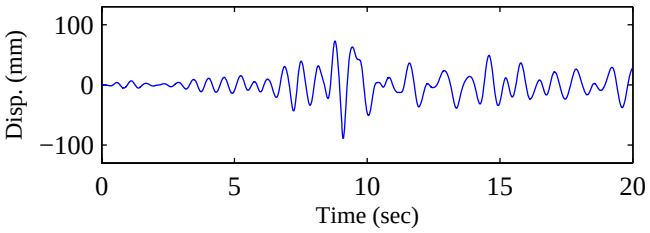

(c) Longitudinal displacement

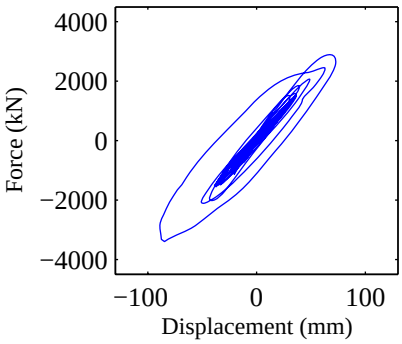

(f) Longitudinal disp.-force

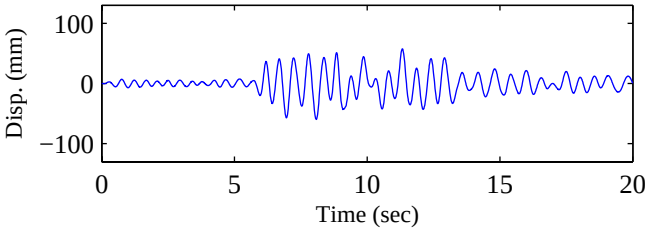

(d) Transverse displacement

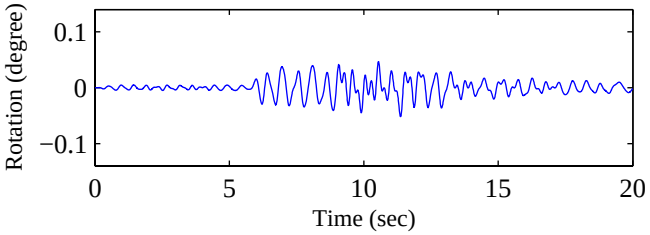

(e) Rotational displacement

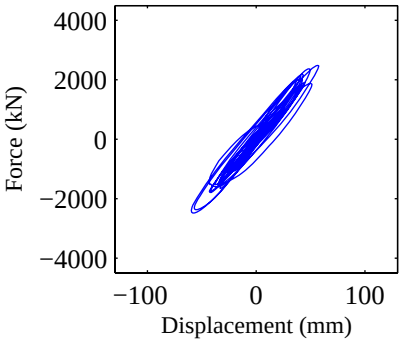

(g) Transverse disp.-force

Response Summary

	Pier1	Pier2	Pier3	Pier4	Joint1	Joint2	Joint3	Joint4
Max Long. Disp.(mm)	99.4	95.5	89.0	90.8	103.5	97.0	81.2	83.0
Max Trans. Disp.(mm)	59.6	59.6	59.7	59.7	29.3	29.3	29.3	29.3
Max Tor. Rot.(degree)	0.051	0.051	0.052	0.052	0.065	0.065	0.063	0.063
Pounding Events	NA	NA	NA	NA	1	1	1	0

Input Earthquake: Loma Prieta, 1986 **Station**: Oakland **Scaling Factor**: 2.02

Input Direction: Diagonal 1 – NS comp.
Diagonal 2 – EW comp.

Skew Angle: 30 degree

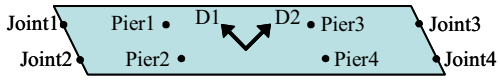

Input Time-histories

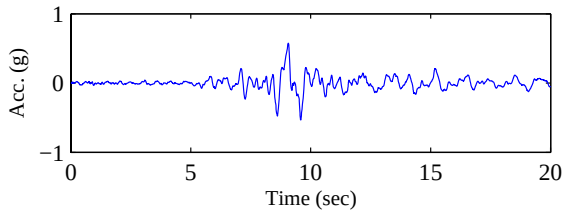

(a) Longitudinal Input

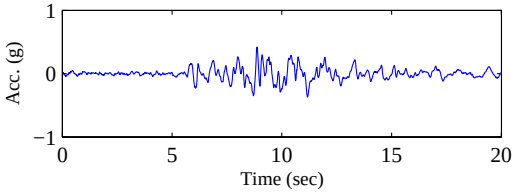

(b) Transverse Input

RC Pier Responses (Pier4)

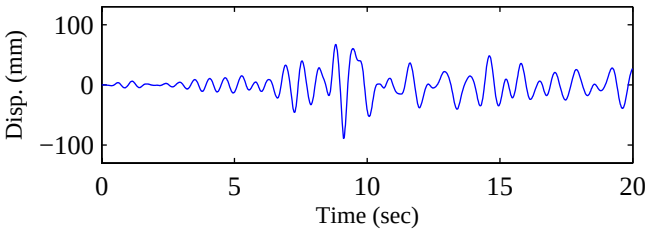

(c) Longitudinal displacement

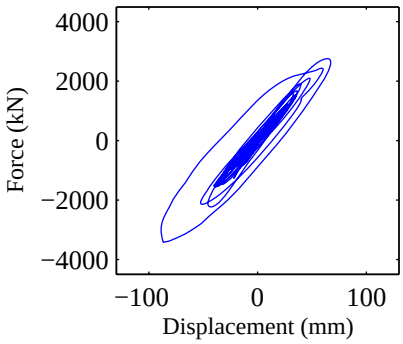

(f) Longitudinal disp.-force

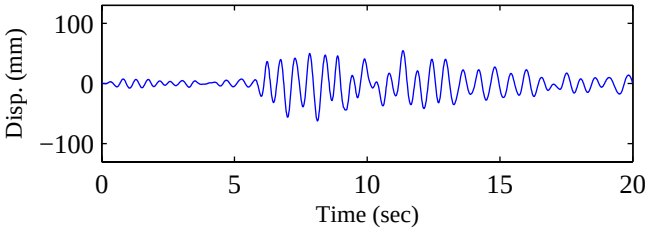

(d) Transverse displacement

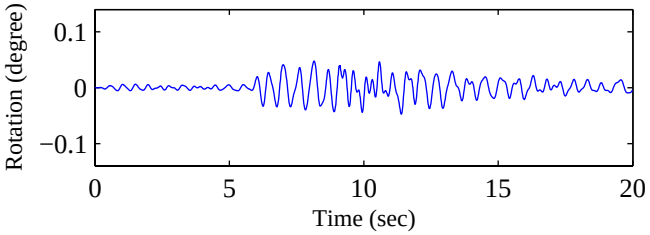

(e) Rotational displacement

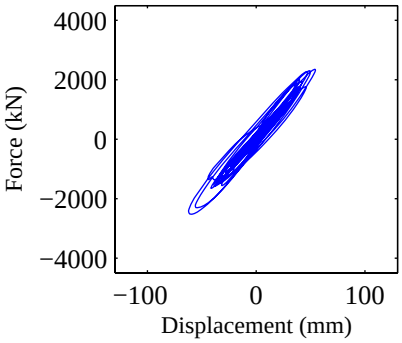

(g) Transverse disp.-force

Response Summary

	Pier1	Pier2	Pier3	Pier4	Joint1	Joint2	Joint3	Joint4
Max Long. Disp.(mm)	99.1	95.1	88.9	90.3	102.9	96.8	81.2	82.7
Max Trans. Disp.(mm)	64.5	62.3	62.3	64.5	28.2	25.1	26.1	28.4
Max Tor. Rot.(degree)	0.043	0.048	0.048	0.043	0.062	0.063	0.064	0.063
Pounding Events	NA	NA	NA	NA	1	1	0	0

Input Earthquake: Loma Prieta, 1986 **Station**: Oakland **Scaling Factor**: 2.02

Input Direction: Diagonal 1 – NS comp.
Diagonal 2 – EW comp.

Skew Angle: 60 degree

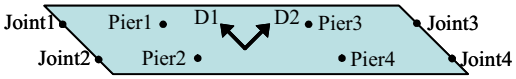

Input Time-histories

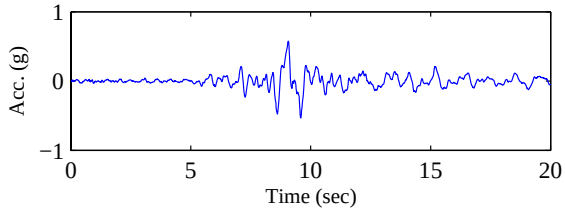

(a) Longitudinal Input

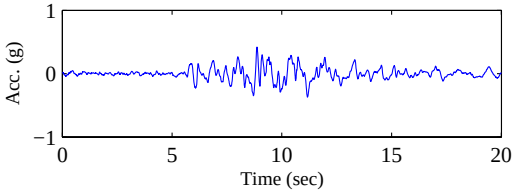

(b) Transverse Input

RC Pier Responses (Pier4)

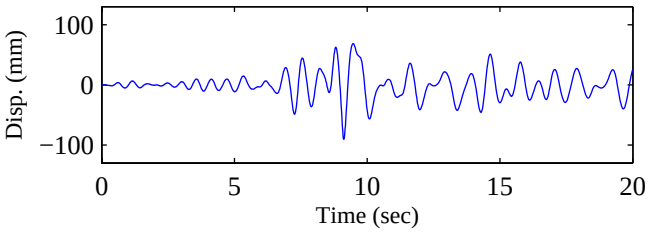

(c) Longitudinal displacement

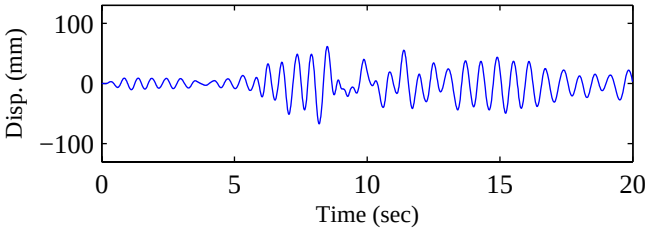

(d) Transverse displacement

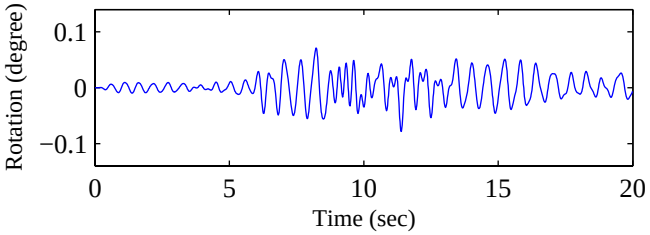

(e) Rotational displacement

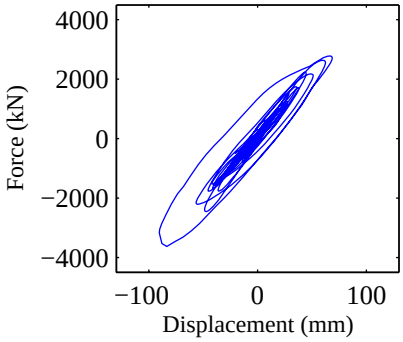

(f) Longitudinal disp.-force

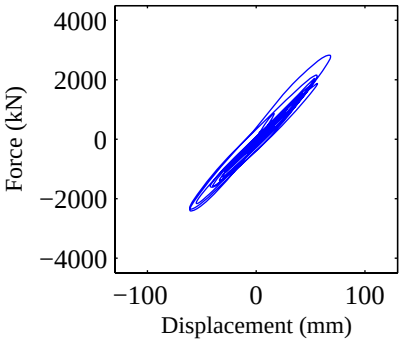

(g) Transverse disp.-force

Response Summary

	Pier1	Pier2	Pier3	Pier4	Joint1	Joint2	Joint3	Joint4
Max Long. Disp.(mm)	99.6	98.1	90.5	90.8	102.9	100.9	82.1	82.6
Max Trans. Disp.(mm)	74.4	67.0	66.9	74.0	34.8	24.6	25.6	34.9
Max Tor. Rot.(degree)	0.057	0.078	0.078	0.057	0.066	0.071	0.071	0.065
Pounding Events	NA	NA	NA	NA	1	1	0	0

Input Earthquake: Loma Prieta, 1986 **Station**: Oakland **Scaling Factor**: 2.02

Input Direction: Longitudinal – 90 comp.
Transverse – 00 comp.

Skew Angle: 0 degree

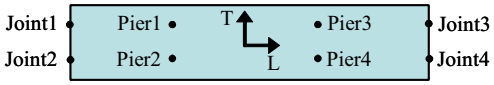

Input Time-histories

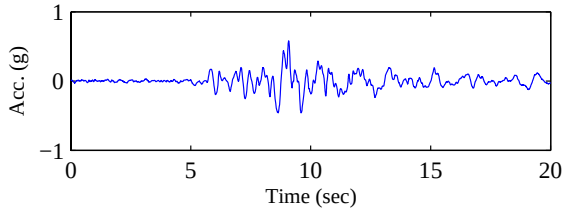

(a) Longitudinal Input

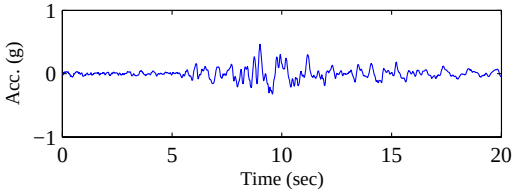

(b) Transverse Input

RC Pier Responses (Pier4)

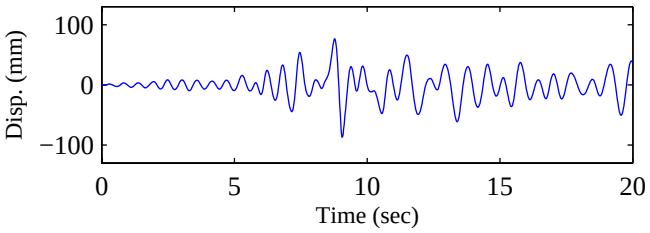

(c) Longitudinal displacement

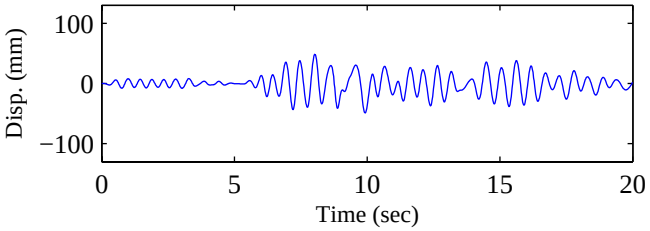

(d) Transverse displacement

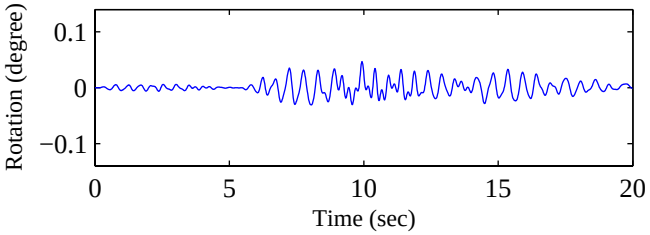

(e) Rotational displacement

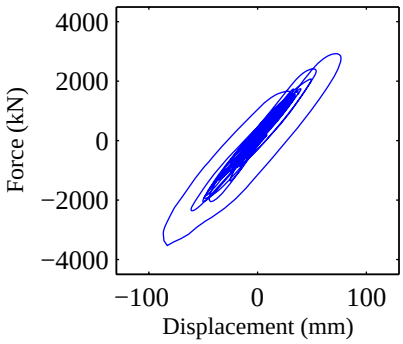

(f) Longitudinal disp.-force

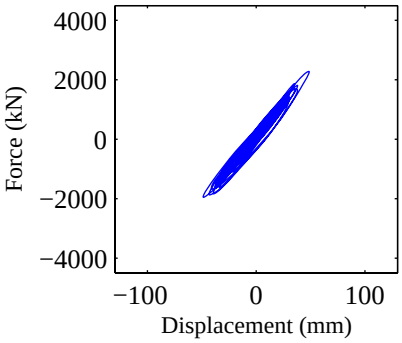

(g) Transverse disp.-force

Response Summary

	Pier1	Pier2	Pier3	Pier4	Joint1	Joint2	Joint3	Joint4
Max Long. Disp.(mm)	92.6	92.8	86.9	86.5	95.2	94.9	80.7	80.8
Max Trans. Disp.(mm)	49.0	49.0	48.9	48.9	21.7	21.7	22.0	22.0
Max Tor. Rot.(degree)	0.047	0.046	0.047	0.048	0.057	0.057	0.057	0.057
Pounding Events	NA	NA	NA	NA	1	1	1	1

Input Earthquake: Loma Prieta, 1986 **Station**: Oakland **Scaling Factor**: 2.02

Input Direction: Longitudinal – 90 comp.
Transverse – 00 comp.

Skew Angle: 30 degree

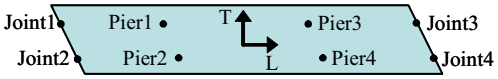

Input Time-histories

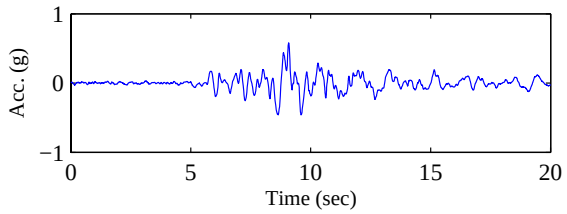

(a) Longitudinal Input

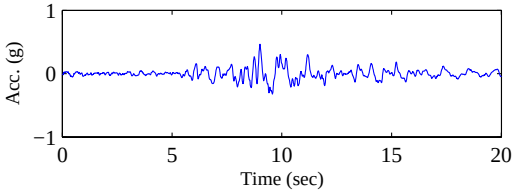

(b) Transverse Input

RC Pier Responses (Pier4)

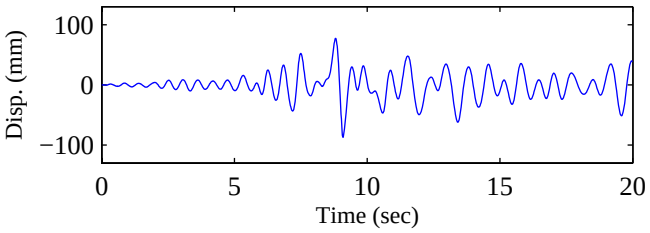

(c) Longitudinal displacement

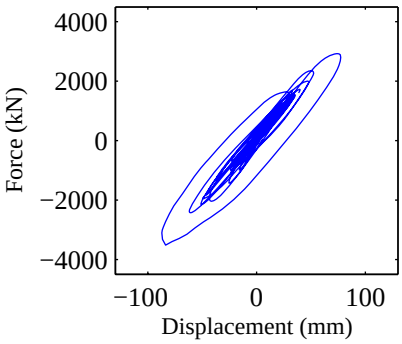

(f) Longitudinal disp.-force

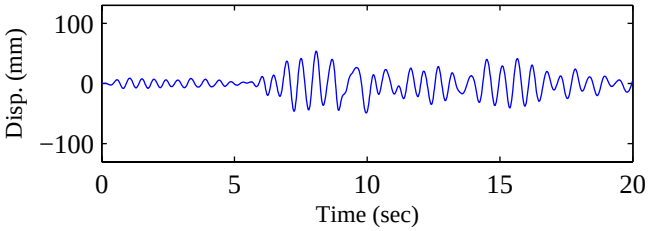

(d) Transverse displacement

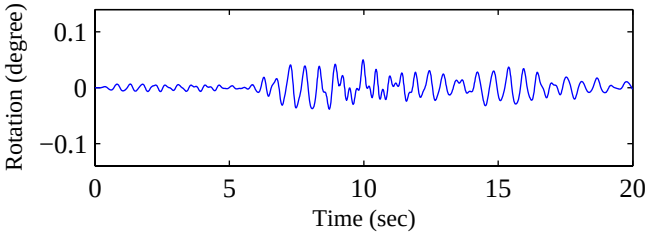

(e) Rotational displacement

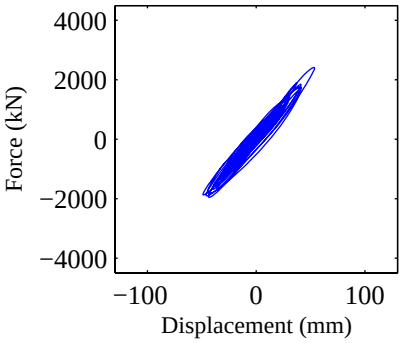

(g) Transverse disp.-force

Response Summary

	Pier1	Pier2	Pier3	Pier4	Joint1	Joint2	Joint3	Joint4
Max Long. Disp.(mm)	93.5	92.9	87.1	87.0	96.4	94.8	80.7	81.1
Max Trans. Disp.(mm)	55.4	53.7	53.8	55.6	25.7	22.2	22.1	25.7
Max Tor. Rot.(degree)	0.046	0.051	0.050	0.046	0.057	0.058	0.057	0.057
Pounding Events	NA	NA	NA	NA	1	1	1	1

Input Earthquake: Loma Prieta, 1986 **Station**: Oakland **Scaling Factor**: 2.02
Input Direction: Longitudinal – 90 comp.
Transverse – 00 comp.
Skew Angle: 60 degree

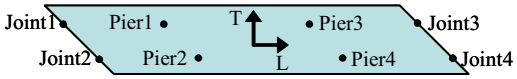

Input Time-histories

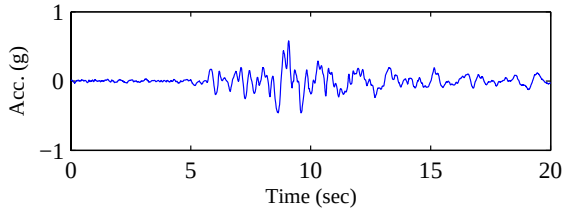

(a) Longitudinal Input

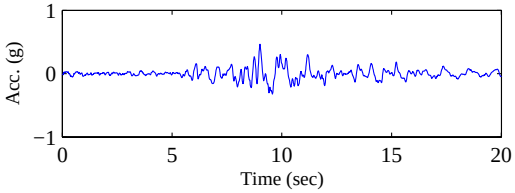

(b) Transverse Input

RC Pier Responses (Pier4)

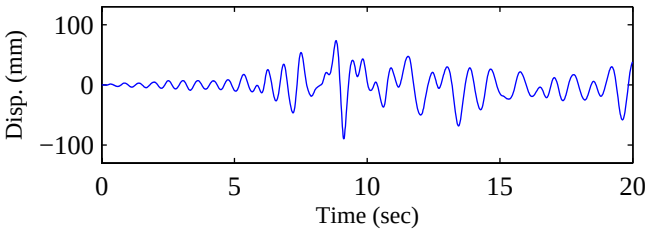

(c) Longitudinal displacement

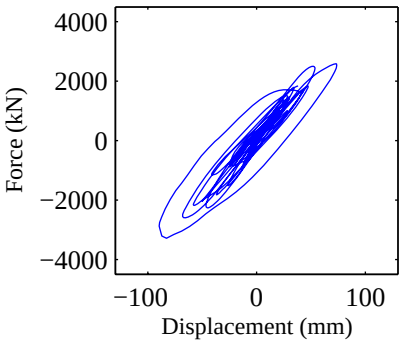

(f) Longitudinal disp.-force

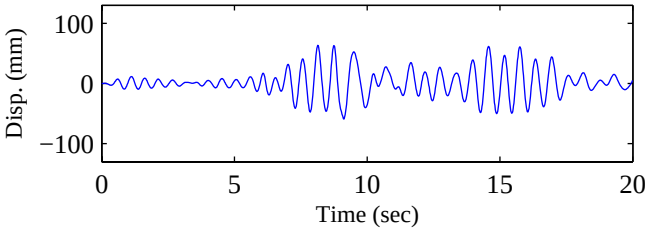

(d) Transverse displacement

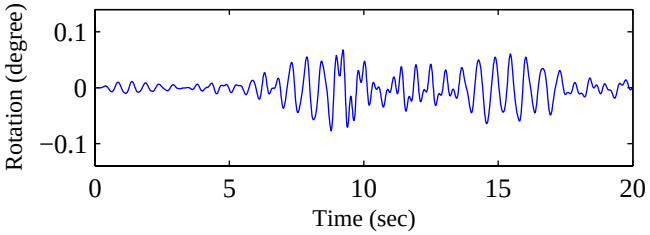

(e) Rotational displacement

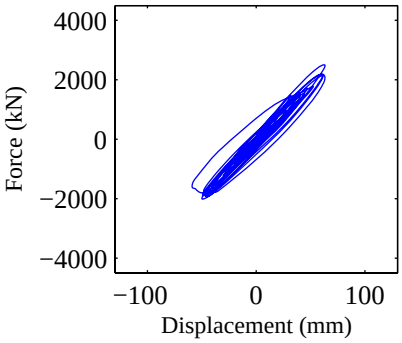

(g) Transverse disp.-force

Response Summary

	Pier1	Pier2	Pier3	Pier4	Joint1	Joint2	Joint3	Joint4
Max Long. Disp.(mm)	98.3	95.5	89.6	89.4	102.5	97.0	81.2	82.5
Max Trans. Disp.(mm)	70.5	63.0	63.3	71.1	41.3	32.5	38.8	41.2
Max Tor. Rot.(degree)	0.053	0.077	0.077	0.054	0.066	0.071	0.073	0.068
Pounding Events	NA	NA	NA	NA	1	1	1	0

Input Earthquake: Kocaeli, 1999 **Station**: Ambarli **Scaling Factor**: 1.48

Input Direction: Longitudinal – 00 comp.
Transverse – 90 comp.

Skew Angle: 0 degree

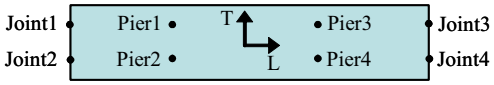

Input Time-histories

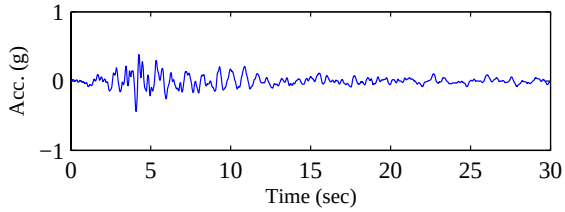

(a) Longitudinal Input

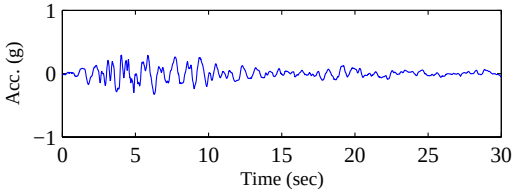

(b) Transverse Input

RC Pier Responses (Pier4)

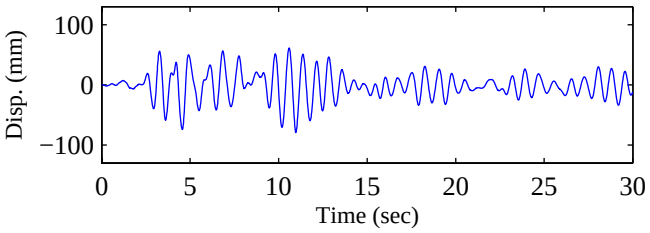

(c) Longitudinal displacement

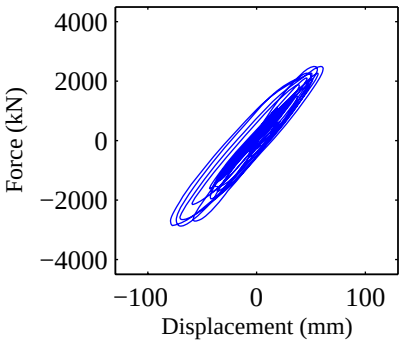

(f) Longitudinal disp.-force

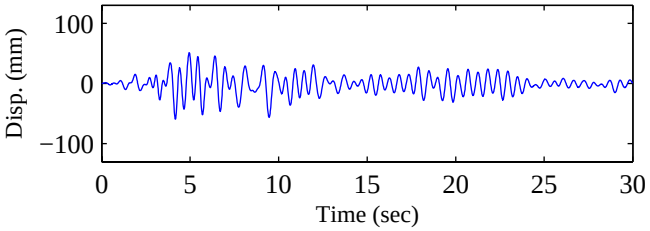

(d) Transverse displacement

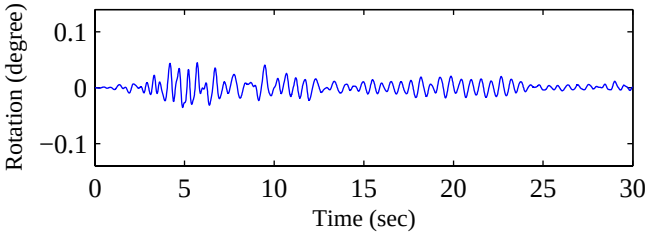

(e) Rotational displacement

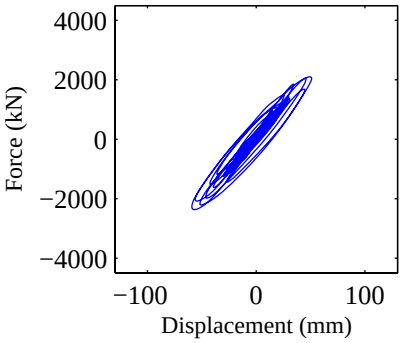

(g) Transverse disp.-force

Response Summary

	Pier1	Pier2	Pier3	Pier4	Joint1	Joint2	Joint3	Joint4
Max Long. Disp.(mm)	79.6	81.5	79.2	78.9	79.9	83.0	77.9	77.2
Max Trans. Disp.(mm)	59.3	59.3	59.3	59.2	25.5	25.5	25.0	25.0
Max Tor. Rot.(degree)	0.045	0.045	0.045	0.046	0.062	0.062	0.062	0.062
Pounding Events	NA	NA	NA	NA	1	2	0	0

Input Earthquake: Kocaeli, 1999 **Station**: Ambarli **Scaling Factor**: 1.48

Input Direction: Longitudinal – 00 comp.
Transverse – 90 comp.

Skew Angle: 30 degree

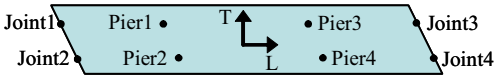

Input Time-histories

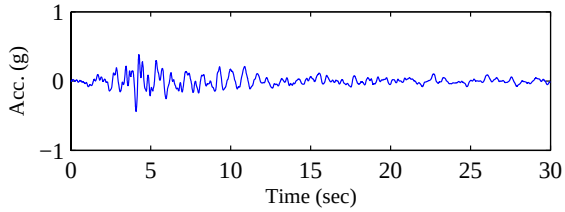

(a) Longitudinal Input

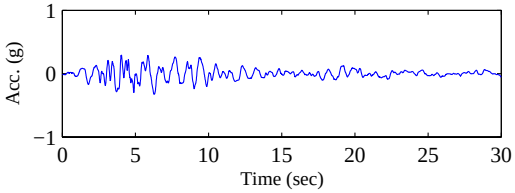

(b) Transverse Input

RC Pier Responses (Pier4)

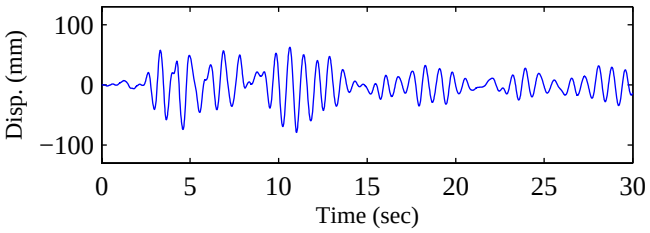

(c) Longitudinal displacement

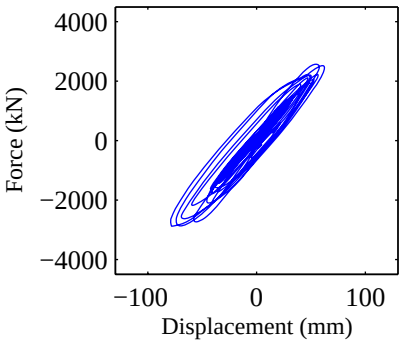

(f) Longitudinal disp.-force

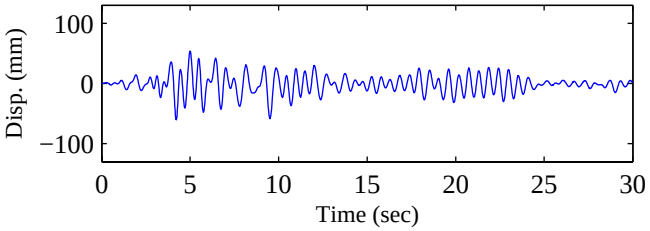

(d) Transverse displacement

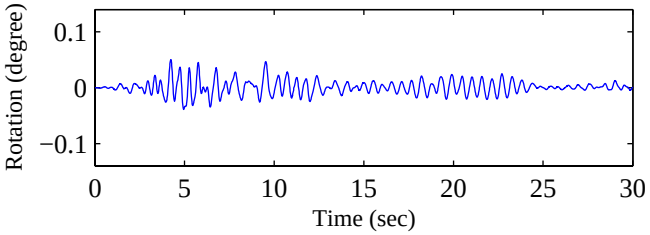

(e) Rotational displacement

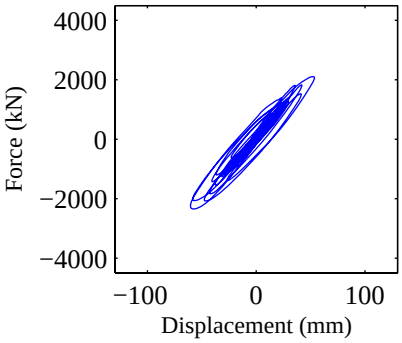

(g) Transverse disp.-force

Response Summary

	Pier1	Pier2	Pier3	Pier4	Joint1	Joint2	Joint3	Joint4
Max Long. Disp.(mm)	79.5	81.5	79.1	78.7	79.7	82.8	77.9	77.2
Max Trans. Disp.(mm)	62.8	60.4	60.6	62.9	27.9	24.5	24.1	27.5
Max Tor. Rot.(degree)	0.046	0.050	0.050	0.046	0.064	0.065	0.065	0.064
Pounding Events	NA	NA	NA	NA	1	2	0	0

Input Earthquake: Kocaeli, 1999 **Station**: Ambarli **Scaling Factor**: 1.48

Input Direction: Longitudinal – 00 comp.
Transverse – 90 comp.

Skew Angle: 60 degree

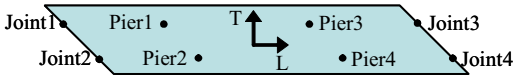

Input Time-histories

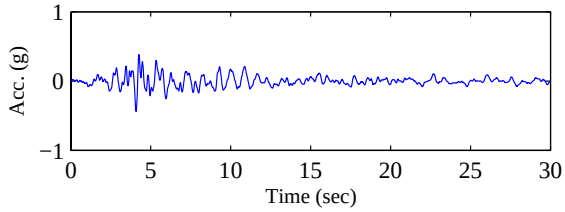

(a) Longitudinal Input

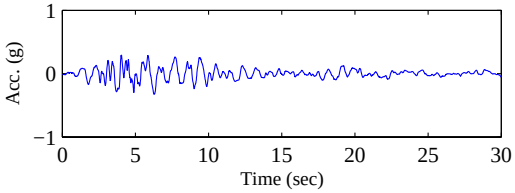

(b) Transverse Input

RC Pier Responses (Pier4)

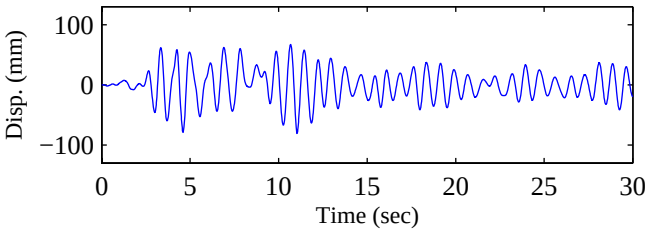

(c) Longitudinal displacement

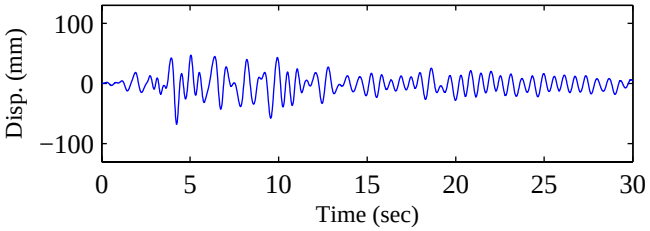

(d) Transverse displacement

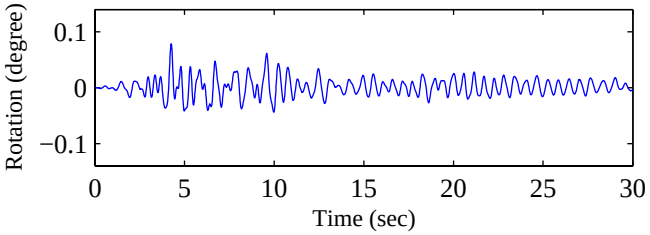

(e) Rotational displacement

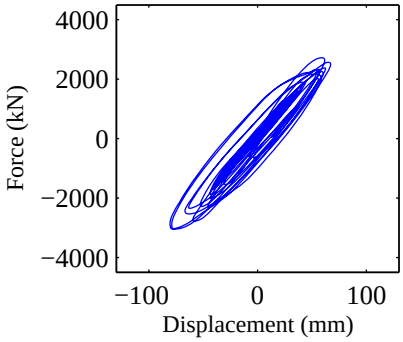

(f) Longitudinal disp.-force

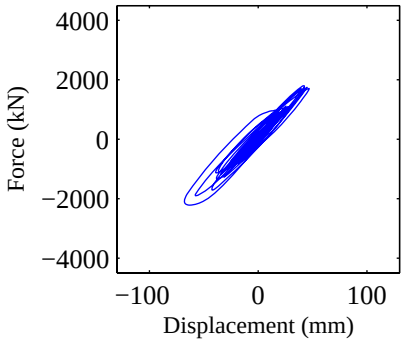

(g) Transverse disp.-force

Response Summary

	Pier1	Pier2	Pier3	Pier4	Joint1	Joint2	Joint3	Joint4
Max Long. Disp.(mm)	81.7	83.5	80.7	79.9	82.2	85.1	78.6	77.6
Max Trans. Disp.(mm)	76.2	67.5	67.8	76.3	29.7	21.7	20.7	29.6
Max Tor. Rot.(degree)	0.060	0.079	0.079	0.059	0.072	0.076	0.076	0.072
Pounding Events	NA	NA	NA	NA	2	2	0	0

Input Earthquake: Kocaeli, 1999 **Station**: Ambarli **Scaling Factor**: 1.48

Input Direction: Diagonal 1 – NS comp.
Diagonal 2 – EW comp.

Skew Angle: 0 degree

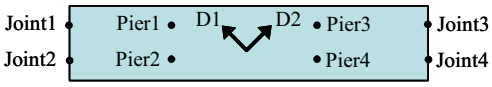

Input Time-histories

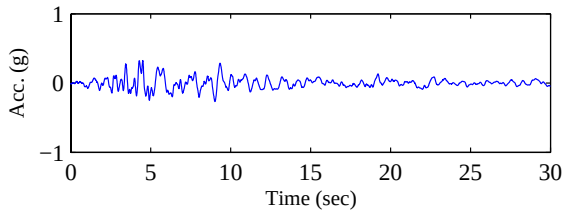

(a) Longitudinal Input

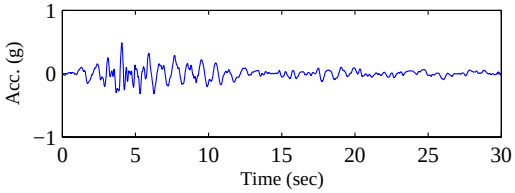

(b) Transverse Input

RC Pier Responses (Pier4)

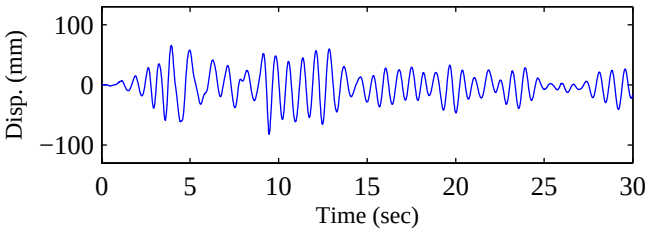

(c) Longitudinal displacement

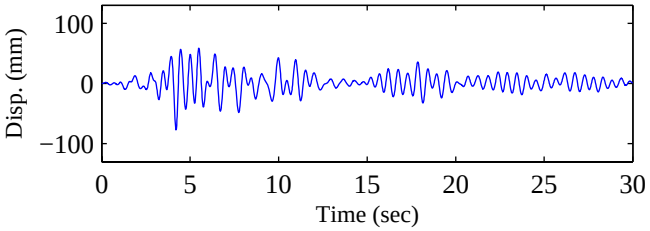

(d) Transverse displacement

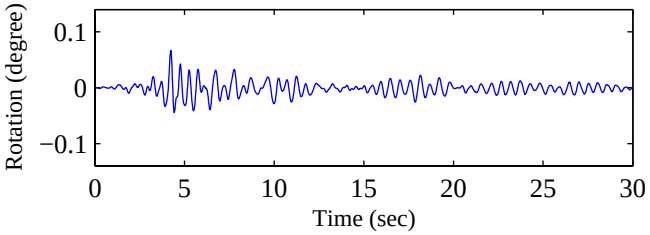

(e) Rotational displacement

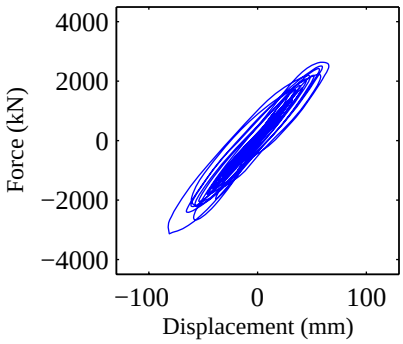

(f) Longitudinal disp.-force

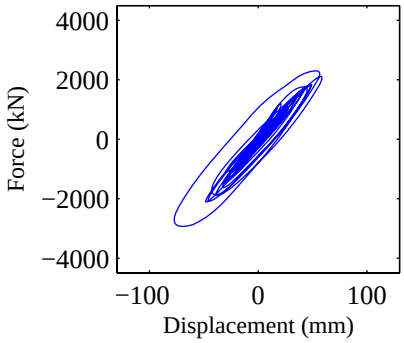

(g) Transverse disp.-force

Response Summary

	Pier1	Pier2	Pier3	Pier4	Joint1	Joint2	Joint3	Joint4
Max Long. Disp.(mm)	86.2	85.4	82.3	82.4	88.0	86.7	78.9	79.2
Max Trans. Disp.(mm)	77.0	77.0	77.2	77.2	30.1	30.1	30.0	30.0
Max Tor. Rot.(degree)	0.066	0.067	0.067	0.065	0.086	0.086	0.086	0.086
Pounding Events	NA	NA	NA	NA	1	1	0	0

Input Earthquake: Kocaeli, 1999 **Station**: Ambarli **Scaling Factor**: 1.48

Input Direction: Diagonal 1 – NS comp.
Diagonal 2 – EW comp.

Skew Angle: 30 degree

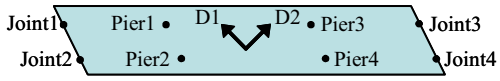

Input Time-histories

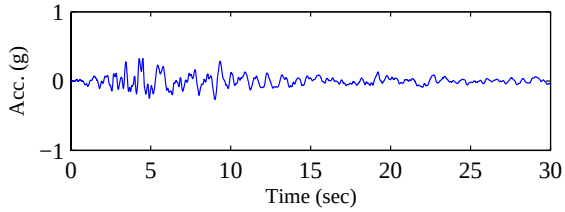

(a) Longitudinal Input

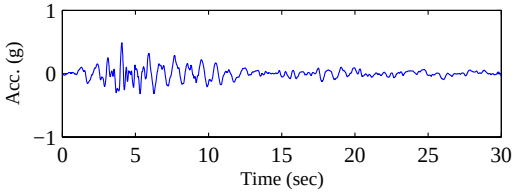

(b) Transverse Input

RC Pier Responses (Pier4)

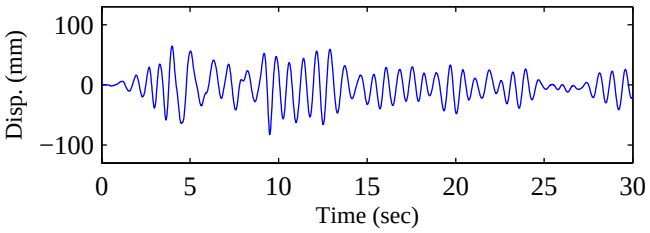

(c) Longitudinal displacement

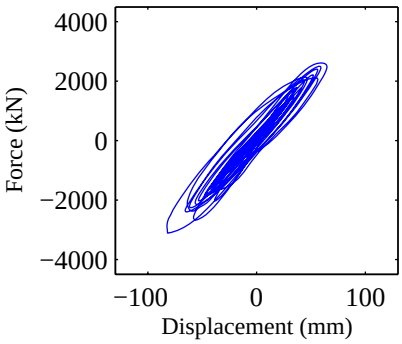

(f) Longitudinal disp.-force

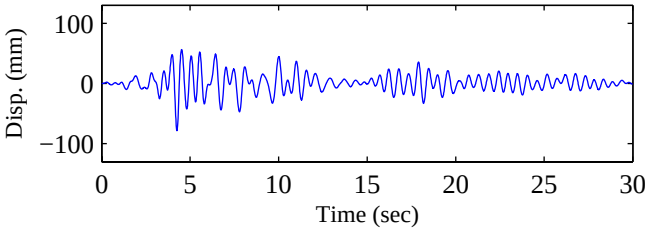

(d) Transverse displacement

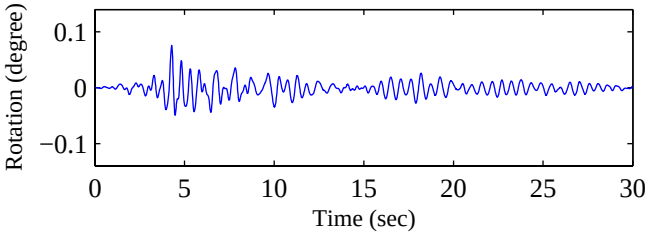

(e) Rotational displacement

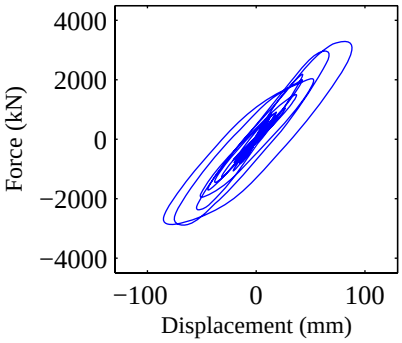

(g) Transverse disp.-force

Response Summary

	Pier1	Pier2	Pier3	Pier4	Joint1	Joint2	Joint3	Joint4
Max Long. Disp.(mm)	86.8	85.7	82.6	82.8	88.8	87.0	79.0	79.4
Max Trans. Disp.(mm)	81.9	78.5	78.5	81.7	32.8	28.8	28.8	32.8
Max Tor. Rot.(degree)	0.067	0.076	0.076	0.067	0.088	0.089	0.089	0.087
Pounding Events	NA	NA	NA	NA	1	1	0	0

Input Earthquake: Kocaeli, 1999 **Station**: Ambarli **Scaling Factor**: 1.48

Input Direction: Diagonal 1 – NS comp.
Diagonal 2 – EW comp.

Skew Angle: 60 degree

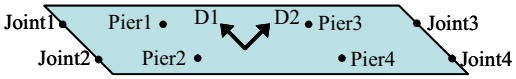

Input Time-histories

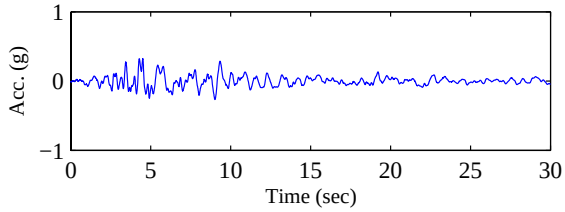

(a) Longitudinal Input

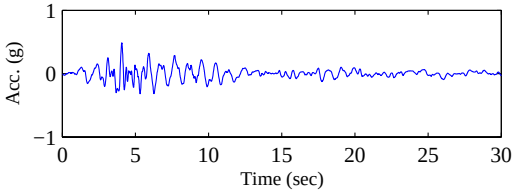

(b) Transverse Input

RC Pier Responses (Pier4)

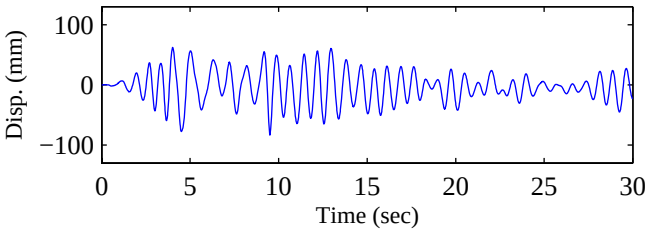

(c) Longitudinal displacement

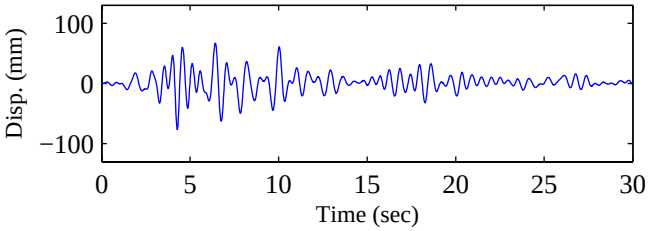

(d) Transverse displacement

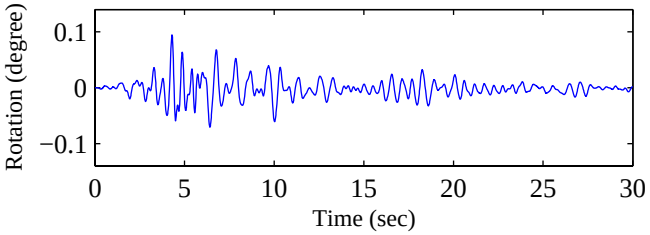

(e) Rotational displacement

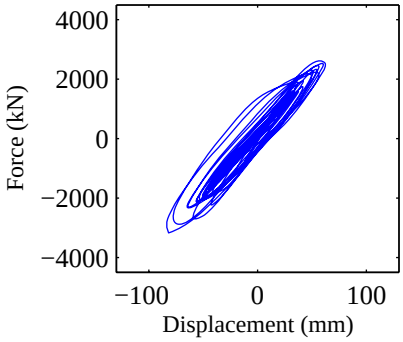

(f) Longitudinal disp.-force

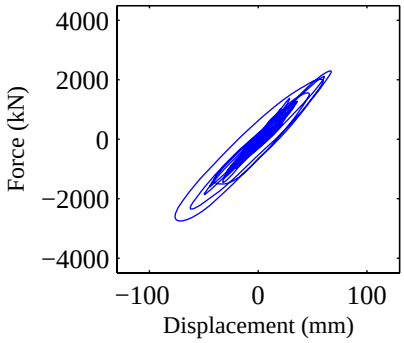

(g) Transverse disp.-force

Response Summary

	Pier1	Pier2	Pier3	Pier4	Joint1	Joint2	Joint3	Joint4
Max Long. Disp.(mm)	88.2	87.8	83.5	83.9	90.3	89.3	79.4	79.8
Max Trans. Disp.(mm)	86.5	76.5	76.6	86.1	36.5	25.5	29.1	39.2
Max Tor. Rot.(degree)	0.068	0.095	0.095	0.067	0.083	0.089	0.088	0.082
Pounding Events	NA	NA	NA	NA	2	1	0	0

Input Earthquake: Kocaeli, 1999 **Station**: Ambarli **Scaling Factor**: 1.48

Input Direction: Longitudinal – 90 comp.
Transverse – 00 comp.

Skew Angle: 0 degree

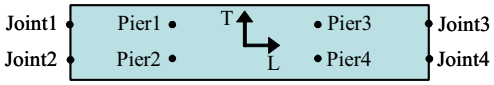

Input Time-histories

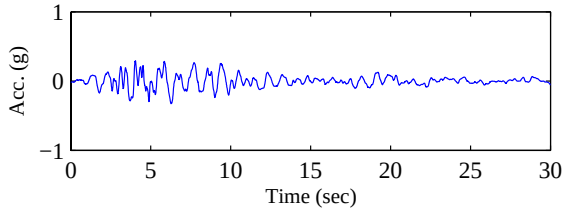

(a) Longitudinal Input

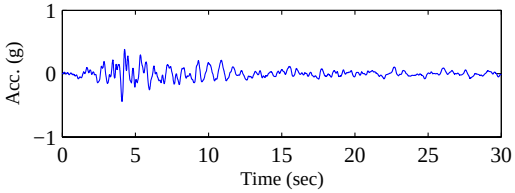

(b) Transverse Input

RC Pier Responses (Pier4)

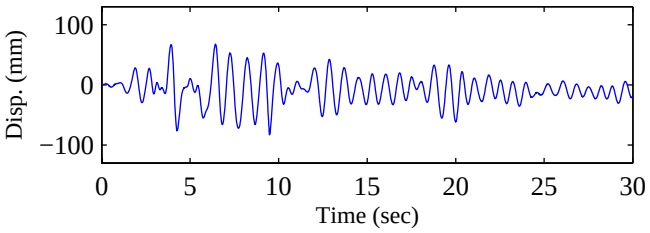

(c) Longitudinal displacement

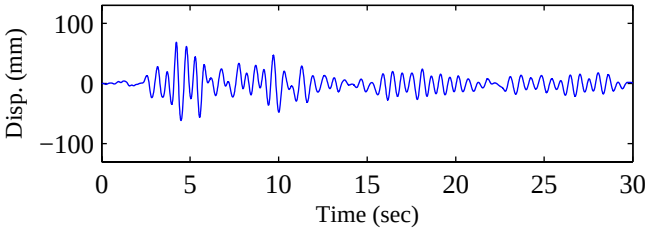

(d) Transverse displacement

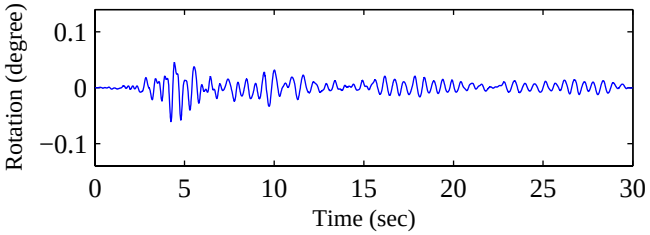

(e) Rotational displacement

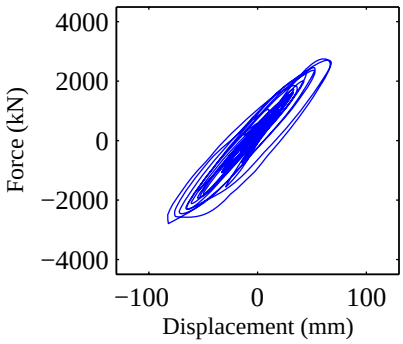

(f) Longitudinal disp.-force

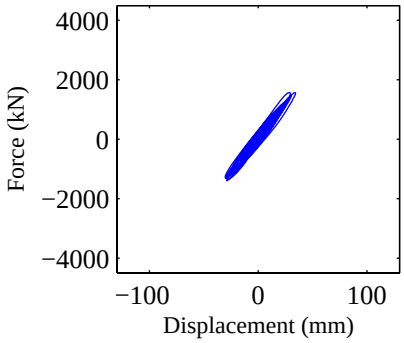

(g) Transverse disp.-force

Response Summary

	Pier1	Pier2	Pier3	Pier4	Joint1	Joint2	Joint3	Joint4
Max Long. Disp.(mm)	88.2	85.8	82.8	83.5	90.5	86.6	78.9	79.7
Max Trans. Disp.(mm)	68.7	68.7	68.7	68.8	31.6	31.6	30.2	30.2
Max Tor. Rot.(degree)	0.066	0.063	0.061	0.064	0.080	0.080	0.079	0.079
Pounding Events	NA	NA	NA	NA	2	1	0	0

Input Earthquake: Kocaeli, 1999 **Station**: Ambarli **Scaling Factor**: 1.48

Input Direction: Longitudinal – 90 comp.
Transverse – 00 comp.

Skew Angle: 30 degree

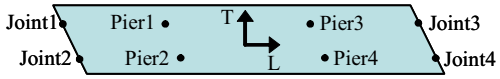

Input Time-histories

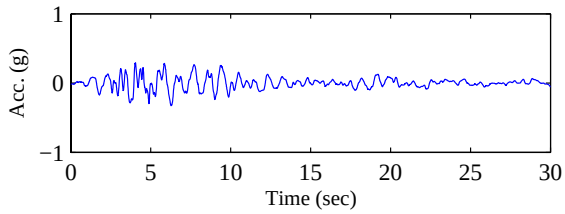

(a) Longitudinal Input

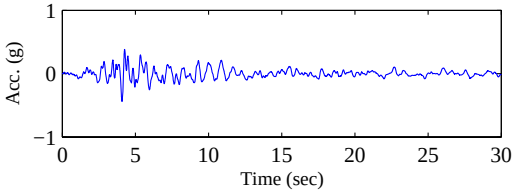

(b) Transverse Input

RC Pier Responses (Pier4)

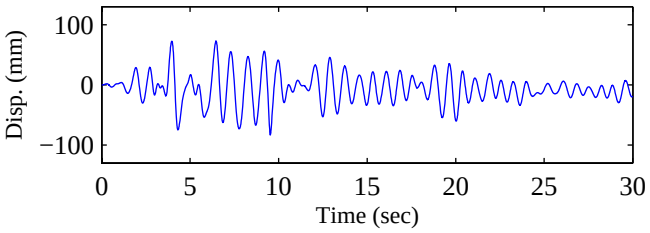

(c) Longitudinal displacement

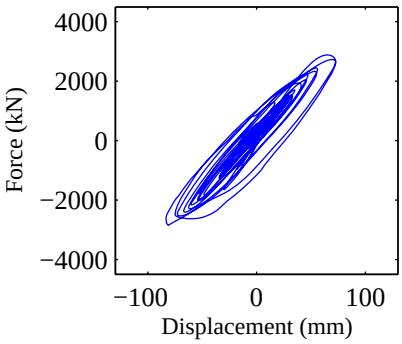

(f) Longitudinal disp.-force

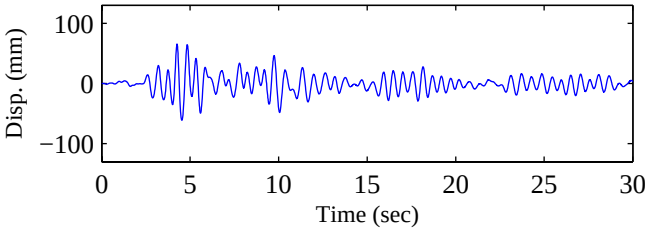

(d) Transverse displacement

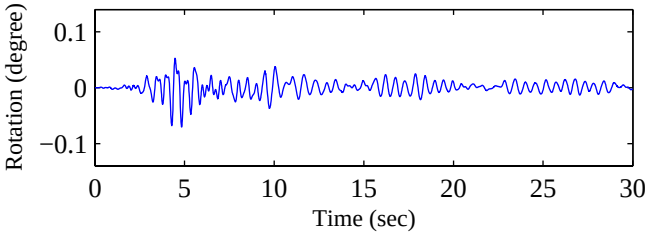

(e) Rotational displacement

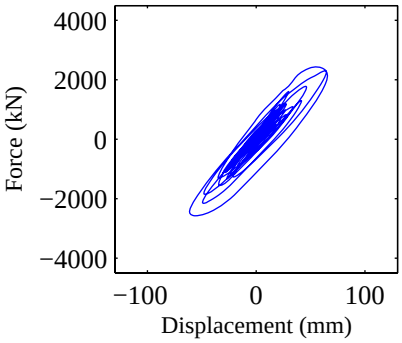

(g) Transverse disp.-force

Response Summary

	Pier1	Pier2	Pier3	Pier4	Joint1	Joint2	Joint3	Joint4
Max Long. Disp.(mm)	89.0	86.4	83.3	83.8	91.4	87.5	79.1	79.9
Max Trans. Disp.(mm)	68.3	65.3	65.5	68.5	35.7	32.4	31.8	35.2
Max Tor. Rot.(degree)	0.065	0.070	0.070	0.064	0.078	0.079	0.079	0.077
Pounding Events	NA	NA	NA	NA	2	1	0	0

Input Earthquake: Kocaeli, 1999 **Station**: Ambarli **Scaling Factor**: 1.48

Input Direction: Longitudinal – 90 comp.
Transverse – 00 comp.

Skew Angle: 60 degree

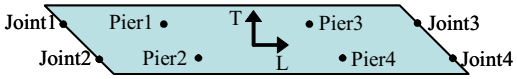

Input Time-histories

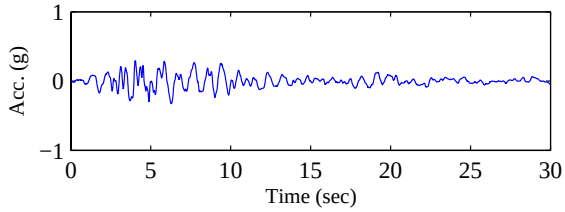

(a) Longitudinal Input

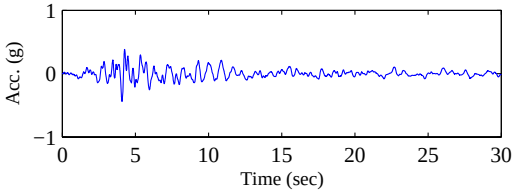

(b) Transverse Input

RC Pier Responses (Pier4)

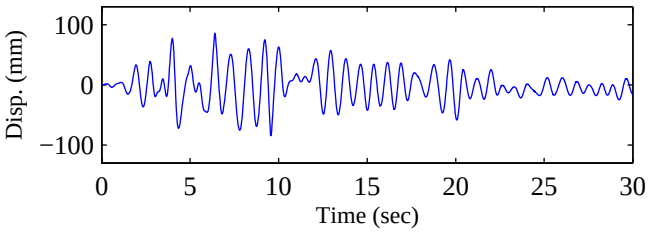

(c) Longitudinal displacement

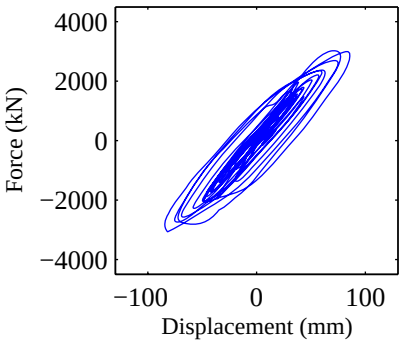

(f) Longitudinal disp.-force

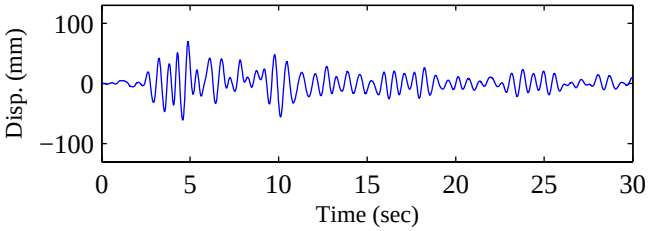

(d) Transverse displacement

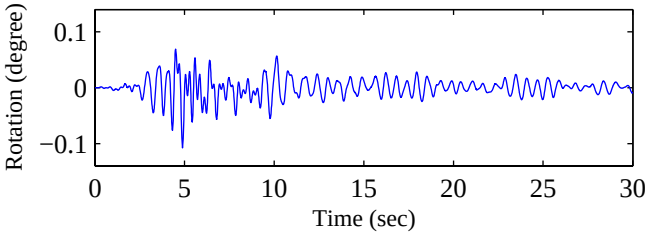

(e) Rotational displacement

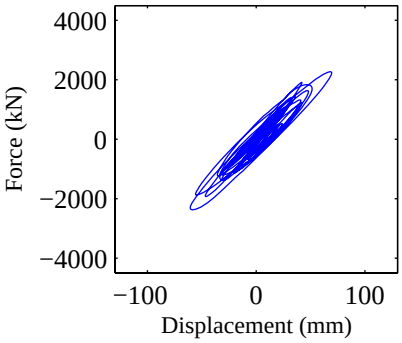

(g) Transverse disp.-force

Response Summary

	Pier1	Pier2	Pier3	Pier4	Joint1	Joint2	Joint3	Joint4
Max Long. Disp.(mm)	90.4	88.9	85.9	85.0	92.9	90.5	88.0	83.2
Max Trans. Disp.(mm)	81.2	69.9	69.4	81.0	42.8	33.7	34.3	42.9
Max Tor. Rot.(degree)	0.079	0.108	0.107	0.079	0.087	0.091	0.090	0.086
Pounding Events	NA	NA	NA	NA	2	1	3	2

List of Recent NSEL Reports

No.	*Authors*	*Title*	*Date*
001	Nagayama, T. and Spencer, B.F.	Structural Health Monitoring Using Smart Sensors	Nov. 2007
002	Sun, S. and Kuchma, D.A.	Shear Behavior and Capacity of Large-Scale Prestressed High-Strength Concrete Bulb-Tee Girders	Nov. 2007
003	Nagle, T.J. and Kuchma, D.A.	Nontraditional Limitations on the Shear Capacity of Prestressed Concrete Girders	Dec. 2007
004	Kwon, O-S. and Elnashai, A.S.	Probabilistic Seismic Assessment of Structure, Foundation, and Soil Interacting Systems	Dec. 2007
005	Nakata, N., Spencer, B.F., and Elnashai, A.S.	Multi-dimensional Mixed-mode Hybrid Simulation: Control and Applications	Dec. 2007
006	Carrion, J. and Spencer, B.F.	Model-based Strategies for Real-time Hybrid Testing	Dec. 2007